

**UNIVERSITY OF THE WITWATERSRAND  
JOHANNESBURG**



**FACULTY OF ENGINEERING AND THE BUILT  
ENVIRONMENT**

**MEASUREMENT AND PREDICTION  
OF DILUTION IN A GOLD MINE  
OPERATING WITH OPEN STOPING  
MINING METHODS**

Petrus Jacobus Le Roux

A thesis submitted to the Faculty of Engineering and the Built Environment, University of the Witwatersrand, Johannesburg, in fulfilment of the requirements for the degree of Doctor of Philosophy.

Johannesburg, 6 October 2015

# **MEASUREMENT AND PREDICTION OF DILUTION IN A GOLD MINE OPERATING WITH OPEN STOPING MINING METHODS**

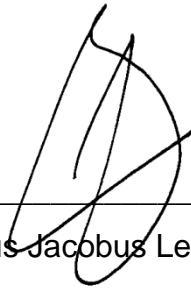
Petrus Jacobus Le Roux

A thesis submitted to the Faculty of Engineering and the Built Environment,  
University of the Witwatersrand, Johannesburg, in fulfilment of the requirements  
for the degree of Doctor of Philosophy.

Johannesburg, 6 October 2015

## **DECLARATION**

I declare that this thesis is my own unaided work. It is being submitted for the Degree of Doctor of Philosophy to the University of the Witwatersrand, Johannesburg. It has not been submitted before for any degree or examination at any other University.

A handwritten signature in black ink, consisting of a large, stylized 'P' and 'L' intertwined, with a horizontal line crossing through the middle.

---

Petrus Jacobus Le Roux

6<sup>th</sup> October 2015

## ABSTRACT

Mining worldwide and definitely in South Africa, is constantly under pressure to reduce its cost structure to sustain profitability. In underground gold mines where an open stope mining method is employed, dilution often has a significant effect on the viability of sustaining profits. Target Mine practices the Open Stope mining Method and it was found that in some open stopes dilution was in excess of 10%, which has a significant impact on the sustainability of the mine.

Dilution in excess of 10% can result in the reduction of the recovered grade from 5,5 to 4,5 grams per ton (g/t). The reduction of 1 g/t in recovered grade results in a potential loss of about ZAR21 Million per month based on a gold price of ZAR240 000 per kilogram. Based on Life of Mine projections, the potential loss of income could be as much as ZAR3,3 Billion. A reduction in dilution would have the opposite effect.

There are numerous factors which affect dilution, of which falls of ground in open stopes are a major contributor. The falls of ground can be attributed to a number of factors such as beam failure, because of a larger than normal expected roof area (hydraulic radius too large), poor ground conditions, and poor blasting. The cost of damage to, or loss of, trackless equipment as a direct result of the falls of ground in open stopes, is very significant. The review of financial figures has indicated that this could be as high as ZAR491 million over the past 10 years at Target Mine. This, combined with the added cost of transport, hoisting, secondary blasting, milling and plant treatment costs of ZAR293 million, results in an estimated opportunity loss of ZAR784 million for the past 10 years at Target Mine.

Currently there is a significant amount of data available in the mining industry, which could be effectively used to develop suitable back analysis techniques, but to date this has not been used effectively. If dilution can have such an impact on current and future mining ventures then the optimization of back analyses for the prediction of dilution in open stoping could assist significantly in the reduction of dilution in massive open stopes.



Rockmass classifications, geotechnical information, blast techniques, blast design, the stress strain environment, and hydraulic radius all have an effect on, or play a role in the evaluation of dilution. Each of these factors will be taken into consideration to ultimately determine a measurable or calculated percentage of dilution in massive open stopes.

The amount of overbreak in an open stope can be determined by subtracting the planned stope volume in  $m^3$  from the actual measured final stope volume in  $m^3$ , which is obtained from the CMS (cavity monitoring system). This is in turn divided by the planned stope volume in  $m^3$  to determine the percentage overbreak. The CMS wireframe is imported into the geological model and its grade re-evaluated. From this, the actual percentage dilution for open stopes can be determined. The dilution obtained can result in a major reduction of recovered grade for the open stope.

When analysing data from Target mine the following was achieved:

- Using 11 years of data a method of measuring and predicting the percentage dilution in open stoping was developed. This took into account rock mass quality, stress-strain state, and the hangingwall hydraulic radius (size of stope hangingwall exposed).
- Implementation of this prediction method resulted in a reduction in falls of ground in open stopes. The benefit of this was a reduction in the damage to mechanised equipment resulting from fewer falls of ground, which had a positive effect on the profit margins of the mine. As a direct result, the recovered grade from the open stopes increased due to the reduction in the amount of dilution.
- A design criterion, Dilution Stress-Strain Index (*DSSI*), was developed which allows the user to calculate, with certainty, the stability of the open stope and determine if major dilution (>10%) can be expected. The following equation can be used:

$$DSSI = \frac{\sigma_m}{q \varepsilon_{vol}}$$

where  $DSSI$  is the Dilution Stress-Strain Index,  $\sigma_m$  is the mean stress where  $\sigma_m = \frac{1}{3}(\sigma_1 + \sigma_2 + \sigma_3)$ ,  $q$  is the slope of the linear trend line and  $\varepsilon_{vol}$  is the volumetric strain where  $\varepsilon_{vol} = \varepsilon_1 + \varepsilon_2 + \varepsilon_3$ . For dilution from hangingwall failure resulting in more than ten percent dilution in open stopes on Target Mine it was found that this is true if the  $\sigma_m > 50\text{MPa}$ ;  $\varepsilon_{vol} > 1,285 \times 10^{-3}$  or  $\sigma_m < 4,8\text{MPa}$ ;  $\varepsilon_{vol} < 0,124 \times 10^{-3}$ . For dilution from sidewall failure resulting in more than ten percent dilution in open stopes on Target Mine it was found that this is true if the  $\sigma_m > 85,3\text{MPa}$ ;  $\varepsilon_{vol} > 2,193 \times 10^{-3}$  or  $\sigma_m < 0,5\text{MPa}$ ;  $\varepsilon_{vol} < 0,013 \times 10^{-3}$ .

Using this design criterion  $DSSI$ , the depth of sidewall failure or hangingwall failure could be determined and the planned open stope wireframe can then be amended to incorporate these failure zones for re-evaluation so as to determine the new stope shape.

To determine the percentage dilution for open stopes on Target Mine, the following equations are proposed:

If  $\frac{\sigma_1}{2.6\sigma_3+54} > 1$  then major sidewall dilution will occur:

$$OS_{HFh} = (0.0021\varepsilon_{volh} + 0.4101) \times 100$$

If  $\frac{\sigma_1}{2.6\sigma_3+34} < 1$  then major hangingwall dilution will occur:

$$OS_{SFS} = (0.2368\varepsilon_{vol_s} + 0.1309) \times 100$$

If  $\frac{\sigma_1}{2.6\sigma_3+54} < 1$  and  $\frac{\sigma_1}{2.6\sigma_3+34} > 1$  then minor dilution will occur:

$$OS_{HFh} = (0.0187\varepsilon_{volh} + 0.0522) \times 100$$

$$OS_{SFn} = (-0.0043\varepsilon_{vol_s} + 0.0677) \times 100$$

$$OSD = \text{Maximum } (OS)$$

where  $OS_{HFS}$  is the open stope hangingwall dilution in percentage for failure in compression;  $OS_{SFS}$  is the open stope sidewall dilution in percentage for failure in compression;  $OS_{HFh}$  is the open stope hangingwall dilution in percentage for failure in tension;  $OS_{SFh}$  is the open stope sidewall dilution in percentage for failure in tension;  $OS_{HFn}$  is the open stope hangingwall dilution in percentage for failure in normal open stope conditions;  $OS_{SFn}$  is the open stope sidewall dilution in percentage for failure in normal open stope conditions; and  $OSD$ , known as the Open Stope Dilution, is the maximum value for the respective  $OS$  value obtained.

To prove the DSSI design method in a wider context, it was decided to apply it to open stoping in a completely different geological environment. Thus, an open stoping mine, Mining Site Two was chosen, situated in the Murchison Greenstone Belt in South Africa on the Antimony Line, an accumulation of ancient metamorphic rocks, which is in contrast with the sedimentary geology in Target Mine. The DSSI criterion has proved very satisfactory in its application on Mining Site Two when compared to other stress and strain-based failure criteria, proving that the DSSI design criterion can be applied to any mining site irrespective of its geological setting or rock mass properties.

## **DEDICATION**

This report is dedicated to my family with special mention to my wife, Ronel, who has been very supportive during my preparation of this document. My family's understanding and patience over the five-year period is truly appreciated.

## **ACKNOWLEDGEMENTS**

I would like to thank my supervisor Professor Dick Stacey for his untiring assistance in guiding me. I would also like to thank Harmony Gold Mining Company Limited for the privilege of presenting this research. The permission to include data and make use of equipment, as well as the assistance received from my colleagues at Brentley, Lucas & Associates, Mining Consultants and Harmony Gold Mining Company Limited, is greatly appreciated.

<b>CONTENTS</b>	<b>Page</b>
<b>DECLARATION.....</b>	<b>III</b>
<b>ABSTRACT.....</b>	<b>IV</b>
<b>DEDICATION .....</b>	<b>VIII</b>
<b>ACKNOWLEDGEMENTS .....</b>	<b>IX</b>
<b>LIST OF FIGURES.....</b>	<b>XIV</b>
<b>LIST OF TABLES.....</b>	<b>XXVIII</b>
<b>LIST OF SYMBOLS .....</b>	<b>29</b>
<b>1 INTRODUCTION.....</b>	<b>31</b>
1.1 BACKGROUND TO THE RESEARCH .....	31
1.2 JUSTIFICATION FOR THE RESEARCH.....	31
1.3 RESEARCH OBJECTIVES .....	33
1.4 RESEARCH METHODOLOGY .....	34
1.5 RESEARCH CONTRIBUTION .....	35
1.6 FACILITIES .....	36
1.7 THESIS OUTLINE .....	36
<b>2 LITERATURE REVIEW ON DILUTION DESIGN METHODS AND OPEN STOPE STABILITY .....</b>	<b>38</b>
2.1 INTRODUCTION .....	38
2.2 DEFINITION OF DILUTION .....	38
2.3 QUANTIFYING DILUTION USING THE CAVITY MONITORING SYSTEM.....	42
2.3.1 CAVITY MONITORING SYSTEM (CMS).....	42
2.3.2 MEASUREMENT OF ACTUAL DILUTION .....	42
2.4 EMPIRICAL OPEN STOPE STABILITY AND DILUTION DESIGN METHODS .....	43
2.4.1 HYDRAULIC RADIUS .....	43
2.4.2 ROCK MASS CLASSIFICATION .....	44
2.4.3 MODIFIED STABILITY NUMBER, $N'$ .....	44
2.4.4 EQUIVALENT LINEAR OVERBREAK SLOUGH (ELOS) .....	50
2.5 THREE-DIMENSIONAL STRESS IN THE MINING ENVIRONMENT .....	53
2.6 FAILURE CRITERIA USED FOR EXCAVATION DESIGN .....	55
2.6.1 MOHR-COULOMB FAILURE CRITERION.....	56
2.7 THREE-DIMENSIONAL FAILURE CRITERIA BASED ON THE MOHR-COULOMB CRITERION .....	59
2.7.1 DRUCKER-PRAGER CRITERION.....	59
2.8 NON-LINEAR FAILURE CRITERIA USED FOR EXCAVATION DESIGN.....	60
2.8.1 HOEK-BROWN FAILURE CRITERION.....	60

2.9	THREE-DIMENSIONAL FAILURE CRITERIA BASED ON THE HOEK–BROWN CRITERION .....	63
2.9.1	GENERALISED ZHANG–ZHU CRITERION .....	64
2.9.2	GENERALISED PAN–HUDSON CRITERION .....	65
2.9.3	GENERALISED PRIEST CRITERION .....	65
2.9.4	SIMPLIFIED PRIEST CRITERION.....	66
2.10	THREE-DIMENSIONAL STRAIN IN THE MINING ENVIRONMENT.....	67
2.11	STRAIN-BASED FAILURE CRITERIA.....	69
2.11.1	STACEY’S EXTENSION STRAIN CRITERION .....	69
2.11.2	SAKURAI’S CRITICAL STRAIN CRITERIA .....	70
2.11.3	FUJII’S CRITICAL TENSILE STRAIN CRITERION .....	71
2.11.4	KWAŚNIEWSKI STRAIN-BASED FAILURE CRITERIA.....	72
2.12	NUMERICAL DESIGN METHODS .....	72
2.12.1	MODELLING OF DILUTION .....	72
2.13	INFLUENCE OF BLASTING ON STOPE HANGINGWALL STABILITY AND DILUTION .....	75
2.13.1	BLASTING VIBRATIONS .....	75
2.14	PLANNING PROCESS ON TARGET MINE.....	77
2.15	SUMMARY.....	79
<b>3</b>	<b>BACKGROUND ON SITE USED FOR DATA COLLECTION.....</b>	<b>80</b>
3.1	INTRODUCTION .....	80
3.2	HISTORY OF GOLD IN THE FREE STATE .....	80
3.3	GENERAL MINE INFORMATION .....	84
3.4	FREE STATE GEOLOGICAL SETTING.....	85
3.4.1	REGIONAL GEOLOGICAL SETTING .....	86
3.4.2	GEOLOGY OF TARGET MINE .....	88
3.5	SUMMARY.....	95
<b>4</b>	<b>DESCRIPTION AND EMPIRICAL DATABASE.....</b>	<b>96</b>
4.1	INTRODUCTION .....	96
4.2	EMPIRICAL DATABASE AND SELECTION OF CASE STUDY STOPES.....	96
4.3	GENERAL OPEN STOPE INFORMATION.....	96
4.4	FINANCIAL IMPLICATION OF DILUTION AND OVERBREAK.....	101
4.4.1	NATURE AND MAGNITUDE OF DILUTION .....	107
4.4.2	FACTORS INITIATING INSTABILITY.....	108
4.5	SUMMARY.....	116
<b>5</b>	<b>DILUTION FACTOR AND DILUTION PREDICTION.....</b>	<b>117</b>
5.1	INTRODUCTION .....	117

5.2	MEASUREMENT OF DILUTION .....	117
5.3	MODIFIED STABILITY NUMBER, $N'$ .....	118
5.4	EQUIVALENT LINEAR OVERBREAK SLOUGH (ELOS).....	121
5.5	SUMMARY.....	126
<b>6</b>	<b>INFLUENCE OF STRESS ON OPEN STOPE HANGINGWALL AND SIDEWALL STABILITY AND DILUTION .....</b>	<b>127</b>
6.1	INTRODUCTION .....	127
6.2	MODELLING METHODOLOGY.....	127
6.2.1	DIPS.....	129
6.2.2	PHASE2 .....	138
6.2.3	JBLOCK .....	145
6.2.4	MAP3D .....	153
6.2.5	FAILURE CRITERIA APPLIED TO MAP3D RESULTS .....	160
6.3	SUMMARY.....	176
<b>7</b>	<b>INFLUENCE OF STRESS AND STRAIN ON OPEN STOPE HANGINGWALL AND SIDEWALL STABILITY AND DILUTION.....</b>	<b>177</b>
7.1	INTRODUCTION .....	177
7.2	APPLICATION OF STRAIN-BASED FAILURE CRITERIA TO CASE STUDIES .....	177
7.3	MEAN STRESS AND VOLUMETRIC STRAIN .....	180
7.4	DILUTION STRESS-STRAIN INDEX .....	181
7.5	APPLYING THE <i>DILUTION STRESS-STRAIN INDEX (DSSI)</i> DESIGN CRITERION TO TARGET MINE .....	182
7.6	PREDICTING DILUTION FROM VOLUMETRIC STRAIN .....	188
7.7	APPLYING THE <i>DILUTION STRESS-STRAIN INDEX (DSSI)</i> DESIGN CRITERION TO MINING SITE TWO .....	191
7.7.1	MINING ENVIRONMENT AT MINING SITE TWO.....	191
7.7.2	GEOLOGICAL SETTING AT MINING SITE TWO .....	193
7.7.3	ANALYSES AND RESULTS OF MINING SITE TWO WHEN APPLYING THE DILUTION STRESS-STRAIN INDEX..	196
7.8	COMPARING CALCULATED OPEN STOPE DILUTION TO OTHER EMPIRICAL METHODS .....	202
<b>8</b>	<b>CONCLUSIONS AND RECOMMENDATIONS.....</b>	<b>205</b>
8.1	KNOWLEDGE CONTRIBUTIONS .....	206
8.2	LIMITATIONS.....	207
8.3	FUTURE WORK.....	207
	<b>REFERENCES .....</b>	<b>208</b>
	<b>BIBLIOGRAPHY.....</b>	<b>215</b>
	<b>APPENDIX A .....</b>	<b>227</b>
	<b>APPENDIX B .....</b>	<b>241</b>



<b>APPENDIX C .....</b>	<b>270</b>
<b>APPENDIX D .....</b>	<b>288</b>
<b>APPENDIX E .....</b>	<b>376</b>
<b>APPENDIX F.....</b>	<b>454</b>
<b>APPENDIX G .....</b>	<b>465</b>

## LIST OF FIGURES

Figure 2.1	Diagram illustrating dilution in an open stope .....	39
Figure 2.2	Diagram for determining dilution in an ore body with a complex structure (Shekhovtsov, 1994)...	41
Figure 2.4	Modified stability graph (Potvin, 1988) .....	45
Figure 2.5	Stability Graph Factor A (After Potvin, 1988; from Hutchinson and Diederichs, 1996).....	46
Figure 2.6	Stability Graph Factor B (After Potvin, 1988; from Hutchinson and Diederichs, 1996).....	47
Figure 2.7	Stability Graph Factor C (After Potvin, 1988; from Hutchinson and Diederichs, 1996).....	48
Figure 2.8	Site-specific average expected dilution data from Pakalnis et al (1995).....	49
Figure 2.9	Equivalent Linear Overbreak/Slough (ELOS), (Clark and Pakalnis, 1997).....	50
Figure 2.10	Estimation of Overbreak/Slough (ELOS) for non-supported hangingwalls and footwalls, after Clark and Pakalnis (1997).....	51
Figure 2.11	Empirical dilution design graph showing the original case histories used to create the graph, after Capes (2009) .....	52
Figure 2.12	Illustration of the procedure for obtaining dilution factor, after Wang (2004) .....	52
Figure 2.13	Illustration stress components on a tetrahedron in three dimensions, after Ryder and Jager (2002).....	54
Figure 2.14	The Mohr-Coulomb failure criterion for shear failure (Brady and Brown, 1985) .....	57
Figure 2.15	Alternative representation of the Mohr-Coulomb failure criterion (Wiles, 2006) .....	58
Figure 2.16	Scaling of Hoek-Brown failure envelope for intact rock to that for rock mass strength (Ulusay and Hudson, 2007).....	62
Figure 2.18	Simple definition of strain, after Ryder and Jager, (2002) .....	68
Figure 2.19	Tunnel failure modes (Kaiser et al. (2000)) .....	75
Figure 2.17	Flowchart showing process to follow when evaluating an open stope for mining .....	78
Figure 3.1	Image showing the relative positions of the St. Helena Mining Lease area (Harmony Financial Report, 2013) .....	83
Figure 3.2	Location of Target Mine (Harrison, 2010).....	85
Figure 3.3	General stratigraphic column of the Witwatersrand Supergroup as proposed by the SACS Task Group (Ryder and Jager, 2002) .....	87
Figure 3.4	Witwatersrand Basin relative to South Africa (Harmony Annual Report, 2009).....	90
Figure 3.5	Target Mine relative to the Witwatersrand Basin in the Free State (Frimmel et al, 2005).....	91
Figure 3.6	Cross section view looking north showing the Eldorado reefs sub-outcropping against the Dreyerskuil reefs .....	94
Figure 3.7	Photo showing the Eldorado reefs sub-outcropping against the Dreyerskuil reefs.....	94
Figure 4.1	Cross section view of a typical open stope design on Target Mine .....	98
Figure 4.2	Plan view of a typical open stope design on Target Mine.....	99
Figure 4.3	General isometric view of a typical open stope design on Target Mine.....	100
Figure 4.4	Photo of a TORO LH514 LHD in an open stope damaged by fall of ground .....	101
Figure 4.5	Graph showing standing time for mechanized equipment – open stoping, damage by falls of ground on Target Mine.....	102
Figure 4.6	Plan view of Target mining block.....	103
Figure 4.7	Plan view of open stopes mined at Target Mine without showing the development and narrow reef stoping .....	104
Figure 4.8	Graph showing mechanized equipment – open stoping, damage by falls of ground per year on Target Mine.....	105

Figure 4.9	Graph showing repair cost of mechanized equipment – open stoping, damage by falls of ground per year on Target Mine.....	105
Figure 4.10	Graph showing total cost due to standing time of mechanized equipment – open stoping, damage by falls of ground per year on Target Mine.....	106
Figure 4.11	Histogram of major principal stress before mining open stopes for all case studies with hangingwall failure.....	107
Figure 4.12	Histogram of major principal stress before mining open stopes for all case studies with sidewall failure .....	108
Figure 4.13	Histogram of major principal stress for all case studies before mining open stopes.....	109
Figure 4.14	Histogram of hydraulic radius for all case studies .....	112
Figure 5.1	Pie Chart showing the percentage major dilution, minor dilution and underbreak for the case studies.....	118
Figure 5.2	Histogram of Modified stability number, $N'$ for all case studies .....	119
Figure 5.3	Plot of case studies on modified stability diagram after Potvin (1988) where average $N' = 16$ for major failure and $N' = 24$ for minor failure .....	119
Figure 5.4	Modification of the modified stability diagram showing percentage trend lines for Target Mine, after Potvin (1988).....	120
Figure 5.5	Plot of case studies showing relation between percentage dilution, hydraulic radius and modified stability number, $N'$ after Pakalnis et al (1995).....	121
Figure 5.6	Histogram of stope ELOS (m) for all case studies.....	122
Figure 5.7	Plot of case studies showing relation between ELOS, hydraulic radius and modified stability number, $N'$ after Clark and Pakalnis (1997) .....	123
Figure 5.8	Modified plot of case studies showing relation between ELOS, hydraulic radius and modified stability number, $N'$ for Target Mine after Clark and Pakalnis (1997) .....	123
Figure 6.1	Sketch showing the dip of the open stope sidewall slopes.....	129
Figure 6.2	Stereonet plot of EA1 joints and second joint set using Dips .....	132
Figure 6.3	Rosette plot of EA1 joints and second joint set using Dips.....	133
Figure 6.4	Stereonet plot of EA3 joints and second joint set using Dips .....	134
Figure 6.5	Rosette plot of EA3 joints and second joint set using Dips.....	135
Figure 6.6	Stereonet plot of EA7 joints and second joint set using Dips .....	136
Figure 6.7	Rosette plot of EA7 joints and second joint set using Dips.....	137
Figure 6.8	Phase2 model setup with joint sets for an open stope that is overtoped .....	138
Figure 6.9	Phase2 model setup showing Edit Joint Network window.....	139
Figure 6.10	Depth of hangingwall failure for an open stope with randomized jointing .....	141
Figure 6.11	Depth of hangingwall failure for open stopes with different middling between narrow reef mining (NRM).....	142
Figure 6.12	Depth of sidewall failure for open stopes with different middling between narrow reef mining (NRM).....	143
Figure 6.13	JBlock model setup for an open stope .....	145
Figure 6.14	Summary of JBlock results for falls of ground per mining step ( $m^3$ ) in the EA1, EA3 and EA7 formations with open stope hangingwall dipping $45^\circ$ .....	147
Figure 6.15	Summary of JBlock results for hangingwall failure depth (m) in the EA1, EA3 and EA7 formations with open stope hangingwall dipping $45^\circ$ .....	147
Figure 6.16	Summary of JBlock results for percentage dilution in the EA1, EA3 and EA7 formations with open stope hangingwall dipping $45^\circ$ .....	148
Figure 6.17	Summary of JBlock results for falls of ground per mining step ( $m^3$ ) in the EA1, EA3 and EA7 formations with open stope hangingwall cutting across strata.....	150

Figure 6.18	Summary of JBlock results for hangingwall failure depth (m) in the EA1, EA3 and EA7 formations with open stope hangingwall cutting across strata.....	150
Figure 6.19	Summary of JBlock results for percentage dilution in the EA1, EA3 and EA7 formations with open stope hangingwall cutting across strata.....	151
Figure 6.20	Map3D model setup for open stopes that is overtoped and not with joint sets .....	153
Figure 6.21	The maximum $\sigma_1$ and $\sigma_3$ stress plot in hangingwall for open stopes with dilution greater and smaller than ten percent.....	156
Figure 6.22	The minimum $\sigma_1$ and $\sigma_3$ stress plot in hangingwall for open stopes with dilution greater and smaller than ten percent.....	156
Figure 6.23	The median $\sigma_1$ and $\sigma_3$ stress plot in hangingwall for open stopes with dilution greater and smaller than ten percent.....	157
Figure 6.24	The average $\sigma_1$ and $\sigma_3$ stress plot in hangingwall for open stopes with dilution greater and smaller than ten percent.....	157
Figure 6.25	The maximum $\sigma_1$ and $\sigma_3$ stress plot in sidewall for open stopes with dilution greater and smaller than ten percent.....	158
Figure 6.26	The minimum $\sigma_1$ and $\sigma_3$ stress plot in sidewall for open stopes with dilution greater and smaller than ten percent.....	158
Figure 6.27	The median $\sigma_1$ and $\sigma_3$ stress plot in sidewall for open stopes with dilution greater and smaller than ten percent .....	159
Figure 6.28	The average $\sigma_1$ and $\sigma_3$ stress plot in sidewall for open stopes with dilution greater and smaller than ten percent .....	159
Figure 6.29	Graph showing the relation between various criteria used and obtained results for open stopes with major hangingwall failure .....	161
Figure 6.30	Graph showing the relation between various criteria used and obtained results for open stopes with major sidewall failure .....	162
Figure 6.31	Graph showing the relation between the Mohr-Coulomb failure criterion and obtained results for open stopes with major hangingwall failure.....	164
Figure 6.32	Graph showing the relation between the Mohr-Coulomb failure criterion and obtained results for open stopes with major sidewall failure.....	164
Figure 6.33	Graph showing the relation between the Hoek-Brown failure criterion and obtained results for open stopes with major hangingwall failure.....	165
Figure 6.34	Graph showing the relation between the Hoek-Brown failure criterion and obtained results for open stopes with major sidewall failure .....	166
Figure 6.35	Graph showing the relation between the Zhang-Zhu Criterion and obtained results for open stopes with major hangingwall failure.....	167
Figure 6.36	Graph showing the relation between the Zhang-Zhu Criterion and obtained results for open stopes with major sidewall failure.....	167
Figure 6.37	Graph showing the relation between the Pan-Hudson Criterion and obtained results for open stopes with major hangingwall failure.....	168
Figure 6.38	Graph showing the relation between the Pan-Hudson Criterion and obtained results for open stopes with major sidewall failure.....	169
Figure 6.39	Graph showing the relation between the Priest Criterion and obtained results for open stopes with major hangingwall failure .....	170
Figure 6.40	Graph showing the relation between the Priest Criterion and obtained results for open stopes with major sidewall failure .....	170
Figure 6.41	Graph showing the relation between the Simplified Priest Criterion and obtained results for open stopes with major hangingwall failure.....	171

Figure 6.42	Graph showing the relation between the Simplified Priest Criterion and obtained results for open stopes with major sidewall failure.....	172
Figure 6.45	Graph showing the hangingwall failure depth predictions obtained for the case studies using various criteria.....	174
Figure 6.46	Graph showing the obtained results using various criteria for the case studies sidewall failure depth.....	175
Figure 7.1	Photo in a borehole at Target Mine open stope hangingwall showing ground conditions with no visible open fractures.....	178
Figure 7.2	The extension strain criterion after Stacey, (1981) applied to case study 1 with a modulus of elasticity $E = 70000$ MPa.....	179
Figure 7.3	The extension strain criterion after Stacey, (1981) applied to case study 1 with a modulus of elasticity $E = 85000$ MPa.....	179
Figure 7.4	Graph showing the relation between mean stress and volumetric strain for open stopes with major and minor hangingwall dilution.....	181
Figure 7.5	Graph showing the relation between mean stress and volumetric strain for open stopes with major and minor sidewall dilution.....	181
Figure 7.6	Flow chart showing the detailed recommended approach for the application of the DSSI design criterion and determining dilution in open stopes.....	185
Figure 7.7	Graph showing the relation between the major and minor stress for the case studies hangingwall.....	186
Figure 7.8	Graph showing the relation between open stope hangingwall and sidewall failure as to determine the failure mode.....	187
Figure 7.9	Application of the DSSI Design criterion to case study 3.....	188
Figure 7.10	Application of the DSSI Design criterion to case study 1.....	188
Figure 7.11	Graph showing the relation between median mean stress, volumetric strain and dilution in the hangingwall.....	189
Figure 7.12	Graph showing the relation between median mean stress, volumetric strain and dilution in the sidewall.....	189
Figure 7.13	Plan view of the generalised geology of the Murchison greenstone belt showing the various stratigraphic units (modified from Poujol et al., 1996).....	192
Figure 7.14	Section view of DXF file opened in Map3D looking north showing the orebody structure and orientation at Mining Site Two.....	192
Figure 7.15	Photo showing the intense buckling of the sidewalls of strike orientated development at Mining Site Two.....	194
Figure 7.16	Cross sectional view looking east showing the orebody structure and orientation at Mining Site Two.....	195
Figure 7.17	Plan view showing the orebody structure and orientation at Mining Site Two.....	196
Figure 7.18	Section view looking north showing the open stopes selected for back analyses on Mining Site Two.....	197
Figure 7.19	Map3D section view of model setup for 29 Level Stope at Mining Site Two.....	198
Figure 7.20	Section view of DXF file opened in Map3D showing survey measurements for 29 Level Stope at Mining Site Two.....	198
Figure 7.21	Graph showing the relation between mean stress and volumetric strain for open stopes with major and minor dilution for Mining Site Two.....	199
Figure 7.22	Plan view of the application of the DSSI Design criterion to Mining Site Two at step 1.....	200
Figure 7.23	Graph showing the relation between open stope hangingwall failure to determine the failure mode at Mining Site Two.....	200

Figure 7.24	Graph showing the relations between median mean stress, volumetric strain and dilution at Mining Site Two.....	201
Figure 7.25	Graph showing total dilution for open stoping per year on Target Mine .....	203
Figure 7.26	Graph showing total cost for dilution and mechanized equipment damage in open stoping per year on Target Mine .....	203
Figure A1	Plan view of case study 1 .....	227
Figure A2	Plan view of case study 2 .....	227
Figure A3	Plan view of case study 3.....	228
Figure A4	Plan view of case study 4.....	228
Figure A5	Plan view of case study 5.....	229
Figure A6	Plan view of case study 6.....	229
Figure A7	Plan view of case study 7.....	230
Figure A8	Plan view of case study 8.....	230
Figure A9	Plan view of case study 9.....	231
Figure A10	Plan view of case study 10.....	231
Figure A11	Plan view of case study 11.....	232
Figure A12	Plan view of case study 12 .....	232
Figure A13	Plan view of case study 13.....	233
Figure A14	Plan view of case study 14.....	233
Figure A15	Plan view of case study 15.....	234
Figure A16	Plan view of case study 16.....	234
Figure A17	Plan view of case study 17.....	235
Figure A18	Plan view of case study 18.....	235
Figure A19	Plan view of case study 19.....	236
Figure A20	Plan view of case study 20.....	236
Figure A21	Plan view of case study 21.....	237
Figure A22	Plan view of case study 22 .....	237
Figure A23	Plan view of case study 23.....	238
Figure A24	Plan view of case study 24.....	238
Figure A25	Plan view of case study 25.....	239
Figure A26	Plan view of case study 26.....	239
Figure A27	Plan view of case study 27.....	240
Figure A28	Plan view of case study 28.....	240
Figure B1	10m stope span overstoped open stope in EA7 with a 2m middling showing joint displacement in black and yielded joints indicated in red .....	241
Figure B2	10m stope span overstoped open stope in EA7 with a 4m middling showing joint displacement in black and yielded joints indicated in red .....	241
Figure B3	10m stope span overstoped open stope in EA7 with a 6m middling showing joint displacement in black and yielded joints indicated in red .....	242
Figure B4	10m stope span overstoped open stope in EA7 with a 8m middling showing joint displacement in black and yielded joints indicated in red .....	242
Figure B5	10m stope span overstoped open stope in EA7 with a 10m middling showing joint displacement in black and yielded joints indicated in red .....	242
Figure B6	10m stope span overstoped open stope in EA7 with a 15m middling showing joint displacement in black and yielded joints indicated in red .....	243
Figure B7	10m stope span overstoped open stope in EA7 with a 20m middling showing joint displacement in black and yielded joints indicated in red .....	243









Figure B77	20m stope span overstoped open stope in EA1 with a 20m middling showing joint displacement in black and yielded joints indicated in red .....	266
Figure B78	25m stope span overstoped open stope in EA1 with a 2m middling showing joint displacement in black and yielded joints indicated in red .....	267
Figure B79	25m stope span overstoped open stope in EA1 with a 4m middling showing joint displacement in black and yielded joints indicated in red .....	267
Figure B80	25m stope span overstoped open stope in EA1 with a 6m middling showing joint displacement in black and yielded joints indicated in red .....	267
Figure B81	25m stope span overstoped open stope in EA1 with a 8m middling showing joint displacement in black and yielded joints indicated in red .....	268
Figure B82	25m stope span overstoped open stope in EA1 with a 10m middling showing joint displacement in black and yielded joints indicated in red .....	268
Figure B83	25m stope span overstoped open stope in EA1 with a 15m middling showing joint displacement in black and yielded joints indicated in red .....	268
Figure B84	25m stope span overstoped open stope in EA1 with a 20m middling showing joint displacement in black and yielded joints indicated in red .....	269
Figure C1	Simulation statistics for 10m stope span situated in EA1 jointsets with flat hangingwall .....	270
Figure C2	Simulation statistics for 10m stope span situated in EA1 jointsets with hangingwall dipping 45° .....	270
Figure C3	Simulation statistics for 15m stope span in EA1 jointsets with flat hangingwall.....	271
Figure C4	Simulation statistics for 15m stope span in EA1 jointsets with hangingwall dipping 45° .....	271
Figure C5	Simulation statistics for 20m stope span in EA1 jointsets with flat hangingwall.....	272
Figure C6	Simulation statistics for 20m stope span in EA1 jointsets with hangingwall dipping 45° .....	272
Figure C7	Simulation statistics for 25m stope span in EA1 jointsets with flat hangingwall.....	273
Figure C8	Simulation statistics for 25m stope span in EA1 jointsets with hangingwall dipping 45° .....	273
Figure C9	Simulation statistics for 10m stope span in EA3 jointsets with flat hangingwall.....	274
Figure C10	Simulation statistics for 10m stope span in EA3 jointsets with hangingwall dipping 45° .....	274
Figure C11	Simulation statistics for 15m stope span in EA3 jointsets with flat hangingwall.....	275
Figure C12	Simulation statistics for 15m stope span in EA3 jointsets with hangingwall dipping 45° .....	275
Figure C13	Simulation statistics for 20m stope span in EA3 jointsets with flat hangingwall.....	276
Figure C14	Simulation statistics for 20m stope span in EA3 jointsets with hangingwall dipping 45° .....	276
Figure C15	Simulation statistics for 25m stope span in EA3 jointsets with flat hangingwall.....	277
Figure C16	Simulation statistics for 25m stope span in EA3 jointsets with hangingwall dipping 45° .....	277
Figure C17	Simulation statistics for 10m stope span in EA7 jointsets with flat hangingwall.....	278
Figure C18	Simulation statistics for 10m stope span in EA7 jointsets with hangingwall dipping 45° .....	278
Figure C19	Simulation statistics for 15m stope span in EA7 jointsets with flat hangingwall.....	279
Figure C20	Simulation statistics for 15m stope span in EA7 jointsets with hangingwall dipping 45° .....	279
Figure C21	Simulation statistics for 20m stope span in EA7 jointsets with flat hangingwall.....	280
Figure C22	Simulation statistics for 20m stope span in EA7 jointsets with hangingwall dipping 45° .....	280
Figure C23	Simulation statistics for 25m stope span in EA7 jointsets with flat hangingwall.....	281
Figure C24	Simulation statistics for 25m stope span in EA7 jointsets with hangingwall dipping 45° .....	281
Figure C25	Summary of JBlock results for a 10m wide excavation in the EA1 formation .....	282
Figure C26	Summary of JBlock results for a 10m wide excavation in the EA3 formation .....	282
Figure C27	Summary of JBlock results for a 10m stope span excavation in the EA7 formation .....	283
Figure C28	Summary of JBlock results for a 15m stope span excavation in the EA1 formation .....	283
Figure C29	Summary of JBlock results for a 15m stope span excavation in the EA3 formation .....	284
Figure C30	Summary of JBlock results for a 15m stope span excavation in the EA7 formation .....	284
Figure C31	Summary of JBlock results for a 20m stope span excavation in the EA1 formation .....	285

Figure C32	Summary of JBlock results for a 20m stope span excavation in the EA3 formation .....	285
Figure C33	Summary of JBlock results for a 20m stope span excavation in the EA7 formation .....	286
Figure C34	Summary of JBlock results for a 25m stope span excavation in the EA1 formation .....	286
Figure C35	Summary of JBlock results for a 25m stope span excavation in the EA3 formation .....	287
Figure C36	Summary of JBlock results for a 25m stope span excavation in the EA7 formation .....	287
Figure E1	Application of the Mohr-Coulomb criterion to case study 1 .....	376
Figure E2	Application of the Hoek-Brown criterion to case study 1 .....	376
Figure E3	Application of the Zhang–Zhu Criterion to case study 1 .....	377
Figure E4	Application of the Pan–Hudson Criterion to case study 1 .....	377
Figure E5	Application of the Priest Criterion to case study 1 .....	378
Figure E6	Application of the Simplified Priest Criterion to case study 1 .....	378
Figure E7	Application of the DSSI design criterion to case study 1 .....	379
Figure E8	CMS wireframe in red showing actual overbreak of case study 1 .....	379
Figure E9	Application of the Mohr-Coulomb criterion to case study 2 .....	380
Figure E10	Application of the Hoek-Brown criterion to case study 2 .....	380
Figure E11	Application of the Zhang–Zhu Criterion to case study 2 .....	381
Figure E12	Application of the Pan–Hudson Criterion to case study 2 .....	381
Figure E13	Application of the Priest Criterion to case study 2 .....	382
Figure E14	Application of the Simplified Priest Criterion to case study 2 .....	382
Figure E15	Application of the DSSI design criterion to case study 2 .....	383
Figure E16	CMS wireframe in red showing actual overbreak of case study 2 .....	383
Figure E17	Application of the Mohr-Coulomb criterion to case study 3 .....	384
Figure E18	Application of the Hoek-Brown criterion to case study 3 .....	384
Figure E19	Application of the Zhang–Zhu Criterion to case study 3 .....	385
Figure E20	Application of the Pan–Hudson Criterion to case study 3 .....	385
Figure E21	Application of the Priest Criterion to case study 3 .....	386
Figure E22	Application of the Simplified Priest Criterion to case study 3 .....	386
Figure E23	Application of the DSSI design criterion to case study 3 .....	387
Figure E24	CMS wireframe in red showing actual overbreak of case study 3 .....	387
Figure E25	Application of the Mohr-Coulomb criterion to case study 4 .....	388
Figure E26	Application of the Hoek-Brown criterion to case study 4 .....	388
Figure E27	Application of the Zhang–Zhu Criterion to case study 4 .....	389
Figure E28	Application of the Pan–Hudson Criterion to case study 4 .....	389
Figure E29	Application of the Priest Criterion to case study 4 .....	390
Figure E30	Application of the Simplified Priest Criterion to case study 4 .....	390
Figure E31	Application of the DSSI design criterion to case study 4 .....	391
Figure E32	Application of the Mohr-Coulomb criterion to case study 5 .....	391
Figure E33	Application of the Hoek-Brown criterion to case study 5 .....	392
Figure E34	Application of the Zhang–Zhu Criterion to case study 5 .....	392
Figure E35	Application of the Pan–Hudson Criterion to case study 5 .....	393
Figure E36	Application of the Priest Criterion to case study 5 .....	393
Figure E37	Application of the Simplified Priest Criterion to case study 5 .....	394
Figure E38	Application of the DSSI design criterion to case study 5 .....	394
Figure E39	CMS wireframe in red showing actual overbreak of case study 5 .....	395
Figure E40	Application of the Mohr-Coulomb criterion to case study 6 .....	395
Figure E41	Application of the Hoek-Brown criterion to case study 6 .....	396
Figure E42	Application of the Zhang–Zhu Criterion to case study 6 .....	396

Figure E43	Application of the Pan–Hudson Criterion to case study 6.....	397
Figure E44	Application of the Priest Criterion to case study 6.....	397
Figure E45	Application of the Simplified Priest Criterion to case study 6.....	398
Figure E46	Application of the DSSI design criterion to case study 6.....	398
Figure E47	Application of the Mohr–Coulomb criterion to case study 7.....	399
Figure E48	Application of the Hoek–Brown criterion to case study 7.....	399
Figure E49	Application of the Zhang–Zhu Criterion to case study 7.....	400
Figure E50	Application of the Pan–Hudson Criterion to case study 7.....	400
Figure E51	Application of the Priest Criterion to case study 7.....	401
Figure E52	Application of the Simplified Priest Criterion to case study 7.....	401
Figure E53	Application of the DSSI design criterion to case study 7.....	402
Figure E54	CMS wireframe in red showing actual overbreak of case study 7.....	402
Figure E55	Application of the Mohr–Coulomb criterion to case study 8.....	403
Figure E56	Application of the Hoek–Brown criterion to case study 8.....	403
Figure E57	Application of the Zhang–Zhu Criterion to case study 8.....	404
Figure E58	Application of the Pan–Hudson Criterion to case study 8.....	404
Figure E59	Application of the Priest Criterion to case study 8.....	405
Figure E60	Application of the Simplified Priest Criterion to case study 8.....	405
Figure E61	Application of the DSSI design criterion to case study 8.....	406
Figure E62	CMS wireframe in red showing actual overbreak of case study 8.....	406
Figure E63	Application of the Mohr–Coulomb criterion to case study 9.....	407
Figure E64	Application of the Hoek–Brown criterion to case study 9.....	407
Figure E65	Application of the Zhang–Zhu Criterion to case study 9.....	408
Figure E66	Application of the Pan–Hudson Criterion to case study 9.....	408
Figure E67	Application of the Priest Criterion to case study 9.....	409
Figure E68	Application of the Simplified Priest Criterion to case study 9.....	409
Figure E69	Application of the DSSI design criterion to case study 9.....	409
Figure E70	CMS wireframe in red showing actual overbreak of case study 9.....	410
Figure E71	Application of the Mohr–Coulomb criterion to case study 10.....	410
Figure E72	Application of the Hoek–Brown criterion to case study 10.....	411
Figure E73	Application of the Zhang–Zhu Criterion to case study 10.....	411
Figure E74	Application of the Pan–Hudson Criterion to case study 10.....	412
Figure E75	Application of the Priest Criterion to case study 10.....	412
Figure E76	Application of the Simplified Priest Criterion to case study 10.....	413
Figure E77	Application of the DSSI design criterion to case study 10.....	413
Figure E78	CMS wireframe in red showing actual overbreak of case study 10.....	414
Figure E79	Application of the Mohr–Coulomb criterion to case study 11.....	414
Figure E80	Application of the Hoek–Brown criterion to case study 11.....	415
Figure E81	Application of the Zhang–Zhu Criterion to case study 11.....	415
Figure E82	Application of the Pan–Hudson Criterion to case study 11.....	416
Figure E83	Application of the Priest Criterion to case study 11.....	416
Figure E84	Application of the Simplified Priest Criterion to case study 11.....	417
Figure E85	Application of the DSSI design criterion to case study 11.....	417
Figure E86	CMS wireframe in red showing actual overbreak of case study 11.....	418
Figure E87	Application of the Mohr–Coulomb criterion to case study 12.....	418
Figure E88	Application of the Hoek–Brown criterion to case study 12.....	419
Figure E89	Application of the Zhang–Zhu Criterion to case study 12.....	419

Figure E90	Application of the Pan–Hudson Criterion to case study 12.....	420
Figure E91	Application of the Priest Criterion to case study 12 .....	420
Figure E92	Application of the Simplified Priest Criterion to case study 12.....	421
Figure E93	Application of the DSSI design criterion to case study 12 .....	421
Figure E94	CMS wireframe in red showing actual overbreak of case study 12 .....	422
Figure E95	Application of the Mohr-Coulomb criterion to case study 13 .....	422
Figure E96	Application of the Hoek-Brown criterion to case study 13 .....	423
Figure E97	Application of the Zhang–Zhu Criterion to case study 13.....	423
Figure E98	Application of the Pan–Hudson Criterion to case study 13.....	423
Figure E99	Application of the Priest Criterion to case study 13 .....	424
Figure E100	Application of the Simplified Priest Criterion to case study 13.....	424
Figure E101	Application of the DSSI design criterion to case study 13 .....	424
Figure E102	CMS wireframe in red showing actual overbreak of case study 13 .....	425
Figure E103	Application of the Mohr-Coulomb criterion to case study 14 .....	425
Figure E104	Application of the Hoek-Brown criterion to case study 14 .....	426
Figure E105	Application of the Zhang–Zhu Criterion to case study 14.....	426
Figure E106	Application of the Pan–Hudson Criterion to case study 14.....	426
Figure E107	Application of the Priest Criterion to case study 14 .....	427
Figure E108	Application of the Simplified Priest Criterion to case study 14.....	427
Figure E109	Application of the DSSI design criterion to case study 14 .....	428
Figure E110	CMS wireframe in red showing actual overbreak of case study 14 .....	428
Figure E111	Application of the Mohr-Coulomb criterion to case study 15 .....	428
Figure E112	Application of the Hoek-Brown criterion to case study 15 .....	429
Figure E113	Application of the Zhang–Zhu Criterion to case study 15.....	429
Figure E114	Application of the Pan–Hudson Criterion to case study 15.....	430
Figure E115	Application of the Priest Criterion to case study 15 .....	430
Figure E116	Application of the Simplified Priest Criterion to case study 15.....	431
Figure E117	Application of the DSSI design criterion to case study 15 .....	431
Figure E118	CMS wireframe in red showing actual overbreak of case study 15 .....	432
Figure E119	Application of the Mohr-Coulomb criterion to case study 16 .....	432
Figure E120	Application of the Hoek-Brown criterion to case study 16 .....	433
Figure E121	Application of the Zhang–Zhu Criterion to case study 16.....	433
Figure E122	Application of the Pan–Hudson Criterion to case study 16.....	433
Figure E123	Application of the Priest Criterion to case study 16 .....	434
Figure E124	Application of the Simplified Priest Criterion to case study 16.....	434
Figure E125	Application of the DSSI design criterion to case study 16 .....	434
Figure E126	CMS wireframe in red showing actual overbreak of case study 16 .....	435
Figure E127	Application of the Mohr-Coulomb criterion to case study 17 .....	435
Figure E128	Application of the Hoek-Brown criterion to case study 17 .....	436
Figure E129	Application of the Zhang–Zhu Criterion to case study 17.....	436
Figure E130	Application of the Pan–Hudson Criterion to case study 17.....	436
Figure E131	Application of the Priest Criterion to case study 17 .....	437
Figure E132	Application of the Simplified Priest Criterion to case study 17.....	437
Figure E133	Application of the DSSI design criterion to case study 17 .....	438
Figure E134	CMS wireframe in red showing actual overbreak of case study 17.....	438
Figure E135	Application of the Mohr-Coulomb criterion to case study 18 .....	438
Figure E136	Application of the Hoek-Brown criterion to case study 18 .....	439

Figure E137	Application of the Zhang–Zhu Criterion to case study 18.....	439
Figure E138	Application of the Pan–Hudson Criterion to case study 18.....	439
Figure E139	Application of the Priest Criterion to case study 18.....	439
Figure E140	Application of the Simplified Priest Criterion to case study 18.....	440
Figure E141	Application of the DSSI design criterion to case study 18.....	440
Figure E142	CMS wireframe in red showing actual overbreak of case study 18.....	440
Figure E143	Application of the Mohr-Coulomb criterion to case study 19.....	441
Figure E144	Application of the Hoek-Brown criterion to case study 19.....	441
Figure E145	Application of the Zhang–Zhu Criterion to case study 19.....	441
Figure E146	Application of the Pan–Hudson Criterion to case study 19.....	442
Figure E147	Application of the Priest Criterion to case study 19.....	442
Figure E148	Application of the Simplified Priest Criterion to case study 19.....	442
Figure E148	Application of the DSSI design criterion to case study 19.....	443
Figure E150	CMS wireframe in red showing actual overbreak of case study 19.....	443
Figure E151	Application of the Mohr-Coulomb criterion to case study 20.....	443
Figure E152	Application of the Hoek-Brown criterion to case study 20.....	444
Figure E153	Application of the Zhang–Zhu Criterion to case study 20.....	444
Figure E154	Application of the Pan–Hudson Criterion to case study 20.....	444
Figure E155	Application of the Priest Criterion to case study 20.....	445
Figure E156	Application of the Simplified Priest Criterion to case study 20.....	445
Figure E157	Application of the DSSI design criterion to case study 20.....	445
Figure E158	CMS wireframe in red showing actual overbreak of case study 20.....	446
Figure E159	Application of the Mohr-Coulomb criterion to case study 21.....	446
Figure E152	Application of the Hoek-Brown criterion to case study 21.....	447
Figure E153	Application of the Zhang–Zhu Criterion to case study 21.....	447
Figure E154	Application of the Pan–Hudson Criterion to case study 21.....	448
Figure E155	Application of the Priest Criterion to case study 21.....	448
Figure E156	Application of the Simplified Priest Criterion to case study 21.....	449
Figure E157	Application of the DSSI design criterion to case study 21.....	449
Figure E158	CMS wireframe in red showing actual overbreak of case study 21.....	450
Figure E159	Application of the Mohr-Coulomb criterion to case study 22.....	450
Figure E160	Application of the Hoek-Brown criterion to case study 22.....	451
Figure E161	Application of the Zhang–Zhu Criterion to case study 22.....	451
Figure E162	Application of the Pan–Hudson Criterion to case study 22.....	451
Figure E163	Application of the Priest Criterion to case study 22.....	452
Figure E164	Application of the Simplified Priest Criterion to case study 22.....	452
Figure E165	Application of the DSSI design criterion to case study 22.....	453
Figure E166	CMS wireframe in red showing actual overbreak of case study 22.....	453
Figure F1	The extension strain criterion after Stacey, (1981) applied to case study 1 with a modulus of elasticity $E = 70000$ MPa.....	454
Figure F2	The extension strain criterion after Stacey, (1981) applied to case study 2 with a modulus of elasticity $E = 70000$ MPa.....	454
Figure F3	The extension strain criterion after Stacey, (1981) applied to case study 3 with a modulus of elasticity $E = 70000$ MPa.....	455
Figure F4	The extension strain criterion after Stacey, (1981) applied to case study 4 with a modulus of elasticity $E = 70000$ MPa.....	455

Figure F5	The extension strain criterion after Stacey, (1981) applied to case study 5 with a modulus of elasticity $E = 70000$ MPa.....	456
Figure F6	The extension strain criterion after Stacey, (1981) applied to case study 6 with a modulus of elasticity $E = 70000$ MPa.....	456
Figure F7	The extension strain criterion after Stacey, (1981) applied to case study 7 with a modulus of elasticity $E = 70000$ MPa.....	457
Figure F8	The extension strain criterion after Stacey, (1981) applied to case study 8 with a modulus of elasticity $E = 70000$ MPa.....	457
Figure F9	The extension strain criterion after Stacey, (1981) applied to case study 9 with a modulus of elasticity $E = 70000$ MPa.....	458
Figure F10	The extension strain criterion after Stacey, (1981) applied to case study 10 with a modulus of elasticity $E = 70000$ MPa.....	458
Figure F11	The extension strain criterion after Stacey, (1981) applied to case study 11 with a modulus of elasticity $E = 70000$ MPa.....	459
Figure F12	The extension strain criterion after Stacey, (1981) applied to case study 12 with a modulus of elasticity $E = 70000$ MPa.....	459
Figure F13	The extension strain criterion after Stacey, (1981) applied to case study 13 with a modulus of elasticity $E = 70000$ MPa.....	460
Figure F14	The extension strain criterion after Stacey, (1981) applied to case study 14 with a modulus of elasticity $E = 70000$ MPa.....	460
Figure F15	The extension strain criterion after Stacey, (1981) applied to Mining Site Two mining step 1 with a modulus of elasticity $E = 60000$ MPa.....	461
Figure F16	The extension strain criterion after Stacey, (1981) applied to Mining Site Two mining step 2 with a modulus of elasticity $E = 60000$ MPa.....	461
Figure F17	The extension strain criterion after Stacey, (1981) applied to Mining Site Two mining step 3 with a modulus of elasticity $E = 60000$ MPa.....	462
Figure F18	The extension strain criterion after Stacey, (1981) applied to Mining Site Two mining step 4 with a modulus of elasticity $E = 60000$ MPa.....	462
Figure F19	The extension strain criterion after Stacey, (1981) applied to Mining Site Two mining step 5 with a modulus of elasticity $E = 60000$ MPa.....	463
Figure F20	The extension strain criterion after Stacey, (1981) applied to Mining Site Two mining step 6 with a modulus of elasticity $E = 60000$ MPa.....	463
Figure F21	The extension strain criterion after Stacey, (1981) applied to Mining Site Two mining step 7 with a modulus of elasticity $E = 60000$ MPa.....	464
Figure F22	The extension strain criterion after Stacey, (1981) applied to Mining Site Two mining step 8 with a modulus of elasticity $E = 60000$ MPa.....	464
Figure G1	Plan view of the application of the DSSI Design criterion to Mining Site Two at mining step 1 ...	465
Figure G2	Plan view of the application of the DSSI Design criterion to Mining Site Two at mining step 2 ...	465
Figure G3	Plan view of the application of the DSSI Design criterion to Mining Site Two at mining step 3 ...	466
Figure G4	Plan view of the application of the DSSI Design criterion to Mining Site Two at mining step 4 ...	466
Figure G5	Plan view of the application of the DSSI Design criterion to Mining Site Two at mining step 5 ...	467

## LIST OF TABLES

Table 2.1	Frequently used <b>PPV</b> predictors (Kamali and Ataei, 2010).....	76
Table 2.2	Parameter estimation for the predictors (Kamali and Ataei, 2010).....	77
Table 4.1	Cost per ton breakdown for overbreaking in open stopes .....	106
Table 4.2	List of recorded data at position A, B and C in radial, transverse and vertical directions (Van Alphen, 1995).....	111
Table 4.2	EA1 Jointing statistics .....	113
Table 4.3	EA3 Jointing statistics .....	113
Table 4.4	EA7 Jointing statistics .....	114
Table 4.5	Second Joint set statistics .....	114
Table 4.6	Rock mass classification using Q' System for all case studies.....	115
Table 5.4	Calculation of percentage dilution from hydraulic radius .....	121
Table 5.1	Summary of Case Studies with major dilution .....	124
Table 5.2	Summary of Case Studies with minor dilution .....	124
Table 5.3	Summary of Case Studies with underbreak .....	125
Table 6.1	Phase2 results as obtained from the simulations .....	144
Table 6.2	JBlock results as obtained from the simulations for hangingwall dipping 45° .....	149
Table 6.3	JBlock results as obtained from the simulations for hangingwall cutting across strata.....	152
Table 6.4	Predicted rock mass unconfined compressive strength $C_0$ using different failure criteria .....	173
Table 7.1	Calculated percentage dilution using the modified stability number method after Potvin (1988), the hydraulic radius method after Pakalnis et al (1995) and the newly developed Open Stope Dilution Method .....	204



**LIST OF SYMBOLS**

Major, intermediate, and minor principal stresses, respectively in MPa	$\sigma_1, \sigma_2$ and $\sigma_3$
Major, Intermediate and Minor principal effective stress in MPa	$\sigma'_1, \sigma'_2$ and $\sigma'_3$
Octahedral effective normal stress in MPa	$\sigma_{\text{oct}}$
Mean effective normal stress acting on the failure plane in MPa	$\sigma_{m,2}$
First invariant of the effective stress tensor in MPa	$I'_1$
Third invariant of the effective stress tensor in MPa	$I'_3$
Modified first invariant of effective stresses tensor in modified Lade in MPa	$I''_1$
Modified third invariant of effective stresses tensor in modified Lade in MPa	$I''_3$
Mean stress in MPa	$\sigma_{\text{mean}}$
Vertical component of virgin stress expressed in MPa	$\sigma_v$
Uniaxial tensile strength of the rock in MPa	$T_o$
Major, intermediate, and minor principal strain, respectively	$\varepsilon_1, \varepsilon_2$ and $\varepsilon_3$
Volumetric strain	$\varepsilon_{\text{vol}}$
Extension strain	$\varepsilon_e$
Extension strain critical value	$\varepsilon_{ec}$
Critical strain	$\varepsilon_0$
Maximum shear strain	$\gamma_{\text{max}}$
Critical shear strain	$\gamma_0$
Octahedral shear stress in MPa	$\tau_{\text{oct}}$
Excess shear stress in MPa	$ESS$
Uniaxial compressive strength (UCS) of rock in MPa	$C_{\text{ucs}}$
Rock mass unconfined compressive strength in MPa	$C_o$
Young's modulus in GPa	$E$
Modulus of longitudinal elasticity	$E_l$

Secant modulus of longitudinal elasticity	$E_{50}$
Secant modulus of shear	$G_{50}$
Poisson's ratio	$\nu$
Cohesion or inherent shear strength in MPa	$S_o$
Angle of internal friction in degrees	$\phi$
Atmospheric pressure	$p_a$
Pore fluid pressure	$P_p$
Biot's parameter	$\alpha$
Drucker–Prager material constant	$\lambda$
Drucker–Prager material constant	$k$
Second invariant of the stress deviator tensor	$J_2$
Lode angle in degrees	$\theta$
Major principal effective stress at failure for the 2D Hoek–Brown criterion	$\sigma'_{1\text{ }hb}$
Minor principal effective stress at failure for the 2D Hoek–Brown criterion	$\sigma'_{3\text{ }hb}$
Upper limit of confining stress	$\sigma'_{3max}$
Hoek–Brown material constant (intact rock)	$m_i$
Hoek–Brown material constant (rock mass)	$m_b$
Hoek–Brown material constant	$s$
Hoek–Brown material constant	$a$
Simplified Priest material constant	$\beta$
Simplified Priest material constant	$w$
Geological Strength Index	$GSI$
Disturbance factor	$D$
Coefficient of correlation	$r$

## **1 INTRODUCTION**

### **1.1 Background to the Research**

In the mining environment, many orebodies have well-defined boundaries between the ore and the waste rock. The orebody is the rock, which carries a mineral/metal that is mined for both economic and material use. The country or waste rock is the uneconomical rock in which the orebody is hosted.

In such orebodies, the introduction of waste due to overbreak rock into the ore dilutes the grade. This is called dilution. With massive disseminated orebodies, dilution is not problematic, but in orebodies with well-defined boundaries, it can have a major impact on the economics of mining due to internal waste rock. In open stoping mining methods<sup>1</sup> the aim is to extract only the ore, leaving the waste behind. This is rarely achieved.

A study undertaken in Canada twenty years ago (Pakalnis et al, 1995), found that approximately 51% of all underground metal mines utilised open stoping mining methods during this period. From surveys conducted at these mines, it was found that the open stopes experienced dilution of up to 20% and sometimes in excess of this. At that time it was significant, since dilution of that magnitude had a significant economic impact on any mining venture (Pakalnis et al, 1995). Research carried out in Australia by Capes (2009) came to the same conclusion.

### **1.2 Justification for the research**

In South African underground gold mines that utilize open stoping mining methods, dilution also has a significant effect on the viability of the mining ventures. At Target mine it was identified that in a number of open stopes the dilution was in excess of 10%, which could have a negative impact on the mine's future.

---

<sup>1</sup> See definition in section 4.3

Dilution of any amount can result in a reduction of the recovered grade. In the case of Target Mine, dilution in excess of 10% can result in the reduction of the recovered grade from 5,5 grams per ton (g/t) to 4,5 g/t. The reduction of 1 g/t in recovered grade results in a loss of about ZAR21 Million per month at the current production levels of 70 000 tons per month extracted. When considered over the life of mine it could amount to a loss of about ZAR3,3 Billion. The opposite can be achieved by increasing the recovered grade. If dilution has such a significant effect on the future of a mining venture, how can dilution be reduced and or forward calculated?

Capes (2009) briefly discussed the costs of dilution, found that it was significant, and increases the cost of both the mining and milling operations. The direct costs associated with dilution are primarily due to the removal of the additional waste material. These costs consist of hauling, transport, crushing, hoisting and milling of waste rock, as well as the additional demands for backfill (Capes, 2009). However, the indirect cost associated with damage to equipment due to falls of ground in open stopes during mucking is neglected. These falls of ground also contribute to dilution significantly. These direct and indirect costs will be discussed in section 4.4.

To date research into the prediction of dilution in open stopes has been undertaken by Potvin (1988); Clark and Pakalnis (1997); Clark (1998); Sutton (1998); Wang (2004); Brady et al. (2005); and Capes (2009) to name a few. Based on this research, dilution can be predicted to some extent, but not with great accuracy.

If the open stope dilution is overestimated, it may result in not mining the stope, since it will be assumed to be uneconomic. For stopes where the dilution is underestimated, it can result in a significant loss in profit. With the current economic situation in South Africa, the need for a method of calculating dilution in open stopes with accuracy is justified.

### 1.3 Research Objectives

The aim and objectives of this thesis will be to develop a method of calculating dilution in open stopes, to be able to determine the expected failure depth into the hangingwall and sidewalls of open stopes with a good degree of certainty. With the methods currently available, this cannot be done with certainty. Using the obtained predictions for failure into the open stopes, the hangingwall and sidewalls of these stopes can then be redesigned to “fail” up to the required stope shape.

The optimization of back analyses for calculating expected dilution in open stoping could have a significant effect in assisting in the reduction of dilution in massive open stopes. Currently in the mining industry, there is a significant amount of data available, which could be used to develop suitable back analysis techniques, but it is not being utilized efficiently at present.

This thesis will:

- Define dilution in the open stope mining environment;
- Discuss the Cavity Monitoring System (CMS) and its use;
- Discuss measurement of actual dilution;
- Discuss the modelling of dilution;
- Define hydraulic radius;
- Discuss the site used for data collection with reference to the geological setting and its orebody;
- Define rock mass classification and its use in determining dilution;
- Determine and define the existing techniques for predicting overbreak and dilution in open stope mining, making use of the modified stability number  $N'$  and equivalent linear overbreak slough (ELOS);
- Discuss the different failure criteria and parameters that could be used to determine the expected failure around open stopes;
- Discuss the effect of blasting vibrations on open stopes and dilution;
- Discuss the current planning process and develop a new thinking framework if required;
- Determine the cost implication of dilution in open stopes;

- Determine the modes and mechanisms of dilution in open stopes;
- Determine a new open stope design methodology;
- Develop a method of calculating the expected overbreak into the hangingwall and sidewalls of open stopes;
- Develop a method of calculating the expected dilution with accuracy;

#### **1.4 Research Methodology**

Dyson (2009) said, *"Every model has to be compared to the real world and, if you can't do that, then don't believe the model"*. Consequently, twenty-eight case studies were selected with sufficient information for the research. In this research, three design methods for underground excavation design will be used:

- a) Empirical methods
- b) Analytical methods
- c) Numerical modelling methods

Empirical design methods involve making use of design criteria and design lines, which are estimated from the analysis of field data for case studies, coupled with engineering judgement. Determining the material strength and loads around excavations, and then applying a failure criterion to establish the stability, describes analytical design methods. Simulating the induced stress distribution around the open stopes, and then applying a failure criterion to establish the stability, represents numerical modelling methods (Wang, 2004).

Rockmass properties, rockmass classifications, blast design, blast techniques, the stress strain environment and hydraulic radius all have some effect on, or play a part in, the evaluation of dilution. This thesis will investigate factors that are responsible for initiating instability in open stopes, to determine the modes and mechanisms of dilution in open stopes and to develop a method of calculating the expected dilution in open stopes.

This will be done as follows for each case study:

- Obtain the actual planned stope volumes;
- Obtain the CMS results;
- Determine the rock mass classification making use of  $Q'$ ;
- Obtain the relevant jointing statistics;
- Calculate the hydraulic radius of the open stope;
- Determine the failure depth into the hangingwall and sidewalls of the open stopes making use of Phase2<sup>2</sup>;
- Determine the failure depth into the hangingwall of the open stopes making use of JBlock<sup>3</sup>;
- Making use of Map3D<sup>4</sup> determine the Major  $\sigma_1$ , intermediate  $\sigma_2$ , and minor  $\sigma_3$  principal stresses, respectively in MPa;
- Making use of Map3D determine the Major  $\varepsilon_1$ , intermediate  $\varepsilon_2$ , and minor  $\varepsilon_3$  principal strains, respectively;
- Determine the modified stability number,  $N'$ ;
- Determine the equivalent linear overbreak slough (ELOS);
- Plot and evaluate the modified stability number,  $N'$  and hydraulic radius results on the stability diagram after Potvin (1988);
- Plot and evaluate the ELOS results on the dilution diagram after Clark and Pakalnis (1997);
- Evaluate the effects of the obtained major, intermediate, and minor principal stresses, respectively in MPa using the failure criteria discussed in section 2.5;
- Evaluate the obtained mean stress<sup>5</sup> and volumetric strain<sup>5</sup>;

## 1.5 Research Contribution

The research will contribute to the understanding of rock behaviour in an open stope environment and the design methodology that could be followed to reduce dilution. Failure depth into the hangingwall and sidewalls of open stopes can be predicted and the calculation of dilution for use in mine design will be done with greater certainty.

<sup>2</sup> See definition in section 6.1.2

<sup>3</sup> See definition in section 6.1.3

<sup>4</sup> See definition in section 6.1.4

<sup>5</sup> See definition in section 5.3

## 1.6 Facilities

Numerical modelling will be used to investigate the mode and mechanism of failure in these open stopes. The following numerical modelling programs, Map3D, Phase2 and JBlock, will be used for conducting back analyses of the open stopes. Making use of Dips, geological data such as joint orientation and the effect thereof on open stope sidewalls, can be simulated (Rocscience, 2015). Target Mine will be used for the case studies as most of the open stopes are situated in different stress environments due to the de-stressing<sup>6</sup> of these stopes and their positions relative to these destressing excavations. The stress environment for the major principal stress  $\sigma_1$  at the position for the planned open stopes ranges from <10MPa to >100MPa.

## 1.7 Thesis Outline

The following paragraph describes the layout of this thesis. Chapter 1 is an introduction. It discusses the background to the research, justification for the research, research objectives, research methodology, research contribution and facilities used. It finally gives an outline of the entire thesis. Chapter 2 gives a literature review on dilution design methods and open stope stability in order to establish the theoretical support of the problem under consideration. In Chapter 3, the background to the site used for data collection is discussed, with general information on the geological setting of the Free State and geology of Target Mine.

Chapter 4 discusses the empirical database, general open stope information, and financial implications of dilution and overbreak on open stopes. The nature and magnitude of dilution will be discussed, highlighting factors initiating instability in open stopes. In Chapter 5 the dilution factor and dilution prediction methods being used in the mining industry will be discussed, as well as the measurement of dilution in open stopes. In Chapter 6 the influence of stress on open stope hangingwall stability and dilution, modelling methodology and the application of different modelling programs such as Dips, Phase2, JBlock and

---

<sup>6</sup> See definition in section 3.6



Map3D will be discussed. Finally, the failure criteria will be applied to the obtained Map3D results.

Chapter 7 will discuss the influence of stress and strain on open stope hangingwall stability and dilution. The application of mean stress and volumetric strain will be evaluated and the newly developed Dilution Stress-Strain Index (DSSI) design criterion will be applied to the case studies, and the results compared to other dilution criteria. Chapter 8 will give a summary and discuss the contribution to knowledge, future work, limitations and lessons learnt during this research.

## 2 LITERATURE REVIEW ON DILUTION DESIGN METHODS AND OPEN STOPE STABILITY

### 2.1 Introduction

Chapter 1 gave a brief overview on the process to be followed in this thesis. In this chapter, a literature review will be presented, explaining the various definitions for dilution, Cavity Monitoring (CMS), measurement of actual dilution underground, modelling of dilution, Hydraulic Radius, Rock Mass Classification, Equivalent Linear Overbreak Slough (ELOS), various failure criteria, the effect of blasting, and the influence of each on the stability of massive open stopes.

### 2.2 Definition of dilution

During the preliminary literature review, it was found that very little research has been carried out regarding dilution in open stopes. Dilution is defined as waste, subgrade rock or backfill that is, by necessity, removed along with the ore in the mining process, subsequently lowering the grade of the ore (Henning and Mitri, 2007). Dilution is measured and recorded on a routine basis by mines, but is not determined in a consistent manner.

Numerous expressions are used to define dilution (Pakalnis et al, 1995):

- a)  $\text{Dilution} = (\text{Tonnes waste mined})/(\text{Tonnes ore mined})$
- b)  $\text{Dilution} = (\text{Tonnes waste mined})/(\text{Tonnes ore mined} + \text{Tonnes waste mined})$
- c)  $\text{Dilution} = (\text{Undiluted in-situ grade reserves})/(\text{Mill head grades obtained for same tonnage})$
- d)  $\text{Dilution} = (\text{Undiluted in-situ grade as derived from drill holes})/(\text{Sample assay grade at draw point})$
- e)  $\text{Dilution} = (\text{Tonnage mucked} - \text{Tonnage blasted})/(\text{Tonnage blasted})$
- f)  $\text{Dilution} = ("x" \text{ amount of metres of footwall over break} + "y" \text{ amount of hanging wall over break})/(\text{ore width})$

- g) Dilution = Difference between backfill tonnage actually placed and theoretically required to fill void
- h) Dilution = Dilution visually observed and assessed
- i) Dilution = (Tonnes drawn from stopes)/(Calculated reserve tonnage) over last ten years

It was found by Pakalnis et al (1995) that the most widely used definitions for calculating dilution are equations (a) and (b) as shown above. For an orebody with a width of "x" metres from the footwall to hangingwall, having "y" metres of overbreak as shown in Figure 2.1, and the depth of overbreak is equal to the orebody width, this results in dilution of 100% when using equation (a) and 50% when using Equation (b). The maximum dilution that can be calculated utilizing Equation (b) is 100%. The use of Equation (a) is recommended as a standard measure of dilution in Canadian mines (Pakalnis et al (1995)).

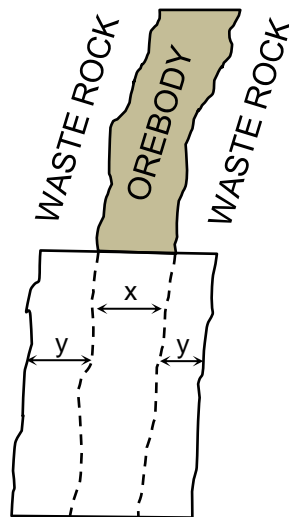


Figure 2.1 Diagram illustrating dilution in an open stope

Shekhovtsov (1994) developed a procedure for determining ore losses and dilution in working deposits with a complicated geological structure. This is one of the few publications dealing with dilution, and the method is summarised below. The term "waste" refers to the external dilution or unplanned dilution that is mined, whereas "ore" refers to that which is expected to be mined. The

complexity of ore masses is evaluated by factors for an irregular orebody  $K_{tw}$  and the amount of rock  $K_r$ , according to the Equations (2.1) and (2.2)

$$K_{tw} = \frac{l_c}{(\sum_1^{n_s} \frac{m}{n_s}) h_s} \quad (2.1)$$

$$K_r = \frac{\sum_1^{n_{r,i}} \bar{m}_{r,i} l_{r,i}}{0,01 \bar{m}_o h_s} \quad (2.2)$$

where  $l_c$  is the contact length of the ore body in a section within an open stope in metres,  $m$ ;  $m_r$  are particular values for the ore body thickness in metres,  $m$ ;  $n_s$  is the number of particular values in an open stope;  $h_s$  is open stope height in metres;  $n_{r,i}$  is the number of rock interlayers;  $\bar{m}_{r,i}$  is the average rock interlayer thickness,  $m$ ;  $l_{r,i}$  is the rock interlayer length (height in metres),  $m$ ;  $\bar{m}_o$  is the average ore body thickness in metres,  $m$ . For complex ore bodies it was suggested that dilution be determined using the following method: the optimum extraction contour as shown in Figure 2.2 is determined on the basis of the generally accepted criterion of maximum profit for 1 ton of used balanced reserves. In Figure 2.2, 1 represents the ore; 2 the internal waste rock band; 3 the ore body contours and 4 the optimum open stope dimension. Over and under breaking of the ore-body are shown in Figure 2.2. The expected orebody losses  $\delta_L$  and dilution  $\delta_R$  can be determined using Equations (2.3) and (2.4)

$$\delta_L = \frac{\sum_{i=1}^n \delta_i h_i}{\sum_{i=1}^n h_i} \quad (2.3)$$

$$\delta_R = \frac{\sum_{j=1}^n \delta_j h_j}{\sum_{j=1}^n h_j} \quad (2.4)$$

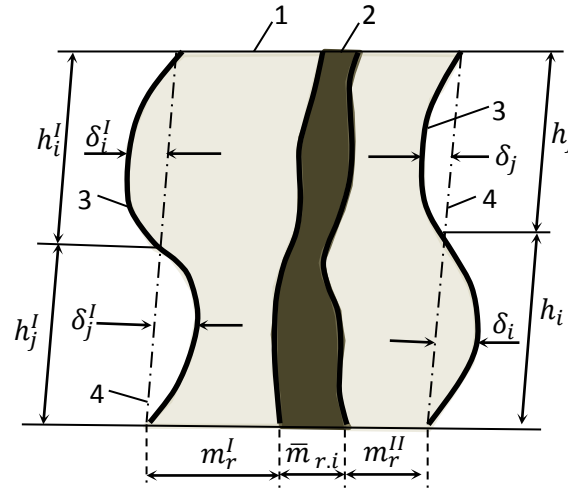


Figure 2.2 Diagram for determining dilution in an ore body with a complex structure (Shekhovtsov, 1994)

where  $n$  is the number of linear measurements  $\delta_i$  and  $\delta_j$  in the direction of losses and dilution respectively with intervals  $h_i$  and  $h_j$  (see Figure 2.2).

Ore losses and dilution at the contact with surrounding waste are determined by Equations (2.5) and (2.6), taking into account drilling and blasting parameters

$$L_c = \frac{\delta_L + 0,51gW + 3d_c}{0,01m_o} \quad (2.5)$$

$$R_c = \frac{(\delta_R - 0,51gW + 3d_c)\gamma_r}{0,01(m_o\gamma_o + \delta_R\gamma_r)} \quad (2.6)$$

where  $\gamma_o$ ,  $\gamma_r$  are the ore and waste rock densities respectively in tons/m<sup>3</sup>;  $W$  is line of least resistance (burden between blast holes) in metres, m;  $d_c$  is explosive charge (blast hole) diameter in metres, m. Average ore thickness in metres  $m_o$  is determined from the expression

$$m_o = \sum_1^n m_i / n \quad (2.7)$$

where  $m_i$  are special values of thickness in metres,  $m$ . In order to retain the optimum extraction design contour, it is necessary to place surrounding blast holes parallel to the contour at a distance of about 0,1m of the line of least resistance.

Ore dilution  $R_{in}$  is determined by the equation

$$R_{in} = \frac{\bar{m}_{r,i}\gamma_o}{0,01(\bar{m}_o\gamma_o + \bar{m}_{r,i}\gamma_o)} \quad (2.8)$$

The average thickness of unconditioned interlayers in metres  $\bar{m}_{r,i}$  is determined by the expression

$$m_{r,i} = \sum_i^n m_j / n \quad (2.9)$$

where  $m_j$  are particular values of thickness of interlayers in metres,  $m$ .

## 2.3 Quantifying Dilution using the Cavity Monitoring System

### 2.3.1 Cavity Monitoring System (CMS)

One of the major problems generally encountered was to quantify dilution that occurred in open stopes. This was due to these stopes being a no entry zone for people, making it difficult to obtain accurate measurements. With the introduction of laser survey systems, this problem was solved and has provided a valuable tool to determine underground excavation volumes precisely and efficiently (Miller et al, 1993). The CMS instrument employs a laser survey integrated within a motorized scanning head. The CMS can be suspended in a stope, mounted on a tripod or inserted down a borehole (Zhou-quan et al, 2008). As the CMS rotates the laser rangefinder, a three-dimensional stope outline is generated. This three-dimensional outline is then imported into STOPECAD from which a volume can be determined.

### 2.3.2 Measurement of Actual Dilution

Using the actual stope volume generated by the CMS and subtracting the actual and planned volumes of extraction from one another, the amount of over breaking can be determined (Pakalnis et al, 1995). The rate of dilution depends on the grade distribution and geometry in the deposit, and on the nature of the mining method being applied. Selective mining methods such as sub-level

stoping with backfill or selective open stope mining normally result in a lower rate of dilution when compared to bulk mining such as block caving (Mult et al, 2008).

Elbrond (1994) compiled dilution and mining loss factors for various mining methods and it was found that dilution varied between 5% and 30%. Mult et al (2008) recommended the use of an average dilution rate of 10% during the exploration stage, which was considered appropriate. The definition of grades sometimes includes “ROM” which stands for “run-of-mine”, meaning the grade after dilution (Mult et al, 2008).

To measure the amount of dilution in an open stope, the planned stope volume in  $\text{m}^3$  is subtracted from the measured final stope volume in  $\text{m}^3$ , which is obtained from the CMS. This is in turn divided by the planned stope volume in  $\text{m}^3$  to determine the percentage overbreak. The obtained CMS wireframe is imported into the geological model and re-evaluated for grade. From this, the percentage dilution for the open stope can be calculated. The dilution obtained can result in a major reduction of recovered grade for the open stope.

## **2.4 Empirical Open Stope Stability and Dilution Design Methods**

### **2.4.1 Hydraulic Radius**

Hydraulic radius is commonly used in massive mining operations as a measure of the size of the extraction area in plan view where the stability for a given rock mass with certain geotechnical characteristics is estimated. The hydraulic radius of an open stope can be calculated as the area of the hangingwall divided by its perimeter. As the hydraulic radius of an open stope increases, the larger the exposed roof area and the more unstable the hangingwall beam becomes. The reason for this is that the beams become less self-supporting, become unstable and eventually fall out under gravity. The result of this is dilution in the stope. Depending on the dip of the orebody, the hydraulic radius may be calculated for the hangingwall and crown of the stope as explained by Brown (2000).

### 2.4.2 Rock Mass Classification

It is acceptable practice to determine the intact rock strength by subjecting it to laboratory tests. However, the rockmass strength is usually weaker as it contains geological structures and planes of weakness such as faults, dykes, joints and stress induced fractures. The stability of an excavation in a jointed rock mass can be influenced by many factors including:

- frequency of jointing
- joint strength
- strength of rock material
- presence of water
- confining stress
- blasting practice

The effect of these factors on the rock mass strength can be taken into account by applying rock mass classification methods (Stacey, 2001).

The two most commonly used classification methods are the Q System developed by Barton et al (1974) and the Geomechanics Classification System developed by Bieniawski (1989). A Geomechanics Classification System was developed specifically for mining applications (Laubscher and Taylor, 1976) and was later refined by Laubscher (1990). The Q system was adapted by Potvin (1988) for use in the evaluation of the stability of open stopes.

### 2.4.3 Modified Stability Number, $N'$

The Modified Stability Number,  $N'$  (Potvin, 1988) was introduced as a modification of the Q System (Barton et al, 1974). It excludes the Q System's Stress Reduction Factor ( $SRF$ ) and includes three specific multiplying factors, which take into account joint orientation, gravity, and rock stress. Initially  $Q'$ , as shown in Equation (2.10), is calculated as:



$$Q' = \left( \frac{RQD}{J_n} \right) \left( \frac{J_r}{J_a} \right) J_w \quad (2.10)$$

In most of the open stopes on Target Mine, dry conditions ( $J_w = 1$ ) are experienced and then  $Q'$  is then expressed as:

$$Q' = \left( \frac{RQD}{J_n} \right) \left( \frac{J_r}{J_a} \right) \quad (2.11)$$

Making use of this relationship an empirical method for open stope design was proposed by Mathews et al (1981). Potvin (1988) modified the method based on more field data, resulting in the stability graph method, which is widely accepted by the Canadian mining industry utilizing open stope mining methods. The Stability Graph links a stability number,  $N'$ , to the hydraulic radius of the open stope hangingwall as shown in Figure 2.4.

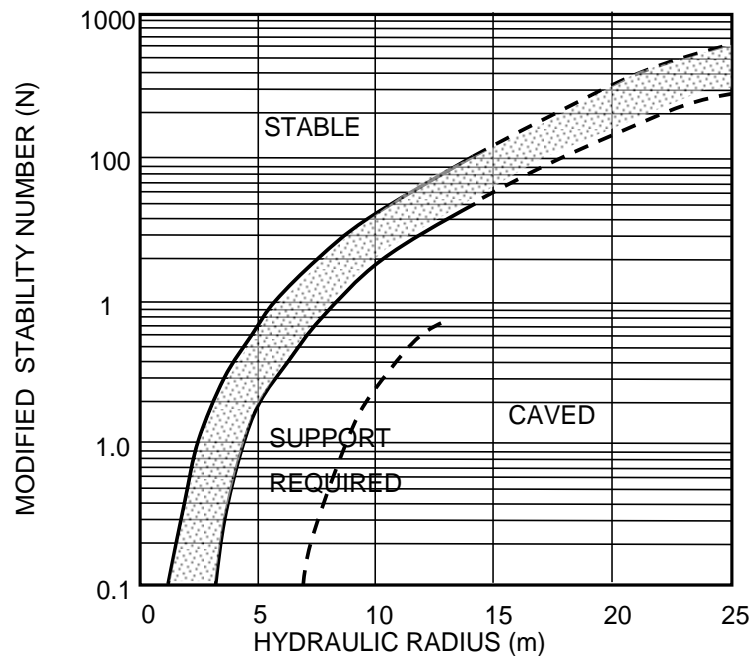


Figure 2.4 Modified stability graph (Potvin, 1988)

The modified stability number  $N'$  is calculated as:

$$N' = Q' \times A \times B \times C$$

A is the stress factor that was modified by Potvin (1988) from a rule of thumb by Mathews et al (1981), which was an attempt to account for the effect of stress in open stope design. The values of A, B, and C are described graphically in the Figures 2.5, 2.6, 2.7 and described in the following paragraphs.

The A-factor can be expressed as the relationship between the intact rock Uniaxial Compressive Strength (UCS)  $C_{ucs}$  and induced stress in the hangingwall to account for any compressive failure. If the obtained value for A is 1, the hangingwall is assumed to be in relaxation or tension as shown in Figure 2.5.

A is given by:

$$A = 1.125R - 0.125 \quad 1 > A > 0.1$$

where  $R$  is the ratio of the  $C_{ucs}$  of the rock material to the maximum induced compressive stress. The maximum induced compressive stress is determined by numerical stress analyses.

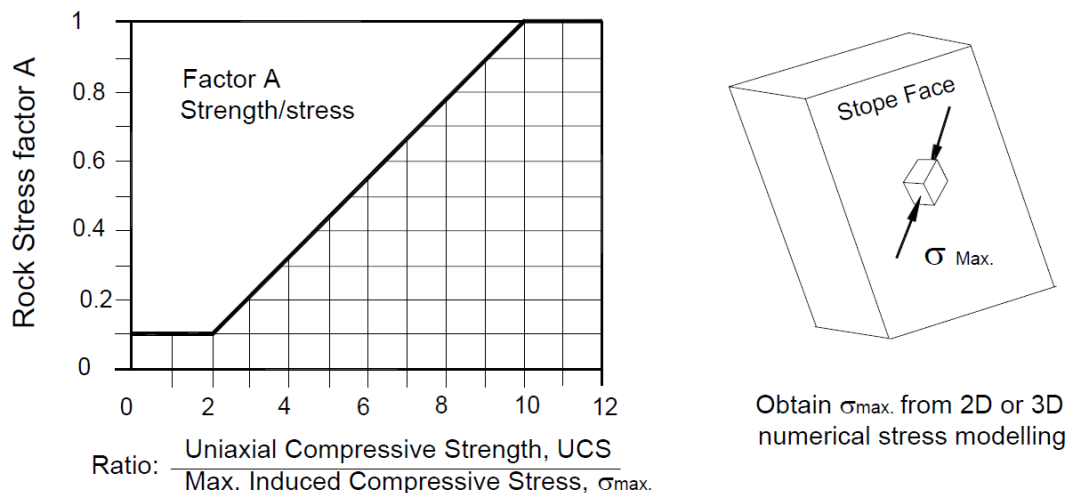


Figure 2.5 Stability Graph Factor A (After Potvin, 1988; from Hutchinson and Diederichs, 1996)

$B$  is a factor, which describes the ease of keyblock fallouts.  $B$  is given by the following equations:

$$\begin{aligned}
 B &= 0.3 - 0.01 & \alpha < 10 \\
 B &= 0.2 & 10 < \alpha < 30 \\
 B &= 0.02\alpha - 0.4 & 30 < \alpha < 60 \\
 B &= 0.0067\alpha + 0.4 & 60 < \alpha < 90
 \end{aligned}$$

where  $\alpha$  is the true angle between the hangingwall surface of the excavation and the joint plane. In the case of numerous joint planes, the smallest angle is applicable. The true angle between the hangingwall surface of the excavation and the joint plane is generally determined using a stereonet as shown in Figure 2.6.

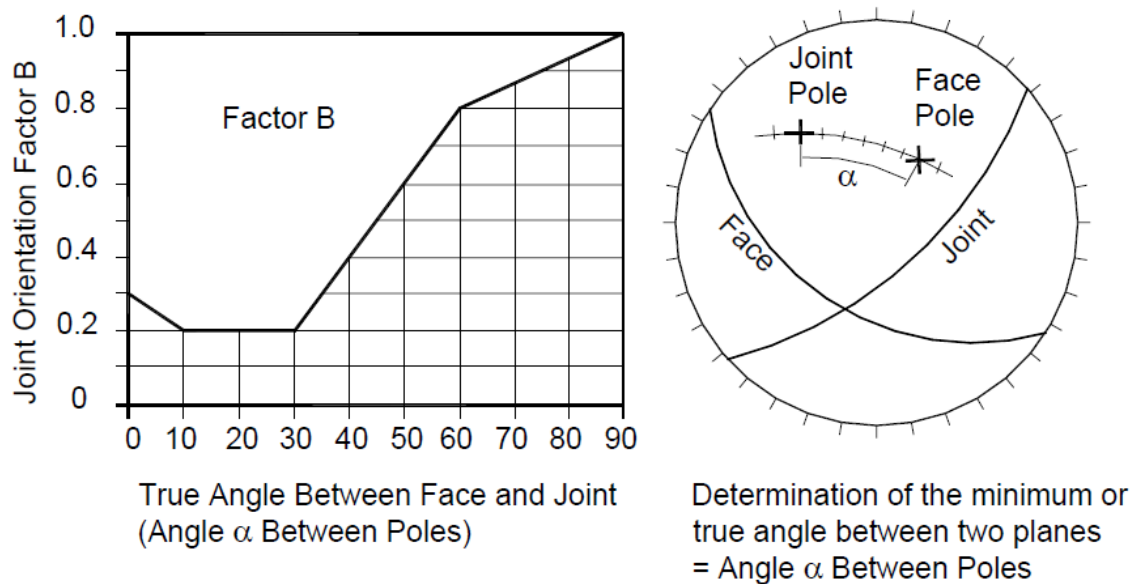


Figure 2.6 Stability Graph Factor B (After Potvin, 1988; from Hutchinson and Diederichs, 1996)

$C$  is the gravitational adjustment factor as shown in Figure 2.7. In the case of gravity falls and slabbing where sliding on joints is not applicable, the factor is given by the following equation:

$$C = 8 - 6 \cos (\text{Dip of stope face})$$

If sliding on joints can be expected, the gravity adjustment factor is given by the following equations:

$$C = 8$$

$$C = 11 - 0.1 (\text{Dip of critical joint})$$

$$\text{Dip of critical joint} < 30^\circ$$

$$\text{Dip of critical joint} > 30^\circ$$

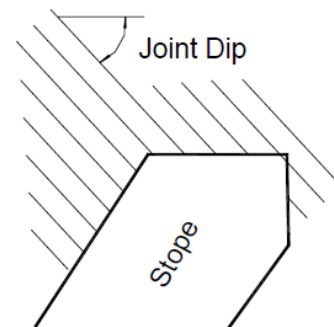
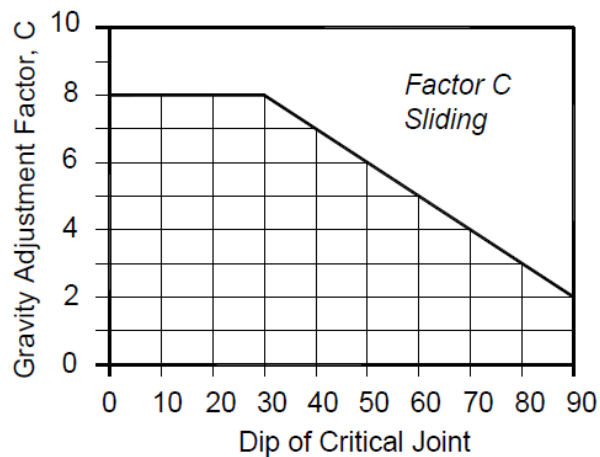
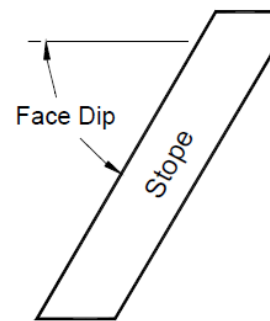
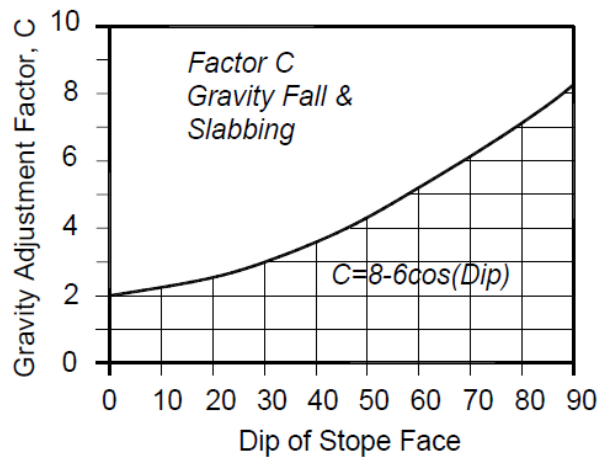


Figure 2.7 Stability Graph Factor C (After Potvin, 1988; from Hutchinson and Diederichs, 1996)

According to Pakalnis et al (1995), the stability graph method is subjective. Research carried out by Pakalnis et al (1995) to quantify the observed stability in terms of dilution values and assessed by survey methods, led to the Dilution Approach as shown in Figure 2.8. The design graph shown in Figure 2.8 compares a stability number, which incorporates the relationship between the excavation geometry, the rock mass quality and the maximum induced compressive stress to estimate the open stope stability. The obtained dilution for each case study is plotted on the graph. This was used to determine the

average percentage dilution that could be expected for open stopes with a specific modified stability number and hydraulic radius.

Rock mass classification systems used for input into open stope stability design do not directly incorporate the response of intact rock properties under different loading conditions according to Potvin (1988). This is due to the consideration that rock engineering is a discipline where input parameters such as loading conditions and material strength are difficult to determine on a mine wide scale. The opening geometry is represented by a term called the shape factor or hydraulic radius (Potvin, 1988).

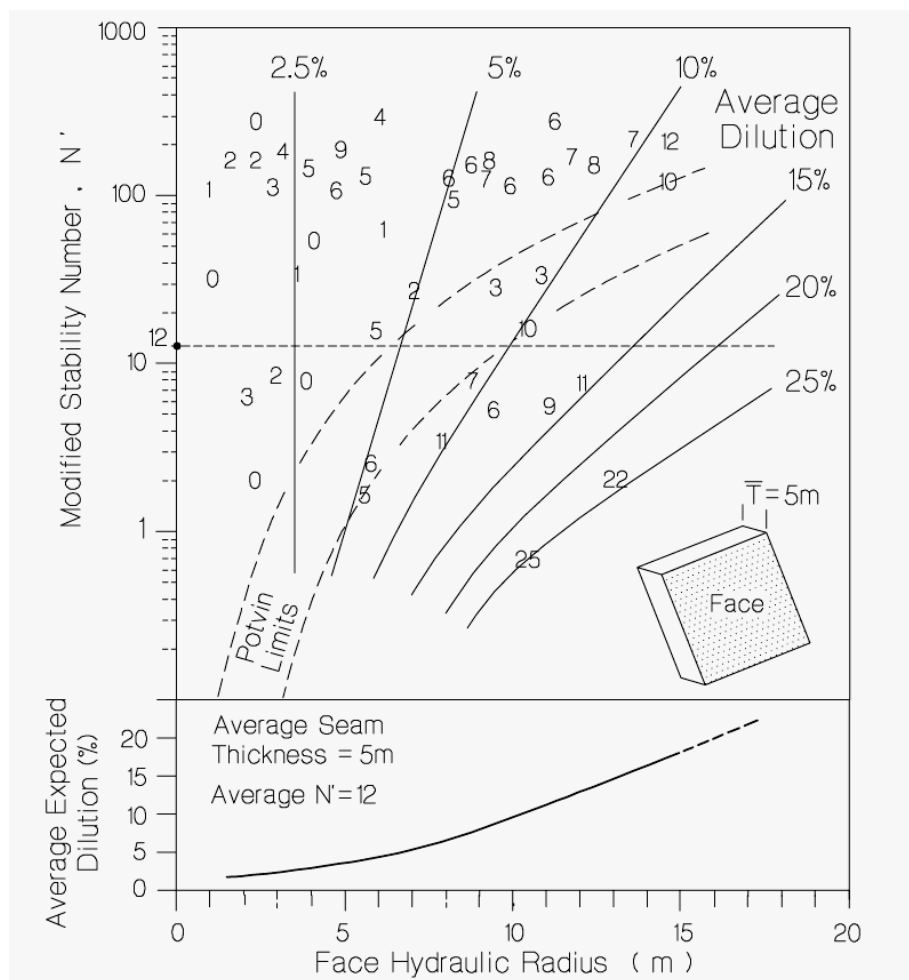


Figure 2.8 Site-specific average expected dilution data from Pakalnis et al (1995)

#### 2.4.4 Equivalent Linear Overbreak Slough (ELOS)

The potential for dilution can be determined from design charts proposed by Clark and Pakalnis (1997) or Capes (2009) as shown in Figure 2.10 and Figure 2.12 respectively. The Equivalent Linear Overbreak Slough (ELOS) is graphically illustrated in Figure 2.9 and is defined as:

$$ELOS = \frac{\text{equivalent linear overbreak}}{\text{slough}} = \frac{\text{volume of slough from stope surface}}{\text{stope height} \times \text{wall strike length}}$$

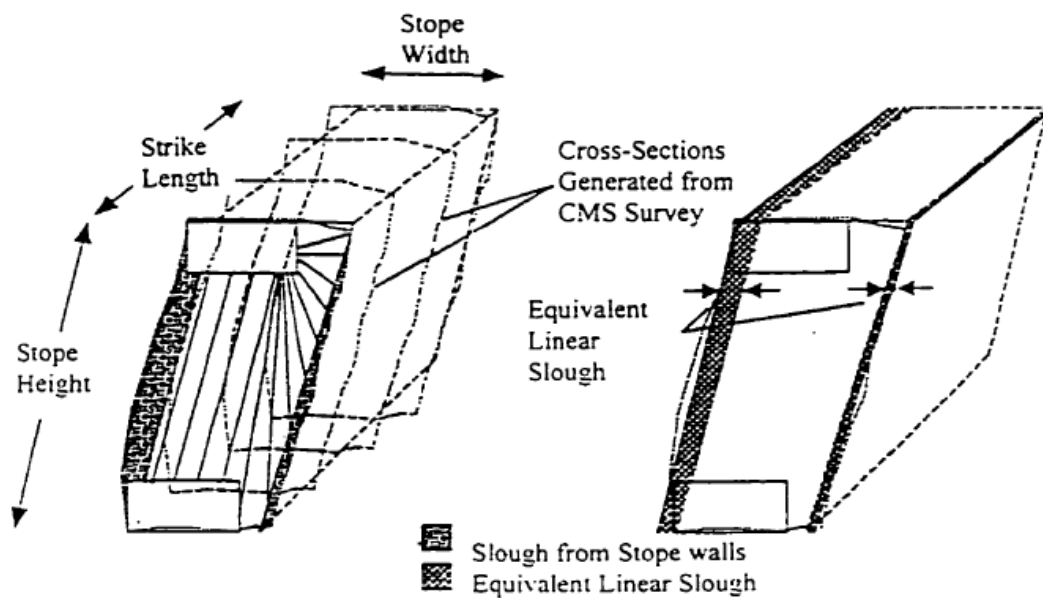


Figure 2.9 Equivalent Linear Overbreak/Slough (ELOS), (Clark and Pakalnis, 1997)

Clark and Pakalnis (1997) developed the dilution graphs, which were then improved by Capes (2009) as an empirical design method, as shown in Figure 2.10 and Figure 2.11. The dilution graph is based on the Modified Stability Graph after Potvin (1988) and has been empirically calibrated so that the degree of stability is represented as the average metres of slough (ELOS) that can be expected to fail from the open stope hangingwall. An estimate of dilution is determined by plotting the modified stability number,  $N'$  versus the hydraulic radius of the open stope hangingwall being assessed (Clark and Pakalnis, 1997).

Wang et al (2002) stated that the dilution graph method ignores or poorly accounts for many factors such as irregular hangingwall geometry, undercutting of the open stope hangingwall and footwall, blasthole diameter, blasthole length and layout, blasthole offset, and stope life and number of blasts, all of which influence open stope dilution. It was also mentioned by Wang et al (2002) that stress is poorly accounted for in the dilution graph design method.

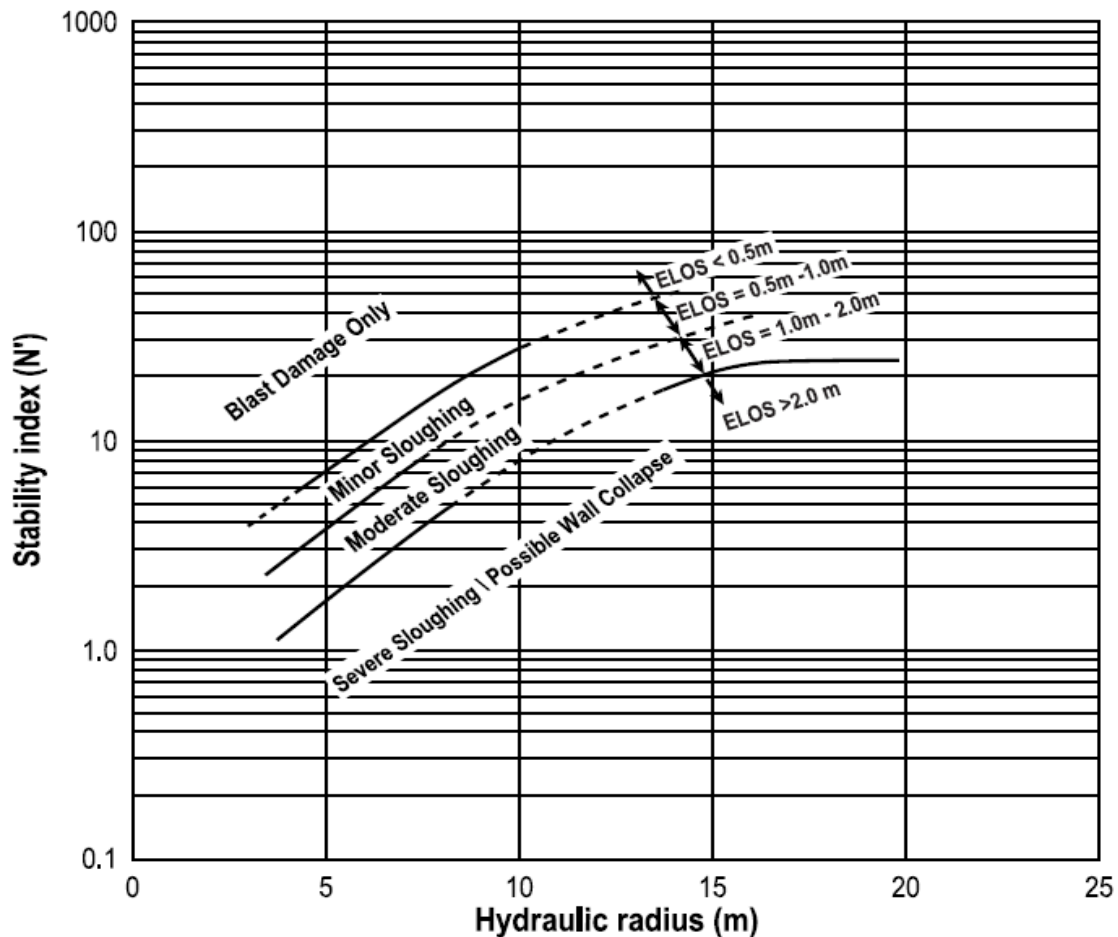


Figure 2.10 Estimation of Overbreak/Slough (ELOS) for non-supported hangingwalls and footwalls, after Clark and Pakalnis (1997)

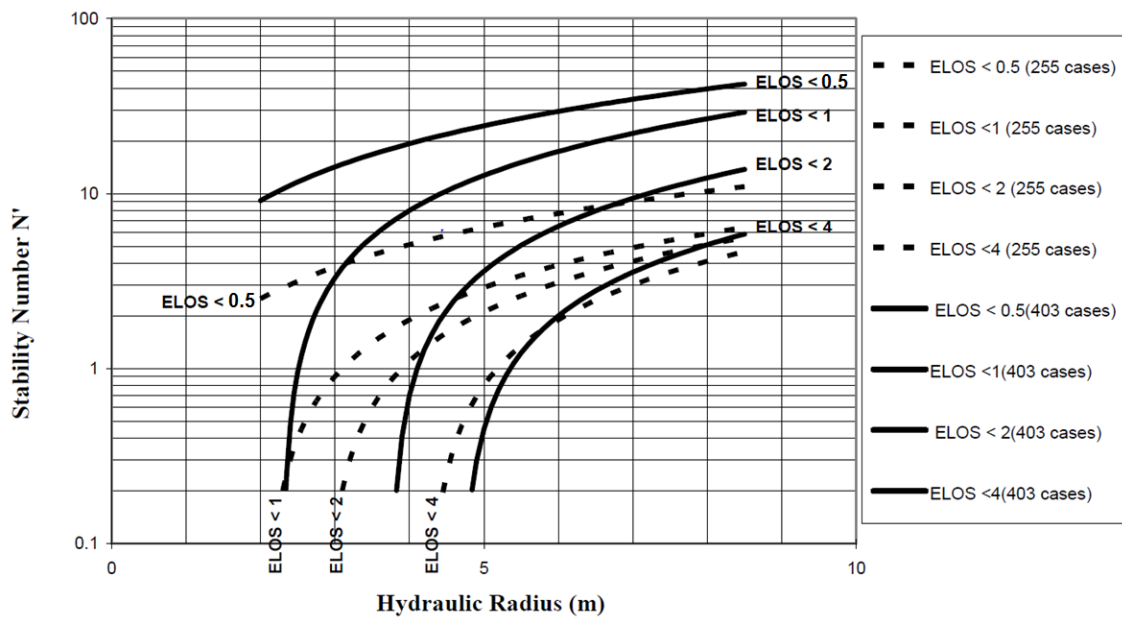


Figure 2.11 Empirical dilution design graph showing the original case histories used to create the graph, after Capes (2009)

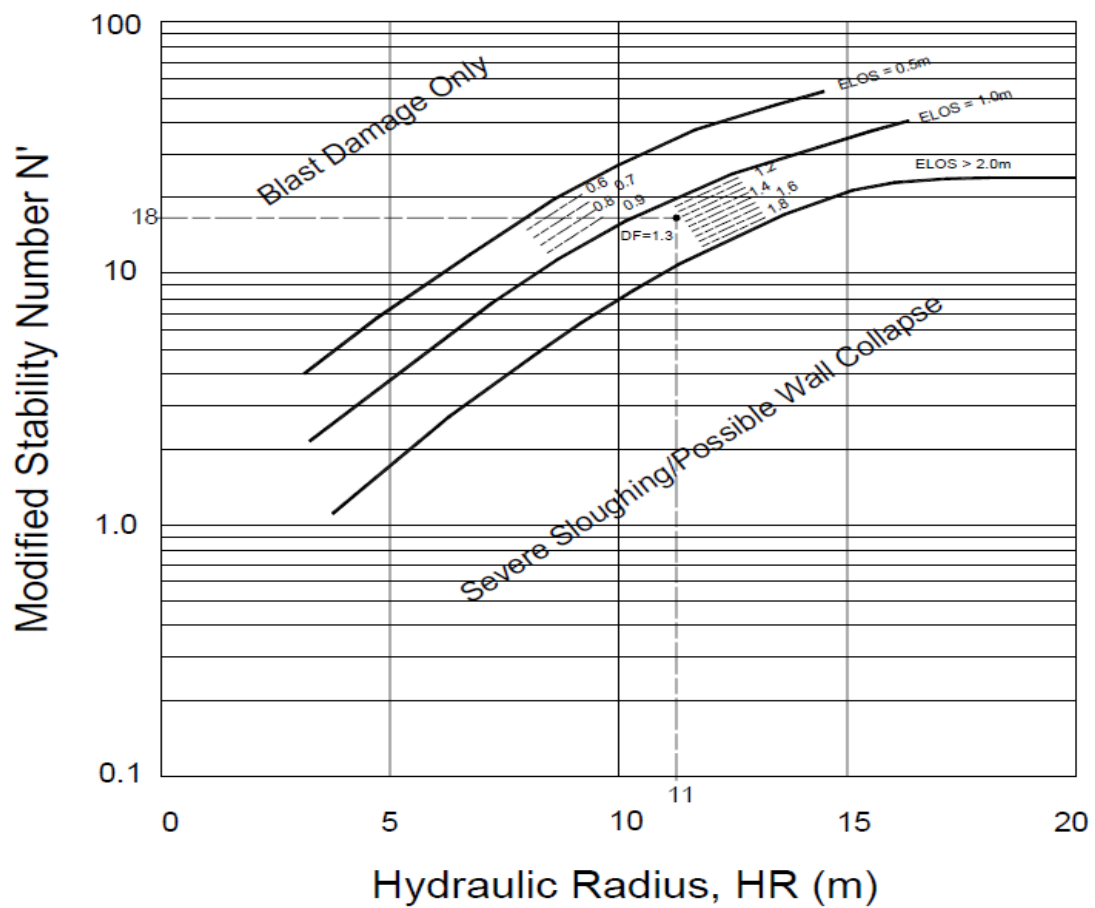


Figure 2.12 Illustration of the procedure for obtaining dilution factor, after Wang (2004)



The dilution factor is defined as the ELOS predicted from the dilution design graph based on the modified stability number,  $N'$  and hydraulic radius for an open stope. Figure 2.12 illustrates how the dilution factor is calculated. The dilution design zones between design lines, for example between ELOS = 1.0m and 2.0m, are divided into even divisions as shown in Figure 2.12. The estimated value obtained from the graph between the design lines is defined as the dilution factor parameter. For example, an open stope hangingwall with a modified stability number,  $N'$  of 18 and hydraulic radius of 11m will have a dilution factor of 1.3. This can be determined by reading the value from the intersection of the modified stability number,  $N'$  and hydraulic radius coordinates. The actual open stope ELOS may differ from the dilution factor value (Wang, 2004). Wang (2004) concluded in his research that the statistical analysis results indicated that the parameters which have a significant influence on open stope hangingwall ELOS are open stope hangingwall exposure time, hydraulic radius, modified stability number  $N'$  and open stope hangingwall undercutting factor. Stress was not included in the statistical analysis carried out by Wang (2004).

A conservative set of design lines was created by Capes (2009) that minimised the number of cases with greater failure than predicted for all of the design lines. According to Capes (2009), there were many improvements made to the dilution graph design lines from Clark (1998). Capes (2009) stated that the limitations of the modified dilution graph are the collected data, from which the new sets of design lines were created. Capes (2009) also stated that inaccurate overbreak predictions could occur if the new design lines were applied to a mine that had a significantly different mining environment.

## 2.5 Three-Dimensional Stress in the Mining Environment

To determine the components of stress on an arbitrarily oriented plane  $ABC$  whose orientation is defined by its normal  $x'$  is shown in Figure 2.13. The direction cosines of this normal, which is the cosines of the angles between the direction  $x'$  and the  $x$ ,  $y$  and  $z$ -axes, are  $\lambda_{xx}$ ,  $\lambda_{xy}$  and  $\lambda_{xz}$ , respectively. Ryder and Jager, (2002) illustrated that the areas of the triangles given in Figure 2.13 are related to the area  $ABC$  by

$$BOC = ABC \lambda_{xx}, AOC = ABC \lambda_{xy}, AOB = ABC \lambda_{xz}$$

The direction cosines  $\lambda_{xx}$ ,  $\lambda_{xy}$  and  $\lambda_{xz}$  are simply the projections on to the x, y, z-axes (i.e. the coordinates) of the endpoint of a unit vector from the origin  $O$  in the direction of  $x'$ . They are linked by the constraint  $\lambda_{xx}^2 + \lambda_{xy}^2 + \lambda_{xz}^2 = 1$  (Ryder and Jager, 2002).

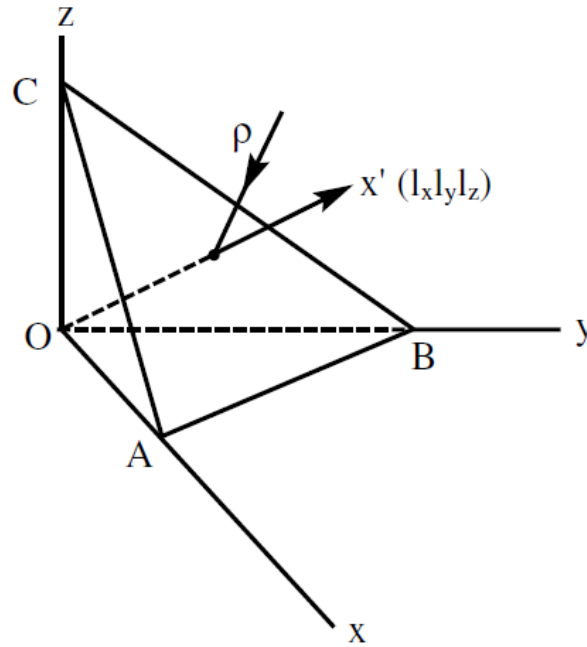


Figure 2.13 Illustration stress components on a tetrahedron in three dimensions, after Ryder and Jager (2002)

This equation  $\sigma_p^3 - I_1 \sigma_p^2 - I_2 \sigma_p - I_3 = 0$  defines the three principal stress values, irrespective of the orientation of the xyz Cartesian coordinate system as shown in Figure 2.13. Where on a principal plane, the traction vector  $p$  is normal to the plane and the three invariants are (Nadai, 1950); (Ryder and Jager, 2002)

$$I_1 = \sigma_{xx} + \sigma_{yy} + \sigma_{zz} = \sigma_1 + \sigma_2 + \sigma_3$$

$$I_2 = -(\sigma_{yy}\sigma_{zz} + \sigma_{zz}\sigma_{xx} + \sigma_{xx}\sigma_{yy}) + \tau_{yz}^2 + \tau_{zx}^2 + \tau_{xy}^2 = -(\sigma_2\sigma_3 + \sigma_3\sigma_1 + \sigma_1\sigma_2)$$

$$I_3 = \sigma_{xx}\sigma_{yy}\sigma_{zz} + 2\tau_{yz}\tau_{zx}\tau_{xy} - \sigma_{xx}\tau_{yz}^2 - \sigma_{yy}\tau_{zx}^2 - \sigma_{zz}\tau_{xy}^2 = \sigma_1\sigma_2\sigma_3$$

which imply that

$$\sigma_{xx}^2 + \sigma_{yy}^2 + \sigma_{zz}^2 + 2\tau_{yz}^2 + 2\tau_{zx}^2 + 2\tau_{xy}^2 = \sigma_1^2 + \sigma_2^2 + \sigma_3^2$$

The normal and shear stress on the plane whose normal  $\lambda_{xx} = \lambda_{xy} = \lambda_{xz} = 3^{-\frac{1}{2}}$  is equally inclined to the principal axes is called the octahedral plane, since it is parallel to a face of an octahedron with vertices on the principal axes. The octahedral normal stress (also called the mean normal stress  $\sigma_m$ ) is given by (Nadai, 1950); (Ryder and Jager, 2002)

$$\sigma_{oct} = \frac{1}{3}(\sigma_1 + \sigma_2 + \sigma_3) = \frac{1}{3} I_1$$

The invariants of stress are of importance since they can be used to express failure criteria (Ryder and Jager, 2002). A number of different criteria are considered in the sections below.

## 2.6 Failure Criteria used for Excavation Design

To understand the behaviour of the rockmass around open stopes, failure criteria are often used. If expected failure can be calculated the amount of expected dilution or overbreak can be determined using numerical analyses. Some of the failure criteria being used in rock engineering will be discussed. These criteria will include the Mohr-Coulomb criterion, Hoek-Brown criterion, Zhang-Zhu Criterion, Pan-Hudson Criterion, Priest Criterion, Simplified Priest Criterion and Drucker-Prager Criterion. The Mohr-Coulomb criterion and Hoek-Brown criterion are two-dimensional criteria in which the intermediate principal stress value is ignored. Three-dimensional criteria such as 3D Hoek-Brown criterion, Zhang-Zhu Criterion, Pan-Hudson Criterion, Priest Criterion, Simplified Priest Criterion and Drucker-Prager Criterion, include the intermediate stress value. In this chapter the theory relevant to these criteria will be reviewed and in section 6.2.5 these criteria will be critically reviewed when being applied to the numerical analyses results. Using these three-dimensional criteria, the influence of the intermediate stress value will be evaluated.

A failure criterion can be defined as the instance where the stress condition at which the ultimate strength of the rock is reached. Failure criteria can be expressed in terms of the major principal stress  $\sigma_1$  that rock can tolerate for a given value of intermediate principal stresses  $\sigma_2$  and minor principal stresses  $\sigma_3$  (Ulusay and Hudson, 2007). This is expressed as  $\sigma_1 = f_1(\sigma_2, \sigma_3)$  or  $f_2(\sigma_1, \sigma_2, \sigma_3) = 0$  in its most simplistic form (Scholz, 1990) where  $f_1$  or  $f_2$  are functions that vary with the selected criterion and can be determined from laboratory tests, theoretically or empirically.

In situ stress measurements at shallow to intermediate depths have shown that rock stresses are mostly anisotropic, i.e.,  $\sigma_1 \neq \sigma_2 \neq \sigma_3$  (Haimson, 1978); (McGarr and Gay, 1978); (Brace and Kohlstedt, 1980). Based on borehole breakout dimensions in crystalline rocks (Vernik and Zoback, 1992) and on calculations of the critical mud weight necessary to maintain wellbore stability (Ewy, 1998), it is shown that rock failure criteria should account for the effect on the strength of the intermediate principal stress. The first true-triaxial compressive tests on rocks, in which  $\sigma_1 \neq \sigma_2 \neq \sigma_3$ , were conducted by Mogi (1971). He subjected rocks to different intermediate principal compressive stresses for the same minor principal stress, and then raised the major principal stress to failure (Ulusay and Hudson, 2007). Mogi demonstrated that, for the rocks tested, strength was a function of  $\sigma_2$  in a manner similar to that predicted theoretically by Wiebols and Cook (1968). Wiebols, Cook and Mogi confirmed independently that the intermediate principal stress has a major effect on rock strength (Ulusay and Hudson, 2007).

### 2.6.1 Mohr-Coulomb Failure Criterion

The Mohr–Coulomb failure criterion is a set of linear equations in principal stress space describing the conditions for which an isotropic material will fail, irrespective of any effect from the intermediate principal stress  $\sigma_2$  being neglected (Ulusay and Hudson, 2007). Mohr–Coulomb failure can be written as a function of major  $\sigma_1$  and minor  $\sigma_3$  principal stresses, or normal stress  $\sigma_n$  and shear stress  $\tau$  on the failure plane (Jaeger and Cook, 1979).

When all of the principal stresses are compressive, the criterion applies reasonably well to rock and where the uniaxial compressive strength  $C_{ucs}$  is greater than the uniaxial tensile strength  $T_o$ , e.g.  $\frac{C_{ucs}}{T_o} > 10$ , some modification is needed (Ulusay and Hudson, 2007).

The Mohr–Coulomb failure criterion is considered as a contribution from Mohr and Coulomb (Nadai, 1950). Mohr's condition is based on the assumption that failure depends on  $\sigma_1$  and  $\sigma_3$ , and that the shape of the failure envelope, the loci of  $\sigma$ ,  $\tau$  acting on a failure plane, can be nonlinear or linear (Mohr, 1900). Coulomb's state is based on a linear failure envelope to determine the critical combination of  $\sigma$ ,  $\tau$  that will result in failure on some plane (Coulomb, 1776). Paul (1968) described a linear failure criterion with an intermediate stress effect, implemented by Meyer and Labuz (2012).

In the investigations of retaining walls by Coulomb (Heyman, 1972), the following relationship was proposed:

$$|\tau| = S_o + \sigma \tan \phi \quad (2.12)$$

where  $S_o$  is the inherent shear strength, also known as cohesion,  $\phi$  is the angle of internal friction, and the coefficient of internal friction  $\mu = \tan \phi$ . The criterion contains two material constants,  $\phi$  and  $S_o$ . The representation of Equation (2.12) in the Mohr diagram is a straight line inclined to the  $\sigma$ -axis by the angle  $\phi$  as shown in Figure 2.14.

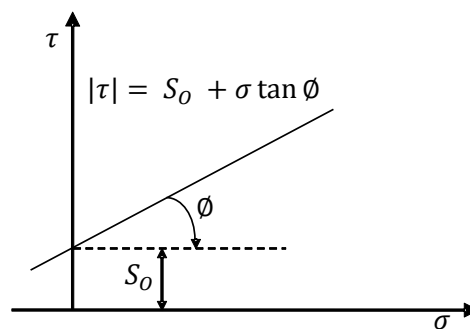


Figure 2.14 The Mohr-Coulomb failure criterion for shear failure (Brady and Brown, 1985)

Designing underground excavations utilizing numerical models can be difficult as they do not necessarily reflect the actual behaviour of the rock mass. In the case of brittle failure this is particularly true, the fundamental assumption of the Mohr-Coulomb criterion  $|\tau| = S_o + \mu\sigma$ , relating the cohesion  $S_o$  to a shear strength  $\tau$  and a simultaneously acting frictional resistance  $\mu\sigma$  not being valid according to Kaiser and Kim (2008). As intact rock is being strained, cohesive bonds start to fail, and only after this does frictional resistance develop. Damage initiation and propagation occur at different stress thresholds according to Diederichs (2003) and the propagation of tensile fractures depends on the level of confinement as established by Hoek (1968) and used to explain brittle failure.

Wiles (2006) explains that the Mohr-Coulomb failure criterion can also be mathematically expressed as shown in Equation (2.13):

$$\sigma_1 = q\sigma_3 + C_o \quad (2.13)$$

where  $\sigma_1$  and  $\sigma_3$  represent, respectively, the major and minor principal stresses,  $C_o$  and  $q$  represent, respectively, the rock mass unconfined compressive strength and slope of the best fit-line as shown in Figure 2.15.

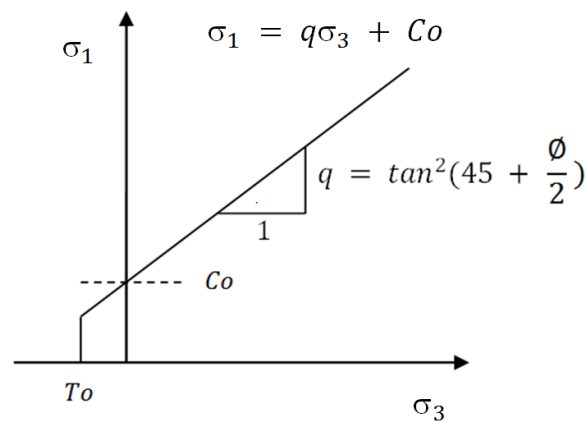


Figure 2.15 Alternative representation of the Mohr-Coulomb failure criterion (Wiles, 2006)

where  $q = \tan^2(45 + \frac{\phi}{2})$ ;  $\phi$  is the friction angle

## 2.7 Three-Dimensional Failure Criteria Based on the Mohr–Coulomb criterion

### 2.7.1 Drucker–Prager Criterion

Drucker and Prager (1952) developed the Drucker–Prager failure criterion as a generalization of the Mohr–Coulomb criterion for soils. The Drucker–Prager failure criterion is based on the assumption that the octahedral shear stress at failure depends linearly on the octahedral normal stress through material constants (Ulusay and Hudson, 2007). It can be expressed as:

$$\sqrt{J_2} = \lambda I'_1 + k \quad (2.14)$$

where  $\lambda$  and  $k$  are material constants,  $J_2$  is the second invariant of the stress deviator tensor and  $I'_1$  is the first invariant of the stress tensor, and are defined as follows:

$$I'_1 = \sigma'_1 + \sigma'_2 + \sigma'_3$$

$$J_2 = \frac{1}{6}[(\sigma'_1 - \sigma'_2)^2 + (\sigma'_1 - \sigma'_3)^2 + (\sigma'_3 - \sigma'_1)^2] \quad (2.15)$$

$\sigma'_1$ ,  $\sigma'_2$ , and  $\sigma'_3$ , are the principal effective stresses. The criterion, when expressed in terms of octahedral shear stress,  $\tau_{\text{oct}}$ , and octahedral normal stress,  $\sigma'_{\text{oct}}$ , takes the form:

$$\tau_{\text{oct}} = \sqrt{\frac{2}{3}}(3\lambda\sigma'_{\text{oct}} + k) \quad (2.16)$$

where  $\sigma'_{\text{oct}} = 1/3 I'_1$  and  $\tau_{\text{oct}} = \sqrt{2/3} J_2$ .

Drucker–Prager criterion can thus be considered as a particular case of Nadai's criterion that states that the mechanical strength of brittle materials takes the form  $\tau_{\text{oct}} = f(\sigma'_{\text{oct}})$ , where  $f$  is a monotonically increasing function (Nadai, 1950); (Addis and Wu, 1993); (Chang and Haimson, 2000); (Yu, 2002).

## 2.8 Non-linear Failure Criteria used for Excavation Design

### 2.8.1 Hoek-Brown Failure Criterion

The Hoek–Brown failure criterion follows a non-linear, parabolic form that separates it from the linear Mohr–Coulomb failure criterion. This criterion is an empirically derived relationship used to describe a non-linear increase in peak strength for isotropic rock with increasing confining stress. The criterion includes procedures developed to provide a practical means to estimate the rock mass strength from actual laboratory test values and underground observations (Ulusay and Hudson, 2007).

This criterion was developed as a means of estimating the rock mass strength by scaling the geological conditions present underground. Based on Hoek's (1968) experiences with brittle rock failure and his use of a parabolic Mohr envelope derived from Griffith's crack theory (Griffith, 1920, 1924) to define the relationship between shear and normal stress at fracture initiation, the criterion was conceived. Hoek and Brown (1980) proceeded through trial and error to fit a variety of parabolic curves to triaxial test data and associating rock failure and fracture initiation with fracture propagation, to derive their criterion (Ulusay and Hudson, 2007).

The non-linear Hoek–Brown failure criterion for intact rock (Hoek and Brown, 1980) was introduced as shown in Equation (2.20):

$$\sigma_1 = \sigma_3 + \sqrt{m C_{ucs} \sigma_3 + s C_{ucs}^2} \quad (2.20)$$

where  $m$  and  $s$  are dimensionless empirical constants and  $C_{ucs}$  is the uniaxial compressive strength (UCS) of rock in MPa. The parameter  $m$  is comparable to the frictional strength of the rock and  $s$  indicates how fractured the rock is, and is related to the rock mass cohesion (Ulusay and Hudson, 2007).

Greater values of  $m$  will give steeply inclined Hoek–Brown envelopes and high instantaneous friction angles at low effective normal stresses for strong brittle



rocks and lower  $m$  values give lower instantaneous friction angles as observed for more ductile rocks (Hoek, 1983). The constant  $s$  varies as a function of how fractured the rock is from a minimum value of zero for heavily fractured rock where the tensile strength has been reduced to zero to as high as 1 for intact rock (Ulusay and Hudson, 2007).

The Hoek–Brown criterion assumes that rock failure is controlled by the major and minor principal stress,  $\sigma_1$  and  $\sigma_3$  as illustrated in Equation (2.20) and the intermediate principal stress,  $\sigma_2$ , does not appear in the equations except insofar as  $\sigma_2 = \sigma_3$  or  $\sigma_2 = \sigma_1$  (Ulusay and Hudson, 2007).

The criterion can be applied to the estimation of rock mass strength properties by adjusting the  $m$  and  $s$  parameters according to the rock mass conditions. For the rock mass response to be isotropic, the assumption required is that any fractures presented are numerous enough that the overall strength behaviour has no preferred failure direction (Ulusay and Hudson, 2007).

The Hoek–Brown criterion has been updated several times to address certain practical limitations, and with experience gained with its use to improve the estimate of rock mass strength (Hoek and Brown, 1988; Hoek et al, 1992, 1995, 2002). It was assumed that the criterion was valid for effective stress conditions thus the principal stress terms in the original equation had been replaced earlier with effective principal stress,  $\sigma_1'$  and  $\sigma_3'$  terms (Hoek, 1983). One of the major updates was the reporting of the ‘generalised’ form of the criterion (Hoek et al, 1995):

$$\sigma_1' = \sigma_3' + C_{ucs} \left( m_b \frac{\sigma_3'}{C_{ucs}} + s \right)^a \quad (2.21)$$

For broken rock the term  $m_b$  was introduced. Hoek et al, (1992) reassessed the original  $m_i$  value and found it to be depending upon the grain size of the intact rock, mineralogy and composition. To address the system’s bias towards hard rock and to better account for poorer quality rock masses by enabling the curvature of the failure envelope to be adjusted, particularly under very low normal stresses, the exponential term  $a$  was added (Hoek et al, 1992).

As shown in Figure 2.16 the Geological Strength Index (GSI) was subsequently introduced together with several relationships relating  $m_b$ ,  $a$  and  $s$ , with the overall structure of the rock mass and surface conditions of the discontinuities (Hoek et al, 1995).

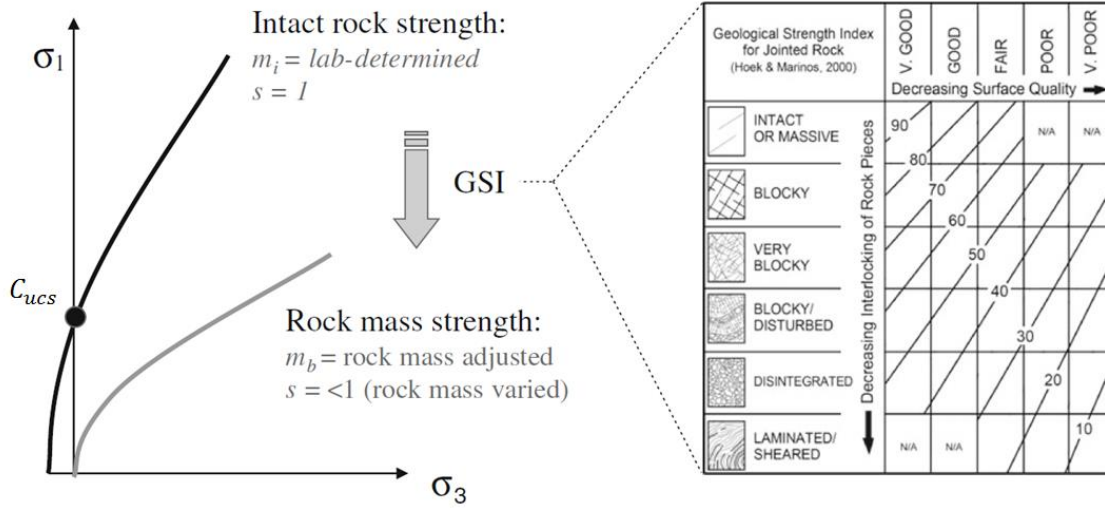


Figure 2.16 Scaling of Hoek-Brown failure envelope for intact rock to that for rock mass strength (Ulusay and Hudson, 2007)

A new factor  $D$ , also known as the blast damage factor, was introduced by Hoek et al (2002), to account for near surface blast damage and stress relaxation in the rock mass. The factor  $D$  can range between 0 and 1 where  $D = 0$  for undisturbed rock and  $D = 1$  for highly disturbed rock mass. The  $m_b$ ,  $a$  and  $s$  were reported as:

$$m_b = m_i \exp\left(\frac{GSI-100}{28-14D}\right) \quad (2.22)$$

$$s = \exp\left(\frac{GSI-100}{9-3D}\right) \quad (2.23)$$

$$a = \frac{1}{2} + \frac{1}{6} \left( e^{-\frac{GSI}{15}} + e^{-\frac{20}{3}} \right). \quad (2.24)$$

where  $m_i$  is a curve fitting parameter derived from triaxial testing of intact rock. The parameter  $m_b$  is a reduced value of  $m_i$ , which accounts for the strength reducing effects of the rock mass conditions defined by GSI as shown in Figure 2.16 (Ulusay and Hudson, 2007). Using the GSI values, adjustments of  $s$

and  $\alpha$  are also done accordingly. Although relationships exist to convert  $\text{RMR}_{89}$  and  $Q$  to GSI (Hoek et al, 1995), it was recommended by Hoek (2007) that the GSI be estimated directly from the charts published on its use as shown in Figure 2.16 (Ulusay and Hudson, 2007).

The advantages of the Hoek–Brown criterion are that it is non-linear in form, which agrees with experimental data obtained over a range of different confining stresses. It also provides an empirical means to estimate the rock mass properties and this was developed through laboratory tests covering a wide range of intact rock types (Ulusay and Hudson, 2007).

## **2.9 Three-Dimensional Failure Criteria Based on the Hoek–Brown Criterion**

Takahashi and Koide (1989) suggested that the intermediate principal stress has a substantial influence on the strength of rock materials. Failure criteria, such as the Mohr-Coulomb and Hoek–Brown criteria, ignore the influence of the intermediate principal stress and therefore may not provide a reliable prediction of rock strength under true-triaxial stress conditions. A number of three-dimensional failure criteria have been developed, such as the Drucker and Prager (1952) criterion and Lade criterion (Kim and Lade, 1984), but these criteria were not primarily developed for the application to rocks (Ulusay and Hudson, 2007).

Three-dimensional versions of the two-dimensional Hoek–Brown failure criterion have been proposed by Pan and Hudson (1988), Priest (2005) and Zhang and Zhu (2007). Zhang (2008) presented a generalised version of the Zhang–Zhu criterion. Melkounian et al (2009) presented an explicit version of the comprehensive Priest criterion. Since these criteria have not been shown to be, nor indeed claimed to be, applicable to fractured rock masses, the parameters  $m_b$ ,  $s$  and  $a$  should be replaced by  $m_i$ , 1.0 and 0.5, respectively, and the criteria limited to the application to intact rock materials (Ulusay and Hudson, 2007).

### 2.9.1 Generalised Zhang–Zhu Criterion

Zhang and Zhu (2007) first presented the Zhang–Zhu criterion. A generalised version of this criterion was presented by Zhang (2008) as follows (Ulusay and Hudson, 2007):

$$s C_{ucs} = C_{ucs} \left(1 - \frac{1}{a}\right) \left(\frac{3\tau_{oct}}{\sqrt{2}}\right)^{\frac{1}{a}} + \frac{3m_b \tau_{oct}}{2\sqrt{2}} - \frac{m_b(3I'_1 - \sigma'_2)}{2} \quad (2.25)$$

$$\tau_{oct} = \frac{\sqrt{(\sigma'_1 - \sigma'_2)^2 + (\sigma'_2 - \sigma'_3)^2 + (\sigma'_3 - \sigma'_1)^2}}{3} \quad (2.26)$$

where  $\sigma'_3$  is the minor effective principal stress at failure,  $\sigma'_2$  is the intermediate effective principal stress at failure,  $\sigma'_1$  is the major effective principal stress at failure,  $\tau_{oct}$  is the octahedral shear stress,  $I'_1$  is the first invariant of the effective stress tensor and the other Hoek–Brown parameters are as defined earlier (Ulusay and Hudson, 2007).

$I'_1$  is given by

$$I'_1 = \frac{\sigma'_1 + \sigma'_2 + \sigma'_3}{3} \quad (2.27)$$

In Equation (2.25),

$$\frac{m_b(3I'_1 - \sigma'_2)}{2} = \frac{m_b(\sigma'_3 + \sigma'_1)}{2}$$

This failure criterion cannot easily be formulated to express  $\sigma'_1$  explicitly in terms of the input data. A numerical strategy must be applied to determine the value of  $\sigma'_1$  that satisfies Equation (2.25) to Equation (2.27).

### 2.9.2 Generalised Pan–Hudson Criterion

It was demonstrated by Zhang and Zhu (2007) that the only difference between their yield criterion and the one proposed by Pan and Hudson (1988) is the absence of the intermediate principal stress in the third term of Equation (2.25). The Pan–Hudson criterion can be written as

$$s C_{ucs} = C_{ucs} \left(1 - \frac{1}{a}\right) \left(\frac{3\tau_{oct}}{\sqrt{2}}\right)^{\frac{1}{a}} + \frac{3m_b \tau_{oct}}{2\sqrt{2}} - m_b I'_1 \quad (2.28)$$

where the parameters are as defined earlier. A numerical strategy is required to determine the value of  $\sigma'_1$  in Equation (2.28). Although there is only a minor difference between the Generalised Pan–Hudson and Generalised Zhang–Zhu criteria, these criteria predict very different strength values (Ulusay and Hudson, 2007).

### 2.9.3 Generalised Priest Criterion

Priest (2005) developed a three-dimensional version of the Hoek–Brown yield criterion by combining the three-dimensional Drucker and Prager (1952) and the two-dimensional Hoek and Brown (1997) criteria. The terminology ‘Priest criterion’ has been adopted following Zhang (2008). The term comprehensive three-dimensional Hoek–Brown criterion was adopted by Priest (2005) to distinguish this failure criterion from the simplified version described in Equations (2.29) to (2.32) (Ulusay and Hudson, 2007).

The term ‘comprehensive’ is misleading, since this criterion is no more comprehensive than the other criteria outlined above. Therefore, this criterion will be referred to as the generalised Priest criterion (Priest, 2009). Solving this formulation presented by Priest (2005), required a numerical solution strategy. This problem was addressed by Melkounian et al (2009) by developing an explicit version of this three-dimensional Hoek–Brown criterion involving the two-dimensional Hoek–Brown failure criterion minimum effective stress at failure  $\sigma'_{3hb}$ , as summarised below (Ulusay and Hudson, 2007):

$$C = s + \frac{m_b(\sigma'_2 + \sigma'_3)}{2C_{ucs}} \quad (2.29)$$

$$E = 2C^a C_{ucs} \quad (2.30)$$

$$F = 3 + 2aC^{a-1}m_b \quad (2.31)$$

$$\sigma'_{3hb} = \frac{\sigma'_2 + \sigma'_3}{2} + \frac{-E \pm \sqrt{E^2 - F(\sigma'_2 - \sigma'_3)^2}}{2F} \quad (2.32)$$

where  $\sigma'_{3hb}$  is the minor principal effective stress at failure for the 2D Hoek–Brown criterion.  $C$ ,  $E$ ,  $F$  and  $P$  have no definition. Equation (2.32) gives two values for  $\sigma'_{3hb}$ , one of which can be positive and the other negative. In a compressive stress environment,  $\sigma'_{3hb}$  will be positive, so Melkounian et al (2009) recommended that the greater or positive root in Equation (2.32) should be adopted (Ulusay and Hudson, 2007).

$$P = C_{ucs} \left\{ \left( \frac{m_b \sigma'_{3hb}}{C_{ucs}} \right) + s \right\}^a \quad (2.33)$$

Finally,

$$\sigma'_1 = 3\sigma'_{3hb} + P - (\sigma'_2 + \sigma'_3). \quad (2.34)$$

#### 2.9.4 Simplified Priest Criterion

A ‘simplified’ three-dimensional version of the Hoek–Brown criterion was proposed by Priest (2005), providing an easily computed estimate for the three-dimensional effective failure stress  $\sigma'_1$  (Ulusay and Hudson, 2007).

$$\sigma'_1 = \sigma'_{1hb} + 2\sigma'_{3hb} - (\sigma'_2 + \sigma'_3) \quad (2.35)$$

where, as before,  $\sigma'_{3hb}$  is the minimum two-dimensional Hoek–Brown failure criterion effective stress at failure, and  $\sigma'_{1hb}$  is the maximum two-dimensional Hoek–Brown failure criterion effective stress at failure, calculated from Equation 2.21, and

$$\sigma'_{3hb} = w\sigma'_2 + (1 - w)\sigma'_3 \quad (2.36)$$

where  $w$  is a weighting factor in the range 0 to 1, which governs the relative influence of  $\sigma'_2$  and  $\sigma'_3$  on the strength of the rock. It was suggested by Priest (2005) that, for a wide range of rock types,  $w$  can be estimated from the following simple power law (Ulusay and Hudson, 2007).

$$w \approx \alpha \sigma'_3{}^\beta \quad (2.37)$$

Priest (2005) suggests that, as a first approximation,

$$\alpha = \beta = 0.15.$$

The simplified Priest criterion has the benefit of being amenable to direct explicit evaluation and so is more suitable for incorporating into numerical modelling software. When the minor principal stress is zero, the simplified Priest criterion underestimates the experimentally determined true-triaxial rock strength. For these conditions, the weighting factor  $w$  in Equation 2.37 is zero, which creates a negative slope for the graph of  $\sigma'_1$  versus  $\sigma'_2$  for the Priest failure criterion (Ulusay and Hudson, 2007).

For all of the criteria examined, with the exception of the simplified Priest criterion, additional input parameters are required beyond  $\sigma'_2$  and the parameters required for the two-dimensional Hoek–Brown criterion. It is possible to obtain a close fit to almost any experimental data by incorporating additional parameters or ‘fudge factors’ into the formulation of a criterion (Ulusay and Hudson, 2007).

## 2.10 Three-Dimensional Strain in the Mining Environment

Strain is defined as the change in length  $\Delta L$  of a strained body, normalised with respect to the original unstrained length  $L$  as shown in Figure 2.18. Ryder and Jager, (2002) explained that the vertical strain  $\varepsilon_{zz}$  could be determined as follows:

$$\varepsilon_{zz} = \Delta L / L$$

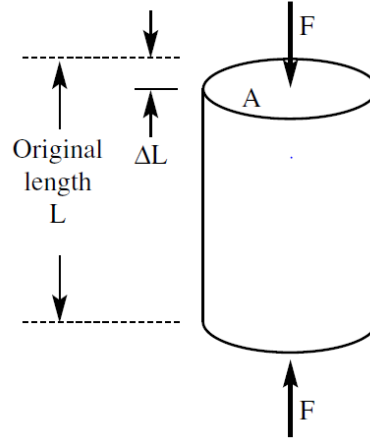


Figure 2.18 Simple definition of strain, after Ryder and Jager, (2002)

Strain is a dimensionless quantity, but is expressed in units of ‘microstrain’ i.e.  $\mu\text{m}/\text{m}$  ( $10^{-6}$ ), or ‘millistrain’ i.e.  $\text{mm}/\text{m}$  ( $10^{-3}$ ), or strain i.e.  $\text{m}/\text{m}$ . Stress and strain at any point in a body are connected by a constitutive law, which means a numerical or mathematical procedure which allows one to infer the state of strain which corresponds to a given state of stress, or vice versa. Constitutive laws can include the theory of linear elasticity, non-linear or time-dependent behaviour that may be relevant to understanding high-stress phenomena in rock engineering (Ryder and Jager, 2002).

Strains in three dimensions can be defined in terms of differentials of the displacement field with components in the x, y and z directions,  $u_x$ ,  $u_y$  and  $u_z$  respectively (Ryder and Jager, 2002):

$$\varepsilon_{xx} = \frac{\partial u_x}{\partial x} \quad \varepsilon_{yy} = \frac{\partial u_y}{\partial y} \quad \varepsilon_{zz} = \frac{\partial u_z}{\partial z}$$

$$\Gamma_{yz} = \Gamma_{zy} = \frac{1}{2} \left( \frac{\partial u_z}{\partial y} + \frac{\partial u_y}{\partial z} \right)$$

$$\Gamma_{zx} = \Gamma_{xz} = \frac{1}{2} \left( \frac{\partial u_x}{\partial z} + \frac{\partial u_z}{\partial x} \right)$$

$$\Gamma_{xy} = \Gamma_{yx} = \frac{1}{2} \left( \frac{\partial u_y}{\partial x} + \frac{\partial u_x}{\partial y} \right)$$



### **Three dimensional principal strains:**

These are given by roots of the cubic

$$\varepsilon_p^3 - I_1 \varepsilon_p^2 - I_2 \varepsilon_p - I_3 = 0$$

where the three strain invariants are given by

$$I_1 = \varepsilon_{xx} + \varepsilon_{yy} + \varepsilon_{zz} = \varepsilon_1 + \varepsilon_2 + \varepsilon_3$$

$$I_2 = -(\varepsilon_{yy}\varepsilon_{zz} + \varepsilon_{zz}\varepsilon_{xx} + \varepsilon_{xx}\varepsilon_{yy}) + (\Gamma_{yz}^2 + \Gamma_{zx}^2 + \Gamma_{xy}^2) = -(\varepsilon_2\varepsilon_3 + \varepsilon_3\varepsilon_1 + \varepsilon_1\varepsilon_2)$$

$$I_3 = \varepsilon_{xx}\varepsilon_{yy}\varepsilon_{zz} + 2\Gamma_{yz}\Gamma_{zx}\Gamma_{xy} - \varepsilon_{xx}\Gamma_{yz}^2 - \varepsilon_{yy}\Gamma_{zx}^2 - \varepsilon_{zz}\Gamma_{xy}^2 = \varepsilon_1\varepsilon_2\varepsilon_3$$

The invariant  $I_1$  is commonly known as ‘volumetric strain’

$$\varepsilon_{vol} = \varepsilon_1 + \varepsilon_2 + \varepsilon_3 \quad (2.38)$$

and is the ratio of change in volume to original volume of a strained element (Ryder and Jager, 2002).

## **2.11 Strain-Based Failure Criteria**

### **2.11.1 Stacey’s extension strain criterion**

The extension strain criterion (Stacey, 1981) was developed to interpret the mechanism of face scaling of bored tunnels and sidewall scaling in mine haulages developed in hard brittle rock. For initiation of brittle rock fracturing to occur, the total extension strain  $\varepsilon_e$  in the rock must exceed a critical value for that rock type. The extension strain criterion may be expressed as follows (Stacey, 1981):

$$\varepsilon_e \geq \varepsilon_{ec} \quad (2.39)$$

where  $\varepsilon_{ec}$  is the extension strain critical value for the rock. Fractures will form normal to the direction of the extension strain in the direction of the minimum principal stress  $\sigma_3$  and is related to the major principal stress  $\sigma_1$ , Intermediate principal stress  $\sigma_2$  and minor principal stress  $\sigma_3$  by the following equation (Stacey, 1981):

$$\varepsilon_3 = \frac{1}{E} [\sigma_3 - \nu(\sigma_1 + \sigma_2)] \quad (2.40)$$

where  $E$  is the modulus of elasticity and  $\nu$  is the Poisson's ratio. Louchnikov, (2011) illustrated the calibration of the extension strain criterion for its use in numerical modelling by measuring the extent of fracturing in production blastholes. By changing the modulus of elasticity the numerical model can be calibrated to match the observed result in the blastholes (Louchnikov, 2011).

### 2.11.2 Sakurai's critical strain criteria

The direct strain evaluation technique after Sakurai (1981) infers that the maximum principal strain  $\varepsilon_1$  can be derived from displacement measurements taken in an excavation and then compared with the allowable critical strain  $\varepsilon_0$  by the following equation (Sakurai, 1981):

$$\varepsilon_0 = \frac{C_{ucs}}{E_l} \quad (2.41)$$

where  $E_l$  is the initial modulus of longitudinal elasticity. The critical strain criterion originally proposed by Sakurai (1981) is expressed by the following equation:

$$\varepsilon_1 = \varepsilon_0 \quad (2.42)$$

The critical strain criterion was modified by Sakurai et al (1995) in order to account for the triaxial stress state and possible shear failure around excavations and was introduced by the following equation:

$$\gamma_{max} = \gamma_0 \quad (2.43)$$

where  $\gamma_{max}$  is the maximum shear strain and  $\gamma_0$  is the critical shear strain. The allowable value for the maximum shear strain can be determined by using the following equations (Sakurai et al, 1995):

$$\gamma_0 = \frac{\tau_{maxf}}{G_{50}} \quad (2.44)$$

$$\tau_{maxf} = \frac{\sigma_c}{2} \quad (2.45)$$

or

$$\tau_{maxf} = \frac{(\sigma_1 - \sigma_3)_f}{2} \quad (2.46)$$

and

$$G_{50} = \frac{E_{50}}{2(1+\nu)} \quad (2.47)$$

where  $\tau_{maxf}$  is the maximum shear stress at strength failure,  $G_{50}$  is the secant modulus of shear at 50% of the ultimate strength and  $E_{50}$  is the secant modulus of longitudinal elasticity at 50% of the ultimate strength. Sakurai et al (1995) determined that the critical shear strain could be directly related to the critical strain as defined by Equation (2.41) by using the following equation:

$$\gamma_0 = \varepsilon_0(1 + \nu) \quad (2.48)$$

### 2.11.3 Fujii's critical tensile strain criterion

Fujii et al (1998) proposed the critical tensile strain criterion for brittle failure of rock as follows:

$$\varepsilon_T = \varepsilon_{TC} \quad (2.49)$$

where  $\varepsilon_T$  is the principal tensile strain and  $\varepsilon_{TC}$  is the critical tensile strain at peak load. According to Fujii et al (1998), the stress will start to drop when the principal tensile strain reaches the critical tensile strain value. This criterion is not applicable to situations where strain-hardening behaviour is expected (Fujii et al 1998).

#### 2.11.4 Kwaśniewski strain-based failure criteria

Kwaśniewski and Takahashi, (2010) first considered the relationship between the octahedral shear strain:

$$\gamma_{oct} = \frac{2}{3} \sqrt{(\varepsilon_1 - \varepsilon_2)^2 + (\varepsilon_2 - \varepsilon_3)^2 + (\varepsilon_3 - \varepsilon_1)^2} \quad (2.50)$$

and mean normal strain:

$$\varepsilon_{m,3} = \frac{1}{3}(\varepsilon_1 + \varepsilon_2 + \varepsilon_3) = \frac{1}{3}\varepsilon_{vol} \quad (2.51)$$

It was found that the mean normal strain  $\varepsilon_{m,2}$  yielded much better results than the mean normal strain  $\varepsilon_{m,3}$  for a functional relationship between the octahedral shear strain and the mean normal strain at strength failure, and the following relationship was proposed (Kwaśniewski and Takahashi, 2010):

$$\varepsilon_{m,2} = \frac{1}{2}(\varepsilon_1 + \varepsilon_3) \quad (2.52)$$

## 2.12 Numerical Design Methods

### 2.12.1 Modelling of Dilution

Henning and Mitri (2007) investigated the relationship of hangingwall dilution in respect to depth, stope dimensions, stress environment, dip angle and stope types. They proposed that no-tension (failure in compression) overbreak represents overbreak that may occur, depending on certain factors that may damage the tensile capacity of the rock mass. Confinement overbreak because

of increasing stress due to the increase in depth, which represents dilution that may occur because of tensile failure of the hangingwall into the open stope.

Wiles (2007) proposed to improve the reliability of numerical model predictions by comparing numerical model results with actual mine response (back analyses). The consistency of results can be improved by refining the numerical model. To achieve this improved representation of the geometry, pre-mining stress state (tectonic stresses and virgin stresses) and refining of the material properties is required.

Coggan et al. (2003) stated that depending on the nature of the stresses around an excavation and the deformation of the rock mass surrounding the excavation, a number of failure mechanisms could exist. These failure mechanisms may be a combination of shear failure on existing fractures or joints, extension of joints and propagation of new fractures through the intact rock. Coggan et al. (2003) demonstrated by using a combined discrete element-finite element code, ELFEN which incorporates a crack propagation mode, the potential of the code to simulate multifaceted rock failure underground. Pine et al. (2006) developed an approach for modelling fractured rock masses, which had two main objectives: to maximize the quality of the geometry of existing rock jointing and to use this information within a loading model which takes full account of the jointing. The rock mass fracture model was based on a combination of clear mapping of rock faces and the fusion of this data into a three-dimensional model. This information was use of the FracMan numerical model.

FRACMAN® Discrete fracture network (DFN) modelling is used for simulating transport and flow in fractured systems. A suite of codes for fracture simulation is an established DFN modelling code known as FracMan. FracMan provides tools for discrete feature spatial analysis, data analysis, geologic modelling, visualization, transport and flow, and geomechanics. From FracMan two-dimensional cross sections can be imported into the finite element computer model, ELFEN, for simulation. From the ELFEN constitutive model for fracture simulation, including Rotating Crack and Rankine material models, in which

fracturing is controlled by fracture energy parameters and tensile strength. For compression and tension stress states, the model is capped using the Mohr-Coulomb criterion in which the softening response is coupled to the tensile model. Fracturing is accommodated by introducing an explicit coupling between the anisotropic degradation of the mutually orthogonal tensile yield surfaces and the inelastic strain accrued by the Mohr-Coulomb yield surface of the rotating crack model.

Pine et al. (2007) proposed a method for modelling discrete fractures in rock masses under tensile and compressive stress fields based on a Mohr-Coulomb failure surface in compression and three independent anisotropic rotating crack models in tension. A clearly time-integrated coupled discrete element/finite element approach was employed with a clear Lagrangian contact algorithm to prevent surfaces penetrating one another, which is created when the tensile strength is depleted. A geomechanical model is created from borehole data and field mapping and integrated into a stochastic 3D discrete fracture network model.

In underground mining, failure modes may include swelling, keyblock failure, scaling, squeezing, etc., which can be simulated using numerical modelling tools such as UDEC, 3DEC, FLAC, Unwedge and Phase2. Shear failure, either along block boundaries or through the rock mass is one of the most commonly recognized failure modes. According to Kaiser et al. (2000), tensile failures are not so common. Brittle tensile, rather than shear, failure modes play a significant role at intermediate to deep stress levels and in massive to moderately jointed rock masses as shown in Figure 2.19. Brittle rock behaviour near excavations is more wide spread than commonly anticipated according to Kaiser et al. (2000).

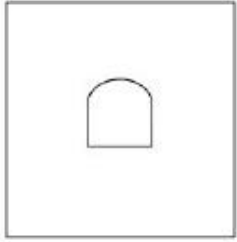
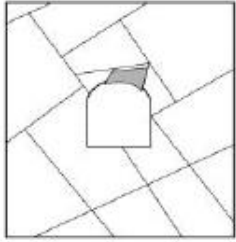
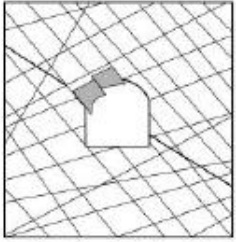

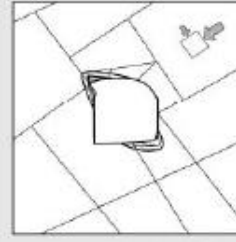
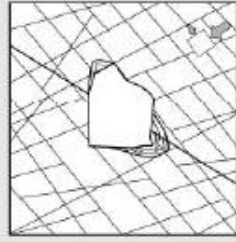

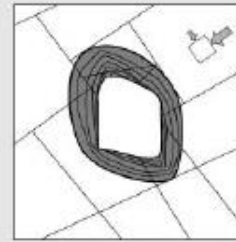
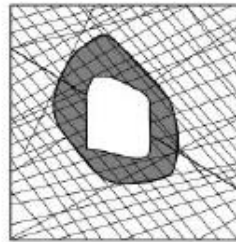
	Massive ( $RMR > 75$ )	Moderately Fractured ( $50 > RMR > 75$ )	Highly Fractured ( $RMR < 50$ )	
Low In-Situ Stress ( $\sigma_1 / \sigma_c < 0.15$ )	 Linear elastic response.	 Falling or sliding of blocks and wedges.	 Unravelling of blocks from the excavation surface.	Low Mining-Induced Stress $\sigma_{max}/\sigma_c < 0.4 \pm 0.1$
Intermediate In-Situ Stress ( $0.15 > \sigma_1 / \sigma_c < 0.4$ )	 Brittle failure adjacent to excavation boundary.	 Localized brittle failure of intact rock and movement of blocks.	 Localized brittle failure of intact rock and unravelling along discontinuities.	Intermediate Induced Stress $0.4 \pm 0.1 < \sigma_{max}/\sigma_c < 1.15 \pm 0.1$
High In-Situ Stress ( $\sigma_1 / \sigma_c > 0.4$ )	 Failure Zone Brittle failure around the excavation.	 Brittle failure of intact rock around the excavation and movement of blocks.	 Squeezing and swelling rocks. Elastic/plastic continuum.	High Mining-Induced Stress $\sigma_{max}/\sigma_c > 1.15 \pm 0.1$

Figure 2.19 Tunnel failure modes (Kaiser et al. (2000))

## 2.13 Influence of Blasting on Stope Hangingwall Stability and Dilution

### 2.13.1 Blasting Vibrations

Blasting vibrations in long hole stoping can have a significant effect on the hangingwall and sidewall stability of open stopes. The hangingwall and sidewalls of the open stopes are unsupported, thus when key blocks in these unsupported walls are subjected to dynamic loading conditions they sometimes tend to fall out, resulting in overbreak. The overbreak can be determined by using the cavity monitoring system to survey the effected open stopes. There

are numerous equations to calculate the peak particle velocity (*PPV*) of the blast. The frequently used *PPV* equations or predictors are listed in Table 2.1.

**Table 2.1 Frequently used *PPV* predictors (Kamali and Ataei, 2010)**

Predictor	Year	Equation	Reference
USBM	1959	$PPV = K \left( \frac{D}{\sqrt{W}} \right)^{-B}$	Duvall and Petkof (1959)
Langfors-Kihlstrom	1963	$PPV = K \left( \frac{D}{\sqrt{W^{2/3}}} \right)^B$	Langfors and Kihlstrom (1963)
General predictor	1964	$PPV = K \cdot D^{-B} \cdot W^A$	Davies et al. (1964)
Ambraseys-Hendron	1968	$PPV = K \left( \frac{D}{\sqrt[3]{W}} \right)^{-B}$	Ambraseys and Hendron (1968)
Bureau of Indian Standards	1973	$PPV = K \left( \frac{W}{D^{2/3}} \right)^B$	Bureau of Indian Standard (1973)
Ghosh-Daemen	1983	$PPV = K \left( \frac{D}{\sqrt{W}} \right)^{-B} \cdot e^{-\alpha D}$	Ghosh and Daemen (1983)
CMRI	1993	$PPV = n + K \left( \frac{D}{\sqrt{W}} \right)^{-1}$	Pal Roy (1993)

The *PPV* equations are based on two important variables, the maximum charge per delay and the distance from the blast site. All these equations listed in Table 2.1 have been based on scaled distance *SD* as shown in Equation (2.53). The scaled distance is the hybrid variable of *D* and *W*. In all formulas *W* and *D* refer to maximum charge per delay and distance from the blast site. The general equation for scaled distance is as follows:

$$SD = \frac{W^{k_1}}{D^{k_2}} \quad (2.53)$$

where *k*<sub>1</sub> and *k*<sub>2</sub> are predefined for each particular predictor. For parameter estimation in these predictors, simple regression analysis was used, except for the general predictor and Ghosh–Daemen (1983) models. The parameter estimation for the predictors is given in Table 2.2 (Kamali and Ataei, 2010).



**Table 2.2 Parameter estimation for the predictors (Kamali and Ataei, 2010)**

Predictor	$K$	$B$	$A$	$\alpha$	$n$
USBM	3621.8	2.6551	-		-
Langfors-Kihlstrom	0.3192	6.7393	-		-
General predictor	91.83	2.57	2.22		-
Ambrases-Hendron	18484	2.6529	-		-
Bureau of Indian Standards	0.3192	3.3697	-		-
Ghosh-Daemen	2.22	3.55	-	0.012	-
CMRI	373.39	-	-	-	-17.921

## 2.14 Planning Process on Target Mine

In planning an open stope for extraction, the first step in the design requires a comprehensive geological model. A geological model will depict the elevation, position of the different reefs and the values of these reefs. To determine the value of the different reef bands the reef needs to be evaluated. This can only be done by developing a reef drive on reef or by drilling boreholes to the area of interest. If a reef drive was developed, infill drilling is done. This core from the infill drilling and boreholes is sent to be evaluated for the gold content. If it is found to be economically feasible to mine, the information is sent to the planning department.

Using the geological model an open stope wireframe is created by the planning department in MINE2-4D, which allows the planning department to simulate the reefs to be mined. These results would depict if the open stope is economically feasible to mine when high and low grade reefs are combined. When feasible, the open stope wireframe is send to the ventilation department and rock engineering department for assessment.

The rock engineering department will first do a rock mass rating in the reef drive and collect as much information as possible, consisting of rock samples for pointload testing, and geological information on possible faults, dykes and joints.

Using the wireframe produced by the planning department the hydraulic radius of the open stope is assessed. If the hydraulic radius is found to be too large, the process will start again at the planning department with a reduced stope size. Using Map3D-SV, analysis is done to evaluate the effect of the open stope on other excavations and for the possibility of Excess Shear Stress (ESS) on geological structures resulting in seismicity. If the hazard is too high, the process will start again at the planning department with new designs and the PPV will be calculated from the blast design done by the planning department as to assess the effect on neighbouring excavations. This process is graphically described in Figure 2.17.

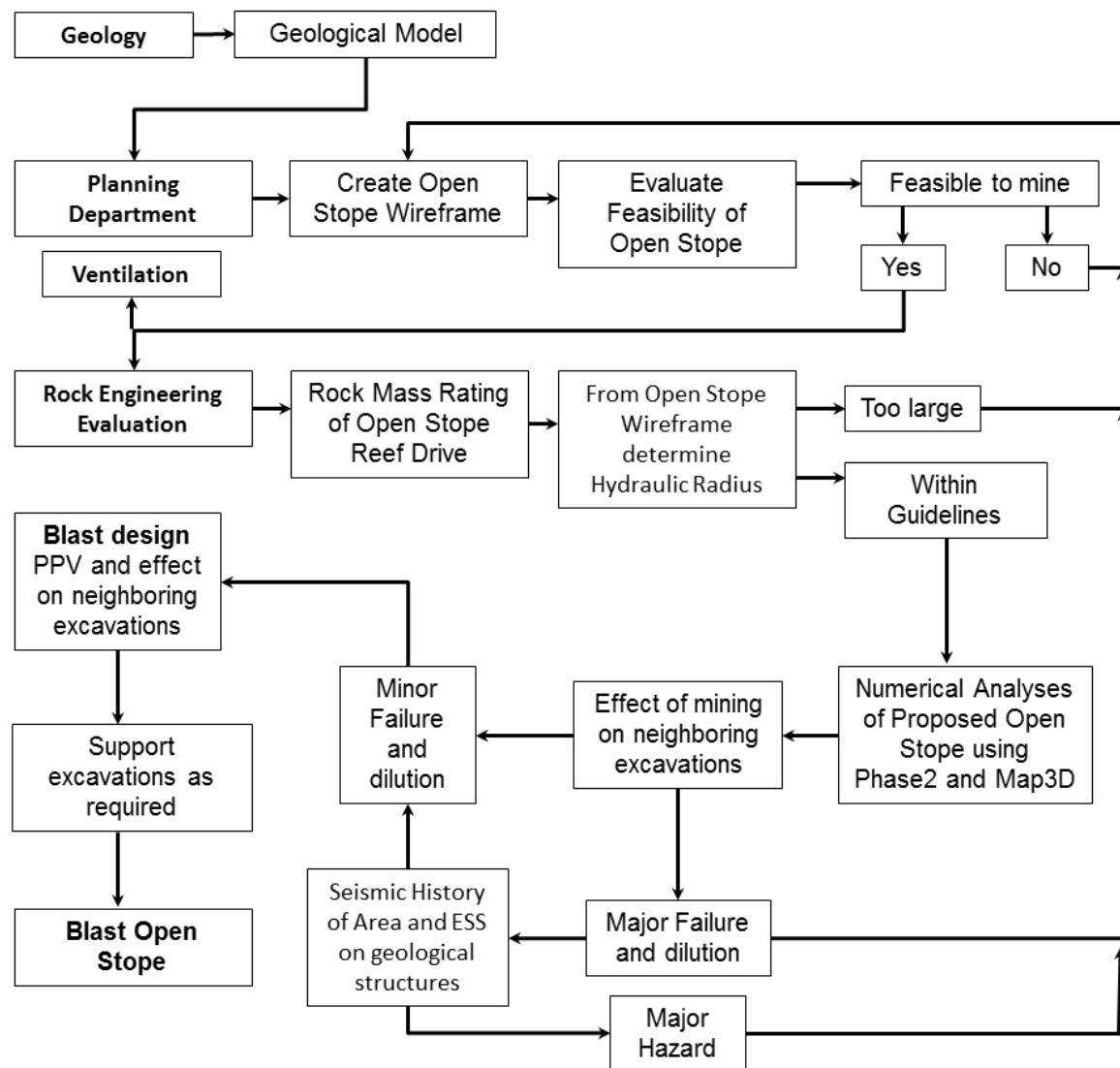


Figure 2.17 Flowchart showing process to follow when evaluating an open stope for mining

## **2.15 Summary**

In this chapter the literature review was discussed explaining the different definitions for dilution, Hydraulic Radius, Rock Mass Classification, and several failure criteria, blasting vibrations and Cavity Monitoring system (CMS) and the influence of each on the stability of massive open stopes. In chapter three, the background on site used for data collection will be discussed.

### **3 BACKGROUND ON SITE USED FOR DATA COLLECTION**

#### **3.1 Introduction**

In chapter two, a literature review was presented. This chapter will give a brief overview of the geological setting of the Free State and the background on Target Mine, the specific mine site used for data collection. In South African underground gold mines there are few mines utilizing open stoping mining methods. It was found that Target Mine had forty-four open stopes mined, of which twenty-eight had significant information available for this research. Other mines, such as South Deep, were also investigated for this research, but only four open stopes have been mined to date, and the empirical data required for the research was not available. This was also the case for open stopes mined at the old Lorraine Mine in the Free State, close to Target Mine, and Cons Murch Mine between Tzaneen and Phalaborwa. The aim of this information is to highlight the differences between Target Mine in South Africa and other open stoping mining operations in Australia and Canada.

#### **3.2 History of Gold in the Free State**

The earliest mention of the discovery of gold in South Africa was when Carel Kruger in 1834, during a hunting expedition to the interior of the Witwatersrand, collected a sample of the ore which he took back to Cape Town to be tested for gold content (Watermeyer and Hoffenberg, 1932).

It is believed that in 1896, Donaldson a prospector and Hinds an engineer, inspected a portion of the farm called Zoeten-Inval for gold bearing ore. This farm belonging to Klopper was located near where the town of Allanridge and Target Mine are situated today. On the farm they excavated an 18m pit and collected samples which they presented to the mining companies in Johannesburg. Unfortunately the mining companies showed no interest in the idea of gold bearing reef being present in the Free State.

The devastated men decided to return to England to have their samples analysed there, and to raise capital for the continuation of their search for gold in the Free State. Unfortunately, the ship Drummond Castle, on which they were sailing back to England, sank in the Bay of Biscay off the coast of France with the loss of all aboard. In 1904, Megson widened and deepened the original pit excavated by Donaldson and Hinds to about 30m and took samples of the exposed strata from this pit, as these indicated some promise of gold (Vista, 1997).

For many years Megson tried to convince mining companies with his samples, until October 1932, when he presented himself to Roberts, a prospector, and Jacobs, a young attorney. Roberts and Megson went back to Odendaalsrus to inspect the pit, widened by Megson, and collected new samples for analysis. These samples were then analysed by Milne, an Analytical Chemist at the University of the Witwatersrand. The results confirmed that the rock samples were definitely gold bearing. The first prospect borehole was drilled on 5 May 1933 and intersected lava formations at a depth of 829m, and a number of gold bearing reefs, one of which contained fair gold values, but this was not enough incentive to attract financial assistance (Vista, 1997).

Unfortunately, Roberts was not able to raise any capital and the drilling was discontinued. In 1933, within the Klerksdorp area, the Anglo American Corporation started drilling and deep boreholes proved the existence of gold-bearing reef, which soon led to the establishment of the Western Reefs Mines. The discovery of gold in payable quantities in this area inspired geologists to look beyond the Vaal River in the Free State region. As prospecting in the Free State was intensified over a wide area in the vicinity of Odendaalsrus, the first high gold value was found in the no.5 borehole, in the area known today as the St. Helena Mining Lease area and shown in Figure 3.1. Early in 1946, the borehole known today as the Geduld 697 yielded good values, followed by the phenomenal results of the Geduld no.1 borehole, and nine months later by the Geduld no.2 borehole, leading to thirteen separate mining properties being

delineated within the new goldfields area. This gave rise to the development of a new town, Welkom, where six of the new mines were situated. St. Helena Mine was the first mine to come into production with the first bar of gold being poured by Anderson, Chairman of Union Corporation, on 26 October 1951 (Vista, 1997).

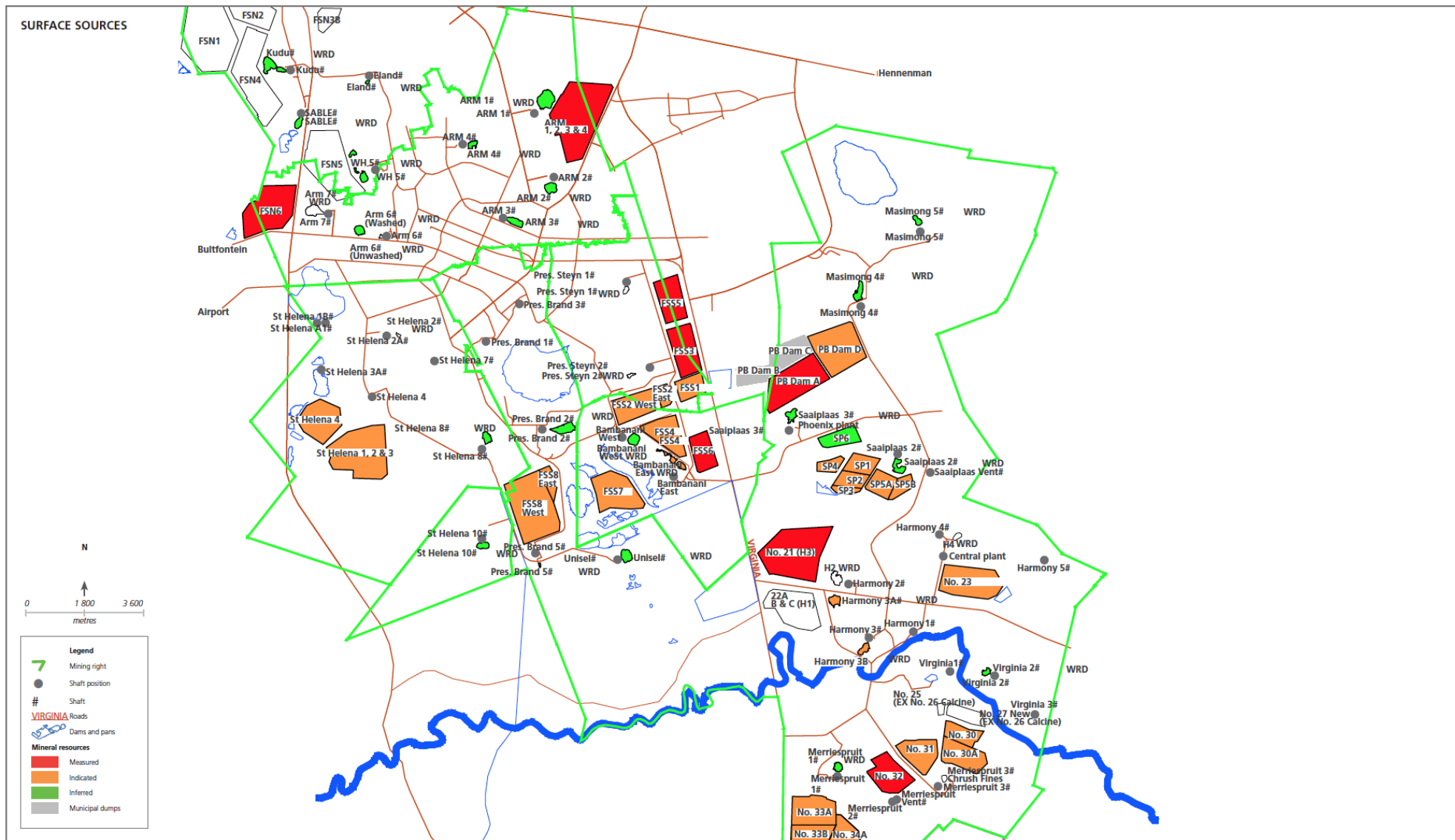


Figure 3.1 Image showing the relative positions of the St. Helena Mining Lease area (Harmony Financial Report, 2013)

### **3.3 General Mine Information**

#### **Location of Target Mine**

Target Mine is situated at the town of Allanridge some 20km from Welkom as shown in Figure 3.2 and is the most northerly mine in the Welkom Goldfields area. Target mine consists of a single surface shaft system with a sub-shaft (Target 1C shaft) and a decline. Ownership of Target Mine was attained in May 2004 by Harmony Gold Mining Company Limited (Harmony Annual Report, 2010).

On the closure of the nearby Lorraine mine in August 1998, the Lorraine 1 and 2 shafts were transferred to Target Mine, and became the Target 1 and 2 shafts. Officially, Target Mine was opened in May 2002. No mining is taking place at Target 2 shaft and it is used as the second escape for Target 1 shaft. Both mechanised (86%) and conventional (14%) mining are undertaken at Target Mine (Harmony Annual Report, 2010).



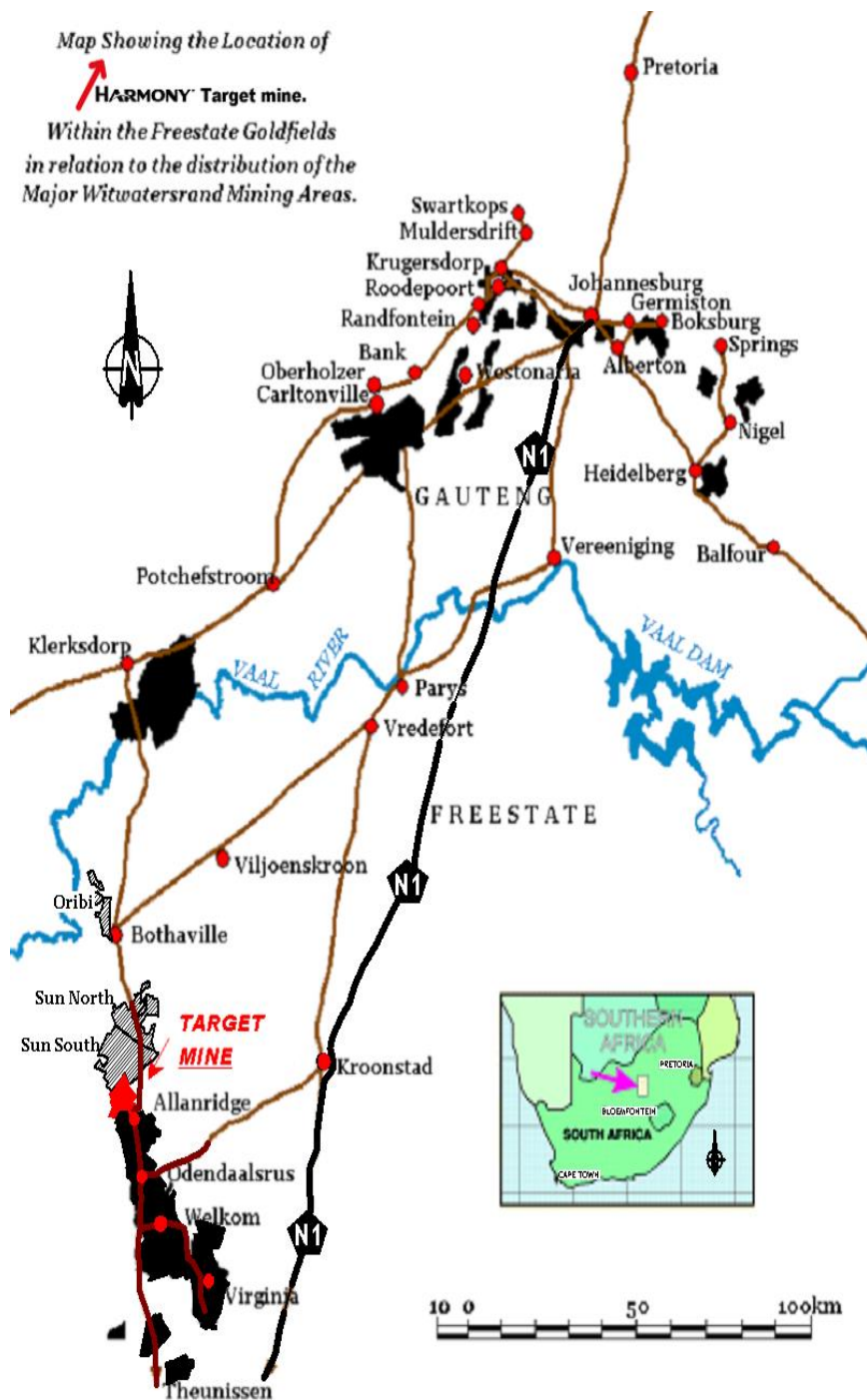


Figure 3.2 Location of Target Mine (Harrison, 2010)

### 3.4 Free State Geological Setting

This Section will describe the geological succession in the Free State, highlighting the differences between the various formations and comparing them with the West Wits area of the Witwatersrand Basin.

### **3.4.1 Regional geological setting**

#### **Stratigraphy in the Witwatersrand Basin**

The Witwatersrand Basin, as shown in Figure 3.4 and Figure 3.5, is the main gold bearing structure within South Africa. The stratigraphic subdivisions and nomenclature are depicted in Figure 3.3 and are described in the following paragraphs (Ryder and Jager, 2002).

The Dominion Group, the lowest member of the Witwatersrand Triad, overlies the Archean granites and outcrops west of Klerksdorp and close to the Vredefort dome where it is highly metamorphosed. It comprises of a lower sedimentary formation, which is approximately 100m in thickness, consisting of conglomerates and quartzites. Five of the conglomerate horizons have been mined for uranium and gold where some grades in excess of 1000 g/t were obtained. The overlying andesitic lava formation is about 650m in thickness and is overlain by about 1550m of acid volcanics (Ryder and Jager, 2002).

The Witwatersrand Supergroup is divided into two main groups - the upper Central Rand Group that varies in thickness from about 1000m to 2700m, and the lower West Rand Group ranging in thickness from 2600m to 5000m. The Central Rand Group is generally arenaceous with few shale formations and has many conglomerate horizons, including most of the major gold bearing reefs. The West Rand Group has a high proportion of shales, amongst which are conspicuous ferruginous members who have been used as markers during geophysical prospecting. Many quartzite horizons are less than 100m in thickness, with generally poor development of conglomerate bands. Further subdivision is provided by five subgroups (Hospital Hill, Government, Jeppestown, Johannesburg and Turffontein) and the twenty-five formations are shown in Figure 3.1 (Ryder and Jager, 2002).

The Ventersdorp Supergroup comprises mainly of volcanic rocks with some occasional sedimentary formations. The Ventersdorp Contact Reef (VCR) can sometimes be found at the base, where it unconformably overlies the Witwatersrand formations (Ryder and Jager, 2002).

		FORMATION		MARKER UNITS AND THEIR CORRELATIVES
CENTRAL RAND GROUP	TURFFONTEIN SUB GROUP	MONDEOR		Deelkraal Reef, VS1, Elsburg Reefs, Elandsrond Reef, EA Reefs, Bastard Reef
		ELSBURG		UK1, EC, VS3
		KIMBERLEY		UK3, VS5, Rosedale Reef, Denny's Reef Beatrice Reef Sand R, Libanon Reef, UK9b, Kimberley Reef
	JOHANNESBURG SUB GROUP	BOOYSENS		UK1, B Reef Daarnkop
		KRUGERSDORP		Bird Lava, Leader Reef, Bird Reef, Basal/Steyn, Vaal Reefs
		LUIPAARDSVLEI		
		RANDFONTEIN		Livingstone Reefs South Reef, Middelvlei Reef, Nigel Reef
		MAIN		Main Reef Leader Main Reef, Carbon Leader, Commonage
		BLYVOORUITZICHT		North, Ada May, Beiso, Rock Tunnel Reefs
	JEPESTOWN SUB GROUP	MARAISBURG		
		ROODEPOORT		
		CROWN		Jepestown Amygdaloid
		BABROSCO		Veldskoer, Inner Basin Reefs
		RIETKUIL		
		KOEDOESLAAGTE		Buffelsdoorn Reef
	GOVERNMENT SUB GROUP	AFRIKANDER		
		ELANDSLAAGTE		Government Reef
		PALMIETFONTEIN		
		TYSSCHENIN		Coronation Reef West Rand Shale Coronation Diamicite
		CORONATION		
		PROMISE		Promise Diamicite
WEST RAND GROUP	HOSPITAL HILL SUB GROUP	BONANZA		Bonanza Reef
		BRIXTON		
		PARKTOWN		
		ORANGE GROVE		

Figure 3.3 General stratigraphic column of the Witwatersrand Supergroup as proposed by the SACS Task Group (Ryder and Jager, 2002)

### **3.4.2 Geology of Target Mine**

In Figure 3.5, the position of the Target ore body is shown in relation to the present known limits of the Witwatersrand basin. From the old Lorraine Gold Mine the orebody is for a large part restricted to a narrow zone trending north-northwest. On Target Mine, the Boulder Beds, have given way to a lateral facies equivalent called the Dreyerskuil and has similar characteristics to the underlying Elsburg Formation (Harrison, 2010).

To the north, the Ventersdorp Contact Reef in the Goldfields was discovered and the characteristics are similar to the VCR elsewhere in the Witwatersrand Goldfields. Target Mine is mining a number of gold reef horizons in the upper Witwatersrand Supergroup. These reefs have the same characteristics as the Eldorado Formation, which was mined on the old Lorraine Gold Mine to the south. The northern limit of Target Mine is restricted by its current mining infrastructure with Gold mineralisation continuing northwards (Harrison, 2010).

The most important reefs on Target Mine are the Elsburg or “EA” and overlying Dreyerskuil reefs, which tend to coalesce towards the sub-outcrop trending north-north westerly. This characteristic is important for the creation of massive mining blocks (Harrison, 2010).

### **Stratigraphy**

#### **Uitkyk Member**

The entire Target Mine lease area is overlain by the Uitkyk Member, which vary in thickness from 2m to 12m and is sericitized polymictic large pebble agglomerate. The Uitkyk Member also referred to as the lower agglomerate as a result of its previously considered volcanic association. Although this genetic characterization has been changed, the name has been retained. Overlying the lower agglomerate up to 18m in thickness is argillaceous quartzwackes intercalated with light grey quartzites and polymictic are loosely packed conglomerate bands. The lower agglomerate is also sometimes referred to as the Lower Dreyerskuil or Lower Boulder Beds at Target Mine (Harrison, 2010).

The upper portions of the member are characterized by the presence of boulder and cobble beds of varying composition ranging from granites, greenstones, green, black and yellow shales, altered porphyritic rocks, cherts, quartz and quartzites (Harrison, 2010).

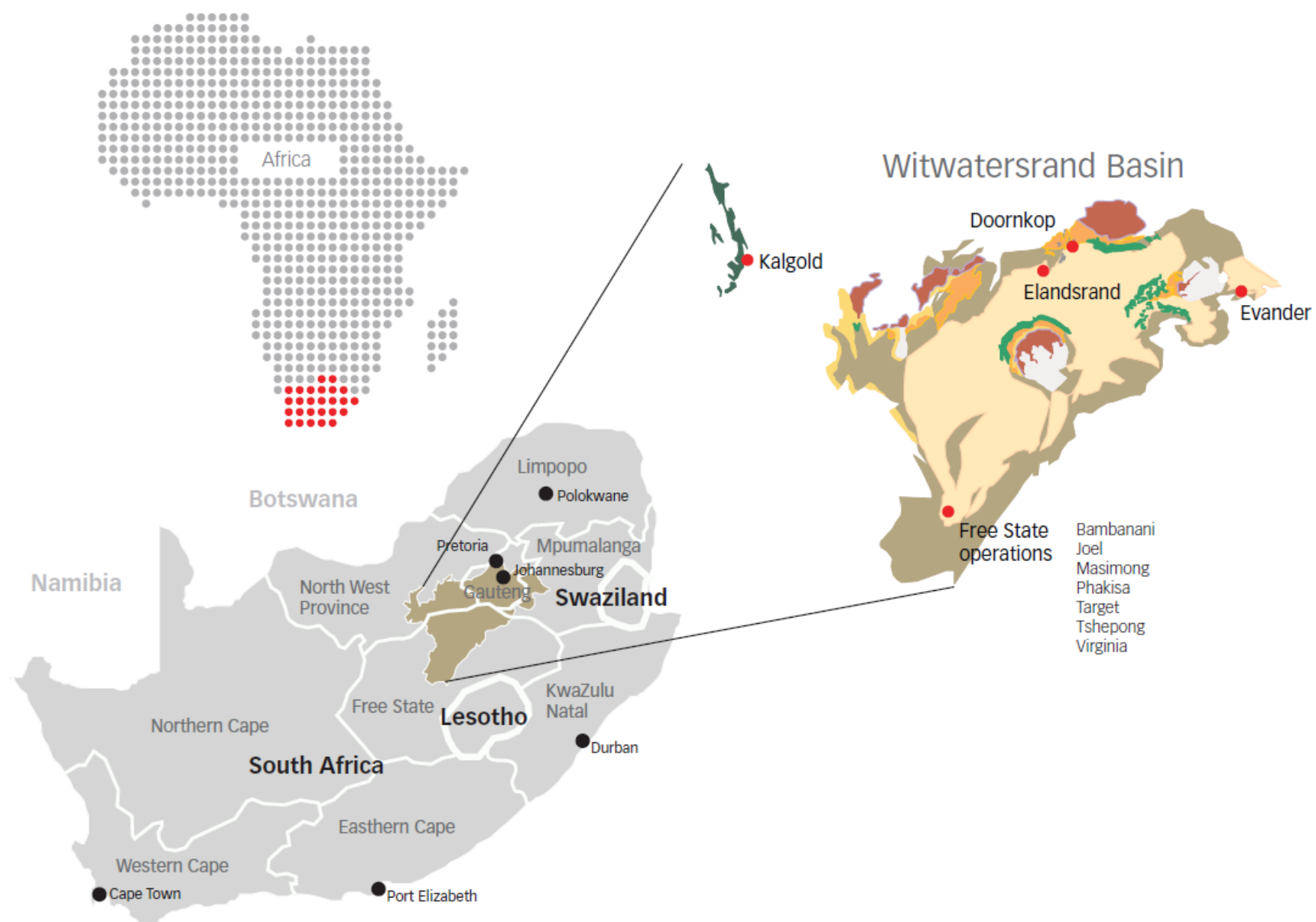


Figure 3.4 Witwatersrand Basin relative to South Africa (Harmony Annual Report, 2009)

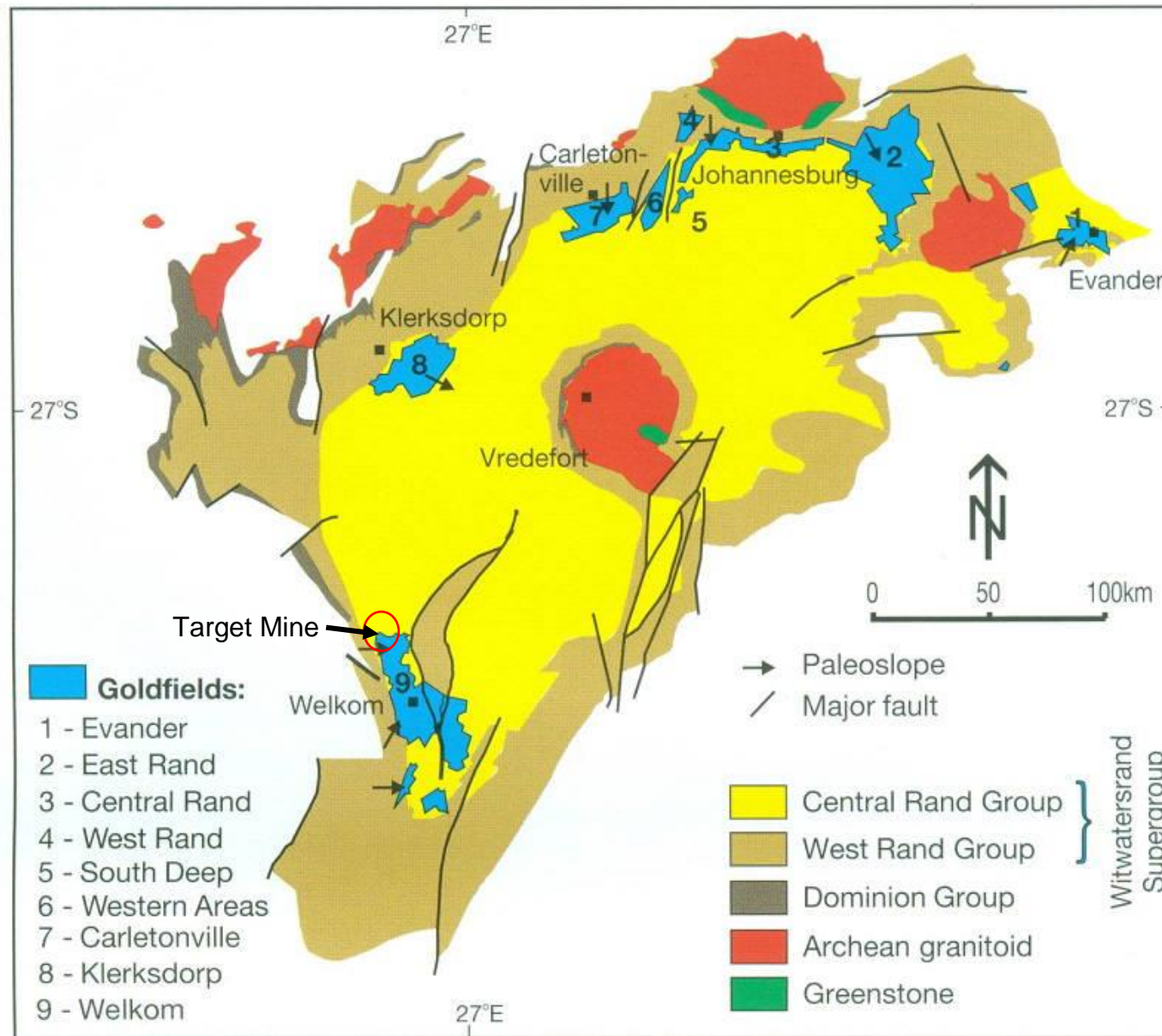


Figure 3.5 Target Mine relative to the Witwatersrand Basin in the Free State (Frimmel et al, 2005)

### **Van den Heeversrust Member (EA Zone)**

The EA Zone comprises interbedded coarse to medium grained, green to black argillaceous quartzwackes, also referred to as subgreywackes, interbedded with polymictic to oligomictic conglomerates and quartzites. The EA developed at Target Mine 1 Shaft is different from that at President Steyn Gold Mine 3 Shaft with regard to the volumetric quantities of immature to mature sediments (Harrison, 2010).

In the north, a relatively high proportion of quartzites with interbedded oligomictic conglomerates exist, while in the south, polymictic conglomerates and greywacke predominate. *“A combination of facies variations, local differences in source areas and tectonics are proposed as a possible explanation for the above”* (Harrison, 2010).

The Eldorado Reefs mined at Target Mine contains the EA1 at the base ranging up through the succession, including the EA2, EA3, EA4, EA5, EA7A, EA7B, EA8 bottom and top, the EA12, EA13 and EA15. There are no distinctive markers, which can be used for identifying the different reefs except for the EA1 with its EB footwall, and the EA8 and EA15 bands (Harrison, 2010).

### **Structure**

As described by Chapman (1969) folding forms the major structural feature and is manifested as an asymmetric syncline whose axis trends N15°W, with a general plunge of 10° - 12° north, although this is variable due to local structural features within the Target Mine lease area (Harrison, 2010).

Due to local faulting and minor folding, the reefs may be vertical in places with dips of the western limb of the syncline often in excess of 55° eastwards. All zones and reefs sub-outcrop either against the Dreyerskuil or against EA reefs, below the EA1 reef as shown in Figure 3.6 and Figure 3.7. The upper EA12 to EA15 reefs generally appear to become more conformable with the Dreyerskuil, while the lower lying EA1 to EA8 reefs sub-outcrop against either higher EA reefs or Boulder Beds (Harrison, 2010).



The underlying Rosedale Member of the Eldorado Formation the Kimberley Formation and the Dagbreek Formation, below the EA1 Reef, although subtle very low angle unconformities exist between each one, all appear conformable with one another. Similar to that of the Uitkyk Beds, the eastern limb of the syncline has an almost constant dip of 10° to 15° to the west (Harrison, 2010).

At Target Mine, a 180m thick reef package is mined, termed the Eldorado Reefs. Reef zones can differ in different areas of the mine. The EA Zone, the zone dealt with in this section, contains the majority of the Eldorado Reefs mined at Target Mine, viz. the EA1 at the base and, ranging up through the succession, the EA2, EA3, EA4, EA5, EA7A, EA7B, EA8 bottom and top, the EA12, EA13 and EA15 (Harrison, 2010).

The EA Zone comprises interbedded green to black, coarse to medium-grained argillaceous quartzwackes (referred to on the mine as subgreywackes), interbedded with polymictic to oligomictic conglomerates and locally quartzites. The EA assemblage as developed at Target Mine 1 Shaft (North), is markedly different from that at Target 3 Shaft (South) with regard to the volumetric quantities of mature to immature sediments. Except for the EA1 with its EB footwall, and the EA8 and EA15 bands, there are no distinctive markers, which can be used for identifying the different reefs. The Eldorado Reefs sub-outcrop against the Dreyerskuil Reefs (Harrison, 2010).

In the south, greywacke and polymictic conglomerates predominate while in the north, a relatively high proportion of quartzites exist, with interbedded oligomictic conglomerates. A combination of facies variations, local differences in source areas and tectonics are proposed as a possible explanation (Harrison, 2010).

Owing to the nature of the Eldorado Reefs that form a massive ore deposit as shown in Figure 3.6, massive open stoping can be utilized. Massive open stoping will be discussed in more detail in section 4.3. Figure 3.6 illustrates the sub-outcrop of the Eldorado reefs against the Dreyerskuil reefs. In Figure 3.7, the actual sub-outcrop was photographed underground.

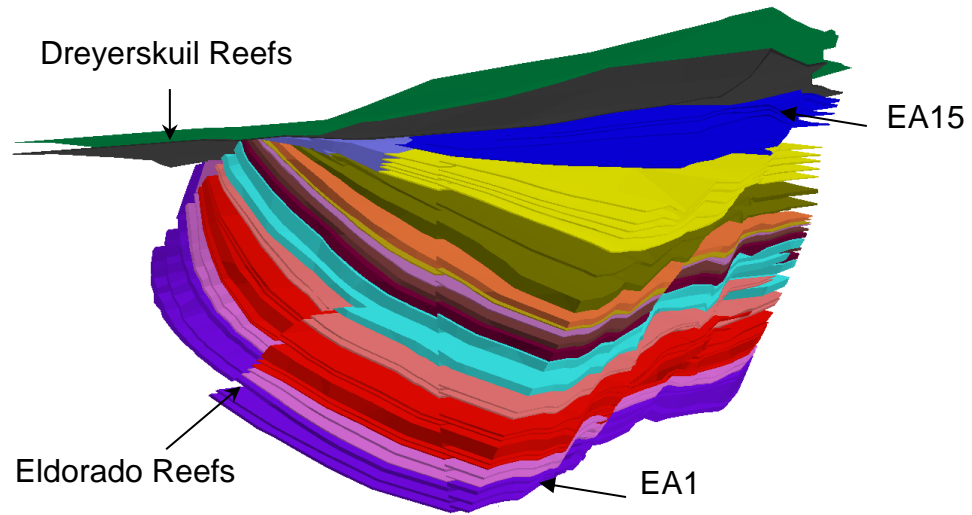


Figure 3.6 Cross section view looking north showing the Eldorado reefs sub-outcropping against the Dreyerskuil reefs

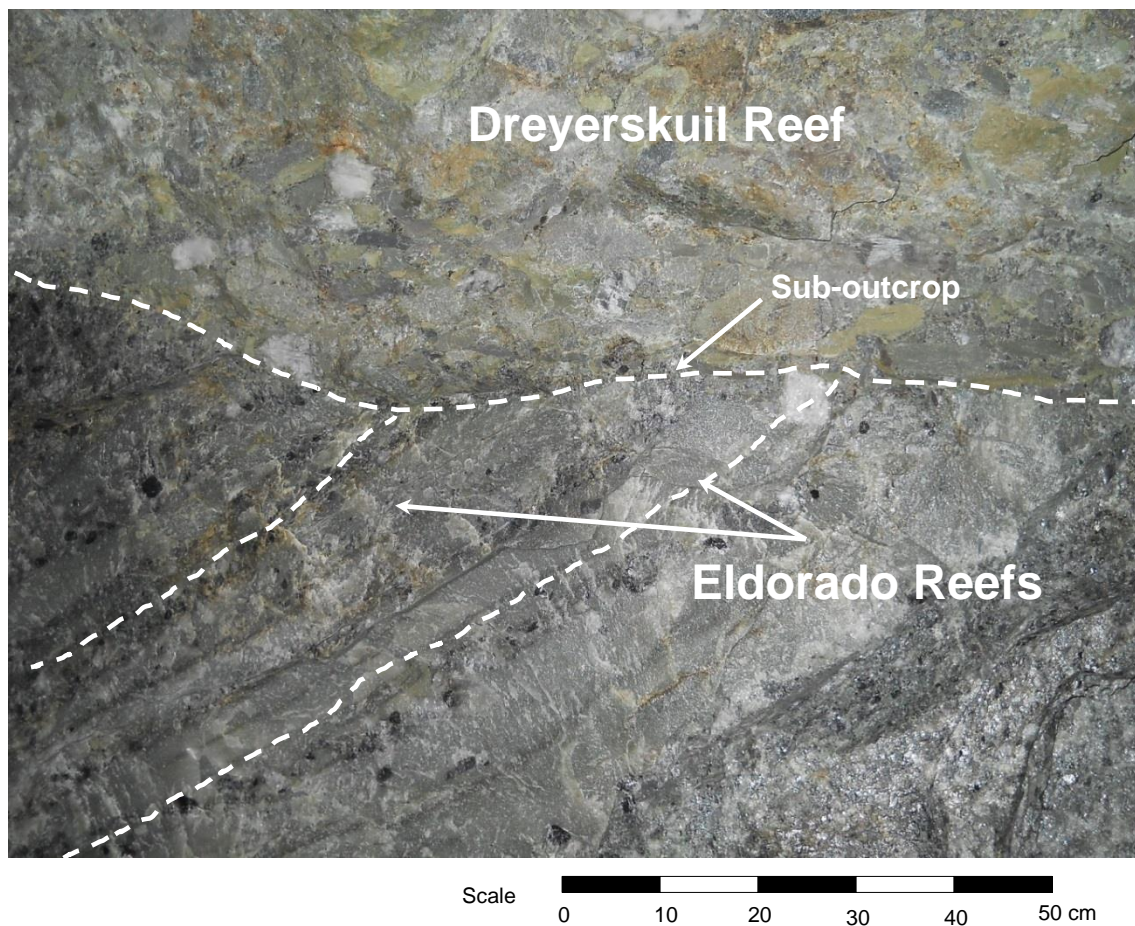


Figure 3.7 Photo showing the Eldorado reefs sub-outcropping against the Dreyerskuil reefs

### **3.5 Summary**

In this chapter brief overviews of the history of mining in the Free State, the geological setting of the Free State, and the background on the site used for data collection were given. The aim of this information was to highlight the difference between this mining operation and other conventional narrow reef mines in the Free State Province of South Africa, and that large open stope mining is uncommon in the South African gold mines. In chapter four, a description of open stope mining on the Target Mine site used for data collection will be given, and the empirical database will be discussed.

## **4 DESCRIPTION AND EMPIRICAL DATABASE**

### **4.1 Introduction**

In chapter three a brief overview of the geological setting of the Free State and the background on the site used for data collection were given. In this chapter, a description of open stope mining on the Target Mine site used for data collection is given, and the empirical database will be discussed. Empirical design methods, consisting of design criteria and design lines that are estimated from the analysis of field data from case studies, coupled with engineering judgement, will be applied.

### **4.2 Empirical Database and Selection of Case Study Stopes**

A comprehensive empirical database was established for this research based on the open stope mining information, rock mass properties, rock mass classification and CMS survey data. The database includes twenty-eight case studies from Target Mine with sufficient information required for this research. The following information was included in the database:

- Planned stope volume
- Stope volume from CMS survey data
- Stope geometry (beam area, circumference, Hydraulic Radius)
- Rock mass properties and classification
- The major principal stress at the open stope hangingwall and sidewall before mining the open stope
- Modified stability number,  $N'$
- Equivalent Linear Overbreak Slough (ELOS)

### **4.3 General Open Stope Information**

Before discussing the selection of open stopes a brief explanation of open stoping, as practiced at Target Mine, will be given. The Target Mine orebody comprises of multiple reefs overlying one another with an orebody 180m in

thickness and 270m wide as discussed in section 3.3.2. The 180m thick reef package being mined is termed the Eldorado Reefs. The dip of the reef varies from as low as 10° in the west to 75° in the east. Compared with most Australian and Canadian open stoping mining operations, Target Mine is unique. In most Australian and Canadian mining operations the hangingwall and footwall comprise of waste rock, with the orebody dipping relatively steeply. At Target Mine the hangingwall, sidewalls and footwall all comprise of reef with different grades, except for the EA1 with its EB footwall, which is waste rock. If the stope is being mined along an existing old stope the western sidewall of this stope will be backfill. The mining direction of these open stopes is from the lowest position of the reef on the west, progressing up towards the east as shown in Figure 4.1.

Due to the depth of the mine, some 2300m to 2500m below surface, a de-stressing slot is mined to create an artificial shallow mining environment where the stress does not exceed 60MPa. This de-stressing slot comprises of narrow reef mining with an average stope width of 1,5m, mined on the Dreyerskuil reefs.

Open stoping is the process by which massive stopes are blasted to mine selected reef packages within the orebody. These open stopes are large in size varying from 10m to 25m in width, 10m to 35m in height and 10m to 100m in length. To establish an open stope, a reef drive is developed on strike at the lowest point where the stope will be situated, as shown in Figure 4.1, Figure 4.2 and Figure 4.3. This reef drive is developed to the mining limit of that specific open stope. At the end of the open stope slot cubbies are developed cutting across the dip of the strata.

In one of the cubbies, a drop raise is developed holing into the top drive for ventilation. Once developed the slot is drilled as well as the blast rings for the open stope. When completed the slot is blasted and cleaned, utilizing remote loading LHD's (load, haul and dump) mechanized equipment.

The open stope is then created, by blasting a maximum of four rings at a time, on retreat, and is cleaned utilizing remote loading LHD's. No personnel are allowed to enter these open stopes at any time.

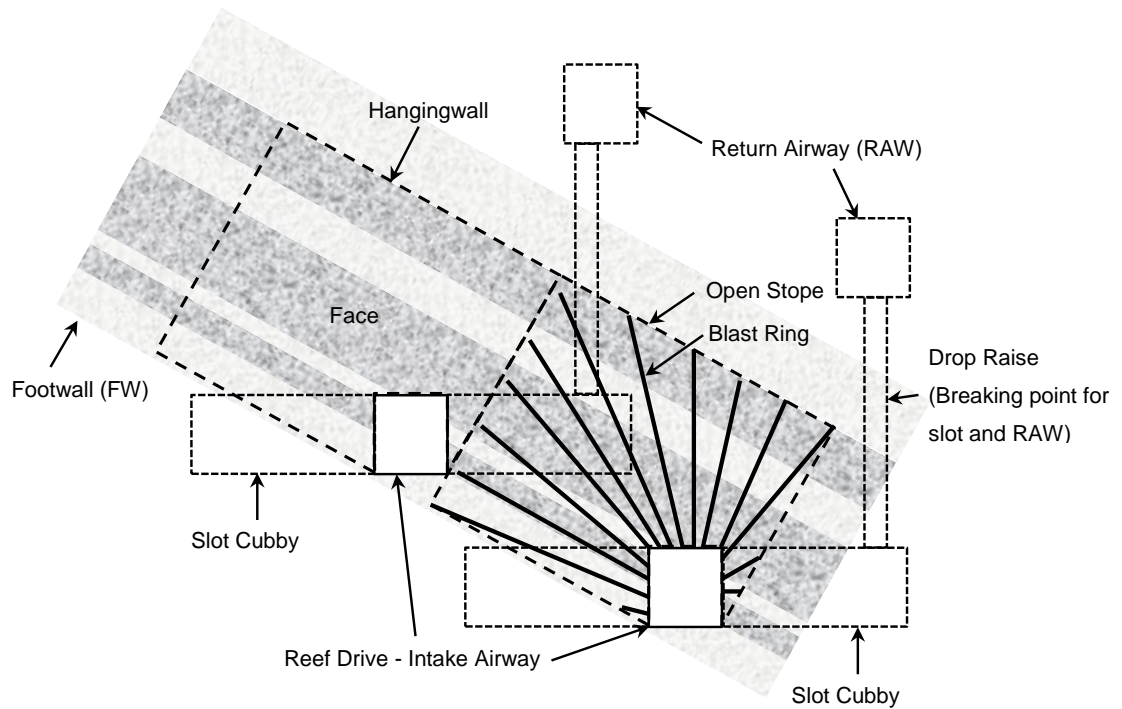


Figure 4.1 Cross section view of a typical open stope design on Target Mine

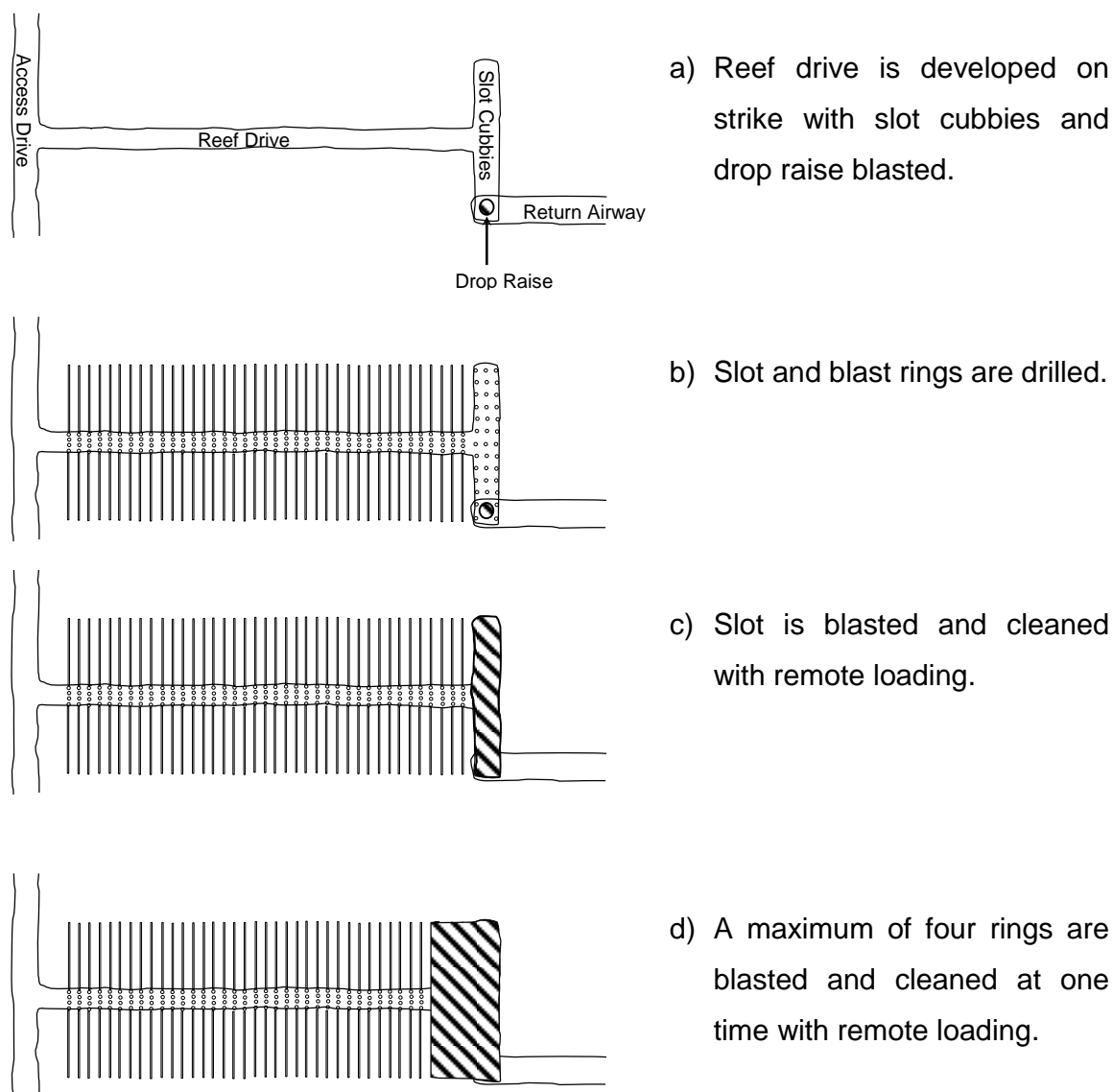


Figure 4.2 Plan view of a typical open stope design on Target Mine

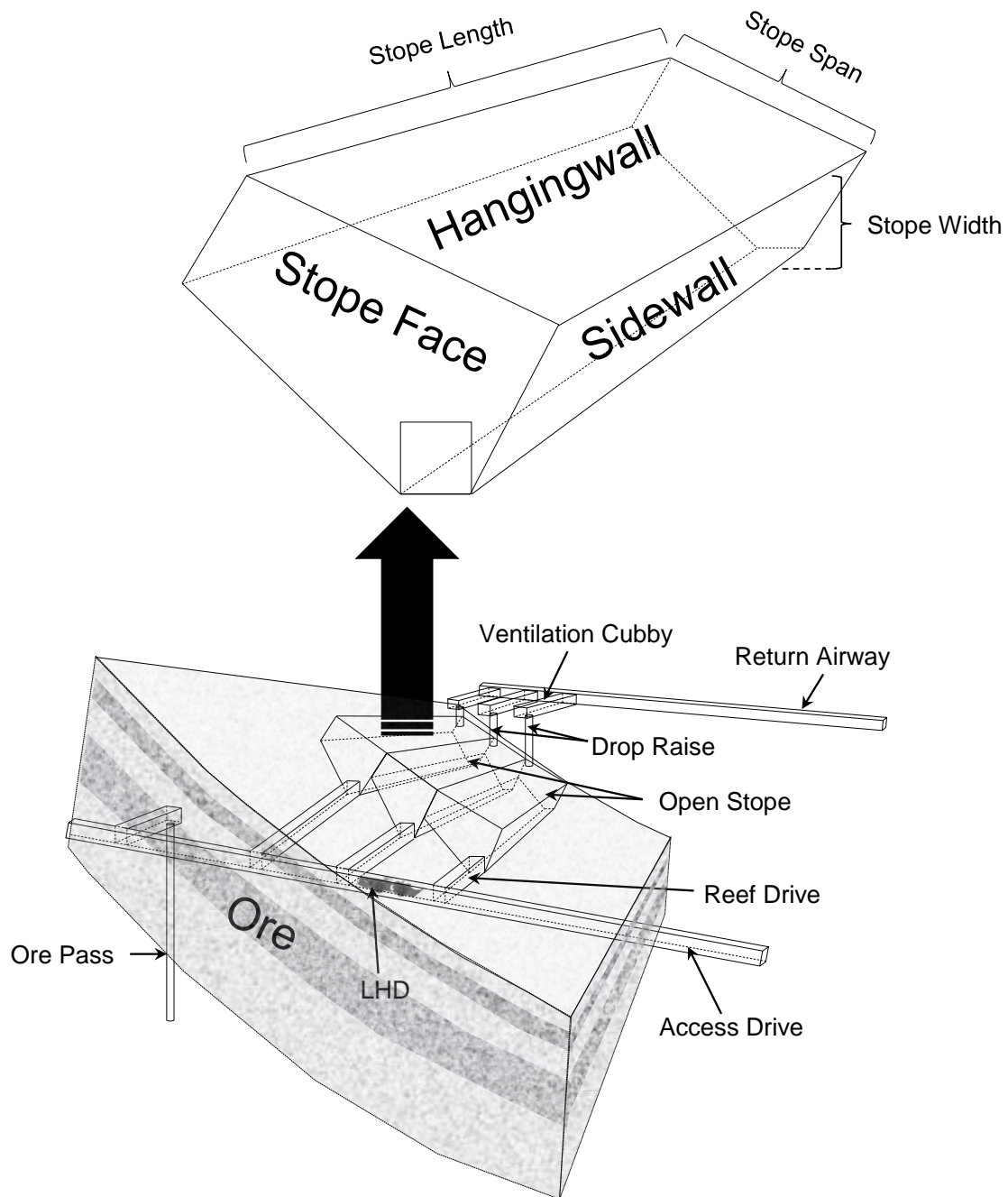


Figure 4.3 General isometric view of a typical open stope design on Target Mine



#### 4.4 Financial Implication of Dilution and Overbreak

Twenty-eight open stopes were used for the back analysis of fall of ground statistics, hours lost per item of mechanized equipment, and the cost implications per ton mined. Figure 4.6 and Figure 4.7 show the plan view of Target Mine and the cross section of the open stopes. In Appendix A, the actual location of each of the case studies on Target Mine is shown. Dilution or overbreak due to falls of ground in open stoping have a huge impact on the profitability of a mining operation. These falls of ground contribute significantly towards dilution as these falls of ground from the hangingwall or sidewalls have to be loaded with the blasted ore.



Figure 4.4 Photo of a TORO LH514 LHD in an open stope damaged by fall of ground

One of the contributing factors to loss in profit is damage and loss of mechanized equipment due to falls of ground in open stopes as shown in Figure 4.4. Only mechanized equipment being used in open stoping was used for the analyses. It was found from back analyses that the average hours lost over the period from 2002 to 2013 was 82 hours per fall of ground damage per item of mechanized equipment.

This is significant, with the average cost per ton mined being increased by approximately ZAR70/ton. The costs of damage to, or loss of, trackless equipment, as a direct result of these falls of ground in open stopes, are very significant, and have totalled about ZAR491 Million over the past 10 years at Target Mine. In Figure 4.5 the hours lost per year, associated with mechanized equipment damage by falls of ground in open stopes, are plotted. From these results, the period 2010 stands out due to the extent of damage to mechanized equipment.

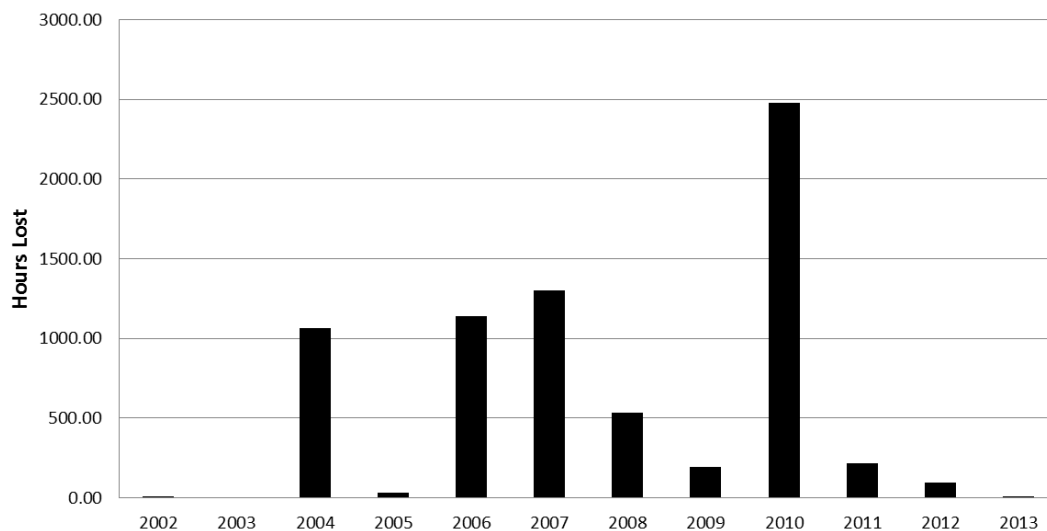


Figure 4.5 Graph showing standing time for mechanized equipment – open stoping, damage by falls of ground on Target Mine

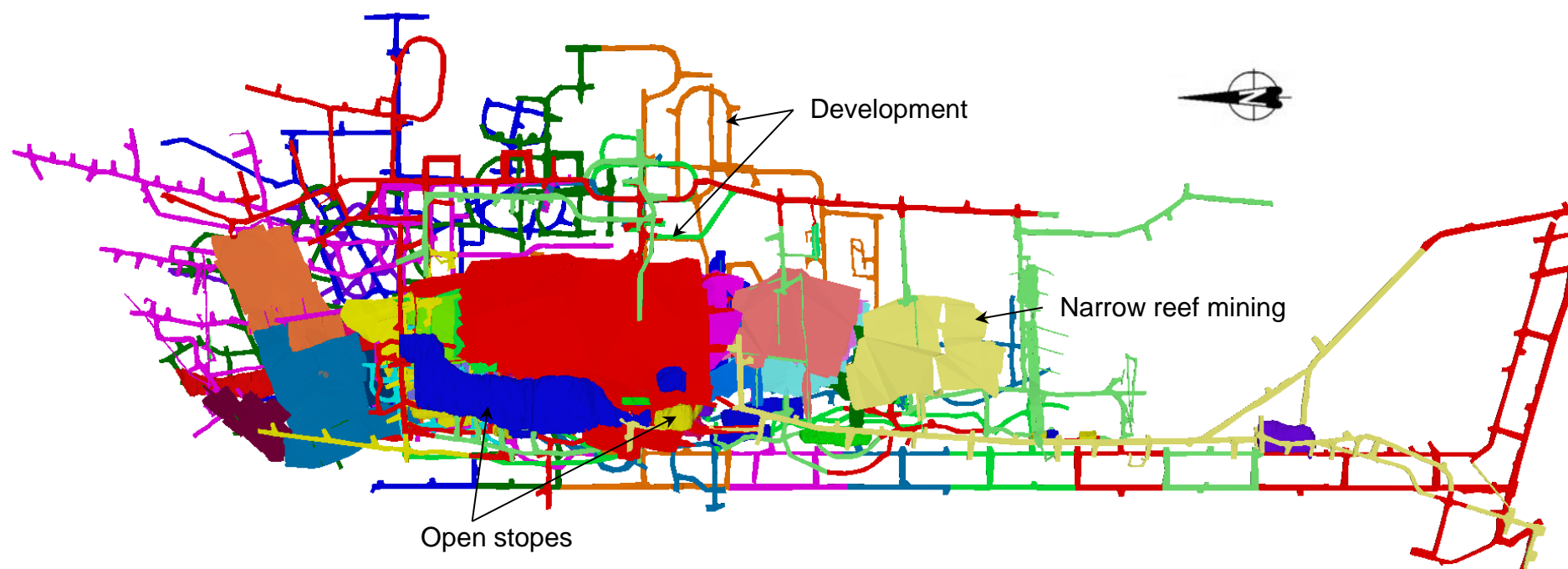


Figure 4.6 Plan view of Target mining block



Figure 4.7 Plan view of open stopes mined at Target Mine without showing the development and narrow reef stoping

Plotting the number of falls of ground causing damage per year, as shown in Figure 4.8, after a high peak in 2004, there was a steady increase over the period 2005 to 2010. From 2010 to 2013 there was a steep decline in falls of ground in open stopes due to design measures put in place. These design measures will be discussed in section 7.

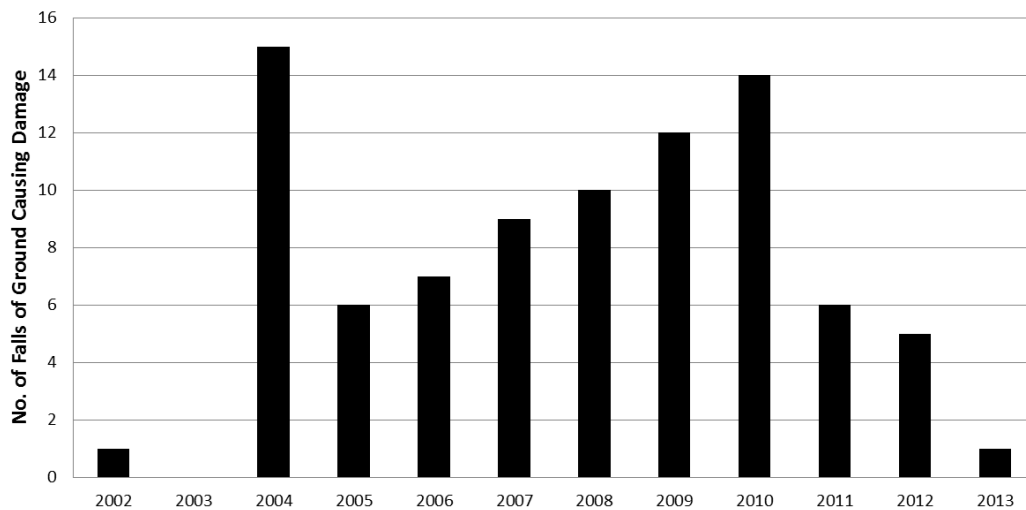


Figure 4.8 Graph showing mechanized equipment – open stoping, damage by falls of ground per year on Target Mine

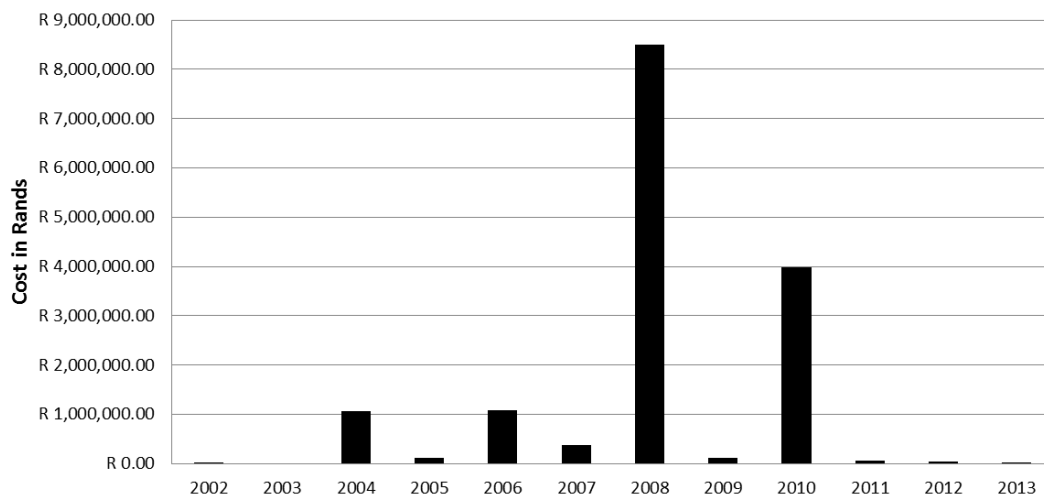


Figure 4.9 Graph showing repair cost of mechanized equipment – open stoping, damage by falls of ground per year on Target Mine

In Figure 4.9 the direct equipment repair costs associated with the damage due to falls of ground are plotted. For the period 2008, a loader was lost due to a major fall of ground as shown in Figure 4.4, and in 2010 a loader was damaged extensively. Plotting the cost associated with standing time and tons not hauled due to damaged mechanized equipment as shown in Figure 4.10, the 2010 period was the worst. Also, a clear cost decrease can be seen for the period 2010 to 2013.

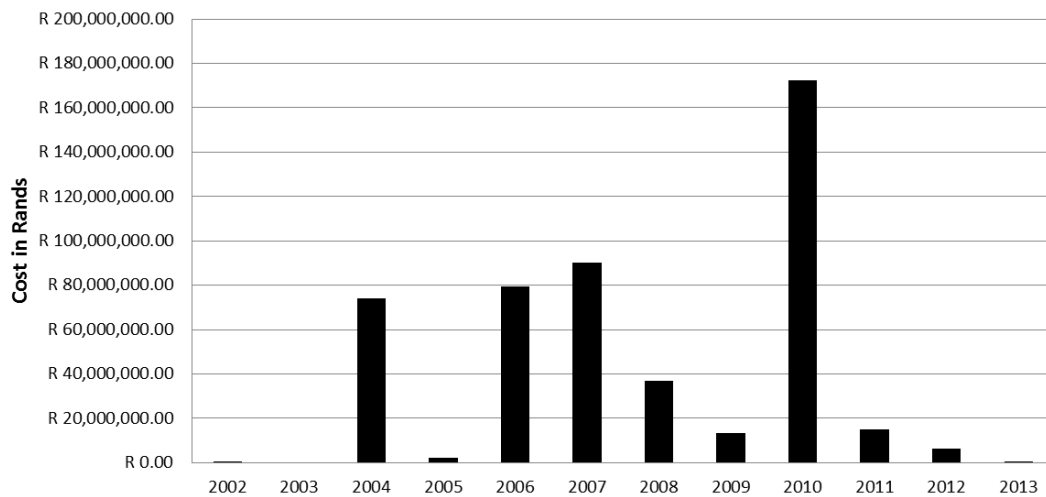


Figure 4.10 Graph showing total cost due to standing time of mechanized equipment – open stoping, damage by falls of ground per year on Target Mine

From 2002 to 2013, it was planned to mine 5.4 Million tons from open stopes on Target Mine, but in fact 6.5 Million tons were removed from these stopes due to overbreaking and falls of ground. The costs associated with removing and treating these tons are shown in Table 4.1:

**Table 4.1 Cost per ton breakdown for overbreaking in open stopes**

Hoisting and transport cost	ZAR161 per ton
Secondary blasting	ZAR2.50 per ton
Milling and plant treatment	ZAR96 per ton
Total cost	ZAR259.50 per ton

Using these figures, a cost could be calculated for overbreaking and falls of ground in open stopes for the period 2002 to 2013. For this period 1.1 Million tons of overbreaking and falls of ground were recorded, with an associated cost of approximately ZAR293 Million. The total cost for removing overbreak or falls of ground, standing time and repairing or replacing mechanized equipment due to falls of ground in open stopes, amounts to approximately ZAR784 Million for the period 2002 to 2013.

#### 4.4.1 Nature and Magnitude of Dilution

It was found during the past 11 years on Target Mine that the major contributors to dilution in open stopes are hangingwall beam failure, poor blasting and some sidewall failure. The magnitude of dilution ranges from as high as 74% to as low as 1.1% for twenty-two of the case studies. The remaining six case studies had underbreak ranging from 2% to as high as 18% due to poor blasting. As previously discussed, it was found that 1.1 Million tons of overbreak was recorded for this period in open stopes. In Figure 4.11 a histogram of the major principal stresses before mining open stopes for all case studies with hangingwall failure is shown. Figure 4.12 shows a histogram of major principal stresses before mining open stopes for all case studies with sidewall failure.

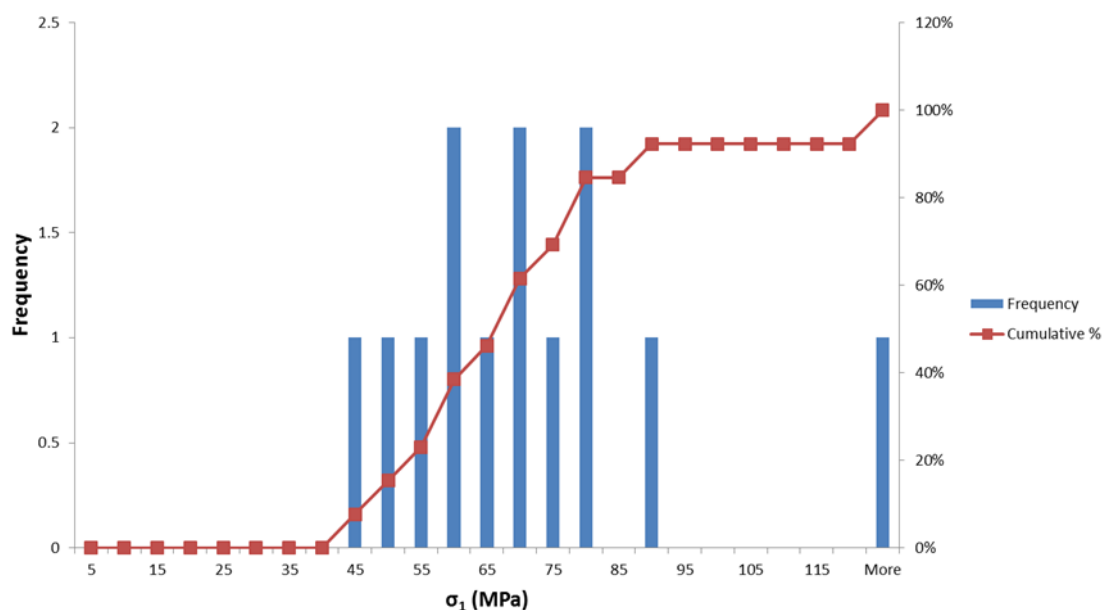


Figure 4.11 Histogram of major principal stress before mining open stopes for all case studies with hangingwall failure

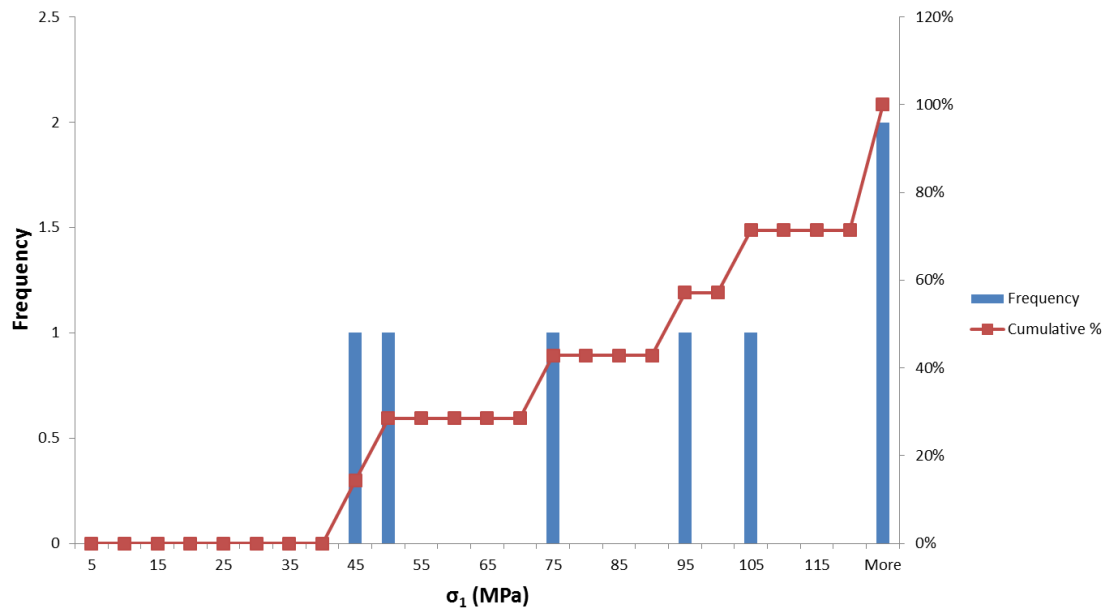


Figure 4.12 Histogram of major principal stress before mining open stopes for all case studies with sidewall failure

#### 4.4.2 Factors Initiating Instability

The following factors tend to initiate instability in open stopes:

##### Major Principal Stress before mining open stope

The stress environment around the open stope has a significant effect on the behaviour of these excavations. Looking at only the major principal stress in isolation from the other stress components does not yield any correlation for hangingwall and sidewall failure in open stopes on Target Mine as shown in Figure 4.11 and 4.12. In Figure 4.13 the histogram for major principal stresses before mining these open stopes is shown. These results are used in calculating the modified stability number,  $N'$  as discussed in section 5.3.



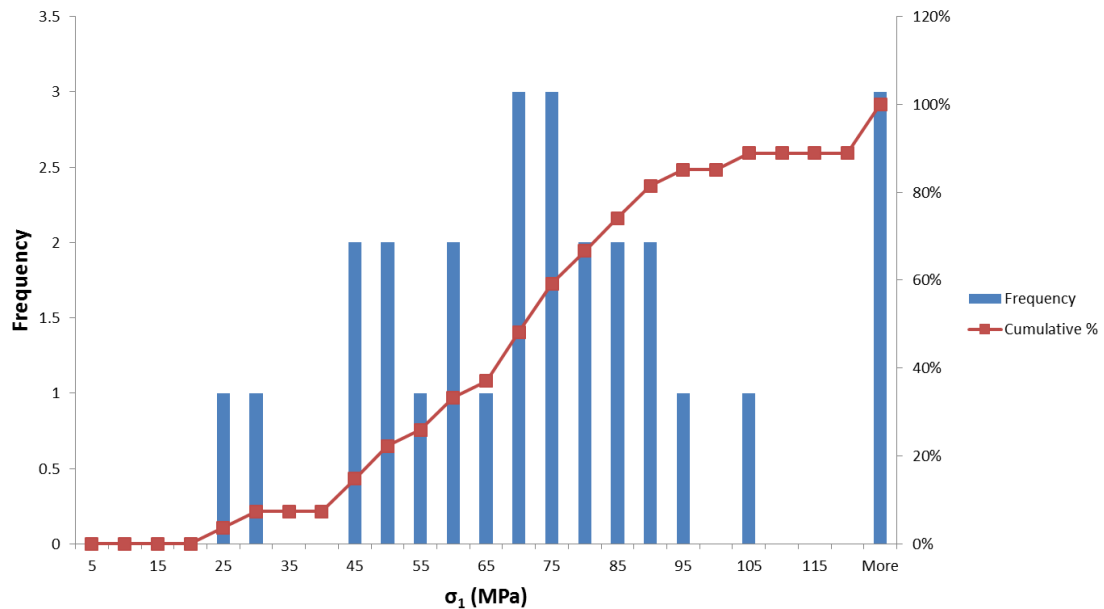


Figure 4.13 Histogram of major principal stress for all case studies before mining open stopes

### **Blasting practice and blast damage**

Poor blasting practice is one of the major contributors to failure and overbreaking in open stopes. The major factors associated with poor blasting are incorrect distance (burden) between the drilled blast holes, holes drilled too long or too short, wrong timing of blast holes for initiation, and over-charging of blast holes with explosives. The blast fractures created by the poor blasting tend to create friable hangingwall and sidewall conditions that tend to be unstable and fall out. In an attempt to ensure good blasting practice, the following procedure is followed at Target Mine.

A drilling layout is issued for each ring to be drilled for the open stope. The layout will state the layout number, the ring number and whether the layout is superseded or not. The layout will also state the orientation of the rig towards the slot of the open stope. Each layout will have a legend to indicate what colours are to be used to mark off the lines and the positions underground. The functional lines on the layout are the Set-up Line (SUL), Laser Line (LL), Survey Line (SL), Ring Line (RL) and Boom Position Lines (BPL) (COP Target Mine, 2014).

The burden between rings, toe spacing, tilt inclination, hole diameter, hole length and total metres to be drilled for the ring will be indicated on the layout. The layout will state the hole number, set-up position (SUL) relative to the Survey Line (SL), boom positions (BPL) relative to the SUL, rotation angle and planned hole length. Each layout will show a section of the ring to be drilled. On the section, the Survey Line (SL) will be denoted by a black cross and the Set-up Line (SUL) and the Boom Position Lines by pink crosses. A plan of the layout will indicate the position of the ring to be drilled. The surveyor will mark off the production drilling layouts in the reef drive (COP Target Mine, 2014).

The planning department for each open stope blast ring will issue a charging layout. Before any open stope blast ring may be charged up with explosives and blasted, the drilling accuracy of the blast holes must be examined by the Survey Department, checking the burden between rings, toe spacing, tilt inclination, hole diameter, hole length and total metres to be drilled. All holes shall be charged according to the charging layout, showing the amount of explosive for each hole (COP Target Mine, 2014).

### **Blasting vibrations (PPV)**

A study conducted on Target Mine, making use of geophones installed to measure the peak particle velocity at distances of 32m, 48m and 206m respectively from the open stope. From this data the input parameters for calculating the blasting vibrations (PPV) relative to other excavations were calculated. The effect of blasting on these excavations was also evaluated (Van Alphen, 1995). The following results were obtained as shown in Table 4.2.

**Table 4.2 List of recorded data at position A, B and C in radial, transverse and vertical directions (Van Alphen, 1995)**

	Measured <i>PPV</i> (mm/s)	Distance from Blast (m)	Scaled Distance
A-radial	2.5	206.3	16.3
B-radial	59	47.7	3.8
C-radial	154.2	32.5	2.6
A-transverse	4.1	206.3	16.3
B-transverse	41.5	47.7	3.8
C-transverse	143.4	32.5	2.6
A-vertical	6.6	206.3	16.3
B-vertical	41	47.7	3.8
C-vertical	110.6	32.5	2.6

From back analyses it was found that  $K = 1181$  and  $B = 2.21$ , for calculating blasting vibrations (*PPV*) on Target Mine as shown in the equation below:

$$PPV = 1181 \left( \frac{D}{\sqrt{W}} \right)^{-2.21} \quad (4.1)$$

During blasting, the ground is dynamically accelerated by the blast and associated vibrations. The dynamic acceleration of the ground could result in falls of ground in the open stope, contributing to dilution. It was found from underground observations, however, that blasting vibrations did not contribute as much to dilution in open stopes as did poor blasting practice.

### **Seismicity and dynamic loading**

Although occasional large seismic events are recorded, damage associated with these events in open stopes is minimal. For the past 11 years no major seismically induced dilution was reported or recorded.

### **Hydraulic radius of open stope**

Hydraulic radius, also known as shape factor, describes the size of a block of ground to be mined, as discussed in section 2.4.1. Hydraulic radius plays a significant role in the stability of open stopes. From back analyses of stopes mined over the past 11 years, it was found that if the hydraulic radius is in excess of 9m, major failure will occur. Figure 4.14 shows a histogram of the hydraulic radius for all case studies evaluated on Target Mine.

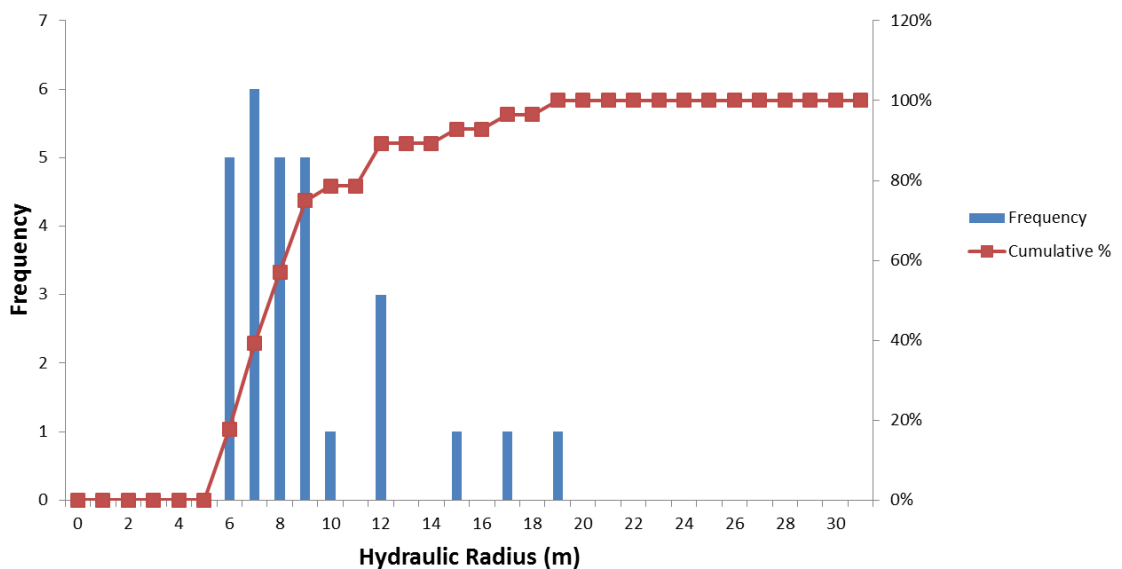


Figure 4.14 Histogram of hydraulic radius for all case studies

### **Geology (Rock Mass properties and Jointing)**

In open stoping, geology and the rock mass properties do have a significant effect on the stability of these stopes. The uniaxial compressive strength (UCS), joint orientation, number of joints, ground water and condition of the joints all play a role in the stability of the stope hangingwall and sidewalls. Jointing and faulting create keyblocks in the hangingwall and sidewalls that can fail, resulting in dilution. In addition, the properties of these geological structures will determine how self-supporting these key blocks will be.

In Table 4.2 to Table 4.4, the spacing, dip, strike direction, dip direction and length of these joints (bedding planes) for the EA1, EA3 and EA7 are shown. The spacing, dip, strike direction, dip direction and length for the second joint set are shown in Table 4.5. Two prominent joint sets were observed in the reef drive for these open stopes used for back analyses, with a random set of joints. These jointing statistics will be used for the numerical analyses making use of Dips and Phase2 as discussed in sections 6.2.2 and 6.2.3. In Table 4.6 the rock mass classification using the Q' System for all case studies is shown and will be used in section 5.3 to calculate the modified stability number, N'.

**Table 4.2 EA1 Jointing statistics**

	EA1 Jointing – Bedding planes				
	Spacing (m)	Dip (°)	Strike direction (°)	Dip Direction (°)	Length (m)
<b>Minimum</b>	0.20	17.0	143.0	53.0	160.0
<b>Maximum</b>	2.00	43.0	163.0	73.0	185.0
<b>Mean</b>	1.04	30.0	157.1	67.1	176.4
<b>Mode</b>	1.20	21.0	160.0	70.0	180.0
<b>Median</b>	1.20	23.0	160.0	70.0	180.0
<b>Standard Deviation</b>	0.59	11.1	6.9	6.9	8.6

**Table 4.3 EA3 Jointing statistics**

	EA3 Jointing – Bedding planes				
	Spacing (m)	Dip (°)	Strike direction (°)	Dip Direction (°)	Length (m)
<b>Minimum</b>	0.30	39.0	117.0	27.0	160.0
<b>Maximum</b>	2.80	50.0	195.0	105.0	217.0
<b>Mean</b>	1.18	45.4	156.5	66.5	185.0
<b>Mode</b>	0.90	45.0	161.0	71.0	181.0
<b>Median</b>	1.00	45.0	162.0	72.0	182.0
<b>Standard Deviation</b>	0.62	3.1	8.9	8.9	13.4

**Table 4.4 EA7 Jointing statistics**

EA7 Jointing – Bedding planes					
	Spacing (m)	Dip (°)	Strike direction (°)	Dip Direction (°)	Length (m)
Minimum	0.50	33.0	138.0	48.0	170.0
Maximum	2.90	49.0	162.0	72.0	179.0
Mean	1.55	40.3	149.4	59.4	174.4
Mode	2.00	44.0	140.4	50.4	173.0
Median	1.50	41.0	148.0	58.0	174.0
Standard Deviation	0.60	4.4	8.2	8.2	2.9

**Table 4.5 Second Joint set statistics**

Second joint set associated with the EA1, EA3 and EA7					
	Spacing (m)	Dip (°)	Strike direction (°)	Dip Direction (°)	Length (m)
Minimum	0.40	17.0	67.0	157.0	180.0
Maximum	1.80	49.0	83.0	173.0	185.0
Mean	1.16	35.8	77.3	167.3	180.9
Mode	1.10	39.0	80.0	170.0	180.0
Median	1.10	37.0	80.0	170.0	180.0
Standard Deviation	0.36	8.9	6.6	6.6	1.8

**Table 4.6 Rock mass classification using Q' System for all case studies**

	Reef Mined	RQD	Jn	Jr	Ja	Q'
Case Study 1	EA3	82.0	6	1.0	4.0	3.4
Case Study 2	EA3	83.0	6	2.0	3.0	9.2
Case Study 3	EA3	67.0	6	1.5	4.0	4.2
Case Study 4	EA3	64.5	6	3.0	2.0	16.1
Case Study 5	EA3	83.0	6	2.0	3.0	9.2
Case Study 6	EA3	64.5	6	3.0	2.0	16.1
Case Study 7	EA3	83.0	6	2.0	3.0	9.2
Case Study 8	EA3	85.0	6	1.0	3.0	4.7
Case Study 9	EA3	83.0	6	2.0	3.0	9.2
Case Study 10	EA7	85.0	6	1.0	3.0	4.7
Case Study 11	EA3	88.0	6	1.5	4.0	5.5
Case Study 12	EA3	85.0	6	1.0	3.0	4.7
Case Study 13	EA7	83.0	6	2.0	3.0	9.2
Case Study 14	EA3	82.0	6	1.0	4.0	3.4
Case Study 15	EA7	68.0	6	0.5	4.0	1.4
Case Study 16	EA3	83.0	6	2.0	3.0	9.2
Case Study 17	EA7	86.5	6	2.0	2.0	14.4
Case Study 18	EA3	69.5	6	3.0	2.0	17.4
Case Study 19	EA1	83.0	6	2.0	3.0	9.2
Case Study 20	EA1	76.0	6	3.0	2.0	19.0
Case Study 21	EA3	76.0	6	3.0	2.0	19.0
Case Study 22	EA1	88.9	6	2.0	1.0	29.6
Case Study 23	EA7	76.0	6	1.0	2.0	6.3
Case Study 24	EA3	69.5	6	3.0	2.0	17.4
Case Study 25	EA3	80.5	6	1.5	1.0	20.1
Case Study 26	EA3	85.0	6	1.0	3.0	4.7
Case Study 27	EA1	75.4	6	2.0	1.0	25.1
Case Study 28	EA1	75.4	6	2.0	1.0	25.1

## 4.5 Summary

In this chapter, a general description of open stope mining was given for the site used during data collection. The direct and indirect financial implications of dilution and overbreak on open stope mining at this site was discussed. For the empirical database, the nature and magnitude of dilution, factors initiating instability such as stress environment, blasting practice and the effect of blast damage, blasting vibrations (*PPV*), effect of seismicity and dynamic loading, hydraulic radius, rock mass properties and jointing, on the stability of the open stopes were evaluated. Chapter five will discuss the dilution factor and dilution prediction methods with the results obtained for Target Mine.



## **5 DILUTION FACTOR AND DILUTION PREDICTION**

### **5.1 Introduction**

In chapter four a general description of open stope mining was given for the Target Mine site used for data collection. The direct and indirect financial implications of dilution on open stope mining were discussed. For the empirical database, the nature and magnitude of dilution and factors initiating instability were evaluated. This chapter will discuss the dilution factor and dilution prediction methods with the results obtained for Target Mine. By applying analytical design methods to the case studies on Target Mine the open stopes will be evaluated.

### **5.2 Measurement of Dilution**

As discussed in section 2.2, the amount of dilution in an open stope can be determined by subtracting the planned stope volume in  $\text{m}^3$  from the actual measured final stope volume in  $\text{m}^3$ , which is obtained from the CMS. This is then in turn divided by the planned stope volume in  $\text{m}^3$  to determine the percentage dilution. The CMS wireframe is imported into the geological model and its grade re-evaluated. The dilution obtained can result in a major reduction of recovered grade for the open stope. Major dilution is defined as measured dilution greater than ten percent. This is a mine management definition, based on the economics of the operation. Minor dilution is where the measured dilution is equal to or less than ten percent, and underbreaking is where the measured dilution is negative (less than zero percent). At Target Mine all open stopes are designed for dilution of 5% and less, but this is rarely achieved. It was found that, in 50% of the case studies, dilution was greater than 10%, and 29% of the case studies had dilution less than 10%, as shown in Figure 5.1. In the remaining 21% of the case studies, underbreak occurred, as shown in Figure 5.1.

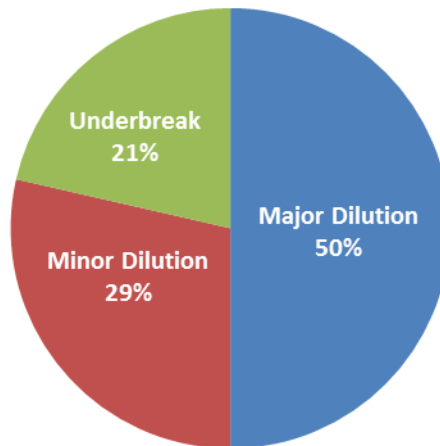


Figure 5.1 Pie Chart showing the percentage major dilution, minor dilution and underbreak for the case studies

### 5.3 Modified stability number, $N'$

Making use of back analyses the Hydraulic radius and modified stability number,  $N'$  for each of the twenty-eight case studies were determined. In Table 5.1 to Table 5.3 and Appendix D the results are shown. These results were collected and obtained from underground observations. The planned dimensions for the open stopes were collected from the mine planning department on Target Mine. The actual open stope measurements were obtained from the survey department using the Cavity Monitoring System (CMS). In Figure 5.2 a histogram of the Modified stability numbers,  $N'$  for all case studies is shown. In Figure 5.3 the twenty-eight case studies are plotted on the modified stability diagram after Potvin (1988). From these results it can be seen that most of the open stopes with major dilution ( $>10\%$ ), plot in the support required zone, with two of the case studies plotting in the transitional zone and one in the caved zone.

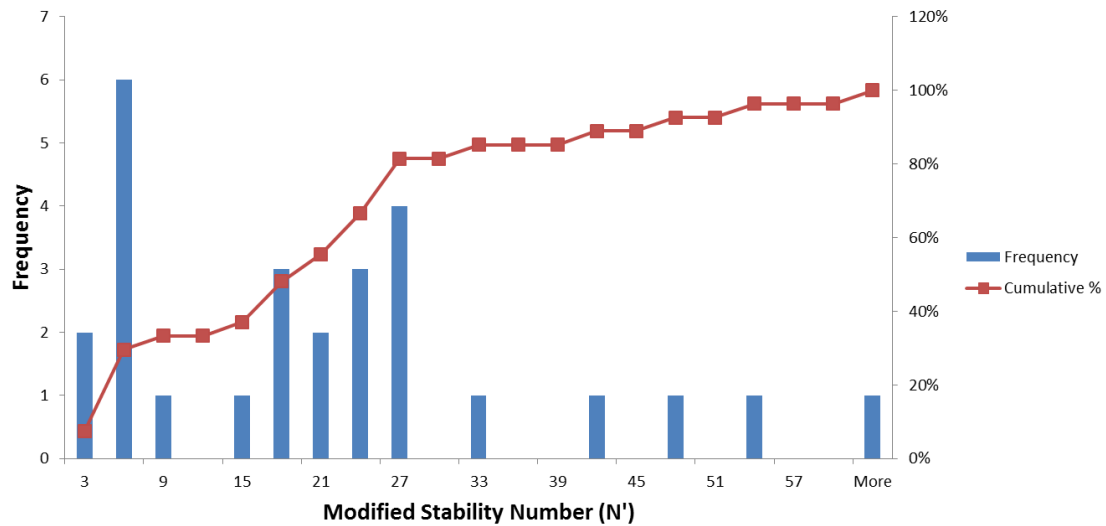


Figure 5.2 Histogram of Modified stability number,  $N'$  for all case studies

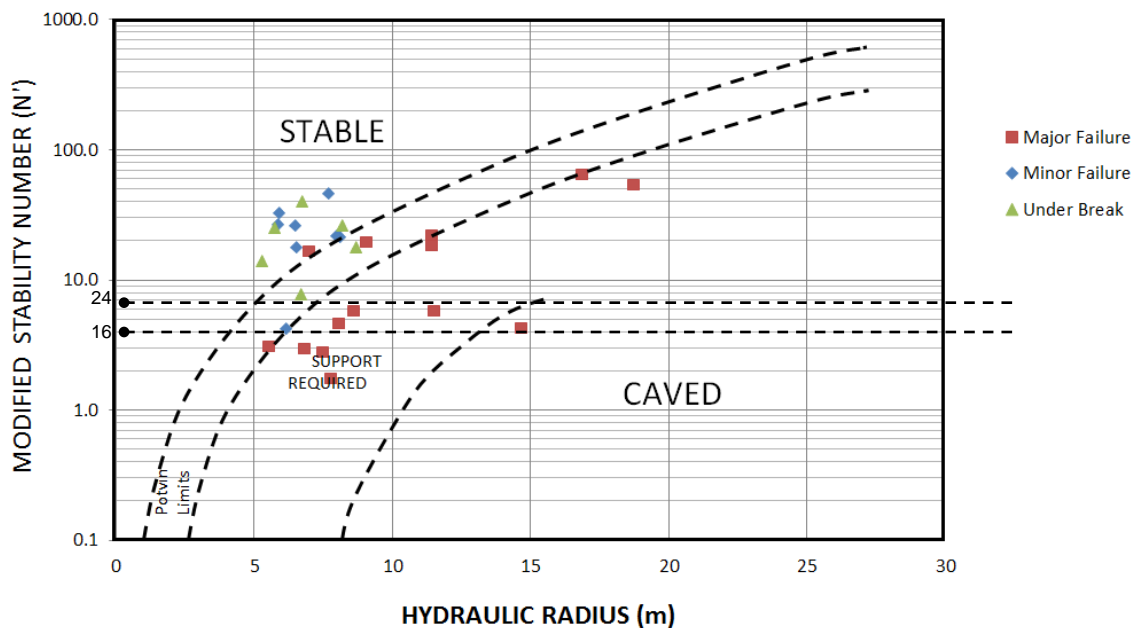


Figure 5.3 Plot of case studies on modified stability diagram after Potvin (1988) where average  $N' = 16$  for major failure and  $N' = 24$  for minor failure

By plotting the percentage dilution for twenty-two of the case studies with dilution greater than zero on the modified stability diagram after Potvin (1988), the diagram was modified to show the expected dilution for an obtained modified stability number versus hydraulic radius, as shown in Figure 5.4. This was done by obtaining the logarithmic trend lines for dilution  $<10\%$ ,  $>10\%$  to  $<20\%$ ,  $>20\%$  to  $<30\%$ ,  $>30\%$  to  $<40\%$ ,  $>40\%$  to  $<50\%$ ,  $>50\%$  to  $<60\%$  and

>60% to <70%. There were no data for >40% to <50% and >50% to <60% dilution and thus the trend lines were estimated as shown on Figure 5.4.

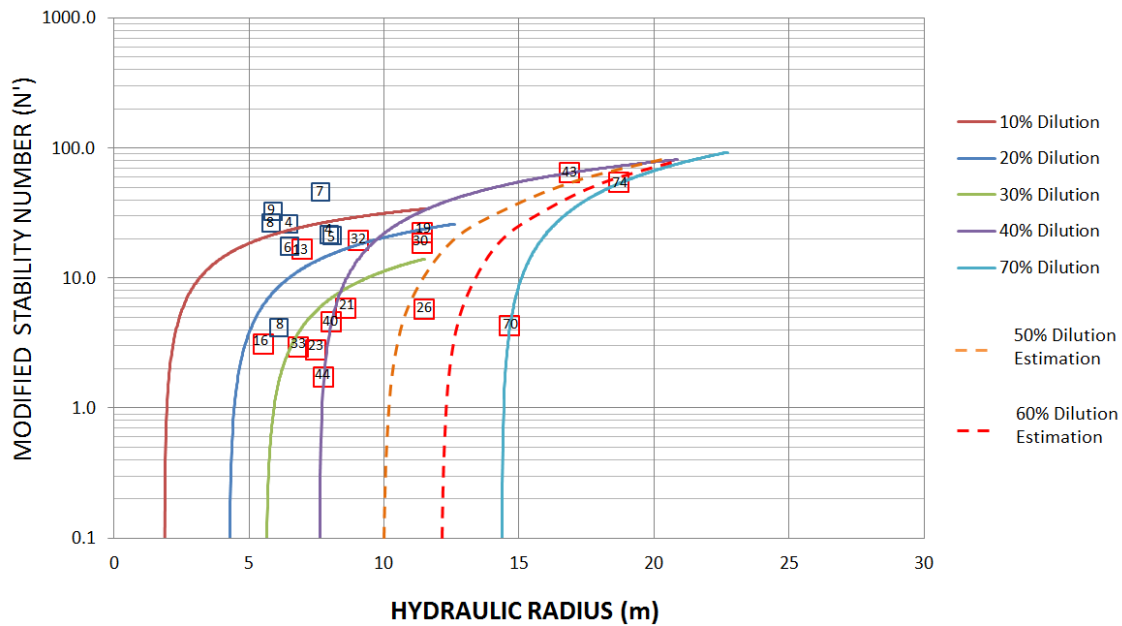


Figure 5.4 Modification of the modified stability diagram showing percentage trend lines for Target Mine, after Potvin (1988)

The percentage dilution, hydraulic radius and modified stability number,  $N'$  for twenty-two of the case studies were plotted on the graph for dilution greater than zero percent as shown in Figure 5.5, after Pakalnis et al (1995). Logarithmic trend lines were established for the following modified stability number,  $N'$  ranges:  $\leq 3$ ; 4 to 10; 11 to 20; 21 to 30 and  $>30$ .

From these logarithmic trend lines, the percentage dilution can be calculated making use of the equations shown in Table 5.4. The fit of each equation to the data obtained from the twenty-two case studies is shown by the  $R^2$  value in Table 5.4 and Figure 5.5. For case studies with a modified stability number,  $N' \leq 3$  and  $N' = 21$  to 30 the  $R^2$  value was just over 0.5, which is not good. For modified stability number,  $N' = 4$  to 10 the  $R^2$  value was just over 0.65, which is more acceptable. For modified stability number,  $N' = 11$  to 20 and  $N' > 30$  the  $R^2$  value was over 0.8, which is good.

**Table 5.4 Calculation of percentage dilution from hydraulic radius**

Modified Stability Number, $N'$	Percentage Dilution	Regression Analysis ( $R^2$ )
$N' \leq 3$	$= 0.5811 \ln(HR) - 0.8278$	0.5364
$N' = 4 \text{ to } 10$	$= 0.5749 \ln(HR) - 0.9565$	0.6585
$N' = 11 \text{ to } 20$	$= 0.4399 \ln(HR) - 0.7268$	0.8017
$N' = 21 \text{ to } 30$	$= 0.1737 \ln(HR) - 0.2755$	0.5053
$N' > 30$	$= 0.5126 \ln(HR) - 0.8951$	0.8534

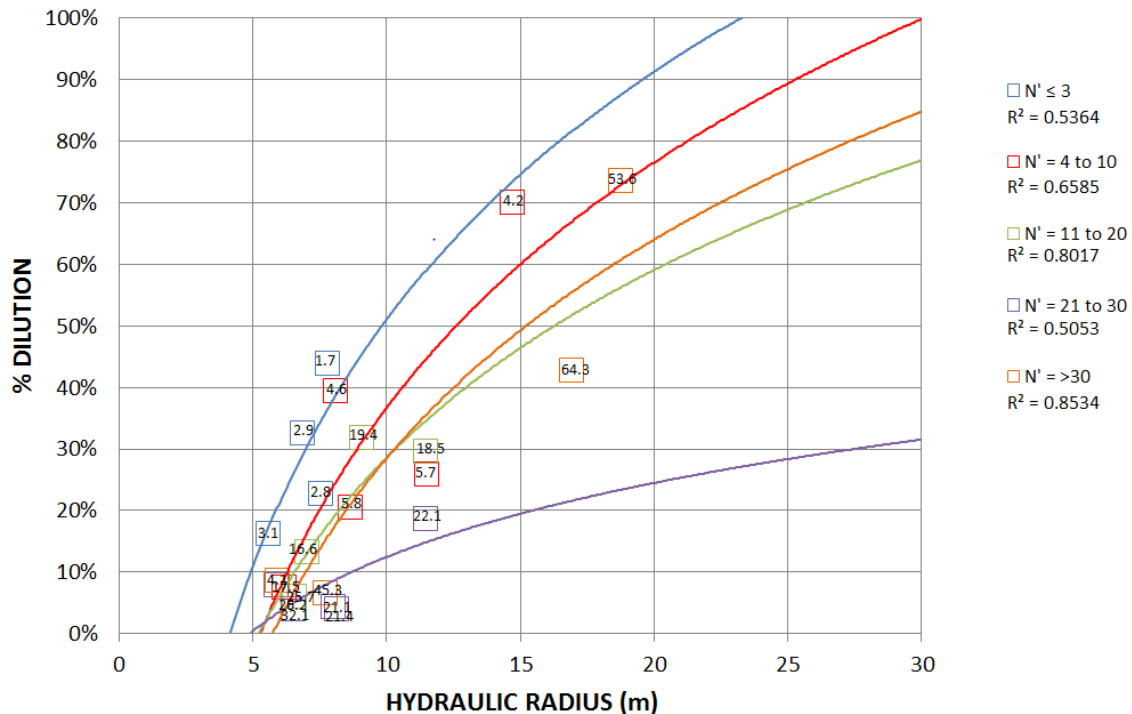


Figure 5.5 Plot of case studies showing relation between percentage dilution, hydraulic radius and modified stability number,  $N'$  after Pakalnis et al (1995)

#### 5.4 Equivalent Linear Overbreak Slough (ELOS)

The dilution factor is defined as the ELOS predicted from the dilution design graph based on the modified stability number,  $N'$ , and hydraulic radius for an open stope, as discussed in section 2.4.4. The twenty-two case studies with dilution greater than zero percent are plotted on the modified stability diagram for ELOS, after Clark and Pakalnis (1997), in Figure 5.7. The calculated ELOS was found to show values from 2.4m up to 23.7m for open stopes with major dilution (>10%). A contributing factor could be that the sidewall dilution is ignored by ELOS, in effect over estimating the dilution factor.

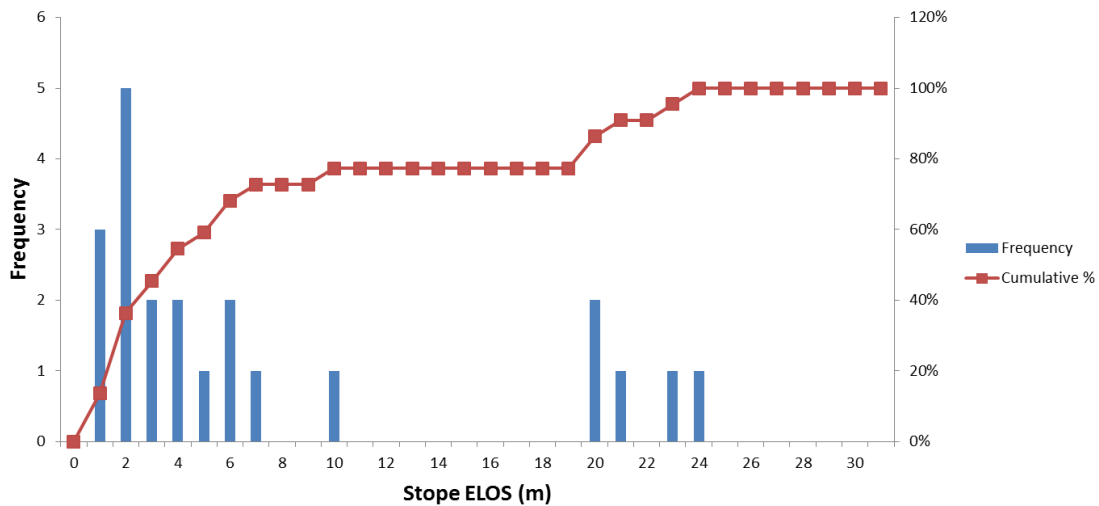


Figure 5.6 Histogram of stope ELOS (m) for all case studies

The modified stability diagram for ELOS after Clark and Pakalnis (1997) was further modified, to attempt to incorporate the ELOS values obtained on Target Mine. It was found that, for Target Mine, the ELOS values are much higher than obtained by Clark and Pakalnis (1997), Wang (2004) and Capes (2009), as shown in Figure 5.7. Due to the limited number of case studies, it was found that, for the ranges of ELOS between 2m to 4m, 4m to 6m and 6m to 12m, the trend lines could not be established. However, for ELOS between 1m and 2m, and greater than 12m, the linear trend lines could be established. Applying the method of establishing the ELOS values as described by Wang (2004), the dashed trend lines obtained for ELOS between 2m to 4m, 4m to 6m and 6m to 12m are shown in Figure 5.8 (estimation). The validities of these trends are questionable, however.

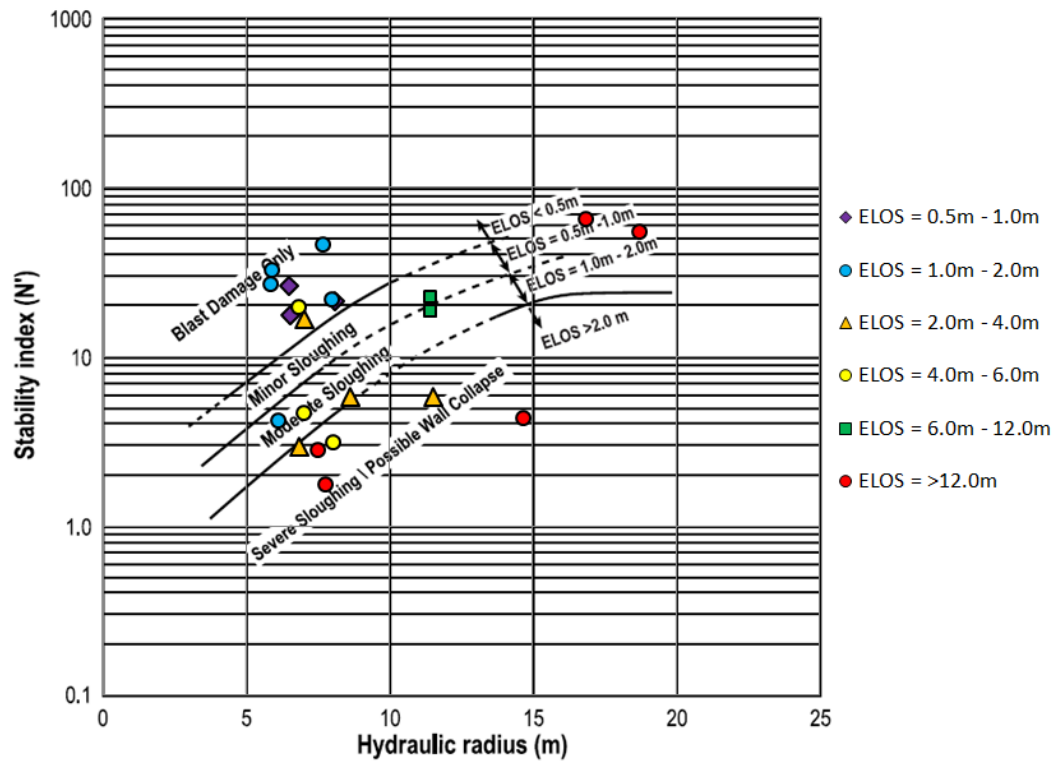


Figure 5.7 Plot of case studies showing relation between ELOS, hydraulic radius and modified stability number,  $N'$  after Clark and Pakalnis (1997)

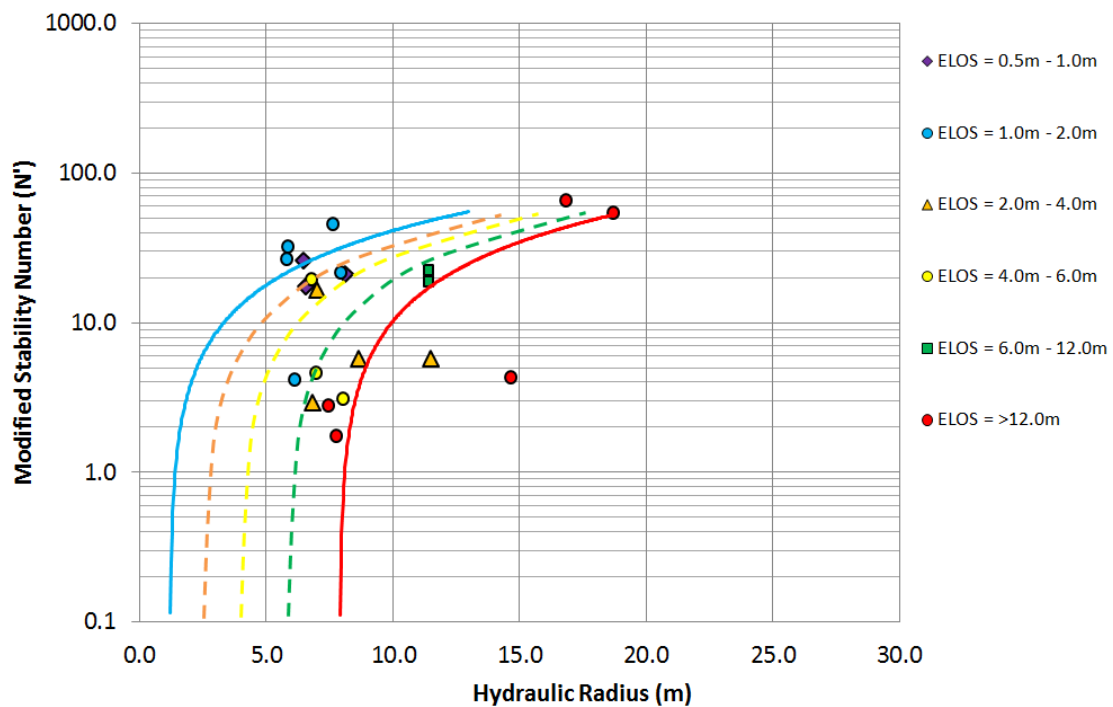


Figure 5.8 Modified plot of case studies showing relation between ELOS, hydraulic radius and modified stability number,  $N'$  for Target Mine after Clark and Pakalnis (1997)

**Table 5.1 Summary of Case Studies with major dilution**

	Planned m <sup>3</sup>	CMS Actual m <sup>3</sup>	Planned Beam area	Planned Circumference	Planned HR	Actual Beam area	Actual Circumference	Actual HR	Dilution	Majority of Dilution is from	Co	$\sigma_1$	R	A	B	C	N'	Q'	ELOS
Case Study 1	8271	12323	1075	157	7	1174	168	7	33%	Hangingwall	250	71	3.5	0.3	0.8	4.0	2.9	3.4	3.5
Case Study 2	16197	23806	1315	145	9	1461	152	10	32%	Sidewall	250	21	11.7	1.0	0.3	7.0	19.4	9.2	5.2
Case Study 3	10665	17691	1582	196	8	1656	194	9	40%	Hangingwall	250	65	3.9	0.3	0.7	5.0	4.6	4.2	4.2
Case Study 4	70724	126508	6780	402	17	2716	117	23	44%	Sidewall	250	22	11.5	1.0	0.8	5.0	64.3	16.1	20.5
Case Study 5	66757	86623	2603	347	7	1043	101	10	23%	Hangingwall	250	140	1.8	0.1	0.8	5.0	2.8	9.2	19.1
Case Study 6	36823	140414	10892	582	19	4363	169	26	74%	Sidewall	250	29	8.5	0.8	0.8	5.0	53.6	16.1	23.7
Case Study 7	32739	109972	8573	585	15	3434	170	20	70%	Sidewall	250	117	2.1	0.1	0.8	5.0	4.2	9.2	22.5
Case Study 8	14596	17464	543	98	6	490	97	5	16%	Hangingwall	250	42	5.9	0.5	0.3	4.0	3.1	4.7	5.9
Case Study 9	84164	120013	3559	312	11	3707	306	12	30%	Hangingwall	250	13	19.2	1.0	0.5	4.0	18.5	9.2	9.7
Case Study 10	28766	33236	1135	162	7	1452	175	8	13%	Sidewall	250	28	8.9	0.9	0.8	5.0	16.6	4.7	3.1
Case Study 11	20654	27936	2950	257	11	3026	278	11	26%	Hangingwall	250	73	3.4	0.3	0.8	5.0	5.7	5.5	2.4
Case Study 12	15198	19167	1213	141	9	1532	170	9	21%	Hangingwall	250	66	3.8	0.3	0.8	5.0	5.8	4.7	2.6
Case Study 13	86855	107079	3551	311	11	2972	309	10	19%	Hangingwall	250	8	29.9	1.0	0.6	4.0	22.1	9.2	6.8
Case Study 14	28128	73018	2027	260	8	2351	272	9	62%	Hangingwall	250	71	3.5	0.3	0.8	4.0	2.9	3.4	3.5

**Table 5.2 Summary of Case Studies with minor dilution**

	Planned m <sup>3</sup>	CMS Actual m <sup>3</sup>	Planned Beam area	Planned Circumference	Planned HR	Actual Beam area	Actual Circumference	Actual HR	Dilution	Majority of Dilution is from	Co	$\sigma_1$	R	A	B	C	N'	Q'	ELOS
Case Study 15	18810	20465	774	132	6	1079	158	7	8%	Sidewall	250	41	6.2	0.6	0.3	7.0	1.7	1.4	19.1
Case Study 16	18353	19567	965	148	7	1562	176	9	6%	Hangingwall	250	34	7.4	0.7	0.8	5.0	26.2	9.2	1.5
Case Study 17	24112	25899	1272	166	8	1021	146	7	7%	Hangingwall	250	60	4.2	0.3	0.5	7.0	17.5	14.4	0.8
Case Study 18	23230	24266	1698	210	8	2083	219	10	4%	Hangingwall	250	33	7.5	0.7	0.6	6.0	45.3	17.4	1.8
Case Study 19	26899	28182	1139	143	8	1159	145	8	5%	Hangingwall	250	47	5.3	0.5	0.6	8.0	21.1	9.2	0.5
Case Study 20	30834	32221	1193	184	6	1405	205	7	4%	Sidewall	250	47	5.3	0.5	0.3	8.0	21.4	19.0	1.1
Case Study 21	14988	16429	570	97	6	754	106	7	9%	Sidewall	250	41	6.1	0.6	0.3	8.0	25.7	19.0	1.0
Case Study 22	12379	13420	920	150	6	940	143	7	8%	Hangingwall	250	49	5.1	0.5	0.3	8.0	32.1	29.6	1.9



**Table 5.3 Summary of Case Studies with underbreak**

	Planned m <sup>3</sup>	CMS Actual m <sup>3</sup>	Planned Beam area	Planned Circumference	Planned HR	Actual Beam area	Actual Circumfe rence	Actual HR	Dilution	Co	$\sigma_1$	R	A	B	C	N'	Q'	ELOS
Case Study 23	10754	9065	704	123	6	601	119	5	-19%	250	34	13.0	1.0	0.8	5.0	25.0	6.3	-2.8
Case Study 24	15105	14444	789	150	5	1249	175	7	-5%	250	60	4.6	0.4	0.5	4.0	13.6	17.4	-0.5
Case Study 25	57885	49340	2942	339	9	3542	370	10	-17%	250	33	3.9	0.3	0.7	4.0	17.5	20.1	-2.4
Case Study 26	14280	13654	839	125	7	776	122	6	-5%	250	47	4.1	0.3	0.8	6.0	7.6	4.7	-0.8
Case Study 27	23095	21942	772	115	7	1072	140	8	-5%	250	47	4.0	0.3	0.8	6.0	39.1	25.1	-1.1
Case Study 28	48620	47678	2002	245	8	1402	164	9	-2%	250	41	3.0	0.2	0.8	6.0	25.8	25.1	-0.7

## **5.5 Summary**

This chapter discussed the dilution factor and dilution prediction methods with the results obtained for Target Mine. Making use of back analyses the Hydraulic radius, modified stability number,  $N'$ , and ELOS were determined for each of the twenty-eight case studies. These results were plotted on the modified stability diagram after Potvin (1988), and this diagram was modified to include trend lines for percentage dilution. These results were then plotted to show the relation between percentage dilution, hydraulic radius and modified stability number,  $N'$  after Pakalnis et al (1995) with trend lines to determine dilution.

The relation between ELOS, hydraulic radius and modified stability number,  $N'$ , was plotted after Clark and Pakalnis (1997) and modified to show trend lines for determining ELOS.

## **6 INFLUENCE OF STRESS ON OPEN STOPE HANGINGWALL AND SIDEWALL STABILITY AND DILUTION**

### **6.1 Introduction**

Chapter five discussed the dilution factor and dilution prediction methods using the results obtained for each of the case studies on Target Mine. Making use of back analyses, the modified stability number,  $N'$ , Hydraulic radius and ELOS were determined for each of the twenty-eight case studies. These results were then plotted on the relevant design graphs. In this chapter the influence of stress on open stope hangingwall and sidewall stability, and the effect on dilution will be discussed. Numerical modelling methods will be applied to simulate the stress distribution around the open stopes from the case studies, and failure criteria applied to evaluate the stability of these excavations and the effects on dilution.

### **6.2 Modelling Methodology**

Making use of back analyses is one of the most important aspects in any engineering field. Compared with other engineering fields such as Aeronautical, Civil and Mechanical engineering, back analysis in Rock engineering is not always being utilized efficiently. Back analyses of open stope overbreak can yield an insight into the true behaviour of these excavations in the mining environment. Knowing that these stopes failed, the magnitude and mode of failure can prove extremely useful. Ultimately, the failure of these stopes should be “designed”, and not be seen as “unexpected failure”.

The geological setting of the open stopes will be evaluated using rock mass classification. The UCS, joint orientation, number of joints, ground water and condition of the joints all play a role in the stability of the stope hangingwall and sidewalls. Open stopes that are de-stressed, and those that are highly stressed will behave differently, and the modes and mechanisms of failure are different.

Numerical modelling will be used to evaluate the mode and mechanism of hangingwall and sidewall failure in these open stopes. When the numerical models were constructed, the principle of Occam's razor was applied, meaning the elimination of all unnecessary information relating to the problem that was analysed (Wiles, 2006). Dips, Map3D, Phase2 and JBlock numerical models were used for conducting back analyses on these open stopes.

Making use of Dips, geological data, such as joint orientation and the effect thereof on open stope sidewalls, can be simulated (Rocscience, 2015). To model the mining on Target Mine, a numerical model is required that will be able to model flat tabular reefs as well as massive open stopes and give results for stress, strain and deformation, and output the  $\sigma_1$ ,  $\sigma_2$ ,  $\sigma_3$ ,  $\varepsilon_1$ ,  $\varepsilon_2$  and  $\varepsilon_3$  values for given coordinates (x, y and z) at multiple mining steps in three dimensions. These requirements are satisfied by MAP3D-SV, an elastic, three-dimensional, boundary element rock stability analysis package. The program is used to construct models, analyse and display displacements (m), strains (unit less), stresses (MPa), energy release rate (MJ/m<sup>2</sup>), excess shear stress (MPa) and strength factors (Wiles, 2006).

To simulate the behaviour of the jointed hangingwalls and sidewalls of the open stopes, Phase2 was used. Phase2 can simulate multiple joints, and the interaction of these joints with the open stope when excavated. Phase2 can determine elastic and inelastic displacements, which are displayed around the open stope and joints at different mining steps in two dimensions (Rocscience, 2015).

The orientation, spacing and length of discontinuities can be used to simulate blocks in the hangingwall of the open stope excavation. The JBlock program was used to generate key blocks, making use of three discontinuity sets (Esterhuizen and Streuders, 1998).

Each of these modelling programs will be discussed in more detail in sections 6.2.1 to 6.2.4.

### 6.2.1 Dips

For analysis of geological data and the orientations thereof, the Dips program can be used. The program allows the analysis and visualisation of structural data in the same manner as manual stereonet. In addition, mean orientation, statistical contouring of orientation, cluster variability, clustering confidence calculation and quantitative feature attribute analysis can be conducted (Rocscience, 2015).

In the research conducted for this thesis, the potential for sidewall instability of the open stopes was evaluated using Dips, to determine the possibility of wedge failures. As in slope stability, the angle of the slope is very important and the lower the dip angle the more stable the dip. In open stope mining at Target Mine, sidewall slopes are normally mined with a dip of  $55^\circ$  as shown in Figure 6.1. The geological input parameters that were used for the analyses are tabled in Table 4.2 to Table 4.5.

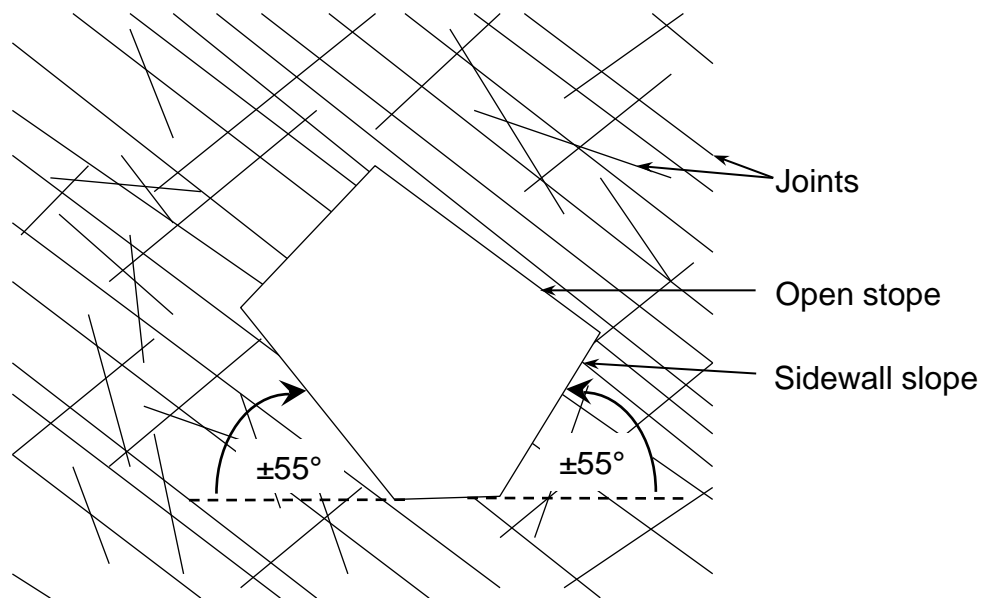


Figure 6.1 Sketch showing the dip of the open stope sidewall slopes

## **Dips Results**

As discussed in the section above, Dips was used to evaluate the interaction of the joint sets and the open stope sidewalls, to identify potential instability. From these analyses the following results were obtained, as shown in Figure 6.2, Figure 6.4 and Figure 6.6.

In Figure 6.2, Figure 6.4 and Figure 6.6 the possibility of wedge sliding is given for the EA1, EA3 and EA7 joint sets and the second joint set intersection. The average slope dip for the open stope sidewalls slope was taken as 55°, determined from actual open stope design, as shown in Figure 6.1. The stopes are mined in a northerly direction. A twenty-eight percent probability of wedge failure in the sidewalls is expected for open stopes mining the EA1 reef as shown in Figure 6.2.

For the EA3 reef a seventy percent probability of wedge failure in the sidewalls is expected for open stopes as shown in Figure 6.4. These results indicate that the EA3 reef formation sidewalls are prone to wedge failure. The predicted failure from the sidewalls correlated with actual underground observations made for stopes being mined in the EA3 reef. For the EA7 reef, the results obtained indicated a forty percent probability of wedge failure in the sidewalls for open stopes as shown in Figure 6.6.

Figure 6.3, Figure 6.5 and Figure 6.7 show rosette diagrams, which are radial histograms of strike density or frequency for the EA1, EA3, EA7 joints and second joint sets respectively. The rosette diagram shows less information than a full stereonet, since one dimension is removed from the diagram. The planes are considered essentially in a two dimensional geometry. Using a vertical rosette cutting a section through the slope as shown in Figure 6.1, quick sliding analyses can be done when the structure strikes parallel to the slope face (Rocscience, 2015).

For visualisation and conveying structural data, rosette diagrams are more appropriate when the structural nature of the rock is simple. The rosette plot

begins with a horizontal plane, which is represented by the outer circle of the stereonet. A radial histogram with arc segments is overlain on the circle, indicating the density of planes intersecting this horizontal surface. The radial orientation limits of the arc segments correspond with the strike of the range of the planes being represented by the segment (Rocscience, 2015).

Each arc segment on a rosette diagram has an equal and opposite counterpart 180° apart. The rosette diagram in Dips does not differentiate between right and left handed strike planes with strikes 180° apart in the same "bin". A "bin" is a range defined by one arc segment. In Dips, each bin is 10 degrees wide by default (Rocscience, 2015).

In Figure 6.3 the rosette diagram of the EA1 joint set and second joint set is shown with 48 planes plotted, 45 planes per arc with a strike density of 36 planes and a trend of N80E. Figure 6.5 shows the rosette diagram of the EA3 joint set and second joint set, 35 planes plotted, 10 planes per arc with a strike density of 9 planes and a trend of N80E. Figure 6.7 shows the rosette diagram of the EA7 joint set and second joint set, 13 planes plotted, 10 planes per arc with a strike density of 9 planes and a trend of N80E.

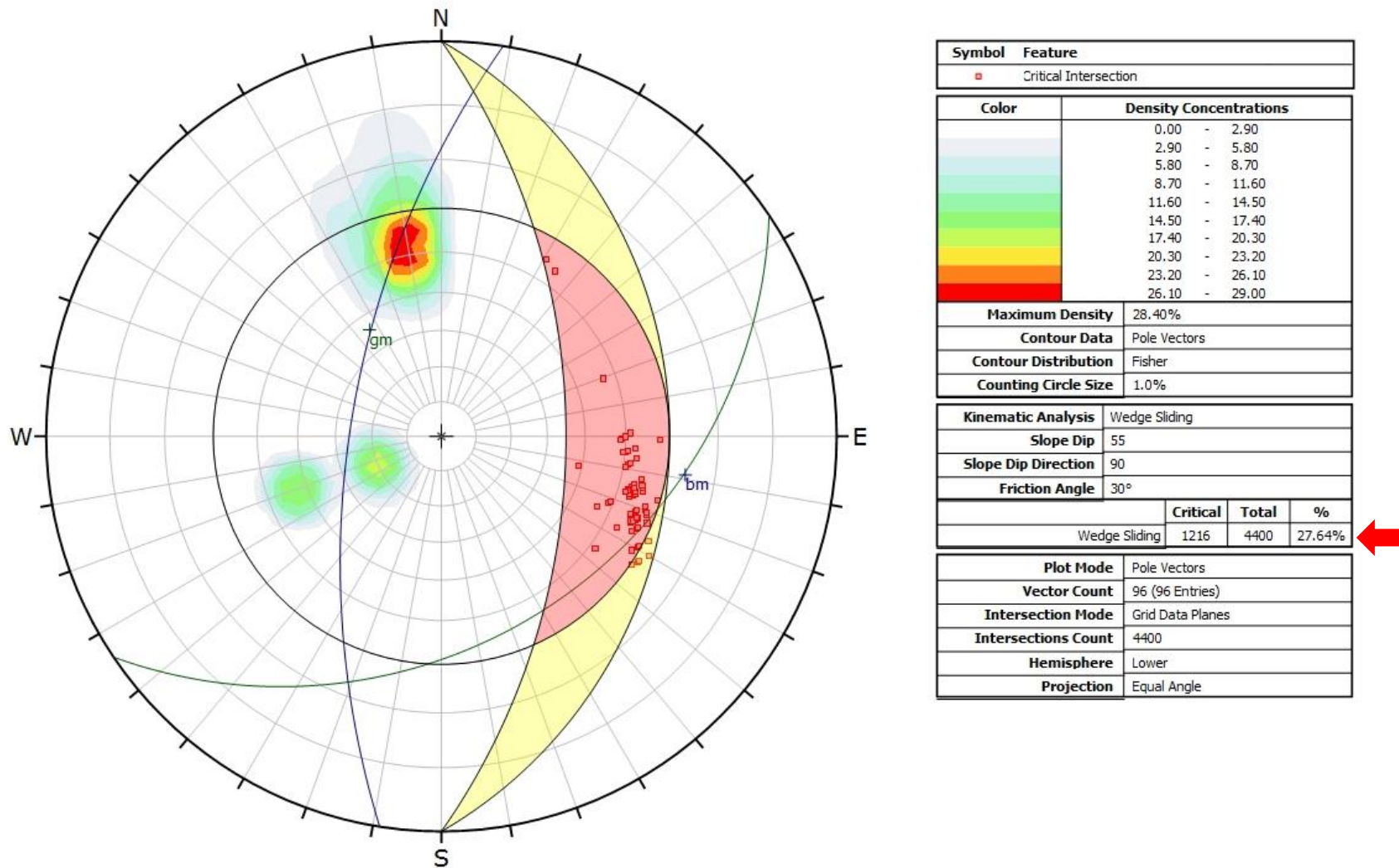


Figure 6.2 Stereonet plot of EA1 joints and second joint set using Dips



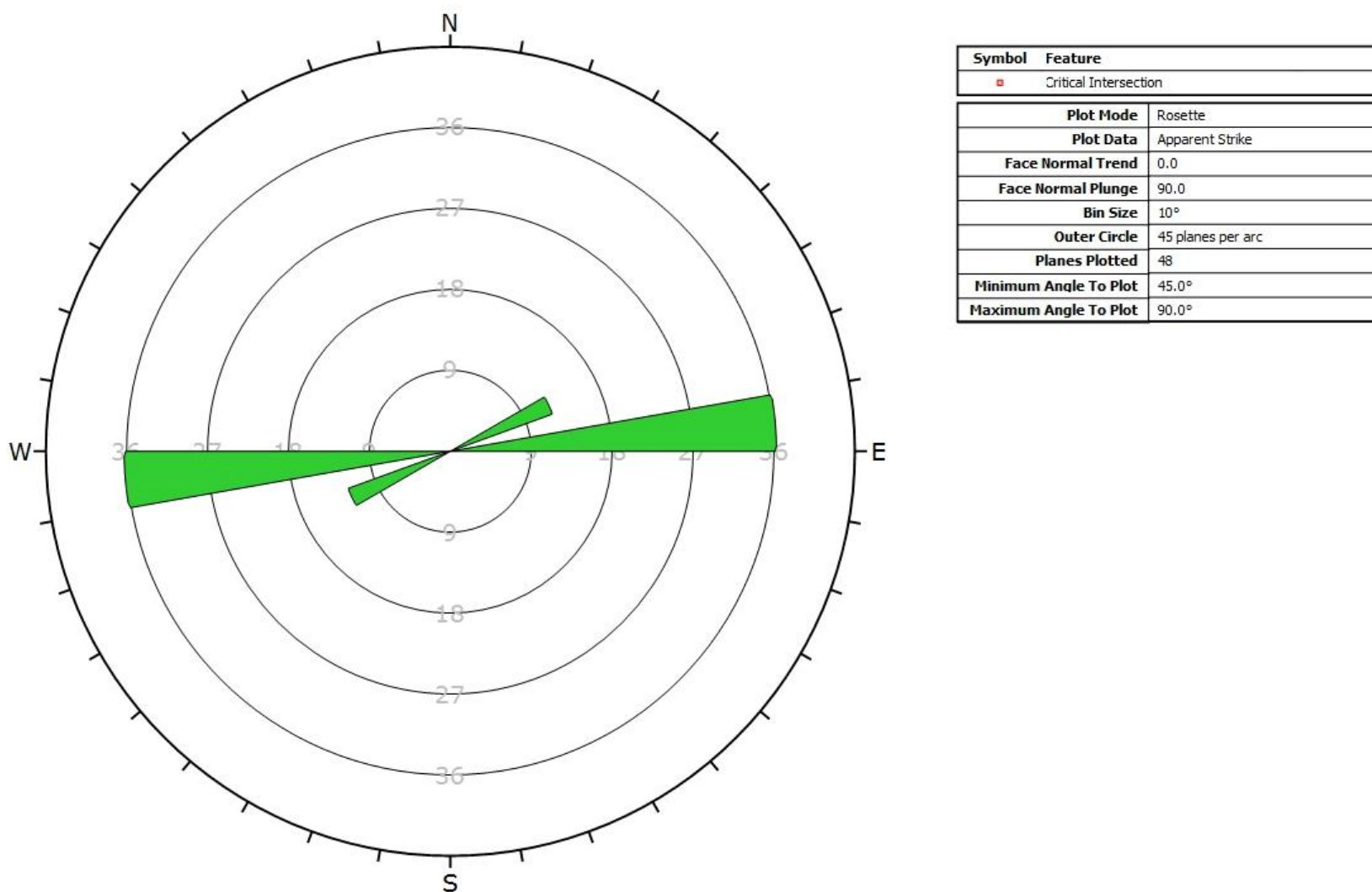


Figure 6.3 Rosette plot of EA1 joints and second joint set using Dips

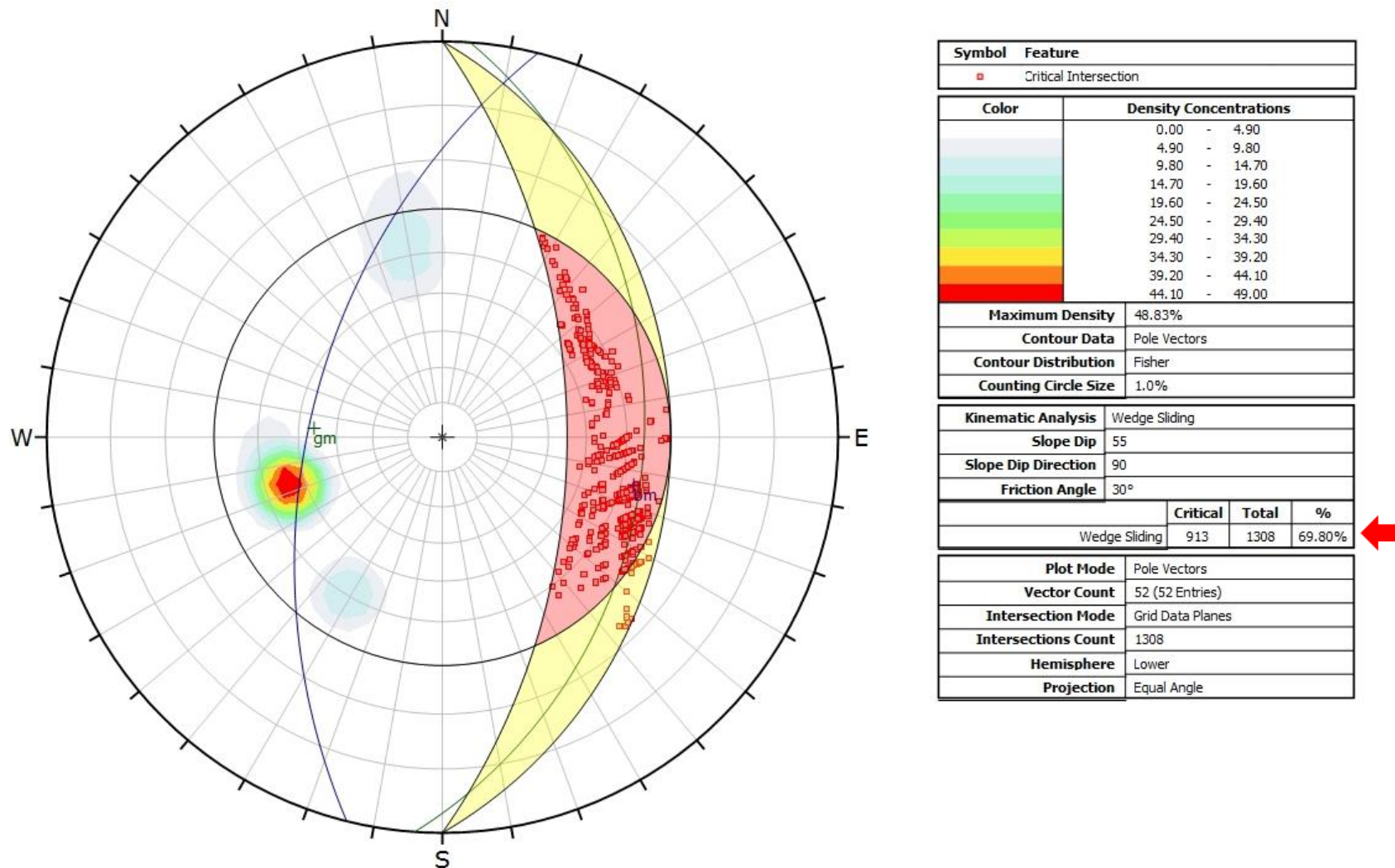


Figure 6.4 Stereonet plot of EA3 joints and second joint set using Dips

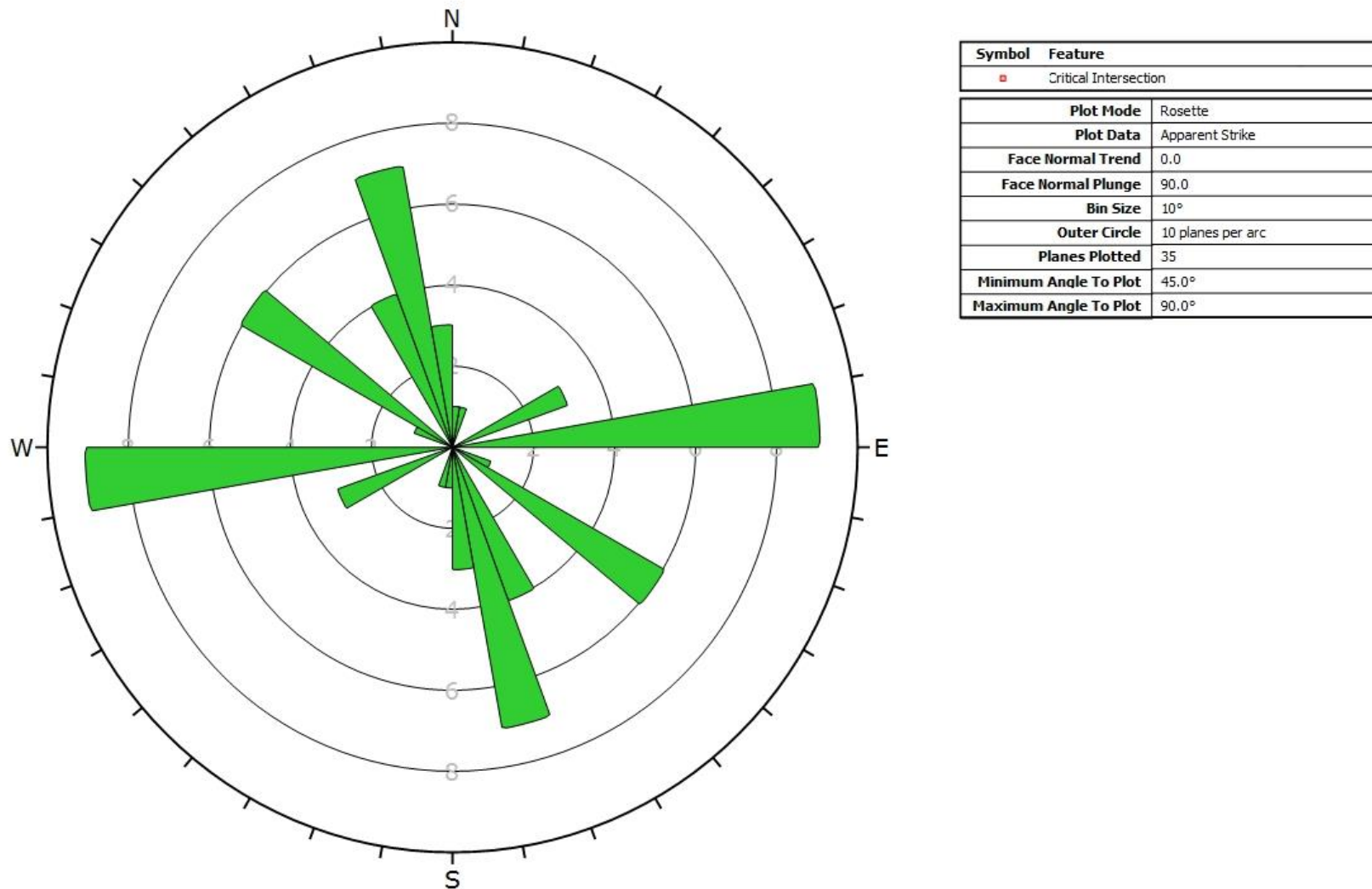


Figure 6.5 Rosette plot of EA3 joints and second joint set using Dips

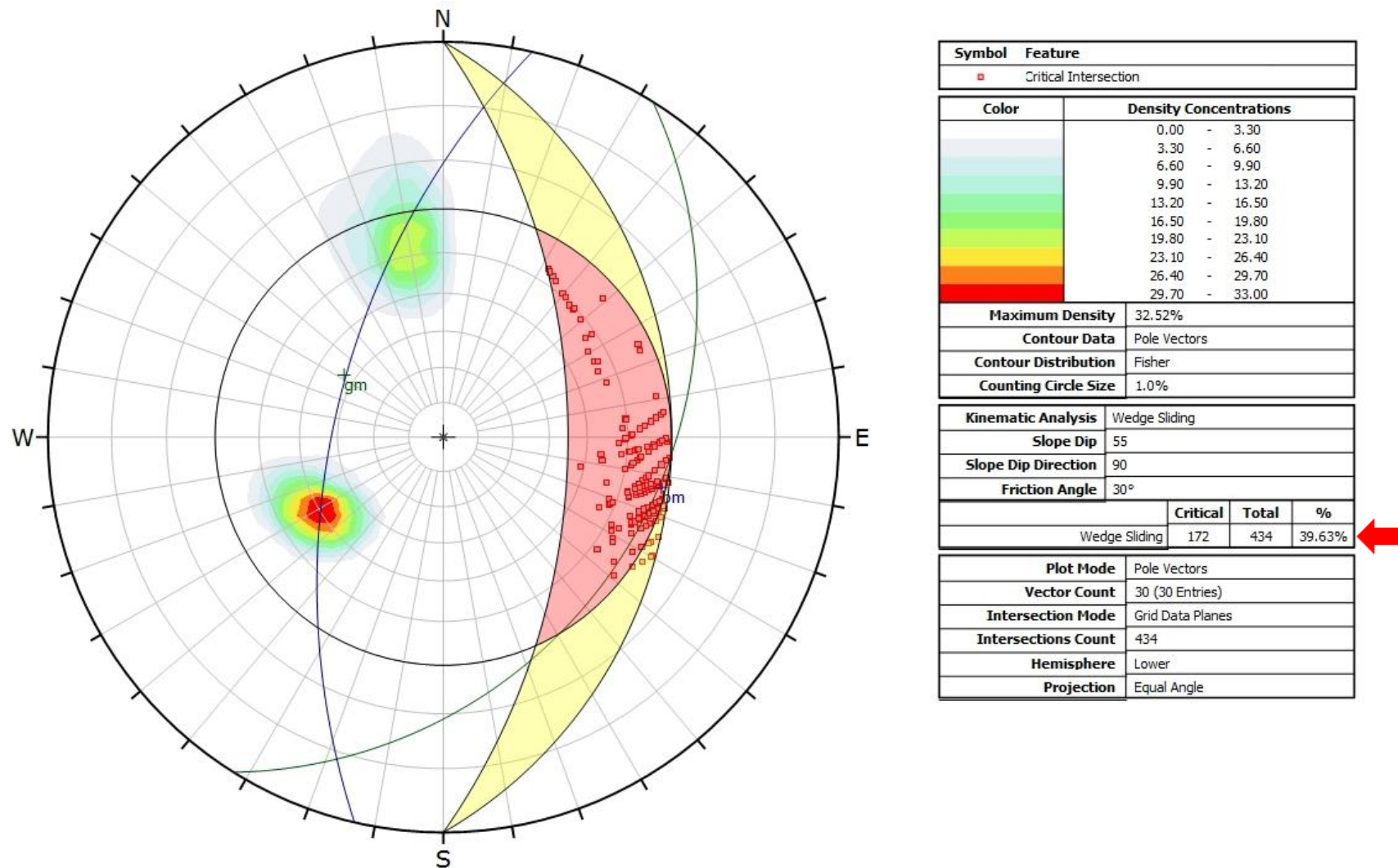


Figure 6.6 Stereonet plot of EA7 joints and second joint set using Dips

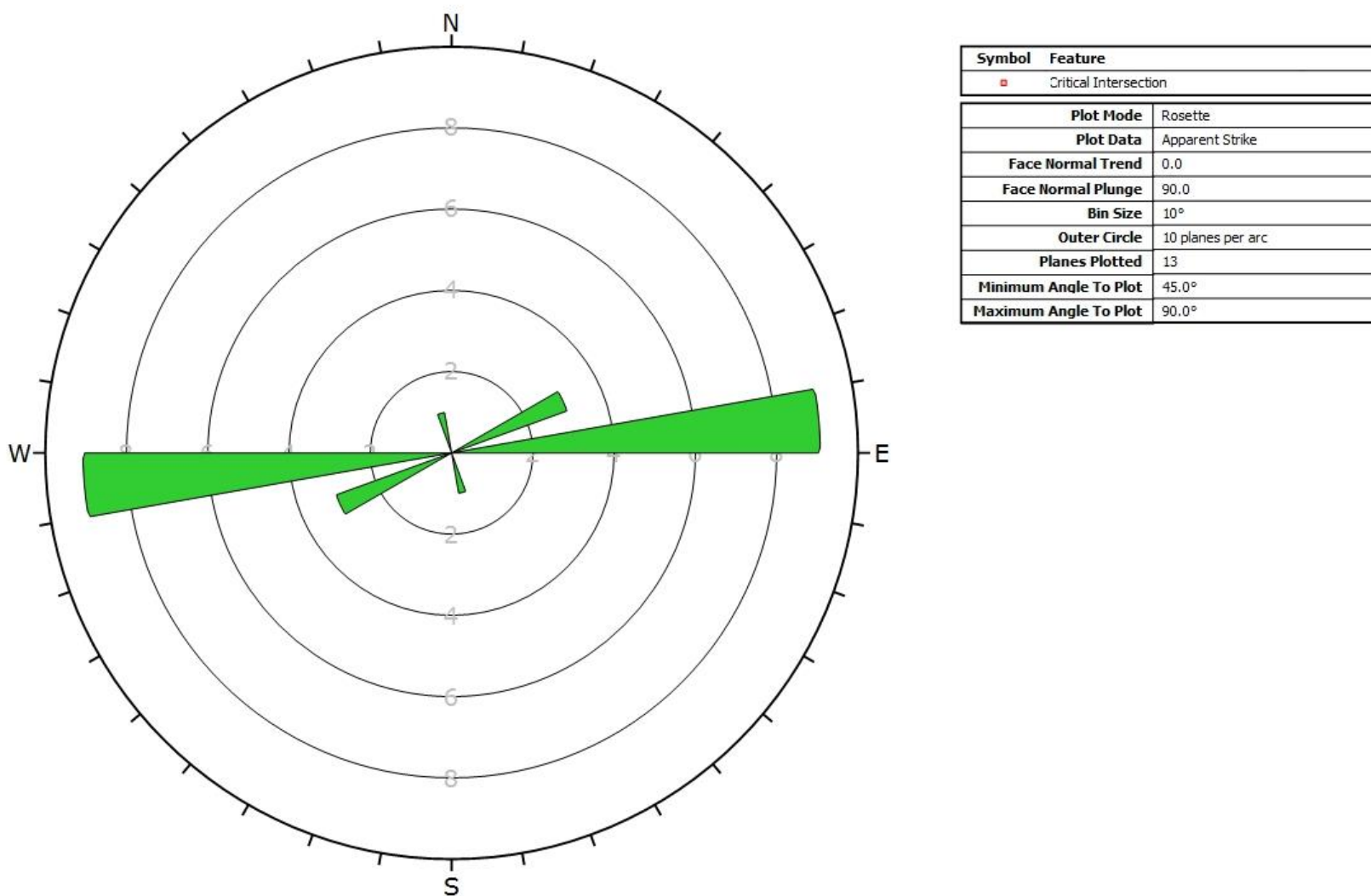


Figure 6.7 Rosette plot of EA7 joints and second joint set using Dips



### 6.2.2 Phase2

Phase2 is a two-dimensional elasto-plastic finite element stress analysis program (Rocscience, 2015). This program was used to analyse the stability and depth of possible failure on the joint sets in the hangingwalls and sidewalls in the open stopes. To simulate the mining method on Target Mine, a narrow reef mining slot is created as shown in Figure 6.8, to produce the shallow mining stress environment that could be expected underground. The lateral extent of the slot is taken as 150m with an average stope width 1.5m.

A range of stope spans (see Figure 4.3) for open stopes was modelled - 10m, 15m, 20m and 25m – and variation in the middling between the narrow reef mining and the open stope was also taken into account for de-stressed open stopes - 2m, 4m, 6m, 8m, 10m, 15m and 20m. Using the same joint input parameters as shown in Table 4.2 to Table 4.5, these joint sets were added to the Edit Joint Network in Phase2. Knowing that the joint spacing for a given joint set varies, the sensitivity of the model was tested with respect to joint spacing and the depth of hangingwall affected. To achieve this, the joint sets in the Edit Joint Network in Phase2 were randomized, as shown in Figure 6.9.

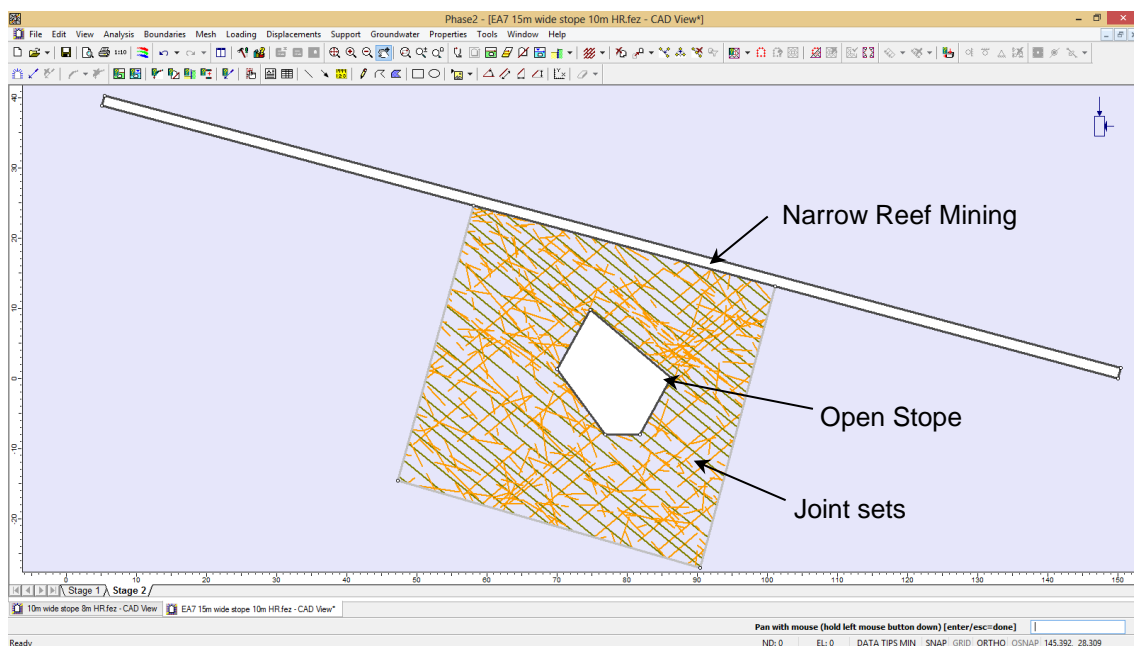


Figure 6.8 Phase2 model setup with joint sets for an open stope that is overstoped

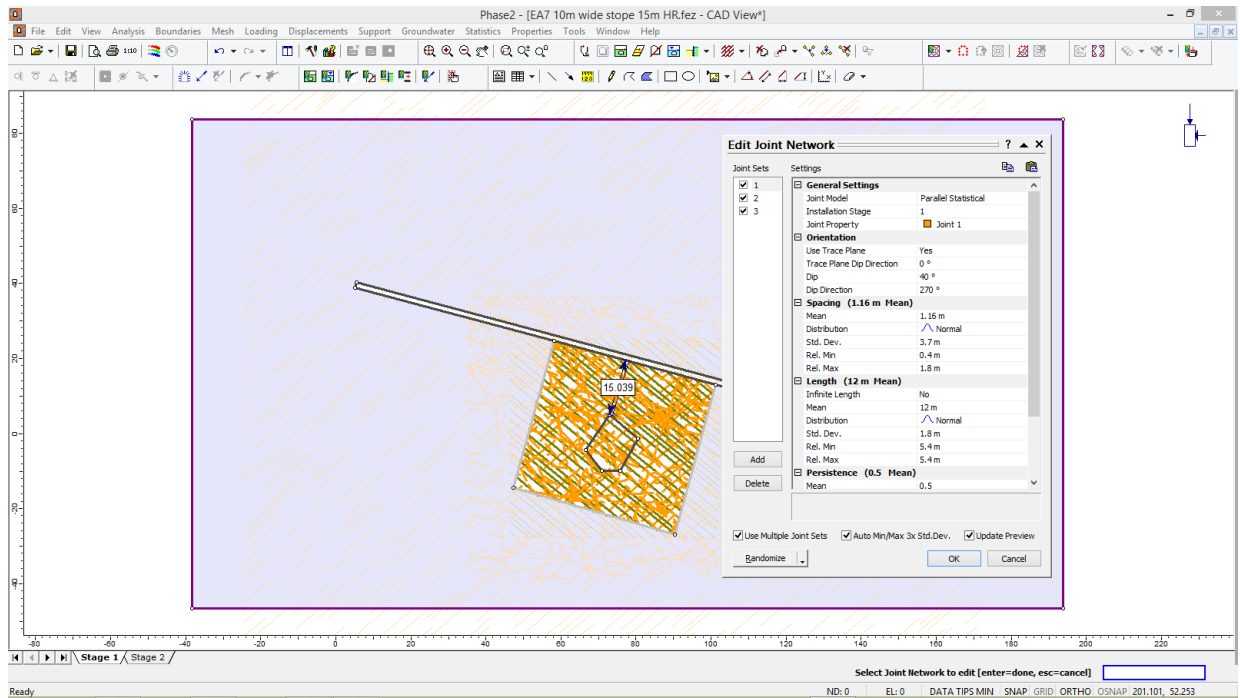


Figure 6.9 Phase2 model setup showing Edit Joint Network window

### **Input Parameters for Phase2**

For this model, the rock in the numerical model was assumed to be homogeneous and isotropic to simplify numerical modelling. Phase2 was used to model the depth of hangingwall and sidewall joint failure in open stopes. The joints in some of the models were randomized to determine how sensitive model behaviour is to joint orientation.

The following input parameters were used for Phase2 (Le Roux, 2004):

Young's modulus	: 70000 MPa
Poisson's ratio	: 0.2
Density	: 2700 kg/m <sup>3</sup>
k-ratio	: 0.5

### **Phase2 Analyses Results**

The open stope hangingwall was the focus, to determine how sensitive the results obtained using Phase2 are to joint orientation. For the sensitivity analyses in Phase2 the joint sets in the models were randomized by computing the analysis ten times for a given setting, using only elastic analysis. Taking the

normal displacement value on the joint sets that indicates instability as equal to or greater than 10mm for the sensitivity analyses, the theoretical depth of failure in the hangingwall could be determined. In Figure 6.10, the sensitivity of joint randomisation is shown. These results indicate that the first 4m of the stope hangingwall is very sensitive to the joint orientation parameter and this sensitivity decreases with depth.

Figures 6.11 show the expected depth of hangingwall failure for different stope widths of 10m, 15m, 20m and 25m, with middling's between the open stope and narrow reef mining of 2m, 4m, 6m, 8m, 10m, 15m and 20m for de-stressed open stopes. From the results, as could logically be expected, it is evident that, as the open stope width increases, so does the failure depth into the hangingwall. For open stopes with a middling of 10m and less between the de-stressing slot and the open stope, the potential for total middling collapse is significant, as shown in Figures 6.11, depending on the open stope mining span. It is also evident from these results that the EA3 reef is more prone to failure, as previously indicated by the Dips analyses. In Table 6.1 a summary of the results obtained is shown in red, indicating open stopes in which the internal middling between the narrow reef mining (NRM) and open stope failed.

Figures 6.12 show the expected sidewall failure depths for different stope widths of 10m, 15m, 20m and 25m, with middlings between the open stope and narrow reef mining of 2m, 4m, 6m, 8m, 10m, 15m and 20m, for de-stressed open stopes. From the results it is evident that, although the sidewalls indicate failure depths greater than those for hangingwall failure, these blocks will not dislodge. In this section a summary of the results has been presented. In Appendix B, all the results obtained are shown.



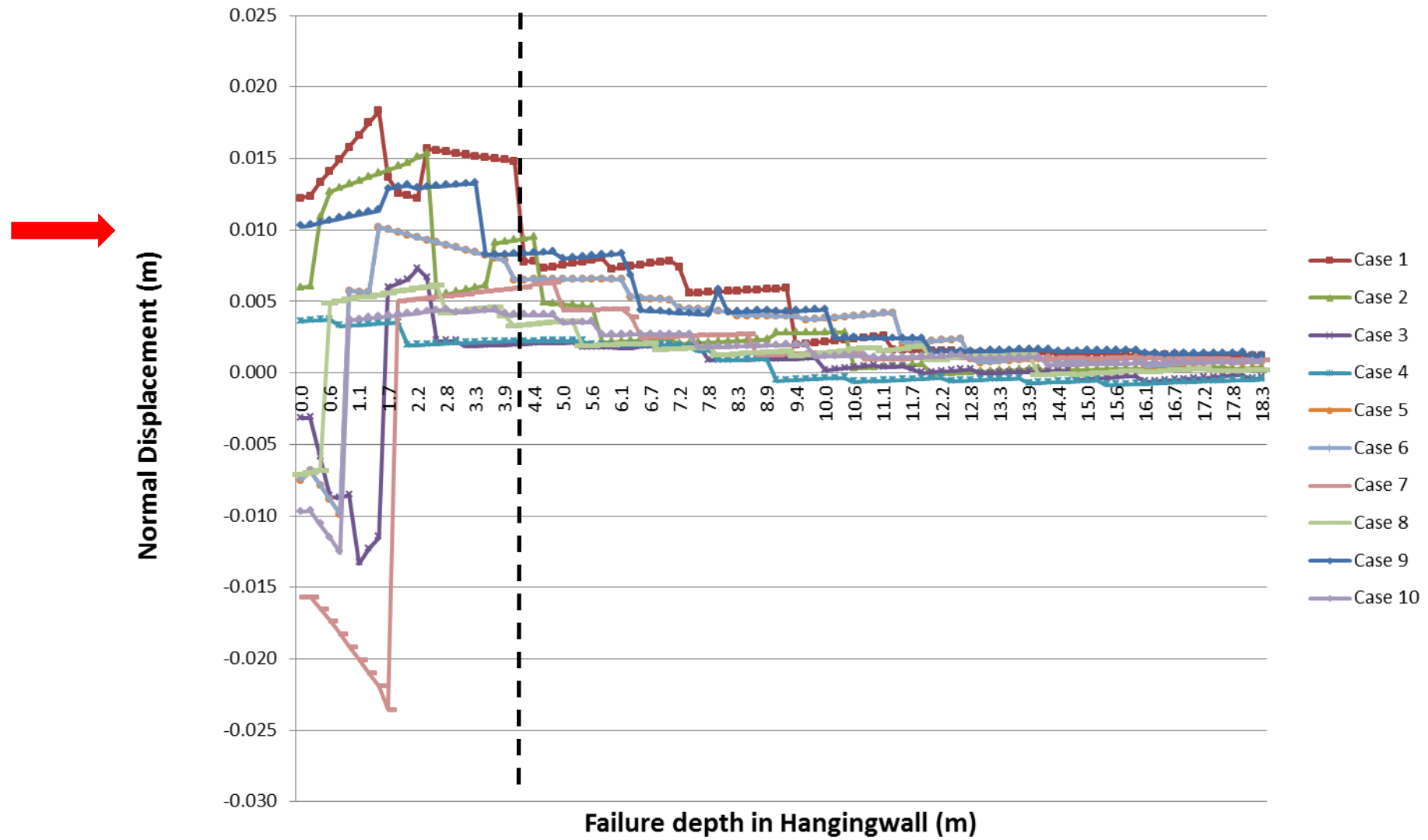


Figure 6.10 Depth of hangingwall failure for an open stope with randomized jointing

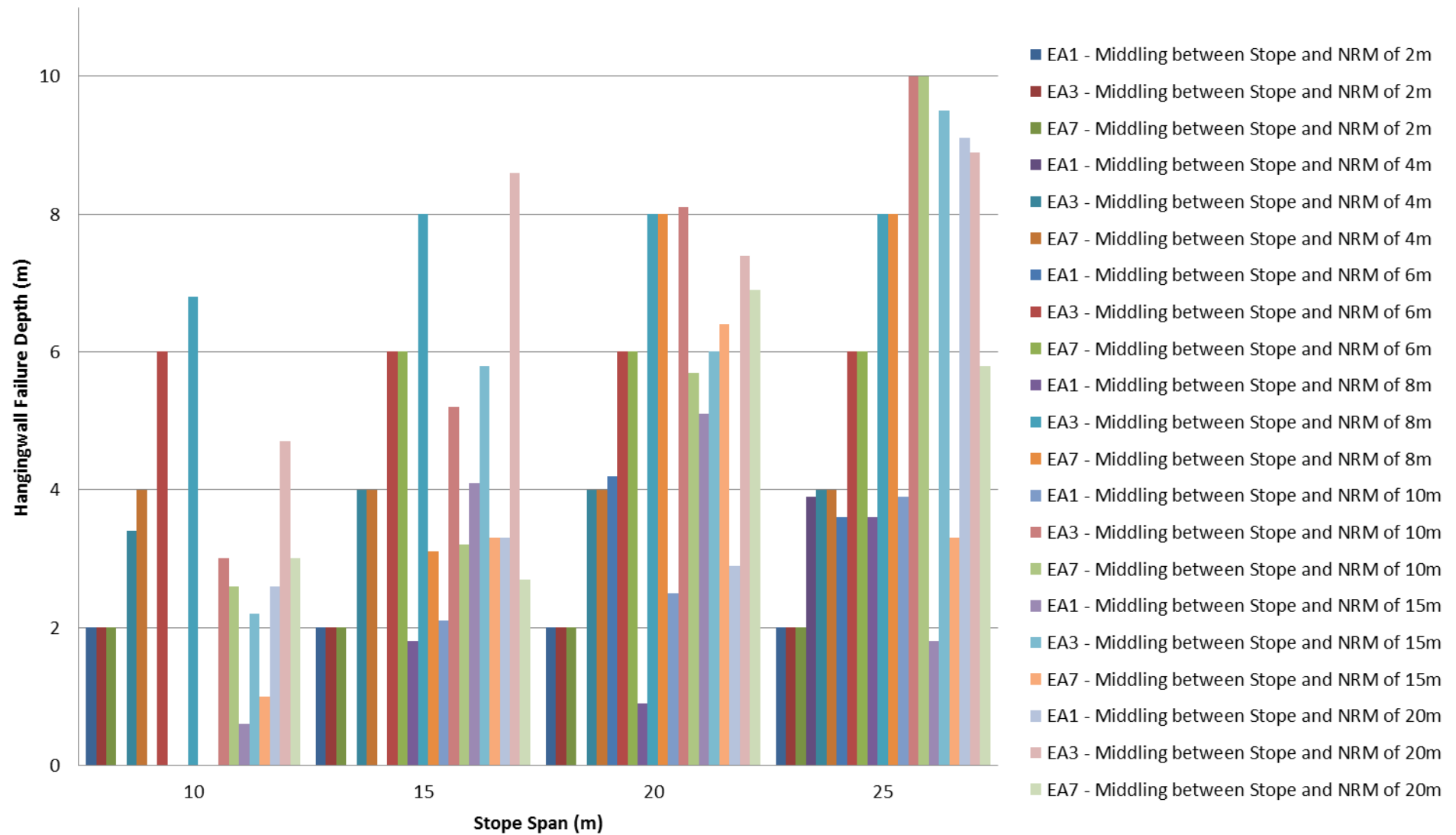


Figure 6.11 Depth of hangingwall failure for open stopes with different midding between narrow reef mining (NRM)

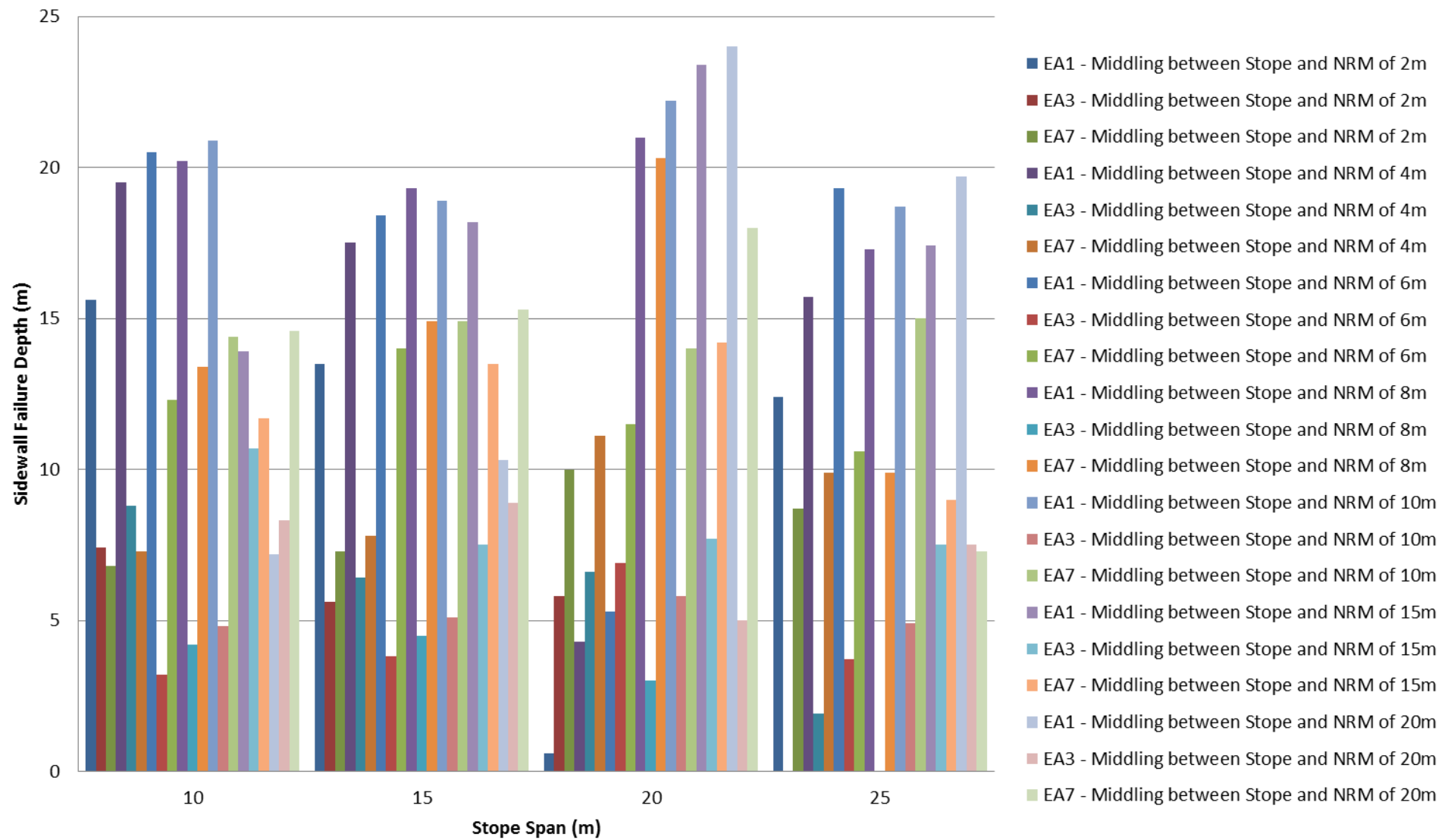


Figure 6.12 Depth of sidewall failure for open stopes with different muddling between narrow reef mining (NRM)

**Table 6.1 Phase2 results as obtained from the simulations**

Stope Span	Middling between stope and NRM	Reef	Failure Depth Hangingwall	Failure Depth Sidewall	Reef	Failure Depth Hangingwall	Failure Depth Sidewall	Reef	Failure Depth Hangingwall	Failure Depth Sidewall
10	2	EA1	2	15.6	EA3	2	7.4	EA7	2	6.8
15	2	EA1	2	13.5	EA3	2	5.6	EA7	2	7.3
20	2	EA1	2	0.6	EA3	2	5.8	EA7	2	10
25	2	EA1	2	12.4	EA3	2	0	EA7	2	8.7
10	4	EA1	0	19.5	EA3	3.4	8.8	EA7	4	7.3
15	4	EA1	0	17.5	EA3	4	6.4	EA7	4	7.8
20	4	EA1	0	4.3	EA3	4	6.6	EA7	4	11.1
25	4	EA1	3.9	15.7	EA3	4	1.9	EA7	4	9.9
10	6	EA1	0	20.5	EA3	6	3.2	EA7	0	12.3
15	6	EA1	0	18.4	EA3	6	3.8	EA7	6	14
20	6	EA1	4.2	5.3	EA3	6	6.9	EA7	6	11.5
25	6	EA1	3.6	19.3	EA3	6	3.7	EA7	6	10.6
10	8	EA1	0	20.2	EA3	6.8	4.2	EA7	0	13.4
15	8	EA1	1.8	19.3	EA3	8	4.5	EA7	3.1	14.9
20	8	EA1	0.9	21	EA3	8	3	EA7	8	20.3
25	8	EA1	3.6	17.3	EA3	8	0	EA7	8	9.9
10	10	EA1	0	20.9	EA3	3	4.8	EA7	2.6	14.4
15	10	EA1	2.1	18.9	EA3	5.2	5.1	EA7	3.2	14.9
20	10	EA1	2.5	22.2	EA3	8.1	5.8	EA7	5.7	14
25	10	EA1	3.9	18.7	EA3	10	4.9	EA7	10	15
10	15	EA1	0.6	13.9	EA3	2.2	10.7	EA7	1	11.7
15	15	EA1	4.1	18.2	EA3	5.8	7.5	EA7	3.3	13.5
20	15	EA1	5.1	23.4	EA3	6	7.7	EA7	6.4	14.2
25	15	EA1	1.8	17.4	EA3	9.5	7.5	EA7	3.3	9
10	20	EA1	2.6	7.2	EA3	4.7	8.3	EA7	3	14.6
15	20	EA1	3.3	10.3	EA3	8.6	8.9	EA7	2.7	15.3
20	20	EA1	2.9	24	EA3	7.4	5	EA7	6.9	18
25	20	EA1	9.1	19.7	EA3	8.9	7.5	EA7	5.8	7.3

### 6.2.3 JBLOCK

JBlock is a computer program developed by Esterhuizen and Streuders (1998) in which a probabilistic method is applied to determine the potential keyblock dimensions and keyblock stability. JBlock is well-suited for the evaluation of the stability of mining excavations when practical limitations prevent the rock engineer from evaluating individual keyblocks, Esterhuizen and Streuders (1998). The open stopes are simulated at different widths of 10m, 15m, 20m and 25m. These open stopes are situated in de-stressed areas where the horizontal stress component is very low. For the analysis of these open stopes, the horizontal stress was conservatively taken to be zero for de-stressed open stopes. In addition, the effect of poor blasting was simulated, to cater for cases in which the open stope hangingwall was not blasted parallel with the dip of the hangingwall strata. To simulate this, the excavation surface (hangingwall) was given a dip of  $0^\circ$  for poor blasting practice and  $45^\circ$  for good blasting practice, to determine the effect of quality blasting on the stability of the hangingwall. The basic layout for simulating an open stope in JBlock is shown in Figure 6.13.

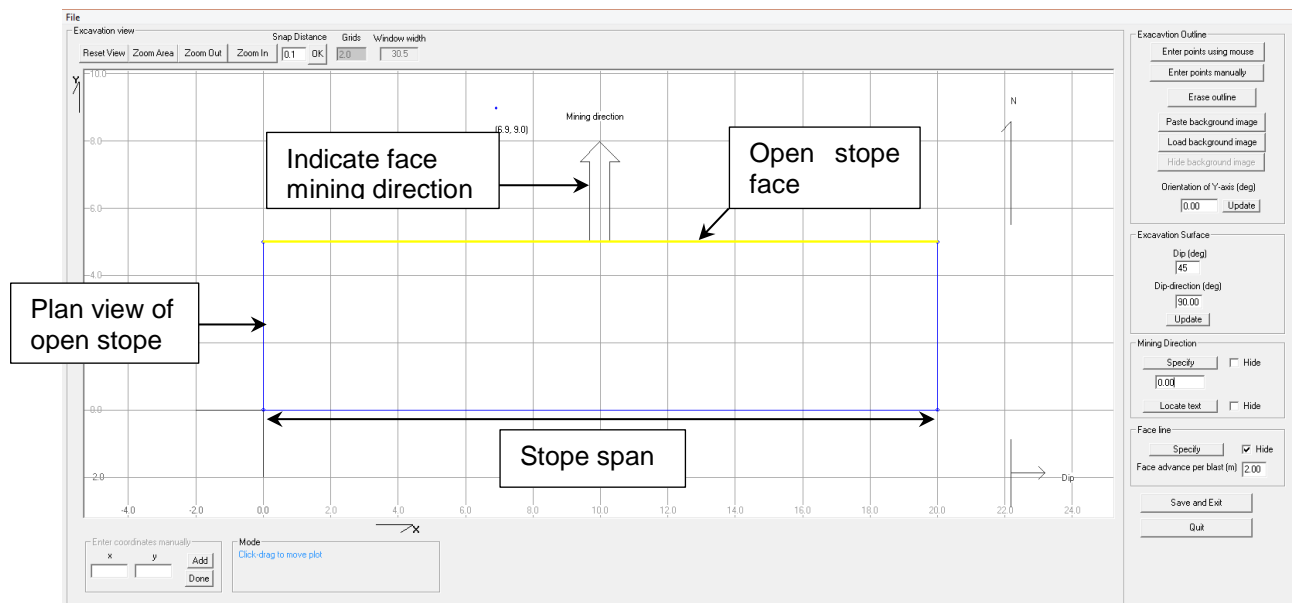


Figure 6.13 JBlock model setup for an open stope

### **Block generation method**

The orientations, spacing's and lengths of discontinuities are used to generate simulated blocks in the hangingwall of the open stope excavation. The joint and fracture input data, showing the variations in the parameters, are presented in Table 4.2, Table 4.3, Table 4.4 and Table 4.5. The rock density was set to 2700 kg/m<sup>3</sup> (Le Roux, 2004). The JBlock program generates blocks with between four and six faces, making use of three discontinuity sets. By applying the keyblock analysis method of Goodman and Shi (1985), each simulated block is evaluated to determine whether it will fail or not.

### **JBLOCK Results**

Using the same joint input parameters as discussed in Table 4.2, Table 4.3, Table 4.4 and Table 4.5, these joint sets were added to the JBlock simulation. The long axis of the open stope is orientated on strike with the short axis on dip.

In Appendix C all the results obtained for the JBlock analyses are shown, and in this section only a summary of the results is presented as shown in Tables 6.2 and 6.3 and Figures 6.14 to 6.19. The mining steps parameter in the analyses was set to 6000, and JBlock increases the number of mining steps by default to achieve model convergence. The de-stressed open stopes are very sensitive to the dip of the hangingwall. If the hangingwall is mined parallel with the dip of the strata, the volumes of falls of ground per mining step are greater than for stopes mining across the strata, as shown in Figures 6.14 to 6.17.

The dilution is determined by dividing the change in volume of the stope by the original volume. Change in volume is determined by multiplying the frequency of falls of ground with the volume of dislodged key blocks in JBlock. The depth of failure is determined by dividing the volume of failure by the area of the stope exposed. The question is can these results be trusted? On closer inspection, it would seem that the falls of ground per mining step increases with increase in width. From experience and underground observations, this is a true reflection of what can be expected as shown in Figure 6.14 and Figure 6.17. In Figure 6.15 and Figure 6.18, the expected failure depth in the hangingwall for open

stopes is shown. These results do not correspond with the actual measured results for open stopes as JBlock underestimates the failure depth and dilution as shown in Figure 6.16 and Figure 6.19.

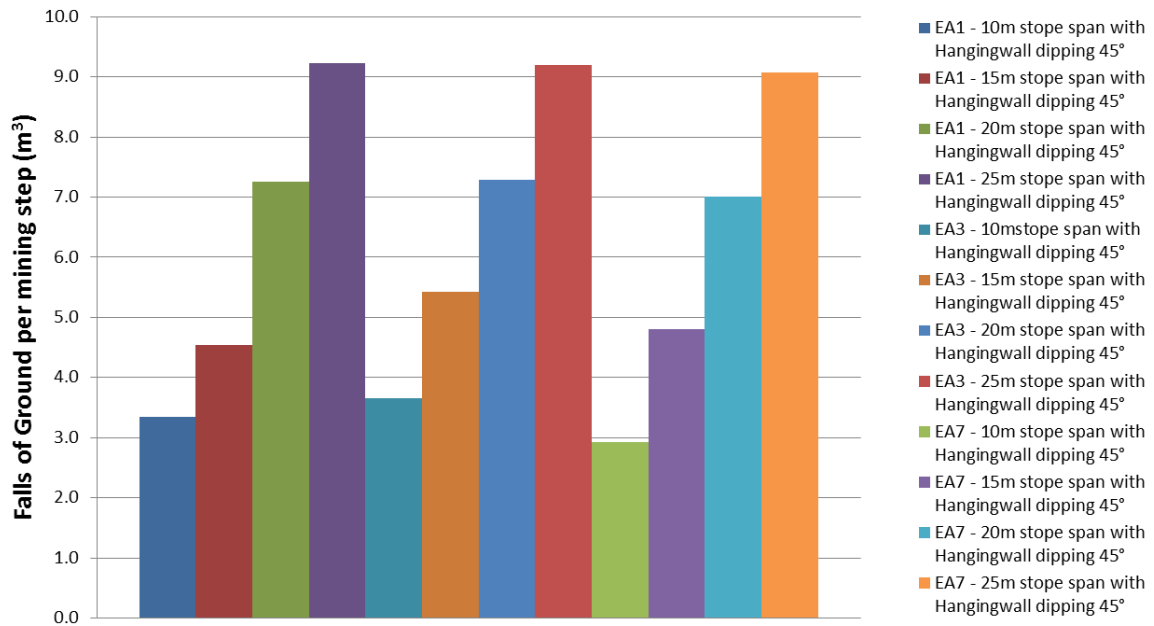


Figure 6.14 Summary of JBlock results for falls of ground per mining step (m³) in the EA1, EA3 and EA7 formations with open stope hangingwall dipping 45°

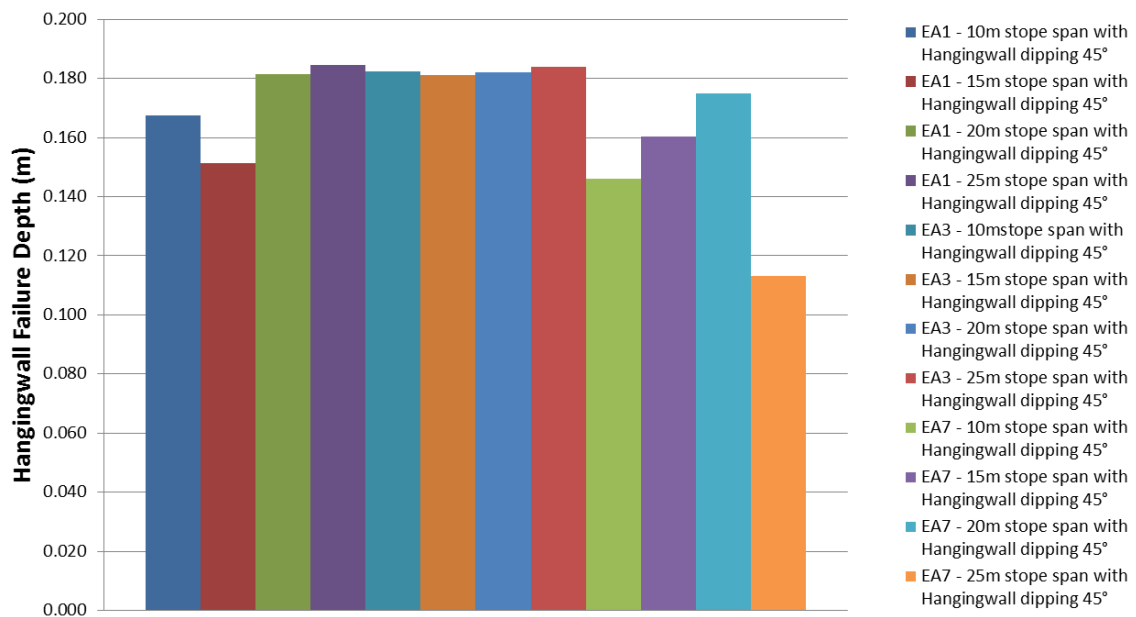


Figure 6.15 Summary of JBlock results for hangingwall failure depth (m) in the EA1, EA3 and EA7 formations with open stope hangingwall dipping 45°

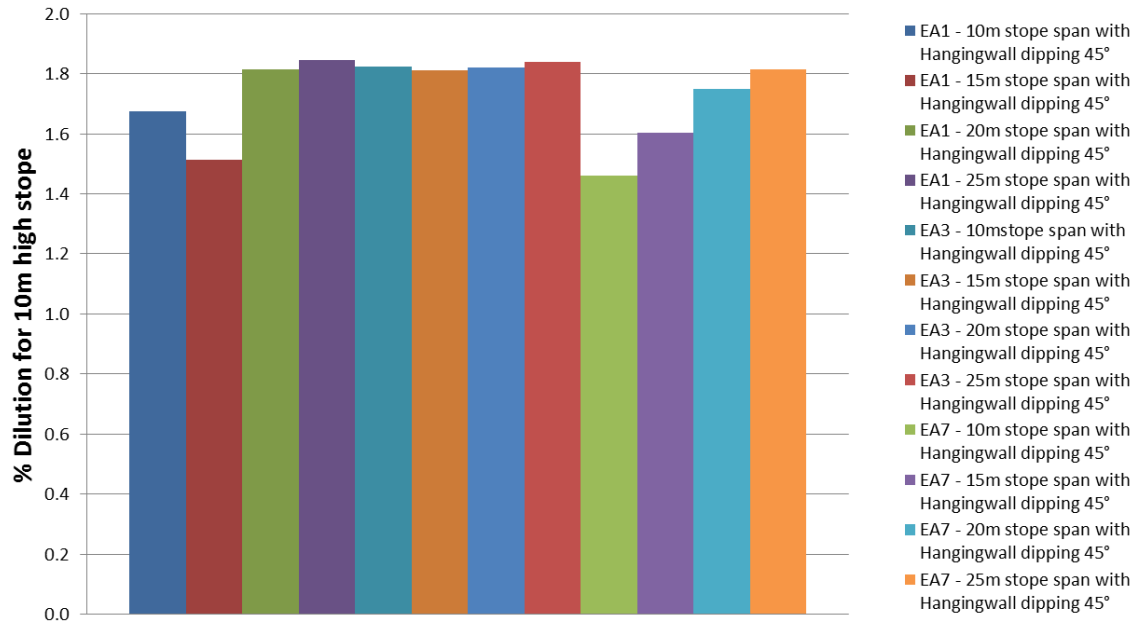


Figure 6.16 Summary of JBlock results for percentage dilution in the EA1, EA3 and EA7 formations with open stope hangingwall dipping 45°



**Table 6.2 JBlock results as obtained from the simulations for hangingwall dipping 45°**

	Mining Steps Simulated by JBlock	Area Mined by JBlock (m <sup>2</sup> )	Area Mined by JBlock per Mining step (m <sup>2</sup> )	FOG (m <sup>3</sup> ) per mining step	% Dilution for 10m high Stope	Average Failure Depth (m) in Hangingwall
EA1 - 10m stope span with Hangingwall dipping 45°	6001	120015	20	3.4	1.7	0.168
EA1 - 15m stope span with Hangingwall dipping 45°	6000	180014	30	4.5	1.5	0.151
EA1 - 20m stope span with Hangingwall dipping 45°	6000	240001	40	7.3	1.8	0.182
EA1 - 25m stope span with Hangingwall dipping 45°	6000	301214	50	9.2	1.8	0.184
EA3 - 10mstope span with Hangingwall dipping 45°	6001	120018	20	3.7	1.8	0.183
EA3 - 15m stope span with Hangingwall dipping 45°	6001	180030	30	5.4	1.8	0.181
EA3 - 20m stope span with Hangingwall dipping 45°	6002	240081	40	7.3	1.8	0.182
EA3 - 25m stope span with Hangingwall dipping 45°	6000	301203	50	9.2	1.8	0.184
EA7 - 10m stope span with Hangingwall dipping 45°	6000	120007	20	2.9	1.5	0.146
EA7 - 15m stope span with Hangingwall dipping 45°	6005	180164	30	4.8	1.6	0.160
EA7 - 20m stope span with Hangingwall dipping 45°	6000	240001	40	7.0	1.8	0.175
EA7 - 25m stope span with Hangingwall dipping 45°	6001	301242	50	9.1	1.8	0.181

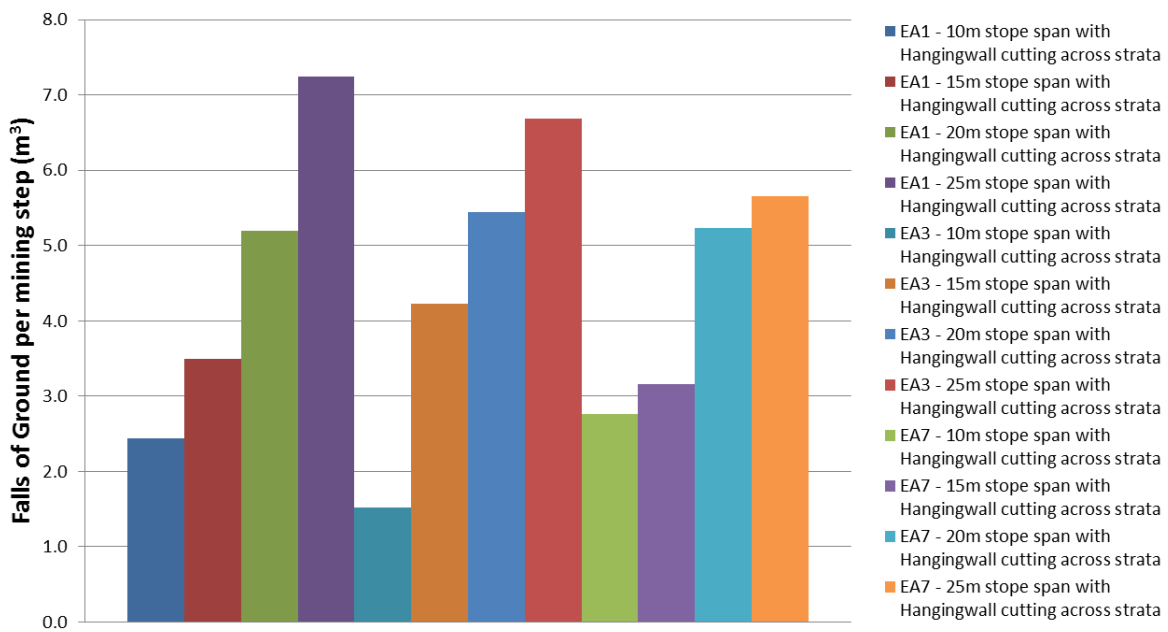


Figure 6.17 Summary of JBlock results for falls of ground per mining step (m³) in the EA1, EA3 and EA7 formations with open stope hangingwall cutting across strata

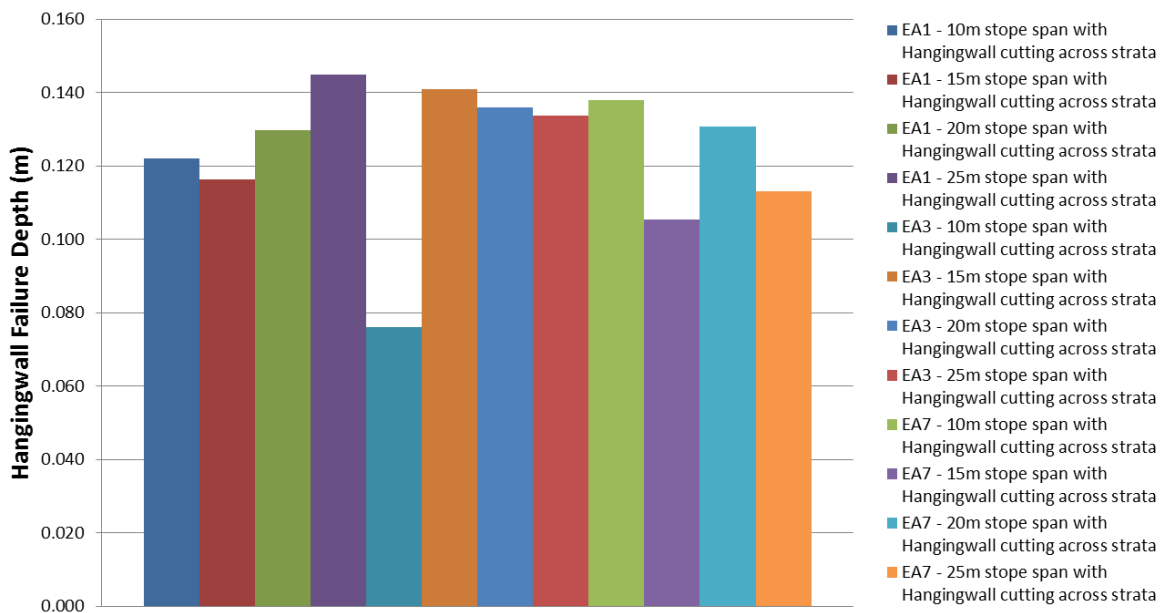


Figure 6.18 Summary of JBlock results for hangingwall failure depth (m) in the EA1, EA3 and EA7 formations with open stope hangingwall cutting across strata

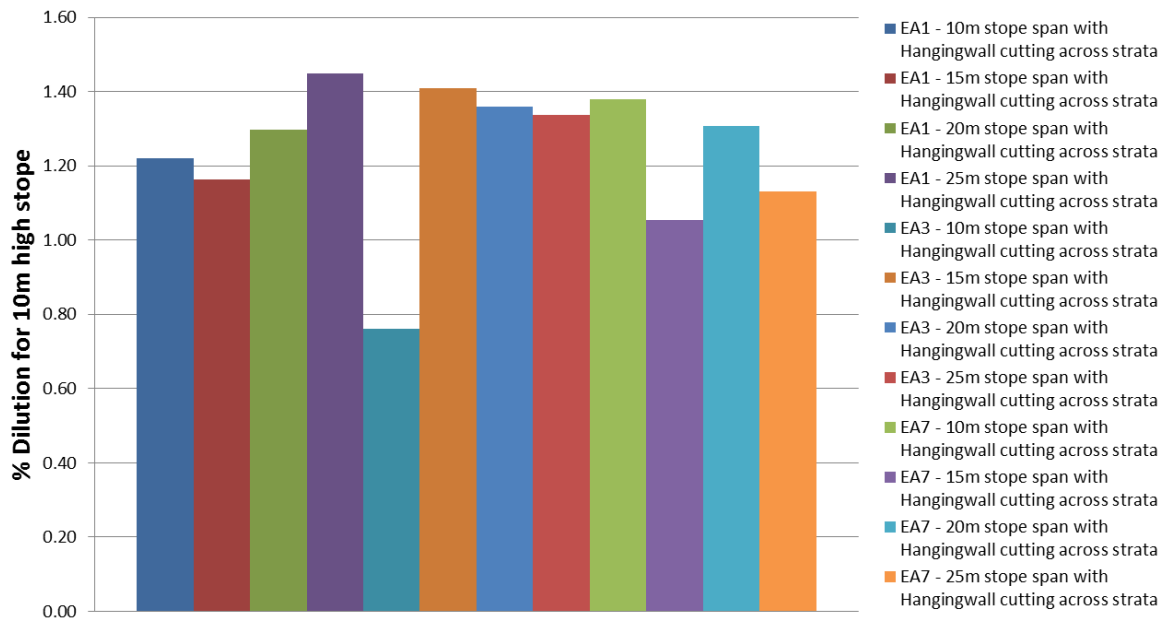


Figure 6.19 Summary of JBlock results for percentage dilution in the EA1, EA3 and EA7 formations with open stope hangingwall cutting across strata

**Table 6.3 JBlock results as obtained from the simulations for hangingwall cutting across strata**

	Mining Steps Simulated by JBlock	Area Mined by JBlock (m <sup>2</sup> )	Area Mined by JBlock per Mining step (m <sup>2</sup> )	FOG (m <sup>3</sup> ) per mining step	% Dilution for 10m high stope	Average Failure Depth (m) in Hangingwall
EA1 - 10m stope span with Hangingwall cutting across strata	6003	120067	20	2.4	1.2	0.122
EA1 - 15m stope span with Hangingwall cutting across strata	6004	180126	30	3.5	1.2	0.116
EA1 - 20m stope span with Hangingwall cutting across strata	6001	240031	40	5.2	1.3	0.130
EA1 - 25m stope span with Hanging wall cutting across strata	6001	301261	50	7.2	1.4	0.145
EA3 - 10m stope span with Hangingwall cutting across strata	6008	120153	20	1.5	0.8	0.076
EA3 - 15m stope span with Hangingwall cutting across strata	6004	180130	30	4.2	1.4	0.141
EA3 - 20m stope span with Hangingwall cutting across strata	6013	240507	40	5.4	1.4	0.136
EA3 - 25m stope span with Hangingwall cutting across strata	6003	301357	50	6.7	1.3	0.134
EA7 - 10m stope span with Hangingwall cutting across strata	6000	120004	20	2.8	1.4	0.138
EA7 - 15m stope span with Hangingwall cutting across strata	6004	180119	30	3.2	1.1	0.105
EA7 - 20m stope span with Hangingwall cutting across strata	6003	240101	40	5.2	1.3	0.131
EA7 - 25m stope span with Hangingwall cutting across strata	6000	301216	50	5.7	1.1	0.113

## 6.2.4 MAP3D

Map3D is based on Banerjee and Butterfield (1981), a very efficient Indirect Boundary Element Method, and incorporates simultaneous use of both fictitious force and displacement discontinuity elements. Special boundary elements are incorporated for the thermal and non-linear analysis versions. This Boundary Element formulation offers many advantages over other stress analysis techniques. Direct Boundary Element formulations require approximately twice the computing effort to assemble and solve the boundary element matrix, compared to the indirect method used in Map3D (Wiles, 2006).

For the back analyses, twenty-eight open stopes were identified where sufficient data were available. Strings, also known as gridlines, were placed on the hangingwall and sidewalls for each of the open stopes and stopes mined using the actual mining extraction sequence as shown in Figure 6.20. These gridlines were placed on the boundaries of the open stope hangingwall and sidewalls. This was done to determine the major principal stress  $\sigma_1$ , intermediate principal stress  $\sigma_2$ , minor principal stress  $\sigma_3$ , major principal strain  $\varepsilon_1$ , intermediate principal strain  $\varepsilon_2$  and minor principal strain  $\varepsilon_3$  values for given coordinates (x, y and z) at multiple mining steps.

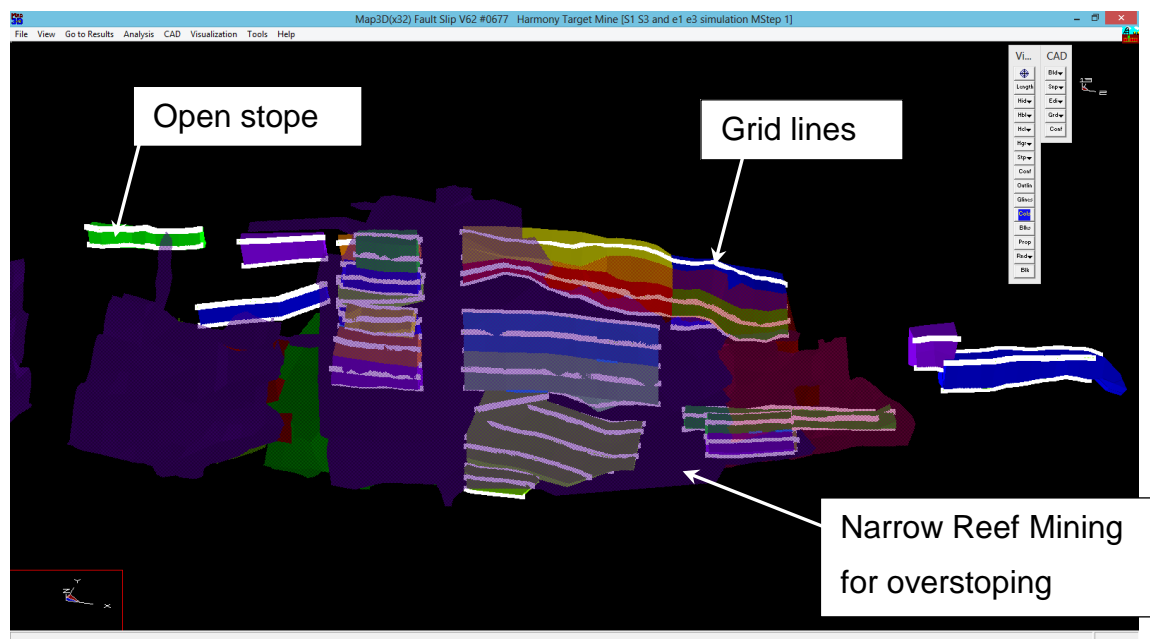


Figure 6.20 Map3D model setup for open stopes that is overstoped and not with joint sets

### **Input Parameters for MAP3D-SV**

The rock mass in the numerical model is assumed to be homogeneous and isotropic to simplify numerical modelling (Wiles, 2006). MAP3D-SV was used to model the mining of the open stopes and to determine the strain and stress values. These stress values for  $\sigma_1$ ,  $\sigma_2$  and  $\sigma_3$  are used as inputs into the Mohr-Coulomb, Hoek-Brown, Zhang–Zhu, Pan–Hudson, Priest, Simplified Priest and Drucker–Prager Criteria to determine whether any of these criteria can be used for assessing failure around open stopes.

The following input parameters were used for MAP3D-SV:

Young's modulus	: 70000 MPa
Poisson's ratio	: 0.2
Density	: 2700 kg/m <sup>3</sup>
k-ratio	: 0.5

These input parameters for Young's modulus, Poisson's ratio and density were obtained from laboratory testing that was conducted at the University of the Witwatersrand by Le Roux (2004) for the Eldorado Reefs. The k-ratio is an estimate based on actual underground observations and back analyses.

### **Map3D Analyses Results**

From the results obtained for the gridlines in Map3D for the twenty-eight case studies the in plane major  $\sigma_1$ , intermediate  $\sigma_2$  and minor  $\sigma_3$  principal stresses around these open stopes were exported for hangingwall and sidewall failure. Only twenty-two of the case studies complied with these criteria. Taking the maximum, minimum, median and average values for each of the case studies hangingwall and sidewalls the results were tested as to determine which values would be fitting to use. In the Figures 6.21 to 6.24 the following principal stress results are plotted;  $\sigma_1$  and  $\sigma_3$  in the hangingwall of the open stopes. In the Figures 6.25 to 6.28 the following principal stress results are plotted;  $\sigma_1$  and  $\sigma_3$  in the sidewalls of the open stopes.

Using regression analysis ( $R^2$ ), a statistical measure of how close the data are to the fitted regression line, the best suitable statistical measure will be determined. It was found that using the median values yielded the best results for open stope failure as shown in Figure 6.23 and Figure 6.27.

For open stopes at Target Mine, it was found that there were three failure modes:

- a) Failure from sidewall in open stopes (compression) as shown in Figure 6.32

$$\text{Failure from sidewalls} = \frac{\sigma_1}{3.6\sigma_3 + 68} \quad (6.1)$$

- b) Failure from hangingwall in open stopes (tension) as shown in Figure 6.23

$$\text{Failure from hangingwall} = \frac{\sigma_1}{2.7\sigma_3 + 23.5} \quad (6.2)$$

- c) Minimum failure (Stable) as shown in Figure 6.23

$$\text{Minimum failure} = \frac{\sigma_1}{2.6\sigma_3 + 44} \quad (6.3)$$

Henning and Mitri (2007) found that the open stope hangingwall might fail in tension or compression, which support these findings. This was a significant find as it clearly shows that there is more than one mode of failure in open stopes and that the effect of the stress environment does play a significant role in the stability of these excavations hangingwall and sidewalls. The most widely accepted failure criteria being used in rock engineering are the Hoek and Brown failure criterion (Hoek and Brown, 1980) and Mohr-Coulomb failure criterion (Coulomb, 1776), which will be discussed in this section.

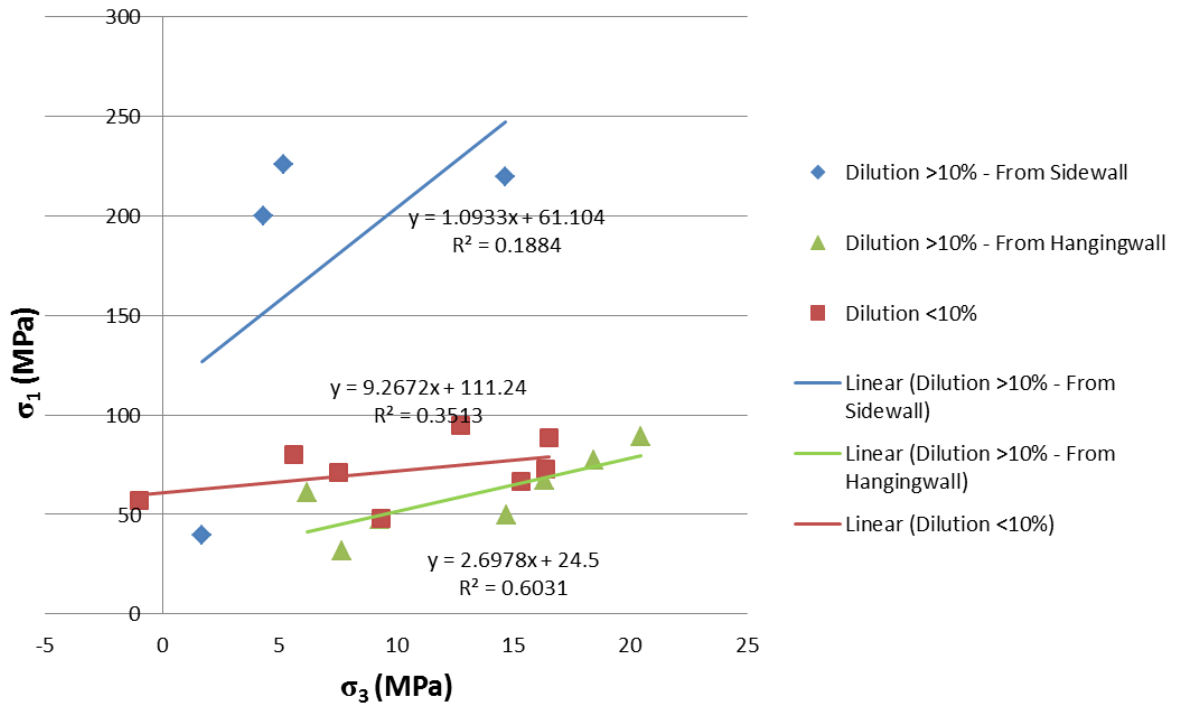


Figure 6.21 The maximum  $\sigma_1$  and  $\sigma_3$  stress plot in hangingwall for open stopes with dilution greater and smaller than ten percent

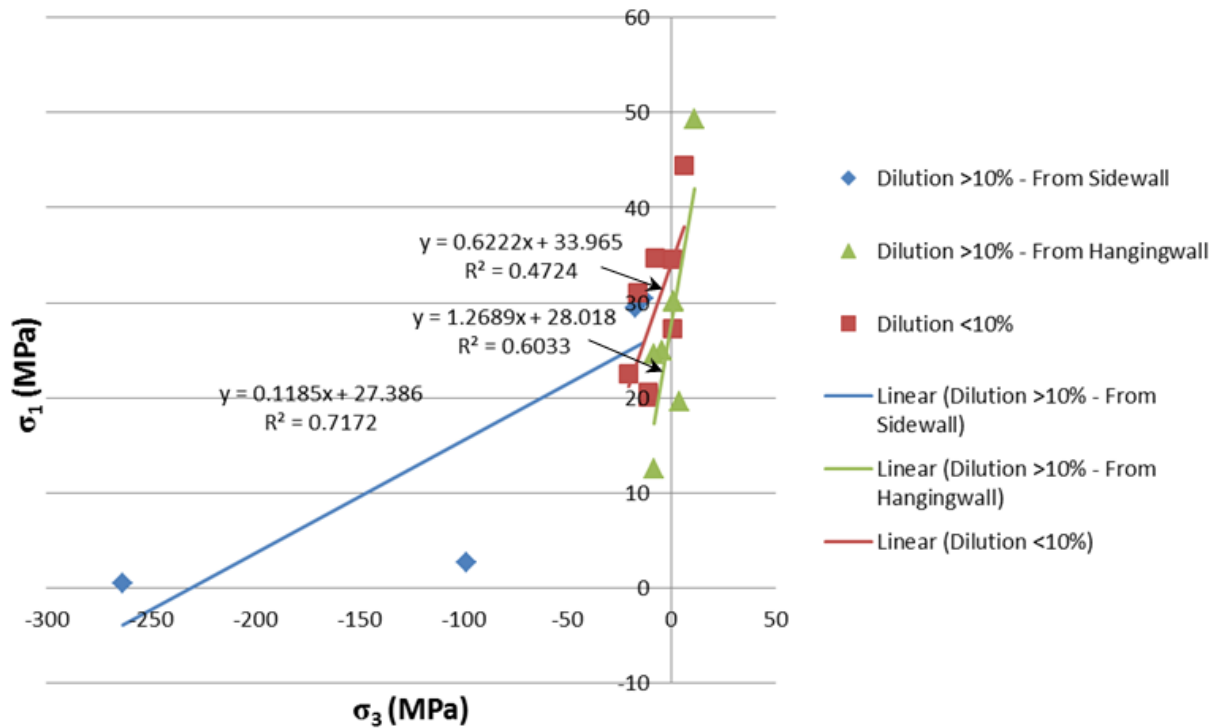


Figure 6.22 The minimum  $\sigma_1$  and  $\sigma_3$  stress plot in hangingwall for open stopes with dilution greater and smaller than ten percent



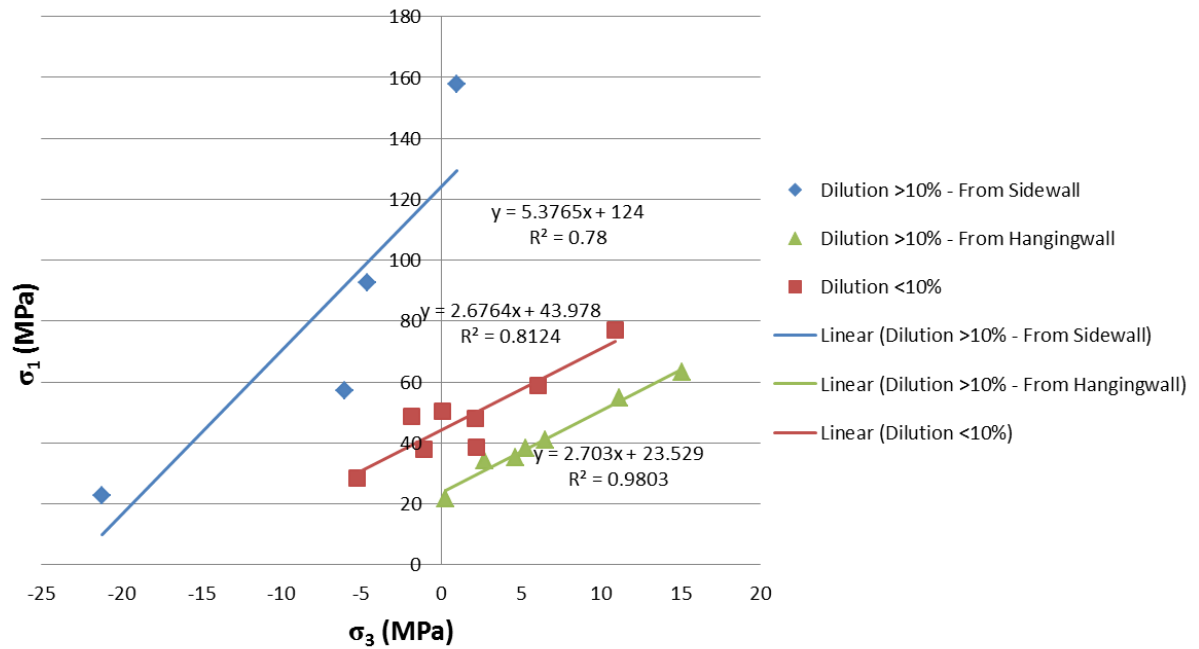


Figure 6.23 The median  $\sigma_1$  and  $\sigma_3$  stress plot in hangingwall for open stopes with dilution greater and smaller than ten percent

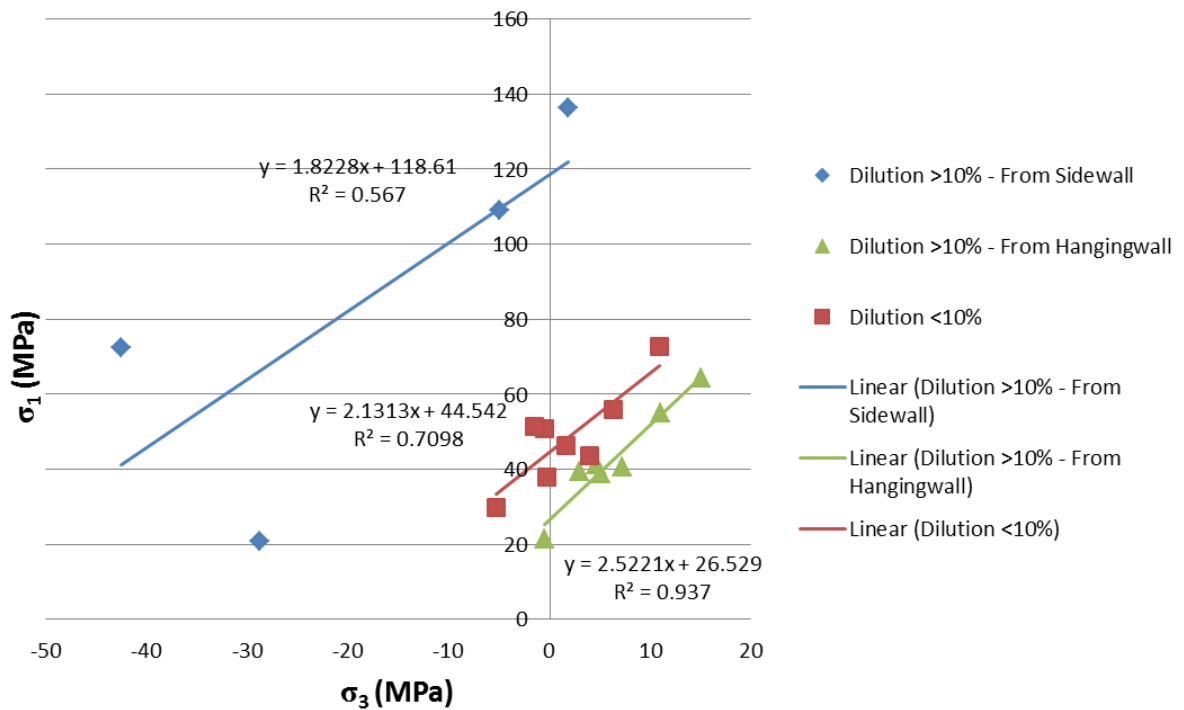


Figure 6.24 The average  $\sigma_1$  and  $\sigma_3$  stress plot in hangingwall for open stopes with dilution greater and smaller than ten percent

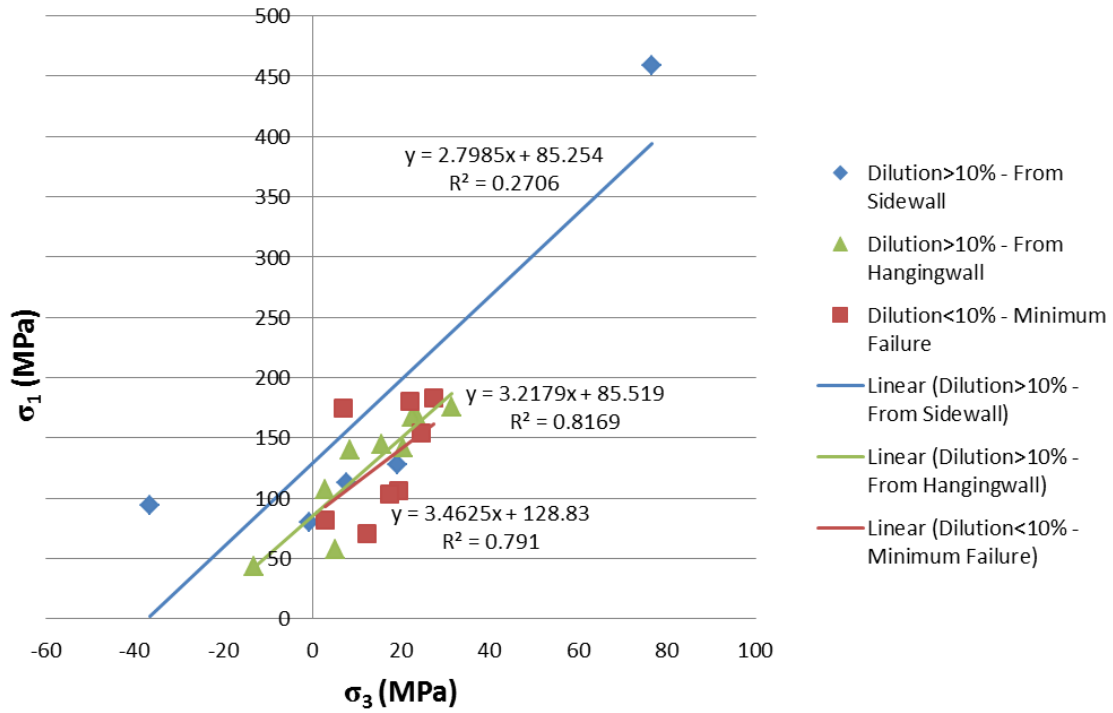


Figure 6.25 The maximum  $\sigma_1$  and  $\sigma_3$  stress plot in sidewall for open stopes with dilution greater and smaller than ten percent

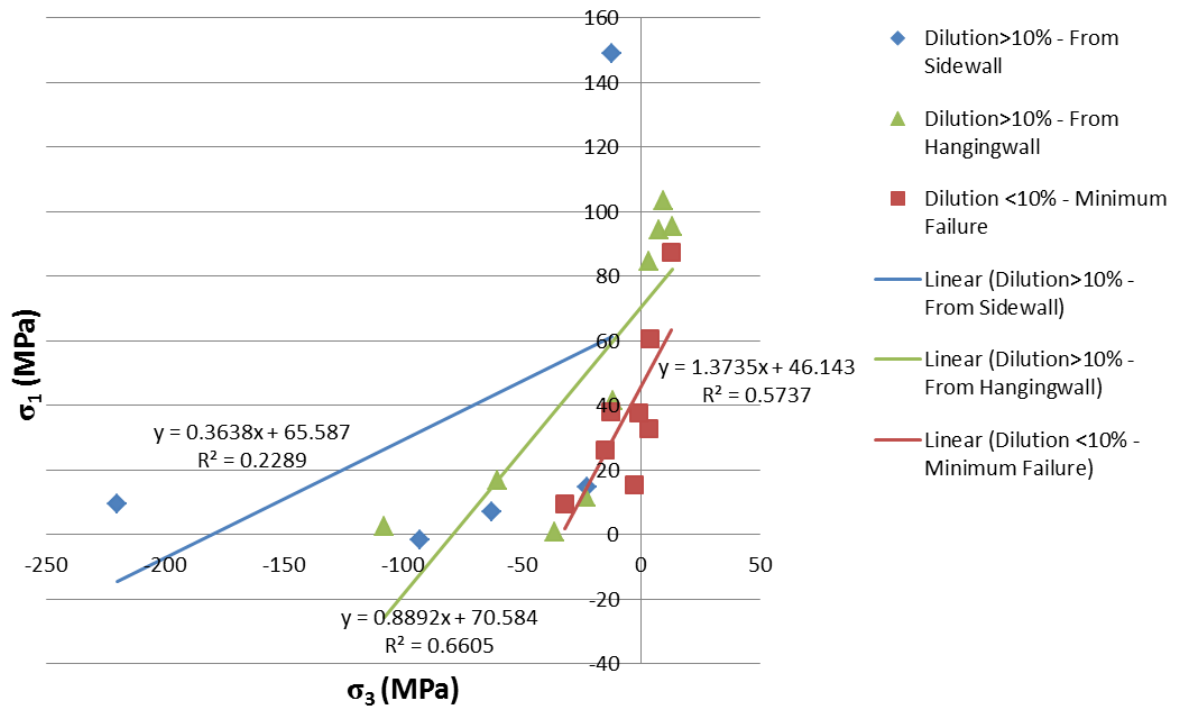


Figure 6.26 The minimum  $\sigma_1$  and  $\sigma_3$  stress plot in sidewall for open stopes with dilution greater and smaller than ten percent

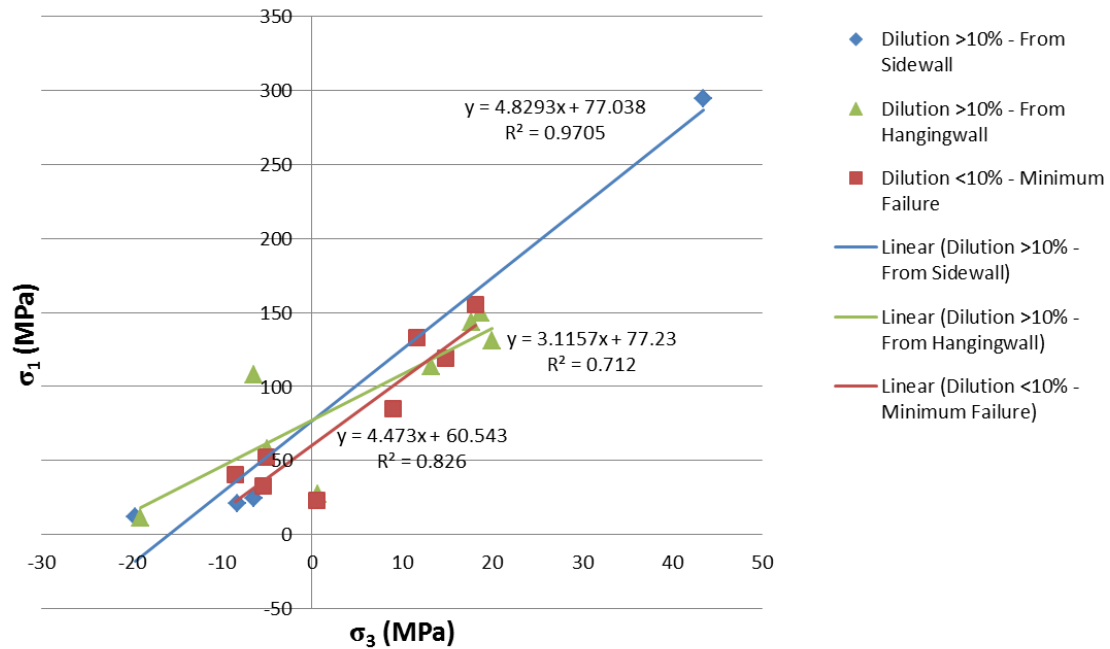


Figure 6.27 The median  $\sigma_1$  and  $\sigma_3$  stress plot in sidewall for open stopes with dilution greater and smaller than ten percent

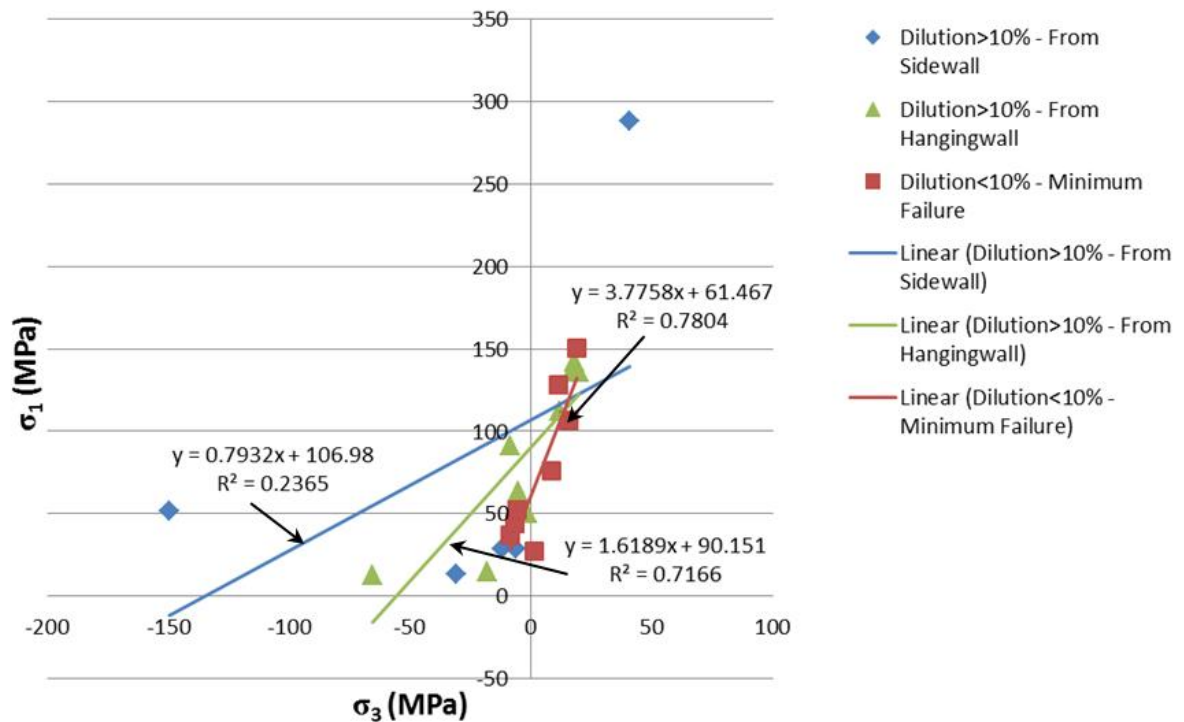


Figure 6.28 The average  $\sigma_1$  and  $\sigma_3$  stress plot in sidewall for open stopes with dilution greater and smaller than ten percent

### **6.2.5 Failure Criteria Applied to Map3D Results**

Using the results obtained from Map3D on the hangingwall and sidewalls for the twenty-two case studies simulated, the failure criteria as discussed in sections 2.6 to 2.9 will be applied. Figure 6.29 and Figure 6.30 show the results of application of the Mohr-Coulomb, Hoek-Brown, Zhang–Zhu, Pan–Hudson, Priest, Simplified Priest and Drucker–Prager Criteria to the  $\sigma_1$ ,  $\sigma_2$  and  $\sigma_3$  results obtained from the Map3D analyses of the open stopes. Each of the criteria mentioned above will be discussed and critically reviewed in the following sections.

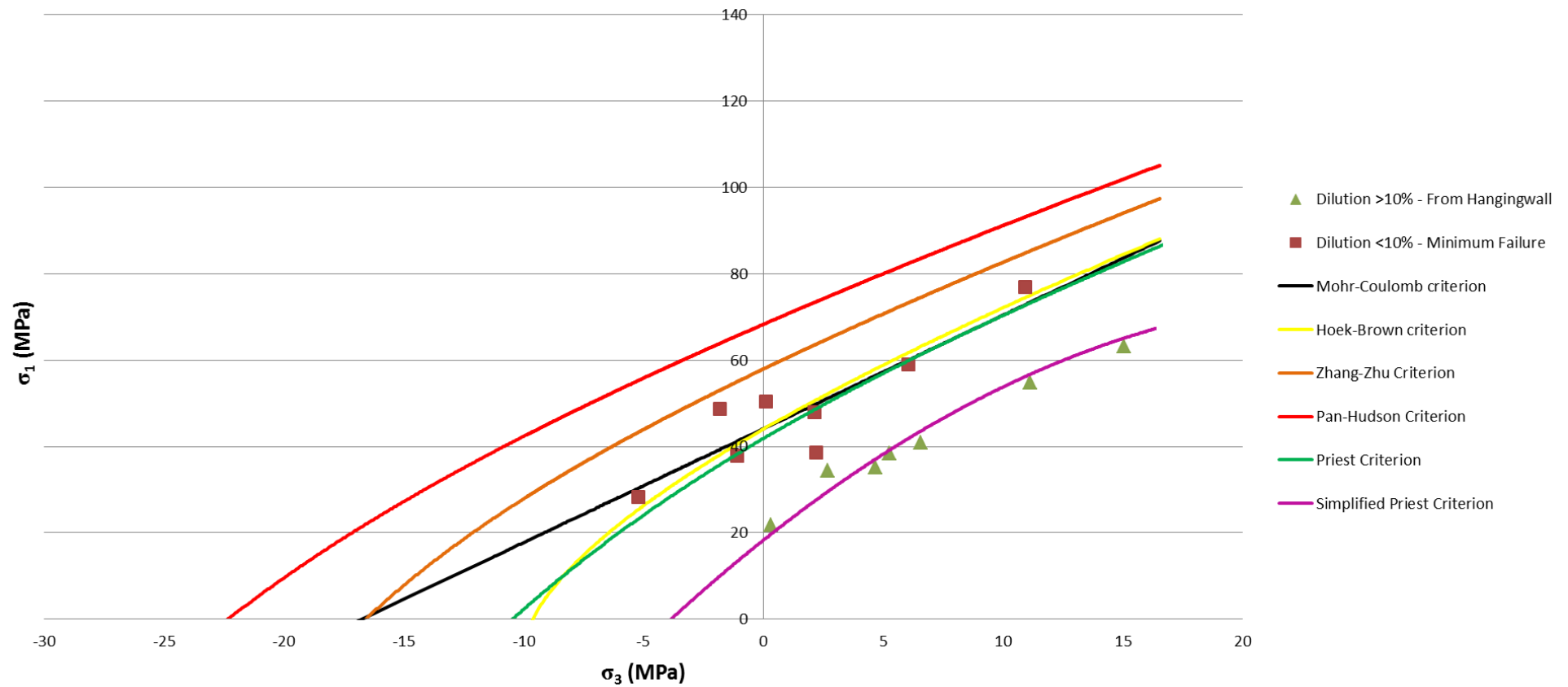


Figure 6.29 Graph showing the relation between various criteria used and obtained results for open stopes with major hangingwall failure

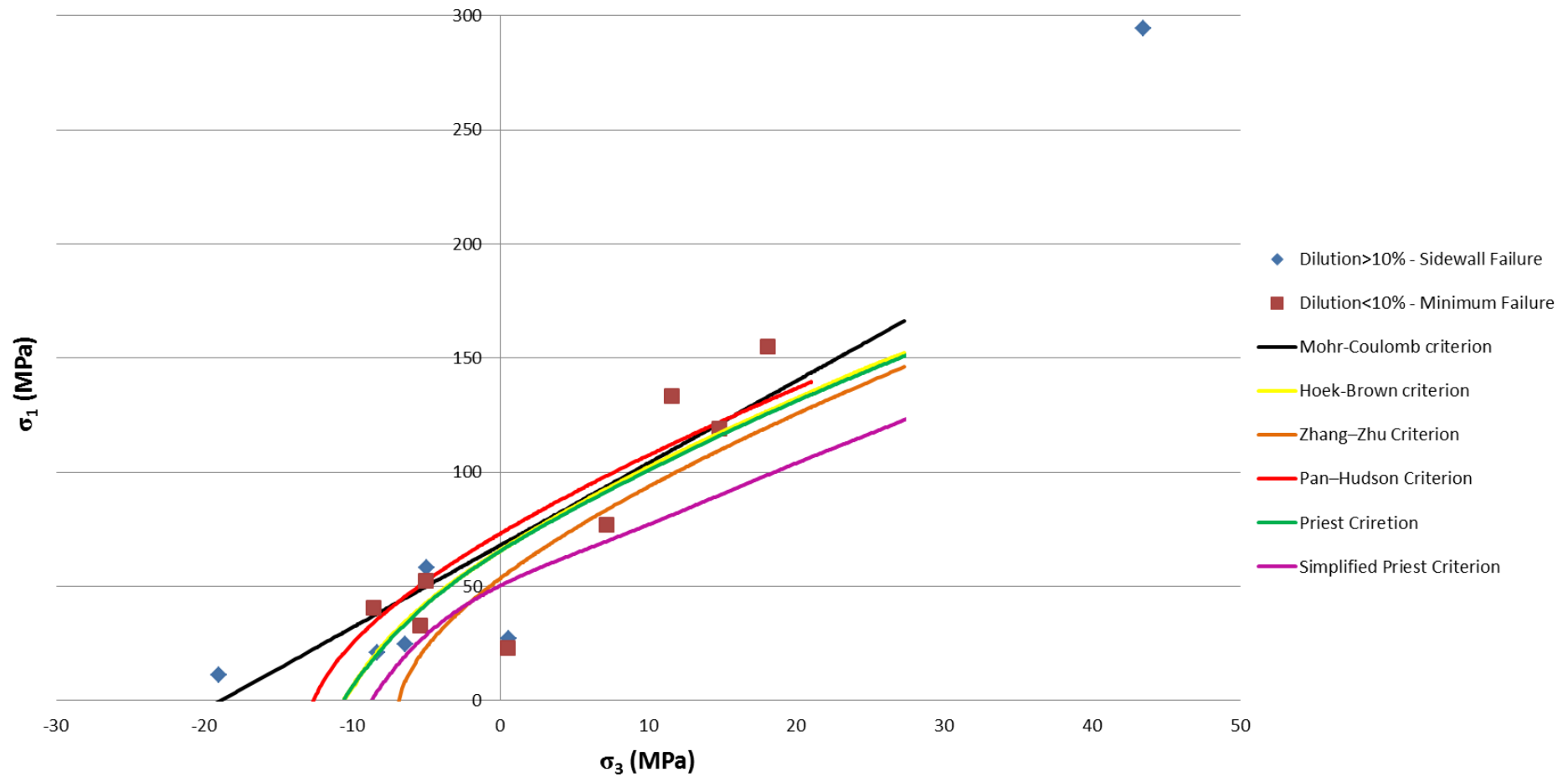


Figure 6.30 Graph showing the relation between various criteria used and obtained results for open stopes with major sidewall failure

### **Mohr-Coulomb failure criterion**

Applying the Mohr-Coulomb failure criterion to the results obtained from Map3D for the case studies' hangingwalls, three distinctive failure zones were identified by plotting the median major  $\sigma_1$  and median minor  $\sigma_3$  principal stresses. These three failure zones corresponded with the case studies where major dilution (>10%) was recorded from the hangingwall or sidewalls as shown in Table 5.1 and minor dilution (<10%) as shown in Table 5.2.

The same approach, as discussed above, was taken in evaluating the case studies' sidewalls. However, for the sidewalls it was found that, for all the case studies, there is no significant difference in the median major  $\sigma_1$  and median minor  $\sigma_3$  principal stresses at the sidewall for major and minor dilution case studies, as shown in Figure 6.32.

From the analyses results, as shown in Figure 6.31 for hangingwall failure around open stopes, the following results were obtained: slope of the best fit-line  $q$  was 2.6, angle of internal friction  $\phi$  of  $27^\circ$  and a rock mass unconfined compressive strength  $C_o$  of 44MPa. Using the analyses results as shown in Figure 6.32 for sidewall failure around open stopes, the following results were obtained: slope of the best fit-line  $q$  was 3.6, angle of internal friction  $\phi$  of  $34^\circ$  and a rock mass unconfined compressive strength  $C_o$  of 68MPa.

The results shown in Table 6.4 for the Mohr-Coulomb failure criterion suggest that the hangingwall and sidewalls of these open stopes have different rock mass unconfined compressive strengths  $C_o$ , which is not a true reflection. It was also found that the angle of internal friction  $\phi$  was different for hangingwall and sidewall failure. The validity of this criterion for the prediction of hangingwall and sidewall failure is therefore questionable.

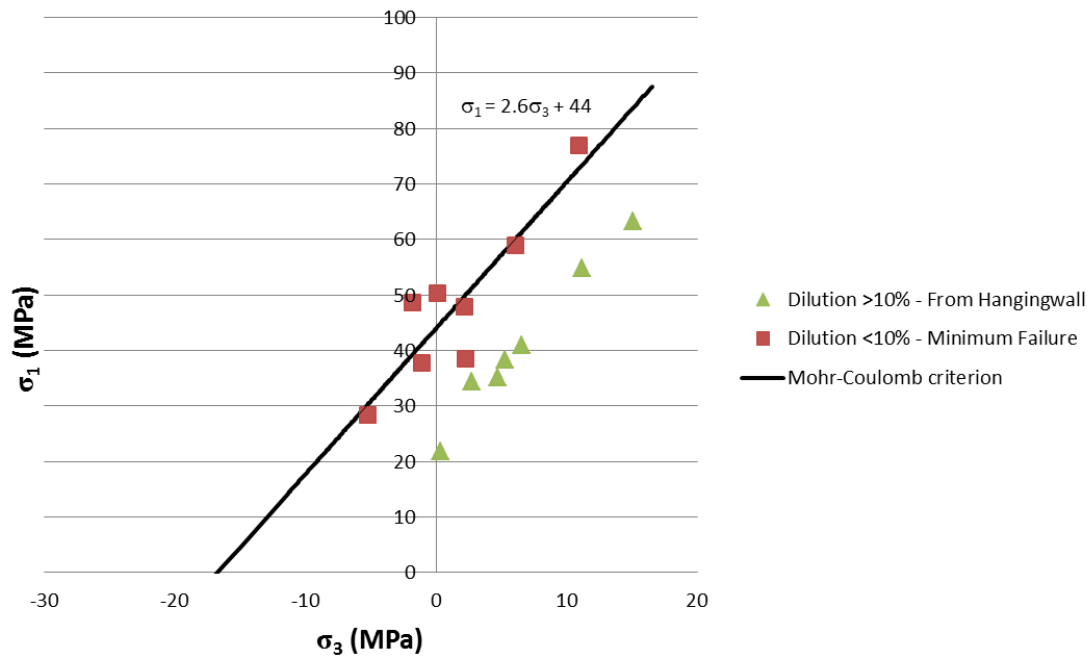


Figure 6.31 Graph showing the relation between the Mohr-Coulomb failure criterion and obtained results for open stopes with major hangingwall failure

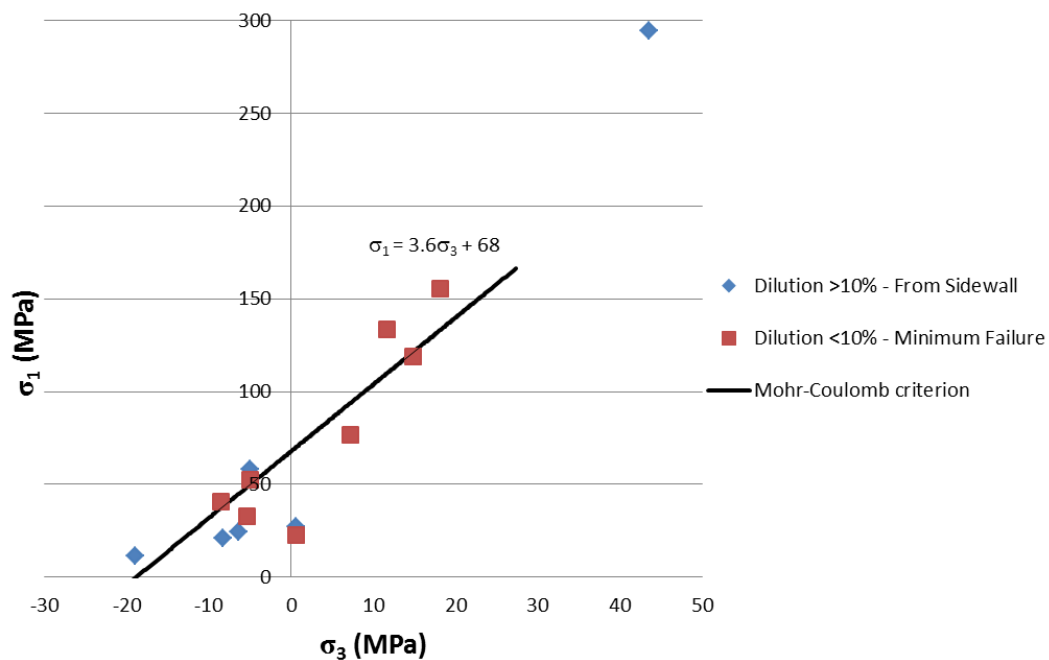


Figure 6.32 Graph showing the relation between the Mohr-Coulomb failure criterion and obtained results for open stopes with major sidewall failure



### Hoek-Brown failure criterion

The material constants for the Hoek-Brown criterion were determined by adjusting the curve to fit the stress results obtained from the numerical analyses. From these results, as shown in Table 6.4, the rock mass unconfined compressive strength  $C_o$  could be determined. As for the Mohr-Coulomb criterion, the results suggest that the hangingwall and sidewalls of these open stopes have a different rock mass unconfined compressive strengths  $C_o$ , which is not the case. When one or more of the principal stresses is tensile the results indicated that no failure would occur. From the analyses results, as shown in Figure 6.33 for hangingwall failure around open stopes, the following results were obtained: rock mass unconfined compressive strength  $C_o = 44.2\text{MPa}$ ;  $m_b = 0.772$ ;  $s = 0.0312$ ;  $a = 0.5$ ;  $GSI = 80$  and  $D = 0.5$ . For sidewall failure around open stopes as shown in Figure 6.34 for the following results were obtained: rock mass unconfined compressive strength  $C_o = 65.9\text{MPa}$ ,  $m_b = 1.658$ ,  $s = 0.0695$ ,  $a = 0.5$ ,  $GSI = 80$  and  $D = 0.5$ .

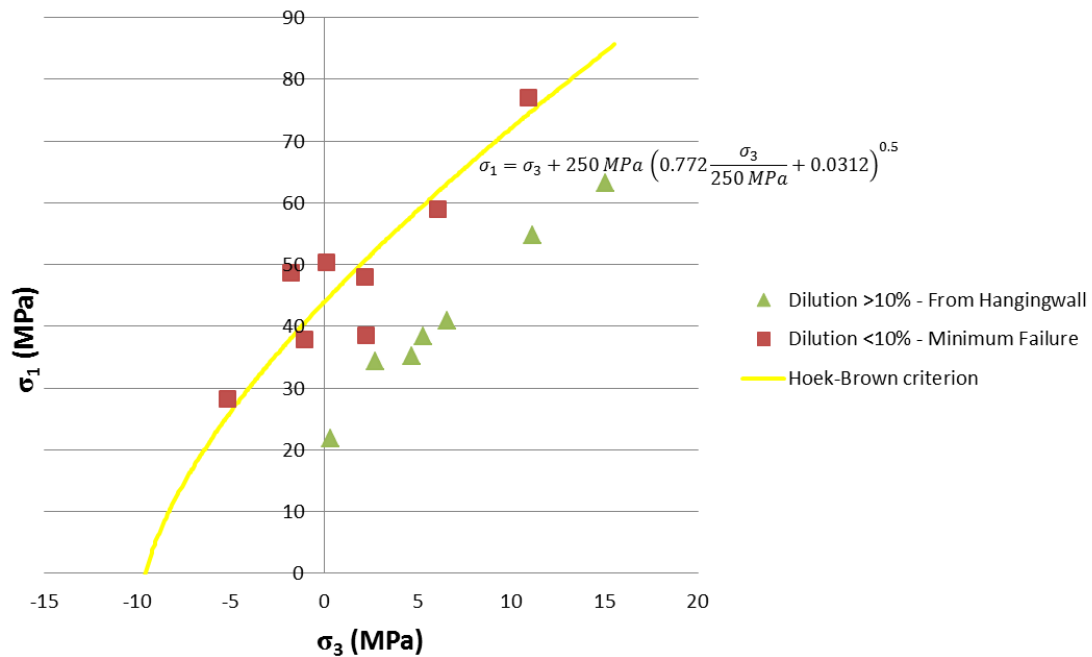


Figure 6.33 Graph showing the relation between the Hoek-Brown failure criterion and obtained results for open stopes with major hangingwall failure

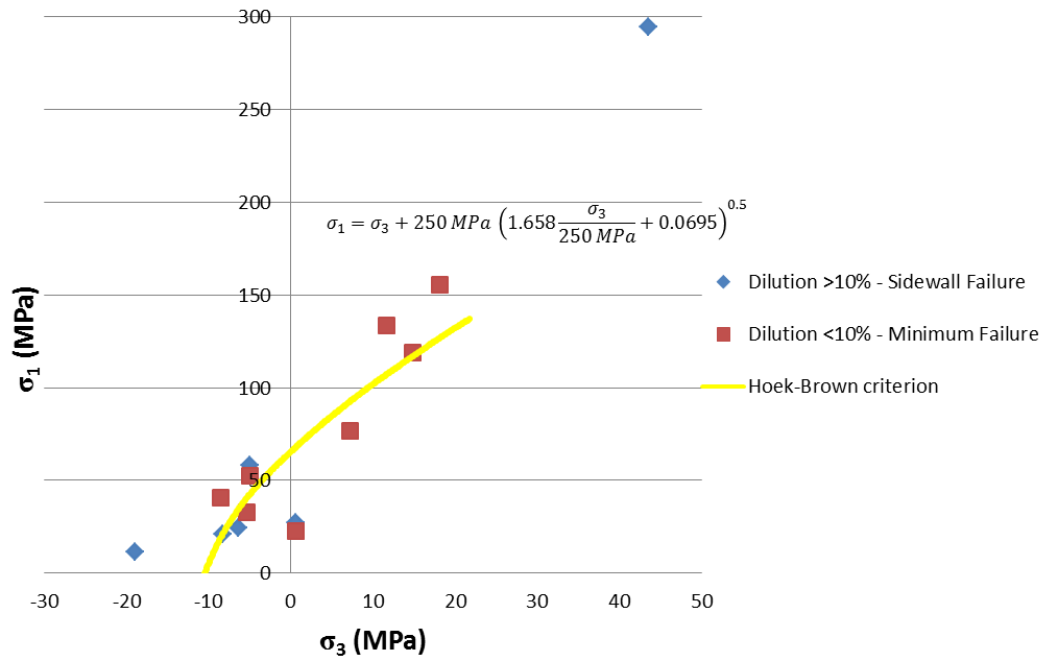


Figure 6.34 Graph showing the relation between the Hoek-Brown failure criterion and obtained results for open stopes with major sidewall failure

### Zhang–Zhu Criterion

From the analyses results, as shown in Figure 6.35 for hangingwall failure around open stopes the following results were obtained: rock mass unconfined compressive strength  $C_o = 58 \text{ MPa}$ ;  $m_b = 0.772$ ;  $s = 0.0540$ ;  $a = 0.5$ ;  $GSI = 80$  and  $D = 0.5$ . For the sidewalls, as shown in Figure 6.36, the following results were obtained: rock mass unconfined compressive strength  $C_o = 53.7 \text{ MPa}$ ,  $m_b = 1.658$ ,  $s = 0.0462$ ,  $a = 0.5$ ,  $GSI = 80$  and  $D = 0.5$ .

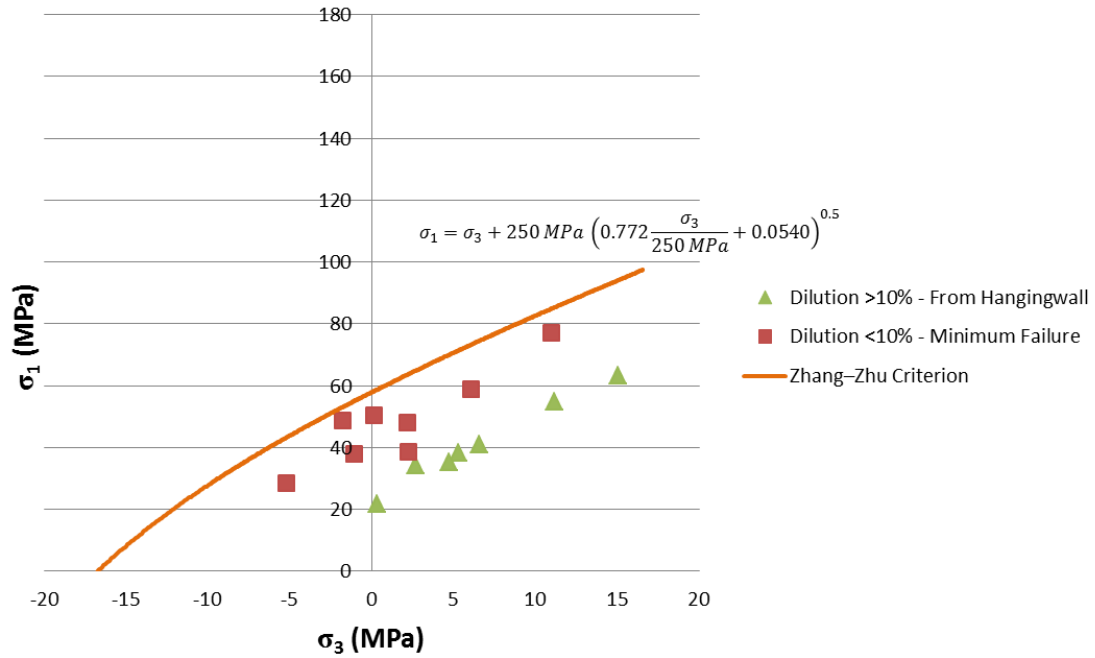


Figure 6.35 Graph showing the relation between the Zhang-Zhu Criterion and obtained results for open stopes with major hangingwall failure

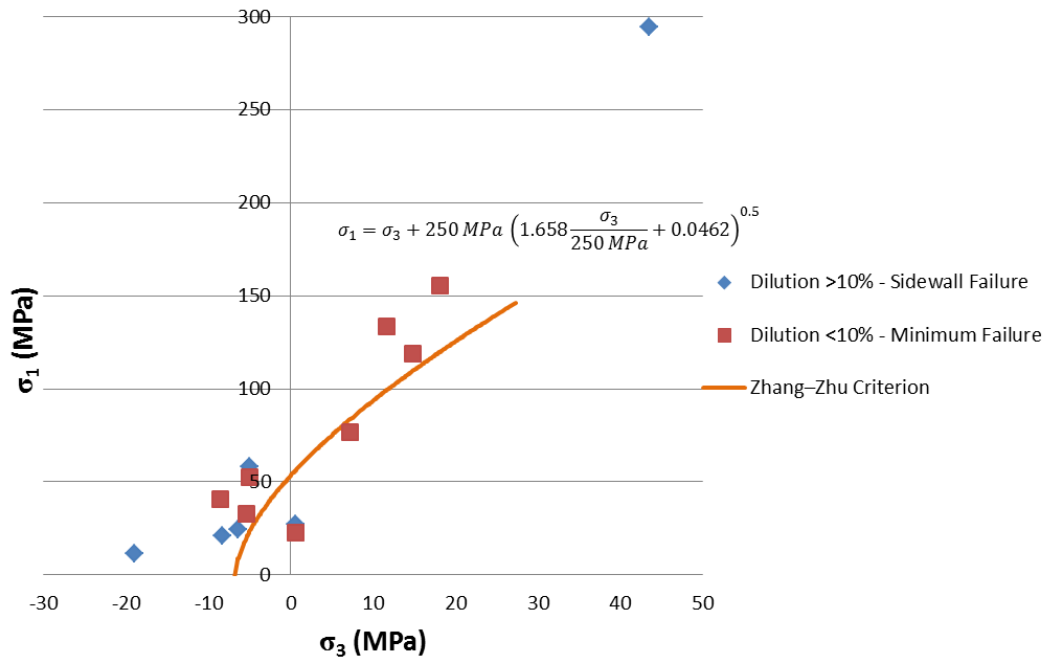


Figure 6.36 Graph showing the relation between the Zhang-Zhu Criterion and obtained results for open stopes with major sidewall failure

### Pan–Hudson Criterion

As shown in Figure 6.37, the following results were obtained for the hangingwall: rock mass unconfined compressive strength  $C_o = 68.5\text{MPa}$ ;  $m_b = 0.772$ ;  $s = 0.0750$ ;  $a = 0.5$ ;  $GSI = 80$  and  $D = 0.5$ . For sidewalls, as shown in Figure 6.38, the following results were obtained: rock mass unconfined compressive strength  $C_o = 73.4\text{MPa}$ ,  $m_b = 1.658$ ,  $s = 0.0861$ ,  $a = 0.5$ ,  $GSI = 80$  and  $D = 0.5$ .

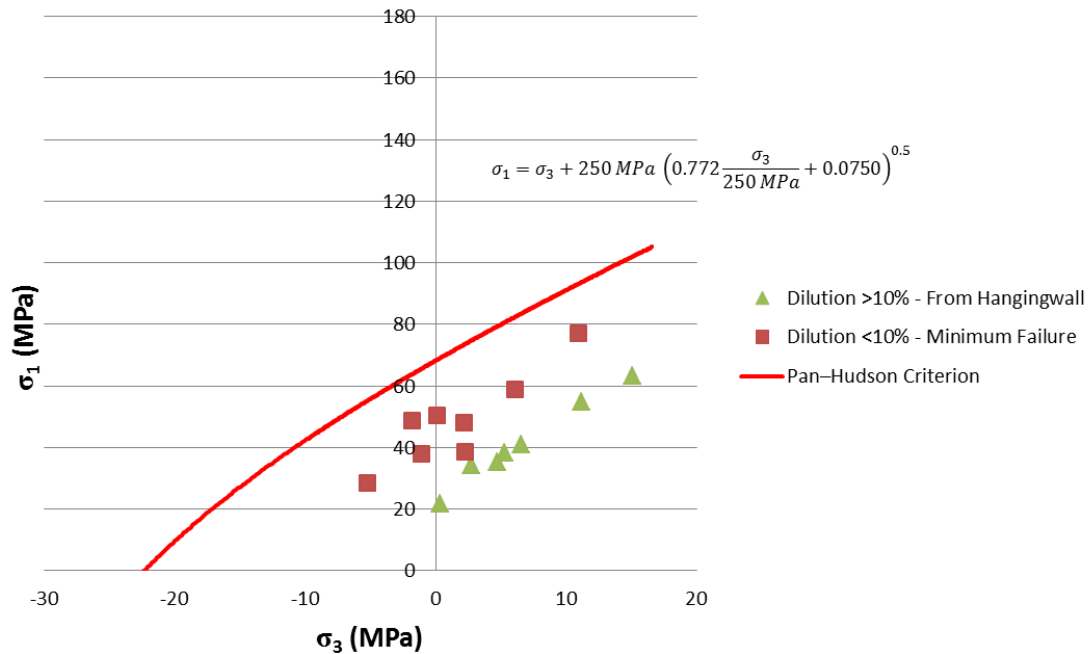


Figure 6.37 Graph showing the relation between the Pan–Hudson Criterion and obtained results for open stopes with major hangingwall failure

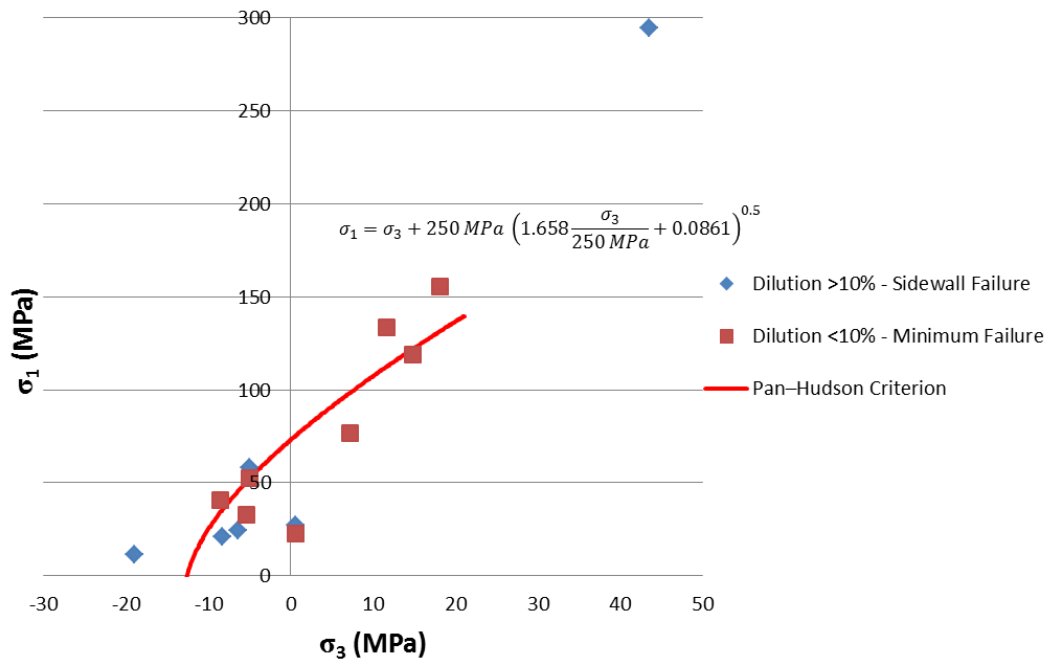


Figure 6.38 Graph showing the relation between the Pan–Hudson Criterion and obtained results for open stopes with major sidewall failure

### **Generalized Priest Criterion**

Applying the generalised Priest criterion to the Map3D results for the principal stresses  $\sigma_1$  and  $\sigma_3$  in the hangingwall and sidewalls of the open stopes, the following results obtained are shown in Figure 6.39 and Figure 6.40. This criterion yielded the same results as the Hoek-Brown criterion, which can be expected since it is based on the Hoek-Brown criterion.

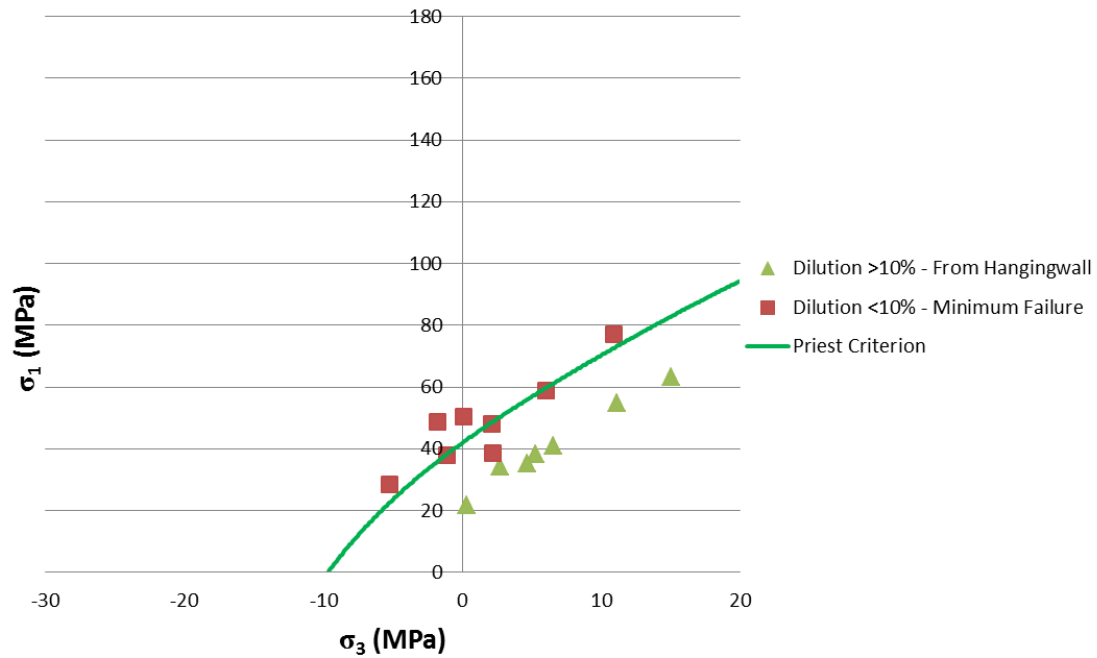


Figure 6.39 Graph showing the relation between the Priest Criterion and obtained results for open stopes with major hangingwall failure

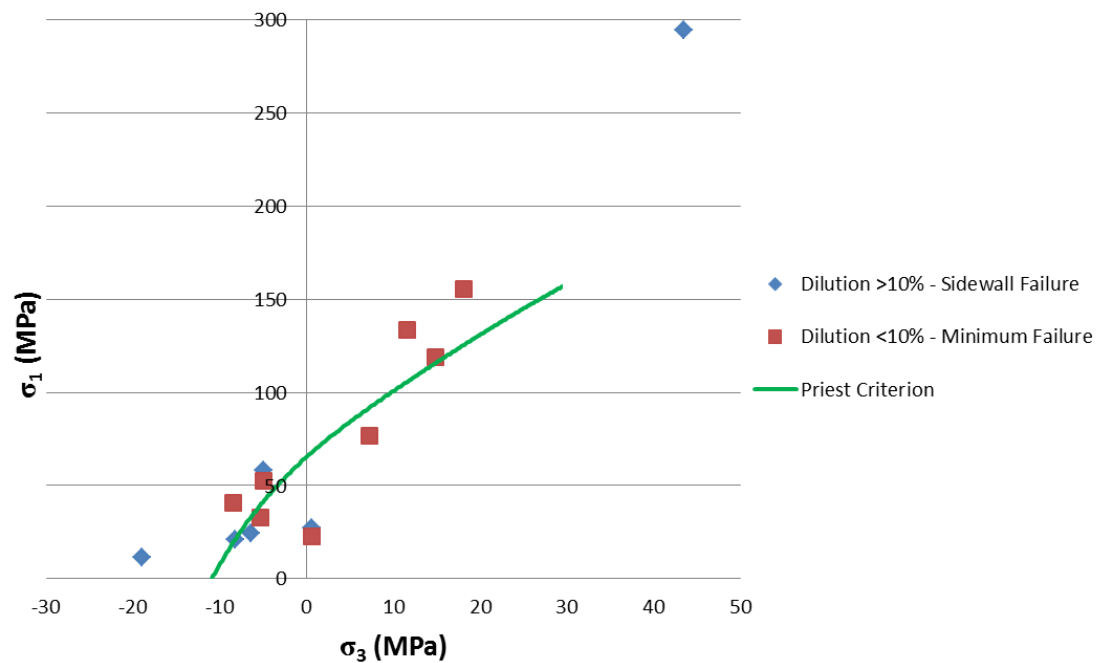


Figure 6.40 Graph showing the relation between the Priest Criterion and obtained results for open stopes with major sidewall failure

### **Simplified Priest Criterion**

The Simplified Priest criterion does not fit the obtained Map3D results and tends to overestimate failure in open stopes, as shown in Figure 6.41 and Figure 6.42.

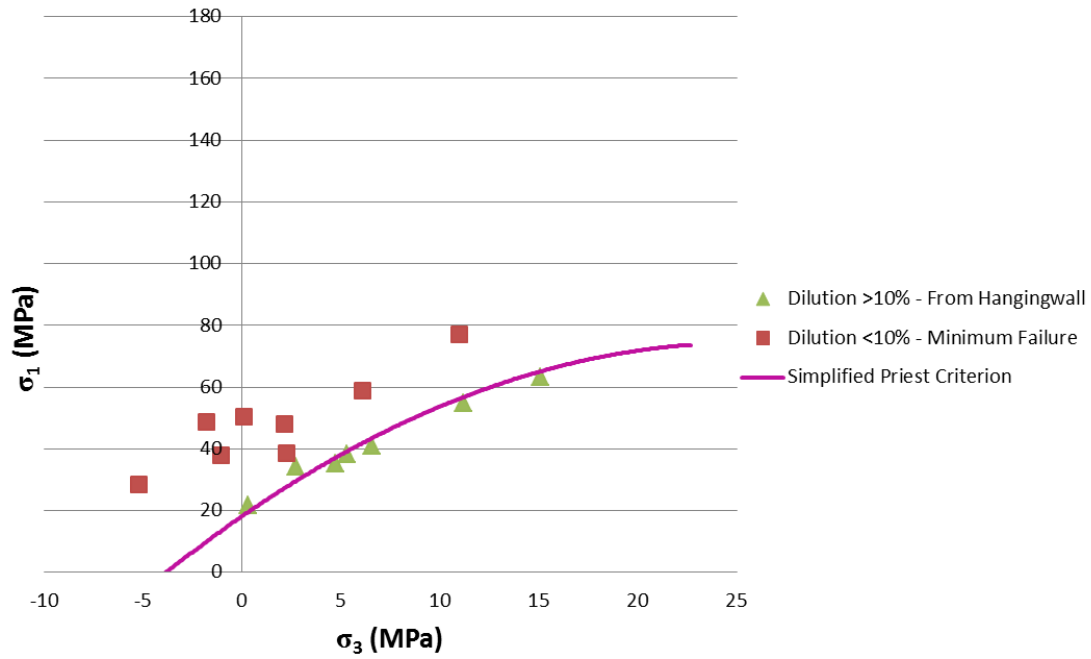


Figure 6.41 Graph showing the relation between the Simplified Priest Criterion and obtained results for open stopes with major hangingwall failure

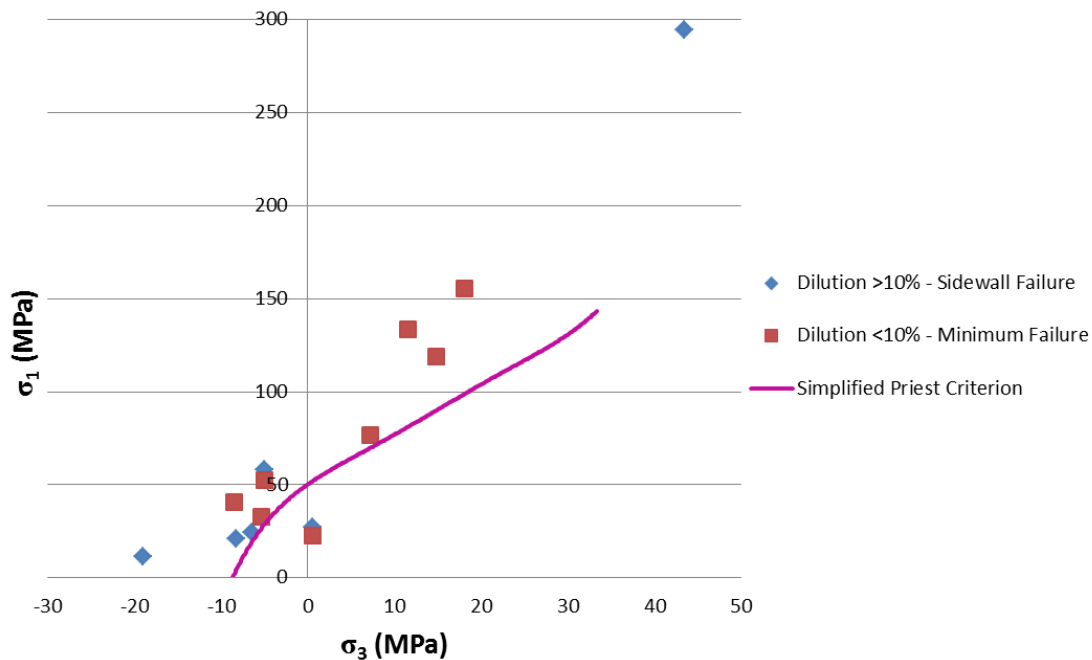


Figure 6.42 Graph showing the relation between the Simplified Priest Criterion and obtained results for open stopes with major sidewall failure

### **Drucker–Prager Criterion**

The Drucker-Prager criterion also does not fit the Map3D results and substantially overestimates the failure around open stopes. Thus it is not suitable for application to open stopes.

### **Outcome of the applied failure criteria**

Using the stresses determined with Map3D, the various stress-based failure criteria discussed above were applied to predict failure depths into the hangingwall and sidewalls of the Target case study open stopes. The results obtained, and the measured overbreaks in the stopes, are shown in Figure 6.45 and Figure 6.46. These results show that the stress-based failure criteria either completely overestimate or under estimate the failure for most of the case studies. It can be concluded that these methods are not appropriate for accurate design of open stopes in the gold mining environment. The application of the failure criteria to the case studies, making use of Map3D, is shown in detail in Appendix E.



**Table 6.4 Predicted rock mass unconfined compressive strength  $C_o$  using different failure criteria**

	Predicted Rock Mass UCS	
	Sidewall	Hangingwall
Mohr-Coulomb criterion	68	44
Hoek-Brown criterion	66	44
Zhang–Zhu Criterion	54	58
Pan–Hudson Criterion	73	68
Priest Criterion	65	44
Simplified Priest Criterion	50	18
Drucker–Prager Criterion	-	-

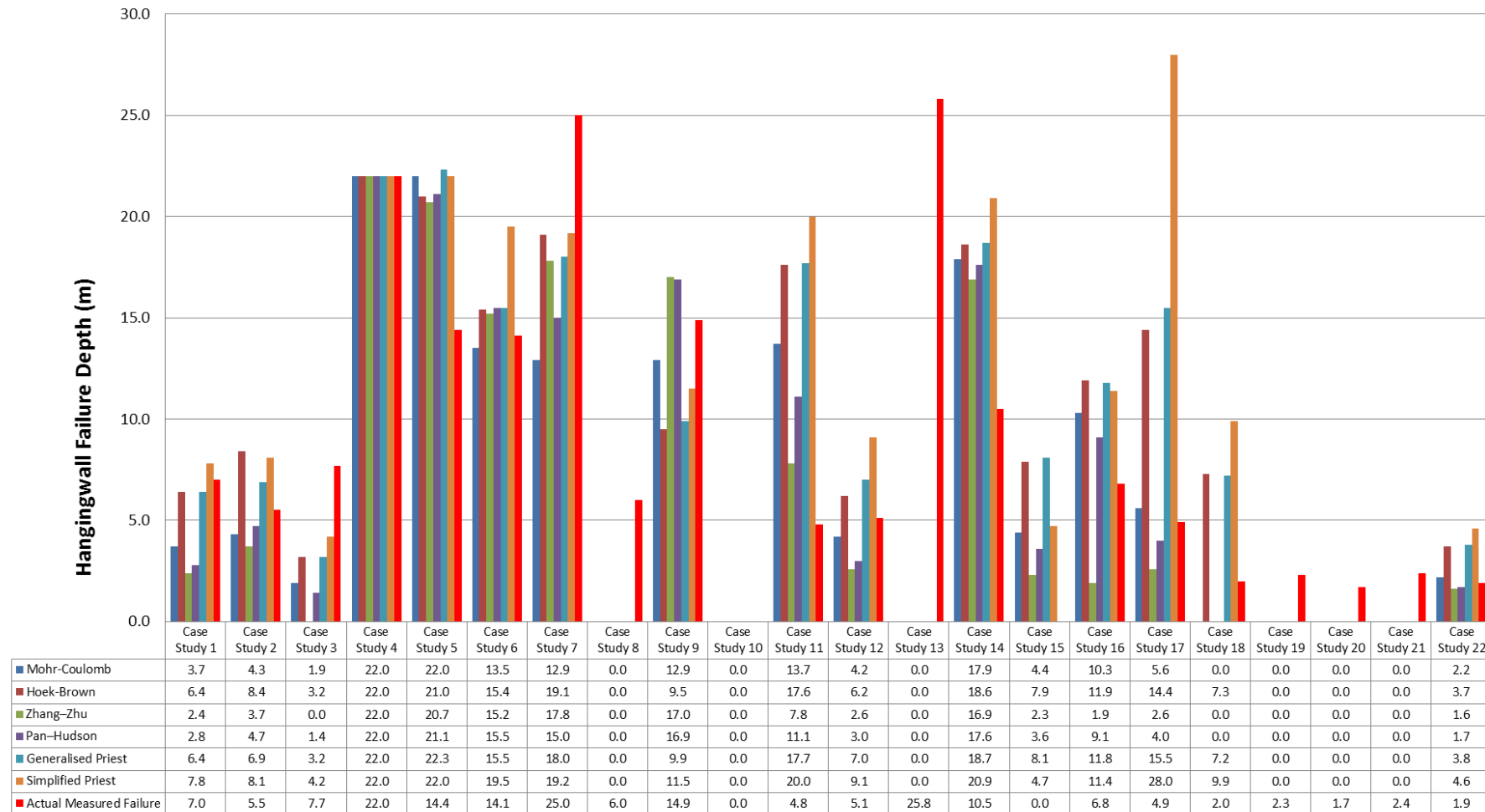


Figure 6.45 Graph showing the hangingwall failure depth predictions obtained for the case studies using various criteria

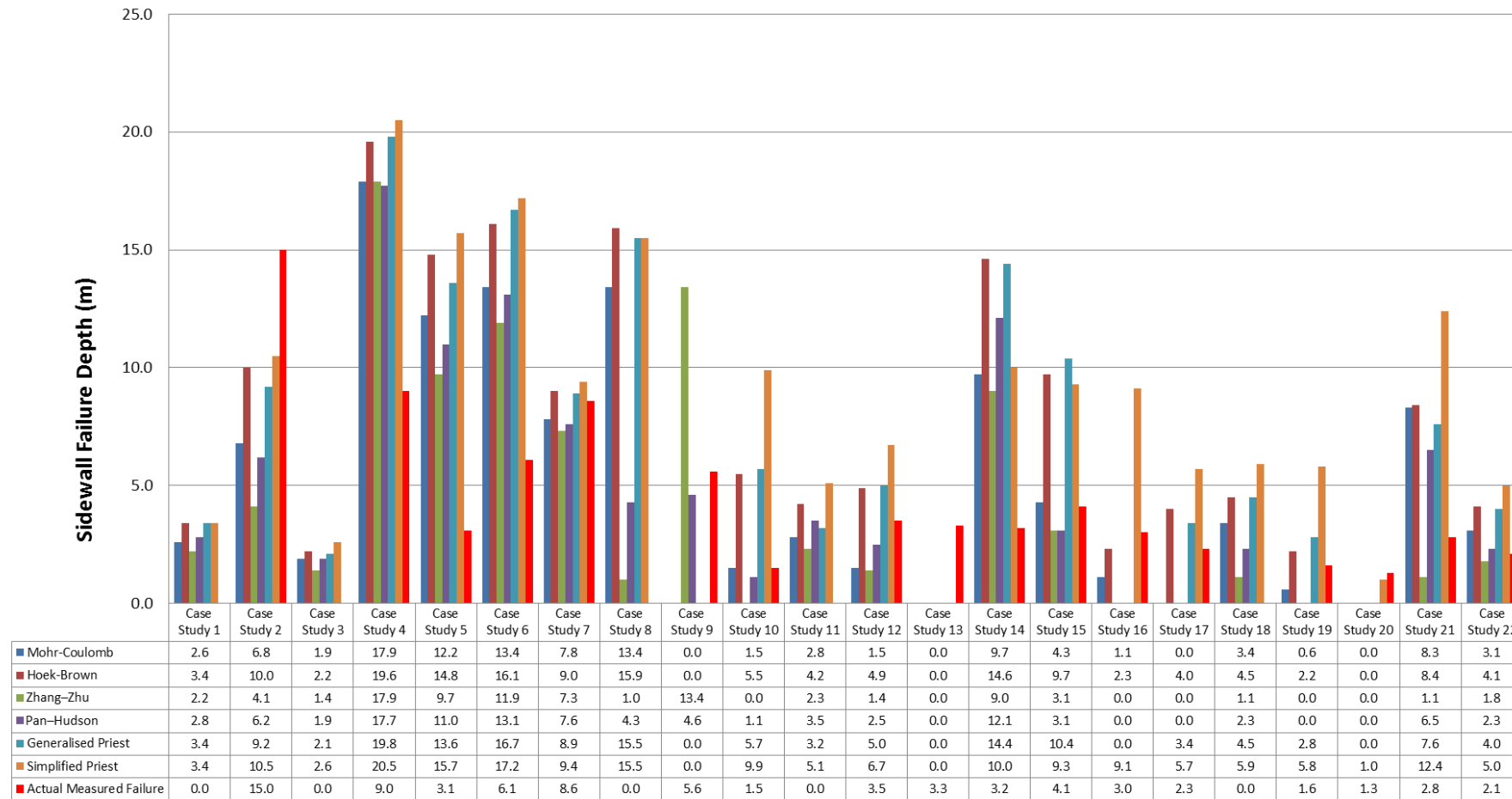


Figure 6.46 Graph showing the obtained results using various criteria for the case studies sidewall failure depth

### **6.3 Summary**

In this chapter, the influence of stress on open stope hangingwall and sidewall stability and the effect on dilution was investigated. Numerical modelling methods were used to simulate the stress distribution around the open stope case studies and then failure criteria were applied to evaluate the stability of the hangingwall and sidewalls of these excavations, and the resulting effects on dilution. In the next chapter, a newly developed Dilution Stress-Strain Index (DSSI) for prediction of failure around stopes, and also for design of stopes, will be discussed.

## **7 INFLUENCE OF STRESS AND STRAIN ON OPEN STOPE HANGINGWALL AND SIDEWALL STABILITY AND DILUTION**

### **7.1 Introduction**

In the previous chapter, the influence of stress on open stope hangingwall and sidewall stability, and the effect on dilution, were discussed. Numerical modelling methods were used to determine the stress distributions around these open stopes for the case studies, and then failure criteria applied to evaluate the stability of the hangingwall and sidewalls, and the effects on dilution. In this chapter, the effect of three-dimensional stress and strain will be comprehensively discussed. The development of a new design criterion will be described, which will assist in predicting failure depths into the hangingwall and sidewalls of open stopes, and in the calculation of dilution in open stopes with greater accuracy. The accuracy of prediction with this criterion will be demonstrated for Target stopes, as well as for another mining site in a different geological environment.

### **7.2 Application of Strain-Based Failure Criteria to Case Studies**

The extension strain criterion after (Stacey, 1981) was applied to the open stope case studies. Calibration of the extension strain criterion for its use on Target Mine was attempted by making use of a borehole camera to measure the extent of these fractures in boreholes drilled from the top down into open stope hangingwalls. Unfortunately, “mist” accumulated in the holes, making it difficult to take measurements, but as shown in Figure 7.1 no open fractures were observed in most of these boreholes. A possible reason for this is that the open stopes have already attained their final shapes.

Making use of the final CMS for the open stopes the extent of these fractures around these open stopes was extrapolated. The model was calibrated by increasing the modulus of elasticity  $E$  until the fracture extent matched with the final CMS for the open stope as shown in Figure 7.2 and 7.3. It was found that

although the modulus of elasticity  $E$  was increased from 70000 MPa to 85000 MPa in an attempt to match the final CMS of the open stope, in case study 1, the result was not satisfactory. All the case study results for the application of the extension strain criterion (Stacey, 1981) are shown in Appendix F. Although the prediction from this criterion matches the expected failure shape in the hangingwall of the open stope as shown in Figure 7.2 and 7.3, the fracture propagation is significantly deeper into the hangingwall than the failure observed for Target Mine, which should be a true reflection. The light grey area in Figure 7.2 and 7.3 indicates the expected fracture propagation depth where the total extension strain  $\varepsilon_e$  in the rock exceeds the critical strain  $\varepsilon_{ec}$  value  $\geq 1$ . The blue area in Figure 7.2 and 7.3 indicates that the total extension strain  $\varepsilon_e$  in the rock is less than the critical strain  $\varepsilon_{ec}$  value, which is  $< 1$  and  $> 0$  and fracture propagation is not expected. The dark grey area in Figure 7.2 and 7.3 indicates that the total extension strain  $\varepsilon_e$  in the rock is less than zero so the rock should still be solid in this area. The lack of success with this strain criterion is perhaps to be expected, since the criterion (Stacey, 1981) applies to the initiation of fractures and not to failure.



Figure 7.1 Photo in a borehole at Target Mine open stope hangingwall showing ground conditions with no visible open fractures

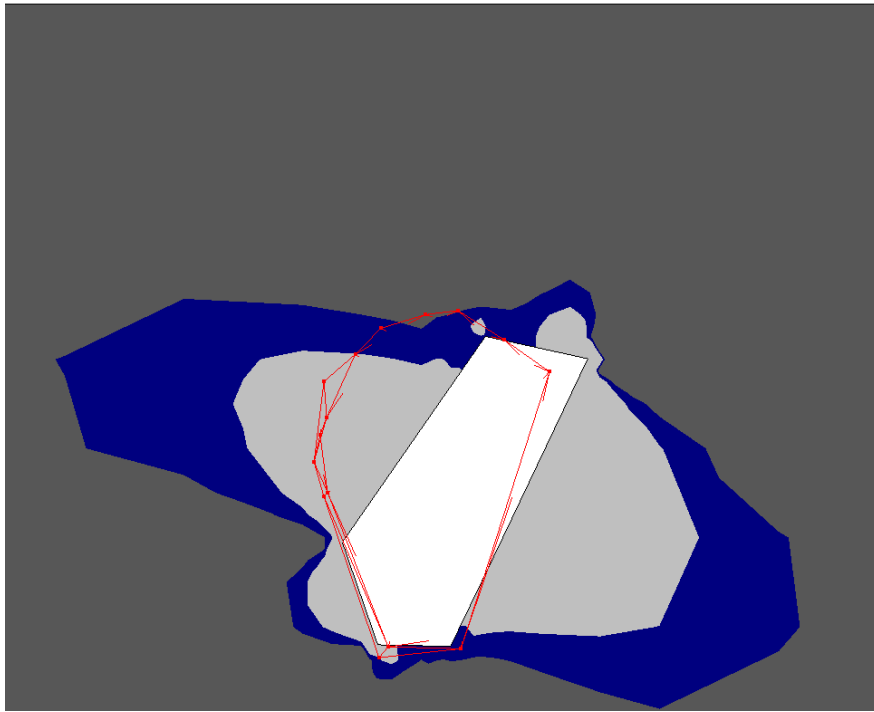


Figure 7.2 The extension strain criterion after Stacey, (1981) applied to case study 1 with a modulus of elasticity  $E = 70000 \text{ MPa}$

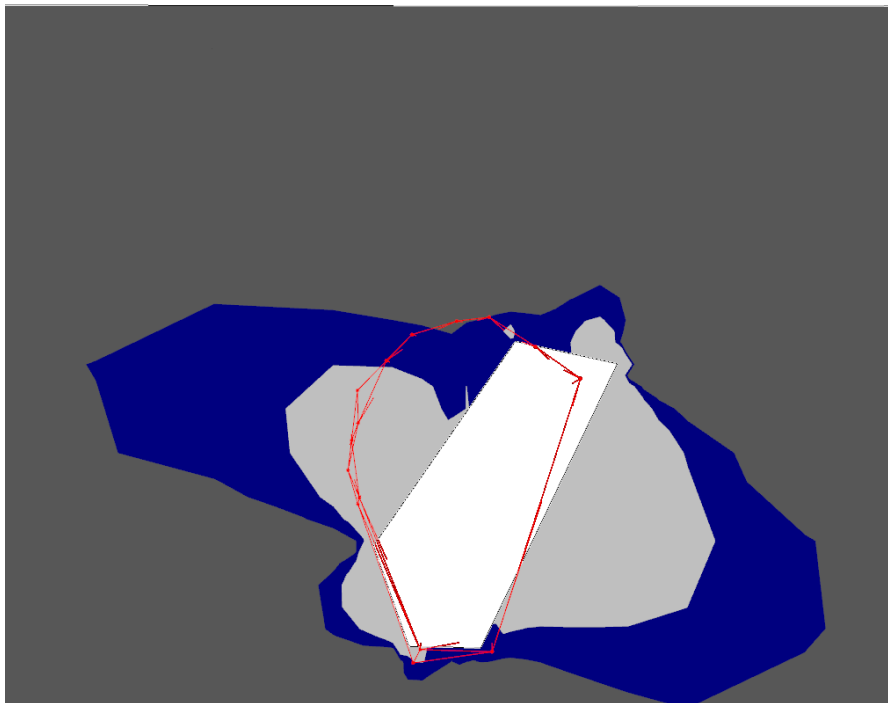


Figure 7.3 The extension strain criterion after Stacey, (1981) applied to case study 1 with a modulus of elasticity  $E = 85000 \text{ MPa}$

### 7.3 Mean Stress and Volumetric Strain

Open stopes have a three-dimensional geometry and are created in a three-dimensional stress field. It is therefore to be expected that the stability of these stopes, and of course the potential dilution, will be dependent on the three-dimensional stress and strain conditions around these stopes. To take these three-dimensional conditions into account, the mean stress,  $\sigma_m$ , also known as the octahedral normal stress, as described in section 2.5, was plotted against volumetric strain,  $\varepsilon_{vol}$ , as described in section 2.10, for open stopes with dilution greater than ten percent, and dilution equal to or smaller than ten percent, in the hangingwall and sidewalls respectively. These results indicate, as expected, a linear relation between the mean stress and volumetric strain - stress and strain are linked in the linear numerical model by constitutive behaviour known as Hooke's Law (Brady and Brown, 1985). This explains the linear relation between mean stress and volumetric strain.

By plotting the results obtained from the gridlines in Map3D, placed at the hangingwall and sidewalls for these simulated case studies with major and minor dilution from the hangingwall and sidewalls respectively, the following results were obtained as shown in Figure 7.4 and 7.5. From these plots it is clear that the major and minor dilution for open stopes fall into distinct clusters shown in red and green respectively, indicating the potential for a suitable criterion for the evaluation of open stopes, which takes into account the three principal stresses and strains. For dilution from hangingwall failure resulting in more than ten percent dilution in open stopes on Target Mine it was found that this is true if the  $\sigma_m > 50\text{MPa}$ ;  $\varepsilon_{vol} > 1,285 \times 10^{-3}$  or  $\sigma_m < 4,8\text{MPa}$ ;  $\varepsilon_{vol} < 0,124 \times 10^{-3}$  as shown in Figure 7.4. For dilution from sidewall failure resulting in more than ten percent dilution in open stopes on Target Mine it was found that this is true if the  $\sigma_m > 85,3\text{MPa}$ ;  $\varepsilon_{vol} > 2,193 \times 10^{-3}$  or  $\sigma_m < 0,5\text{MPa}$ ;  $\varepsilon_{vol} < 0,013 \times 10^{-3}$  as shown in Figure 7.5. This new criterion is dealt with in the next section.



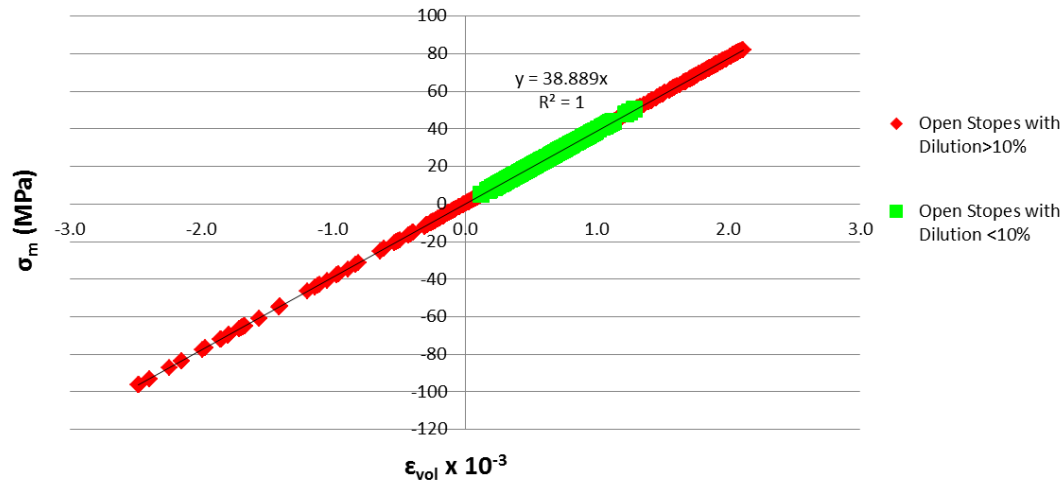


Figure 7.4 Graph showing the relation between mean stress and volumetric strain for open stopes with major and minor hangingwall dilution

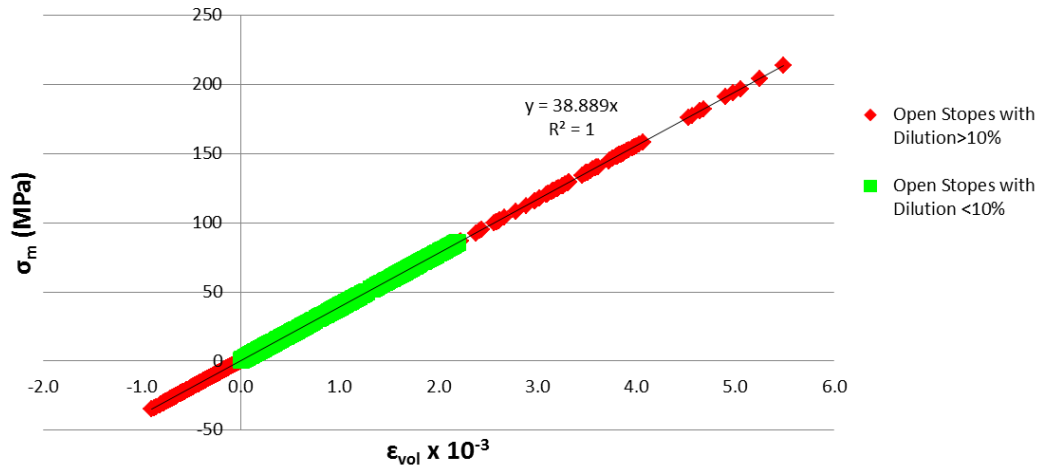


Figure 7.5 Graph showing the relation between mean stress and volumetric strain for open stopes with major and minor sidewall dilution

#### 7.4 Dilution Stress-Strain Index

Evaluating the stress-strain environment around these open stopes the following were observed from the numerical analyses. It would appear that there is a good relation between mean stress in MPa and volumetric strain in millistrains. A design criterion is proposed for open stopes allowing the prediction of the failure extent in the hangingwall and sidewalls of open stopes with accuracy. From the back analyses, it was found that for hard quartzite rock the tolerance for stress-strain changes in the immediate vicinity of the open

stopes were very small. The relation between mean stress  $\sigma_m$  and volumetric strain  $\varepsilon_{vol}$  can be mathematically expressed as follows:

$$\sigma_m = q\varepsilon_{vol}$$

$$\varepsilon_{vol} = \frac{\sigma_m}{q}$$

where  $q = 38.889$  GPa, which is the slope of the linear trend line as shown on Figures 7.4 and 7.5. The  $q$ -value can be different for each operation depending on the Young's Modulus ( $E$ ) and Poisson's Ratio ( $\nu$ ). As failure of these simulated open stopes is bounded by Hooke's Law, the Dilution Stress-Strain Index ( $DSSI$ ) is the relation between mean stress and volumetric strain and can be mathematically expressed as follows:

$$DSSI = \frac{\sigma_m}{q\varepsilon_{vol}} \quad (7.1)$$

This is a new criterion for determining the expected failure depth in the hangingwall or sidewalls of excavations, and does not appear in any literature reviewed. It is not apparent that any application of this criterion, or similar criterion, has been published, since no reference to such an application was discovered during the review of literature. Although octahedral normal stress form the basis of this criterion this is a completely new method of determining failure depth. In this method the assumption is made that if the volumetric strain exceeds the critical value for mean stress, failure will occur. This method considers all three Principal stresses and strains components, which agrees with the actual environment these open stopes are being excavated in.

## **7.5 Applying the *Dilution Stress-Strain Index (DSSI)* design criterion to Target Mine**

A full 3D numerical program is required to simulate the 3D environment in which these open stopes will be excavated. Using Map3D, areas within the open stope hangingwall or sidewall can be identified where instability may occur.

Before applying the DSSI to Target Mine Open stopes, the detailed recommended approach for the application of the design criterion will be discussed.

### **3D Numerical Analyses (Map3D)**

Build a full 3D model of the open stope making use of fictitious forces including all the relevant mining before mining this open stope in the numerical model for back analyses. This must be done for each case study being used for back analyses. At each case study place gridlines on the open stope excavation hangingwall and sidewalls boundaries. Ensure that the gridlines are placed in the centre of the excavation hangingwall and sidewalls. Ensure that there are at least 50 and more points on each gridline. Place a sufficient number of vertical grid planes cutting across the open stope, which will be used later for DSSI analyses. The relevant stress input parameters for the k-ratio with the Young's Modulus ( $E$ ) and Poisson's Ratio ( $\nu$ ) determined from laboratory tests to be used. Then run the numerical model.

### **Results from Analyses**

Obtain the gridline results for the open stope excavation after being mined (mining step 2) and export  $\sigma_1$ ,  $\sigma_3$ ,  $\sigma_m$  and  $\varepsilon_{vol}$  for major and minor dilution in the open stope hangingwall and sidewalls. Ensure that the volumetric strain  $\varepsilon_{vol}$  to be exported, is in millistrains. Determine the statistical median from these exported results for  $\sigma_1$ ,  $\sigma_3$ ,  $\sigma_m$  and  $\varepsilon_{vol}$  for major and minor dilution in open stope hangingwall and sidewalls. The obtained median mean stress value for each case study will be used when applying the DSSI. Plot on a graph the  $\sigma_1$  and  $\sigma_3$  median results for each case study for major and minor dilution in open stope hangingwall and sidewalls as shown in Figure 7.11. From these results, determine the failure mode for major and minor dilution in open stope hangingwall and sidewalls. Making use of the minor dilution data the failure envelope cut-off can be determined as shown in Figure 7.7.

### **Applying DSSI and determining dilution in open Stopes**

Making use of obtained median mean stress value  $\sigma_m$  determined for each case study, the DSSI can be applied for major failure in open stope hangingwall and sidewalls in Map3D on the vertical grid planes. Now the open stope CMS can be imported into Map3D as a DXF file and superimposed on the grid planes to compare the results as shown in Figure 7.9. This is part of the calibration process. If a good correlation is found between the DSSI prediction and the open stope CMS, the criterion can be used; if not, the model calibration process must be continued until a reasonable result is obtained.

To calibrate the model, the Young's Modulus ( $E$ ) and Poisson's Ratio ( $\nu$ ) can be changed until the results match. When the model is calibrated the same Young's Modulus ( $E$ ) and Poisson's Ratio ( $\nu$ ) must be applied for all case studies being used. Apply the DSSI for major failure in open stope hangingwall and sidewalls in Map3D on the vertical grid planes for a planned open stope, and measure the failure depth. The DSSI failure lobes can also be exported as a DXF file and compared to the design stope shape, to determine the expected dilution, as shown in Figure 7.10. Using this information the stope shape can be amended (reduced in size) so that the final shape corresponds with the actual required planned shape due to the expected failure depth. The flow chart shown in Figure 7.6 gives the detailed recommended approach.

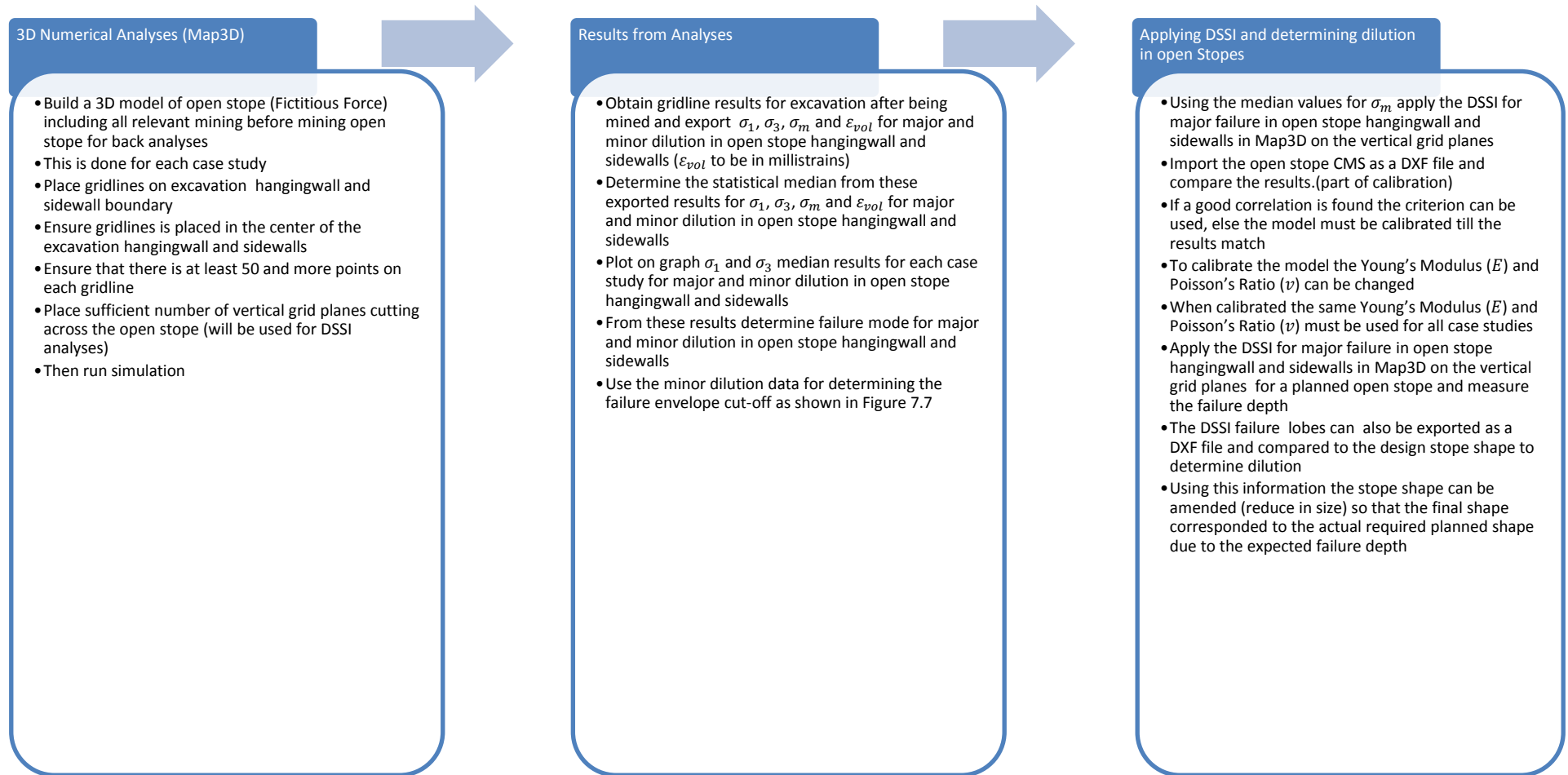


Figure 7.6 Flow chart showing the detailed recommended approach for the application of the DSSI design criterion and determining dilution in open stopes

Applying the methodology shown in Figure 7.6, the open stope case studies were evaluated. Following the steps recommended, when plotting the results for mean stress in MPa versus volumetric strain in millistrains there is a clear linear relation. Making use of Equation (7.1), hangingwall and sidewall failure in open stopes can be predicted by the following equation proposed for Target Mine, with  $\varepsilon_{vol}$  in millistrains:

$$DSSI = \left( \frac{MEDIAN(\sigma_m)}{38.889\varepsilon_{vol}} \right) > 1 \quad (7.2)$$

After the DSSI design criterion was established for hangingwall failure and sidewall failure on Target Mine, the obtained median major principal stress  $\sigma_1$  and median minor principal stress  $\sigma_3$  were plotted for each of the twenty-two case studies as shown in Figure 7.7. Using the obtained results for the twenty-two case studies, the failure mode for the open stopes with major hangingwall or sidewall dilution could be determined. The same was done for open stopes with minor dilution <10%. A failure envelope was established using the minor dilution <10% trend line. By allowing for a failure envelope indicated as Minor Dilution on the graph shown in Figure 7.8, upper and lower failure limits were found to be where  $\sigma_1 = 2.6\sigma_3 + 54$  and  $\sigma_1 = 2.6\sigma_3 + 34$ , respectively for open stopes with minor dilution.

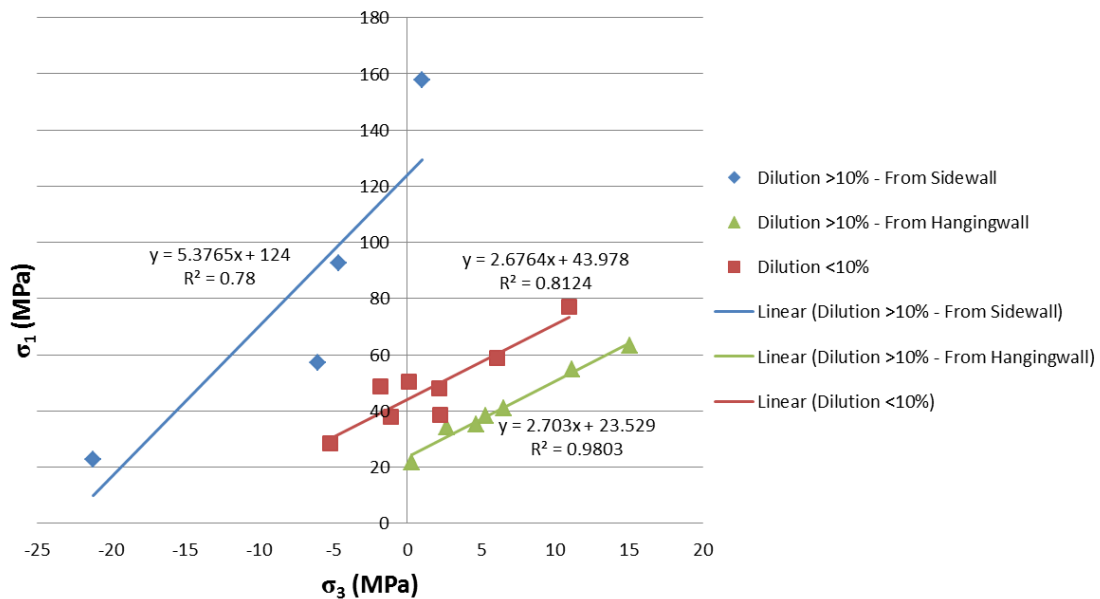


Figure 7.7 Graph showing the relation between the major and minor stress for the case studies hangingwall

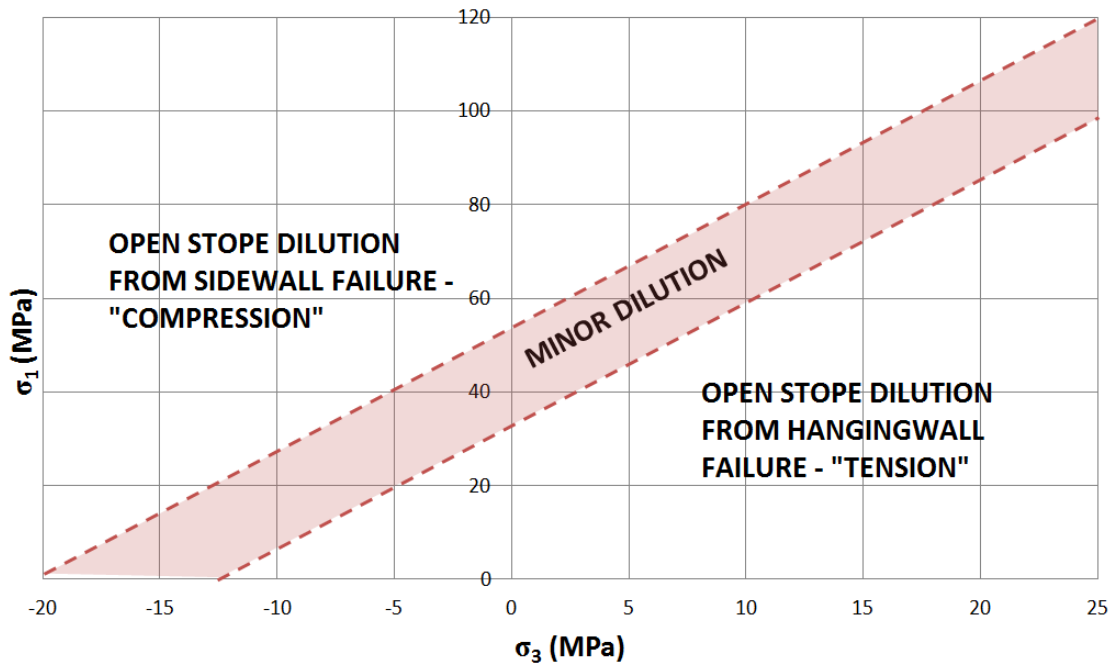


Figure 7.8 Graph showing the relation between open stope hangingwall and sidewall failure as to determine the failure mode

Making use of the graph shown in Figure 7.8, and depending on where these results for median major principal stress  $\sigma_1$  and median minor principal stress  $\sigma_3$  plot for each open stope, the appropriate hangingwall or sidewall median mean stress value can be applied to the DSSI Equation (7.2). Figure 7.9 below indicates such areas in light grey around the open stope for hangingwall failure whereby the DSSI design criterion was applied to case study 1. The contour range for plotting the DSSI design criterion was set to minimum 0 (zero) and the maximum to 1, with intervals of 1 in Map3D. This means that if the DSSI obtained value is  $> 1$ , it will be indicated as light grey on the grid plane. The predicted failure corresponded very well with the actual observed failure in the hangingwall as shown by the CMS of the open stope plotted in red on Figure 7.9 and Appendix E.

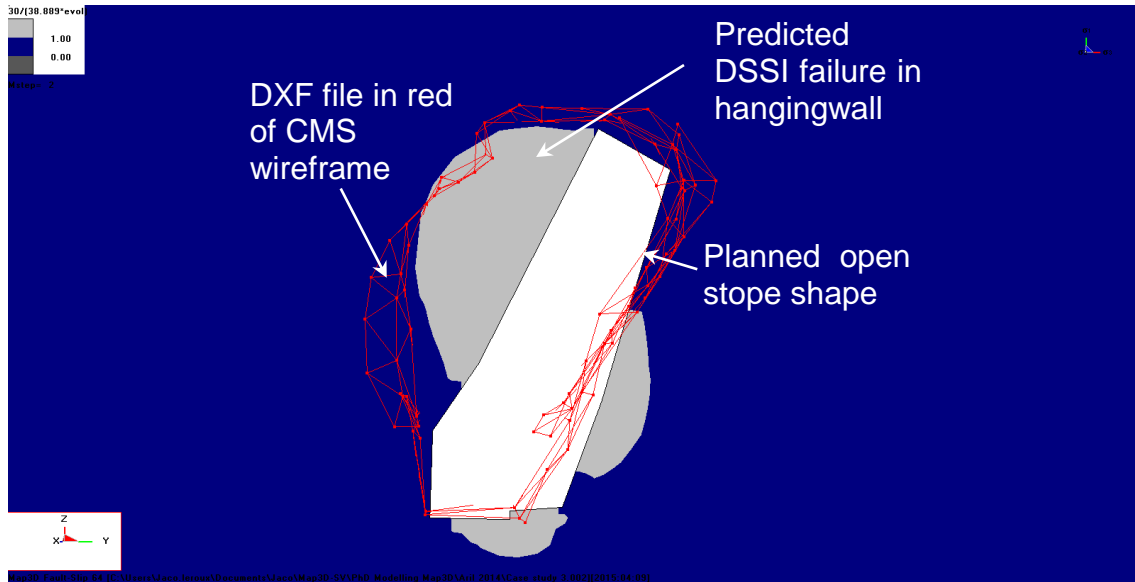


Figure 7.9 Application of the DSSI Design criterion to case study 3

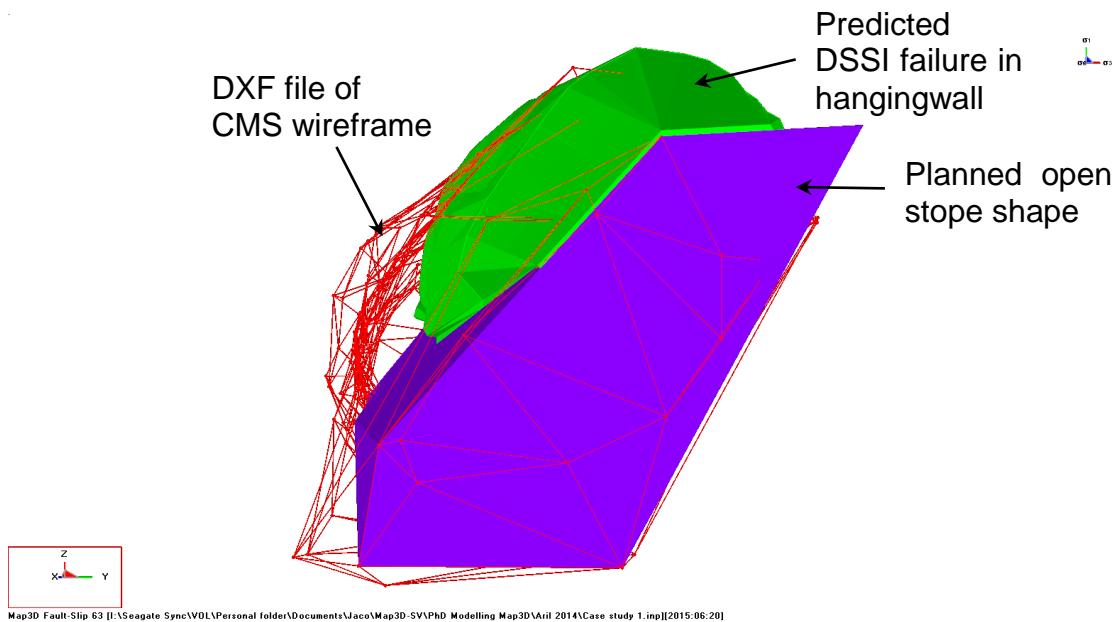


Figure 7.10 Application of the DSSI Design criterion to case study 1

## 7.6 Predicting Dilution from Volumetric Strain

Using the median mean stress  $\sigma_m$  and median volumetric strain  $\varepsilon_{vol}$  results obtained from the case studies, these results were plotted relative to the percentage dilution obtained for each case study with the major dilution from the hangingwall or sidewalls and minor dilution as shown in Figures 7.11 and 7.12. This information proved useful in predicting the actual expected dilution in the



open stopes from the hangingwall or sidewalls. Making use of regression analysis ( $R^2$ ), the trend lines for the twenty-two case studies were established. It was found that for dilution >10% from the sidewalls the regression coefficient ( $R^2$ ) was 97%, which is very good. The regression analysis indicated  $R^2$  for dilution >10% from the hangingwall as 58%.

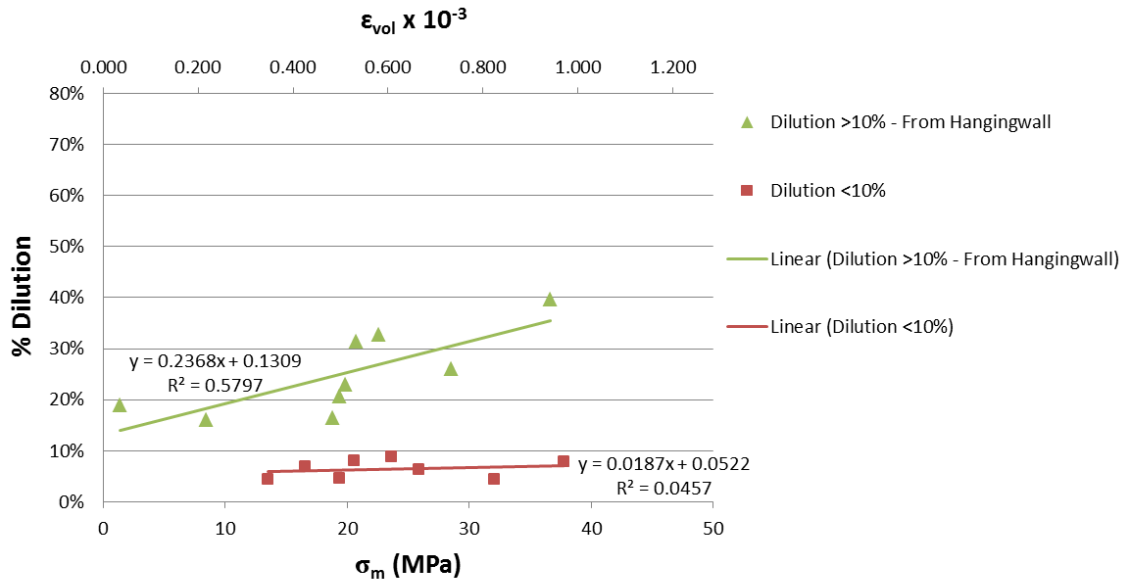


Figure 7.11 Graph showing the relation between median mean stress, volumetric strain and dilution in the hangingwall

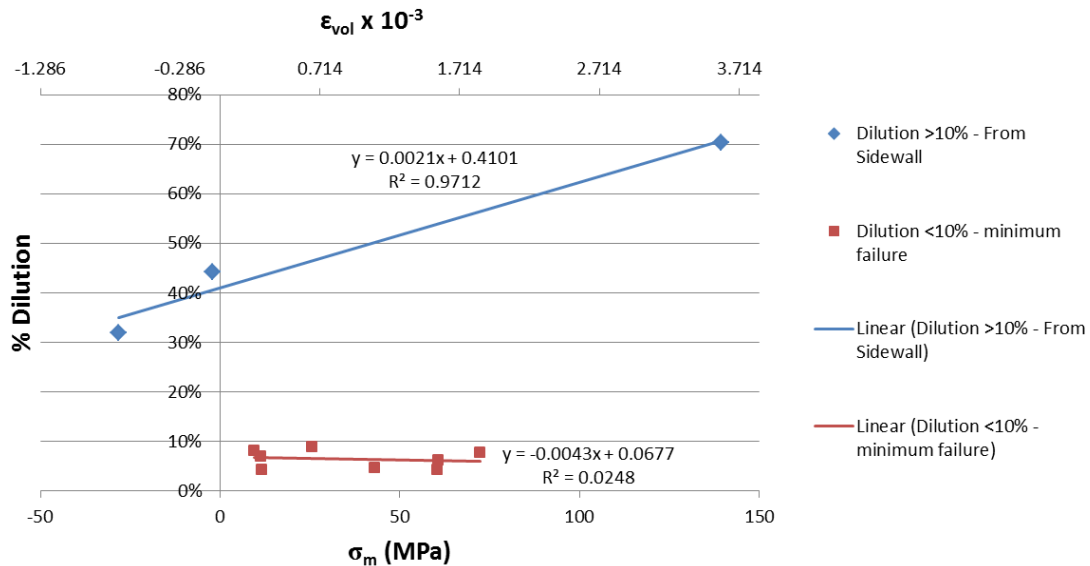


Figure 7.12 Graph showing the relation between median mean stress, volumetric strain and dilution in the sidewall

From the graphs in Figure 7.11 and Figure 7.12, the following equations are proposed for calculating major hangingwall, major sidewall or minor dilation in open stopes on Target Mine:

If  $\frac{\sigma_1}{2.6\sigma_3+54} > 1$  then major sidewall dilation will occur as shown in Figure 7.8:

$$OS_{HFh} = (0.0021\varepsilon_{vol_h} + 0.4101) \times 100 \quad (7.3)$$

If  $\frac{\sigma_1}{2.6\sigma_3+34} < 1$  then major hangingwall dilation will occur as shown in Figure 7.8:

$$OS_{SFs} = (0.2368\varepsilon_{vol_s} + 0.1309) \times 100 \quad (7.4)$$

If  $\frac{\sigma_1}{2.6\sigma_3+54} < 1$  and  $\frac{\sigma_1}{2.6\sigma_3+34} > 1$  then minor dilation will occur as shown in Figure 7.8:

$$OS_{HFh} = (0.0187\varepsilon_{vol_h} + 0.0522) \times 100 \quad (7.5)$$

$$OS_{SFh} = (-0.0043\varepsilon_{vol_s} + 0.0677) \times 100 \quad (7.6)$$

$$OSD = \text{Maximum } (OS) \quad (7.7)$$

where  $OS_{HFh}$  is the open stope hangingwall dilation in percentage for failure in compression;  $OS_{SFs}$  is the open stope sidewall dilation in percentage for failure in compression;  $OS_{HFh}$  is the open stope hangingwall dilation in percentage for failure in tension;  $OS_{SFh}$  is the open stope sidewall dilation in percentage for failure in tension;  $OS_{HFh}$  is the open stope hangingwall dilation in percentage for failure in normal open stope conditions;  $OS_{SFh}$  is the open stope sidewall dilation in percentage for failure in normal open stope conditions; and  $OSD$ , known as the Open Stope Dilation, is the maximum value for the respective  $OS$  value obtained.

Making use of the Graph shown in Figure 7.8, the relation between open stope hangingwall and sidewall failure and ultimately dilution can be determined. This is done by plotting the obtained  $\sigma_1$  and  $\sigma_3$  median results for each separate case study on Figure 7.8 and reading off the Graph if there will be expected hangingwall dilution, sidewall dilution or minor dilution. Thus for sidewall dilution, Equations (7.3) will be used. For hangingwall dilution, Equations (7.4) will be used. For minor dilution Equations (7.5) and (7.6) will be used. After calculating the expected dilution using the relevant equations, only the maximum calculated dilution (*OSD*) value is used for the open stope being evaluated.

## **7.7 Applying the *Dilution Stress-Strain Index (DSSI)* design criterion to Mining Site Two**

As shown above in Section 7.6, the DSSI criterion has proved very satisfactory in its application to Target Mine, which was the primary purpose. However, to prove the design method in a wider context, it was decided to apply it to open stoping in a completely different geological environment. Thus, an open stoping mine in an ancient metamorphic environment was chosen, in contrast with the sedimentary geology in Target Mine. A generalized overview will be given of the second mining site used for the application of the Dilution Stress-Strain Index (DSSI) design criterion. Owing to the sensitive nature of the dilution data used for the analyses, the mining company wishes the name of the mine to remain confidential, and therefore the mine will be referred to as Mining Site Two.

### **7.7.1 Mining Environment at Mining Site Two**

Mining Site Two is situated in the Murchison Greenstone Belt in South Africa on the Antimony Line, which is an accumulation of ancient lavas and sediments as shown in Figure 7.13 (Poujol et al., 1996). The mineralized ore occurs as discontinuous lenses in siliceous carbonates and siliceous chlorites. The ore zones are bounded by Talc schist on both the hangingwall and footwall in an asymmetric manner as shown in Figure 7.16 and 7.17.

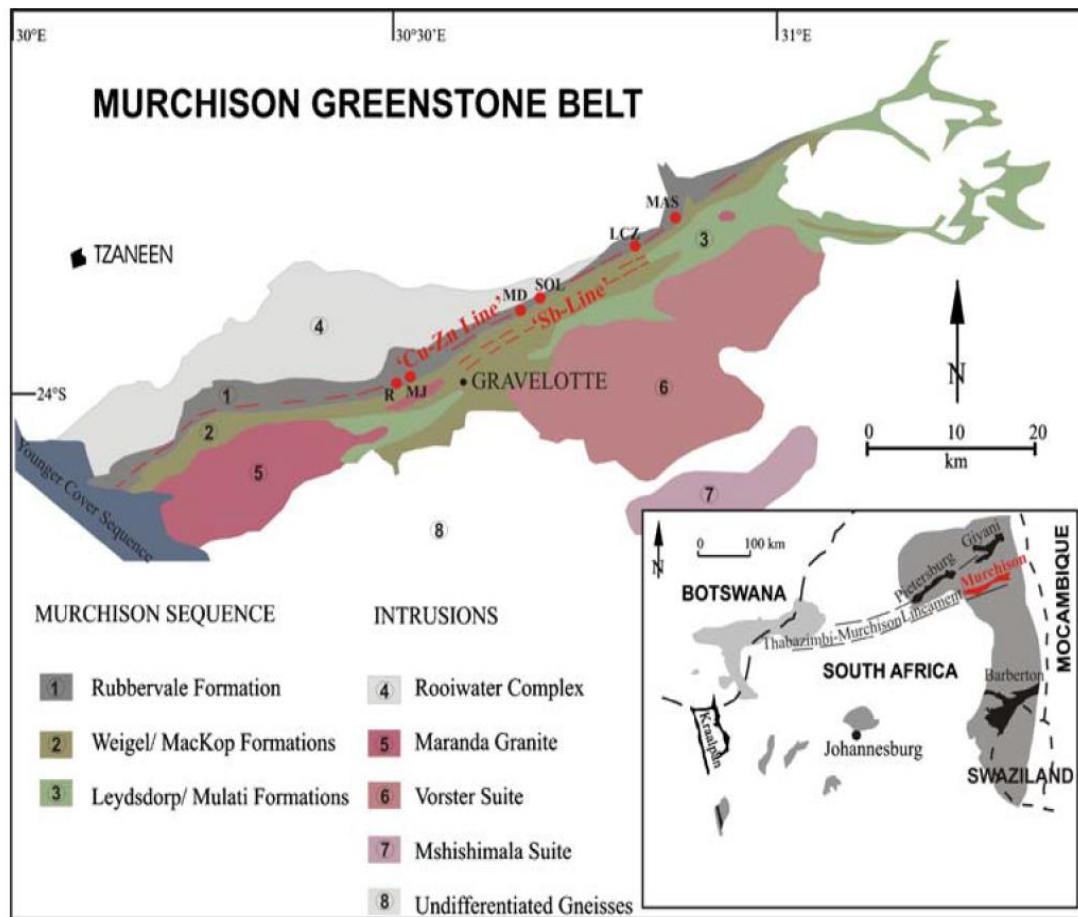


Figure 7.13 Plan view of the generalised geology of the Murchison greenstone belt showing the various stratigraphic units (modified from Poujol et al., 1996)

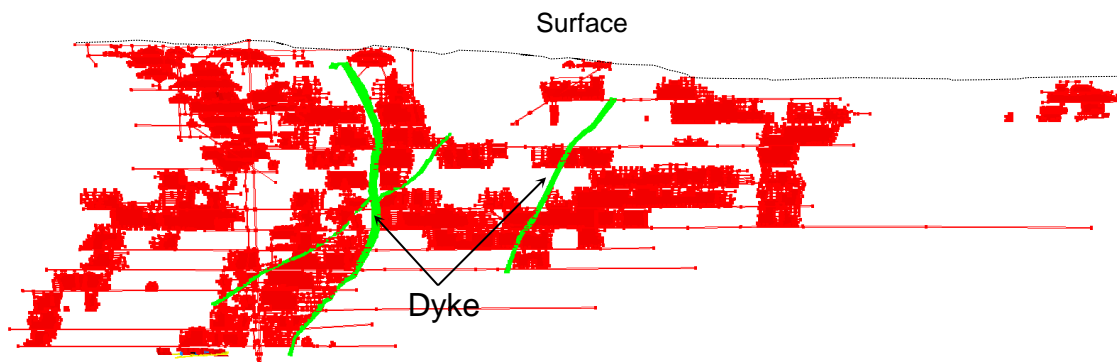


Figure 7.14 Section view of DXF file opened in Map3D looking north showing the orebody structure and orientation at Mining Site Two

### **7.7.2 Geological setting at Mining Site Two**

The mining depths are between shallow mining, meaning less than 1000m, and intermediate depth mining of up to 1100m, with open stopes, which were mined up to surface at some places as shown in Figure 7.14. The strikes of the orebodies are east-northeast and west-southwest. The orebodies are generally steeply dipping and plunge to the north or south at angles up to 65° as shown in Figure 7.16 and 7.17. The orebodies mined are disjointed and lenticular in shape and vary in thickness from 2m to 25m. They are located in massive quartz carbonated rock, which is competent, but subsequent shearing has altered the ore zone in some places from quartz carbonate to talc carbonate schist. In areas where the orebody is in contact with the talc carbonate schist, scaling of the open stope hangingwall and footwall takes place, resulting in excessive dilution on Mining Site Two.

The country rock consists of chlorite schist with varying amounts of quartz and carbonate. The country rock is fairly competent and most of the main development is located in this zone, as shown in Figures 7.16 and 7.17. The orebodies are en échelon structures located as multiple orebodies in some cases on Mining Site Two as shown in Figures 7.16 and 7.17. The Northern Freestate orebody is located further north of the Southern Antimony hosting reefs as shown in Figure 7.17.

Excavations situated at the intermediate mining depth are renowned for the intense buckling of sidewalls when orientated on strike, due to the high vertical stress and the anisotropic strength of the country rock, as shown in Figure 7.15. The Sheared Quartz Chlorite Schist and Sheared Quartz Carbonate Schist are brittle and severely vertically foliated. The behaviour of the schistose material is extremely sensitive to the direction of loading on Mining Site Two.

The uniaxial compressive strength for Sheared Quartz Carbonate Schist varies greatly between the extreme cases of loading perpendicular or parallel to the schistosity. The uniaxial compressive strength perpendicular to the foliation was between 142MPa and 177MPa. Parallel to the foliation it was found that the

uniaxial compressive stress was significantly lower at 22MPa to 27MPa. Open stopes situated in the talc schist zones experience excessive dilution over time on Mining Site Two.



Figure 7.15 Photo showing the intense buckling of the sidewalls of strike orientated development at Mining Site Two

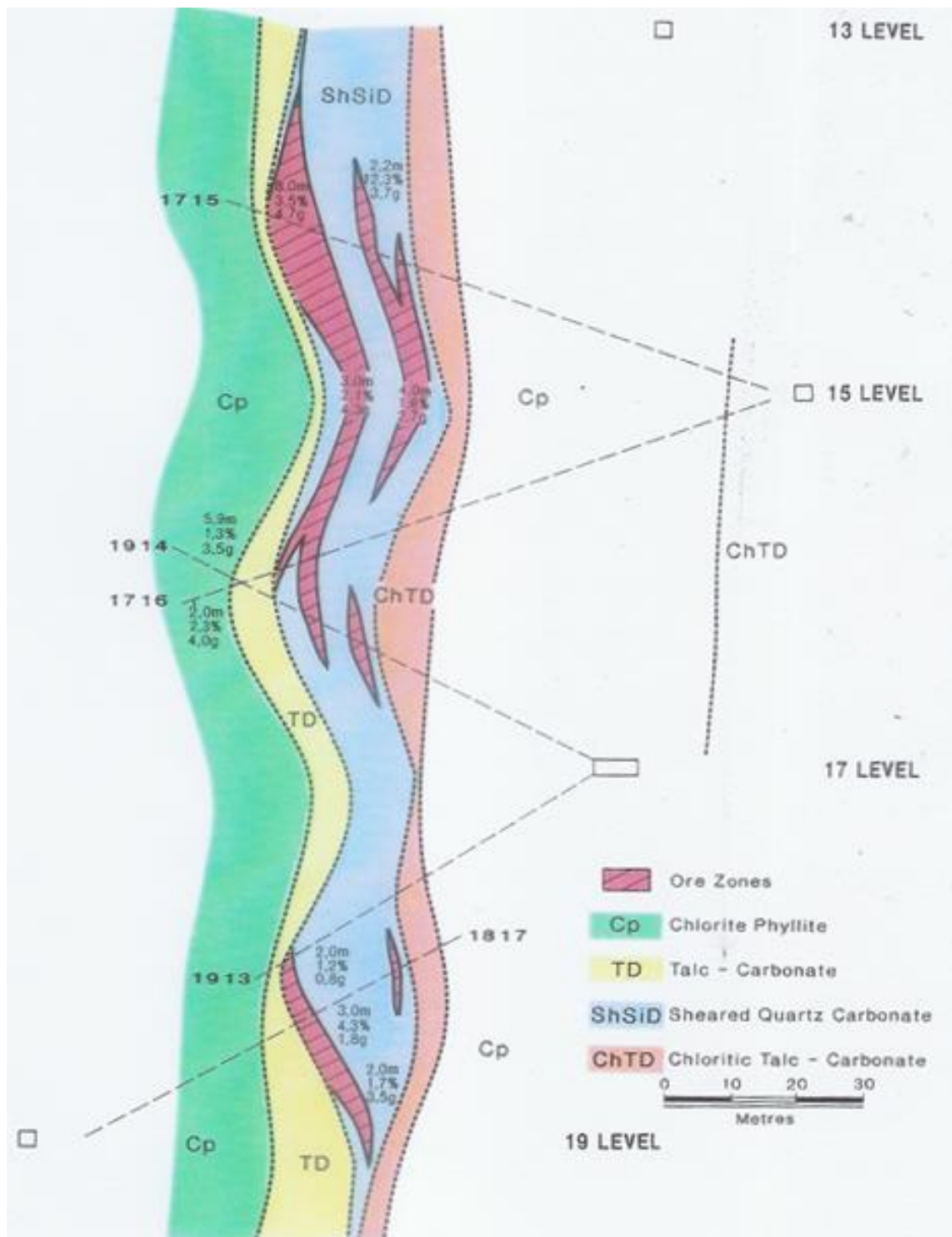


Figure 7.16 Cross sectional view looking east showing the orebody structure and orientation at Mining Site Two



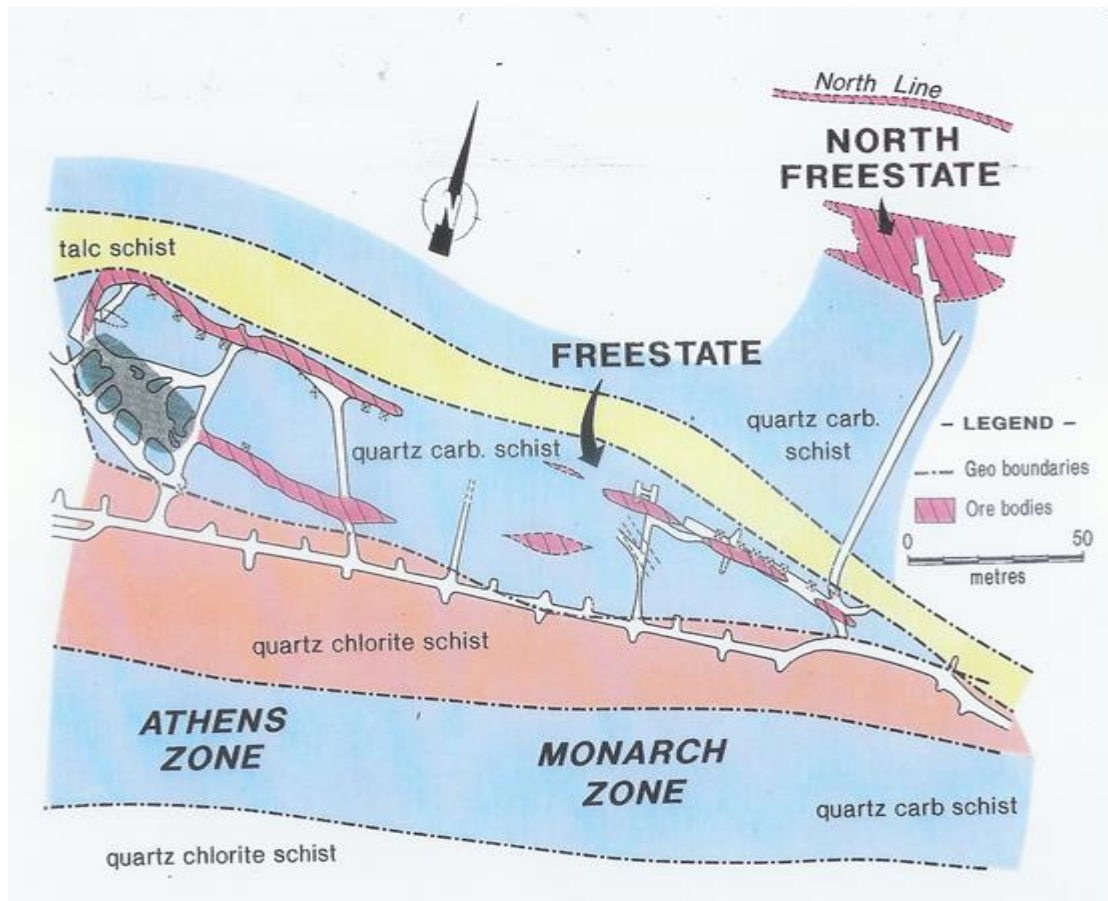


Figure 7.17 Plan view showing the orebody structure and orientation at Mining Site Two

The general mining method at this site is sublevel open stoping, with occasional long hole retreat mining where orebody widths are greater than 10m. This long hole retreat mining method is similar to the mining method practised on Target Mine, the difference being that the hangingwall and footwall are bounded by waste rock. On Mining Site Two the accepted percentage dilution is 15%, which is different to Target Mine where a cut-off of 10% is used. Thus, major dilution for these analyses will be all stopes where the percentage dilution is  $> 15\%$  and minor dilution will be for stopes where the percentage dilution is  $< 15\%$ .

### 7.7.3 Analyses and results of Mining Site Two when applying the Dilution Stress-Strain Index

For these analyses it was found that only two of the open stopes at Mining Site Two had sufficient data, meaning planned volume extractions and actual measured stope dimensions, to illustrate the ease of applying the Dilution Stress-Strain Index to other mines different from Target Mine, as shown in



Figure 7.18. The actual stope dimensions after mining were not determined by CMS, but measured by the mine using normal surveying equipment as shown in Figure 7.20. The accuracy of these surveyed dimensions is questionable. These open stopes are situated at a depth of approximately 1000m below surface on 31 level and 29 level and in a completely different geological environment from Target Mine. Applying the same methodology as discussed in section 7.5, Map3D was used to simulate these open stopes by placing gridlines on the boundary of the open stope hangingwall and footwall at each mining step as shown in Figure 7.19. The mining steps are illustrated in different colours in the model and were simulated as per mine planning for this stope during the time of extraction, as shown in Figure 7.19.

The following input parameters were used for Map3D:

Young's modulus	: 60000 MPa
Poisson's ratio	: 0.25
Density	: 2790 kg/m <sup>3</sup>
k-ratio	: 0.87

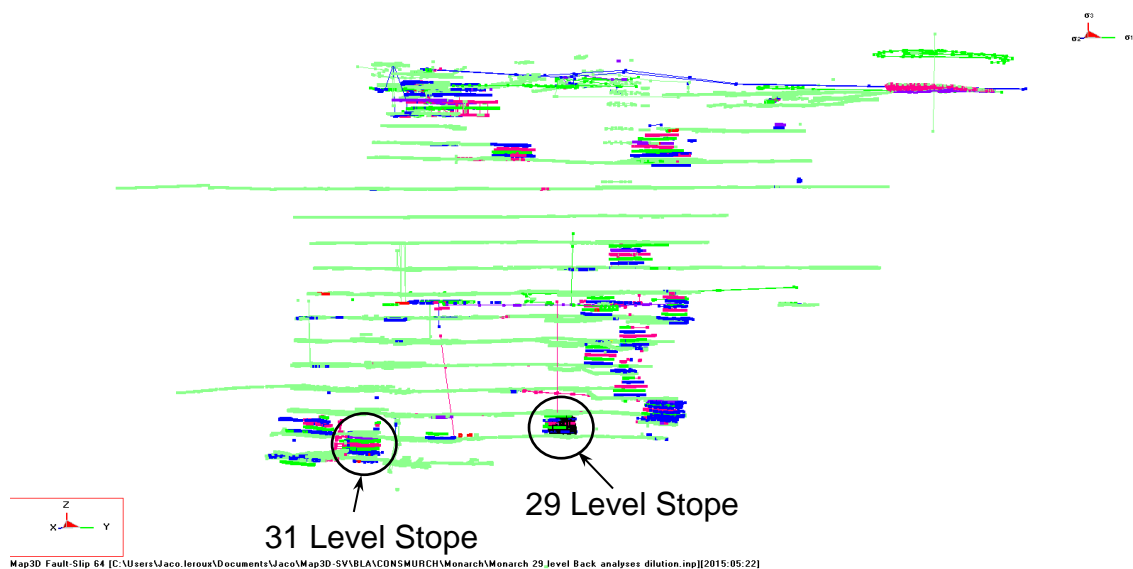


Figure 7.18 Section view looking north showing the open stopes selected for back analyses on Mining Site Two

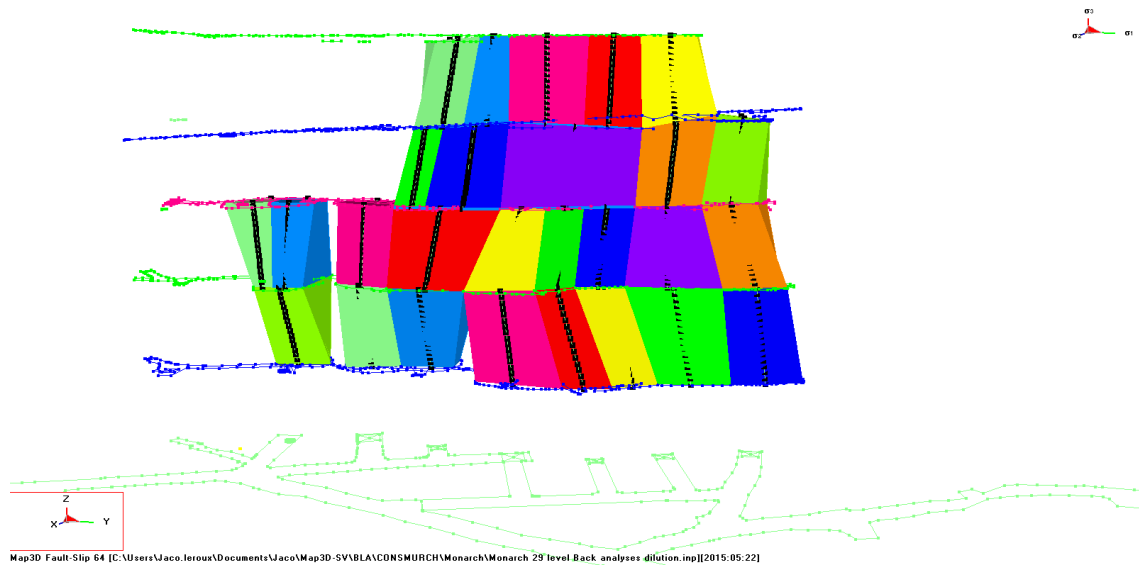


Figure 7.19 Map3D section view of model setup for 29 Level Stope at Mining Site Two

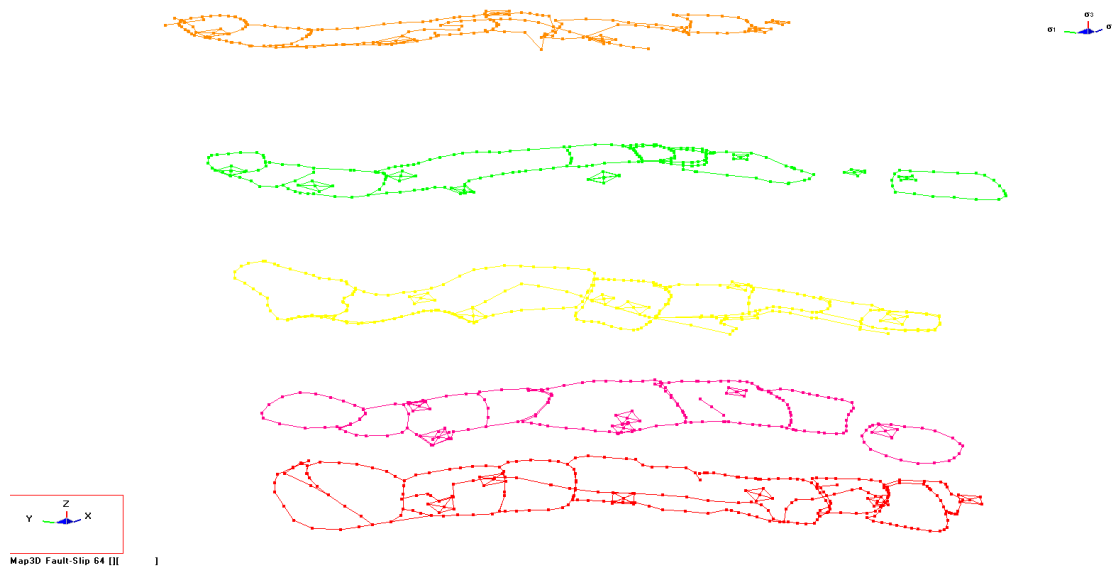


Figure 7.20 Section view of DXF file opened in Map3D showing survey measurements for 29 Level Stope at Mining Site Two

It was found that failures in these open stopes at Mining Site Two were restricted to hangingwall and footwall failure only. The median major principal stress  $\sigma_1$ , median minor principal stress  $\sigma_3$ , median mean stress in MPa and median volumetric strain in millistrains for the different open stope mining steps were obtained. When plotting these results for mean stress in MPa versus volumetric strain in millistrains for failure in the hangingwall and footwall resulting in more than fifteen percent dilution in open stopes on Mining Site

Two, it was found that this is true if  $\sigma_m > 12\text{MPa}$ ;  $\varepsilon_{vol} > 0,3 \times 10^{-3}$ , as shown in Figure 7.21.

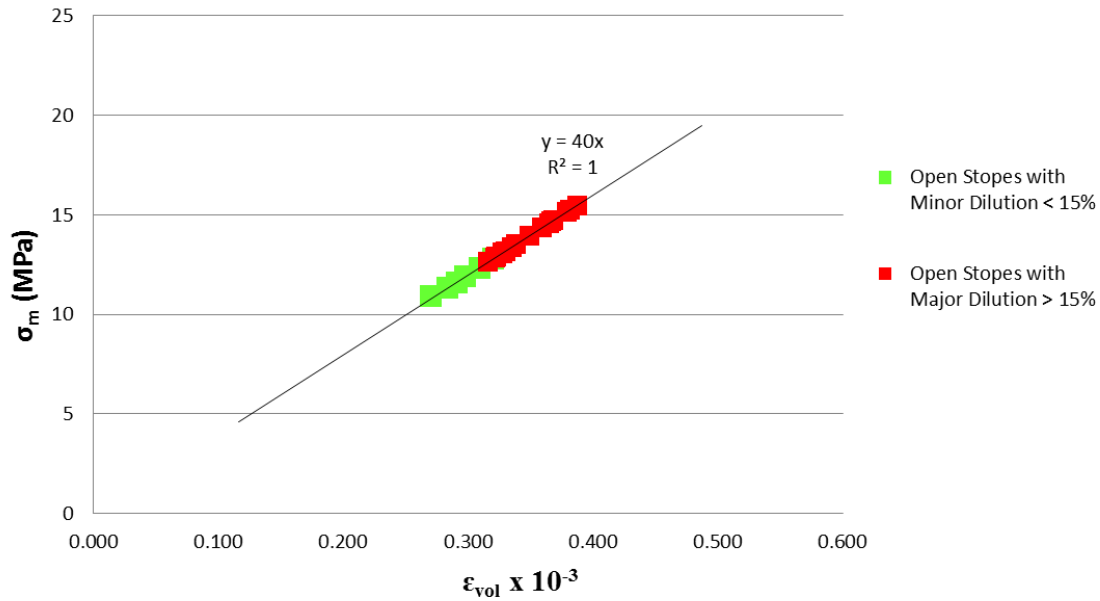


Figure 7.21 Graph showing the relation between mean stress and volumetric strain for open stopes with major and minor dilution for Mining Site Two

For failure of the hangingwall and footwall, the following equation is proposed for Mining Site Two, with  $\varepsilon_{vol}$  in millistrains:

$$DSSI = \left( \frac{MEDIAN(\sigma_m)}{q \varepsilon_{vol}} \right) > 1$$

$$DSSI = \left( \frac{MEDIAN(\sigma_m)}{40 \varepsilon_{vol}} \right) > 1 \quad (7.8)$$

Note that the  $q$ -value for Mining Site Two is different from that for Target Mine. This is due to the difference in Young's modulus of 60000 MPa and Poisson's ratio of 0.25 used during the numerical analyses. Figure 7.22 below indicates the predicted failure zones around the open stope in light grey, when the design criterion was applied to Mining Site Two. The predicted failure extent corresponded very well with the actual observed failure in the hangingwall and footwall, as shown by the survey measurements of the open stope plotted in red on Figure 7.22. The results for other mining steps are shown in Appendix G.



Figure 7.22 Plan view of the application of the DSSI Design criterion to Mining Site Two at step 1

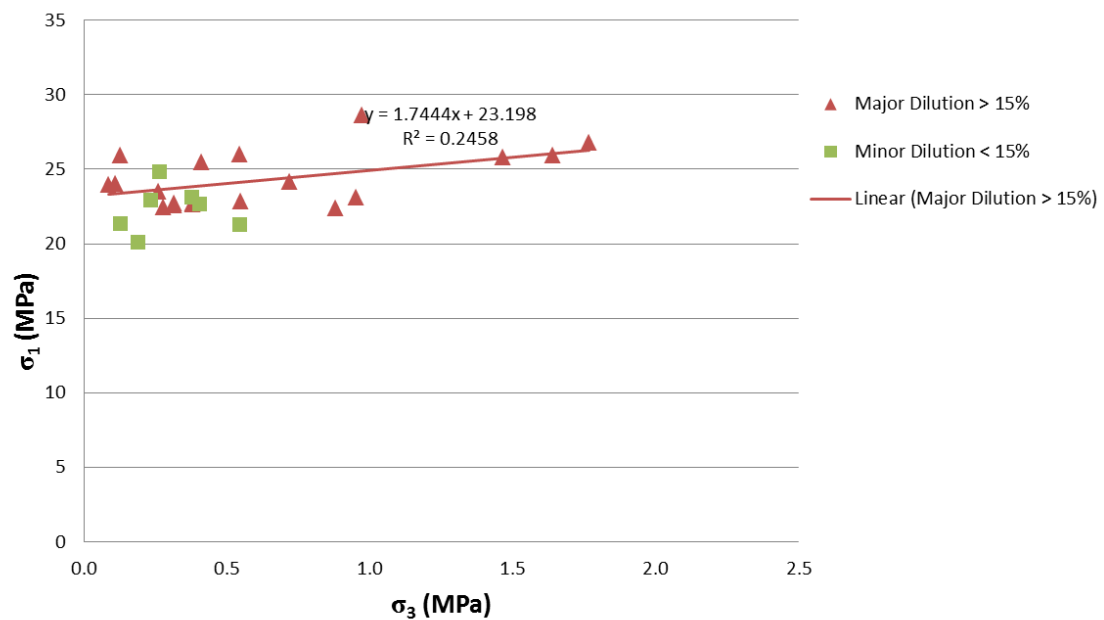


Figure 7.23 Graph showing the relation between open stope hangingwall failure to determine the failure mode at Mining Site Two

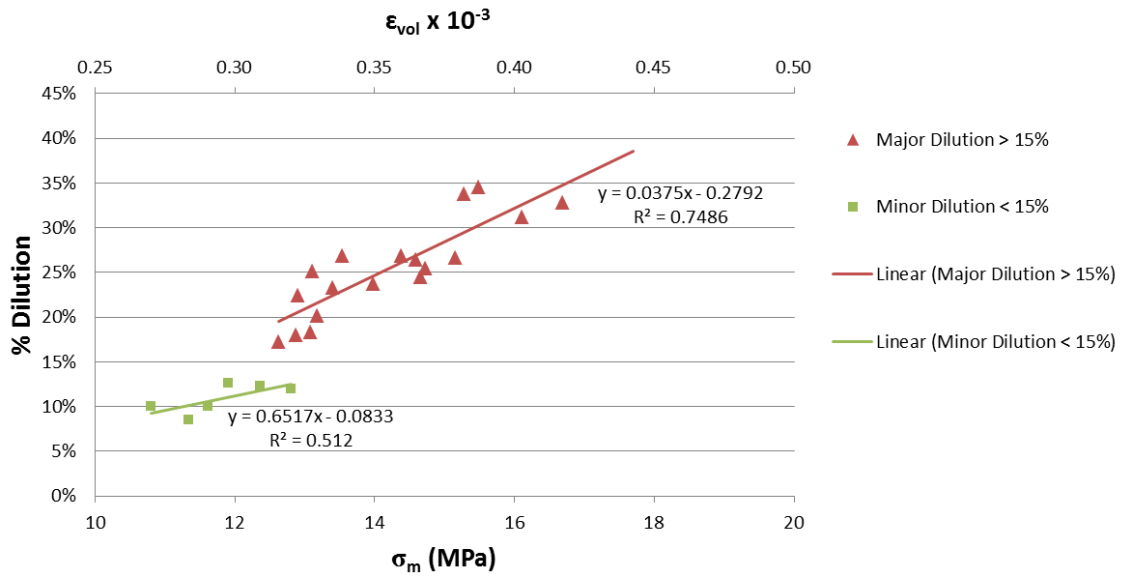


Figure 7.24 Graph showing the relations between median mean stress, volumetric strain and dilution at Mining Site Two

In Figure 7.23, the failure limit was found to be where  $\sigma_1 = 1.7\sigma_3 + 23.2$  for open stopes with minor dilution. From the graph in Figure 7.24 the percentage overbreak and in turn, the percentage dilution for open stopes at Mining Site Two, could be determined, and the following equations are proposed for Mining Site Two:

If  $\frac{\sigma_1}{1.7\sigma_3 + 23.2} > 1$  then major hangingwall and footwall dilution will occur:

$$OS_{HF} = (0.0375\varepsilon_{vol_h} - 0.2792) \times 100 \quad (7.9)$$

If  $\frac{\sigma_1}{1.7\sigma_3 + 23.2} < 1$  then minor hangingwall dilution will occur:

$$OS_{HF} = (0.6517\varepsilon_{vol_h} - 0.0833) \times 100 \quad (7.10)$$

where  $OS_{HF}$  is the open stope hangingwall dilution in percentage.

## **7.8 Comparing Calculated Open Stope Dilution to other Empirical Methods**

A comparison of the results predicted using the DSSI criterion with the percentage dilution predicted using the modified stability diagram (Potvin, 1988) as shown in Figure 5.3, and the site-specific average expected dilution as shown in Figure 5.4 (Pakalnis et al, 1995), is shown in Table 7.1. A 5% standard deviation between the actual and obtained results was used, highlighted in green if less and red if more. The comprehensive results are shown in Appendix D. Both the Potvin (1988) modified stability diagram and the hydraulic radius method (Pakalnis et al, 1995) tend to overestimate the amount of dilution expected. As shown in Table 7.1, the Open Stope Dilution (*OSD*) method using the DSSI criterion yields very reliable results. The effect of standing time after the open stope was blasted and time delay before being CMS can account for the difference in dilution experienced in case studies 4, 5, 6 and 7.

After the commencement of application of the DSSI design criterion in 2011 on Target Mine, a significant reduction in dilution was recorded, as shown in Figure 7.25. Being able to predict dilution very accurately in open stopes, these open stopes could be re-designed to “fail” to the desired final open stope shape. The DSSI design criterion has clearly influenced the sustainability and economics from 2011 at Target Mine, as shown in Figure 7.26. The resulting enormous financial benefit at Target mine has been quantified, as described in Section 4, and this has proved the value of the design approach using the new DSSI criterion. There is also no reason why the design approach could not have the same impact on any other mining operation, as shown in the application on Mining Site Two. In the current economic environment, this could determine the difference between continuing or closing a mining operation.

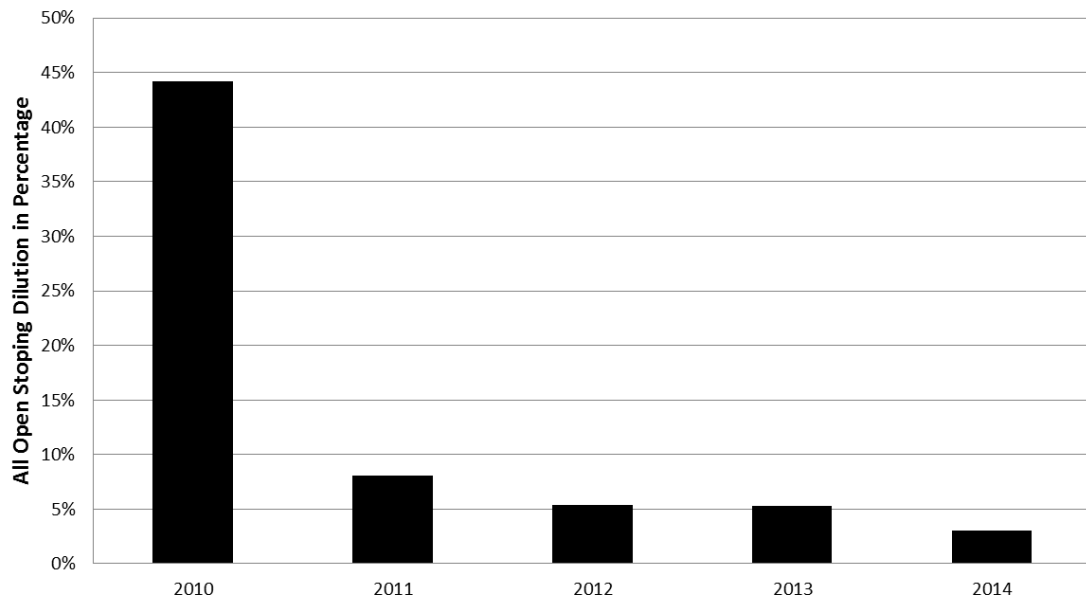


Figure 7.25 Graph showing total dilution for open stopping per year on Target Mine

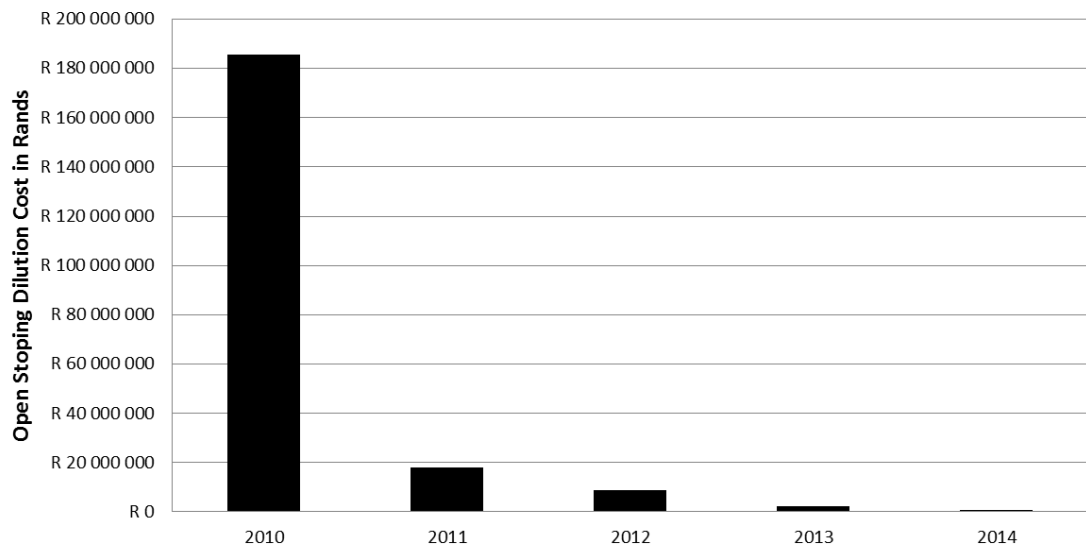


Figure 7.26 Graph showing total cost for dilution and mechanized equipment damage in open stopping per year on Target Mine

**Table 7.1 Calculated percentage dilution using the modified stability number method after Potvin (1988), the hydraulic radius method after Pakalnis et al (1995) and the newly developed Open Slope Dilution Method**

	% Dilution	Majority of Dilution is from	% Dilution Potvin (1988)	% Dilution Amended Pakalnis et al (1995)	% Dilution OSD	% Difference between actual and Potvin (1988)	% Difference between actual and Amended Pakalnis et al (1995)	% Difference between actual and OSD
Case Study 1	32.9	Hangingwall	32.0	28.9	26.8	-0.9	-4.0	-6.1
Case Study 2	32.0	Hangingwall	19.0	24.3	12.0	-13.0	-7.7	-20.0
Case Study 3	39.7	Hangingwall	40.0	24.3	35.4	0.3	-15.4	-4.3
Case Study 4	44.1	Sidewall	40.0	55.3	41.0	-4.1	11.2	-3.1
Case Study 5	22.9	Sidewall	40.0	34.3	41.2	17.1	11.4	18.3
Case Study 6	73.8	Sidewall	70.0	60.7	41.0	-3.8	-13.1	-32.8
Case Study 7	70.2	Sidewall	70.0	58.7	41.8	-0.2	-11.5	-28.4
Case Study 8	16.4	Hangingwall	28.0	2.8	24.5	11.6	-13.6	8.1
Case Study 9	16.1	Hangingwall	45.0	34.5	18.2	28.9	18.4	2.1
Case Study 10	13.4	Hangingwall	15.0	12.9	23.3	1.6	-0.5	9.9
Case Study 11	26.1	Hangingwall	54.0	44.7	30.4	27.9	18.6	4.3
Case Study 12	20.7	Hangingwall	41.0	28.2	24.9	20.3	7.5	4.2
Case Study 13	18.9	Hangingwall	20.0	14.8	13.9	1.1	-4.1	-5.0
Case Study 14	61.5	Sidewall	40.0	36.5	41.1	-21.5	-25.0	-20.4
Case Study 15	8.1	Sidewall	9.0	3.1	6.7	0.9	-5.0	-1.4
Case Study 16	6.2	Hangingwall	12.0	9.9	6.5	5.8	3.7	0.3
Case Study 17	6.9	Sidewall	8.0	15.0	6.6	1.1	8.1	-0.3
Case Study 18	4.3	Sidewall	14.0	8.8	6.1	9.7	4.5	1.8
Case Study 19	4.6	Sidewall	12.0	8.6	6.3	7.4	4.0	1.7
Case Study 20	4.3	Hangingwall	9.0	4.9	6.8	4.7	0.6	2.5
Case Study 21	8.8	Sidewall	8.0	1.4	6.5	-0.8	-7.4	-2.3
Case Study 22	7.8	Hangingwall	29.0	8.6	7.0	21.2	0.8	-0.8
<b>Standard Deviation</b>			<b>18.7</b>	<b>18.3</b>	<b>13.8</b>			



## 8 CONCLUSIONS AND RECOMMENDATIONS

The objective of the research described in this thesis was to develop a method of calculating dilution in open stopes, and to be able to determine the expected failure depth into the hangingwall and sidewalls of open stopes with a high degree of certainty. With the existing methods available, this could not be done with certainty, and a very large database is required (Capes, 2009). Rockmass properties, rockmass classifications, blast design, blast techniques, the stress strain environment and hydraulic radius all have some effect on, or play a part in the evaluation of dilution. It was found however, that the stress strain environment actually plays a significant role in the behaviour of open stopes at depth. Twenty-eight case studies at Target mine were selected with sufficient information for the research.

The research in this thesis:

- Defined dilution in the open stope mining environment;
- Discussed the Cavity Monitoring System (CMS) and its use;
- Discussed measurement of actual dilution;
- Discussed the modelling of dilution;
- Defined hydraulic radius;
- Discussed the site used for data collection with reference to its geological setting and its orebody;
- Defined rock mass classification and its use in determining dilution;
- Determined and defined the existing techniques for predicting overbreak and dilution in open stope mining, making use of the modified stability number,  $N'$ , and equivalent linear overbreak slough (ELOS);
- Discussed the different failure criteria and parameters that could be used to determine the expected failure around open stopes;
- Discussed the effect of blasting vibrations on open stopes and dilution;
- Discussed the current planning process and developed a new thinking framework;

- Determined the cost implication of dilution in open stopes as discussed in section 4.4;
- Determined the modes and mechanisms of dilution in open stopes;
- Determined a new open stope design methodology as described in section 7.5;
- Developed a method of calculating the expected overbreak into the hangingwall and sidewalls of open stopes, making use of the DSSI design criterion, as discussed in section 7.4;
- Developed a method of calculating the expected dilution with accuracy making use of OSD;

The results of predictions of the extents of failure into the open stope hangingwall or sidewalls, based on application of the DSSI design criterion, allow open stopes to be redesigned to “fail” up to the required stope shape and thus to reduce dilution.

## **8.1 Knowledge Contributions**

This research contributed to the understanding of rock behaviour in an open stope environment and the design methodology that should be followed to reduce dilution. It was also illustrated that, even with very limited information available, as shown on Mining Site Two, relatively accurate results could be obtained for the open stope design. This is significant, since when a new mine is designed there is very limited information available, and the expected dilution is normally assumed to be within a certain value, which could completely underestimate or overestimate dilution. The design approach that has resulted from the research allows failure depth into the hangingwall and sidewalls of open stopes to be predicted accurately, and dilution can be calculated for use in mine design with a high degree of certainty. The applicability of the DSSI design criterion to alternative mining operations was demonstrated as described in section 7.7.4. Proof of the value of the new DSSI design criterion is the significant impact that it has had on the

economics of Target Mine, and that it has ensured the future of mining at this operation.

## **8.2 Limitations**

Making use of the modified stability graph method after Potvin (1988) and ELOS after Capes (2009) requires a significantly large database of open stopes, and does not cater for small mines such as Target Mine where the total number of open stopes mined was only forty-four. This limited the potential for successful application of these methods at Target mine.

The effect of time on the stability of the open stopes was not taken into account due to limited available information. The effect of standing time after the open stope was blasted, and the time delay before being backfilled could account for the difference between predicted and actual dilution experienced in case studies 4, 5, 6 and 7. These stopes stood for a significant time before they were measured using CMS.

## **8.3 Future Work**

It is recommended that future research should include further applications of the DSSI criterion to a wider range of open stopes in a variety of geological environments. It is also clear that time is an important factor regarding failure around open stopes. This is a topic associated with the research described in this thesis – little research has been carried out into time-dependent behaviour of rocks and rock masses, which therefore is an important topic for future research.

## REFERENCES

- Addis, M.A. and Wu, B. (1993) The role of the intermediate principal stress in wellbore stability studies: evidence from hollow cylinder tests. *Int J Rock Mech Min Sci Geomech Abstr* 30(7),pp.1027–1030.
- Ambraseys, N.R. and Hendron, A.J. (1968) Dynamic behavior of rock masses in *Rock Mechanics in Engineering Practices*, London, Wiley.
- Banerjee, P.K. and Butterfield, R. (1981) *Boundary Element Methods in Engineering Science*. McGraw-Hill Book Company (UK) Limited, London.
- Barton N., Lien I.R and Lunde J. (1974) Engineering classification of rock masses for design of tunnel support, *Rock Mechanics* vol 6,pp.186-236.
- Bieniawski, Z.T. (1989) *Engineering Rock Mass Classification*, John Wiley and Sons, New York.
- Brace, W.F. and Kohlstedt, D.L. (1980) Limits on lithospheric stress imposed by laboratory experiments. *J Geophys Res* 85,pp.6248–6252.
- Brady, B.H.G., and Brown, E.T. (1985) *Rock mechanics for underground mining*. London: Allen and Unwin.
- Brady, T., Pakalnis, R., and Clark, L. (2005) *Design in Weak Rock Masses*, Nevada Underground Mining Operations, SME-AGM, Salt Lake City,pp.9.
- Brown, E.T. (2000) Block Caving Geomechanics, *The International Caving Study I 1997 – 2000*, JKMRRC Monograph Series in Mining and Mineral Processing 3,pp.127-138.
- Bureau of Indian Standard. (1973) Criteria for safety and design of structures subjected to underground blast, *ISI Bull IS-6922*.
- Capes, G.W. (2009) Open stope hangingwall design based on general and detailed data collection in rock masses with unfavorable hangingwall conditions, PhD. Thesis, University of Saskatchewan.
- Chang, C. and Haimson, B.C. (2000) True triaxial strength and deformability of the German Continental Deep Drilling Program (KTB) deep hole amphibolite. *J Geophys Res* 105(B8):18999–19013.
- Chapman, K. (1969) *The geology of Loraine Gold Mines, Limited*, A brief description, Unpublished company report, Anglovaal Limited, Johannesburg.
- Clark, L. and Pakalnis, R., (1997) An empirical design approach for estimating unplanned dilution from open stope hanging walls and footwalls, *CIM AGM*, Calgary, Alberta.
- Clark, L., (1998) *Minimizing Dilution in Open Stope Mining with a Focus on Open Stope Design and Narrow Vein Longhole Blasting*. M.Sc. Thesis, University of British Columbia.
- CMRI (1993) *Vibration standards*, Central Mining Research Institute, Dhanbad.

- COP Target Mine (2014) Mandatory code of practice to combat rockfall and rockburst accidents in tabular metalliferous mines and to combat rockmass failure accidents in massive mining operations.
- Coggan, J.S., Pine, R. J., Stead, D. and Rance, M.J. (2003) Numerical modelling of brittle rock failure using a combined finite-discrete element approach: implications for rock engineering design, ISRM 2003–Technology roadmap for rock mechanics, South African Institute of Mining and Metallurgy, pp.211-218.
- Coulomb, C.A. (1776) Sur une application des regles maximis et minimis a quelques problems de statique, relatives a l'architecture. Acad Sci Paris Mem Math Phys 7, pp.343–382.
- Davies, B., Farmer, I.W. and Attewell, P.B. (1964) Ground vibrations from shallow sub-surface blasts, The Engineer, London, pp.553-559.
- Diederichs, M.S. (2003) Rock fracture and collapse under low confinement conditions. Rock Mechanics and Rock Engineering 36 (5), pp.339-381.
- Drucker, D.C. and Prager, W. (1952) Soil mechanics and plastic analysis or limit design. Q Appl Mech 10(2), pp.157–164.
- Duvall, W.I. and Petkof, B. (1959) Spherical propagation of explosion generated strain pulses in rock, USBM Report of Investigation 5483, pp.21.
- Dyson, F. (2009) New York Times 30 April 2009.
- Elbrond, J. (1994) Economic effects of ore losses and rock dilution, Elsevier Science, Amsterdam, CIM Bull 87(978), pp.131-134.
- Esterhuizen, G.S. and Streuders, S.B. (1998) Rockfall hazard evaluation using probabilistic keyblock analysis, The Journal of The South African Institute of Mining and Metallurgy, Vol 98, pp.59-64.
- Ewy, R.T. (1998) Wellbore stability predictions using a modified Lade criterion. In: Proceedings of Eurock 98: SPE/ISRM Rock Mechanics in Petroleum Engineering, vol 1, pp.247–254.
- Frimmel, H.E., Groves, D.I., Kirk, J., Ruiz, J., Chesley, J. and Minter, W.E.L. (2005) The formation and preservation of the Witwatersrand goldfields, the largest gold province in the world In: Hedenquist JW, Thompson JFH, Goldfarb RJ, Richards JP (eds) Economic Geology One Hundreth Anniversary Volume. Society of Economic Geologists, Littleton, pp.769-797.
- Fujii, Y., Kiyama, T., Ishijima, Y. and Kodama, J. (1998) Examination of a rock failure criterion based on circumferential tensile strain, Pure and applied Geophysics, Vol. 152, pp.551-577.
- Ghosh, A. and Daemen, J.K. (1983) A simple new blast vibration predictor, Proceedings of the 24th US Symposium on Rock Mechanics, College Station, Texas, pp.151-161.
- Goodman, R.E. and Shi, G. (1985) Block Theory and its Application to Rock Engineering. Prentice Hall.
- Griffith, A.A. (1920) The phenomena of rupture and flow in solids. Philos Trans R Soc Lond Ser A Math Phys Sci 221(587), pp.163–198.

- Griffith, A.A. (1924) The theory of rupture. In: Biezeno CB, Burgers JM (eds) Proceedings of the First International Congress for Applied Mechanics. Delft. J. Waltman Jr, Delft, pp.55–63.
- Haimson, B. (1978) The hydrofracturing stress measurement technique- method and recent field results. *Int J Rock Mech Min Sci Geomech Abstr* 15, pp.167–178.
- Harmony Annual Report, 2009
- Harmony Annual Report, 2010
- Harmony Financial Report, 2013
- Harrison, A.G. (2010) Mineral Resource Statement, Target Mine 2010.
- Henning, J.G. and Mitri, H.S. (2007) Numerical modelling of ore dilution in blasthole stoping, *International Journal of Rock Mechanics & Mining Sciences*, vol 44. 5, pp.692-703.
- Heyman, J. (1972) Coulomb's Memoir on Statics. Cambridge University Press, London.
- Hoek, E. (1968) Brittle failure of rock. In: Stagg KG, Zienkiewicz OC (eds) *Rock mechanics in engineering practice*. Wiley, New York, pp.99–124.
- Hoek, E. and Brown, E.T. (1980) *Underground excavations in rock*. The Institution of Mining and Metallurgy, London.
- Hoek, E. (1983) Strength of jointed rock masses, 23rd Rankine Lecture. *Geotechnique* 33(3), pp.187–223.
- Hoek, E. and Brown, E.T. (1988) The Hoek–Brown failure criterion—a 1988 update. In: Curran J (ed) *Proceedings of the 15th Canadian Rock Mechanics Symposium*. University of Toronto, Toronto, pp.31–38.
- Hoek, E., Wood, D., Shah, S. (1992) A modified Hoek–Brown criterion for jointed rock masses. In: Hudson JA (ed) *Rock characterization: ISRM Symposium, Eurock '92*, Chester, UK. Thomas Telford, London, pp.209–213.
- Hoek, E., Kaiser, P.K. and Bawden, W.F. (1995) *Support of Underground Excavations in Hard Rock*, A.A.Balkema, Rotterdam, Brookfield.
- Hoek, E. and Brown, E.T. (1997) Practical estimates of rock mass strength. *Int J Rock Mech Min Sci Geomech Abstr* 34, pp.1165–1186.
- Hoek, E., Carranza-Torres, C.T. and Corkum, B. (2002) Hoek–Brown failure criterion—2002 edition. In: Hammah R, Bawden W, Curran J, Telesnicki M (eds) *Proceedings of the Fifth North American Rock Mechanics Symposium (NARMS-TAC)*, University of Toronto Press, Toronto, pp.267–273.
- Hoek, E. and Marinos, P. (2007) A brief history of the development of the Hoek-Brown failure criterion. *Soils and Rocks*, No. 2., November 2007.
- Hutchinson, D.J. and Diederichs, M.S. (1996) *Cablebolting in underground mines*. BiTech Publishers Ltd. pp.265-273.
- Jaeger, J.C. and Cook, N.G.W. (1979) *Fundamentals of rock mechanics*. Chapman and Hall Ltd., London
- Kaiser, P.K., Diederichs, M.S., Martin, D., Sharpe, J. and Steiner, W. (2000) *Underground works in hard rock tunnelling and mining*. In: *GeoEng2000, Proceedings of the International Conference on Geotechnical and Geological*

- Engineering, Melbourne, Technomic Publishing Company, Lancaster, pp.841–926.
- Kaiser, P.K. and Kim, B-H. (2008) Rock Mechanics Advances for Underground Construction in Civil Engineering and Mining, Keynote lecture, Korea Rock Mechanics Symposium, Seoul, pp.1-16.
- Kamali, M. and Ataei, M. (2010) Prediction of blast induced ground vibrations in Karoun III power plant and dam: a neural network, The Journal of The Southern African Institute of Mining and Metallurgy, vol 110, pp.481-490.
- Kim, M.K. and Lade, P.V. (1984) Modelling rock strength in three dimensions. Int J Rock Mech Min Sci Geomech Abstr 21, pp.21–33.
- Kwaśniewski, M. and Takahashi, M. (2010) Strain-based failure for rocks: State of the art and recent advances, Rock Mechanics in Civil and Environmental Engineering – Zhao, Labiouse, Dudt & Mathier (eds), pp.45-56.
- Langefors, U. and Kihlstrom, B. (1963) The modern technique of rock blasting, New York, Wiley.
- Laubscher, D.H. (1990) A geomechanics classification system for the rating of rock mass in mine design, JI S. Afr. Inst. Min. Metall., Vol 90, No 10, pp.257-273.
- Laubscher, D.H. and Taylor, H.W. (1976) The importance of geomechanics classification of jointed rock masses in mining operations, Proc. Symp. Exploration for Rock Engineering, Johannesburg, Vol 1, A.A. Balkema, pp.119-128.
- Le Roux, P.J. (2004) Project on Rock Mass Properties for the Free State, Mechanical Properties of Rocks and Rock Masses, University of the Witwatersrand, South Africa.
- Louchnikov, V. (2011) Simple calibration of the extension strain criterion for its use in numerical modelling, Australian Centre for Geomechanics, Perth, ISBN 978-0-9806154-6-3, pp.85-96
- Mathews, K.E., Hoek, E., Wyllie, D.C. and Stewards, S.B.V. (1981) Prediction of stable excavations for mining at depth below 1000 metres in hard rock, CANMET report DSS Serial No. OSQ80-00081, DSS File No. 17SQ.23440-0-9020. Ottawa: Department of Energy, Mines and Resources.
- McGarr, A. and Gay, N.C. (1978) State of stress in the earth's crust. Annu Rev Earth Planet Sci 6, pp.405-436.
- Melkounian, N., Priest, S.D and Hunt, S.P. (2009) Further development of the three-dimensional Hoek–Brown yield criterion. Rock Mech Rock Eng 42(6), pp.835–847.
- Meyer, J.P. and Labuz, J.F. (2012) Linear failure criteria with three principal stresses. Int J Rock Mech Min Sci, Submitted
- Miller, F., Potvin, Y. and Jacob, D. (1993) Laser measurement of open stope dilation, International Journal of Rock Mechanics & Mining Sciences Abstracts, vol 30, 2 April 1993, pp.A134.
- Mogi, K. (1971) Fracture and flow of rocks under high triaxial compression. J Geophys Res 76(5), pp.1255–1269.

- Mohr, O. (1900) Welche Umstände bedingen die Elastizitätsgrenze und den Bruch eines Materials? *Zeit des Ver Deut Ing* 44,pp.1524–1530.
- Mult, H.C., Dalheimer, M. and Wagner, M. (2008) Conversion of Geological Data into Mining Data for Ore Deposits, *Economic Evaluations in Exploration*, Chapter 4, pp.55-58.
- Nadai, A. (1950) *Theory of flow and fracture of solids*, vol 1. McGraw- Hill, New York.
- Pakalnis, R.C., Poulin, R. and Hadjigeorgiou, J. (1995) Quantifying the cost of dilution in underground mines, *Mining Engineering*,pp.1136-1141.
- Pal Roy, P. (1993) Putting ground vibration predictors into practice, *Colliery Guardian*, vol 241, 1993,pp.63-67.
- Pan, X.D and Hudson, J.A. (1988) A simplified three-dimensional Hoek–Brown yield criterion. In: Romana M (ed) *Rock mechanics and power plants*, A.A. Balkema, Rotterdam,pp.95–103.
- Paul, B. (1968) Generalized pyramidal fracture and yield criteria. *Int J Solids Struct* 4,pp.175–196.
- Pine, R.J., Coggan, J.S., Flynn, Z.N. and Elmo, D. (2006) The development of a new numerical modelling approach for naturally fractured rock masses, *Rock Mechanics and Rock Engineering*, 2006.
- Pine, R.J., Owen, D.R.J., Coggan, J.S. and Rance, J.M. (2007) A new discrete fracture modelling approach for rock masses, *Géotechnique* vol 57, 9, 2007,pp.757-766.
- Potvin, Y. (1988) *Empirical open stope design in Canada*, PhD Thesis, University of British Columbia, Vancouver, 1988.
- Poujol, M., Robb, L.J., Respaut, J.P. and Anhaeusser, C.R. (1996). Ga greenstone belt formation in the northeastern Kaapvaal Craton: implications for the origin of the Witwatersrand Basin. *Economic Geology*, Vol.91,pp.1455-1461.
- Priest, S.D. (2005) Determination of shear strength and three-dimensional yield strength for the Hoek–Brown criterion. *Rock Mech Rock Eng* 38(4),pp.299–327.
- Priest, S.D. (2009) Comparisons between selected three-dimensional yield criteria applied to rock. *Rock Mech Rock Eng* 43,pp.379–389.
- Rocscience (2015) <http://www.Rocscience.com/products/overview> (Dips, Unwedge and Phase2)
- Ryder, J.A. and Jager, A.J. (2002) *A Textbook on Rock Mechanics for Tabular Hard Rock Mines*, The Safety in Mines Research Advisory Committee (SIMRAC), Johannesburg, 2002.
- Sakurai, S. (1981) Direct strain evaluation technique in construction of underground openings. *Proceedings of the 22nd U.S. Symposium on Rock Mechanics*, June 29 – July 2, 1981, Cambridge, MA,pp.278–282.
- Sakurai, S., Kawashima, I. and Otani, T. (1995) A criterion for assessing the stability of tunnels, In L. Ribeiro e Sousa & N.F. Grossmann (eds), *Safety and Environmental Issues in Rock Engineering; Proc. ISRM Intern. Symp. EUROCK '93*, Lisbon, 21–24 June 1993, Rotterdam: Vol. 2,pp.969-973.
- Scholz, C.H. (1990) *The mechanics of earthquake and faulting*. Cambridge University Press, New York.



- Shekhovtsov, V.S. (1994) Procedure for determining ore loss and dilution in working deposits with a complicated structure, *Journal of Mining Science*, vol 29. 6, Nov. 1994.
- Stacey, T.R. (1981) A simple extension strain criterion for fracture of brittle rock. *Int. J. Rock Mech. Min. Sci. & Geomech. Abstr.* Vol. 18, pp.469–474.
- Stacey, T.R. (2001) Best practice rock engineering handbook for “other” mines, *Safety in Mines Research Advisory Committee*, December 2001.
- Sutton, D. (1998) Use of the Modified Stability Graph to Predict Stope Instability and Dilution at Rabbit Lake Mine, Saskatchewan, University of Saskatchewan Design Project, Canada.
- Takahashi, M. and Koide, H. (1989) Effect of intermediate principal stress on strength and deformation behavior of sedimentary rocks at the depth shallower than 2000 m. In: Maury V, Fourmaintraux D (eds) *Rock at Great Depth*, vol 1. Balkema, Rotterdam, pp.19–26.
- Ulusay, R. and Hudson, J.A. (2007) The complete ISRM suggested methods for rock characterization, testing and monitoring: 1974–2006, pp.971-1010.
- Van Alphen, P.P. (1995) Pillar extraction, Blast Consult, Loraine Gold Mine - 1#, Internal report.
- Vernik, L. and Zoback, M.D. (1992) Estimation of maximum horizontal principal stress magnitude from stress-induced well bore breakouts in the Cajon Pass scientific research borehole. *J Geophys Res* 97, pp.5109–5119.
- Vista Local paper (1997) Goldfields, Free State, Special Anniversary Edition, April 1997.
- Watermeyer, G.A. and Hoffenberg, S.N. (1932) *Witwatersrand Mining Practice*, pp.393-403.
- Wang, J., Milne, D., Yao, M. and Allen, G. (2002) Factors Influencing Open Stope Dilution at Hudson Bay Mining and Smelting, North American Rock Mechanics Symposium (NARMS) Proceedings, 2002, Toronto, pp.195-202
- Wang, J., (2004) Influence of stress, undercutting, blasting, and time on open stope stability and dilution. PhD. Thesis, University of Saskatchewan.
- Wiebols, G.A. and Cook, N.G.W. (1968) An energy criterion for the strength of rock in polyaxial compression. *Int. J. Rock Mech. Min. Sci. Geomech. Abstr.*, 5, pp.529–549.
- Wiles, T.D. (2006) Course Notes, Mine Modelling Report.
- Wiles, T.D. (2007) Evidence Based Model Calibration for Reliable Predictions, Australian Centre for Geomechanics, Deep Mining, pp.3-20.
- Wiles, T.D. (2006) MAP3D User's Manual, Mine Modelling Report.
- Yu, M-H. (2002) Advances in strength theories for materials under complex stress state in the 20th century. *App Mech Rev* 55(3), pp.169–218.
- Zhang, L. (2008) A generalized three-dimensional Hoek–Brown strength criterion. *Rock Mech Rock Eng* 41(6), pp.893–915.
- Zhang, L. and Zhu, H. (2007) Three-dimensional Hoek–Brown strength criterion for rocks. *J Geotech Geoenviron ASCE* 133(9), pp.1128–1135.

Zhou-quan, L., Xiao-ming, L., Bao, Z., Hao, L. and Chang, L. (2008) Cavity 3D modelling and correlative techniques based on cavity monitoring, Journal of Central South University of Technology, vol 15. 5.

## BIBLIOGRAPHY

- Akai, K. and Mori, H. (1970) Ein versuch uber Bruchmecanismus von Sandstein under mehrachsigen Spannungzustand. In: ISRM Proc. 2nd Int Congress Rock Mech. ISRM, Belgrade, vol 2, Paper 3–30.
- Al-Ajmi, A.M. and Zimmerman, R.W. (2005) Relation between the Mogi and the Coulomb failure criteria. *Int J Rock Mech Min Sci* 42(3),pp.431–439.
- Al-Ajmi, A.M. and Zimmerman, R.W. (2006) Stability analysis of vertical boreholes using the Mogi–Coulomb failure criterion. *Int J Rock Mech Min Sci* 43(8),pp.1200–1211.
- Amborzi, T. and Turk, G. (2003) Prediction of subsidence due to underground mining by artificial neural networks, *Computers & Geosciences*, vol 29,pp.627–637.
- Andreev, G.E. (1995) *Brittle Failure of Rock Material*. Balkema, Rotterdam.
- Aubertin, M., Li, L., Simon, R. and Khalfi, S. (1999) Formulation and application of a short-term strength criterion for isotropic rocks. *Can Geotech J* 36(5),pp.947–960.
- Aubertin, M. and Simon, R. (1996) A multiaxial failure criterion that combines two quadratic surfaces. In: Aubertin M, Hassani F, Mitri H (eds) *Rock mechanics—tools and techniques. Proceedings of second North American rock mechanical symposium*, Montreal. A.A. Balkema, Rotterdam,pp.1729–1736.
- Baecher, G.B., Lanney, N.A. and Einstein, H.H. (1978) Statistical Description of Rock Properties and Sampling. *Proceedings of the 18th U.S. Symposium on Rock Mechanics*, 5C1-8.
- Barton, N.R. (1972) A model study of rock-joint deformation, *Int. J. Rock Mech. Min. Sci.*, Vol 9,pp.579-602.
- Basu, D. and Sen, M. (2005) Blast induced ground vibration norms—A critical review, *National Seminar on Policies, Statutes & Legislation in Mines*.
- Beer, G. and Meek, J.L. (1982) Design curves for roofs and hangingwalls in bedded rock based on voussoir beam and plate solutions. *Trans. Instn. Min. Metall.* Vol 91,pp.A18-22.
- Beer, G., Meek, J. and Cowling, R. (1983) Prediction of the behaviour of shale hangingwalls of deep underground excavations. *Proc. Fifth ISRM Congress*, Melbourne Australia, 1983,pp.D45-51.
- Benz, T. and Schwab, R. (2008) A quantitative comparison of six rock failure criteria. *Int J Rock Mech Min Sci* 45(7),pp.1176–1186.
- Benz, T., Schwab, R., Kauther, R.A. and Vermeer, P.A. (2008) A Hoek–Brown criterion with intrinsic material strength factorization. *Int J Rock Mech Min Sci* 45(2),pp.210–222.
- Brace, W.F. (1964) Brittle fracture of rocks. In: *State of stress in the Earth's crust: Proceedings of the International Conference*. American Elsevier Publishing Co., New York,pp.110–178.

- Brady, B.H.G., and Brown, E.T., (1993) Rock mechanics for underground mining, 2nd edition. Chapman & Hall.
- Brady, T., Pakalnis, R., and Clark, L. (2005) Design in Weak Rock Masses, Nevada Underground Mining Operations, SME-AGM, Salt Lake City, pp.9.
- Brook, N. (1985) The Equivalent Core Diameter Method of Size and Shape Correction in Point Load Testing, *Int. J. Rock Mech. Min. Sci. & Geomech. Abstr.* vol 22. 2,pp.61-70.
- Brown, E.T. (2008) Estimating the mechanical properties of rock masses. In: Potvin Y, Carter J, Dyskin A, Jeffrey R (eds) *Proceedings of the 1st Southern Hemisphere International Rock Mechanics Symposium*, Australian Centre for Geomechanics, Perth,pp.3–22.
- Buck, S.G. and Minter, W.E.L. (1985) Placer formation by fluvial degradation of an alluvial fan sequence: The Proterozoic Carbon Leader Placer, Witwatersrand Supergroup, South Africa, *Journal Geological Society London*,vol 142,pp.757-764.
- Budavari, S. (1983) Rock Mechanics in Mining Practice, The South African Institute of Mining and Metallurgy,pp.33–131.
- Butler, R.F. (1992) Paleomagnetism: magnetic domains to geologic terranes (Chapter 6), Blackwell Science.
- Cai, J.G. and Zhao, J. (1997) Use of neural networks in rock tunneling. *Proceedings of Computing Methods and Advances in Geomechanics*, IACMAG, China,pp.613–618.
- Callow, M.J.W. and Myers, R.E. (1986) A tectono-stratigraphic model for the development of the Welkom Fan Placer deposits: Orange Free State Goldfields, Geological Society South Africa,pp.455-460.
- Capes, G.W. and Milne, D.A. (2008) Compilation of Dilution Graph Data for Open Stope Hangingwall Design, SHIRMS, Perth, Western Australia,pp.149-162.
- Chang, C. and Haimson, B.C. (2007) Effect of fluid pressure on rock compressive failure in a nearly impermeable crystalline rock: implication on mechanism of borehole breakouts. *Eng Geol* 89,pp.230–242.
- Chang, C. and Haimson, B.C. (2005) Nondilatant deformation and failure mechanism in two Long Valley Caldera rocks under true triaxial compression. *Int J Rock Mech Min Sci Geomech Abstr* 42,pp.402–414.
- Chakraborty, A.K., Guha, P., Chattopadhyay, B., Pal, S. and Das, J. A (2004) Fusion Neural Network for Estimation of Blasting Vibration, N.R. Pal et al. (eds.): *ICONIP 2004*, LNCS 3316, pp. 008.1013, Springer-Verlag Berlin Heidelberg.
- Cividini, A. (1993) Constitutive behaviour and numerical modelling. In: Hudson J (ed) *Comprehensive rock engineering*, vol 1. Pergamon Press, Oxford,pp.395–426.
- Colmenares, L.B. and Zoback, M.D. (2001) Statistical evaluation of six rock failure criteria constrained by polyaxial test data. In: Elsworth D, Tinucci JP, Heasley KA (eds) *Rock mechanics in the national interest. Proceedings of 38th US Rock Mechanics Symposium*, Washington DC. A.A. Balkema,pp.1251–1258.

- Colmenares, L.B. and Zoback, M.D. (2002) A statistical evaluation of intact rock failure criteria constrained by polyaxial test data for five different rocks. *Int J Rock Mech Min Sci* 39(6),pp.695–729.
- COMRO (1988) An Industry Guide to Methods Of Ameliorating the Hazards of Rockfalls and Rockbursts,pp.12-16, 33.
- Crandell, F.J. (1949) Ground vibration due to blasting and its effect upon structures, *Journal of Boston Society of Civil Engineers*.
- Cundall, P.A. and Damjanac, B. (2009) A comprehensive 3D model for rock slopes based on micromechanics, Universidad de Los Andes, Santiago, Chile.
- Das, S.K. and Basudhar, P.K. (2009) Comparison of intact rock failure criteria using various statistical methods. *Acta Geotech* 4:pp.223–231.
- Dehler, W. and Labuz, J.F. (2007) Stress path testing of an anisotropic sandstone. *J Geotech Eng* 133(1),pp.116–119.
- Deng, J., Yue, Z.Q., Tham, L.G. and Zhu, H.H. (2003) Pillar design by combining finite element methods, neural networks and reliability: a case study of the Feng
- Huangshan copper mine, China, *International Journal of Rock Mechanics & Mining Sciences*, vol 40,pp.585-599.
- Dershowitz, W. (1985) Rock Joint Systems. Ph.D. Thesis, Massachusetts Institute of Technology, Cambridge, MA.
- Diederichs, M.S., and Kaiser, P.K. (1999) Tensile strength and abutment relaxation as failure control mechanisms in underground excavations. *Int. Rock Mech. Min. Sci.* 36(1999),pp.69-96.
- Diederichs, M.S., and Kaiser, P.K. (1999) Stability of large excavations in laminated hard rock masses: the voussoir analogue revisited. *Int. Journal of Rock Mech. And Mining Sci.* 36(1999),pp.97-117.
- Diederichs, M.S. (2007) Mechanistic interpretation and practical application of damage and spalling prediction criteria for deep tunnelling. *Can Geotech J* 44(9),pp.1082–1116.
- Diederichs, M.S., Kaiser, P.K. and Eberhardt, E. (2004) Damage initiation and propagation in hard rock tunnelling and the influence of nearface stress rotation. *Int J Rock Mech Min Sci* 41(5),pp.785–812.
- Diederichs, M.S., Carvalho, J.L. and Carter, T.G. (2007) A modified approach for prediction of strength and post yield behaviour for high GSI rock masses in strong, brittle ground. , 1st Canada-U.S. Rock Mech. Symp.,pp.249-257.
- Diering, J.A.C and Stacey, T.R. (1987) Three-dimensional Stress Analysis: a Practical Planning Tool for Mining Problems, APCOM 87, Proceedings of the Twentieth International Symposium on the Application of Computers and Mathematics in the Mineral Industries, vol 1: Mining, Johannesburg, SAIMM,pp.33- 42.
- Duvall, W.I. and Fogelson, D.E. (1962) Review of criteria for estimating damage to residences from blasting vibration, US Bureau of Mines R.I. 5968.

- Dysart, P.S. and Pulli, J.J. (1990) Regional seismic event classification at the noress array: seismological measurements and the use of trained neural networks, *Bull Seismol Soc Am*, vol 80, pp.1910-1933.
- Eberhardt, E., Stead, D., Coggan, J. S. and Willenberg, H. (2003) Hybrid finite-/discrete-element modelling of progressive failure in massive rock slopes, *ISRM 2003-Technology roadmap for rock mechanics*, South African Institute of Mining and Metallurgy, pp.275-279.
- Evans, W.H., (1941) The strength of underground strata. *Trans. Instn. Min. Metall.*, 50, pp. 475-532.
- Ewy, R.T. (1999) Wellbore-stability predictions by use of a modified Lade criterion. *SPE Drill Compl* 14(2), pp.85–91.
- Finnie, G.J. (1999) Using neural networks to discriminate between genuine and spurious seismic events in mines, *Pure Appl Geophys*, vol 154, pp.41-56.
- Fisher, R. (1953) Dispersion on a sphere. *Proc. Royal Society London*, A217, pp.295-305.
- Ghazvinian, A.H., Fathi, A. and Moradian, Z.A. (2008) Failure behavior of marlstone under triaxial compression. *Int J Rock Mech Min Sci* 45(5), pp.807–814.
- Gupta, R.N., Pal Roy, P. and Singh, B. (1988) Prediction peak particle velocity and air pressure generated by buried explosion, *International Journal of mining and geological engineering*.
- Hadjigeorgiou, J., Ghanmi, A. and Paraszczak, J. (1998) 3-D numerical modelling of radial-axial rock splitting. *Geotech Geol Eng* 16(1), pp.45–57.
- Haimson, B. and Chang, C. (2000) A new true triaxial cell for testing mechanical properties of rock, and its use to determine rock strength and deformability of Westerly granite. *Int J Rock Mech Min Sci* 37(1–2), pp.285–296.
- Haimson, B. and Chang, C. (2002) True triaxial strength of the KTB amphibolite under borehole wall conditions and its use to estimate the maximum horizontal in situ stress. *J Geophys Res* 107, pp.2257–2271.
- Haimson, B. (2006) True triaxial stresses and the brittle fracture of rock. *Pure Appl Geophys* 163(5–6), pp.1101–1130.
- Haimson, B., Lin, W., Oku, H., Hung, J-H. and Song, S-R. (2010) Integrating borehole breakout dimensions, strength criteria, and leak-off test results to constrain the state of stress across the Chelungpu Fault, Taiwan. *Tectonophysics* 482, pp.65–72.
- Haimson, B. and Rudnicki, J.W. (2010) The effect of the intermediate principal stress on fault creation and angle in siltstone. *J Struct Geol* 32, pp.1701–1711.
- Hajiabdolmajid, V., Kaiser, P.K. and Martin, C.D. (2002) Modelling brittle failure of rock, *International Journal of Rock Mechanics & Mining Sciences*, vol 39, pp.731-741.
- Hajiabdolmajid, V., Kaiser, P.K. and Martin, C.D. (2003) Mobilised strength components in brittle failure of rock, *Géotechnique* 53, vol 3, pp.327-336.
- Handin, J., Heard, H.C. and Magouirk, J.N. (1967) Effect of the intermediate principal stress on the failure of limestone, dolomite, and glass at different temperature and strain rate. *J Geophys Res* 72, pp.611–640.

- Holmberg, R. and Persson, P.A. (1979) Design of tunnel perimeter blasthole patterns to prevent rock damage, Proc. IMM Tunnelling '79 Conference, London, pp.280-283.
- International Society for Rock Mechanics (1975) Commission on Terminology, Symbols and Graphic Representation, Terminology (English, French, German), Final Draft: July 1975.
- Jager, A.J. and Ryder, J.A. (1999) A Handbook on Rock Engineering Practice for Tabular Hard Rock Mines, The Safety in Mines Research Advisory Committee (SIMRAC), Johannesburg.
- Jimeno, L.C., Jimeno, L.E. and Carcedo, A.J.F. (1995) Drilling and Blasting of Rocks, A.A. Balkema, Rotterdam, pp.333-365.
- Kabongo, K.K. (1997) Explosives and Blasting Technology, Department of Mining Engineering, Course MINN 564, University of the Witwatersrand.
- Kahraiman, A. (2001) Analysis of Ground Vibrations Caused by Bench Blasting at Can Open-pit Lignite Mine in Turkey, Environmental Geology, vol 41, pp.653-661.
- Kaiser, P.K. (2007) Rock mechanics challenges and opportunities in underground construction and mining, Keynote lecture, 1st Canada-U.S. Rock Mechanics Symposium, pp.47.
- Kaiser, P.K. (2006) Tunnel stability in highly stressed, brittle ground - Rock mechanics considerations for Alpine tunneling, Geologie und Geotechnik der Basistunnels, Keynote lecture at GEAT'05 Symposium, Zürich, Switzerland, pp.183-201.
- Kaiser, P.K., McCreath, D.R. and Tannant, D.D. (1996) Canadian Rockburst Support Handbook, Mining Research Directorate, Sudbury, Canada, 314 p.; also Drift support in burst-prone ground, CIM Bulletin, 89(998), pp.131-138.
- Kataka, M.O., Hildyard, M.W. and Sellers, E.J. (2003) Integration of Seismic Observations from Deep Level Gold Mines with Dynamic Numerical Modelling, ISRM 2003 – Technology Roadmap for Rock Mechanics, South African Institute of Mining and Metallurgy, pp.617-622.
- Khandelwal, M. and Singh, T.N. (2006) Prediction of blast induced ground vibrations and frequency in opencast mine: A neural network approach, Journal of Sound and Vibration, vol 289, pp.711-725.
- Khandelwal, M. and Singh, T.N. (2002) Prediction of waste dump stability by an intelligent approach, Proceedings of the national symposium on new equipment–new technology, management and safety, ENTMS, Bhubaneshwar, pp.38-45.
- Kimberley Working Group. (1998) Regional characteristics of the Kimberley succession with implications for enhanced exploitation and exploration, CSIR report.
- Kingsley, C.S. (1986) Stratigraphic Framework and model of sedimentation of the Eldorado sequence in the Welkom Goldfields, Geocongress, extended abstracts, Geological Society South Africa, pp.461-464.
- Labuz, J.F. and Bridell, J.M. (1993) Reducing frictional constraint in compression testing through lubrication. Int J Rock Mech Min Sci Geomech Abstr 30(4), pp.451–455.

- Lachenicht, R., Wiles, T. and van Aswegen, G. (2001) The Integration of Numerical Modelling with Seismic Monitoring through the MAP3Di Boundary Element Method: Part II Applications, Proc. of the Fifth International Symposium on Rockburst and Seismicity in Mines (RASiM5), Johannesburg, South Africa, pp.389-398.
- Lade, P.V. (1982) Three-parameter failure criterion for concrete. *J Eng Mech Div Am Soc Civ Eng* 108, pp.850–863.
- Lade, P.V. (1993) Rock strength criteria: the theories and the evidence. In: Hudson J, Brown ET (eds) *Comprehensive rock engineering*. Elsevier Inc, London, pp.225–284.
- Landolt-Börnstein (1982) Numerical data and functional relationships in science and technology. In: Angenheister G (ed) *Physical properties of rocks*. Springer, Berlin, pp.1b.
- Lade, P.V. (1977) Elasto-plastic stress–strain theory for cohesionless soils with curved yield surfaces. *Int J Solids Struct* 13: pp.1019–1035.
- Laubscher, D.H. (1993) Planning mass mining operations, *Comprehensive Rock Engineering: Principles, Practice and Projects*, ed J Hudson, Pergamon Press, Vol 2, pp.547-583.
- Laubscher, D.H. (1994) Cave mining – state of the art, *Jl S. Afr. Inst. Min. Metall.*, Vol 94, pp.279-293.
- Lawrence, S., Giles, C.L. and Tsoi, A.C. (1997) Lessons in Neural Network Training: Training may be harder than expected, *Proceedings of the Fourteenth National Conference on Artificial Intelligence, AAAI-97*, Menlo Park, California: AAAI Press, pp.540-545.
- Lee, H. and Haimson, B. (2011) True triaxial strength, deformability, and brittle failure of granodiorite from the San Andreas Fault Observatory at Depth. *Int J Rock Mech Min Sci* 48, pp.1199–1207.
- Li, L., Gamache, M. and Aubertin, M. (2000) Parameter determination for nonlinear stress criteria using simple regression model. *Can Geotech J* 37(6), pp.1332–1347.
- Lundborg, N. (1957) Keeping the lid on flyrock in open-pit blasting. *E/MJ*.
- Lubarda, V.A., Mastilovic, S. and Knap, J. (1996) Brittle–ductile transition in porous rocks by cap model. *J Eng Mech* 122(7), pp.633–642.
- Marinos, V., Marinos, P. and Hoek, E. (2005) The geological strength index: applications and limitations. *Bull Eng Geol Environ* 64(1), pp.55–65.
- MacDonald, P., Wiles, T. and Villeneuve, T. (1988) Rock Mechanics Aspects of Vertical Retreat Mining at 2000m Depth at Creighton Mine Canada, *Conference on Applied Rock Engineering*, Inst. Min. and Metallurgy, London, England, pp.151-157.
- Maity, D. and Saha, A. (2004) Damage assessment in structure from changes in static parameters using neural networks, *Sadhana*, vol 29, pp.315-327.
- Mariset, S.D., Wiles, T.D. and Martin, C.D. (1997) Energy Release Rate Study for Deep Level Mine Development at Creighton Mine, *Mine Modelling Report*.



- Martin, C.D., Kaiser, P.K. and McCreath, D.R. (1999) Hoek–Brown parameters for predicting the depth of brittle failure around tunnels. *Can Geotech J* 36(1),pp.136–151.
- Maulenkamp, F. and Grima, M.A. (1999) Application of neural networks for the prediction of the unconfined compressive strength (UCS) from Equotip Hardness, *International Journal of Rock Mechanics & Mining Sciences*, vol 36, 1999,pp.29-39.
- McCarthy, T.S. (2006) The Witwatersrand Supergroup, *The Geology of South Africa*, Geological Society of South Africa, 2006,pp.155-186.
- Miall, A.D. (1981) Alluvial sedimentary basins: Tectonic setting and basin architecture, *Sedimentation and tectonics in alluvial basins*, Geological Association of Canada special paper 23, 1981.
- Michelis, P. (1985) Polyaxial yielding of granular rock. *J Eng Mech* 111(8),pp.1049–1066.
- Michelis, P. (1987) True triaxial cyclic behavior of concrete and rock in compression. *Int J Plas* 3(2),pp.249–270.
- Mitchell, G.R., Gavine G.H. (2005) Motivation – Capital for further exploration at Target North, Internal Harmony report, unpublished, 2005,pp.35.
- Minter, W.E.L., Hill, W.C.N., Kidger, R.J., Kingsley, C.S. and Snowden, P.A. (1986) The Welkom Goldfield, *Mineral Deposits of Southern Africa*, Geological Society South Africa, 1986,pp.497-539.
- Mogi, K. (1967) Effect of the intermediate principal stress on rock failure. *J Geophys Res* 72(20),pp.5117–5131.
- Mogi K (1972) Effect of the triaxial stress system on fracture and flow of rocks. *Phys Earth Planet In* 5,pp.318–324.
- Mogi K (1974) On the pressure dependence of strength of rocks and the Coulomb fracture criterion. *Tectonophysics* 21,pp.273–285.
- Mogi K (2007) *Experimental rock mechanics*. Taylor & Francis Group, London.
- Mogilnicki, M.A. and Assibey-Bonsu, W. (1994) A case study of the impact of support and information effects of Resource/Reserve estimates to be used for medium term mine planning in the Witwatersrand type deposits, *Proceedings of the Conference on Mining Geostatistics*, 1994.
- Mohamed, M.T. (2009) Artificial neural network for prediction and control of blasting vibrations in Assiut (Egypt) limestone quarry, *International Journal of Rock Mechanics & Mining Sciences*, vol 46, 2009,pp.426-431.
- Monjezi, M. and Dehghani, H. (2008) Evaluation of effect of blasting pattern parameters on back break using neural networks, *International Journal of Rock Mechanics & Mining Sciences*, vol 45, 2008,pp.1446-1453.
- Monjezi, M., Singh, T.N., Khandelwal, M., Sinha, S., Singh, V. and Hosseini, I. (2006) Prediction and analysis of blast parameters using artificial neural network, *Noise Vibrations Worldwide*, vol 37, 2006,pp.8-16.
- Murrell, S.A.F. (1963) A criterion for brittle fracture of rocks and concrete under triaxial stress, and the effect of pore pressure on the criterion. In: Fairhurst C (ed)

- Proceedings of the 5th Symposium on Rock Mechanics. University of Minnesota, Minneapolis, pp.563–577.
- Musil, M. and Plesinger, A. (1996) Discrimination between local micro earthquakes and quarry blasts by multi-layer perceptions and Kohonen maps, *Bull Seismol Soc Am*, vol 86, 1996, pp.1077-1090.
- New, B.M. (1986) Ground vibration caused by civil engineering works, Transport and Road Research Laboratory, Research Report 53, 1986, pp.19.
- Northrop, W.D. (2003) A logical approach to the evaluation of a stacked multi-reef Witwatersrand gold deposit, *Application of Computers and Operations Research in the Minerals Industries*, South African Institute of Mining and Metallurgy, 2003, pp.19-25.
- Northrop, W.D. (2003) Target Division Resources – A Review for CPR Purposes, Sep. 2003.
- Napier, J.A.L. (1987) The Application of Excess Shear Stress to the Design of Mine Layouts. *Journal of the South African Institute of Mining and Metallurgy*, vol 87, no 12, 1987, pp.397– 405.
- Olivier, H.J. (1965) The tectonics of the upper division of the Witwatersrand System in the Loraine area of the Orange Free State Goldfields, *Transactions Geological Society South Africa*, 1965, pp.143-175.
- Oku, H., Haimson, B. and Song, S.R. (2007) True triaxial strength and deformability of the siltstone overlying the Chelungpu fault (Chi–Chi earthquake), Taiwan. *Geophys Res Lett* 34:L09306.
- Oliver, P., Wiles, T. and MacDonald, P. (1987) Rockburst Control Measures at INCO's Creighton Mine, *Proc. 6th Conf. Ground Control in Mining*, West Virginia, USA, 1987.
- Oxford English Dictionary. Second Edition 1989.
- Pakalnis, R.T., Miller, H.D.S. and Madill, T. (1985) Open stope design - a dilution approach, *Proc of the Symposium on Rock Mass Characterization*, Randburg, South Africa, 8 Nov. 1985, pp.93-98.
- Pande, G.N., Beer, G. and Williams, J.R. (1990) *Numerical Methods in Rock Mechanics*, John Wiley and Sons Ltd., 1990.
- Pariseau, W.G. (1972) Plasticity theory for anisotropic rocks and soils. In: Grey KE (ed) *Basic and applied rock mechanics. Proceedings of the tenth US Rock Mechanics Symposium*, NY SME/AIME, pp.267–295.
- Pariseau, W.G. (2007) Fitting failure criteria to laboratory strength tests. *Int J Rock Mech Min Sci* 44(4), pp.637–646.
- Paterson, M.S and Wong, T-f (2005) *Experimental rock deformation—the brittle field*, 2nd edn. Springer-Verlag, Berlin.
- Paul, B. (1961) Modification of the Coulomb–Mohr theory of fracture. *J Appl Mech* 28, pp.259–268.
- Paul, B. and Gangal, M. (1967) Initial and subsequent fracture curves for biaxial compression of brittle materials. In: Fairhurst C (ed) *Failure and breakage of rock*, *Proc 8th Symp Rock Mech*. University of Minnesota, MN, pp.113–141.

- Pincus, H. (2000) Closed-form/least-squares failure envelopes for rock strength. *Int J Rock Mech Min Sci* 37, pp.763–785.
- Prechelt, L. (1998) Early Stopping - but when? *Neural Networks: Tricks of the trade*, Springer Berlin/Heidelberg, vol 1524, 1998, pp.55-69.
- Priest, S.D. (2010) Comparisons between selected three-dimensional yield criteria applied to rock. *Rock Mech Rock Eng* 43(4), pp.379–389.
- Qiang, W., Siyuan, Y. and Jia, Y. (2008) The prediction of size-limited structures in a coal mine using Artificial Neural Networks, *International Journal of Rock Mechanics & Mining Sciences*, vol 45, 2008, pp.999-1006.
- Rudajev, V. and Ciz, R. (1999) Estimation of mining tremor occurrence by using neural networks, *Pure Appl Geophys*, vol 154, 1999, pp.57-72.
- Ryder, J.A. (1988) Excess Shear Stress in the Assessment of Geologically Hazardous Situations, *Journal of the South African Institute of Mining and Metallurgy*, vol 88. 1, 1988, pp.27–39.
- Sarle, W. (1995) Stopped Training and Other Remedies for Overfitting, *Proceedings of the 27th Symposium on the Interface of Computing Science and Statistics*, 1995, pp.352-360.
- Schwartz, A.E. (1964) Failure of rock in the triaxial shear test. In: Spokes EM, Christiansen CR (eds) *Proceedings of sixth US symposium on rock mechanics*. University of Missouri, Rolla, pp.109–151.
- Shield, R.T. (1955) On Coulomb's law of failure in soils. *J Mech Phys Sol* 4, pp.10–16.
- Singh, T.N. and Singh, V. (2005) An intelligent approach to prediction and control ground vibration in mines, *Geotechnical and Geological Engineering*, vol 23, 2005, pp.249-262.
- Singh, T.N. (2004) Artificial neural network approach for prediction and control of ground vibrations in mines, *Mining Technology*, vol 113, 2004, pp.251-255.
- Singh, T.N., Kanchan, R., Saigal, K. and Verma, A.K. (2004) Prediction of P-wave velocity and anisotropic properties of rock using Artificial Neural Networks technique, *J Sci Ind Res*, vol 63, 2004, pp.32-38.
- Singh, V.K., Singh, D. and Singh, T.N. (2001) Prediction of strength properties of some schistose rock, *Int J Rock Mech Min Sci*, vol 38, 2001, pp.269–284.
- Smith, N.D. and Minter, W.E.L. (1979) Sedimentological controls of Gold and Uranium in Local Developments of the Leader Reef, Welkom Goldfield, and Elsburg No. 5 Reef, Klerksdorp Goldfield; Witwatersrand basin, E.G.R.U. Information Circular No. 137, 1979.
- Smith, P.D. and Hetherington, J.G. (1994) *Blast and ballistic loading of structure*, Elsevier Science, Butterworth-Heinemann Ltd., Oxford, 1994.
- Snowden, V. (1996) Practical interpretation of Resource Classification Guide Lines AusIMM Annual Conference, 1996, pp.16.
- Starfield, A.M. and Cundall P.A. (1988) Towards a Methodology for Rock Mechanics Modelling, *Int. J. Rock Mech. Min. Sci. & Geomech. Abstr.*, vol 25. 3, 1988, pp.99-106.

- Steffen, Robertson and Kirsten (South Africa) Pty Ltd (2007) An Independent Competent Person's Report on the Mining Assets of Harmony Gold Mining Company Limited, Public Report, [www.harmony.co.za](http://www.harmony.co.za), March 2007.
- Sönmez, H. and Ulusay, R. (2002) A discussion on the Hoek–Brown failure criterion and suggested modifications to the criterion verified by slope stability case studies. *Yerbilimleri* 26:pp.77–99.
- Tucker, R.F. (2003) Geological Aspects of the Target-Sun Gold Prospect.
- Vardoulakis, I., Labuz, J.F., Papamichos, E. and Tronvoll, J. (1998) Continuum fracture mechanics of uniaxial compression of brittle materials. *Int J Solids Struct* 35,pp.4313–4335.
- Vieira, F.M.C.C. and Durrheim, R.J. (2001) Probabilistic Mine Design Methods to Reduce Rockburst Risk, Rockburst and Seismicity in Mines – RaSiM5, South African Institute of Mining and Metallurgy,pp.251-262.
- Vermeer, P.A. and De Borst, R. (1984) Non associated plasticity for soils, concrete and rock. *Heron* 29,pp.3–64.
- Vutukuri, V.S., Lama, R.D. and Saluja, D. (1974) Handbook on the mechanical properties of rocks. Trans Tech Pub, Clausthal.
- Wiles, T.D. (2009) A mining analysis program in three dimensions, Mine Modelling Pty Ltd. Mt Eliza, Victoria, Australia.
- Wiles, T.D. (1988) Accuracy and Applicability of Elastic Stress Analysis Methods in Mining, 15th Canadian Rock Mechanics Symposium, Toronto, Canada,pp.207-220.
- Wiles, T.D. and Curran, J.H. (1982) A General 3-D Displacement Discontinuity Method, *Proc. 4th Int. Conf. Numerical Methods in Geomechanics*, Vol 1,pp.103-111.
- Wiles, T.D. and Kaiser, P.K. (1990) A New Approach for Statistical Treatment of Stress Tensors, Specialty Conference on Stress, Ottawa, Ontario.
- Wiles, T.D. and Kaiser, P.K. (1994) In Situ Stress Determination Using the Under-Excavation Technique - Part II: Applications, *Int. J. Rock Mech. Min. Sci. & Geomech. Abstr.*, vol 31. 5,pp.447-456.
- Wiles, T.D. and Kaiser, P.K. (1994) Failure Process Modelling - a Fracture Mechanics Approach to Discing, Laurentian University.
- Wiles, T.D. and MacDonald, P. (1988) Correlation of Stress Analysis Results with Visual and Microseismic Monitoring at Creighton Mine, *Computers and Geotechnics*, vol., no 5. 2,pp.105-122.
- Wiles, T.D. and MacDonald, P. (1990) Rock Mechanics Aspects of Regional Faulting around Creighton Mine, 31st U.S. Rock Mechanics Symposium, Golden, Colorado.
- Wiles, T.D. (1998) Correlation Between Local Energy Release Density and Observed Bursting Conditions at Creighton Mine, Mine Modelling Report.
- Wiles, T.D. (1995) DBEM3D Back-Analysis of AECL's Mine-by-Experiment, Mine Modelling Report.

- Wiles, T.D. (1991) Issues of Ease of Use, Error and Accuracy Control in MAP3D, Mining Analysis Program in 3-Dimensions, Proc. 2nd Canadian Conference on Computer Applications in the Mineral Industry, Vancouver, B.C., pp.669-677.
- Wiles, T.D. (2002) Loading System Stiffness – a Parameter to Evaluate Rockburst Potential, First International Seminar on Deep and High Stress Mining, Australian Centre for Geomechanics, Perth, Australia.
- Wiles, T.D. (1989) Non-Linear Modelling of Mining at Great Depth: A Case History at Creighton Mine, Int. Symposium Rock Mechanics, Pau, France, vol 2, pp.621-628.
- Wiles, T.D. (1990) Plasticity in the Boundary Element Method, Year 1, 2 and 3 Interim Report on Numerical Modelling, DSS file no.14SQ.23440-6-9033.
- Wiles, T.D. (2006) Reliability of Numerical Modelling Predictions, International Journal of Rock Mechanics and Mining Sciences, vol 43, pp.454-472.
- Wiles, T.D. (2005) Rockburst Prediction Using Numerical Modelling: Realistic Limits for Failure Prediction Accuracy, 6th International Symposium on Rockbursts and Seismicity in Mines (RaSiM 6), Perth, Australia.
- Wiles, T.D., Lachenicht, R. and van Aswegen, G. (2001) Integration of Deterministic Modelling with Seismic Monitoring for the Assessment of Rockmass Response to Mining: Part I Theory, Proc. of the Fifth International Symposium on Rockburst and Seismicity in Mines (RASiM5), Johannesburg, South Africa, pp.379-388.
- Wiles, T.D., Villaescusa, E. and Windsor, C.R. (2004) Rock Reinforcement Design for Overstressed Rock Using Three Dimensional Numerical Modelling, 5th Int. Symposium on Ground Support in Mining and Underground Construction, Perth, Australia.
- Wilson, J.W. and More-O'Ferrall, R.C. (1968–1969) The Application of the Electrical Resistance Analogue to Mining Operations, Association of Mine Managers of South Africa, Papers and Discussions, pp.209-280.
- Winter, H. de la R. (1964) The geology of the Northern Section of the Orange Free State Goldfield, The geology of some ore deposits of Southern Africa, Geological Society South Africa, pp.417-450.
- Winter, H. de la R. (1986) Cratonic Foreland model for Witwatersrand Basin development in a continental arc-plate tectonic setting, Geological Society South Africa, pp.75-80.
- Working Group on Revision of the Point Load Test Method, International Society for Rock Mechanics, Commission on Testing Methods, Int. J. Rock Mech. Min. Sci. & Geomech. Abstr., vol 22. 2, 1985, pp.51-60.
- Yang, Y. and Zhang, Q. (1997) Analysis for the results of point load testing with artificial neural network, Proceedings of computing methods and advances in geomechanics, IACMAG, China, pp.607-612.
- Yi X, Ong S, Russell, J.E. (2006) Quantifying the effect of rock strength criteria on minimum drilling mud weight prediction using polyaxial rock strength test data. Int J Geomech ASCE 6(4), pp.260–268.
- Yi X, Valko P.P, Russell, J.E. (2005) Effect of rock strength criterion on the predicted onset of sand production. Int J Geomech ASCE 5(1), pp.66–73.

Zhao, J. (2000) Applicability of Mohr–Coulomb and Hoek–Brown strength criteria to the dynamic strength of brittle rock. *Int J Rock Mech Min Sci* 37(7),pp.1115–1121.

Page 227

Page 228



Page 229

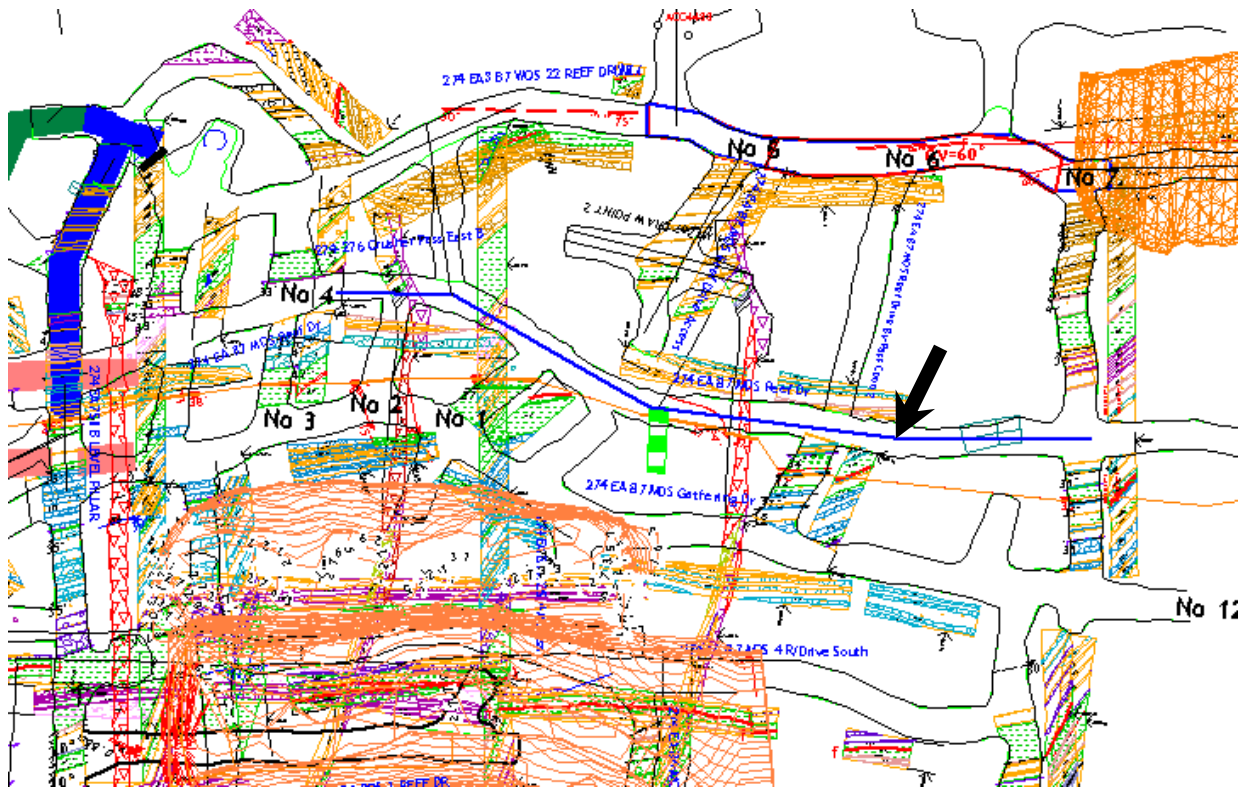


Figure A7 Plan view of case study 7

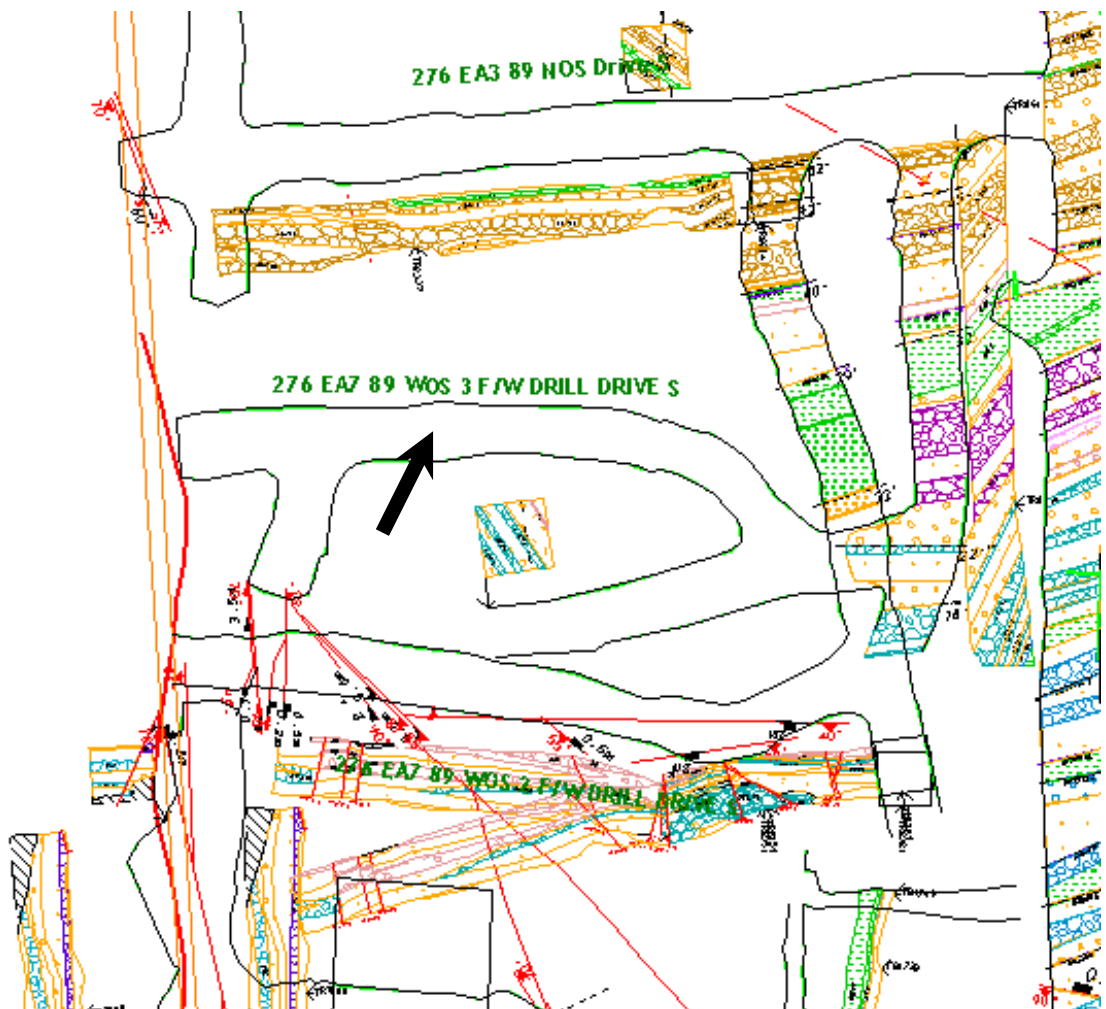


Figure A8 Plan view of case study 8



Page 231

The map displays a complex network of roads and land parcels. Key features include:

- Roads:** Access Reef Drive, Exploration Drive North, Reef Drive North.
- Land Parcels:** Various colored areas representing different land uses or ownership.
- Infrastructure:** Utility lines, drainage systems, and other engineering details.
- Annotations:** Numerous handwritten notes and labels providing additional context.

A large black arrow points to a specific location on the map, likely indicating a point of interest or a key feature.

Page 232

[illegible]

Page 233



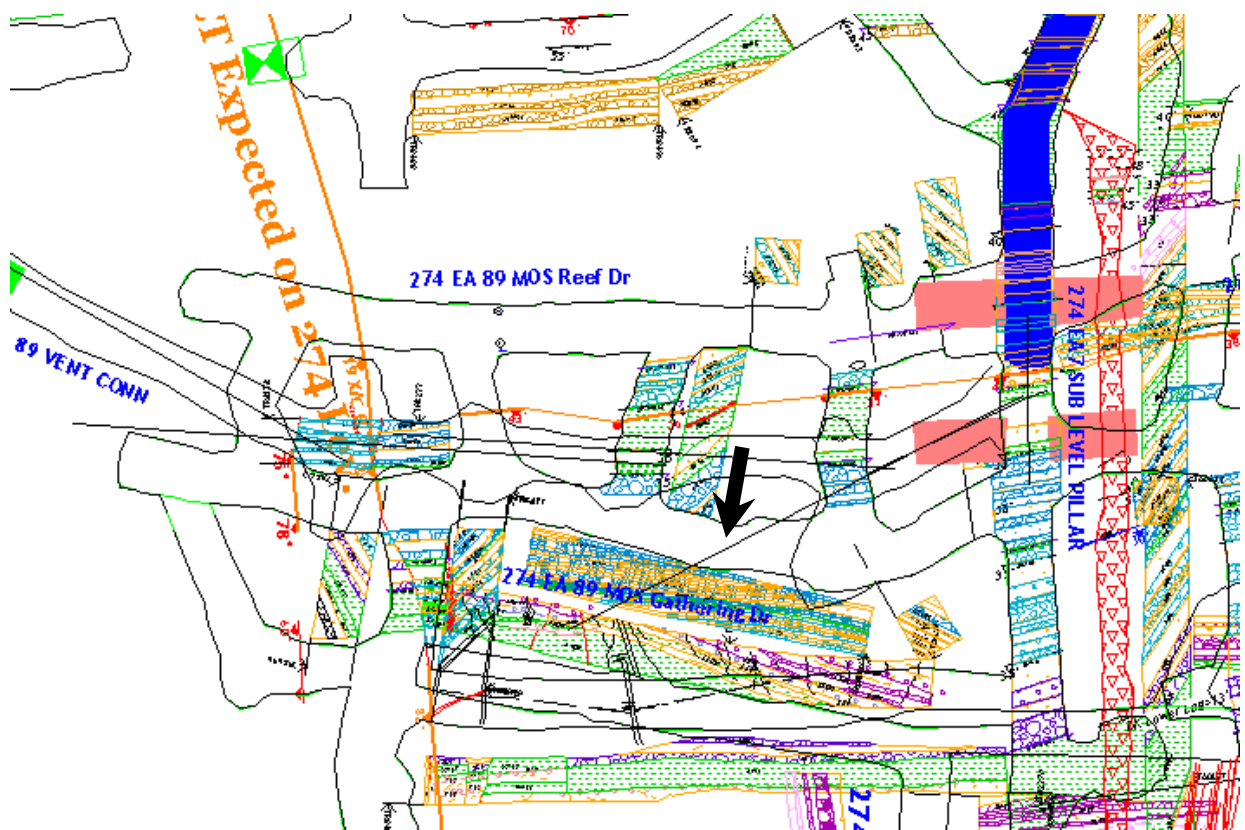


Figure A15 Plan view of case study 15

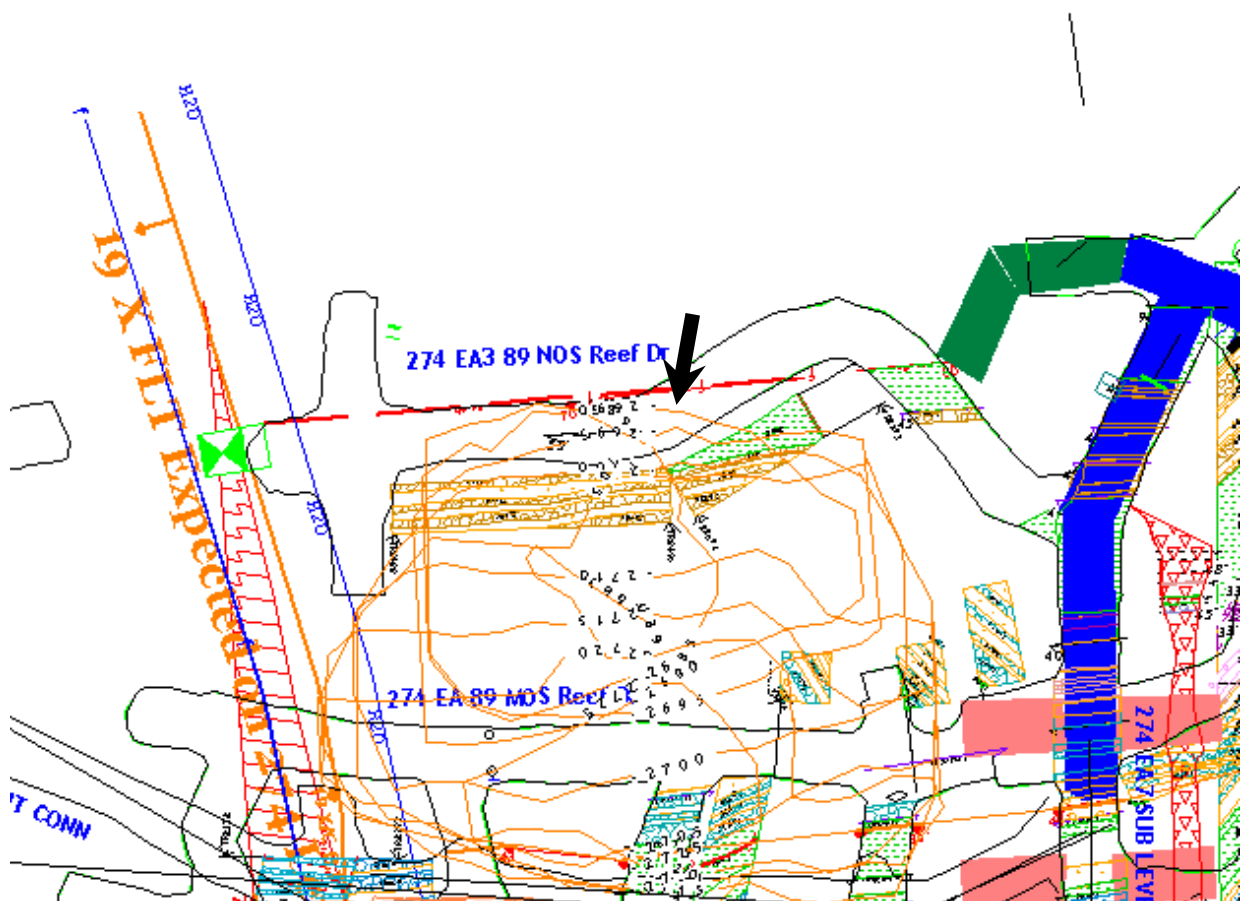


Figure A16 Plan view of case study 16

[illegible]

Page 235

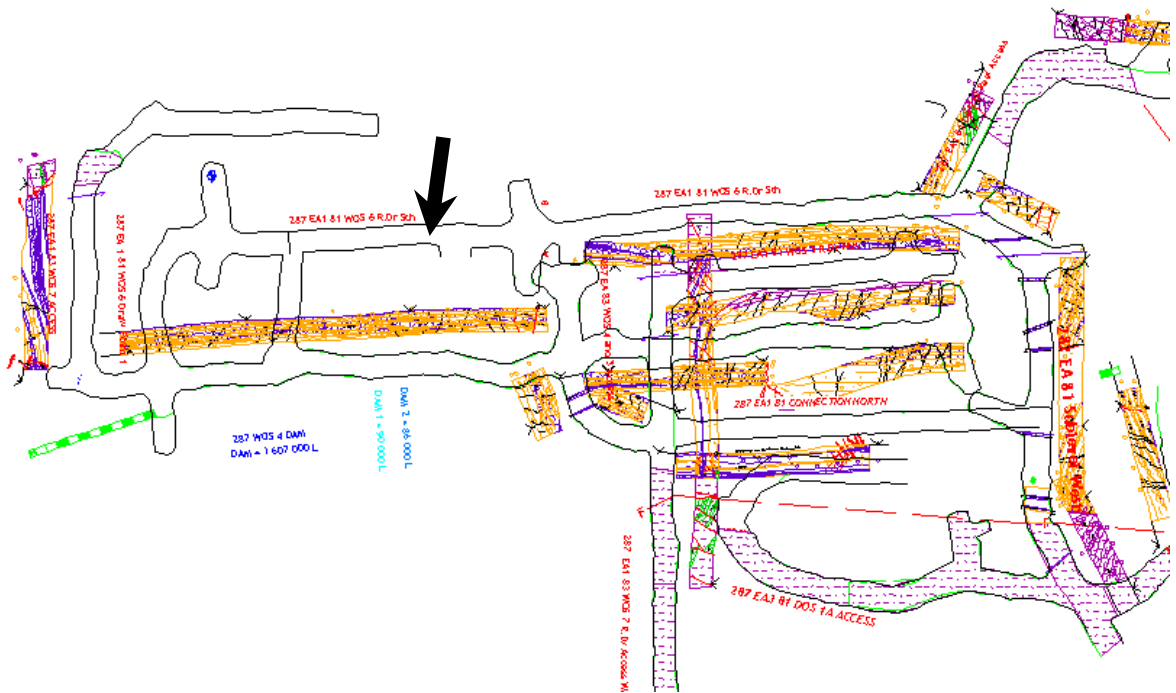


Figure A19 Plan view of case study 19

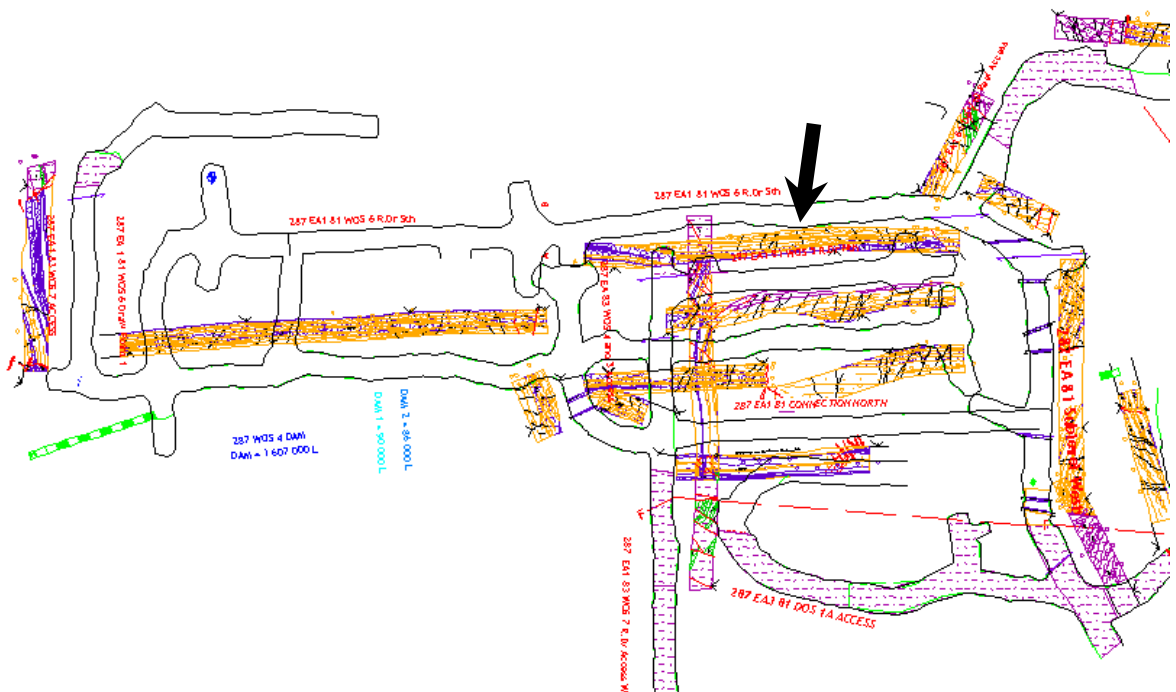


Figure A20 Plan view of case study 20





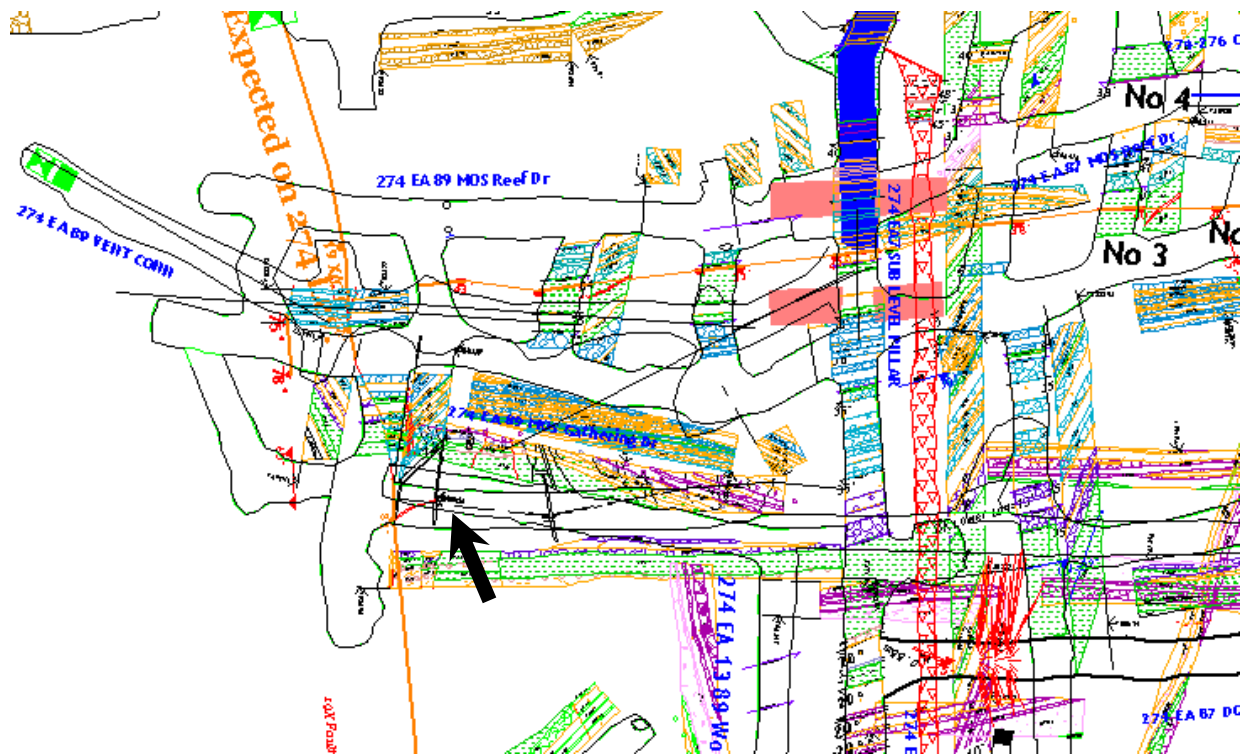


Figure A23 Plan view of case study 23

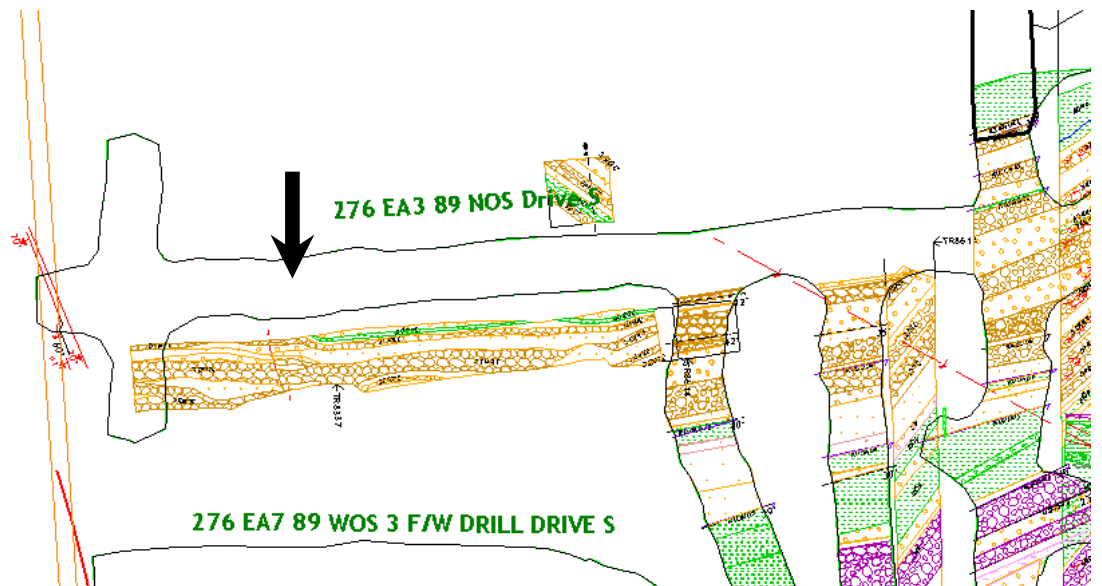


Figure A24 Plan view of case study 24

Page 239





Figure A27 Plan view of case study 27



Figure A28 Plan view of case study 28

## APPENDIX B

### Results of Phase<sup>2</sup> Modelling

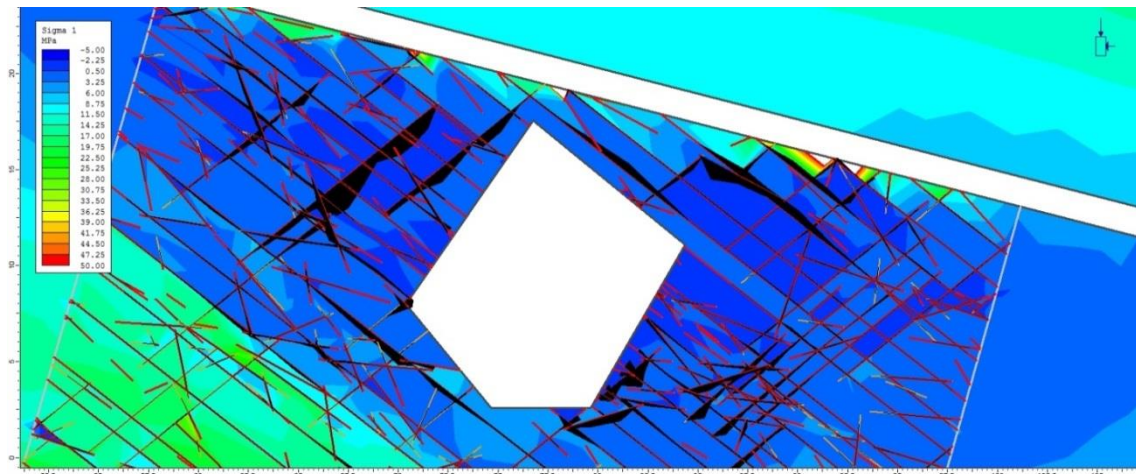


Figure B1 10m stope span overtopped open stope in EA7 with a 2m middling showing joint displacement in black and yielded joints indicated in red

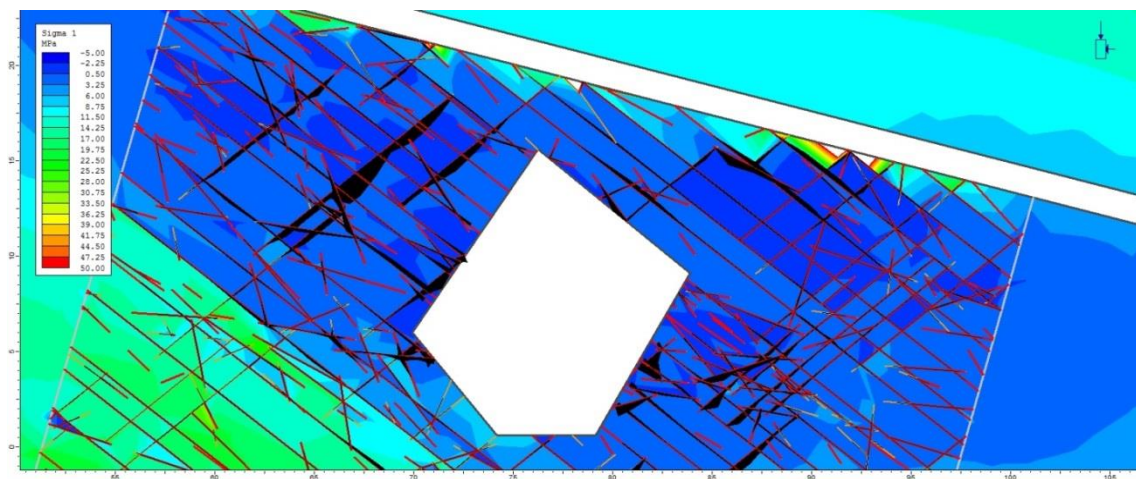


Figure B2 10m stope span overtopped open stope in EA7 with a 4m middling showing joint displacement in black and yielded joints indicated in red



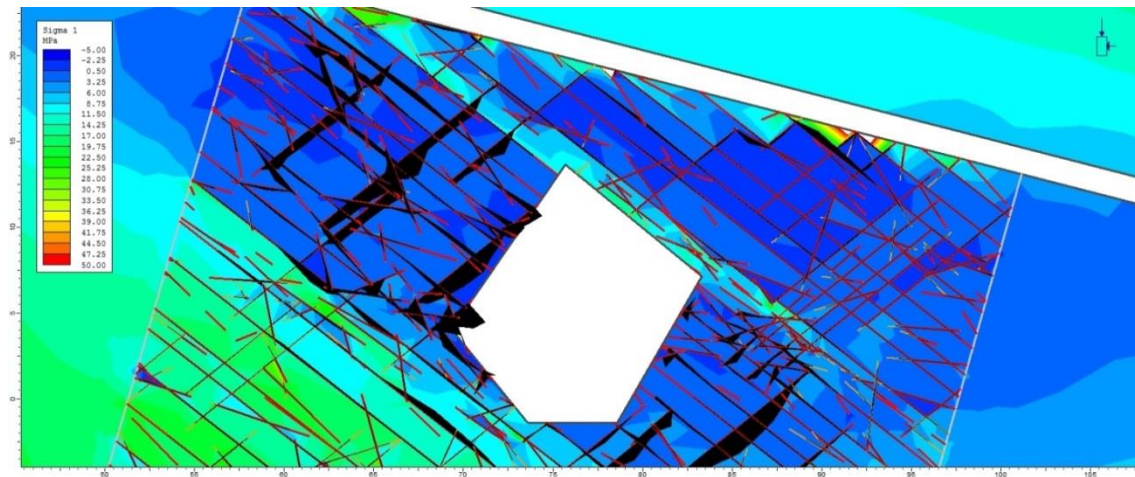


Figure B3 10m stope span overstoped open stope in EA7 with a 6m middling showing joint displacement in black and yielded joints indicated in red

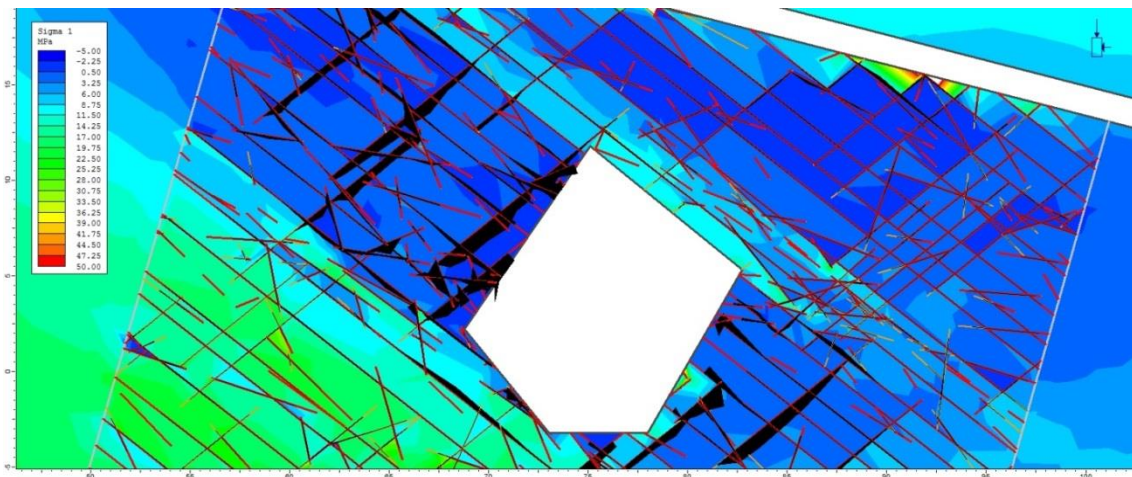


Figure B4 10m stope span overstoped open stope in EA7 with a 8m middling showing joint displacement in black and yielded joints indicated in red

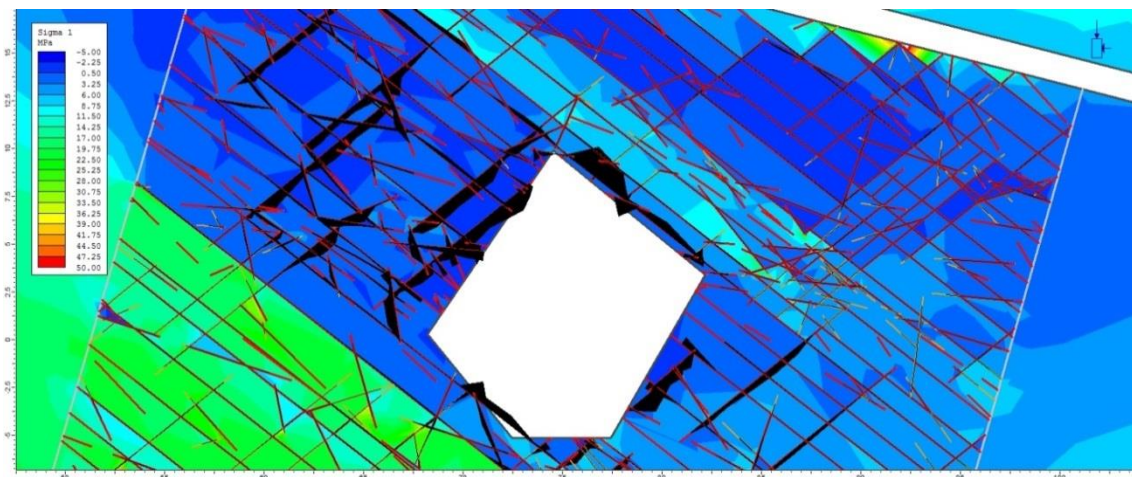


Figure B5 10m stope span overstoped open stope in EA7 with a 10m middling showing joint displacement in black and yielded joints indicated in red



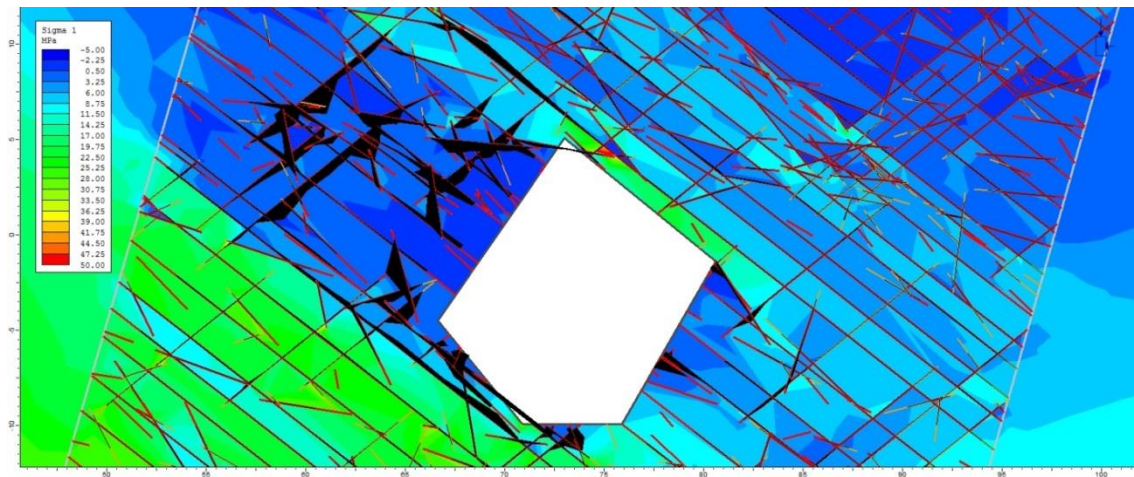


Figure B6 10m stope span overtopped open stope in EA7 with a 15m middling showing joint displacement in black and yielded joints indicated in red

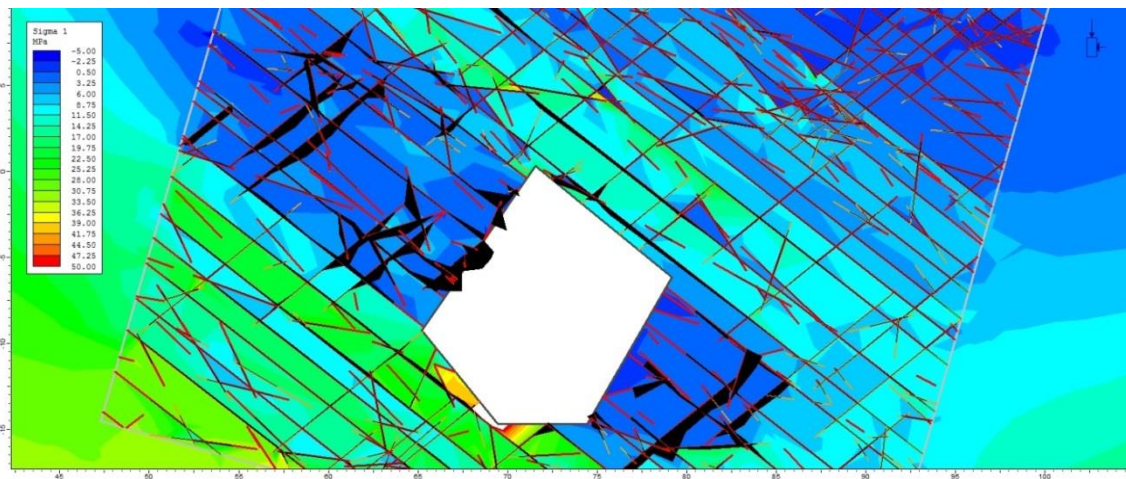


Figure B7 10m stope span overtopped open stope in EA7 with a 20m middling showing joint displacement in black and yielded joints indicated in red

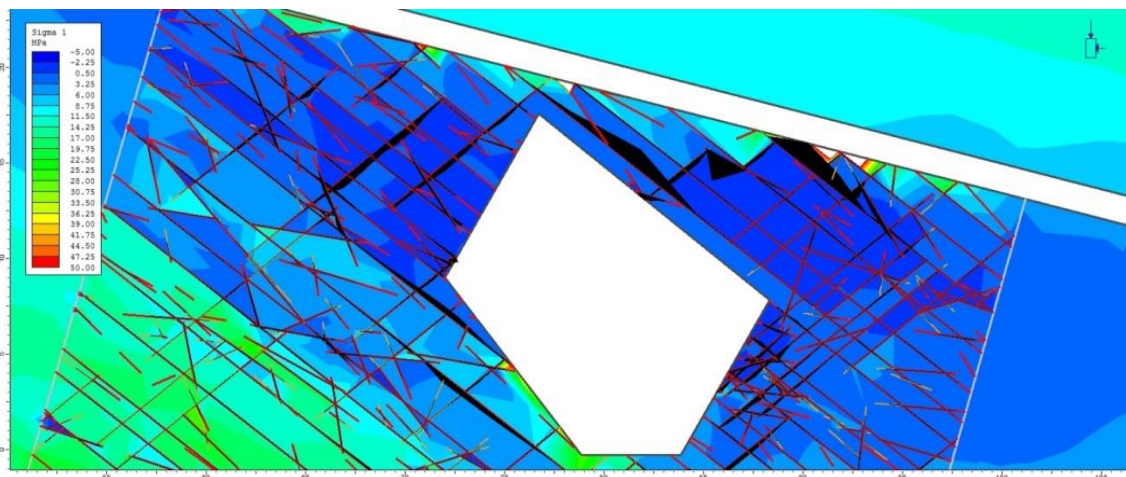


Figure B8 15m stope span overtopped open stope in EA7 with a 2m middling showing joint displacement in black and yielded joints indicated in red



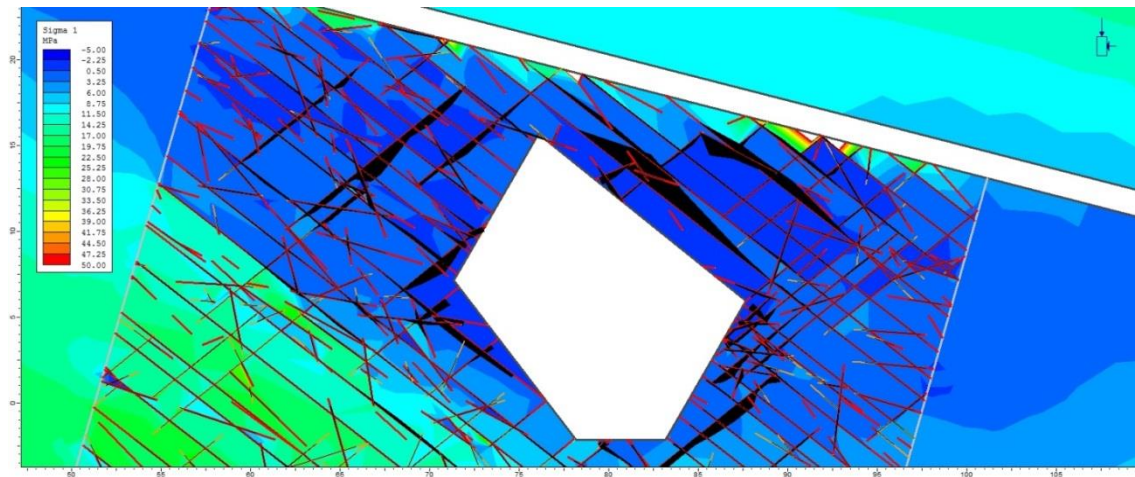


Figure B9 15m stope span overstoped open stope in EA7 with a 4m middling showing joint displacement in black and yielded joints indicated in red

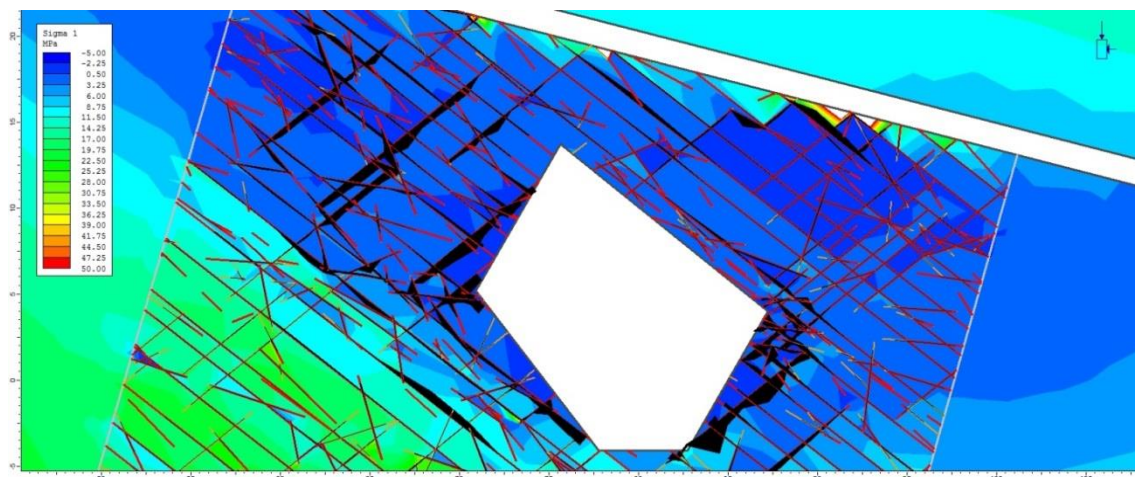


Figure B10 15m stope span overstoped open stope in EA7 with a 6m middling showing joint displacement in black and yielded joints indicated in red

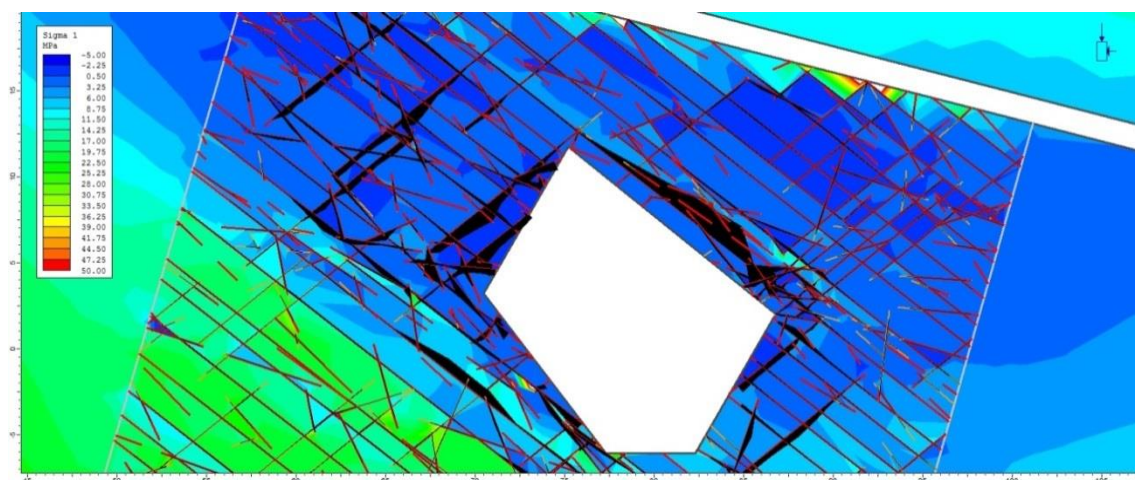


Figure B11 15m stope span overstoped open stope in EA7 with a 8m middling showing joint displacement in black and yielded joints indicated in red



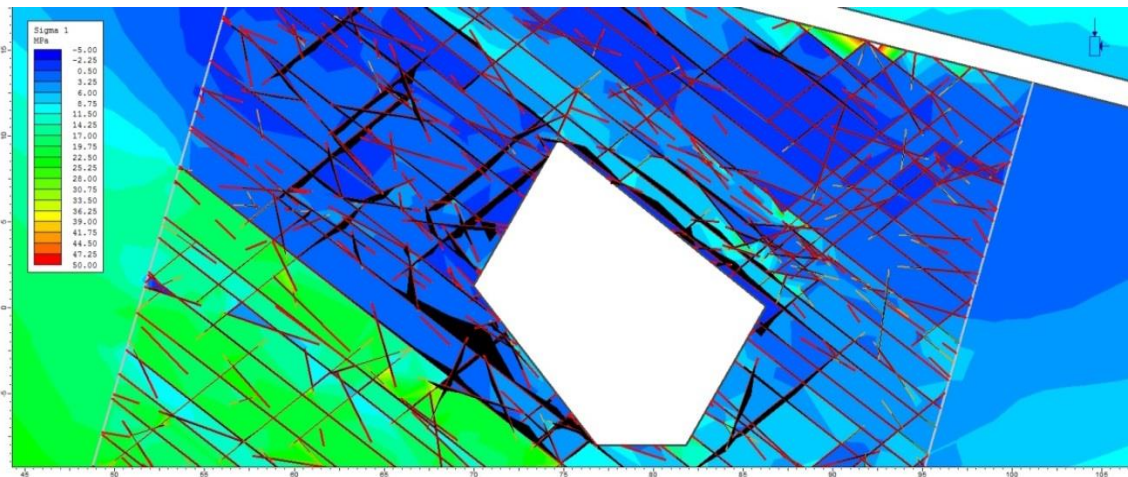


Figure B12 15m stope span overstoped open stope in EA7 with a 10m middling showing joint displacement in black and yielded joints indicated in red

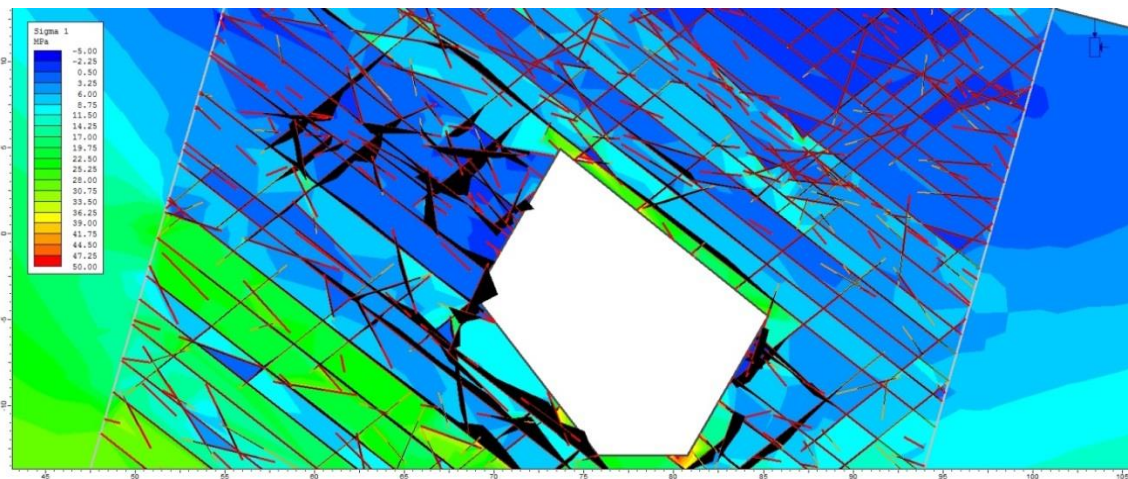


Figure B13 15m stope span overstoped open stope in EA7 with a 15m middling showing joint displacement in black and yielded joints indicated in red

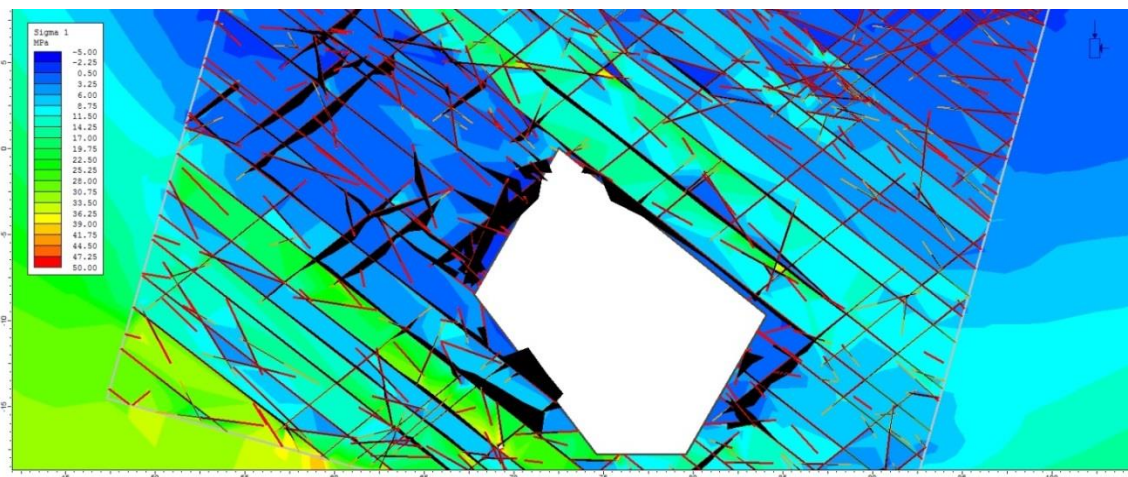


Figure B14 15m stope span overstoped open stope in EA7 with a 20m middling showing joint displacement in black and yielded joints indicated in red



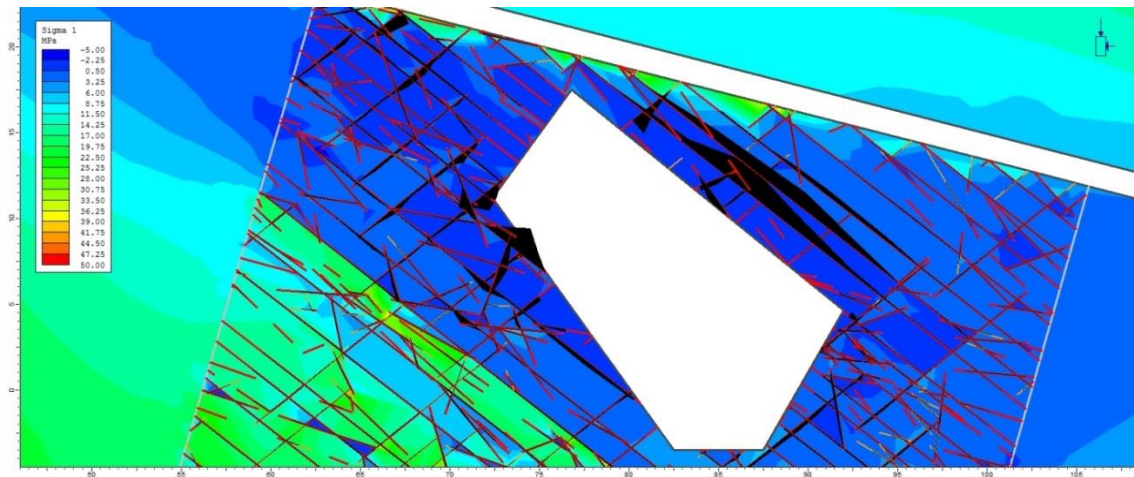


Figure B15 20m stope span overtopped open stope in EA7 with a 2m middling showing joint displacement in black and yielded joints indicated in red

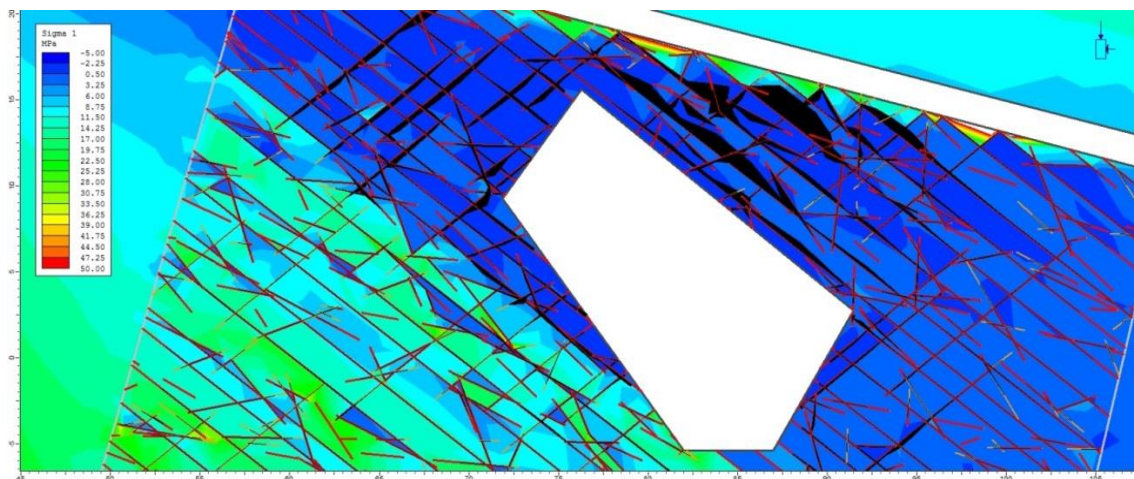


Figure B16 20m stope span overtopped open stope in EA7 with a 4m middling showing joint displacement in black and yielded joints indicated in red

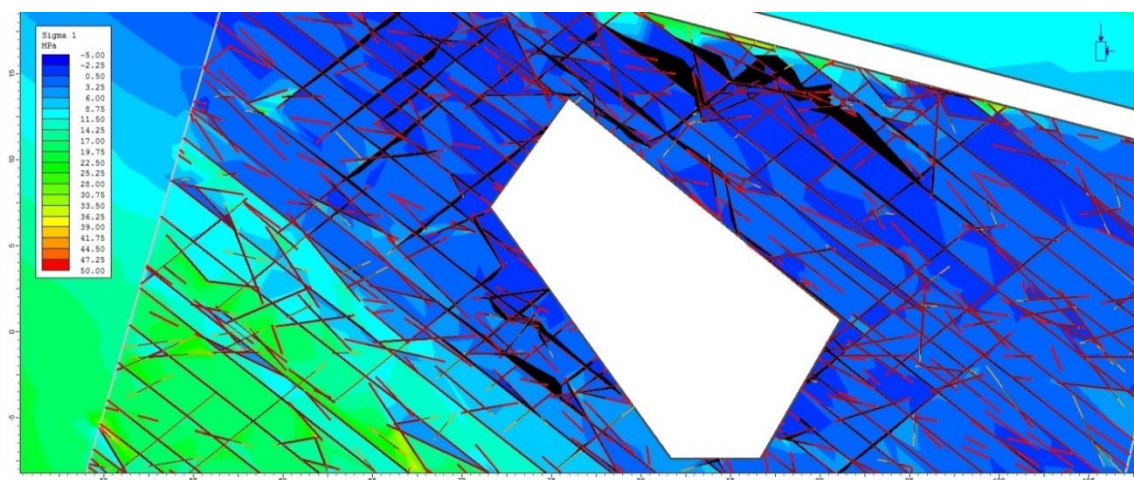


Figure B17 20m stope span overtopped open stope in EA7 with a 6m middling showing joint displacement in black and yielded joints indicated in red



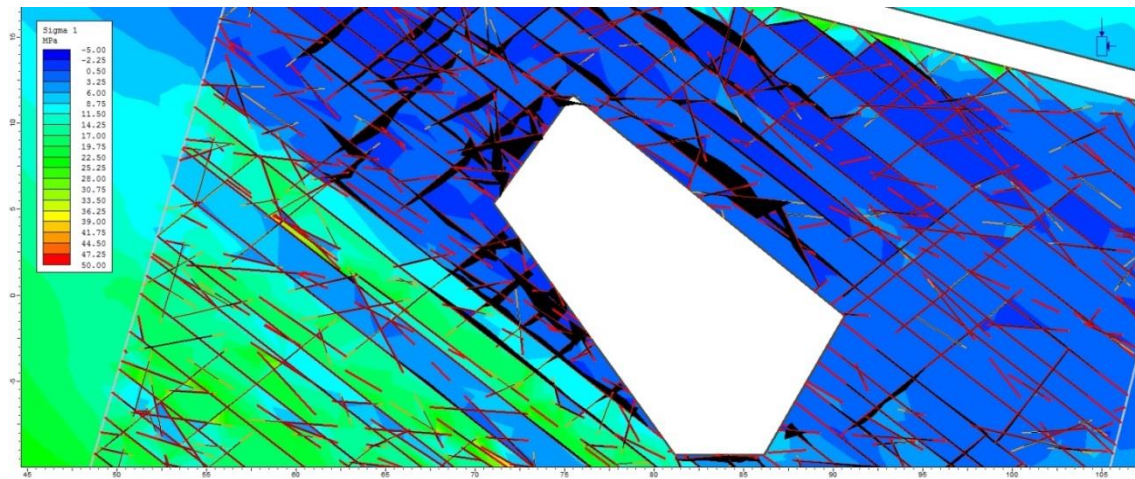


Figure B18 20m stope span overstoped open stope in EA7 with a 8m middling showing joint displacement in black and yielded joints indicated in red

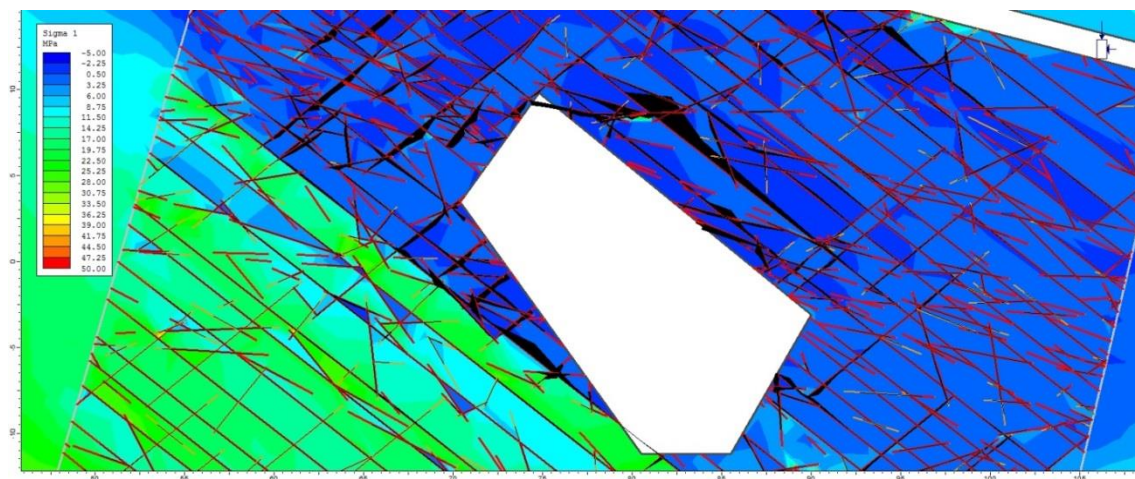


Figure B19 20m stope span overstoped open stope in EA7 with a 10m middling showing joint displacement in black and yielded joints indicated in red

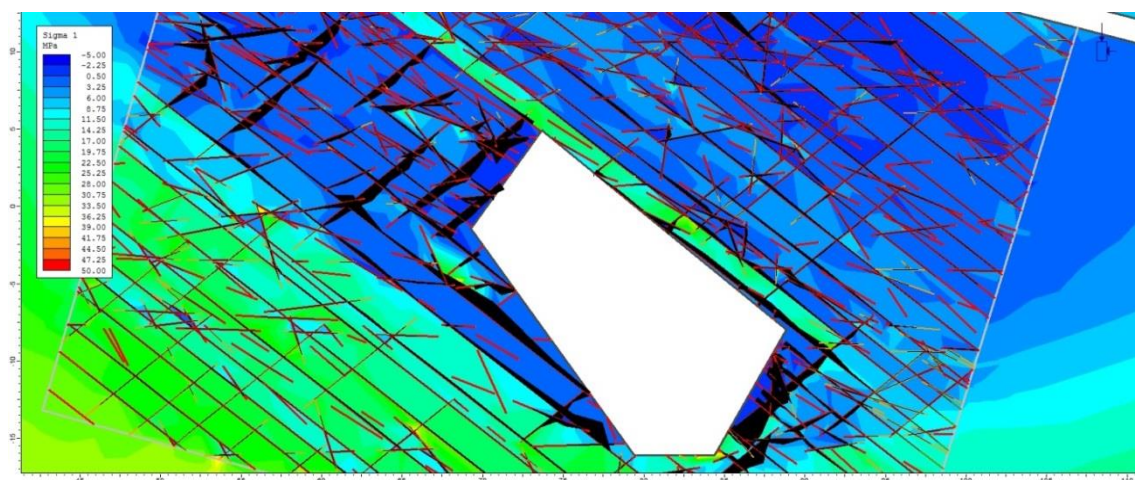


Figure B20 20m stope span overstoped open stope in EA7 with a 15m middling showing joint displacement in black and yielded joints indicated in red



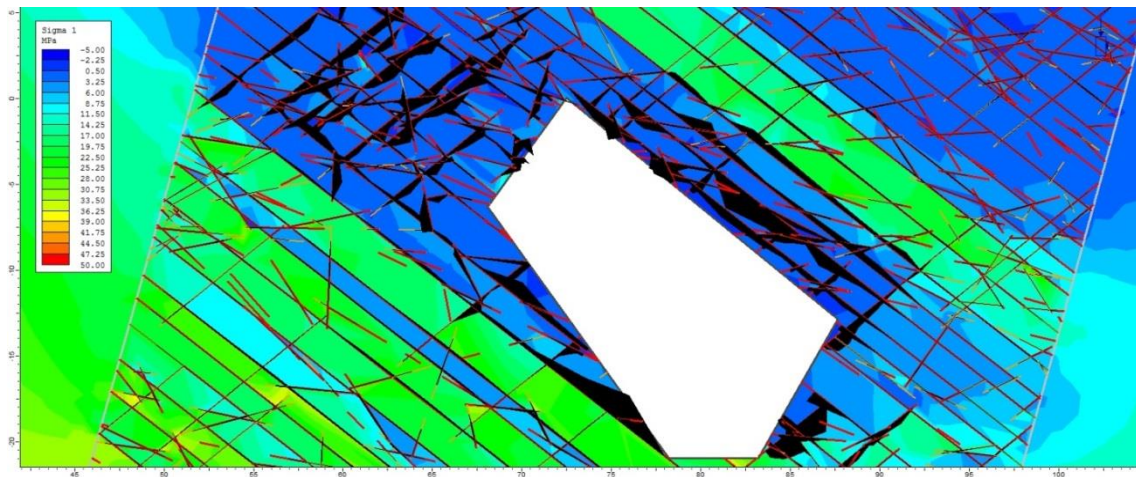


Figure B21 20m stope span overstoped open stope in EA7 with a 20m middling showing joint displacement in black and yielded joints indicated in red

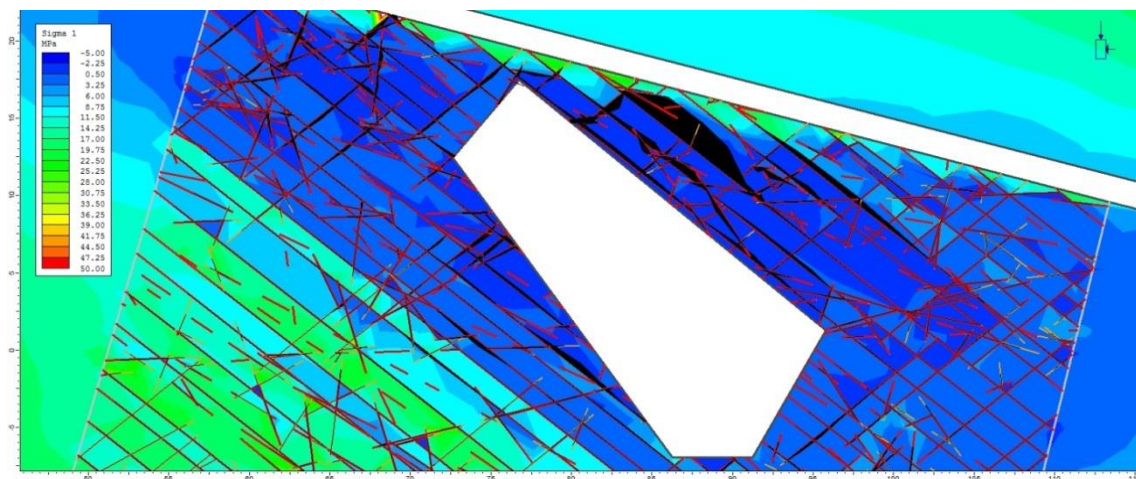


Figure B22 25m stope span overstoped open stope in EA7 with a 2m middling showing joint displacement in black and yielded joints indicated in red

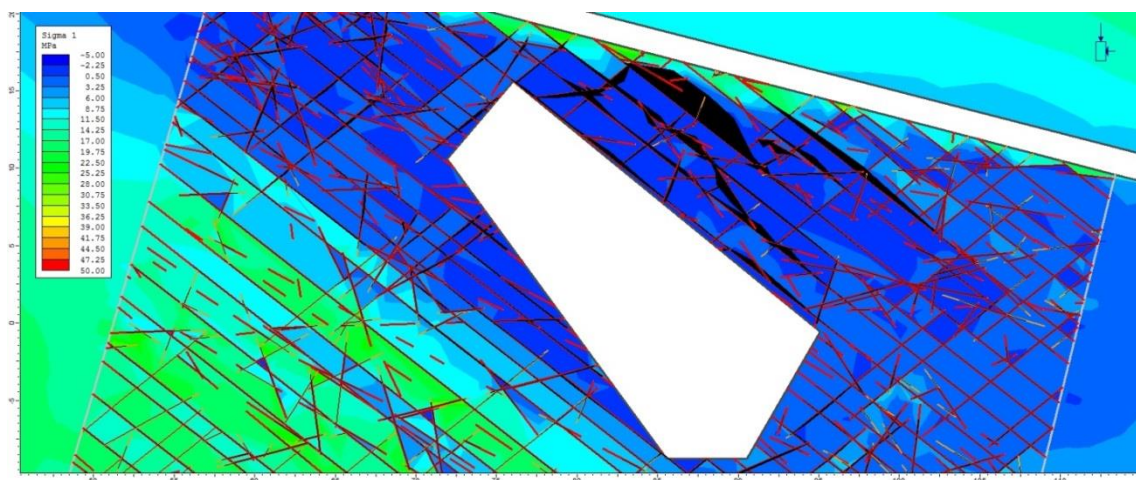


Figure B23 25m stope span overstoped open stope in EA7 with a 4m middling showing joint displacement in black and yielded joints indicated in red



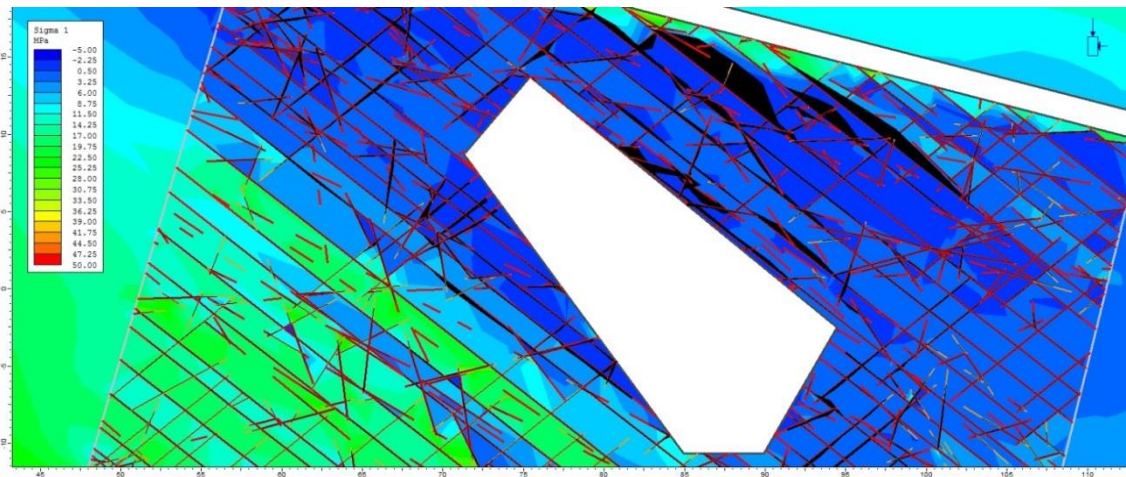


Figure B24 25m stope span overtopped open stope in EA7 with a 6m middling showing joint displacement in black and yielded joints indicated in red

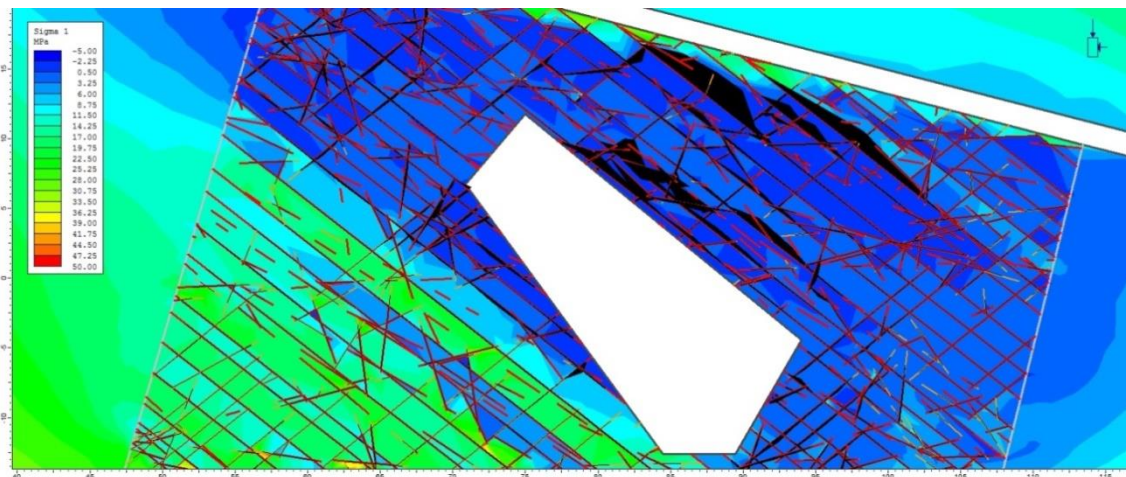


Figure B25 25m stope span overtopped open stope in EA7 with an 8m middling showing joint displacement in black and yielded joints indicated in red

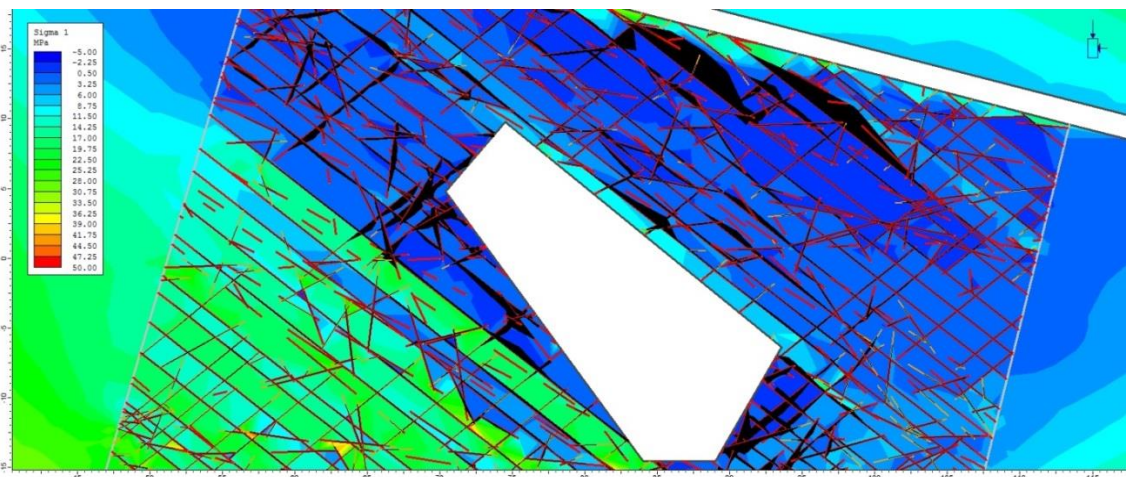


Figure B26 25m stope span overtopped open stope in EA7 with a 10m middling showing joint displacement in black and yielded joints indicated in red



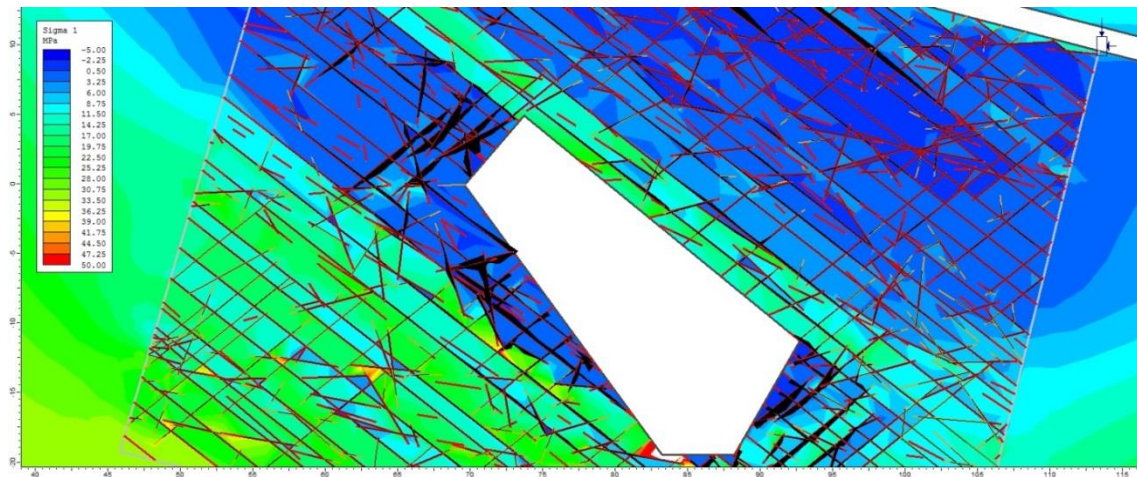


Figure B27 25m stope span overtopped open stope in EA7 with a 15m middling showing joint displacement in black and yielded joints indicated in red

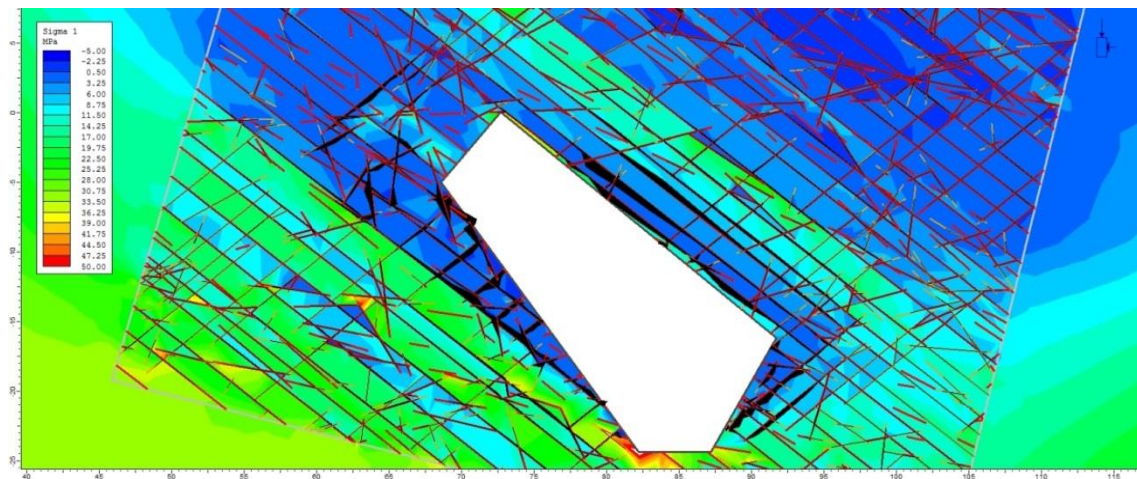


Figure B28 25m stope span overtopped open stope in EA7 with a 20m middling showing joint displacement in black and yielded joints indicated in red

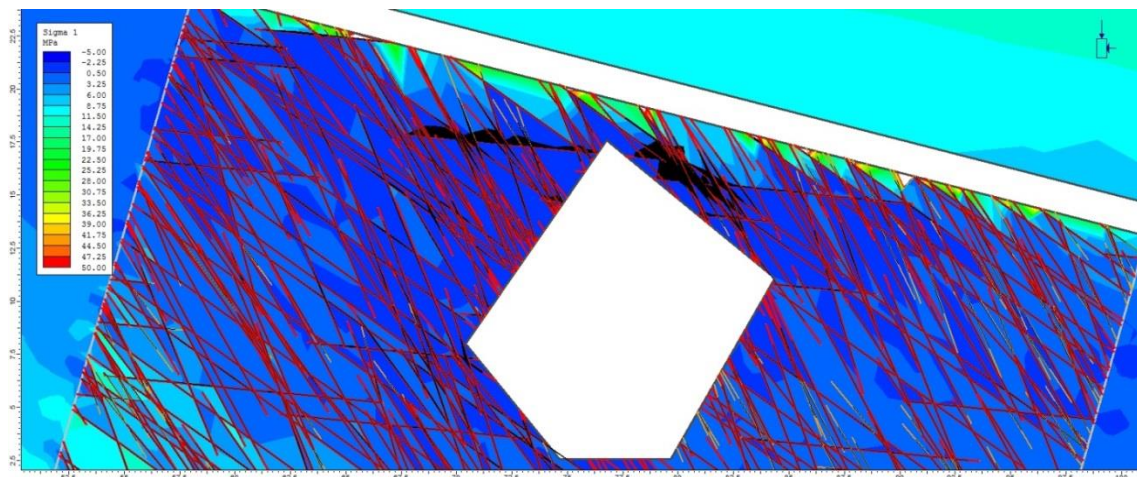


Figure B29 10m stope span overtopped open stope in EA3 with a 2m middling showing joint displacement in black and yielded joints indicated in red



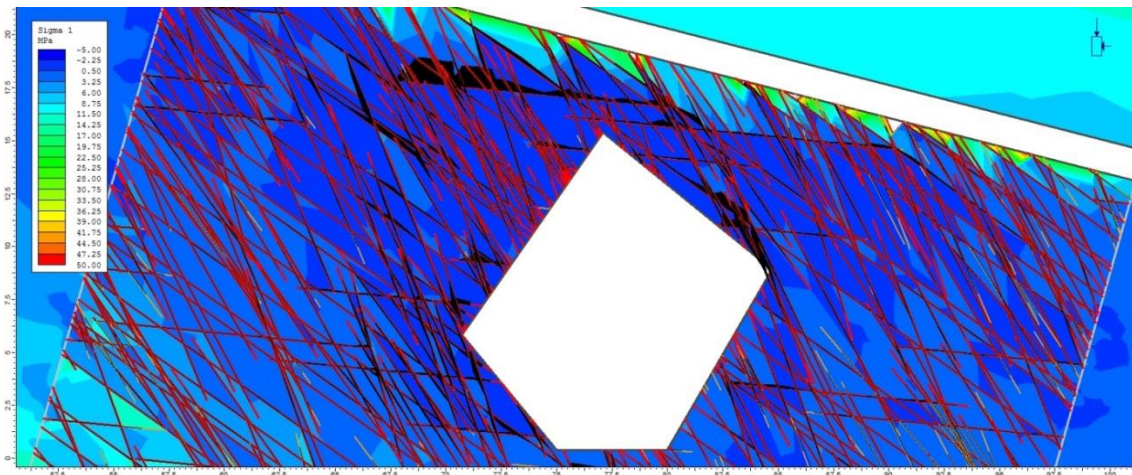


Figure B30 10m stope span overtopped open stope in EA3 with a 4m middling showing joint displacement in black and yielded joints indicated in red

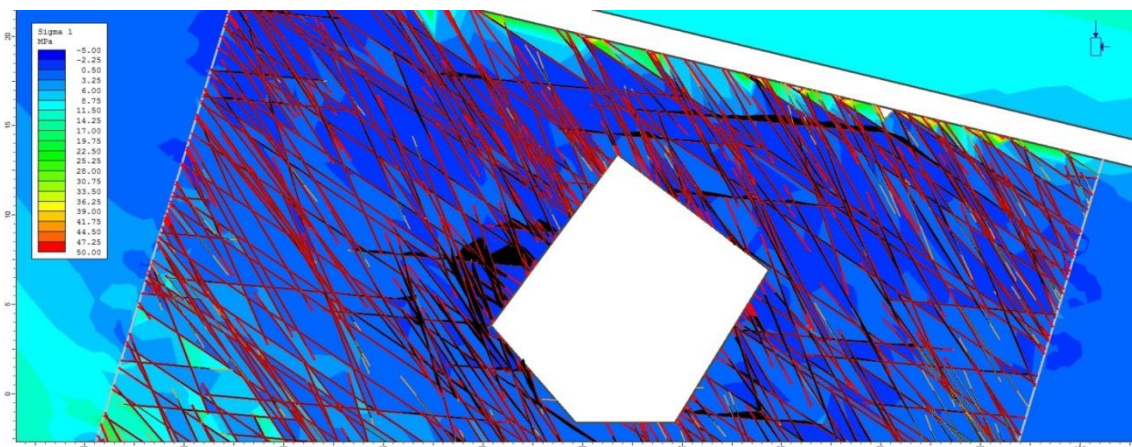


Figure B31 10m stope span overtopped open stope in EA3 with a 6m middling showing joint displacement in black and yielded joints indicated in red

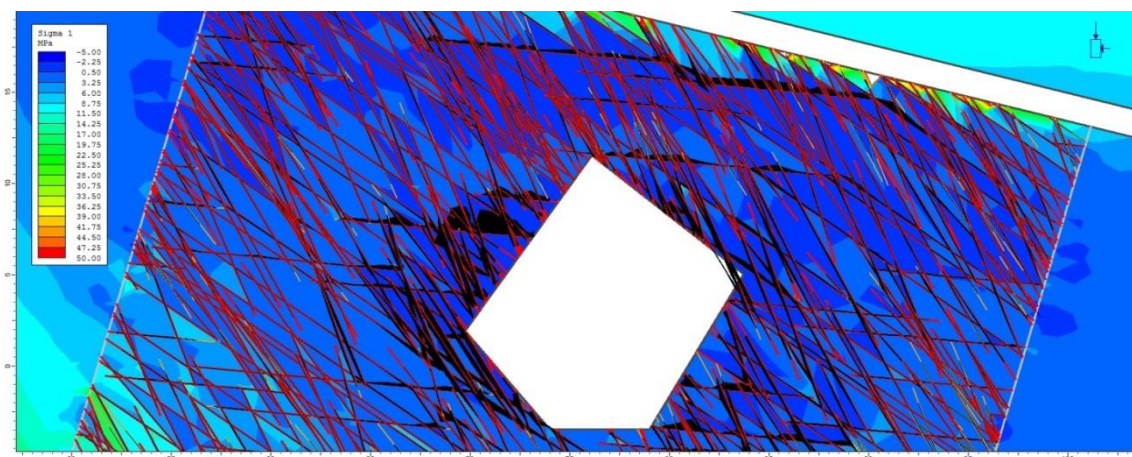


Figure B32 10m stope span overtopped open stope in EA3 with an 8m middling showing joint displacement in black and yielded joints indicated in red



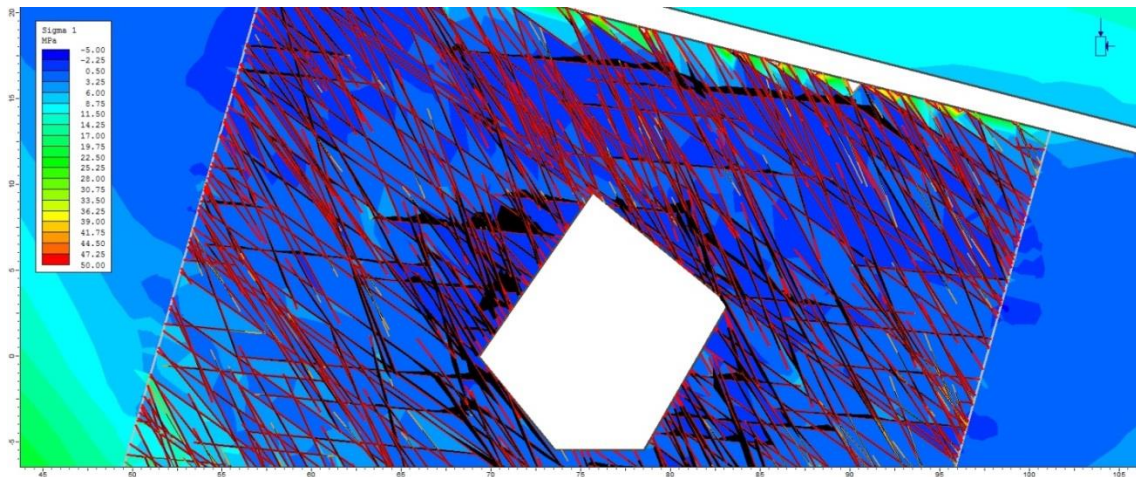


Figure B33 10m stope span overtopped open stope in EA3 with a 10m middling showing joint displacement in black and yielded joints indicated in red

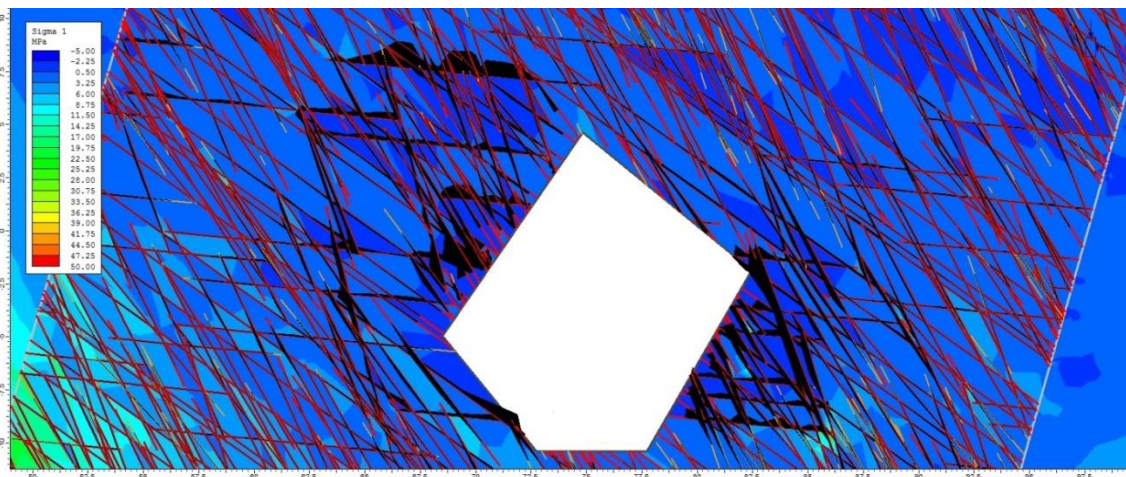


Figure B34 10m stope span overtopped open stope in EA3 with a 15m middling showing joint displacement in black and yielded joints indicated in red

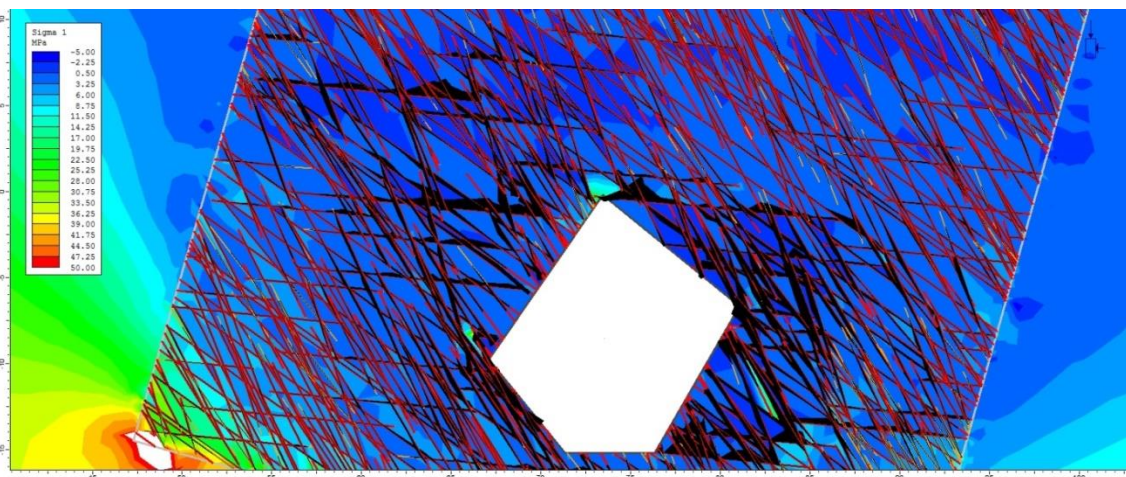


Figure B35 10m stope span overtopped open stope in EA3 with a 20m middling showing joint displacement in black and yielded joints indicated in red



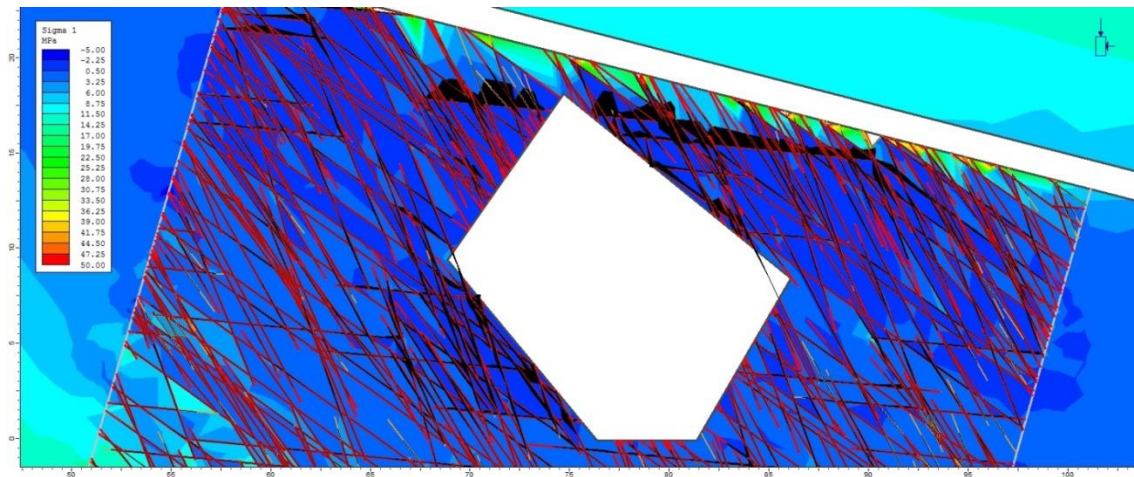


Figure B36 15m stope span overtopped open stope in EA3 with a 2m middling showing joint displacement in black and yielded joints indicated in red

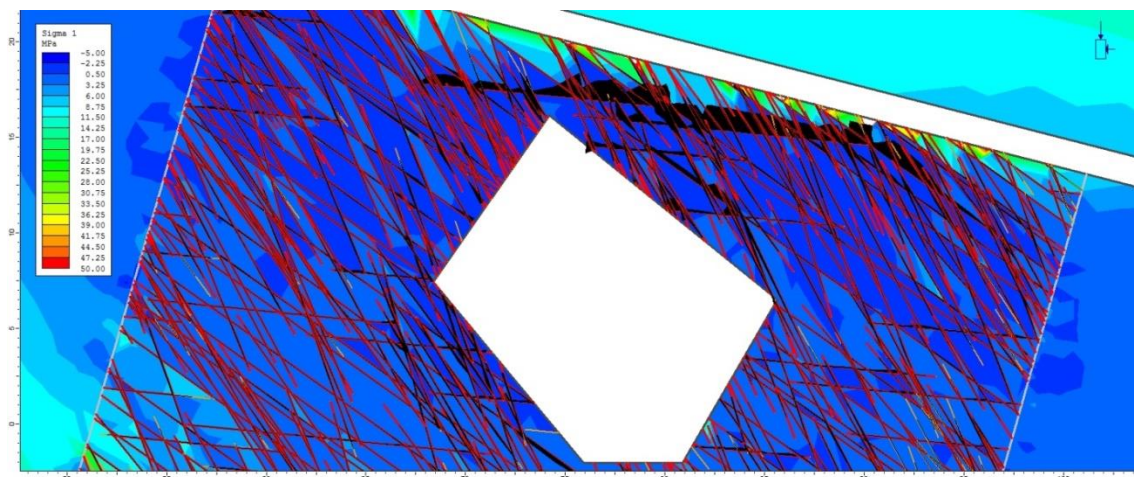


Figure B37 15m stope span overtopped open stope in EA3 with a 4m middling showing joint displacement in black and yielded joints indicated in red

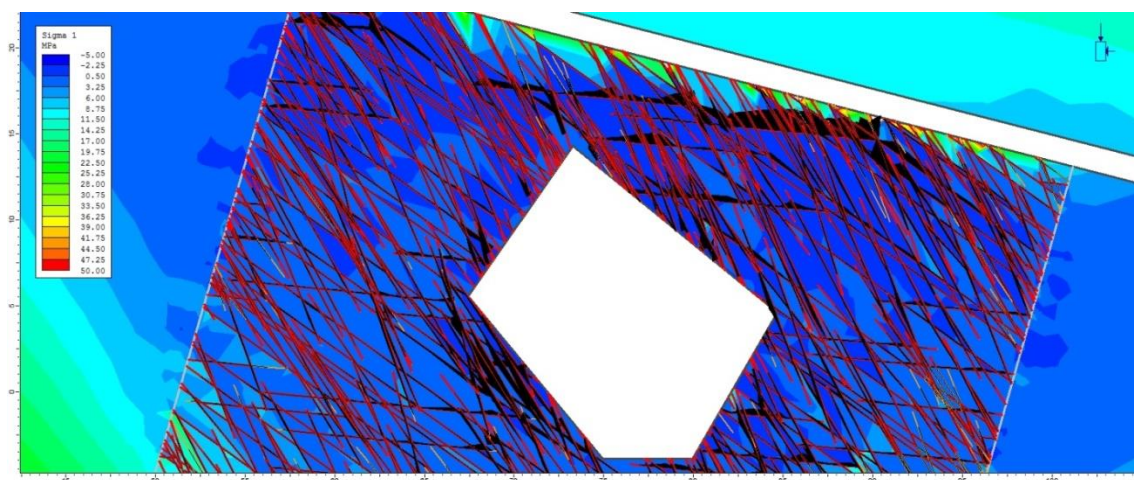


Figure B38 15m stope span overtopped open stope in EA3 with a 6m middling showing joint displacement in black and yielded joints indicated in red



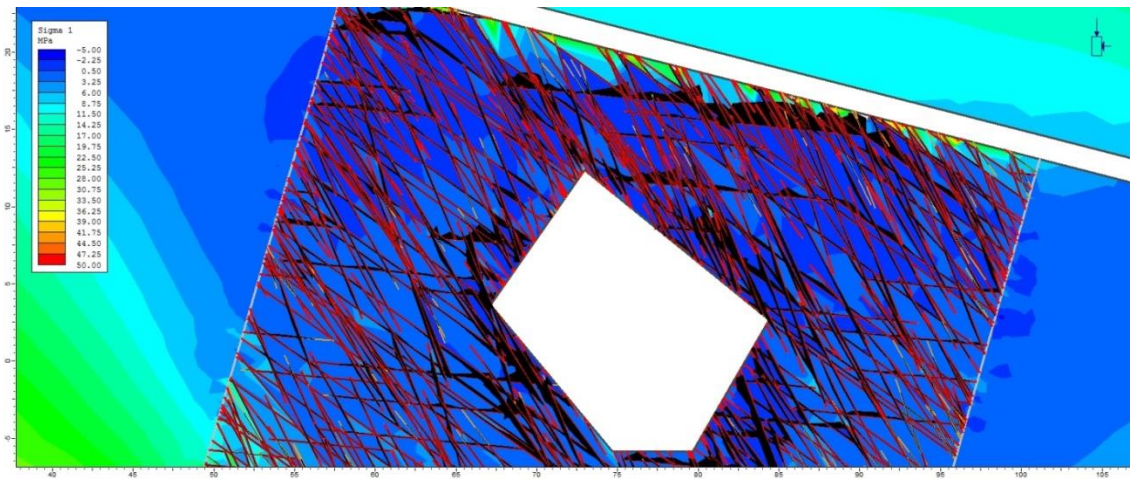


Figure B39 15m stope span overstoped open stope in EA3 with a 8m middling showing joint displacement in black and yielded joints indicated in red

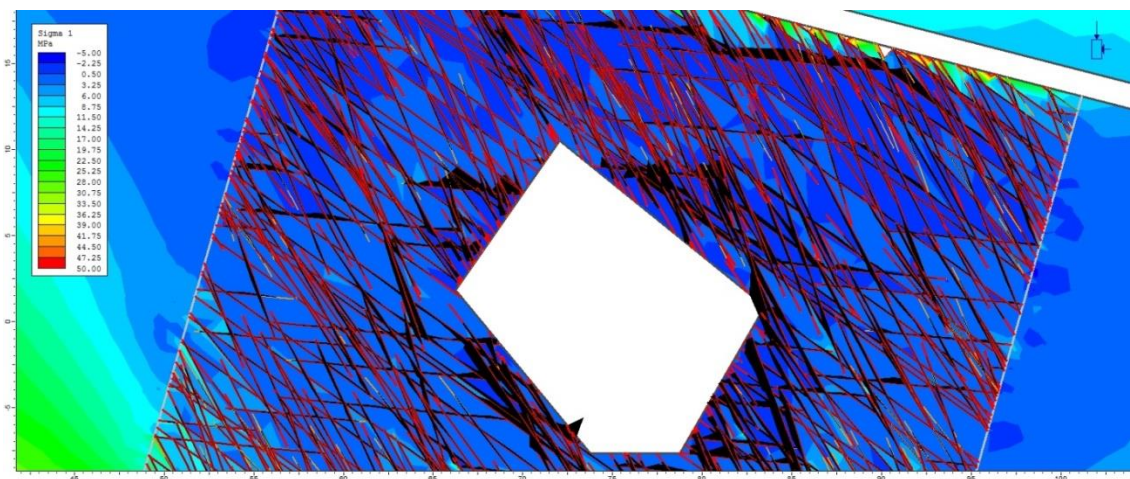


Figure B40 15m stope span overstoped open stope in EA3 with a 10m middling showing joint displacement in black and yielded joints indicated in red

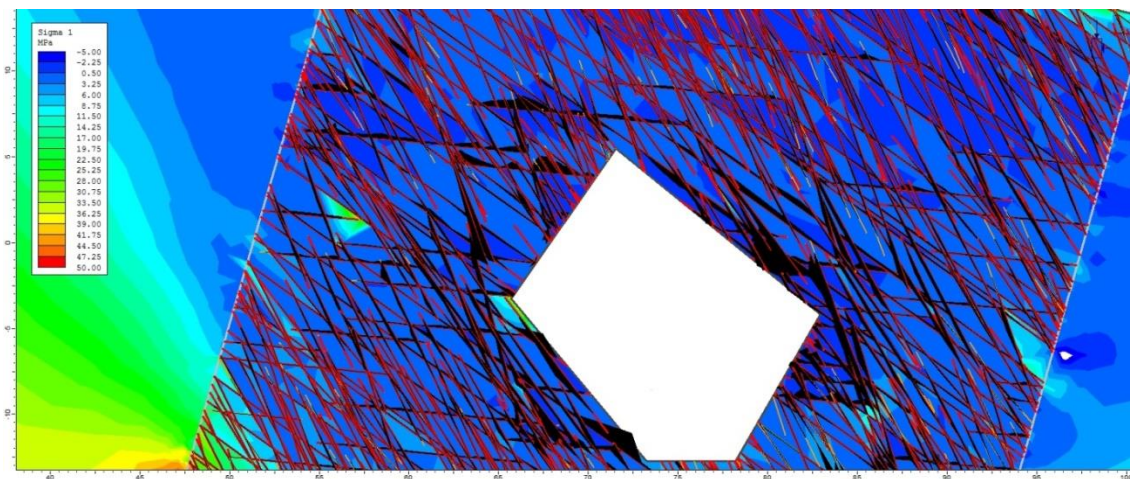


Figure B41 15m stope span overstoped open stope in EA3 with a 15m middling showing joint displacement in black and yielded joints indicated in red



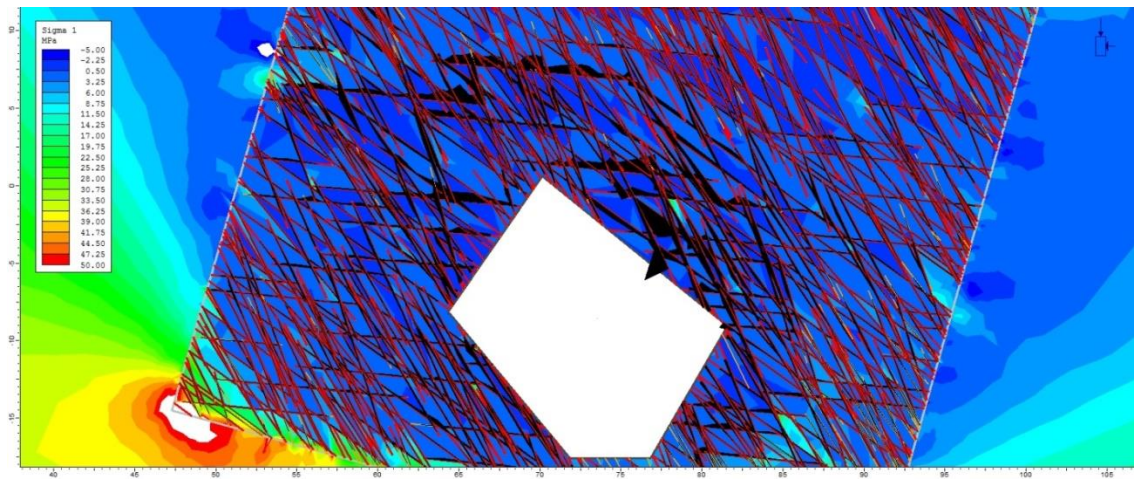


Figure B42 15m stope span overtopped open stope in EA3 with a 20m middling showing joint displacement in black and yielded joints indicated in red

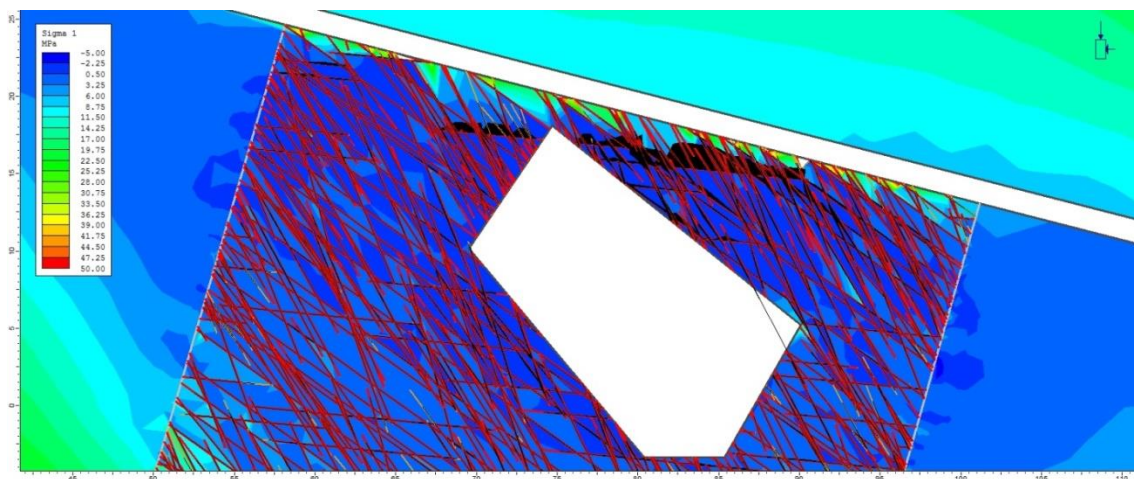


Figure B43 20m stope span overtopped open stope in EA3 with a 2m middling showing joint displacement in black and yielded joints indicated in red

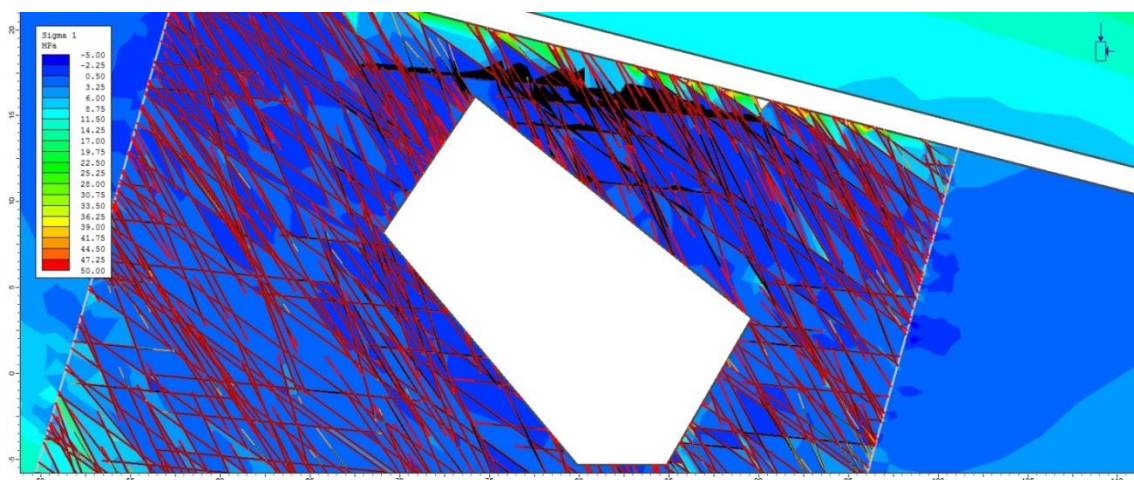


Figure B44 20m stope span overtopped open stope in EA3 with a 4m middling showing joint displacement in black and yielded joints indicated in red



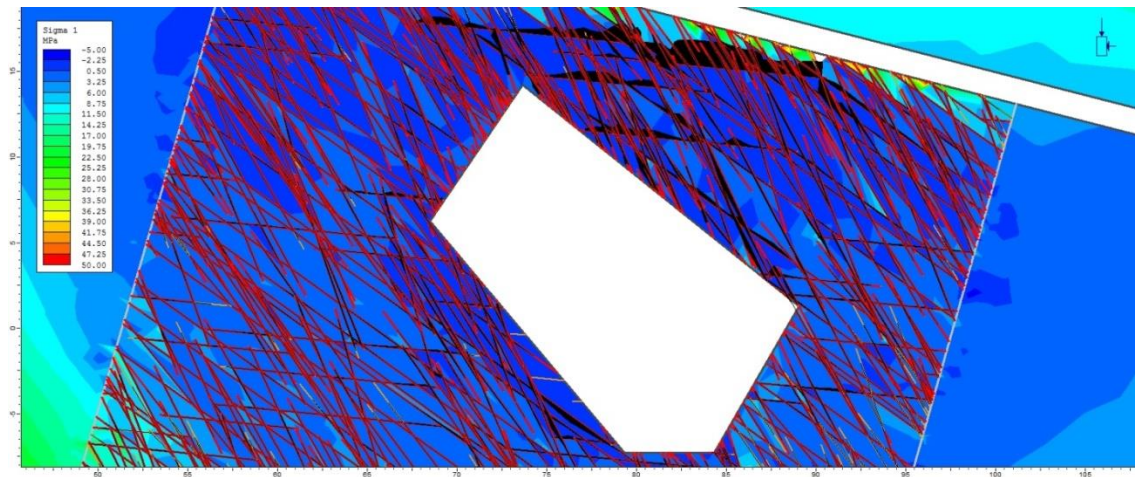


Figure B45 20m stope span overtopped open stope in EA3 with a 6m middling showing joint displacement in black and yielded joints indicated in red

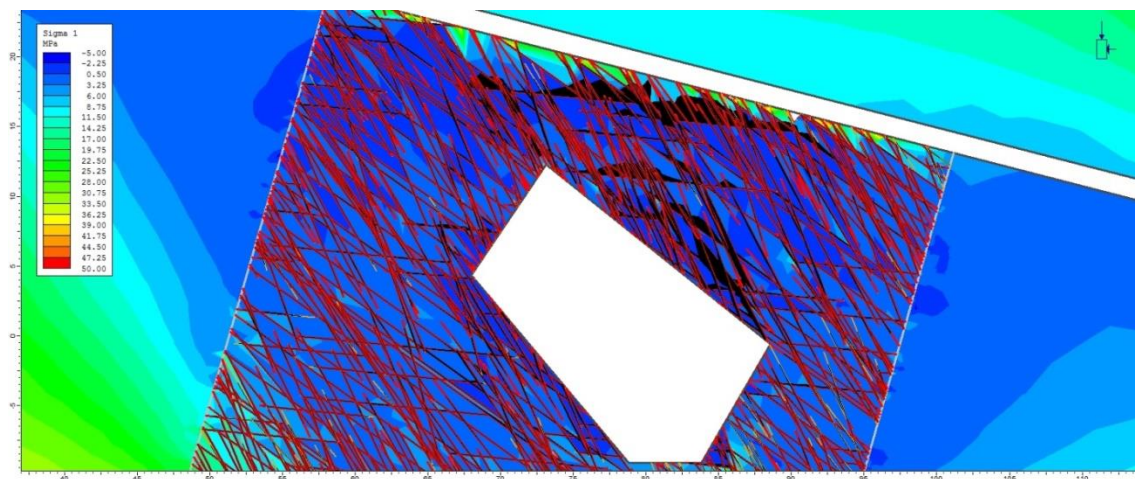


Figure B46 20m stope span overtopped open stope in EA3 with an 8m middling showing joint displacement in black and yielded joints indicated in red

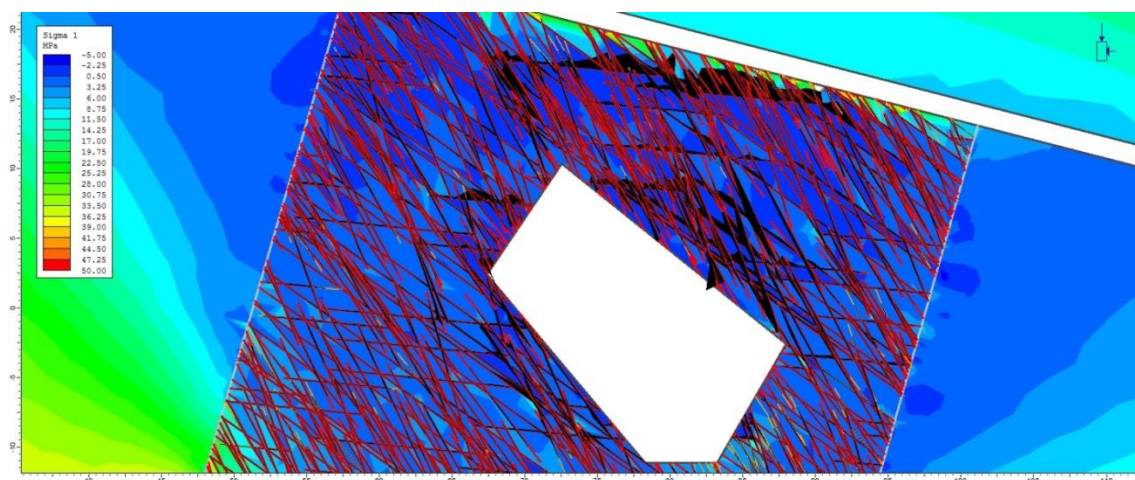


Figure B47 20m stope span overtopped open stope in EA3 with a 10m middling showing joint displacement in black and yielded joints indicated in red



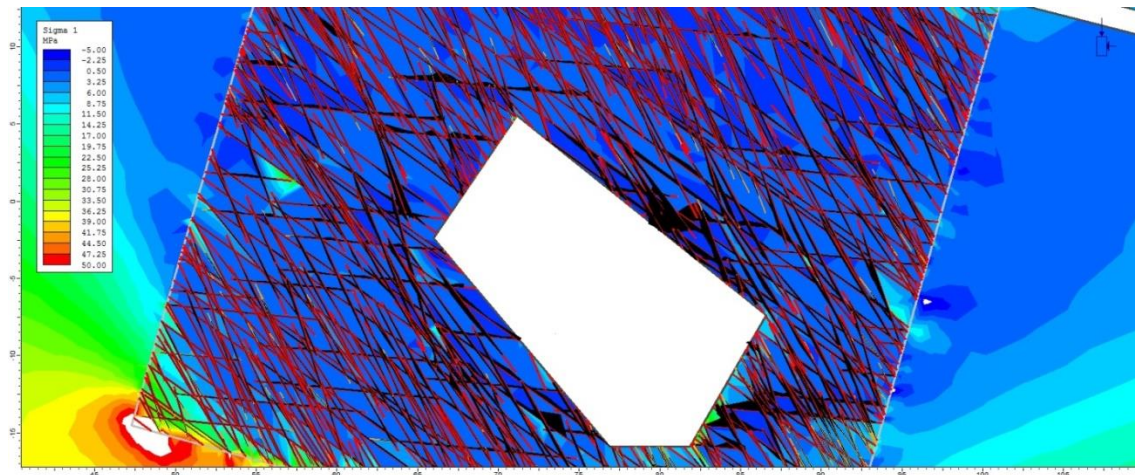


Figure B48 20m stope span overtopped open stope in EA3 with a 15m middling showing joint displacement in black and yielded joints indicated in red

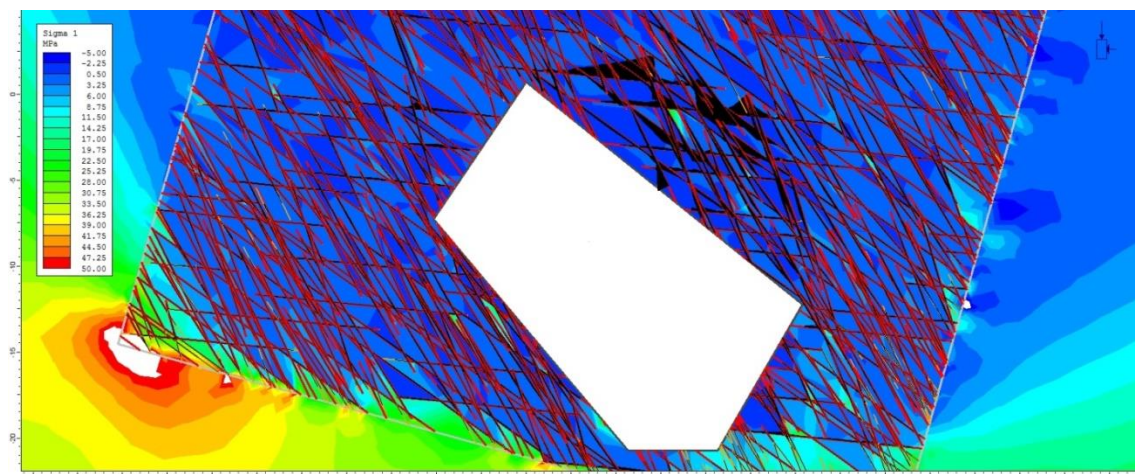


Figure B49 20m stope span overtopped open stope in EA3 with a 20m middling showing joint displacement in black and yielded joints indicated in red

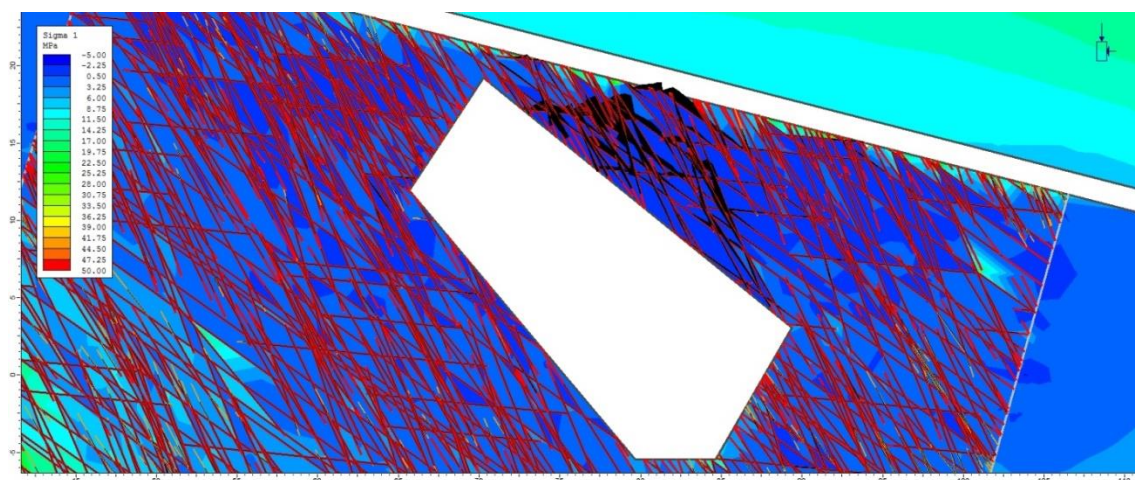


Figure B50 25m stope span overtopped open stope in EA3 with a 2m middling showing joint displacement in black and yielded joints indicated in red



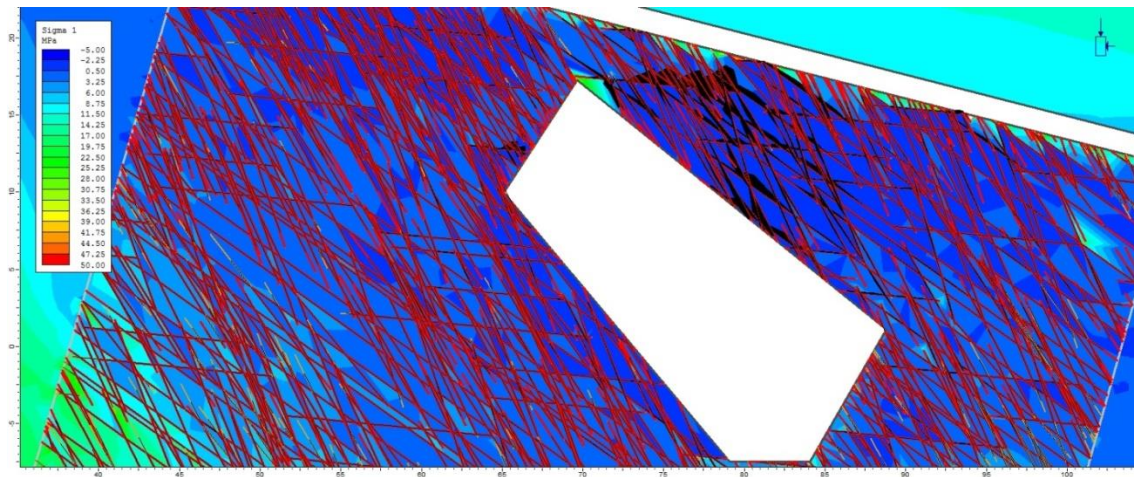


Figure B51 25m stope span overtopped open stope in EA3 with a 4m middling showing joint displacement in black and yielded joints indicated in red

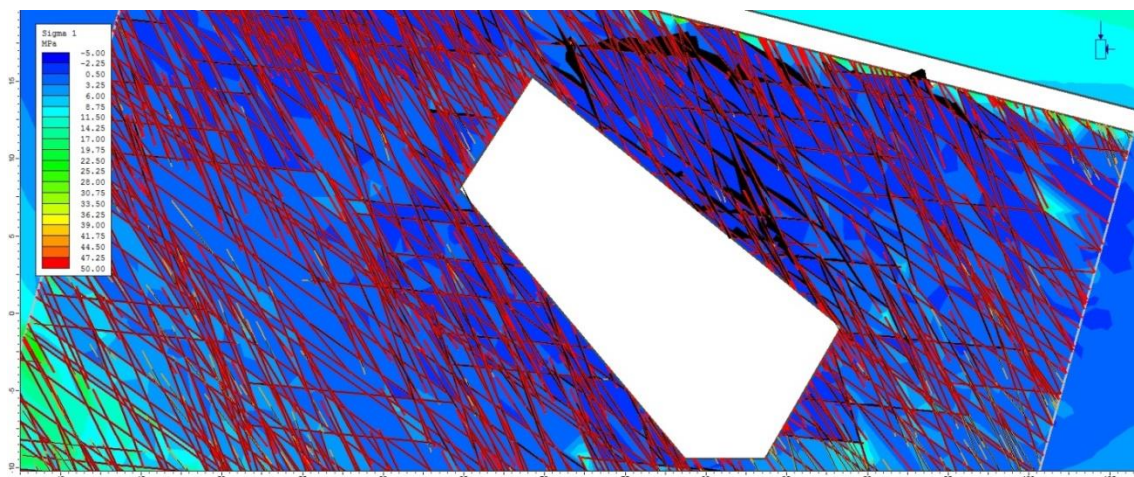


Figure B52 25m stope span overtopped open stope in EA3 with a 6m middling showing joint displacement in black and yielded joints indicated in red

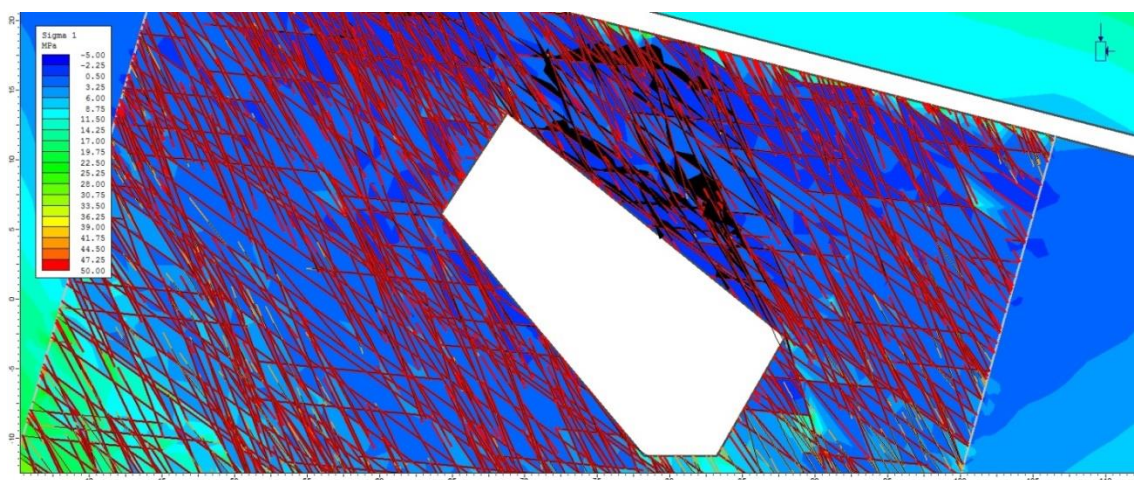


Figure B53 25m stope span overtopped open stope in EA3 with an 8m middling showing joint displacement in black and yielded joints indicated in red



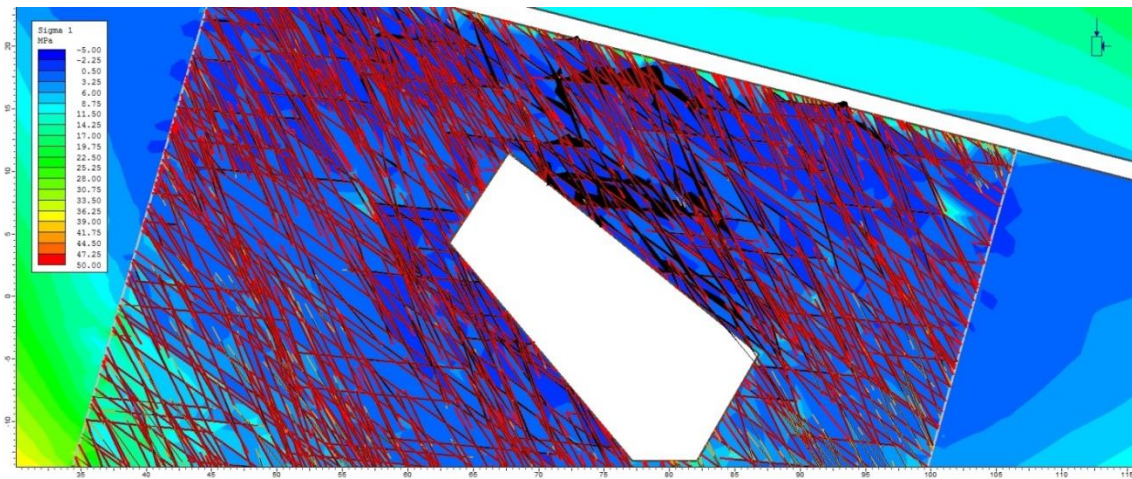


Figure B54 25m stope span overtopped open stope in EA3 with a 10m middling showing joint displacement in black and yielded joints indicated in red

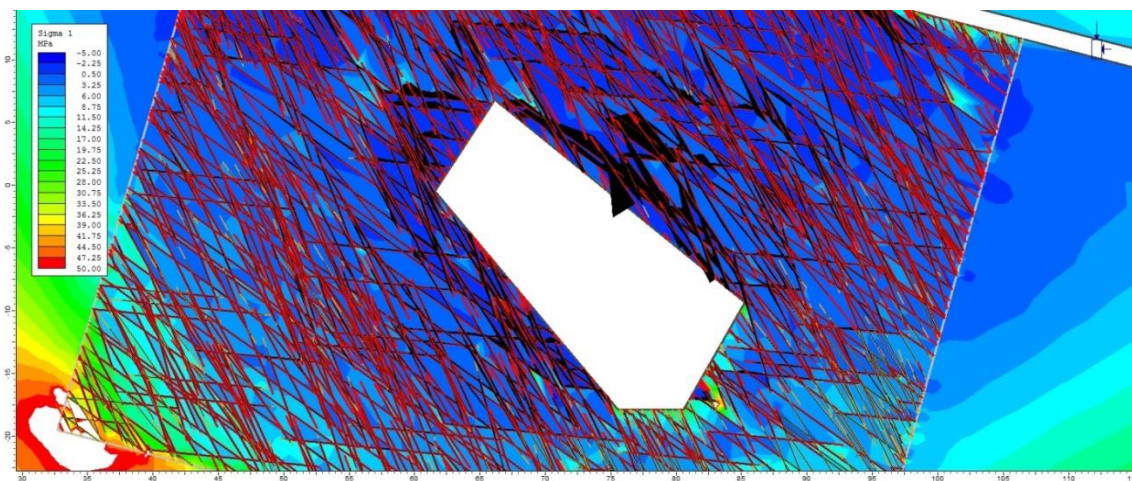


Figure B55 25m stope span overtopped open stope in EA3 with a 15m middling showing joint displacement in black and yielded joints indicated in red

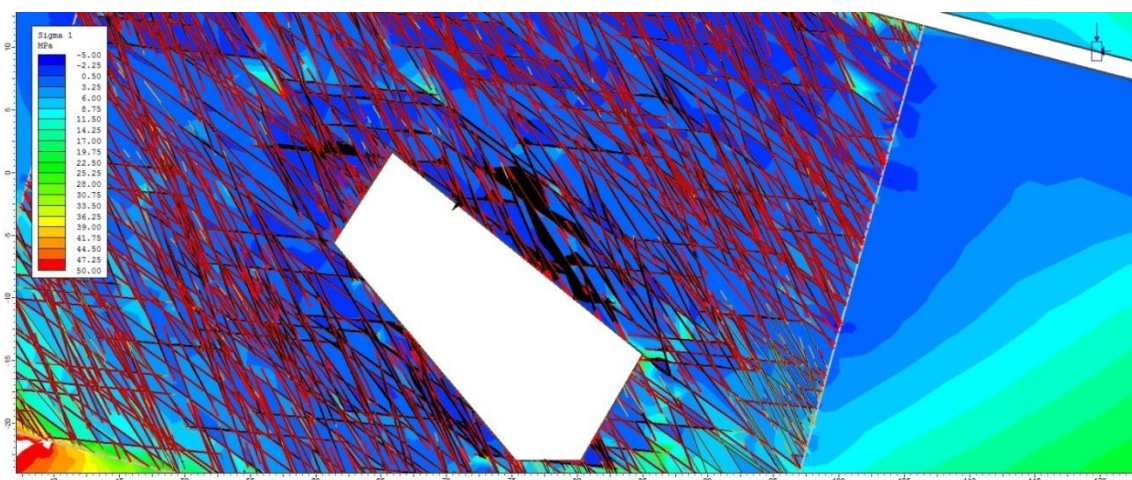


Figure B56 25m stope span overtopped open stope in EA3 with a 20m middling showing joint displacement in black and yielded joints indicated in red



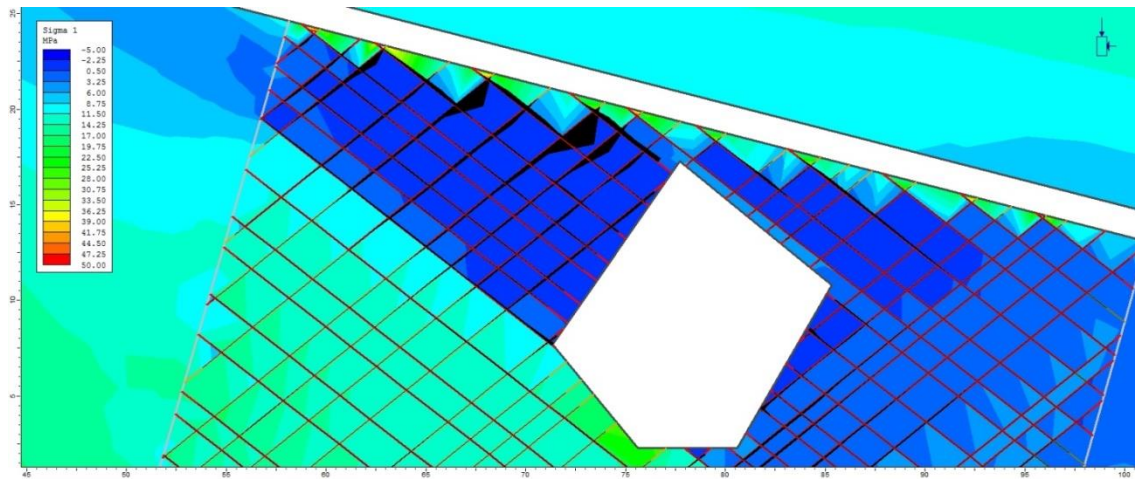


Figure B57 10m stope span overtopped open stope in EA1 with a 2m middling showing joint displacement in black and yielded joints indicated in red

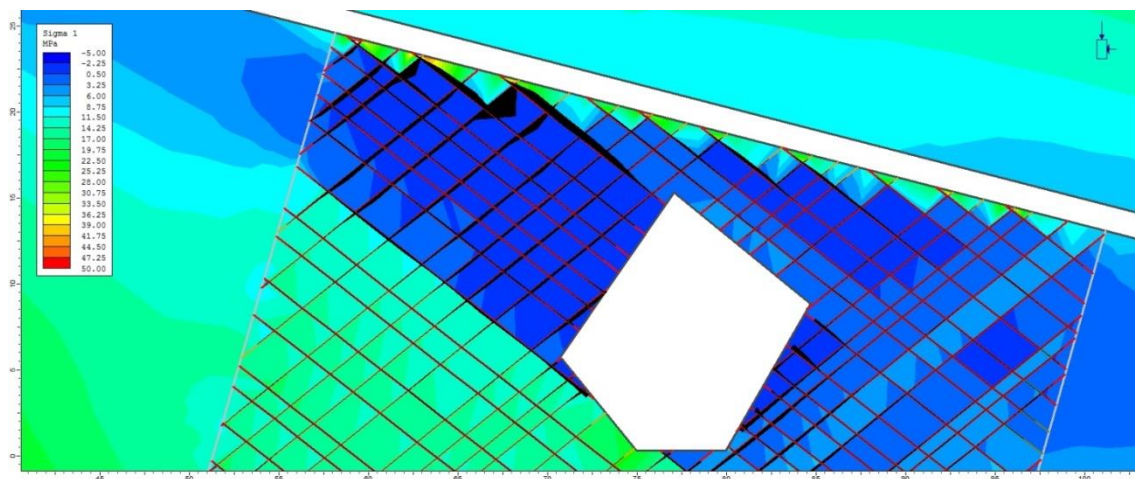


Figure B58 10m stope span overtopped open stope in EA1 with a 4m middling showing joint displacement in black and yielded joints indicated in red

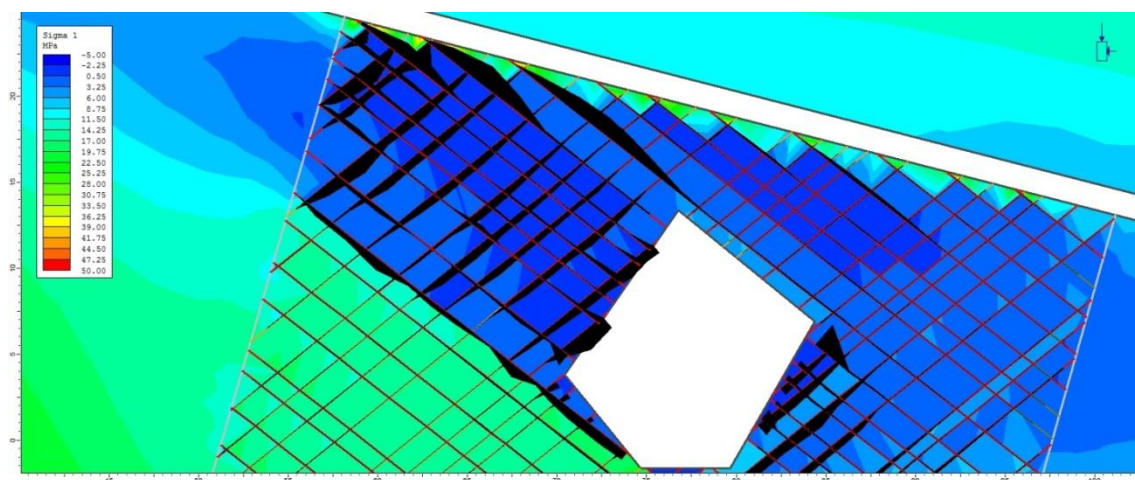


Figure B59 10m stope span overtopped open stope in EA1 with a 6m middling showing joint displacement in black and yielded joints indicated in red



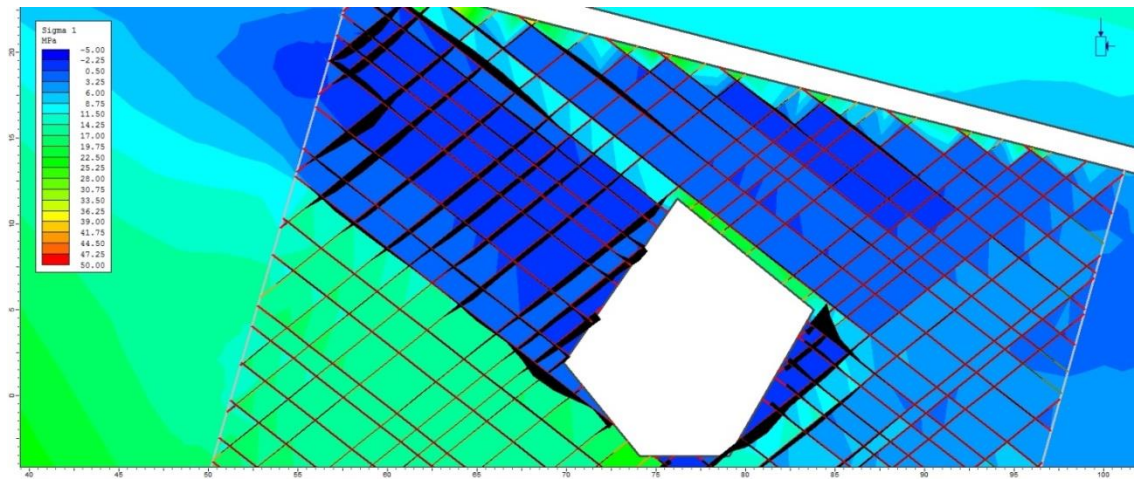


Figure B60 10m stope span overtopped open stope in EA1 with a 8m middling showing joint displacement in black and yielded joints indicated in red

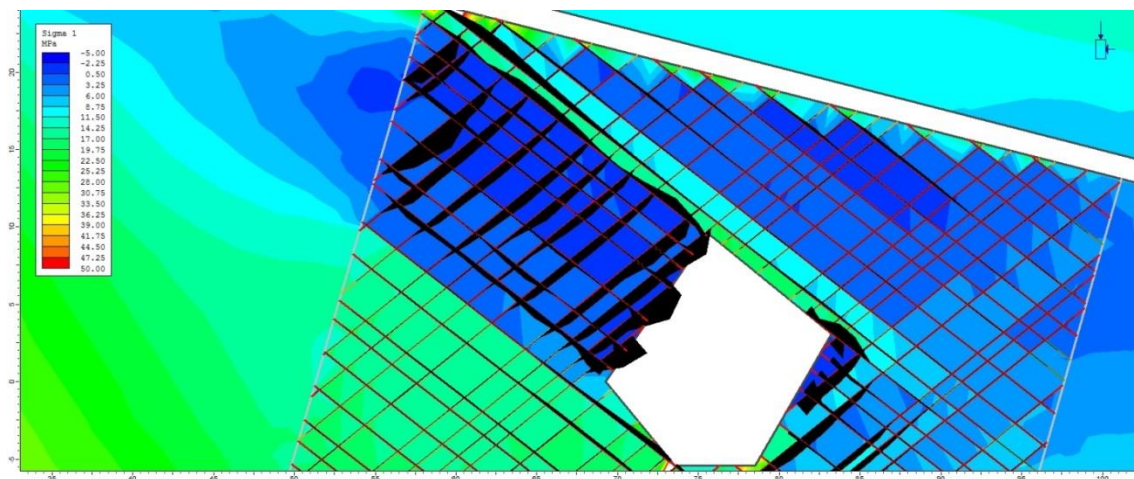


Figure B61 10m stope span overtopped open stope in EA1 with a 10m middling showing joint displacement in black and yielded joints indicated in red

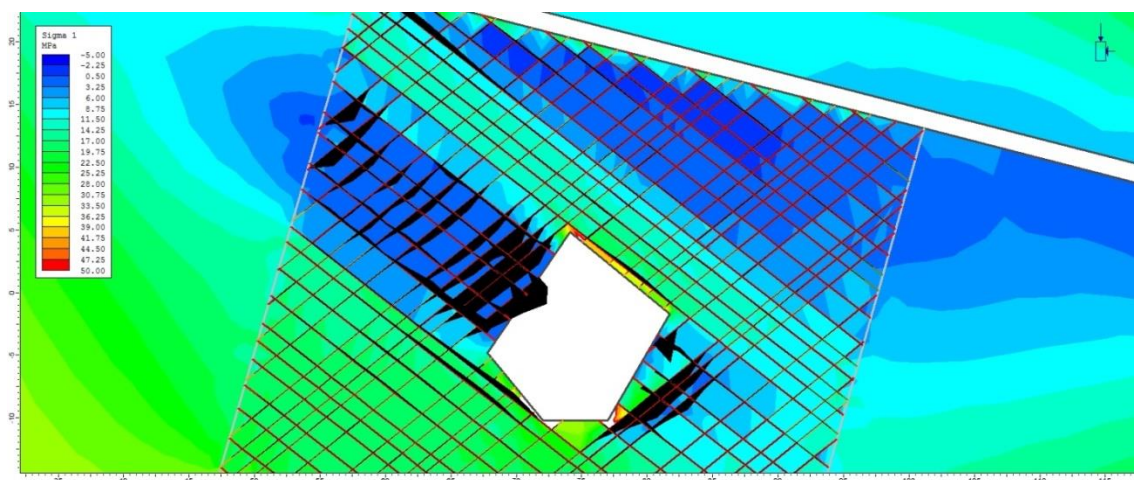


Figure B62 10m stope span overtopped open stope in EA1 with a 15m middling showing joint displacement in black and yielded joints indicated in red



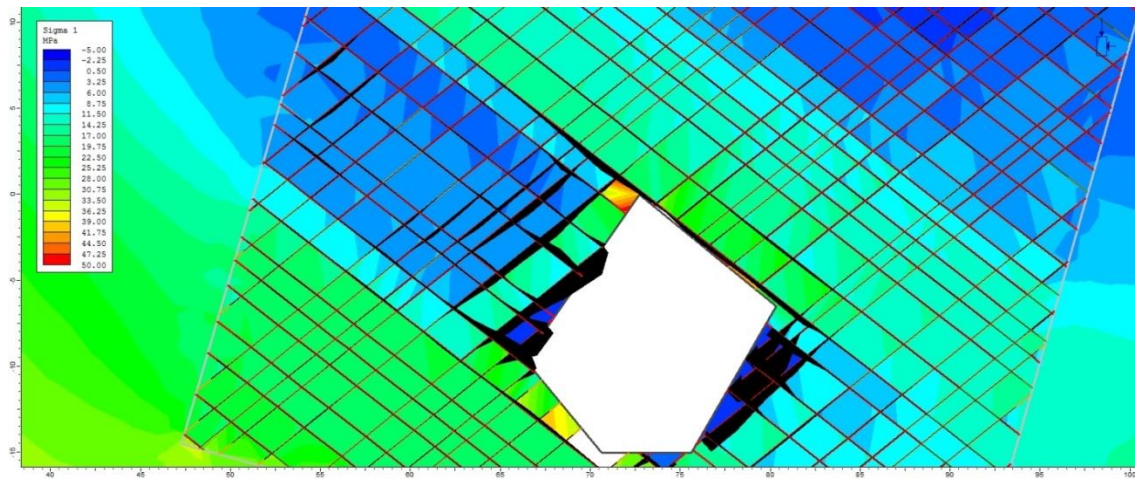


Figure B63 10m stope span overtopped open stope in EA1 with a 20m middling showing joint displacement in black and yielded joints indicated in red

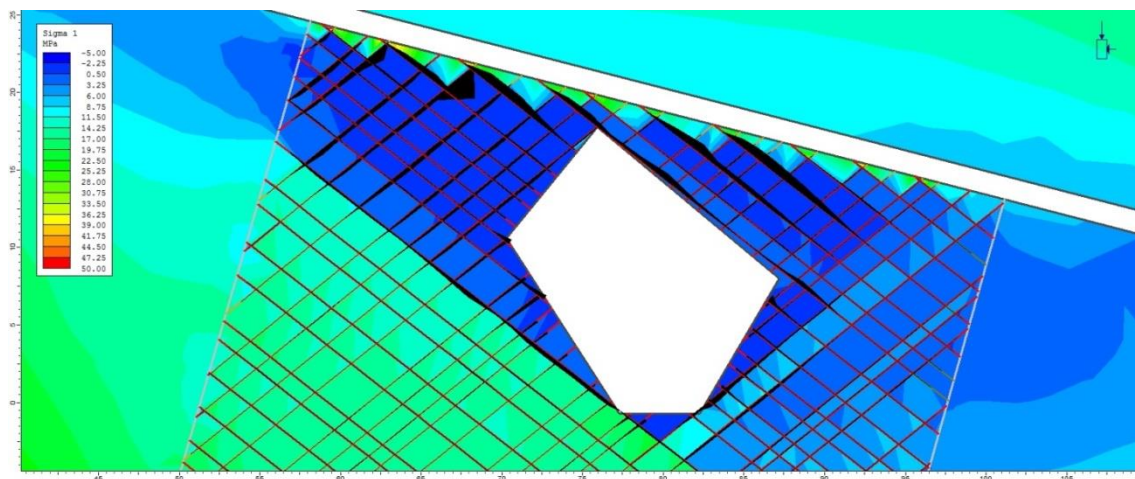


Figure B64 15m stope span overtopped open stope in EA1 with a 2m middling showing joint displacement in black and yielded joints indicated in red

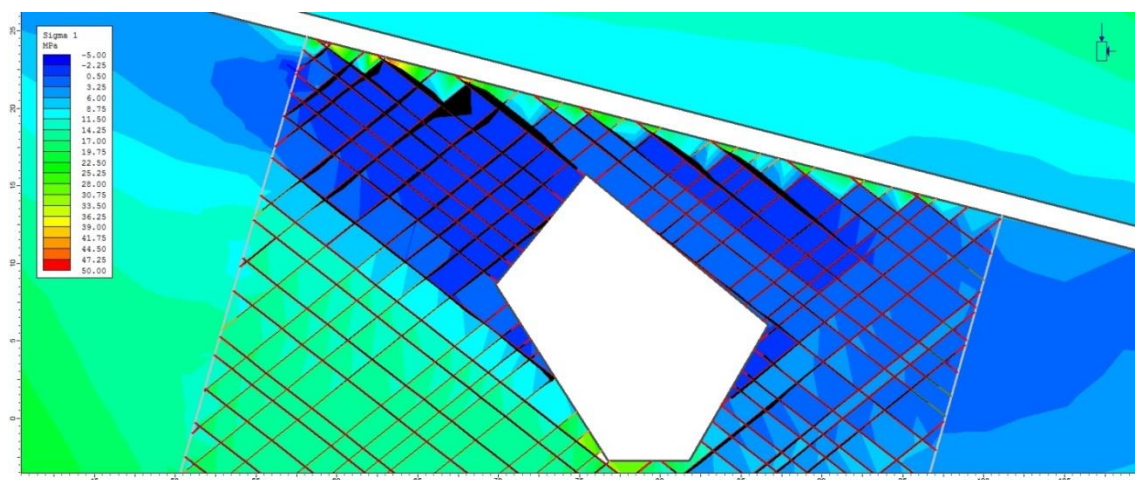


Figure B65 15m stope span overtopped open stope in EA1 with a 4m middling showing joint displacement in black and yielded joints indicated in red



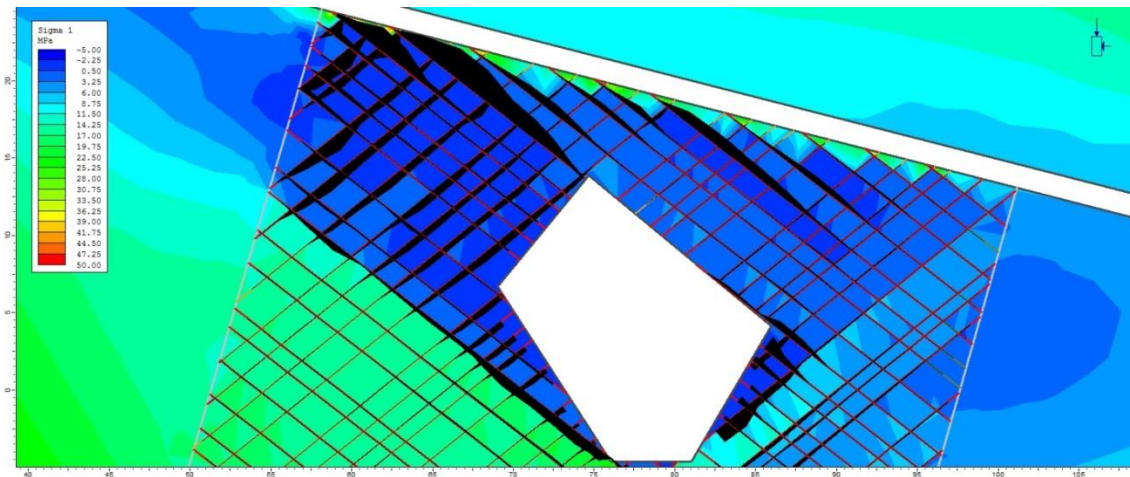


Figure B66 15m stope span overtopped open stope in EA1 with a 6m middling showing joint displacement in black and yielded joints indicated in red

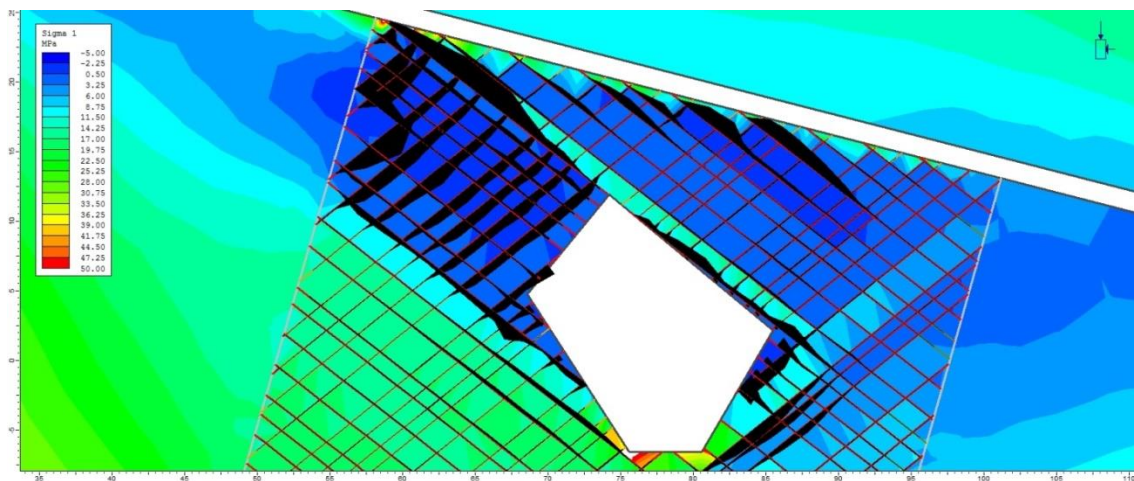


Figure B67 15m stope span overtopped open stope in EA1 with an 8m middling showing joint displacement in black and yielded joints indicated in red

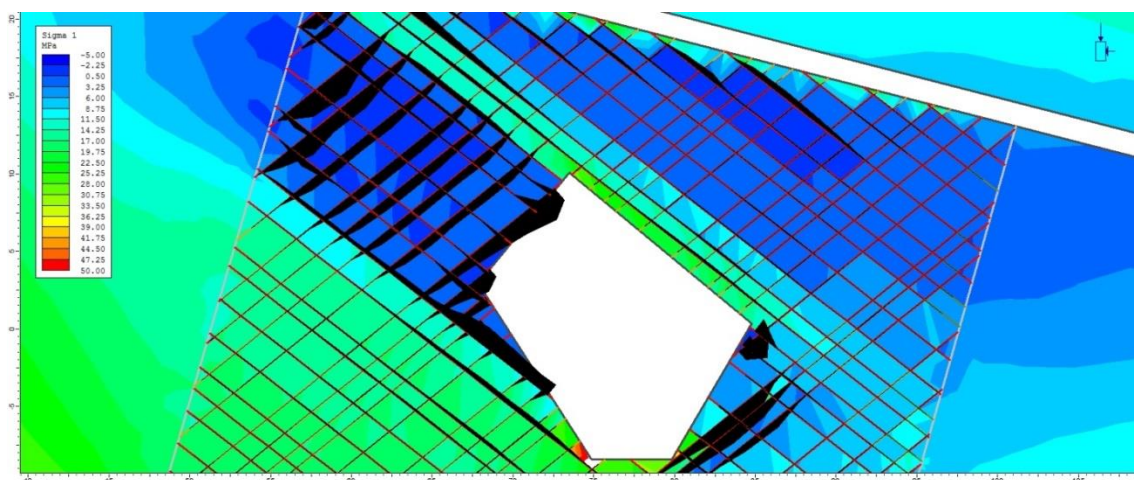


Figure B68 15m stope span overtopped open stope in EA1 with a 10m middling showing joint displacement in black and yielded joints indicated in red



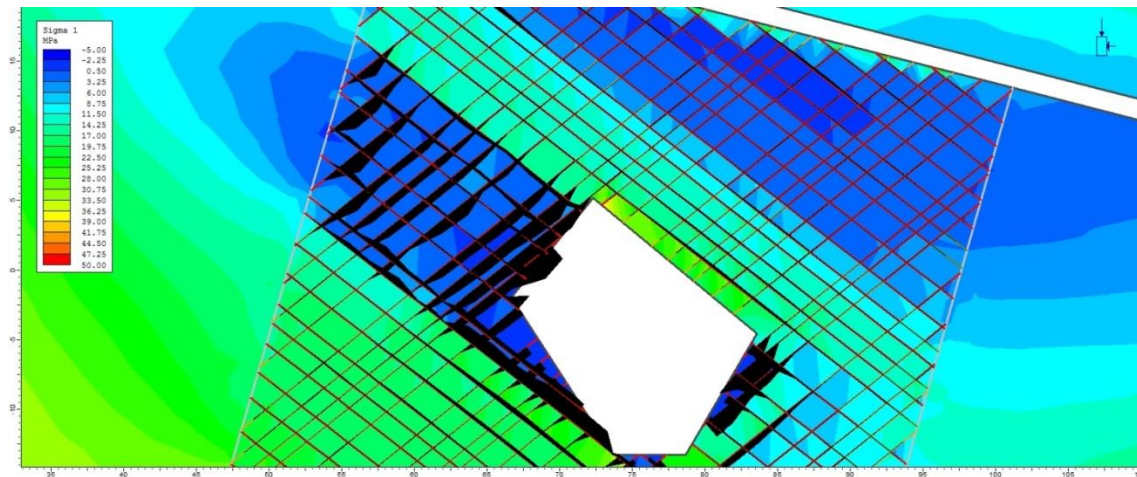


Figure B69 15m stope span overtopped open stope in EA1 with a 15m middling showing joint displacement in black and yielded joints indicated in red

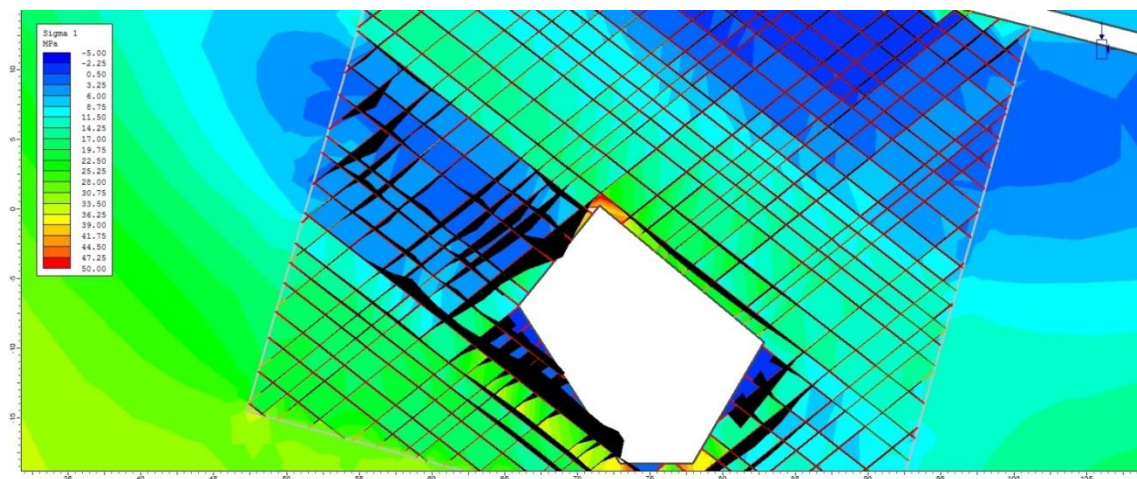


Figure B70 15m stope span overtopped open stope in EA1 with a 20m middling showing joint displacement in black and yielded joints indicated in red

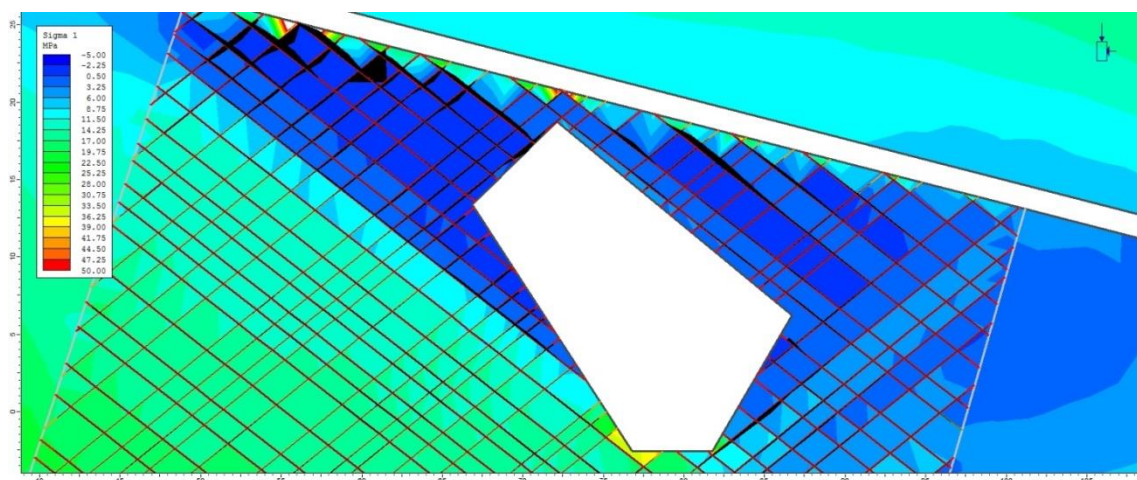


Figure B71 20m stope span overtopped open stope in EA1 with a 2m middling showing joint displacement in black and yielded joints indicated in red



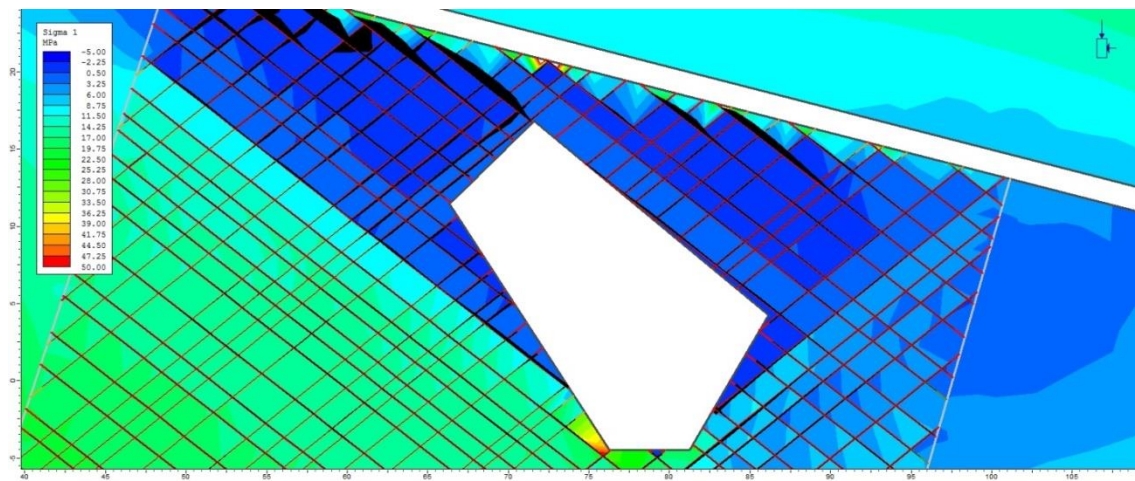


Figure B72 20m stope span overtopped open stope in EA1 with a 4m middling showing joint displacement in black and yielded joints indicated in red

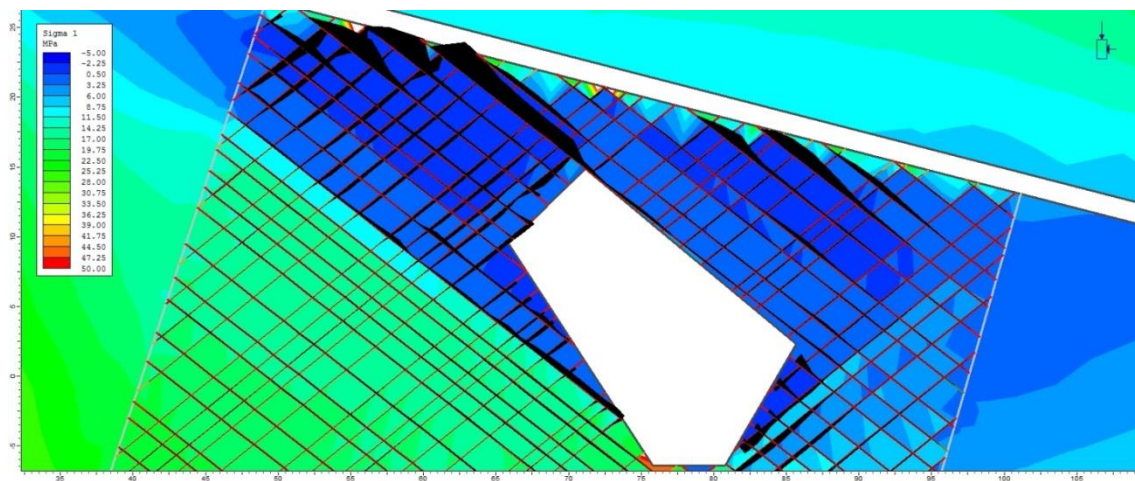


Figure B73 20m stope span overtopped open stope in EA1 with a 6m middling showing joint displacement in black and yielded joints indicated in red

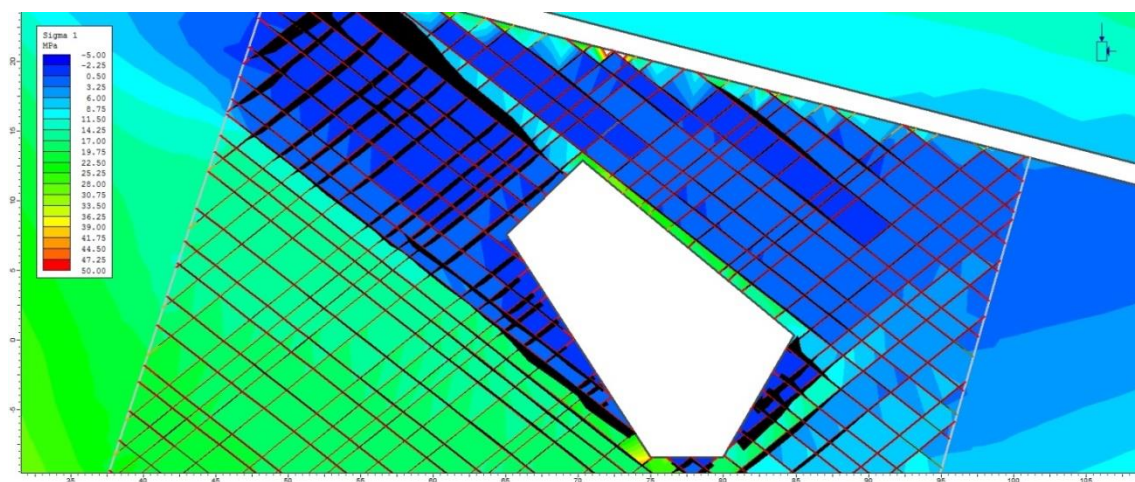


Figure B74 20m stope span overtopped open stope in EA1 with an 8m middling showing joint displacement in black and yielded joints indicated in red



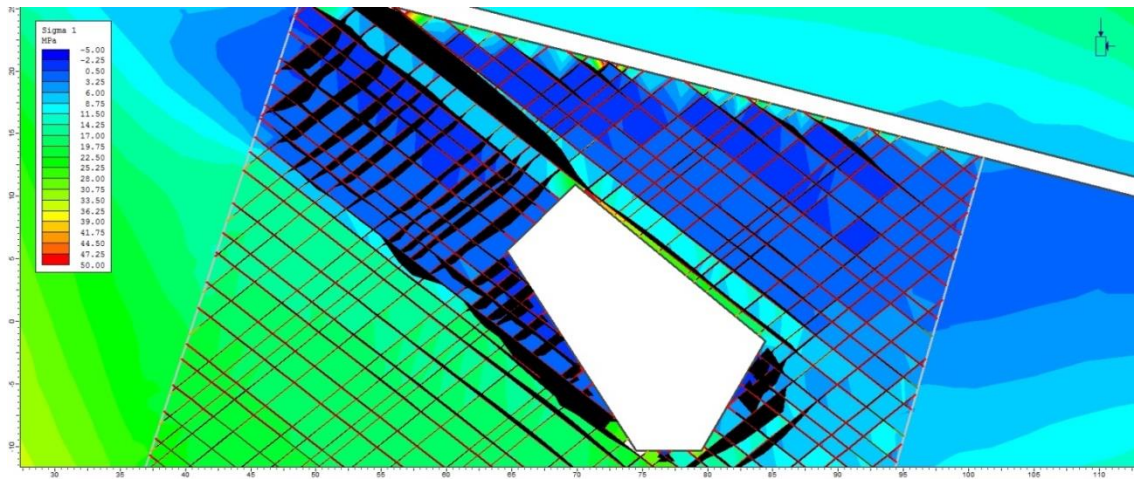


Figure B75 20m stope span overtopped open stope in EA1 with a 10m middling showing joint displacement in black and yielded joints indicated in red

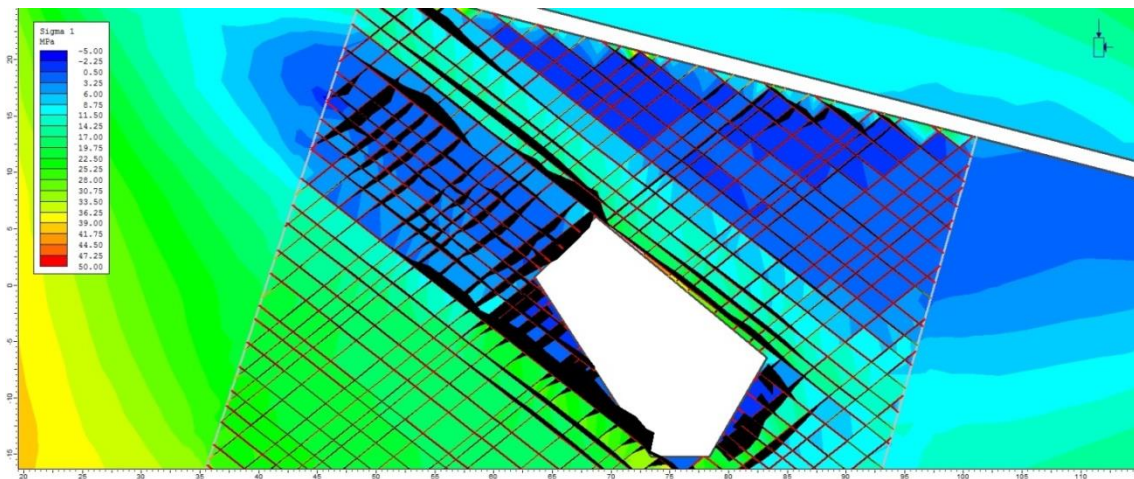


Figure B76 20m stope span overtopped open stope in EA1 with a 15m middling showing joint displacement in black and yielded joints indicated in red

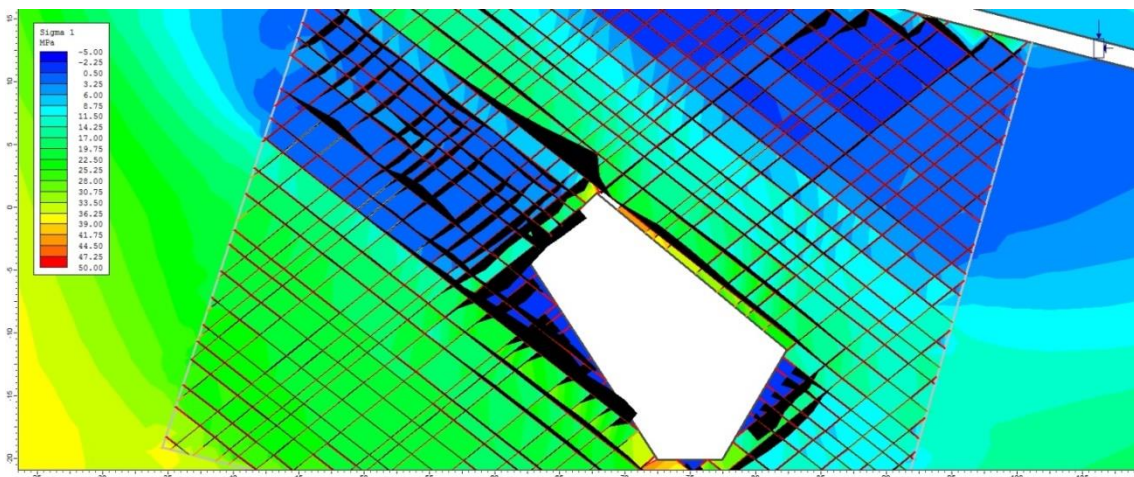


Figure B77 20m stope span overtopped open stope in EA1 with a 20m middling showing joint displacement in black and yielded joints indicated in red



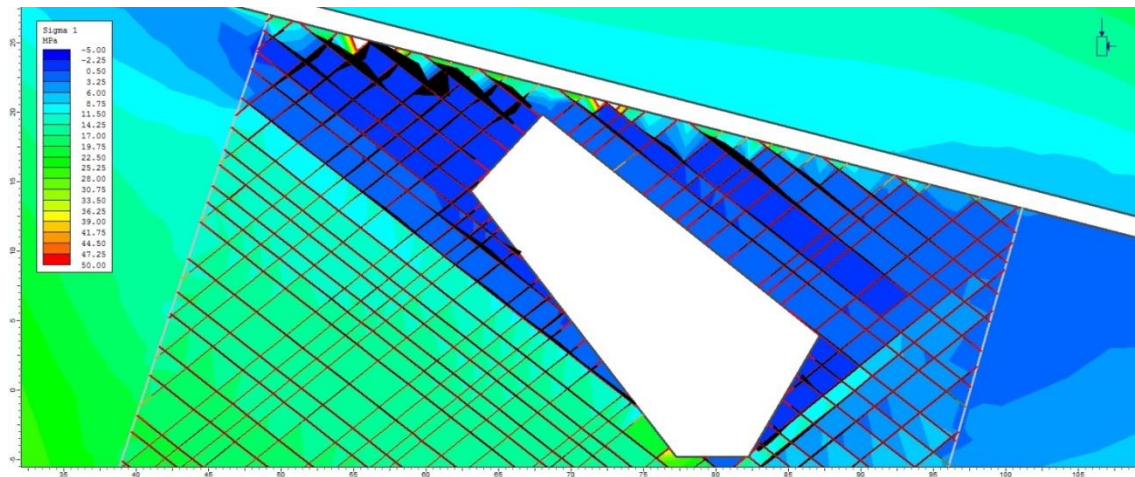


Figure B78 25m stope span overtopped open stope in EA1 with a 2m middling showing joint displacement in black and yielded joints indicated in red

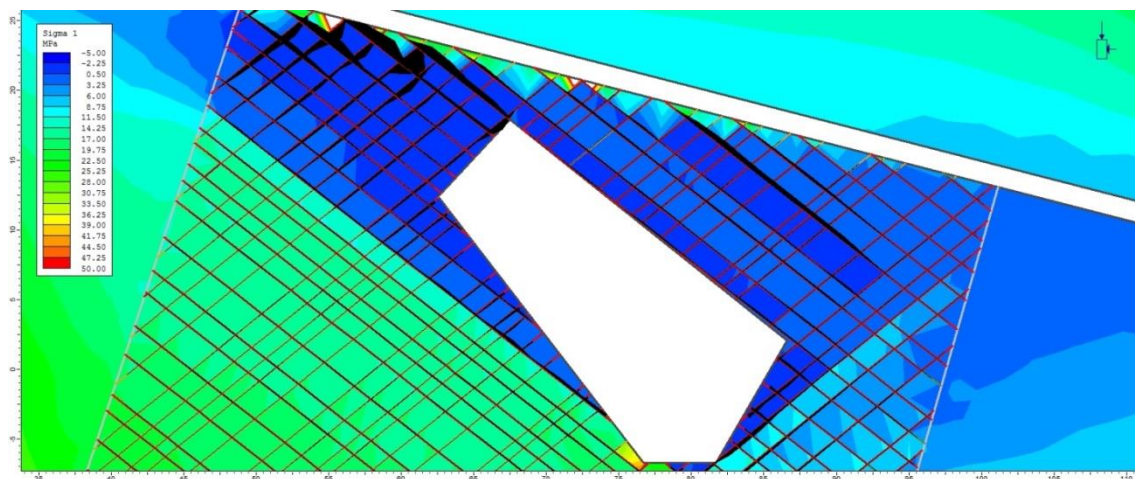


Figure B79 25m stope span overtopped open stope in EA1 with a 4m middling showing joint displacement in black and yielded joints indicated in red

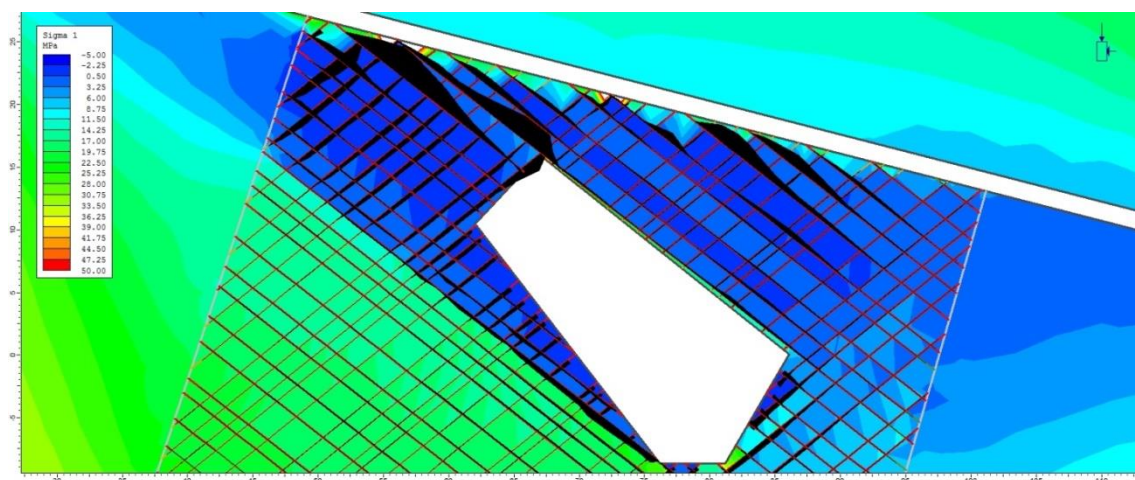


Figure B80 25m stope span overtopped open stope in EA1 with a 6m middling showing joint displacement in black and yielded joints indicated in red



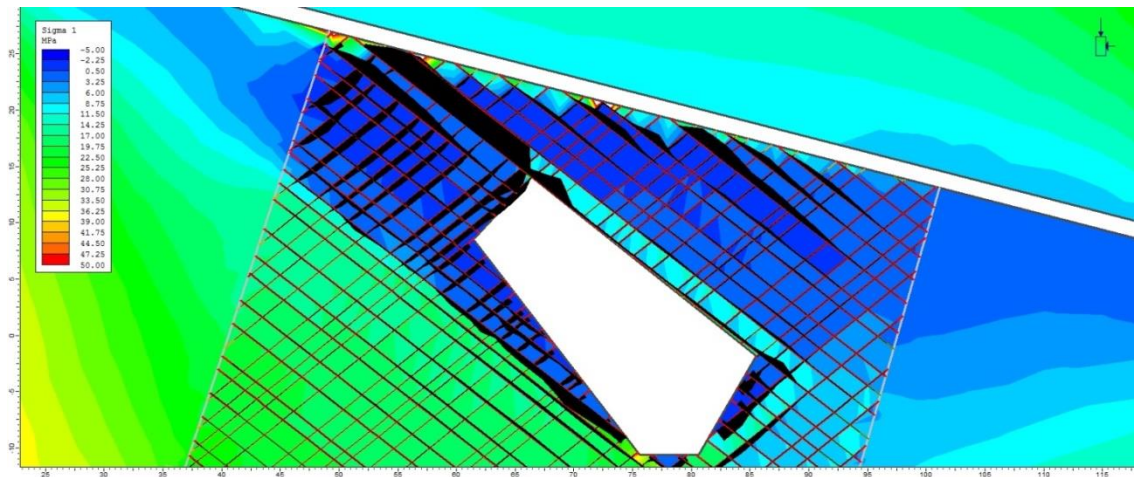


Figure B81 25m stope span overtopped open stope in EA1 with a 8m middling showing joint displacement in black and yielded joints indicated in red

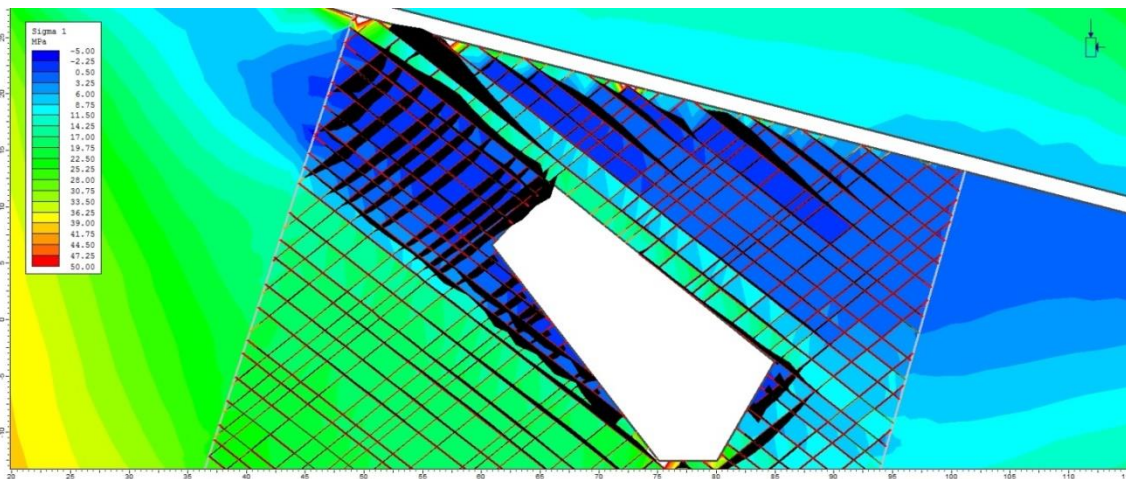


Figure B82 25m stope span overtopped open stope in EA1 with a 10m middling showing joint displacement in black and yielded joints indicated in red

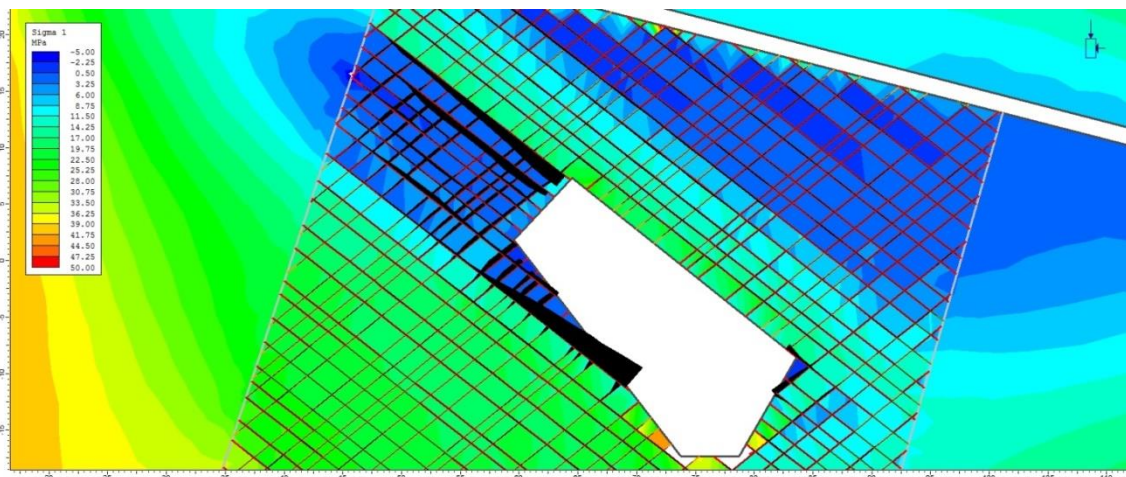
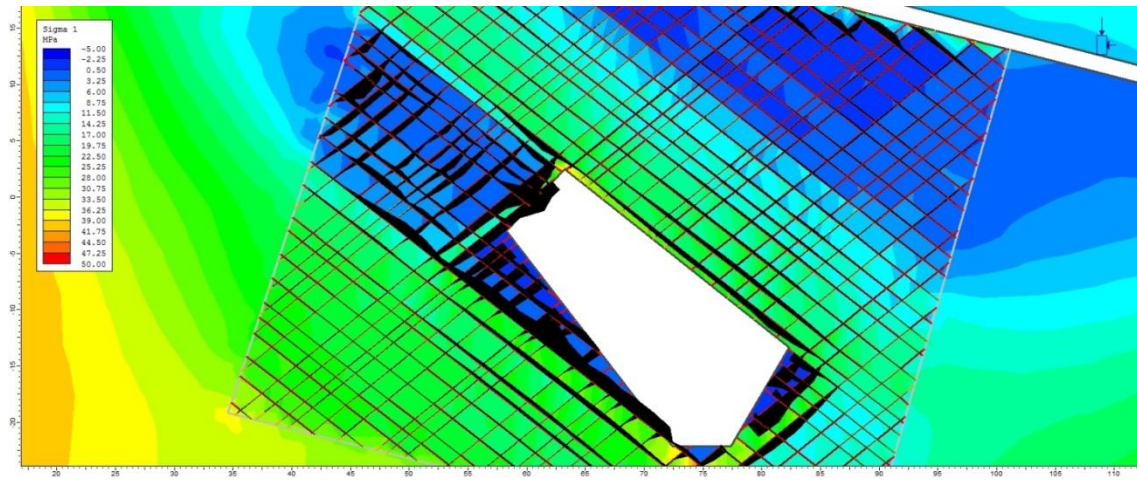


Figure B83 25m stope span overtopped open stope in EA1 with a 15m middling showing joint displacement in black and yielded joints indicated in red



## APPENDIX C

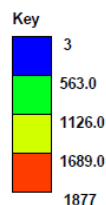
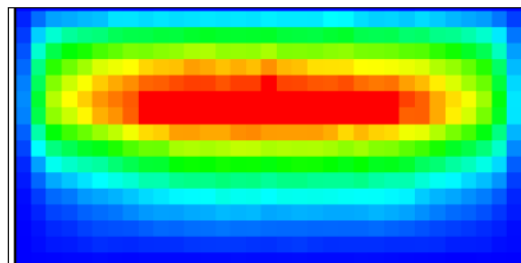
### Results of JBlock Modelling

#### Simulation Statistics

Total simulation area	120 067
Percent area that is a keyblock	71.6%
Total no. of keyblocks	529 300
Total no. of failed keyblocks	37 654
Average rockfalls per mining step	6.27
Average failure volume per mining step	2.44

#### Hazard Results

Zone	Label	Falls/1000m <sup>2</sup>	Injuries/1000m <sup>2</sup>
------	-------	--------------------------	-----------------------------



Distribution of keyblock falls

#### Excavation data:

Excavation dip	0.0
Excavation dip dir.	90.0
Excavation dip range	0.0
Excavation map y-dir	0.0
Dip stress (kPa)	0.0
Strike stress (kPa)	0.0
Rock density (kg/m <sup>3</sup> )	2700.0
Seismic acceleration m/s	0.00

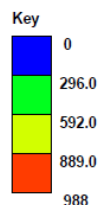
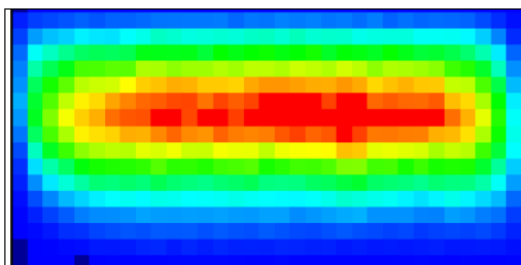
Figure C1 Simulation statistics for 10m stope span situated in EA1 jointsets with flat hangingwall

#### Simulation Statistics

Total simulation area	120 015
Percent area that is a keyblock	51.4%
Total no. of keyblocks	279 800
Total no. of failed keyblocks	19 411
Average rockfalls per mining step	3.23
Average failure volume per mining step	3.35

#### Hazard Results

Zone	Label	Falls/1000m <sup>2</sup>	Injuries/1000m <sup>2</sup>
------	-------	--------------------------	-----------------------------



Distribution of keyblock falls

#### Excavation data:

Excavation dip	45.0
Excavation dip dir.	90.0
Excavation dip range	0.0
Excavation map y-dir	0.0
Dip stress (kPa)	0.0
Strike stress (kPa)	0.0
Rock density (kg/m <sup>3</sup> )	2700.0
Seismic acceleration m/s	0.00

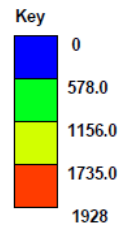
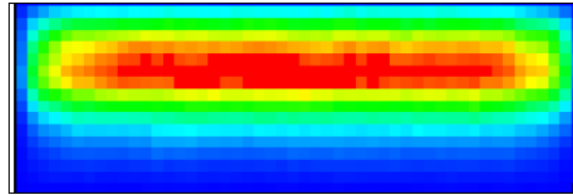
Figure C2 Simulation statistics for 10m stope span situated in EA1 jointsets with hangingwall dipping 45°

## Simulation Statistics

Total simulation area	180 126
Percent area that is a keyblock	59.8%
Total no. of keyblocks	876 200
Total no. of failed keyblocks	65 882
Average rockfalls per mining step	10.97
Average failure volume per mining step	3.49

## Hazard Results

Zone	Label	Falls/1000m <sup>2</sup>	Injuries/1000m <sup>2</sup>
------	-------	--------------------------	-----------------------------



Distribution of keyblock falls

## Excavation data:

Excavation dip	0.0
Excavation dip dir.	90.0
Excavation dip range	0.0
Excavation map y-dir	0.0
Dip stress (kPa)	0.0
Strike stress (kPa)	0.0
Rock density (kg/m <sup>3</sup> )	2700.0
Seismic acceleration m/s	0.00

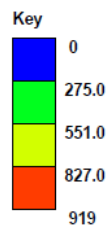
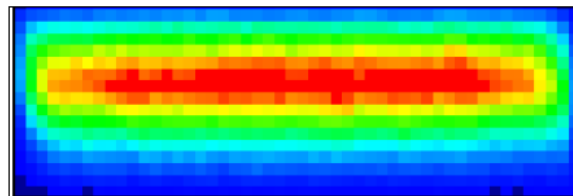
Figure C3 Simulation statistics for 15m stope span in EA1 jointsets with flat hangingwall

## Simulation Statistics

Total simulation area	180 014
Percent area that is a keyblock	47.6%
Total no. of keyblocks	466 400
Total no. of failed keyblocks	33 948
Average rockfalls per mining step	5.66
Average failure volume per mining step	4.54

## Hazard Results

Zone	Label	Falls/1000m <sup>2</sup>	Injuries/1000m <sup>2</sup>
------	-------	--------------------------	-----------------------------



Distribution of keyblock falls

## Excavation data:

Excavation dip	45.0
Excavation dip dir.	90.0
Excavation dip range	0.0
Excavation map y-dir	0.0
Dip stress (kPa)	0.0
Strike stress (kPa)	0.0
Rock density (kg/m <sup>3</sup> )	2700.0
Seismic acceleration m/s	0.00

Figure C4 Simulation statistics for 15m stope span in EA1 jointsets with hangingwall dipping 45°

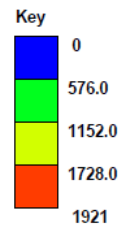
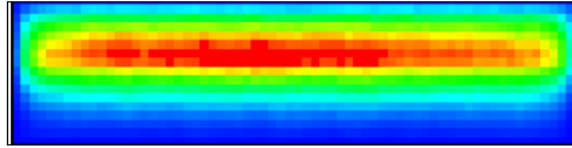


## Simulation Statistics

Total simulation area	240 031
Percent area that is a keyblock	77.1%
Total no. of keyblocks	1 096 600
Total no. of failed keyblocks	78 899
Average rockfalls per mining step	13.15
Average failure volume per mining step	5.19

## Hazard Results

Zone	Label	Falls/1000m <sup>2</sup>	Injuries/1000m <sup>2</sup>
------	-------	--------------------------	-----------------------------



Distribution of keyblock falls

Excavation data:

Excavation dip	0.0
Excavation dip dir.	90.0
Excavation dip range	0.0
Excavation map y-dir	0.0
Dip stress (kPa)	0.0
Strike stress (kPa)	0.0
Rock density (kg/m <sup>3</sup> )	2700.0
Seismic acceleration m/s	0.00

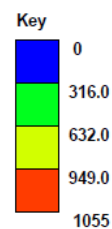
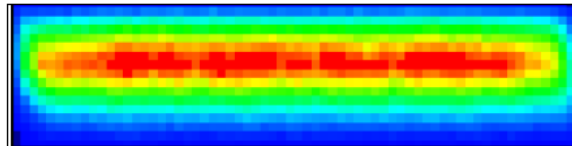
Figure C5 Simulation statistics for 20m stope span in EA1 jointsets with flat hangingwall

## Simulation Statistics

Total simulation area	240 001
Percent area that is a keyblock	48.6%
Total no. of keyblocks	607 100
Total no. of failed keyblocks	43 928
Average rockfalls per mining step	7.32
Average failure volume per mining step	7.26

## Hazard Results

Zone	Label	Falls/1000m <sup>2</sup>	Injuries/1000m <sup>2</sup>
------	-------	--------------------------	-----------------------------



Distribution of keyblock falls

Excavation data:

Excavation dip	45.0
Excavation dip dir.	90.0
Excavation dip range	0.0
Excavation map y-dir	0.0
Dip stress (kPa)	0.0
Strike stress (kPa)	0.0
Rock density (kg/m <sup>3</sup> )	2700.0
Seismic acceleration m/s	0.00

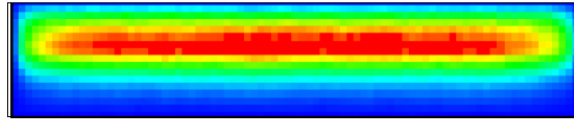
Figure C6 Simulation statistics for 20m stope span in EA1 jointsets with hangingwall dipping 45°

## Simulation Statistics

Total simulation area	301 261
Percent area that is a keyblock	75.0%
Total no. of keyblocks	1 500 300
Total no. of failed keyblocks	108 527
Average rockfalls per mining step	18.08
Average failure volume per mining step	7.24

## Hazard Results

Zone	Label	Falls/1000m <sup>2</sup>	Injuries/1000m <sup>2</sup>
------	-------	--------------------------	-----------------------------



Distribution of keyblock falls

## Excavation data:

Excavation dip	0.0
Excavation dip dir.	90.0
Excavation dip range	0.0
Excavation map y-dir	0.0
Dip stress (kPa)	0.0
Strike stress (kPa)	0.0
Rock density (kg/m <sup>3</sup> )	2700.0
Seismic acceleration m/s	0.00

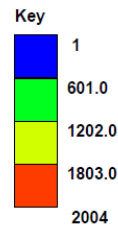


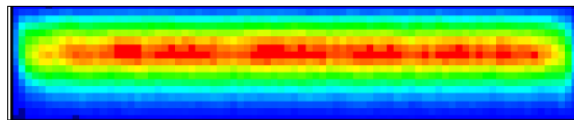
Figure C7 Simulation statistics for 25m stope span in EA1 jointsets with flat hangingwall

## Simulation Statistics

Total simulation area	301 214
Percent area that is a keyblock	48.1%
Total no. of keyblocks	748 500
Total no. of failed keyblocks	54 688
Average rockfalls per mining step	9.11
Average failure volume per mining step	9.22

## Hazard Results

Zone	Label	Falls/1000m <sup>2</sup>	Injuries/1000m <sup>2</sup>
------	-------	--------------------------	-----------------------------



Distribution of keyblock falls

## Excavation data:

Excavation dip	45.0
Excavation dip dir.	90.0
Excavation dip range	0.0
Excavation map y-dir	0.0
Dip stress (kPa)	0.0
Strike stress (kPa)	0.0
Rock density (kg/m <sup>3</sup> )	2700.0
Seismic acceleration m/s	0.00

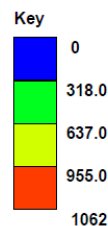


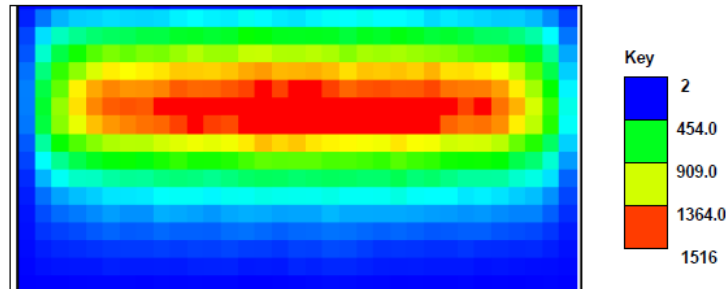
Figure C8 Simulation statistics for 25m stope span in EA1 jointsets with hangingwall dipping 45°

## Simulation Statistics

Total simulation area	120 153
Percent area that is a keyblock	58.6%
Total no. of keyblocks	498 700
Total no. of failed keyblocks	34 192
Average rockfalls per mining step	5.69
Average failure volume per mining step	1.52

## Hazard Results

Zone	Label	Falls/1000m <sup>2</sup>	Injuries/1000m <sup>2</sup>
------	-------	--------------------------	-----------------------------



Distribution of keyblock falls

## Excavation data:

Excavation dip	0.0
Excavation dip dir.	90.0
Excavation dip range	0.0
Excavation map y-dir	0.0
Dip stress (kPa)	0.0
Strike stress (kPa)	0.0
Rock density (kg/m <sup>3</sup> )	2700.0
Seismic acceleration m/s	0.00

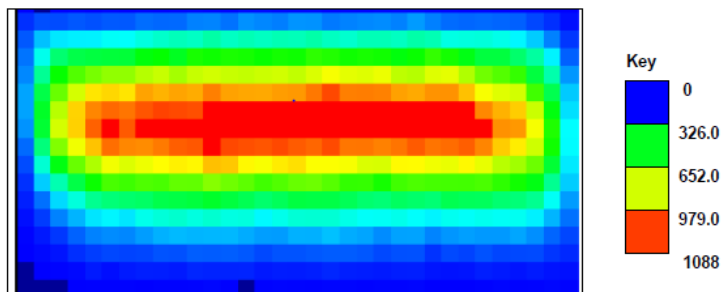
Figure C9 Simulation statistics for 10m stope span in EA3 jointsets with flat hangingwall

## Simulation Statistics

Total simulation area	120 018
Percent area that is a keyblock	46.7%
Total no. of keyblocks	328 800
Total no. of failed keyblocks	23 762
Average rockfalls per mining step	3.96
Average failure volume per mining step	3.65

## Hazard Results

Zone	Label	Falls/1000m <sup>2</sup>	Injuries/1000m <sup>2</sup>
------	-------	--------------------------	-----------------------------



Distribution of keyblock falls

## Excavation data:

Excavation dip	45.0
Excavation dip dir.	90.0
Excavation dip range	0.0
Excavation map y-dir	0.0
Dip stress (kPa)	0.0
Strike stress (kPa)	0.0
Rock density (kg/m <sup>3</sup> )	2700.0
Seismic acceleration m/s	0.00

Figure C10 Simulation statistics for 10m stope span in EA3 jointsets with hangingwall dipping 45°

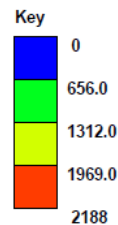
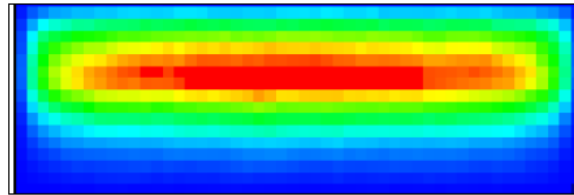


## Simulation Statistics

Total simulation area	180 130
Percent area that is a keyblock	71.6%
Total no. of keyblocks	795 300
Total no. of failed keyblocks	58 051
Average rockfalls per mining step	9.67
Average failure volume per mining step	4.23

## Hazard Results

Zone	Label	Falls/1000m <sup>2</sup>	Injuries/1000m <sup>2</sup>
------	-------	--------------------------	-----------------------------



Distribution of keyblock falls

## Excavation data:

Excavation dip	0.0
Excavation dip dir.	90.0
Excavation dip range	0.0
Excavation map y-dir	0.0
Dip stress (kPa)	0.0
Strike stress (kPa)	0.0
Rock density (kg/m <sup>3</sup> )	2700.0
Seismic acceleration m/s	0.00

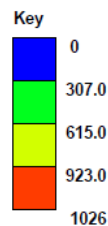
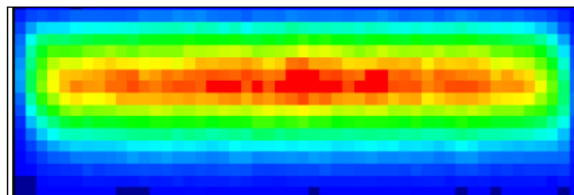
Figure C11 Simulation statistics for 15m stope span in EA3 jointsets with flat hangingwall

## Simulation Statistics

Total simulation area	180 030
Percent area that is a keyblock	54.2%
Total no. of keyblocks	448 000
Total no. of failed keyblocks	32 116
Average rockfalls per mining step	5.35
Average failure volume per mining step	5.43

## Hazard Results

Zone	Label	Falls/1000m <sup>2</sup>	Injuries/1000m <sup>2</sup>
------	-------	--------------------------	-----------------------------



Distribution of keyblock falls

## Excavation data:

Excavation dip	45.0
Excavation dip dir.	90.0
Excavation dip range	0.0
Excavation map y-dir	0.0
Dip stress (kPa)	0.0
Strike stress (kPa)	0.0
Rock density (kg/m <sup>3</sup> )	2700.0
Seismic acceleration m/s	0.00

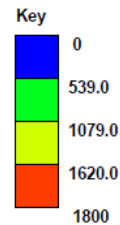
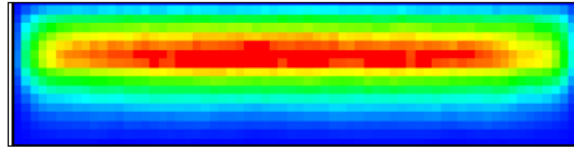
Figure C12 Simulation statistics for 15m stope span in EA3 jointsets with hangingwall dipping 45°

## Simulation Statistics

Total simulation area	240 507
Percent area that is a keyblock	69.5%
Total no. of keyblocks	968 800
Total no. of failed keyblocks	70 134
Average rockfalls per mining step	11.66
Average failure volume per mining step	5.44

## Hazard Results

Zone	Label	Falls/1000m <sup>2</sup>	Injuries/1000m <sup>2</sup>
------	-------	--------------------------	-----------------------------



Distribution of keyblock falls

Excavation data:

Excavation dip	0.0
Excavation dip dir.	90.0
Excavation dip range	0.0
Excavation map y-dir	0.0
Dip stress (kPa)	0.0
Strike stress (kPa)	0.0
Rock density (kg/m <sup>3</sup> )	2700.0
Seismic acceleration m/s	0.00

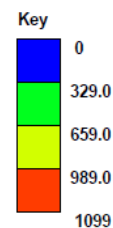
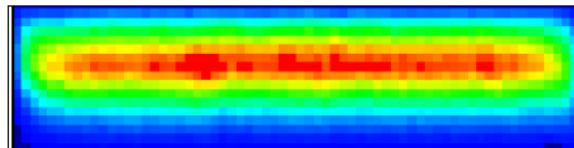
Figure C13 Simulation statistics for 20m stope span in EA3 jointsets with flat hangingwall

## Simulation Statistics

Total simulation area	240 081
Percent area that is a keyblock	49.9%
Total no. of keyblocks	617 200
Total no. of failed keyblocks	44 806
Average rockfalls per mining step	7.47
Average failure volume per mining step	7.28

## Hazard Results

Zone	Label	Falls/1000m <sup>2</sup>	Injuries/1000m <sup>2</sup>
------	-------	--------------------------	-----------------------------



Distribution of keyblock falls

Excavation data:

Excavation dip	45.0
Excavation dip dir.	90.0
Excavation dip range	0.0
Excavation map y-dir	0.0
Dip stress (kPa)	0.0
Strike stress (kPa)	0.0
Rock density (kg/m <sup>3</sup> )	2700.0
Seismic acceleration m/s	0.00

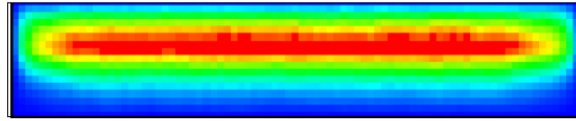
Figure C14 Simulation statistics for 20m stope span in EA3 jointsets with hangingwall dipping 45°

## Simulation Statistics

Total simulation area	301 357
Percent area that is a keyblock	73.9%
Total no. of keyblocks	1 209 600
Total no. of failed keyblocks	85 912
Average rockfalls per mining step	14.31
Average failure volume per mining step	6.69

## Hazard Results

Zone	Label	Falls/1000m <sup>2</sup>	Injuries/1000m <sup>2</sup>
------	-------	--------------------------	-----------------------------



Distribution of keyblock falls

## Excavation data:

Excavation dip	0.0
Excavation dip dir.	90.0
Excavation dip range	0.0
Excavation map y-dir	0.0
Dip stress (kPa)	0.0
Strike stress (kPa)	0.0
Rock density (kg/m3)	2700.0
Seismic acceleration m/s	0.00

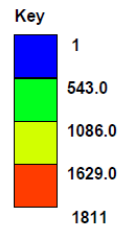


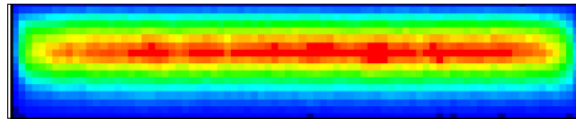
Figure C15 Simulation statistics for 25m stope span in EA3 jointsets with flat hangingwall

## Simulation Statistics

Total simulation area	301 203
Percent area that is a keyblock	47.1%
Total no. of keyblocks	733 800
Total no. of failed keyblocks	55 108
Average rockfalls per mining step	9.18
Average failure volume per mining step	9.19

## Hazard Results

Zone	Label	Falls/1000m <sup>2</sup>	Injuries/1000m <sup>2</sup>
------	-------	--------------------------	-----------------------------



Distribution of keyblock falls

## Excavation data:

Excavation dip	45.0
Excavation dip dir.	90.0
Excavation dip range	0.0
Excavation map y-dir	0.0
Dip stress (kPa)	0.0
Strike stress (kPa)	0.0
Rock density (kg/m3)	2700.0
Seismic acceleration m/s	0.00

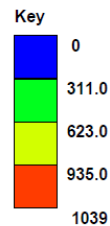


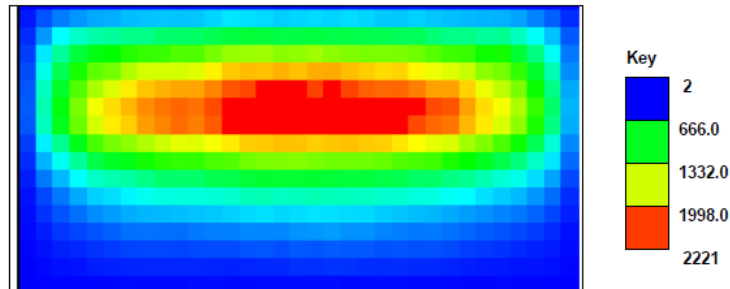
Figure C16 Simulation statistics for 25m stope span in EA3 jointsets with hangingwall dipping 45°

## Simulation Statistics

Total simulation area	120 004
Percent area that is a keyblock	73.7%
Total no. of keyblocks	502 500
Total no. of failed keyblocks	33 912
Average rockfalls per mining step	5.65
Average failure volume per mining step	2.76

## Hazard Results

Zone	Label	Falls/1000m <sup>2</sup>	Injuries/1000m <sup>2</sup>
------	-------	--------------------------	-----------------------------



Distribution of keyblock falls

## Excavation data:

Excavation dip	0.0
Excavation dip dir.	90.0
Excavation dip range	0.0
Excavation map y-dir	0.0
Dip stress (kPa)	0.0
Strike stress (kPa)	0.0
Rock density (kg/m <sup>3</sup> )	2700.0
Seismic acceleration m/s	0.00

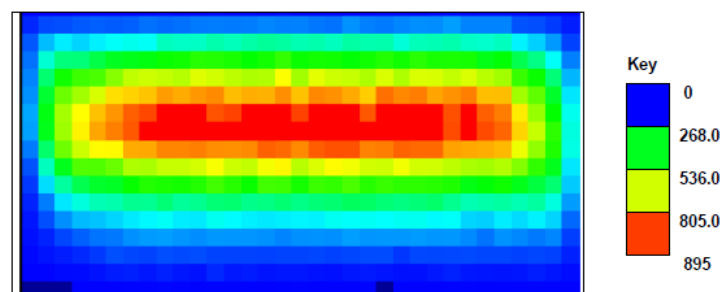
Figure C17 Simulation statistics for 10m stope span in EA7 jointsets with flat hangingwall

## Simulation Statistics

Total simulation area	120 007
Percent area that is a keyblock	49.8%
Total no. of keyblocks	303 000
Total no. of failed keyblocks	20 668
Average rockfalls per mining step	3.44
Average failure volume per mining step	2.92

## Hazard Results

Zone	Label	Falls/1000m <sup>2</sup>	Injuries/1000m <sup>2</sup>
------	-------	--------------------------	-----------------------------



Distribution of keyblock falls

## Excavation data:

Excavation dip	45.0
Excavation dip dir.	90.0
Excavation dip range	0.0
Excavation map y-dir	0.0
Dip stress (kPa)	0.0
Strike stress (kPa)	0.0
Rock density (kg/m <sup>3</sup> )	2700.0
Seismic acceleration m/s	0.00

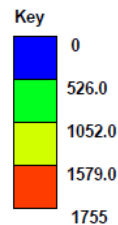
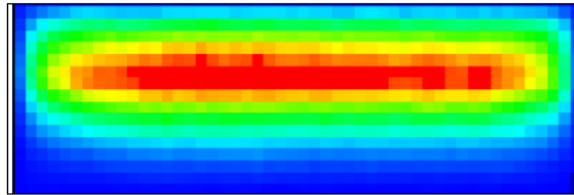
Figure C18 Simulation statistics for 10m stope span in EA7 jointsets with hangingwall dipping 45°

## Simulation Statistics

Total simulation area	180 119
Percent area that is a keyblock	66.5%
Total no. of keyblocks	661 700
Total no. of failed keyblocks	47 327
Average rockfalls per mining step	7.88
Average failure volume per mining step	3.16

## Hazard Results

Zone	Label	Falls/1000m <sup>2</sup>	Injuries/1000m <sup>2</sup>
------	-------	--------------------------	-----------------------------



Distribution of keyblock falls

## Excavation data:

Excavation dip	0.0
Excavation dip dir.	90.0
Excavation dip range	0.0
Excavation map y-dir	0.0
Dip stress (kPa)	0.0
Strike stress (kPa)	0.0
Rock density (kg/m <sup>3</sup> )	2700.0
Seismic acceleration m/s	0.00

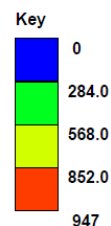
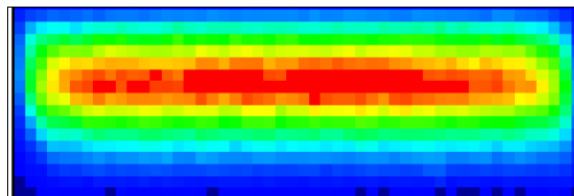
Figure C19 Simulation statistics for 15m stope span in EA7 jointsets with flat hangingwall

## Simulation Statistics

Total simulation area	180 164
Percent area that is a keyblock	40.7%
Total no. of keyblocks	454 100
Total no. of failed keyblocks	34 300
Average rockfalls per mining step	5.71
Average failure volume per mining step	4.81

## Hazard Results

Zone	Label	Falls/1000m <sup>2</sup>	Injuries/1000m <sup>2</sup>
------	-------	--------------------------	-----------------------------



Distribution of keyblock falls

## Excavation data:

Excavation dip	45.0
Excavation dip dir.	90.0
Excavation dip range	0.0
Excavation map y-dir	0.0
Dip stress (kPa)	0.0
Strike stress (kPa)	0.0
Rock density (kg/m <sup>3</sup> )	2700.0
Seismic acceleration m/s	0.00

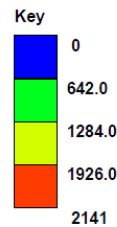
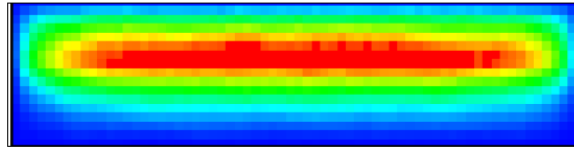
Figure C20 Simulation statistics for 15m stope span in EA7 jointsets with hangingwall dipping 45°

## Simulation Statistics

Total simulation area	240 101
Percent area that is a keyblock	76.5%
Total no. of keyblocks	929 200
Total no. of failed keyblocks	67 017
Average rockfalls per mining step	11.16
Average failure volume per mining step	5.23

## Hazard Results

Zone	Label	Falls/1000m <sup>2</sup>	Injuries/1000m <sup>2</sup>
------	-------	--------------------------	-----------------------------



Distribution of keyblock falls

## Excavation data:

Excavation dip	0.0
Excavation dip dir.	90.0
Excavation dip range	0.0
Excavation map y-dir	0.0
Dip stress (kPa)	0.0
Strike stress (kPa)	0.0
Rock density (kg/m <sup>3</sup> )	2700.0
Seismic acceleration m/s	0.00

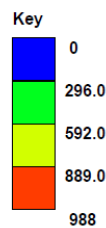
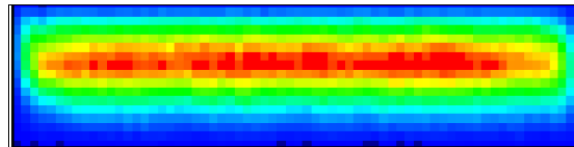
Figure C21 Simulation statistics for 20m stope span in EA7 jointsets with flat hangingwall

## Simulation Statistics

Total simulation area	240 001
Percent area that is a keyblock	46.9%
Total no. of keyblocks	628 700
Total no. of failed keyblocks	45 667
Average rockfalls per mining step	7.61
Average failure volume per mining step	7.00

## Hazard Results

Zone	Label	Falls/1000m <sup>2</sup>	Injuries/1000m <sup>2</sup>
------	-------	--------------------------	-----------------------------



Distribution of keyblock falls

## Excavation data:

Excavation dip	45.0
Excavation dip dir.	90.0
Excavation dip range	0.0
Excavation map y-dir	0.0
Dip stress (kPa)	0.0
Strike stress (kPa)	0.0
Rock density (kg/m <sup>3</sup> )	2700.0
Seismic acceleration m/s	0.00

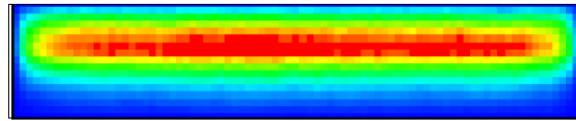
Figure C22 Simulation statistics for 20m stope span in EA7 jointsets with hangingwall dipping 45°

## Simulation Statistics

Total simulation area	301 216
Percent area that is a keyblock	55.8%
Total no. of keyblocks	1 178 700
Total no. of failed keyblocks	86 235
Average rockfalls per mining step	14.37
Average failure volume per mining step	5.66

## Hazard Results

Zone	Label	Falls/1000m <sup>2</sup>	Injuries/1000m <sup>2</sup>
------	-------	--------------------------	-----------------------------



Distribution of keyblock falls

## Excavation data:

Excavation dip	0.0
Excavation dip dir.	90.0
Excavation dip range	0.0
Excavation map y-dir	0.0
Dip stress (kPa)	0.0
Strike stress (kPa)	0.0
Rock density (kg/m3)	2700.0
Seismic acceleration m/s	0.00

## Key

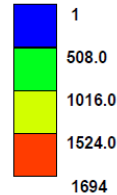


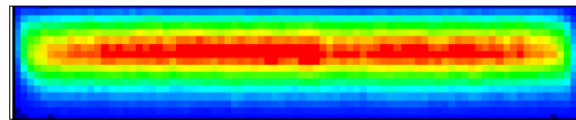
Figure C23 Simulation statistics for 25m stope span in EA7 jointsets with flat hangingwall

## Simulation Statistics

Total simulation area	301 242
Percent area that is a keyblock	47.5%
Total no. of keyblocks	782 400
Total no. of failed keyblocks	57 087
Average rockfalls per mining step	9.51
Average failure volume per mining step	9.07

## Hazard Results

Zone	Label	Falls/1000m <sup>2</sup>	Injuries/1000m <sup>2</sup>
------	-------	--------------------------	-----------------------------



Distribution of keyblock falls

## Excavation data:

Excavation dip	45.0
Excavation dip dir.	90.0
Excavation dip range	0.0
Excavation map y-dir	0.0
Dip stress (kPa)	0.0
Strike stress (kPa)	0.0
Rock density (kg/m3)	2700.0
Seismic acceleration m/s	0.00

## Key

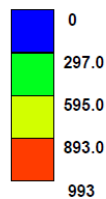


Figure C24 Simulation statistics for 25m stope span in EA7 jointsets with hangingwall dipping 45°



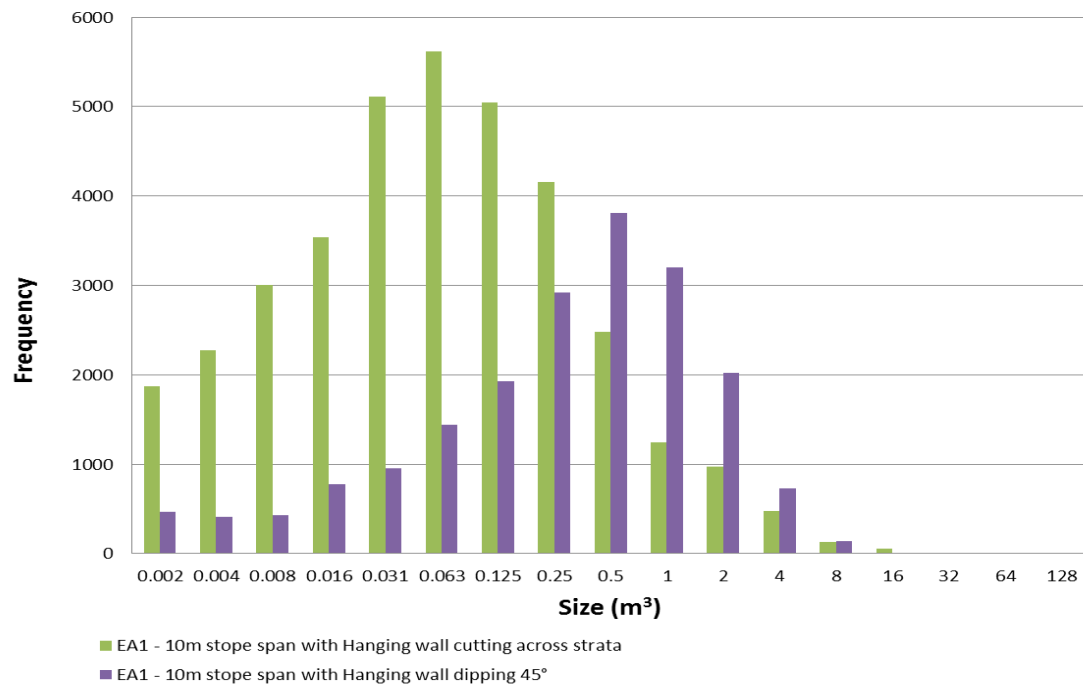


Figure C25 Summary of JBlock results for a 10m wide excavation in the EA1 formation

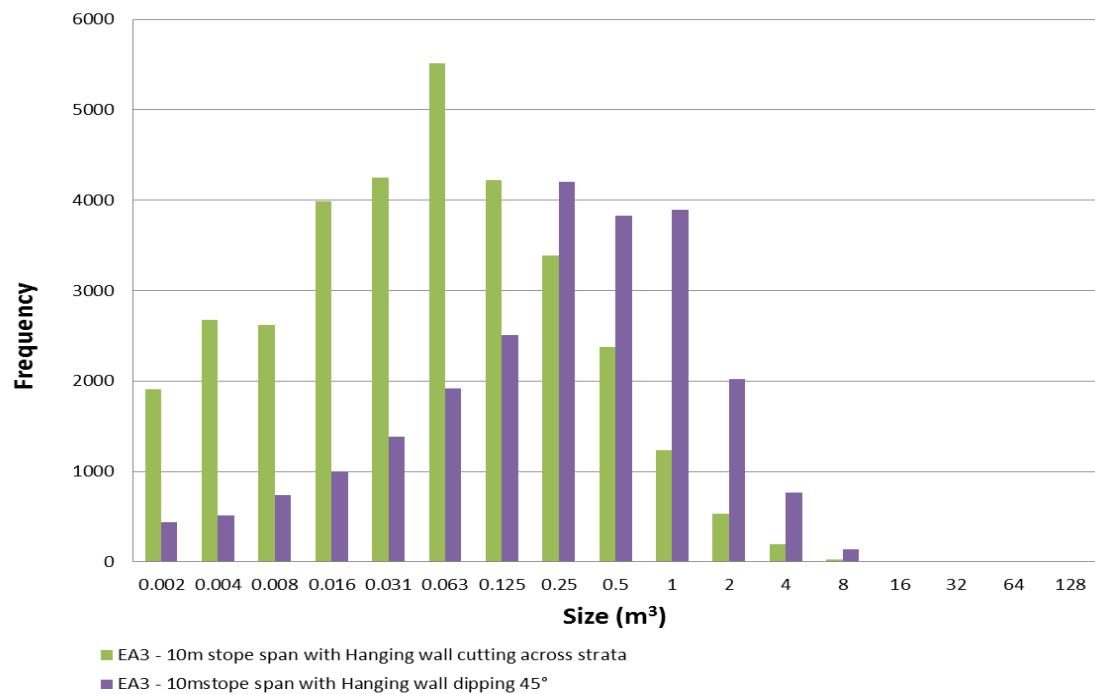


Figure C26 Summary of JBlock results for a 10m wide excavation in the EA3 formation

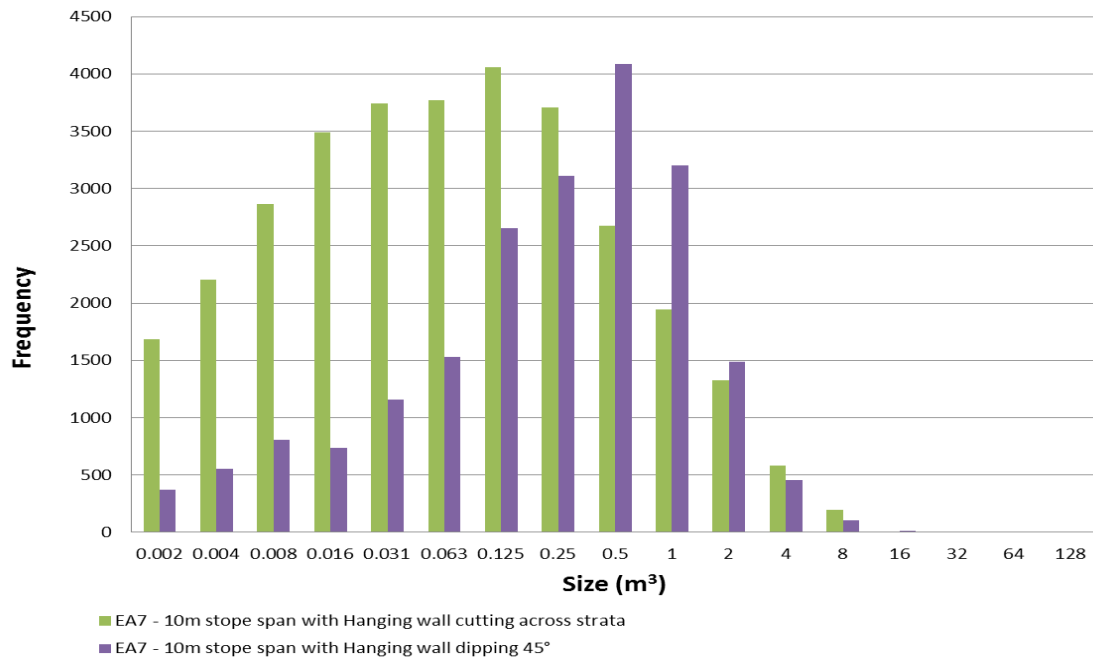


Figure C27 Summary of JBlock results for a 10m stope span excavation in the EA7 formation

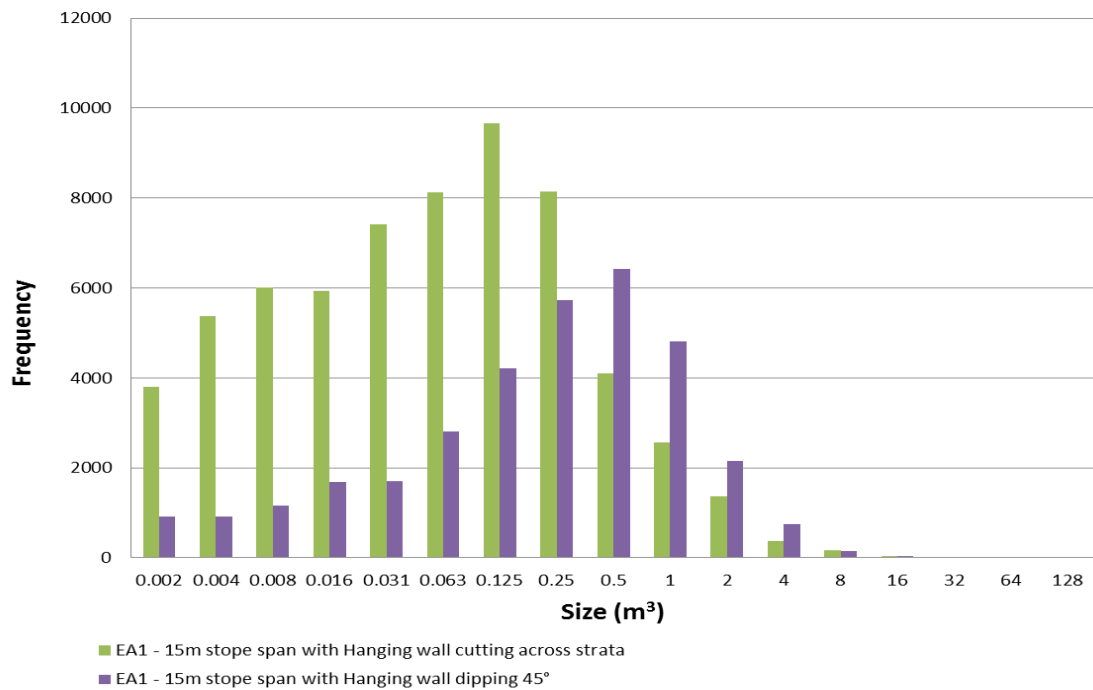


Figure C28 Summary of JBlock results for a 15m stope span excavation in the EA1 formation

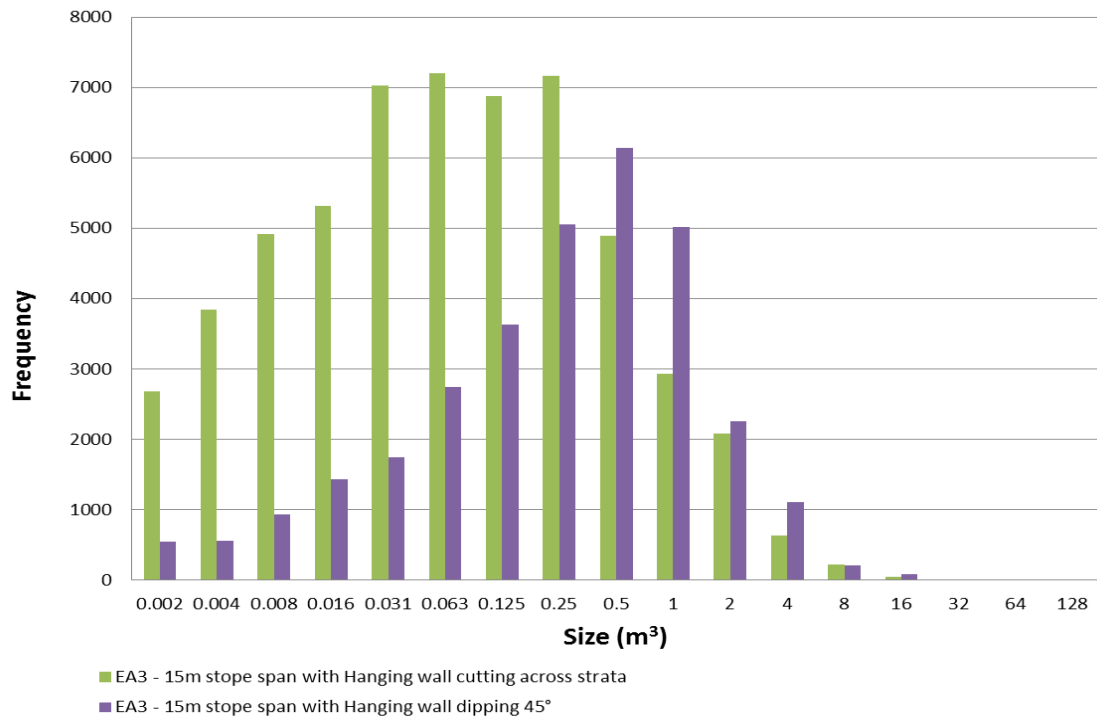


Figure C29 Summary of JBlock results for a 15m stope span excavation in the EA3 formation

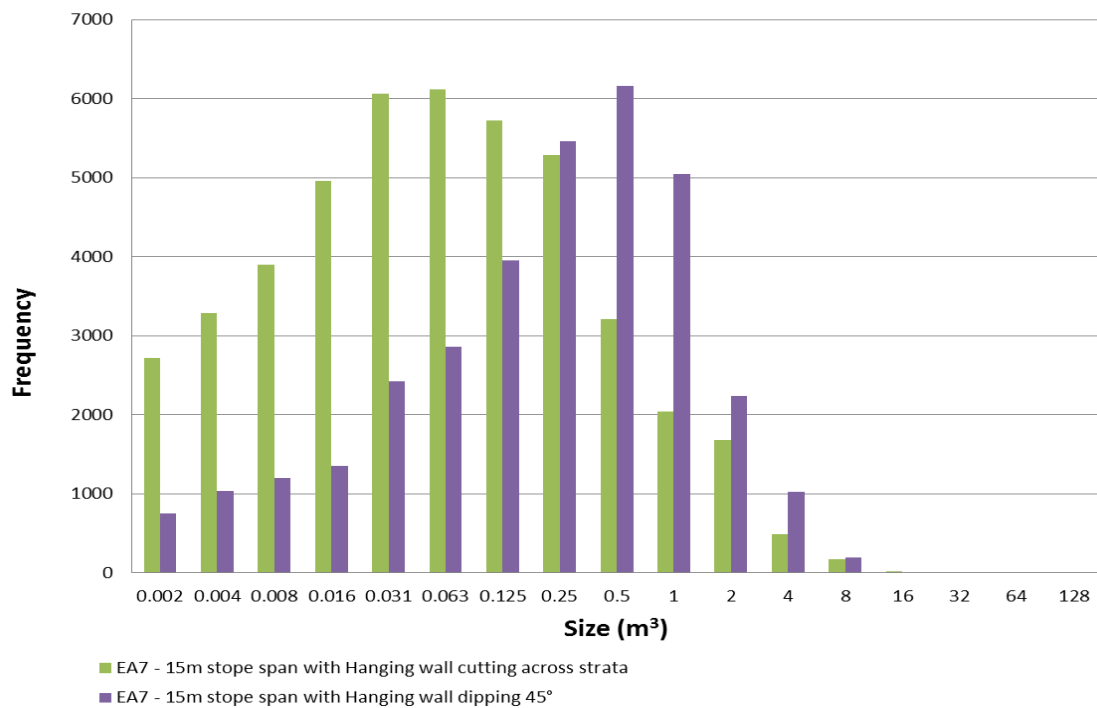


Figure C30 Summary of JBlock results for a 15m stope span excavation in the EA7 formation

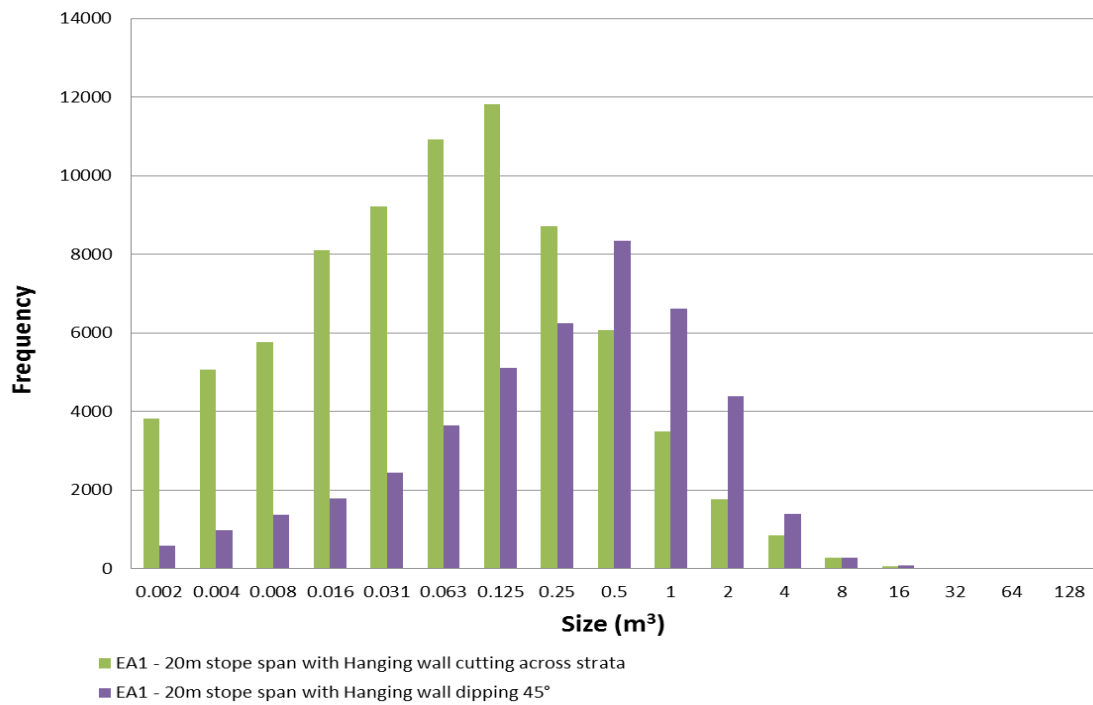


Figure C31 Summary of JBlock results for a 20m stope span excavation in the EA1 formation

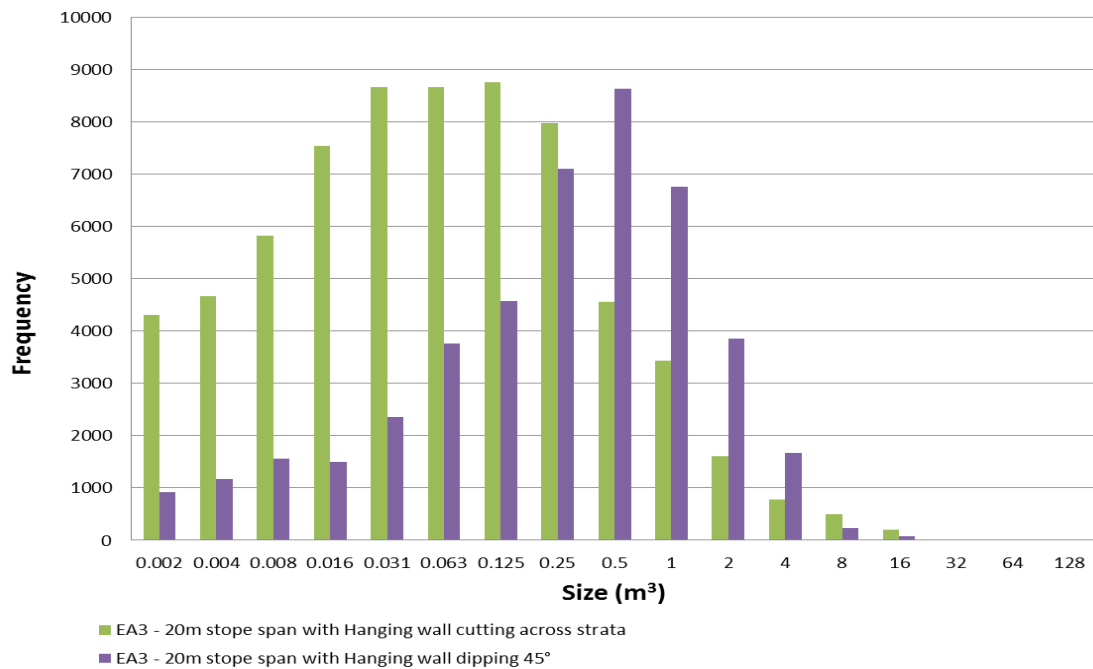


Figure C32 Summary of JBlock results for a 20m stope span excavation in the EA3 formation

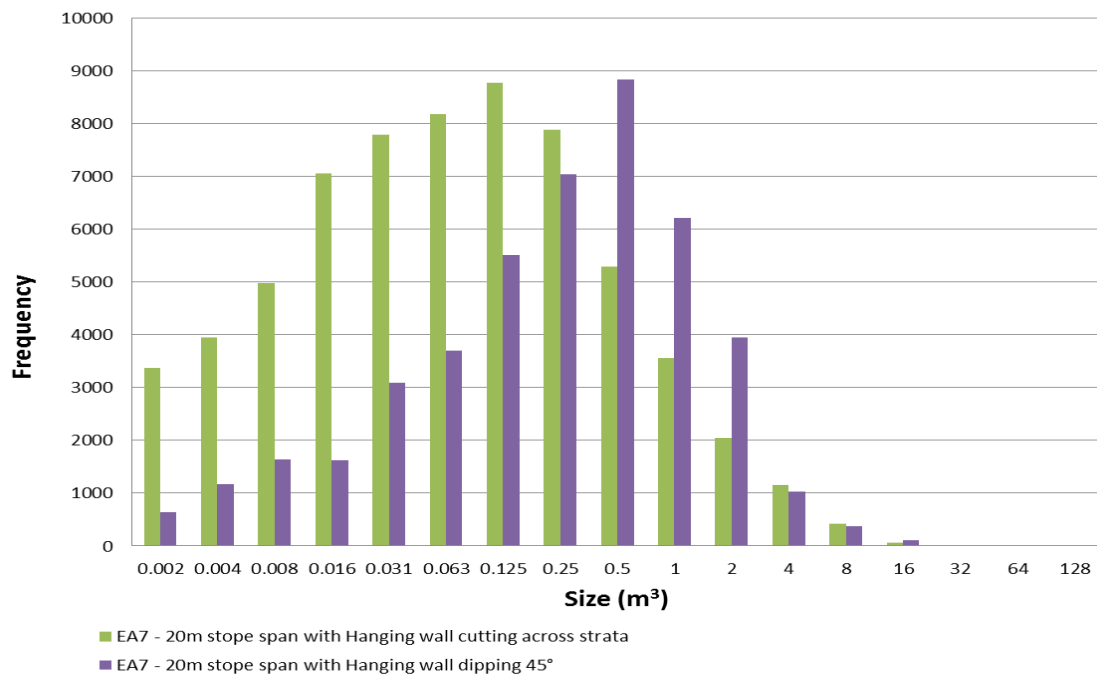


Figure C33 Summary of JBlock results for a 20m stope span excavation in the EA7 formation

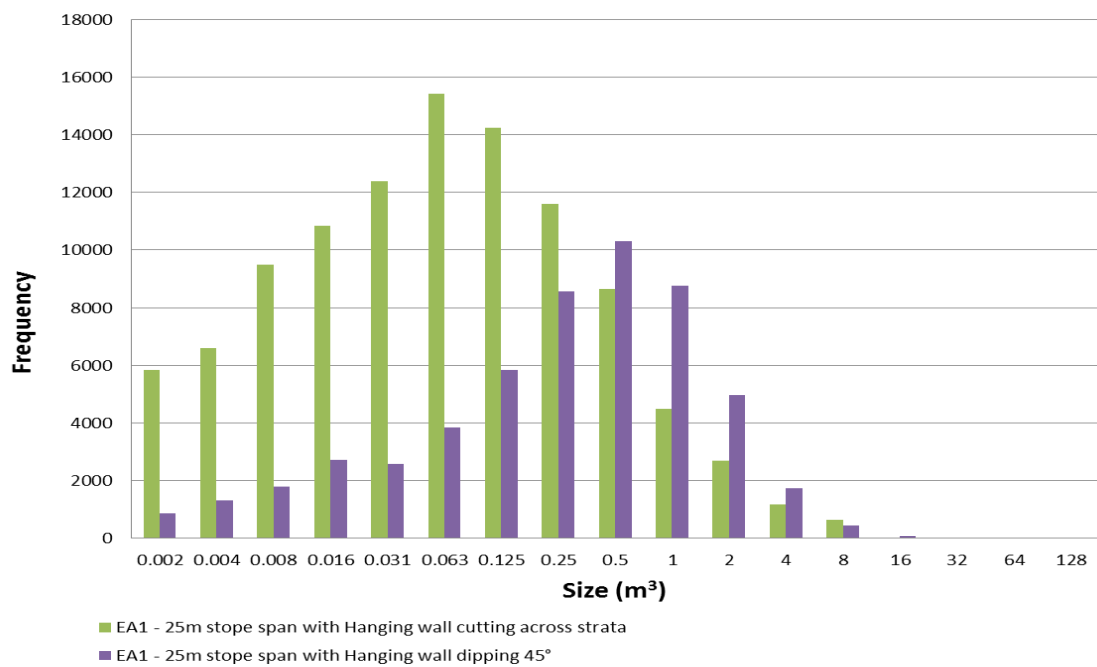


Figure C34 Summary of JBlock results for a 25m stope span excavation in the EA1 formation

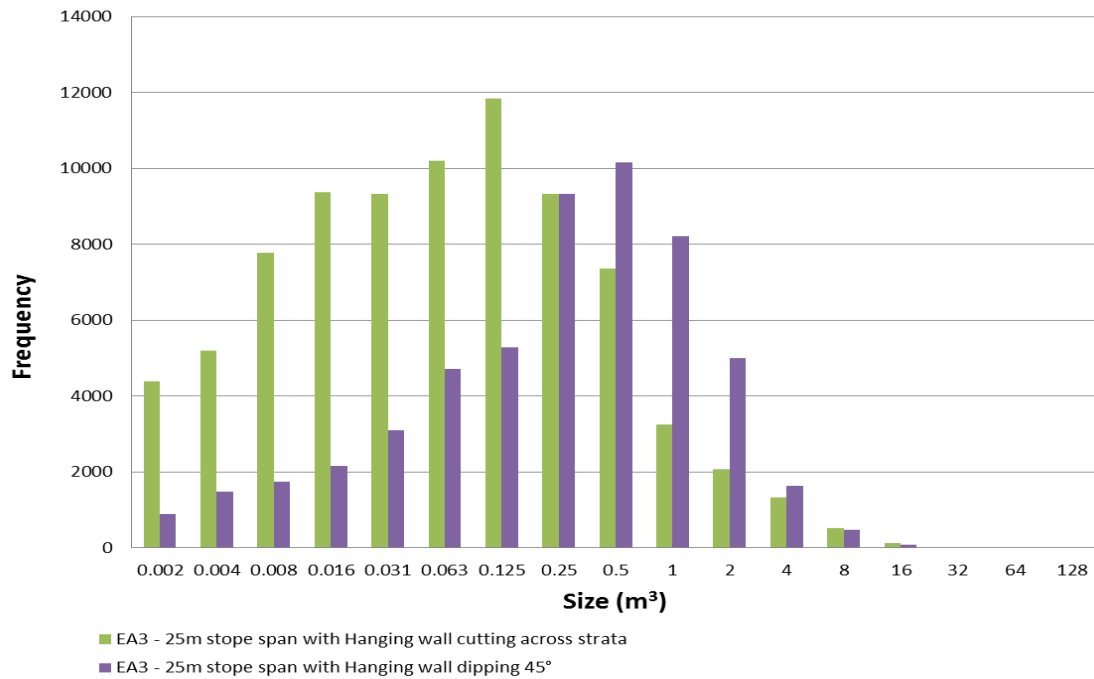


Figure C35 Summary of JBlock results for a 25m stope span excavation in the EA3 formation

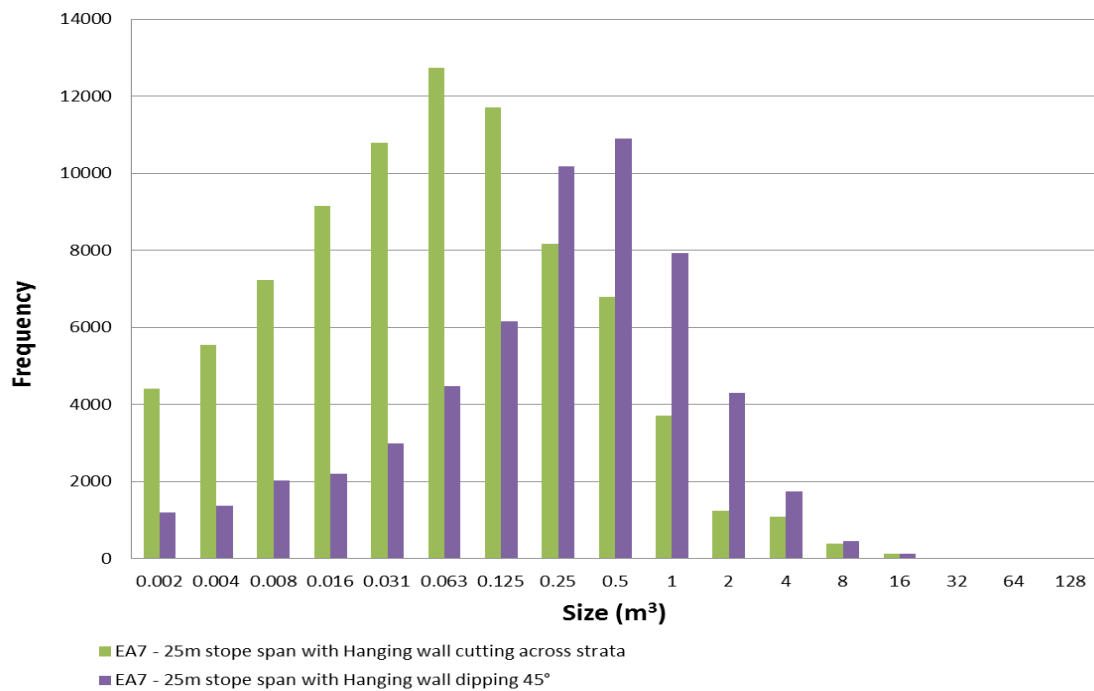
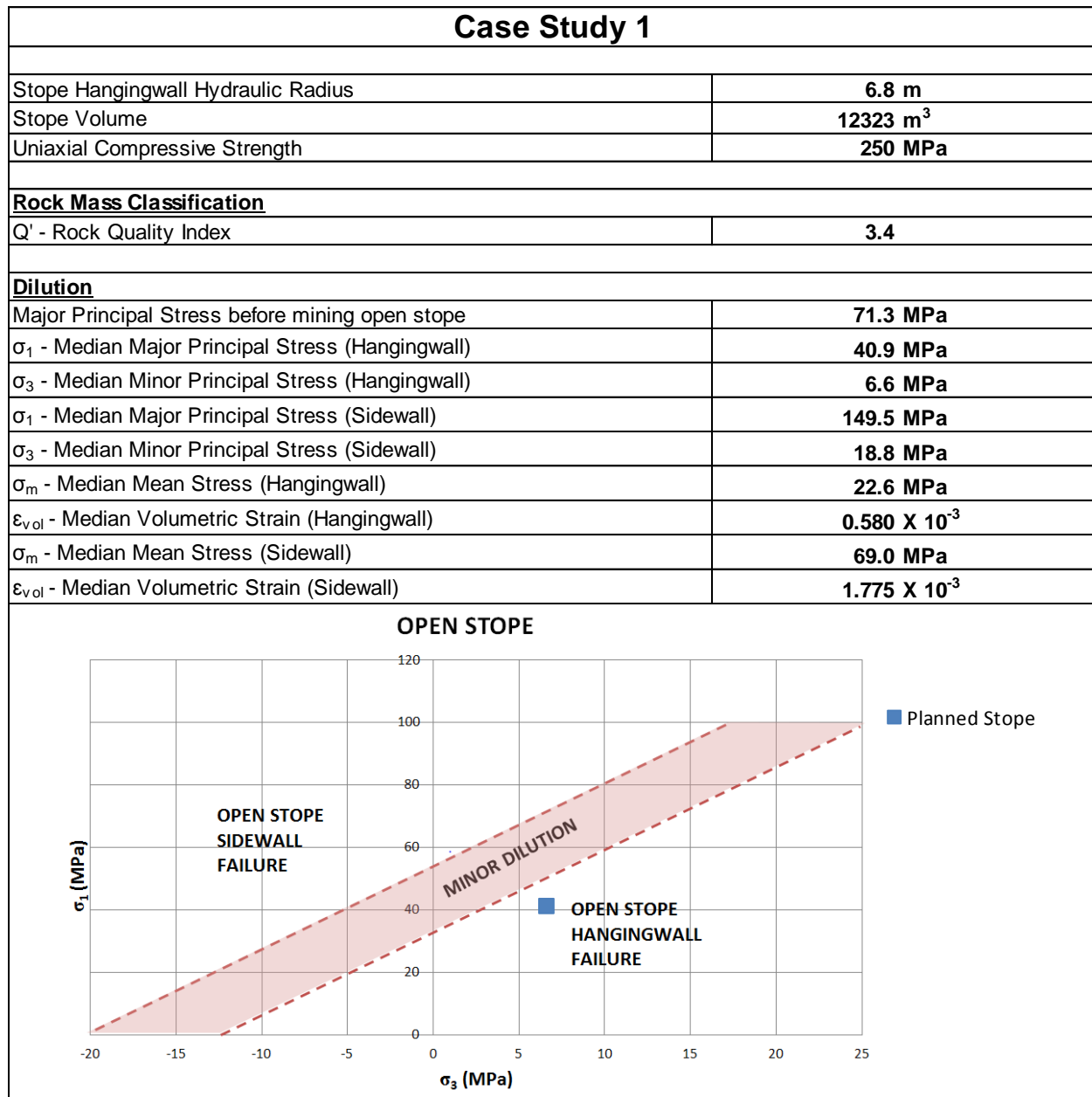


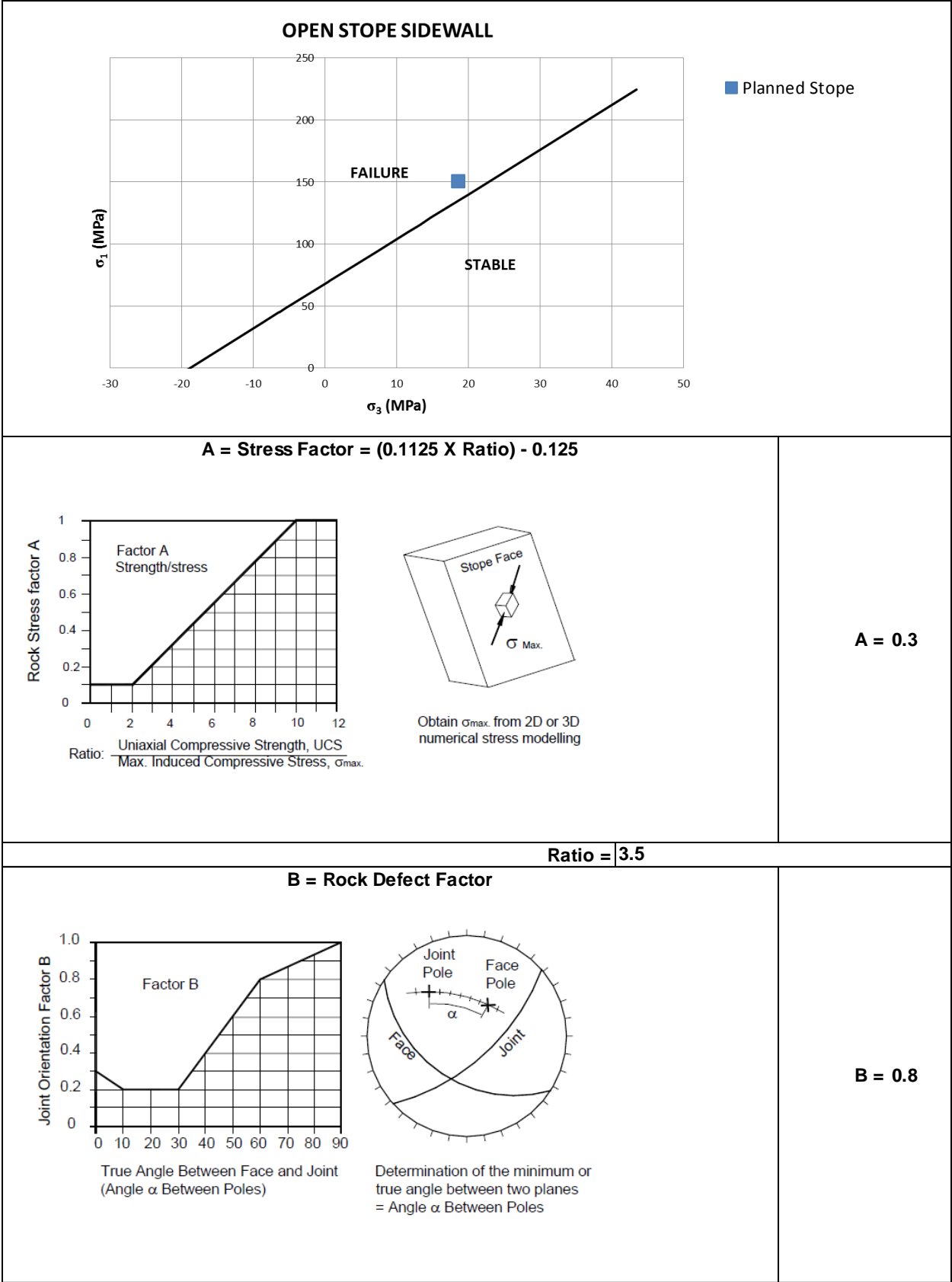
Figure C36 Summary of JBlock results for a 25m stope span excavation in the EA7 formation

## APPENDIX D

### Case Studies evaluations

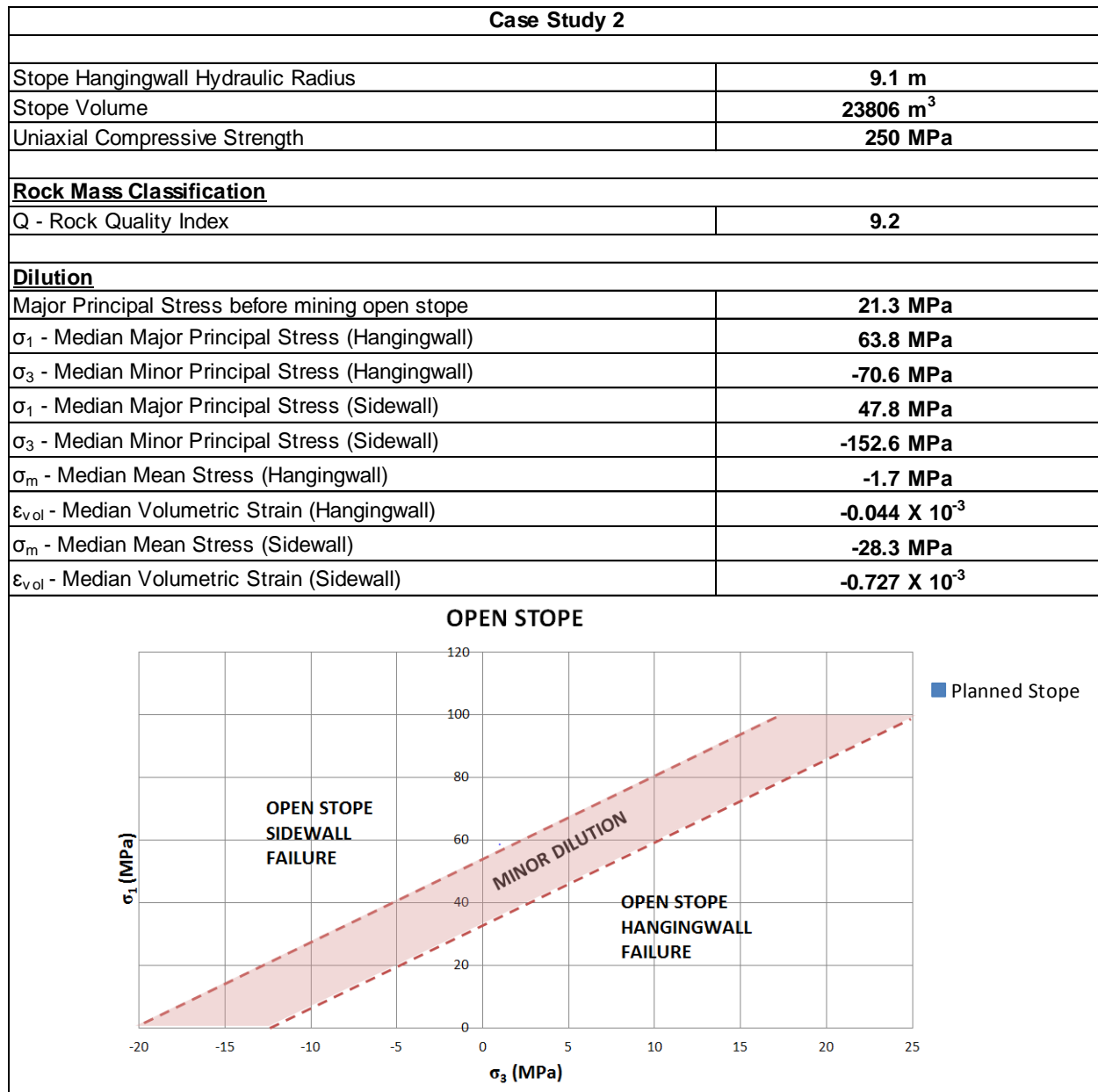


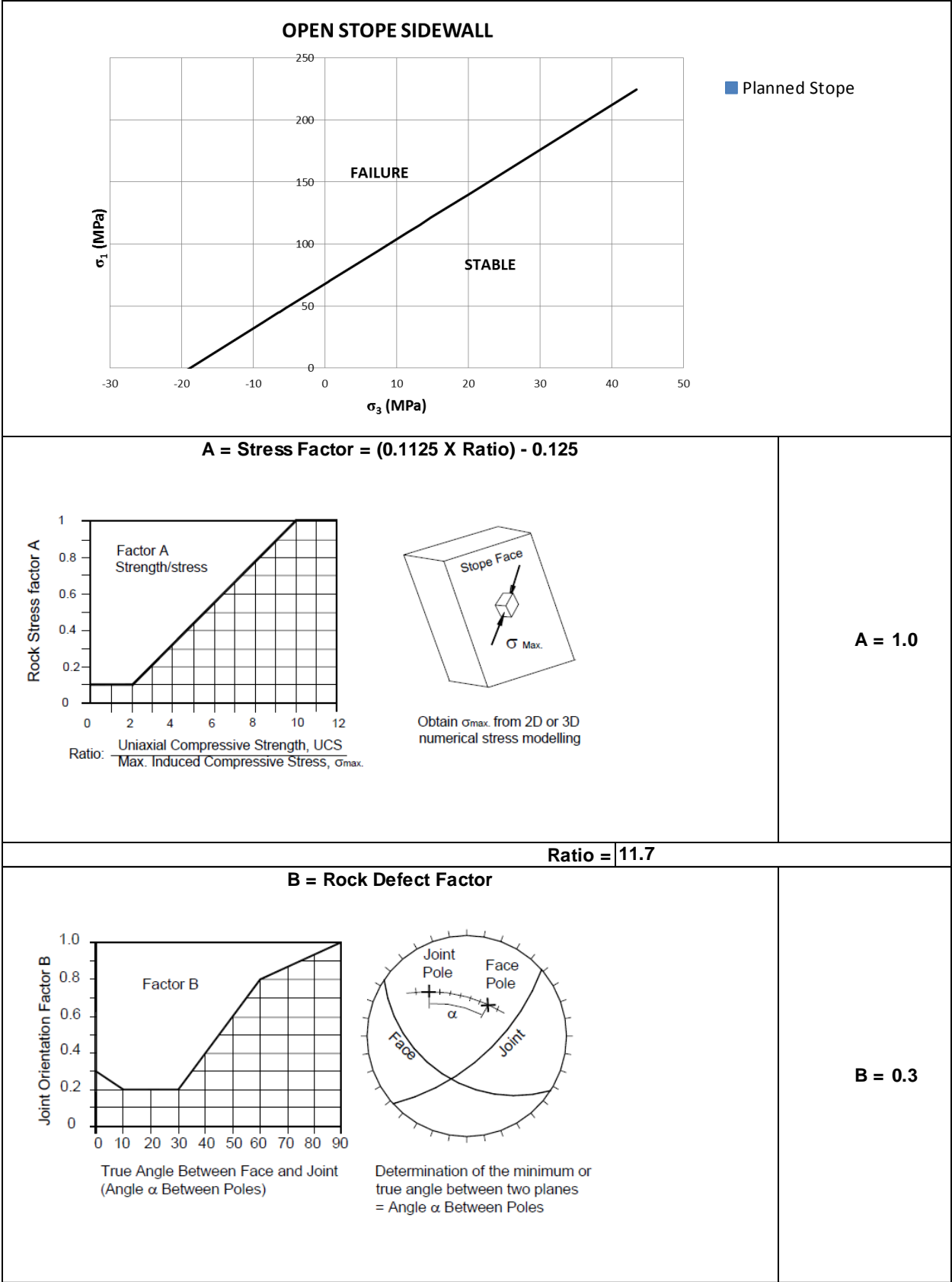






<p>A line graph showing % Dilution (0% to 100%) on the y-axis versus HYDRAULIC RADIUS (m) (0 to 30) on the x-axis. Five curves are plotted for different N' values: N' ≤ 3 (blue), N' = 4 to 10 (red), N' = 11 to 20 (green), N' = 21 to 30 (purple), and N' &gt; 30 (orange). A red square is plotted at approximately (6.5, 30%).</p>	<p><b><u>Expected Dilution (2):</u></b></p>	<p><b>28.9%</b></p>
<p>A line graph showing % Dilution (0% to 80%) on the y-axis versus <math>\sigma_m</math> (MPa) (-50 to 150) on the x-axis. The top x-axis shows <math>\epsilon_{vol} \times 10^{-3}</math> values: -1.286, -0.286, 0.714, 1.714, 2.714, 3.714. A red square is plotted at approximately (25, 27%).</p>	<p><b><u>Expected Hangingwall Dilution (3):</u></b></p>	<p><b>26.8%</b></p>
<p>A line graph showing % Dilution (0% to 80%) on the y-axis versus <math>\sigma_m</math> (MPa) (-50 to 150) on the x-axis. The top x-axis shows <math>\epsilon_{vol} \times 10^{-3}</math> values: -1.286, -0.286, 0.714, 1.714, 2.714, 3.714. A red square is plotted at approximately (75, 0%).</p>	<p><b><u>Expected Sidewall Dilution (4):</u></b></p>	<p><b>0.0%</b></p>
<p><b>Expected Dilution for Open Stope using OSD</b></p>		<p><b>26.8%</b></p>

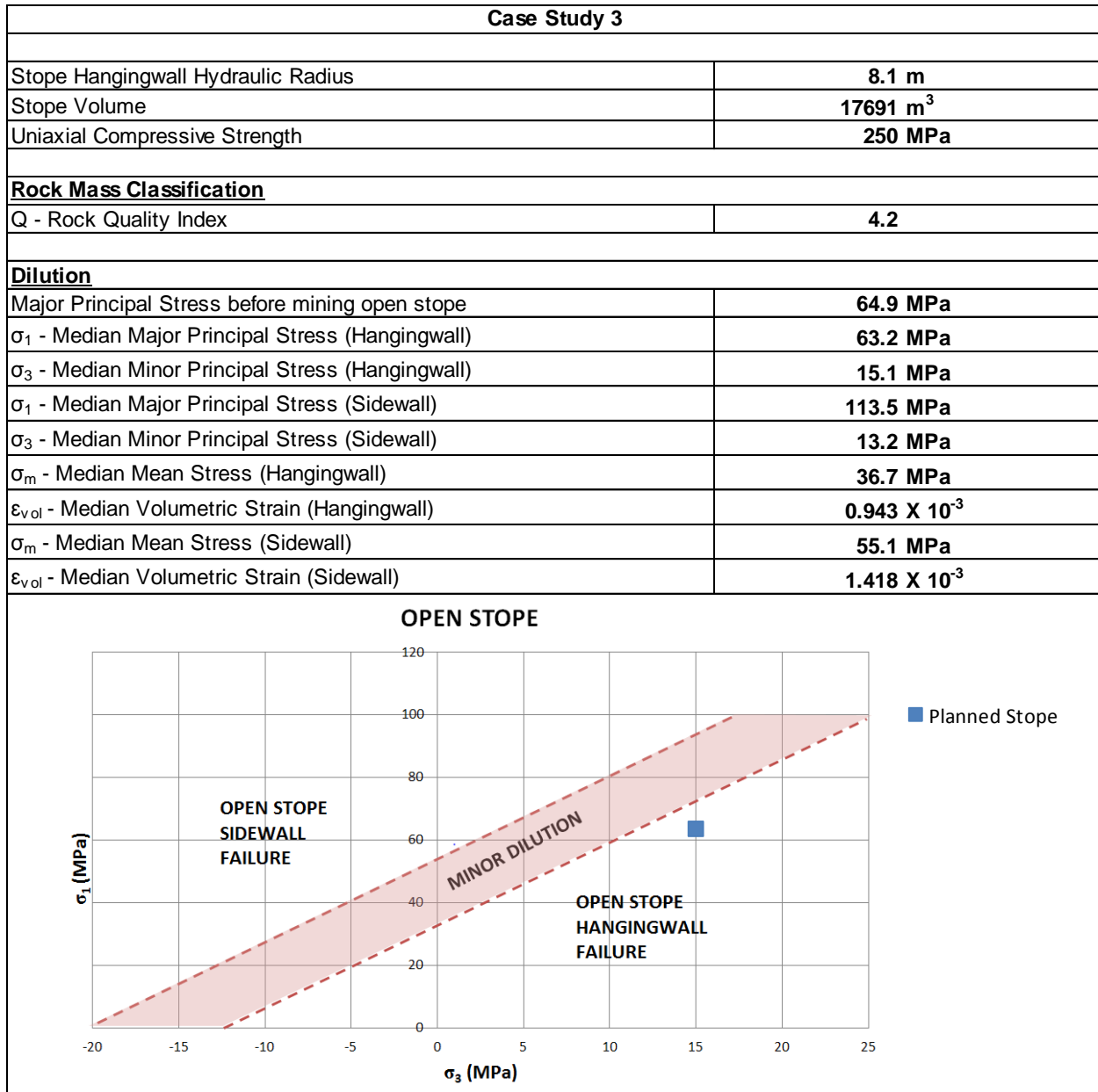


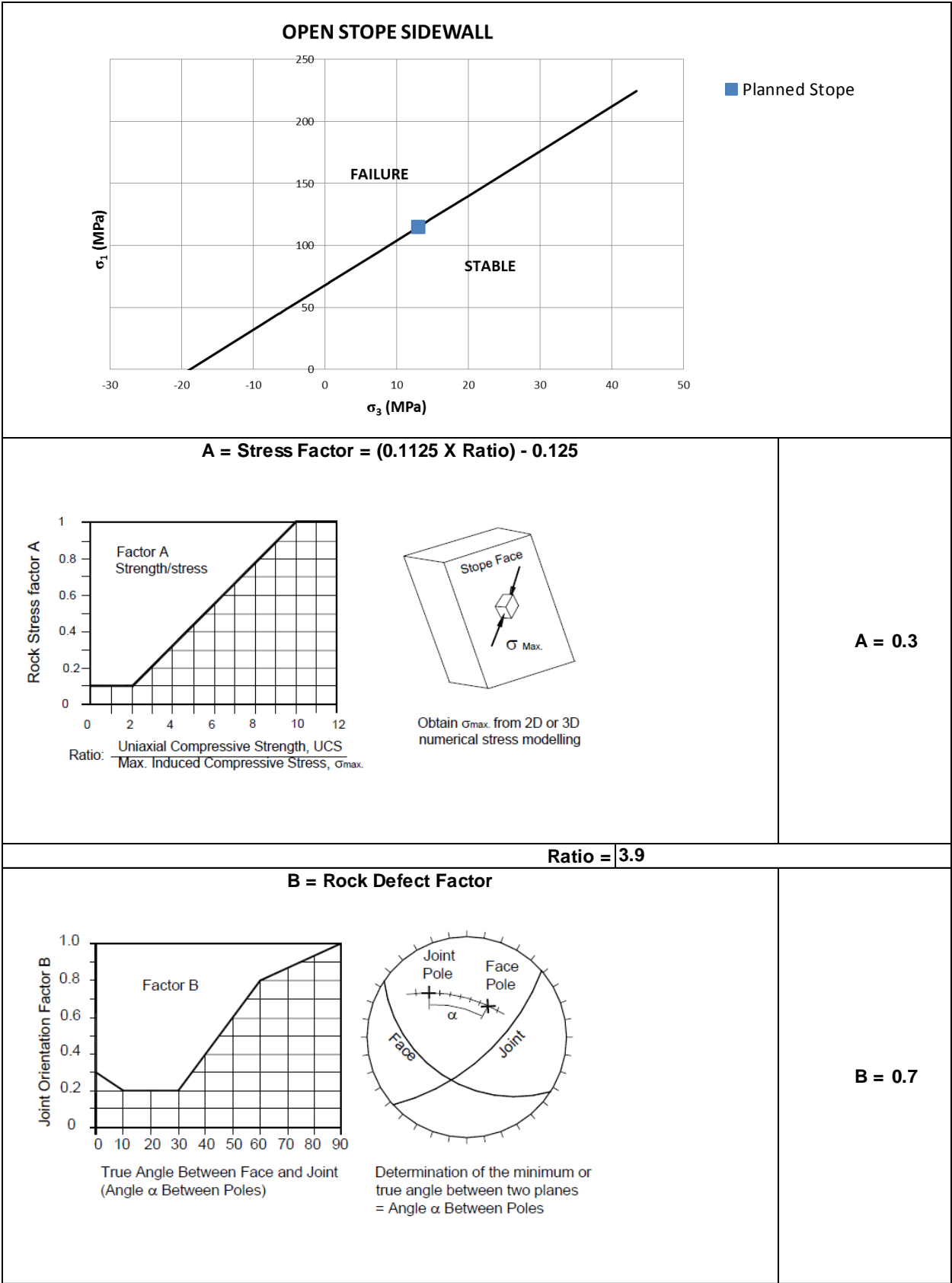


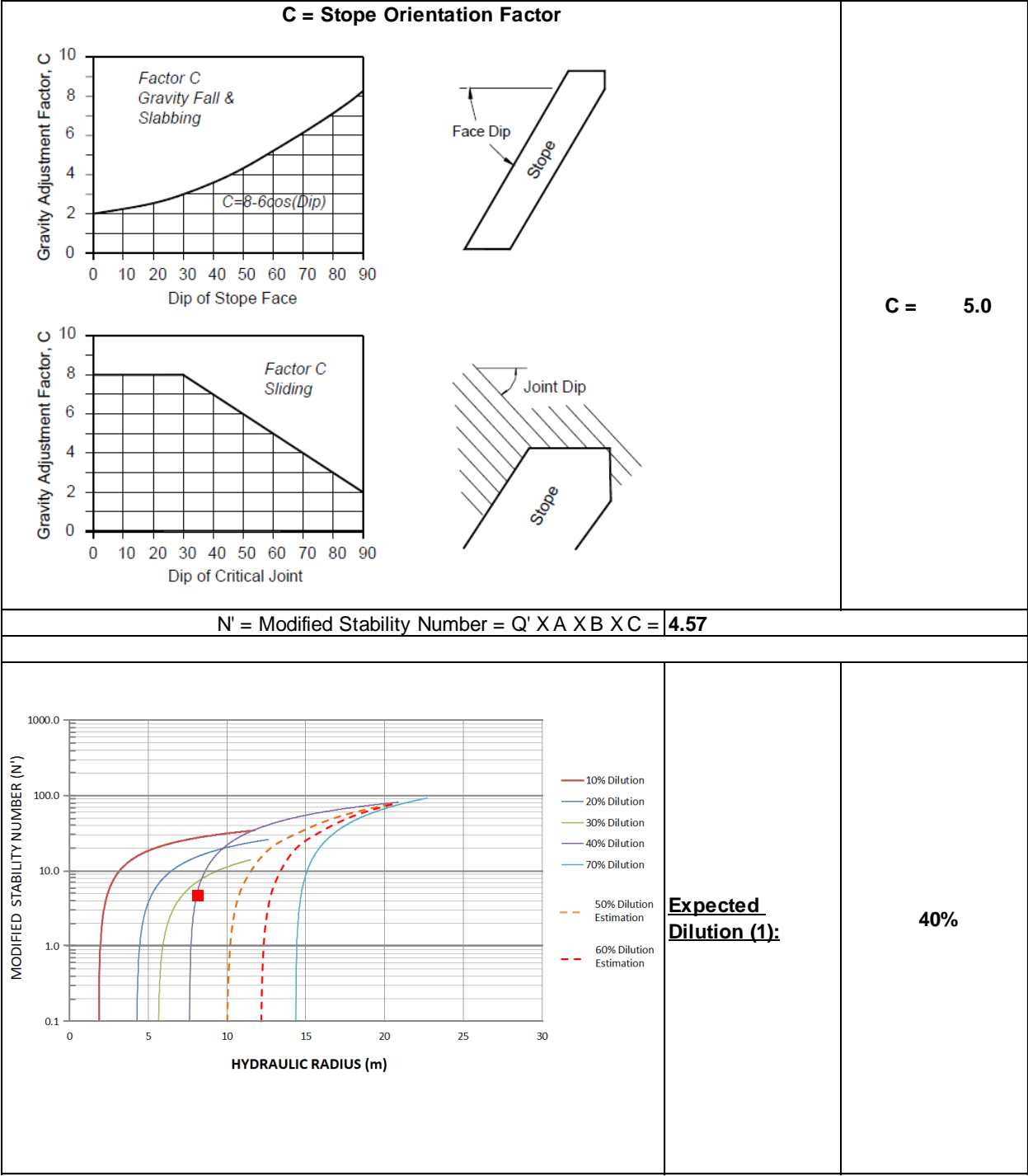


<p>A line graph showing % Dilution (0% to 100%) on the y-axis versus HYDRAULIC RADIUS (m) (0 to 30) on the x-axis. Five curves are plotted for different N' values: N' ≤ 3 (blue), N' = 4 to 10 (red), N' = 11 to 20 (green), N' = 21 to 30 (purple), and N' &gt; 30 (orange). A red square is plotted on the red curve at a hydraulic radius of approximately 9 m and a dilution of 24.3%.</p>	<p><b><u>Expected Dilution (2):</u></b></p>	<p><b>24.3%</b></p>
<p>A line graph showing % Dilution (0% to 80%) on the y-axis versus σ<sub>m</sub> (MPa) (-50 to 150) on the x-axis. The top x-axis also shows ε<sub>vol</sub> × 10<sup>-3</sup> values: -1.286, -0.286, 0.714, 1.714, 2.714, 3.714. A red square is plotted at σ<sub>m</sub> = 0 MPa and a dilution of 12.0%.</p>	<p><b><u>Expected Hangingwall Dilution (3):</u></b></p>	<p><b>12.0%</b></p>
<p>A line graph showing % Dilution (0% to 80%) on the y-axis versus σ<sub>m</sub> (MPa) (-50 to 150) on the x-axis. The top x-axis also shows ε<sub>vol</sub> × 10<sup>-3</sup> values: -1.286, -0.286, 0.714, 1.714, 2.714, 3.714. A red square is plotted at σ<sub>m</sub> = -25 MPa and a dilution of 0.0%.</p>	<p><b><u>Expected Sidewall Dilution (4):</u></b></p>	<p><b>0.0%</b></p>
<p><b>Expected Dilution for Open Stope using OSD</b></p>		<p><b>12.0%</b></p>

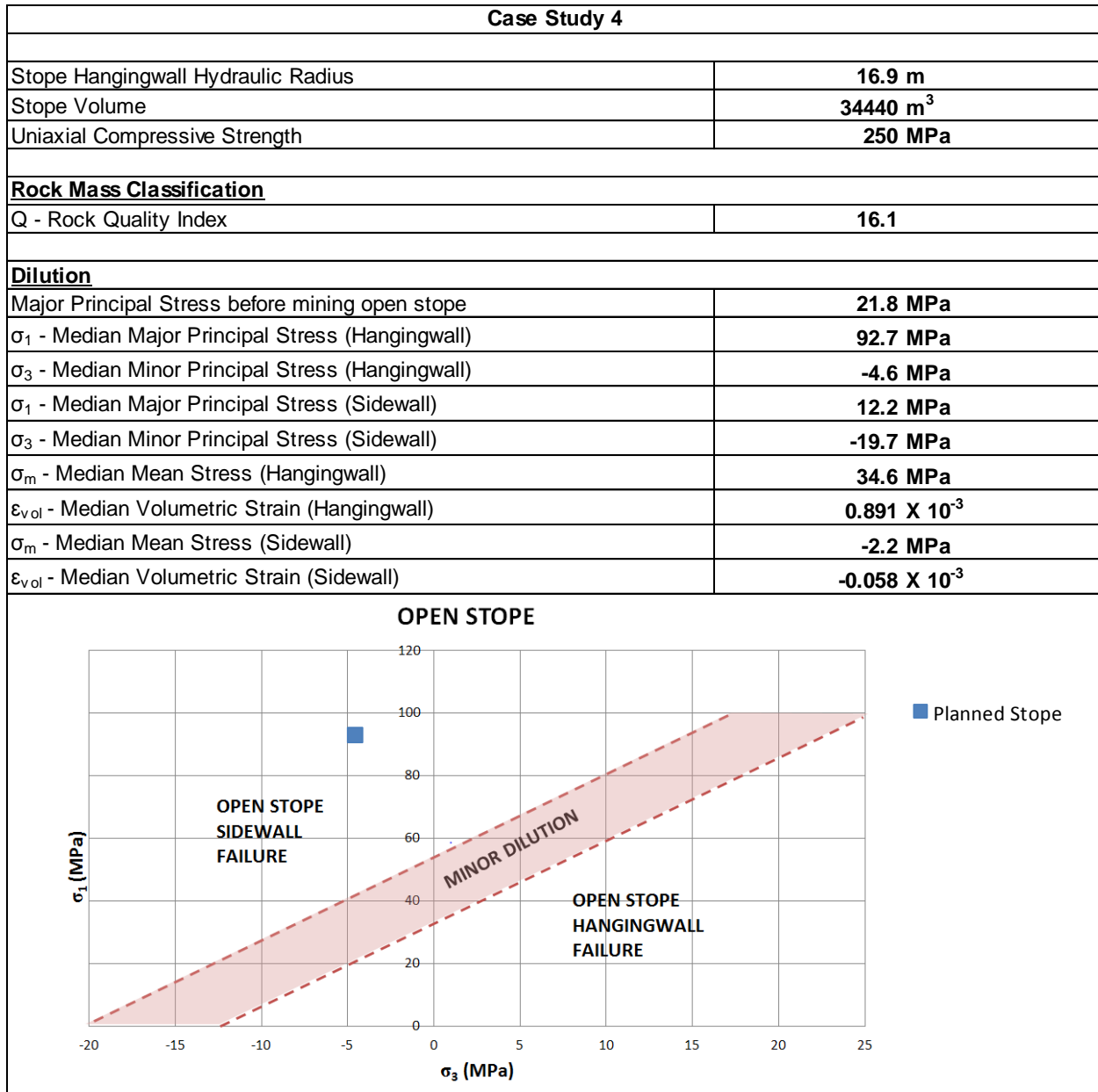


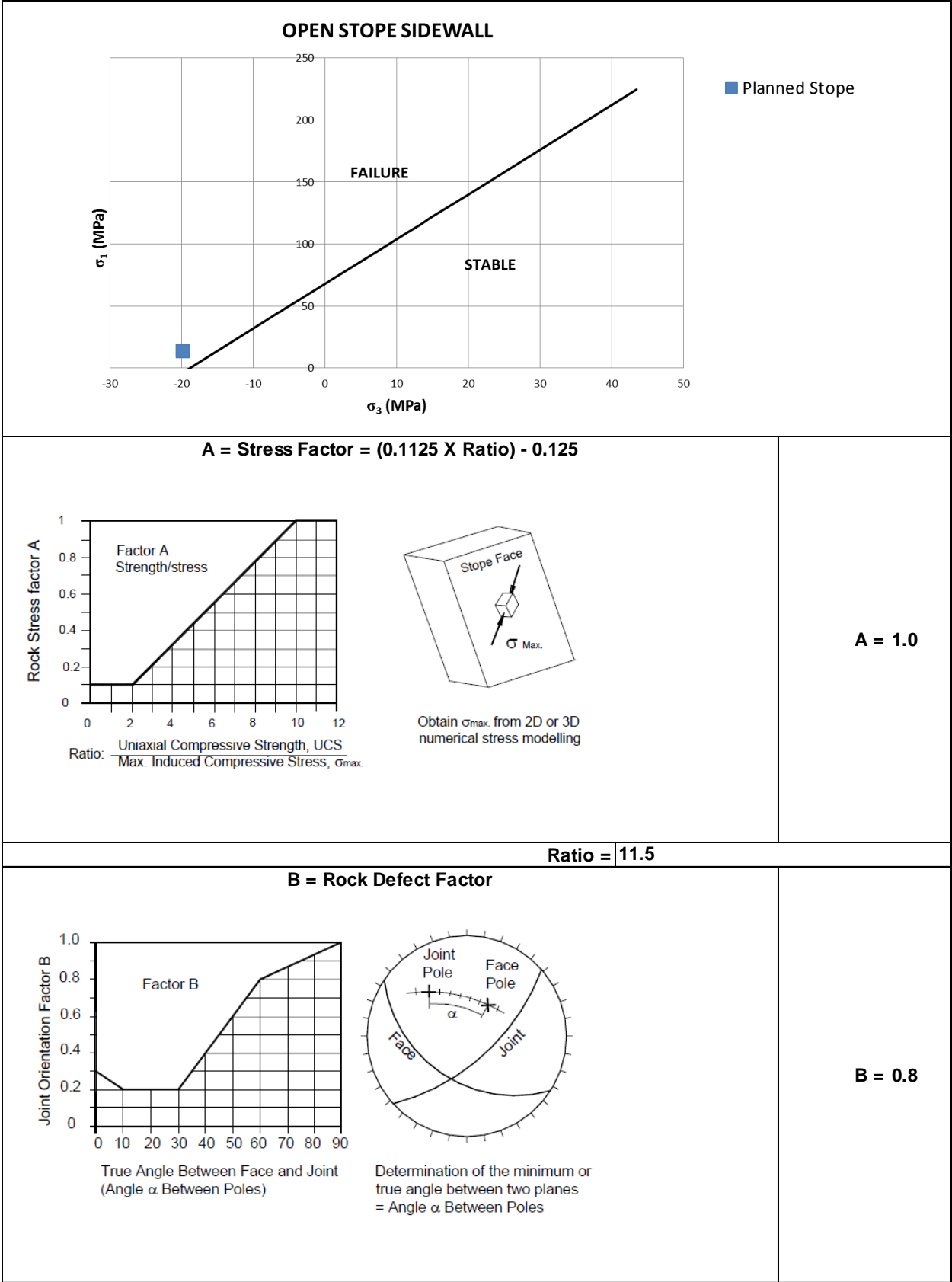






<p>The graph shows % Dilution on the y-axis (0% to 100%) and Hydraulic Radius (m) on the x-axis (0 to 30). Five curves are plotted for different N' values: N' ≤ 3 (blue), N' = 4 to 10 (red), N' = 11 to 20 (green), N' = 21 to 30 (purple), and N' &gt; 30 (orange). A red square is plotted at approximately (8, 24.3%).</p>	<p><b><u>Expected Dilution (2):</u></b></p>	<p><b>24.3%</b></p>
<p>The graph shows % Dilution on the y-axis (0% to 80%) and σm (MPa) on the x-axis (-50 to 150). A red square is plotted at approximately (35, 35.4%). The top x-axis shows εvol x 10<sup>-3</sup> values: -1.286, -0.286, 0.714, 1.714, 2.714, 3.714.</p>	<p><b><u>Expected Hangingwall Dilution (3):</u></b></p>	<p><b>35.4%</b></p>
<p>The graph shows % Dilution on the y-axis (0% to 80%) and σm (MPa) on the x-axis (-50 to 150). A red square is plotted at approximately (55, 0.0%). The top x-axis shows εvol x 10<sup>-3</sup> values: -1.286, -0.286, 0.714, 1.714, 2.714, 3.714.</p>	<p><b><u>Expected Sidewall Dilution (4):</u></b></p>	<p><b>0.0%</b></p>
<p><b>Expected Dilution for Open Stope using OSD</b></p>		<p><b>35.4%</b></p>





**C = Stope Orientation Factor**

Gravity Adjustment Factor, C

Factor C  
Gravity Fall &  
Slabbing

$C = 8 - 6\cos(Dip)$

Dip of Stope Face

Face Dip

Stope

Gravity Adjustment Factor, C

Factor C  
Sliding

Dip of Critical Joint

Joint Dip

Stope

**C = 5.0**

**N' = Modified Stability Number = Q' X A X B X C = 64.33**

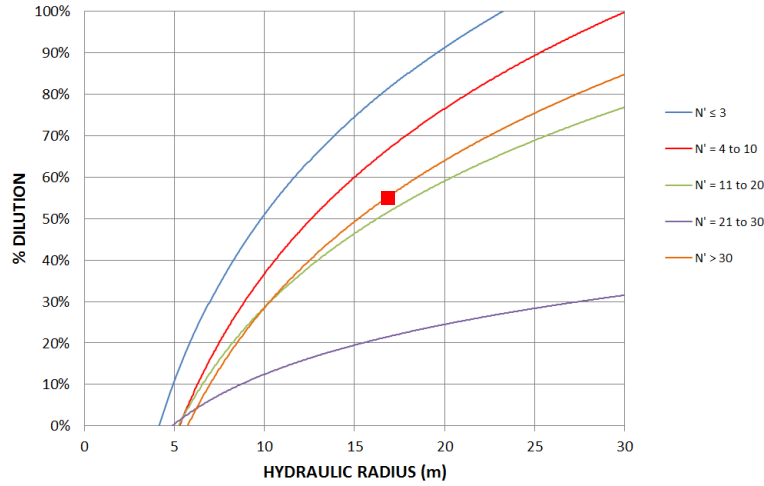
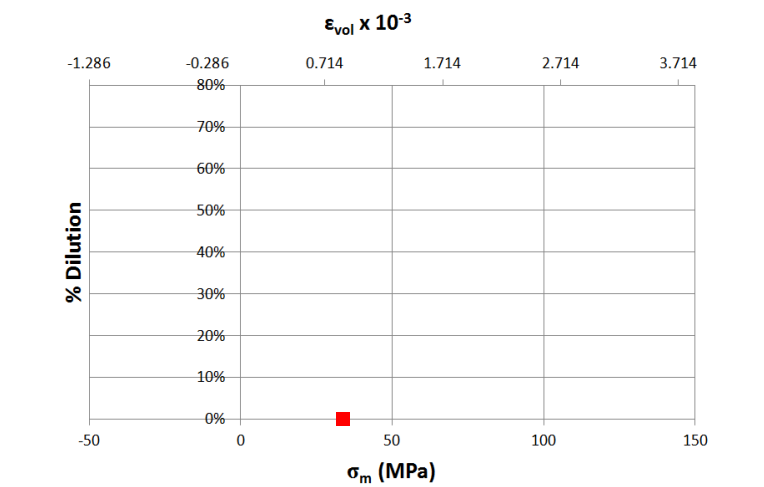
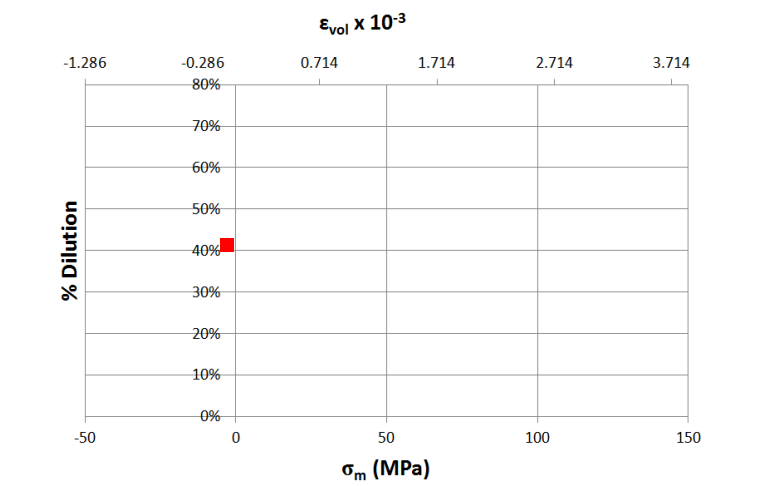
MODIFIED STABILITY NUMBER (N')

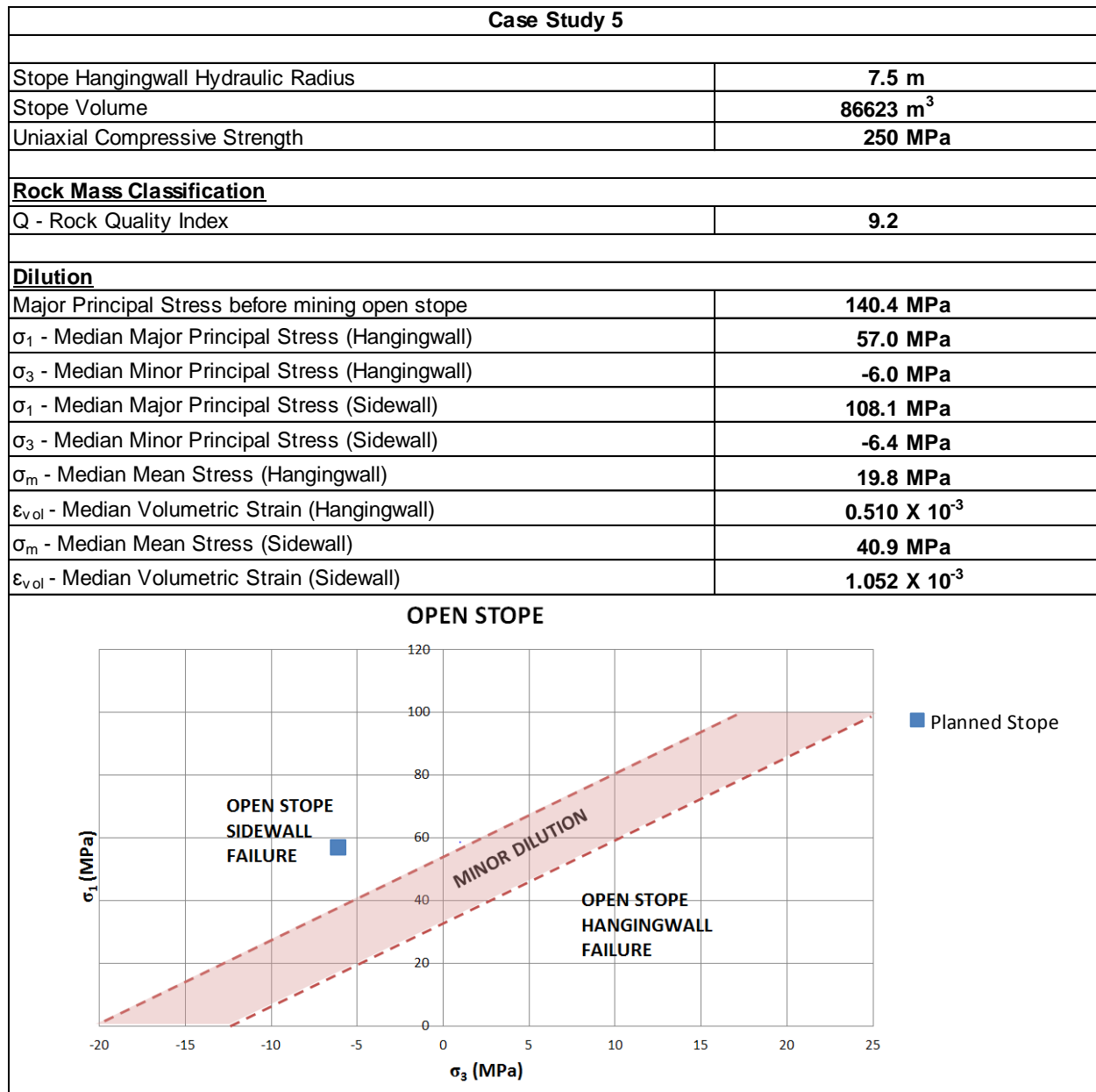
HYDRAULIC RADIUS (m)

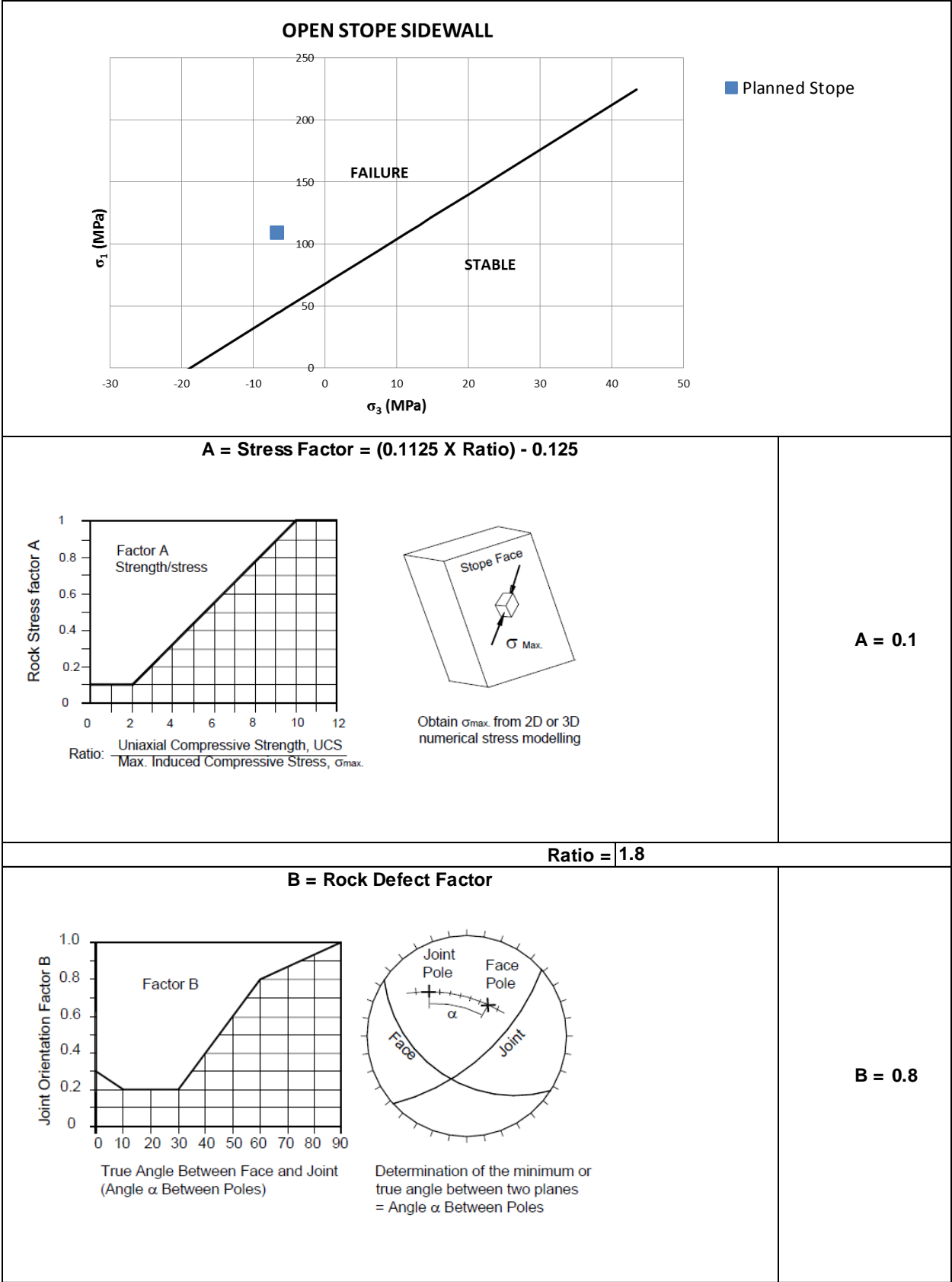
- 10% Dilution
- 20% Dilution
- 30% Dilution
- 40% Dilution
- 50% Dilution Estimation
- 60% Dilution Estimation
- 70% Dilution

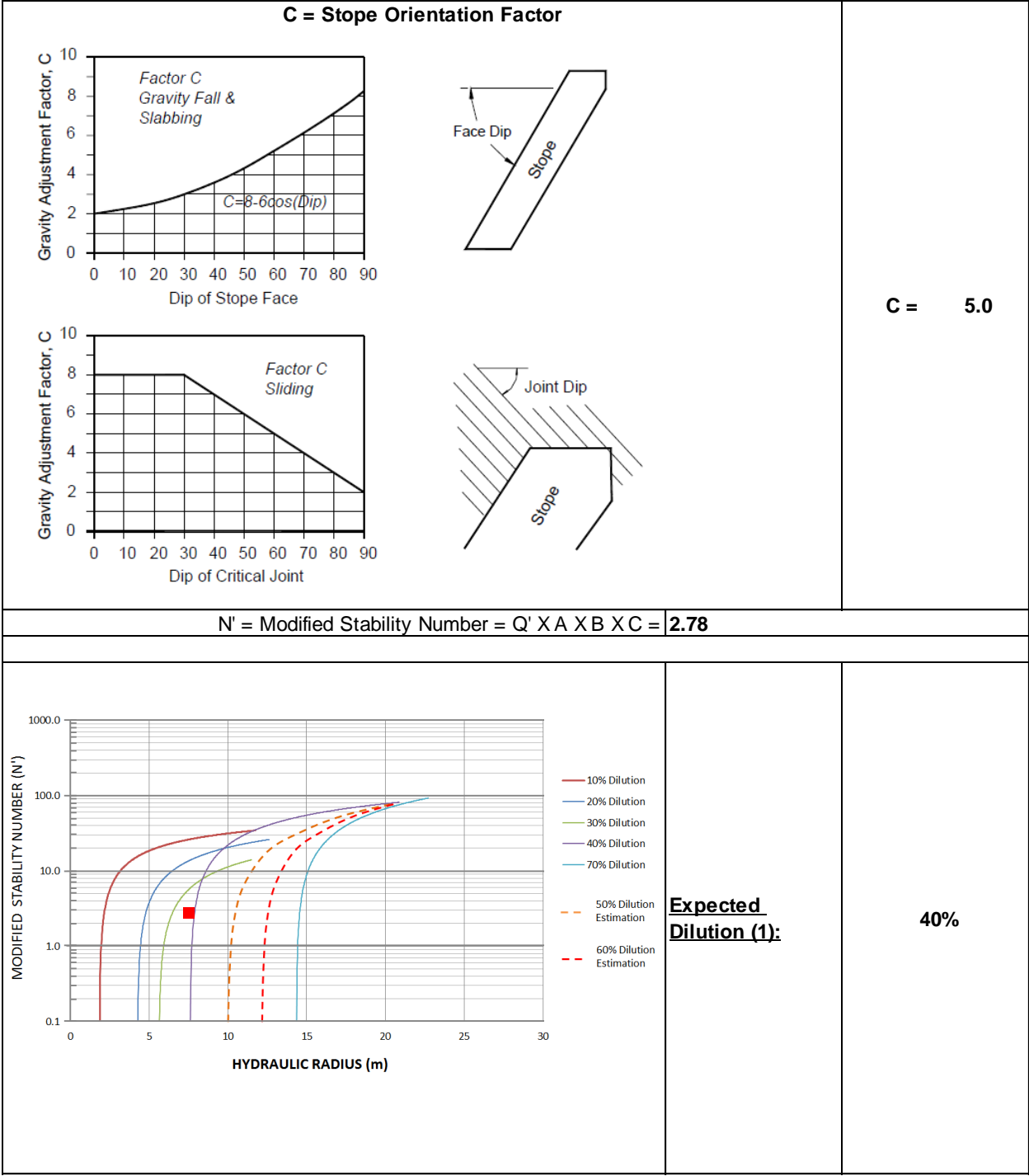
**Expected Dilution (1): 40%**

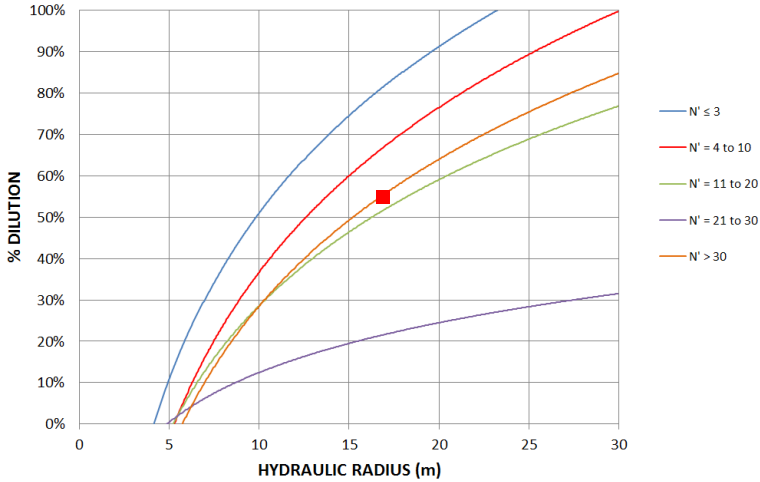
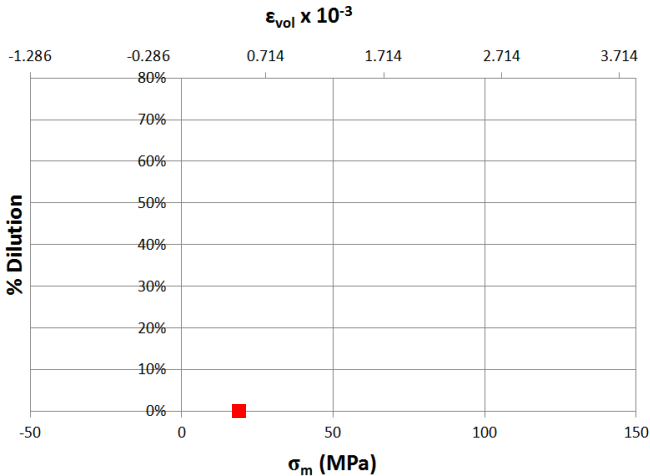
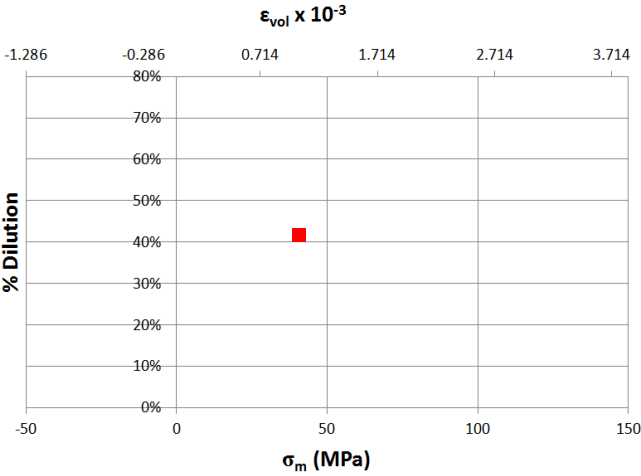


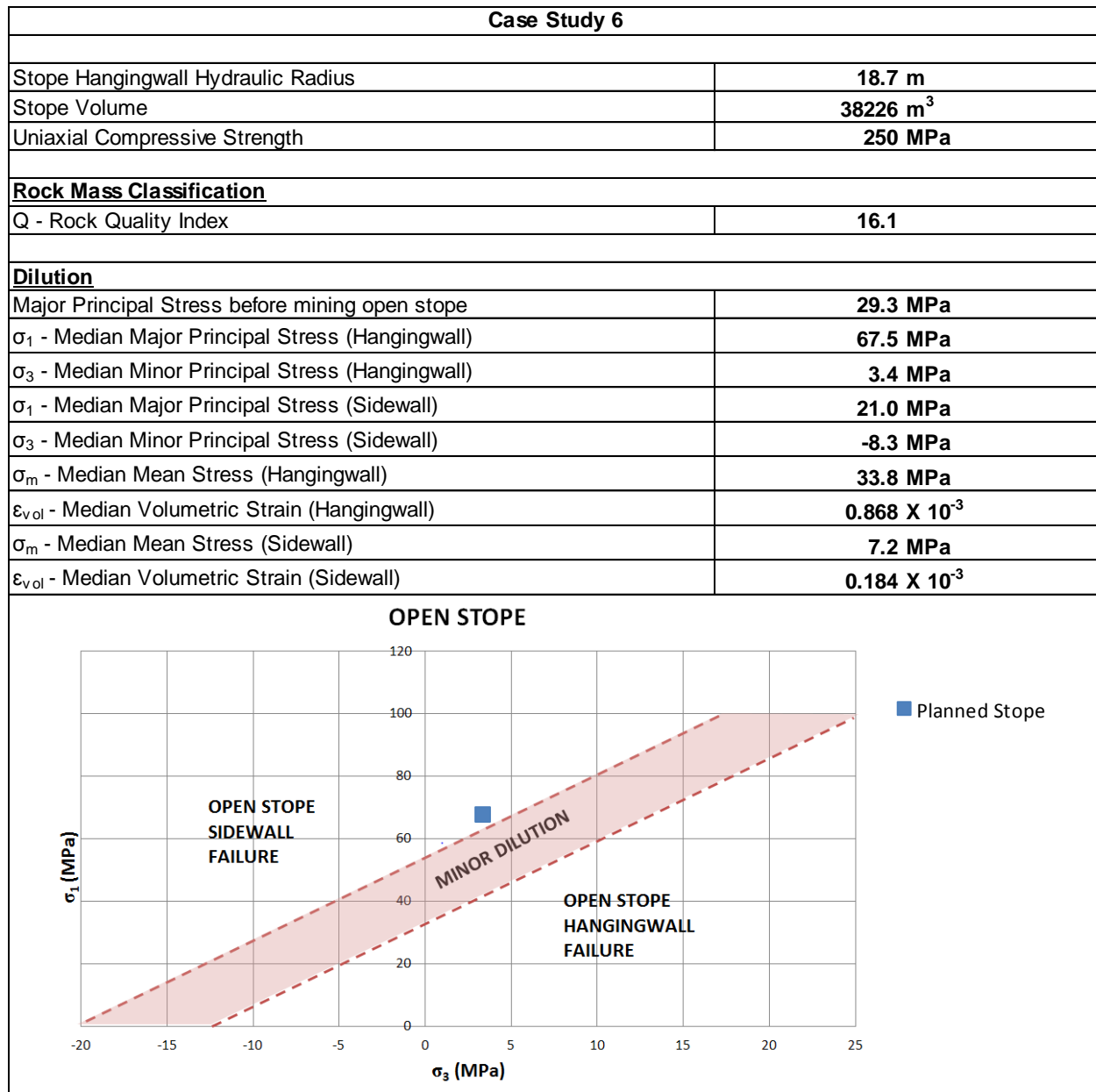
 <p>Graph showing % Dilution (Y-axis, 0% to 100%) versus HYDRAULIC RADIUS (m) (X-axis, 0 to 30). The graph includes curves for different values of <math>N'</math>:</p> <ul style="list-style-type: none"><li><math>N' \leq 3</math> (Blue line)</li><li><math>N' = 4 \text{ to } 10</math> (Red line)</li><li><math>N' = 11 \text{ to } 20</math> (Green line)</li><li><math>N' = 21 \text{ to } 30</math> (Purple line)</li><li><math>N' &gt; 30</math> (Orange line)</li></ul> <p>A red square indicates the expected dilution for <math>N' = 4 \text{ to } 10</math> at a hydraulic radius of approximately 17 m, resulting in 55.3% dilution.</p>	<p><b><u>Expected Dilution (2):</u></b></p>	<p><b>55.3%</b></p>
 <p>Graph showing % Dilution (Y-axis, 0% to 80%) versus <math>\sigma_m</math> (MPa) (X-axis, -50 to 150). The graph also includes a secondary X-axis for <math>\epsilon_{vol} \times 10^{-3}</math> with values: -1.286, -0.286, 0.714, 1.714, 2.714, 3.714.</p> <p>A red square indicates the expected hangingwall dilution at <math>\sigma_m = 30</math> MPa, resulting in 0.0% dilution.</p>	<p><b><u>Expected Hangingwall Dilution (3):</u></b></p>	<p><b>0.0%</b></p>
 <p>Graph showing % Dilution (Y-axis, 0% to 80%) versus <math>\sigma_m</math> (MPa) (X-axis, -50 to 150). The graph also includes a secondary X-axis for <math>\epsilon_{vol} \times 10^{-3}</math> with values: -1.286, -0.286, 0.714, 1.714, 2.714, 3.714.</p> <p>A red square indicates the expected sidewall dilution at <math>\sigma_m = 0</math> MPa, resulting in 41.0% dilution.</p>	<p><b><u>Expected Sidewall Dilution (4):</u></b></p>	<p><b>41.0%</b></p>
<p><b>Expected Dilution for Open Stope using OSD</b></p>		<p><b>41.0%</b></p>

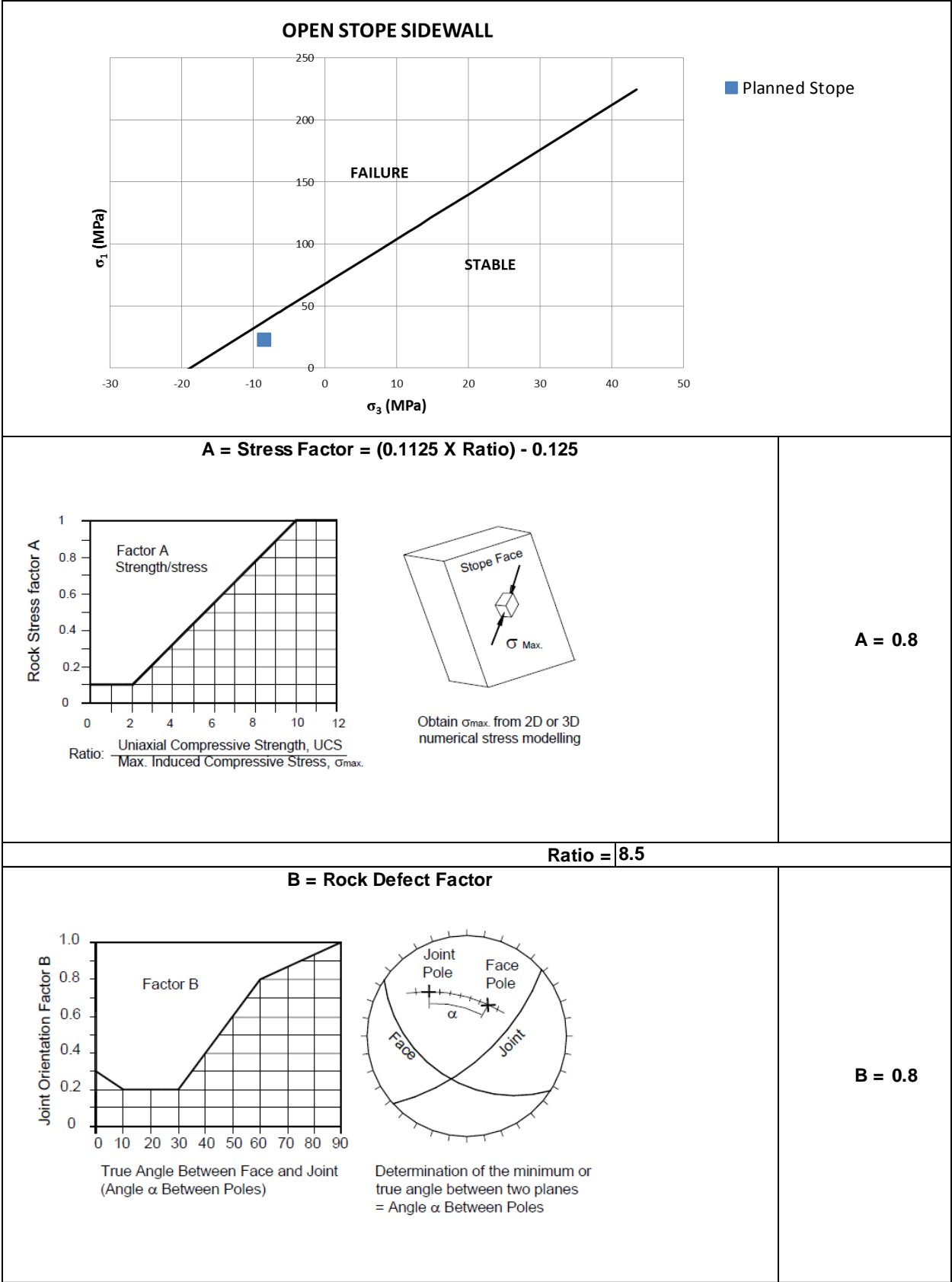






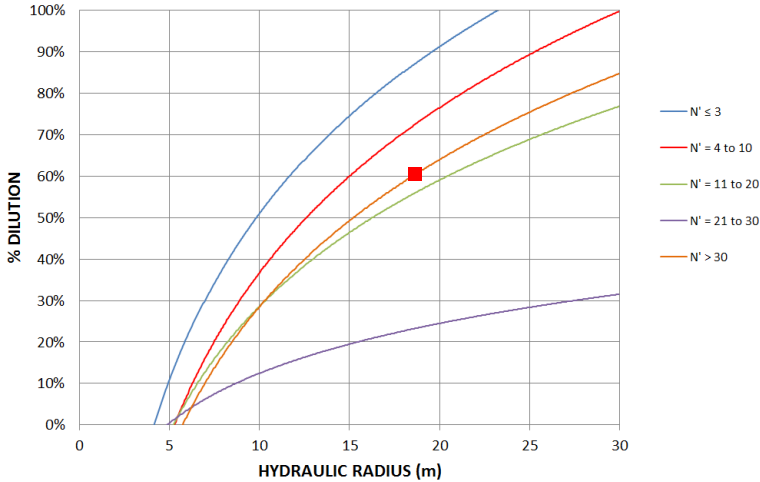
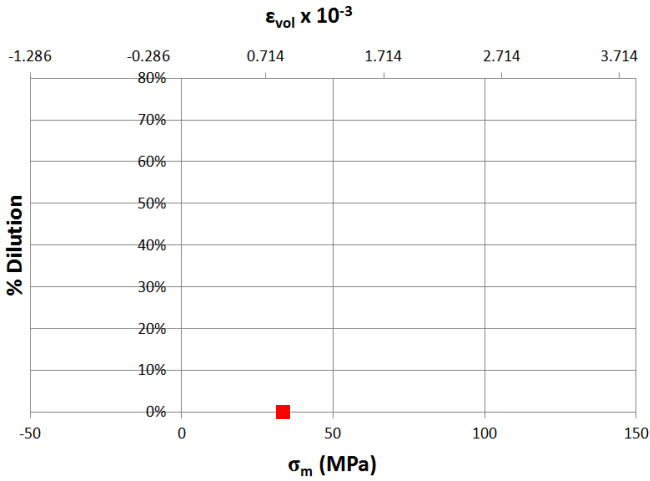
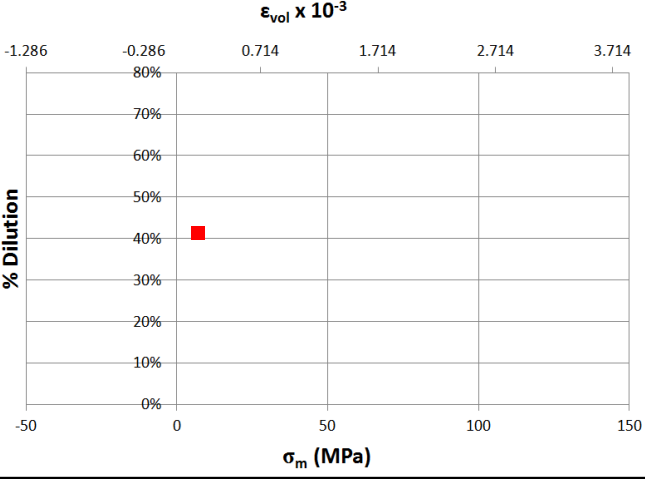
 <p>Graph showing % Dilution (Y-axis, 0% to 100%) versus HYDRAULIC RADIUS (m) (X-axis, 0 to 30). The graph includes curves for different values of <math>N'</math>: <math>N' \leq 3</math> (blue), <math>N' = 4</math> to 10 (red), <math>N' = 11</math> to 20 (green), <math>N' = 21</math> to 30 (purple), and <math>N' &gt; 30</math> (orange). A red square is plotted at approximately 17m radius and 55% dilution.</p>	<p><b><u>Expected Dilution (2):</u></b></p>	<p><b>34.3%</b></p>
 <p>Graph showing % Dilution (Y-axis, 0% to 80%) versus <math>\sigma_m</math> (MPa) (X-axis, -50 to 150). The graph also shows <math>\epsilon_{vol} \times 10^{-3}</math> (top X-axis, -1.286 to 3.714). A red square is plotted at approximately 20 MPa and 0% dilution.</p>	<p><b><u>Expected Hangingwall Dilution (3):</u></b></p>	<p><b>0.0%</b></p>
 <p>Graph showing % Dilution (Y-axis, 0% to 80%) versus <math>\sigma_m</math> (MPa) (X-axis, -50 to 150). The graph also shows <math>\epsilon_{vol} \times 10^{-3}</math> (top X-axis, -1.286 to 3.714). A red square is plotted at approximately 40 MPa and 41.2% dilution.</p>	<p><b><u>Expected Sidewall Dilution (4):</u></b></p>	<p><b>41.2%</b></p>
<p><b>Expected Dilution for Open Stope using OSD</b></p>		<p><b>41.2%</b></p>

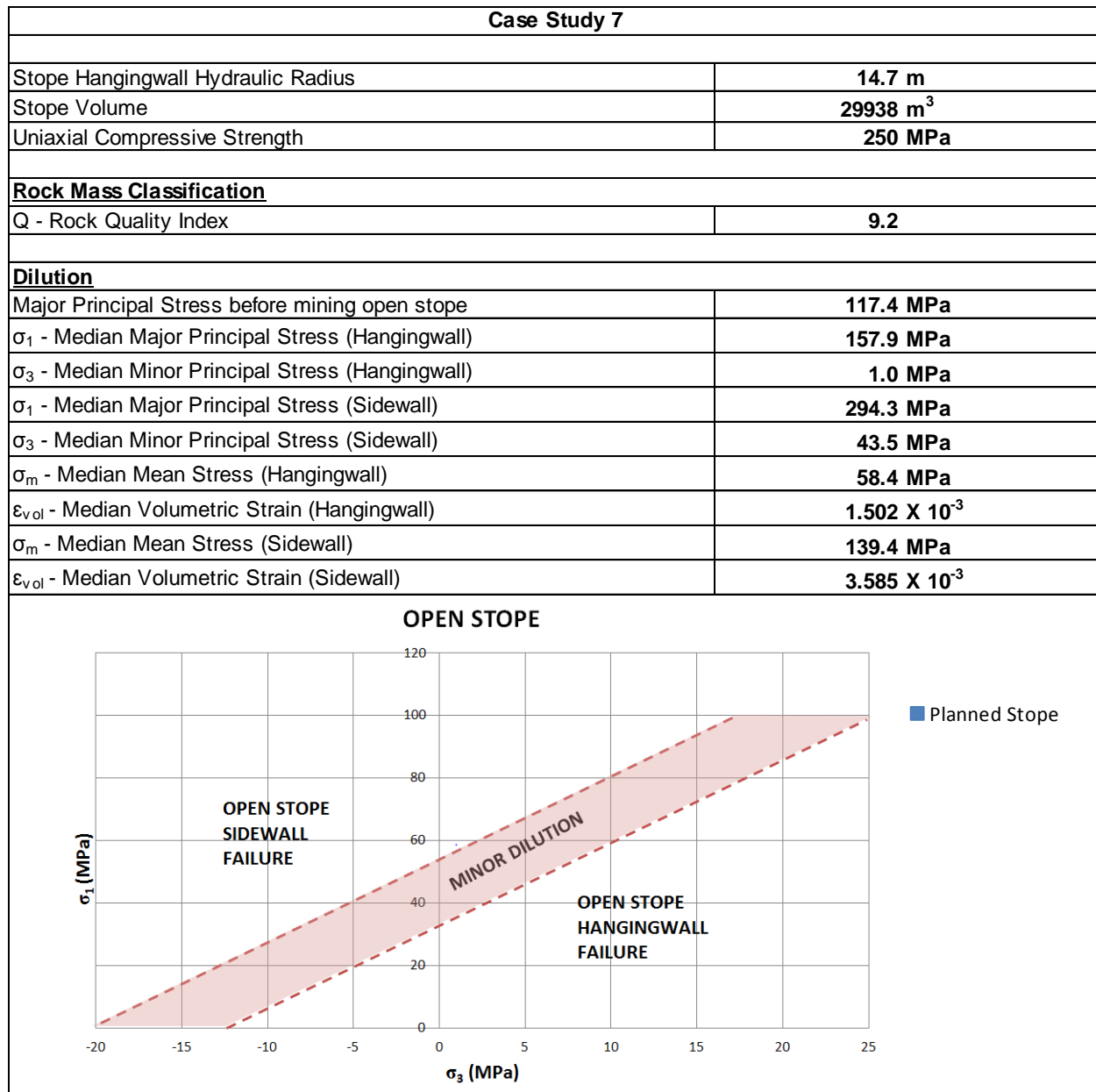


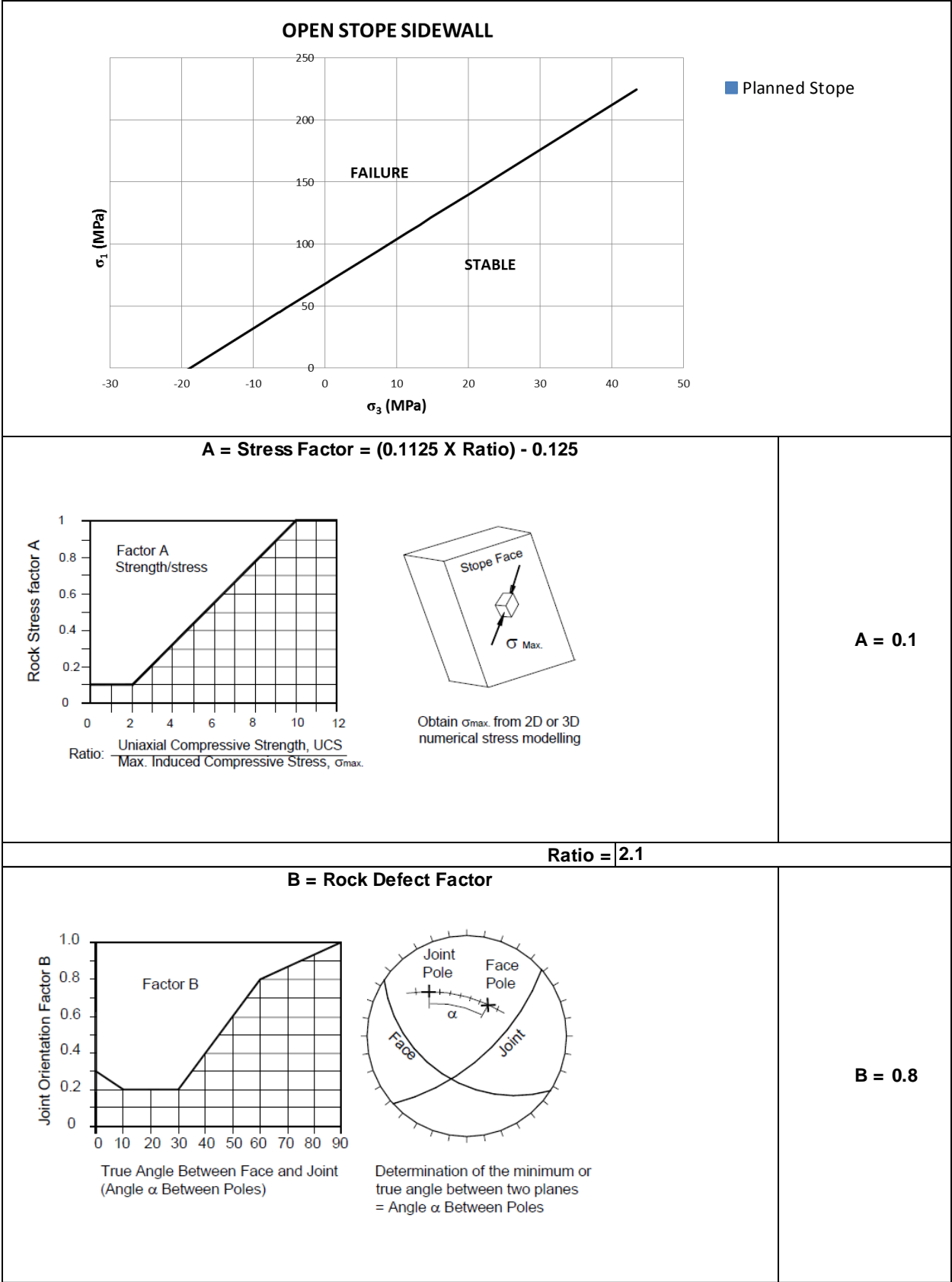




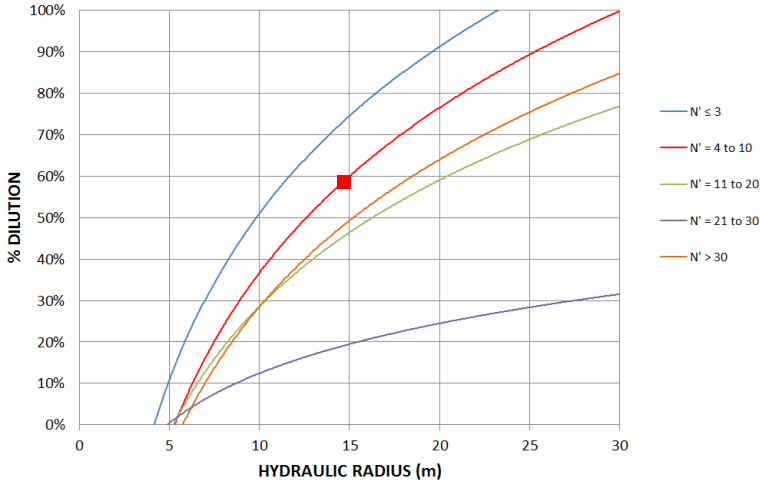
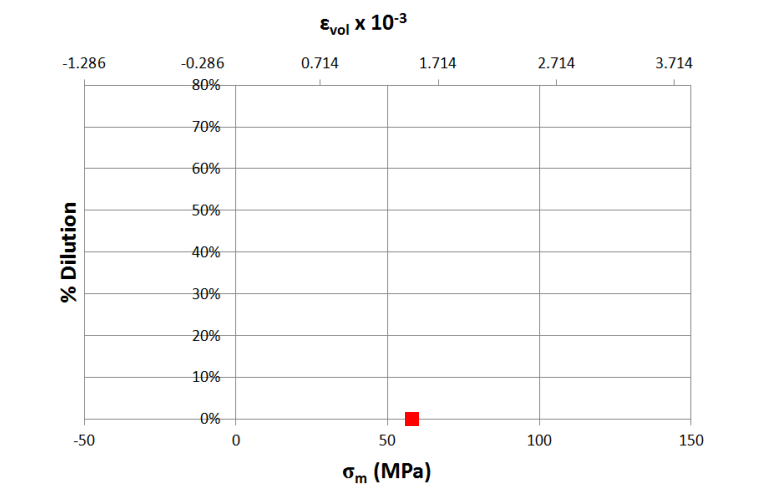
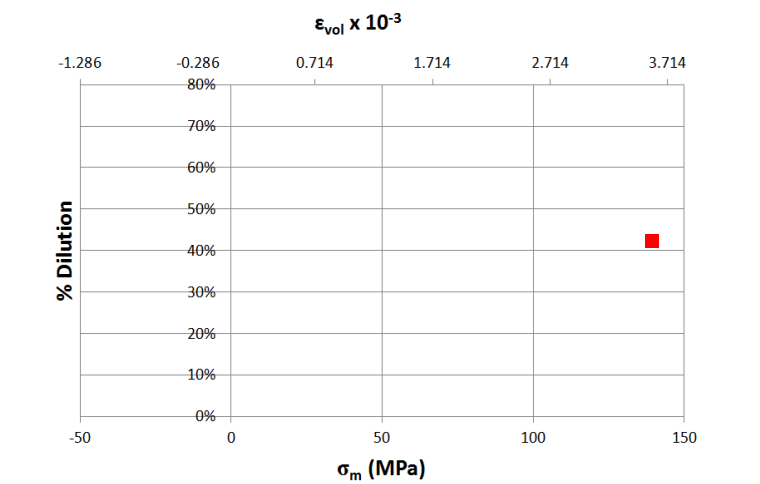


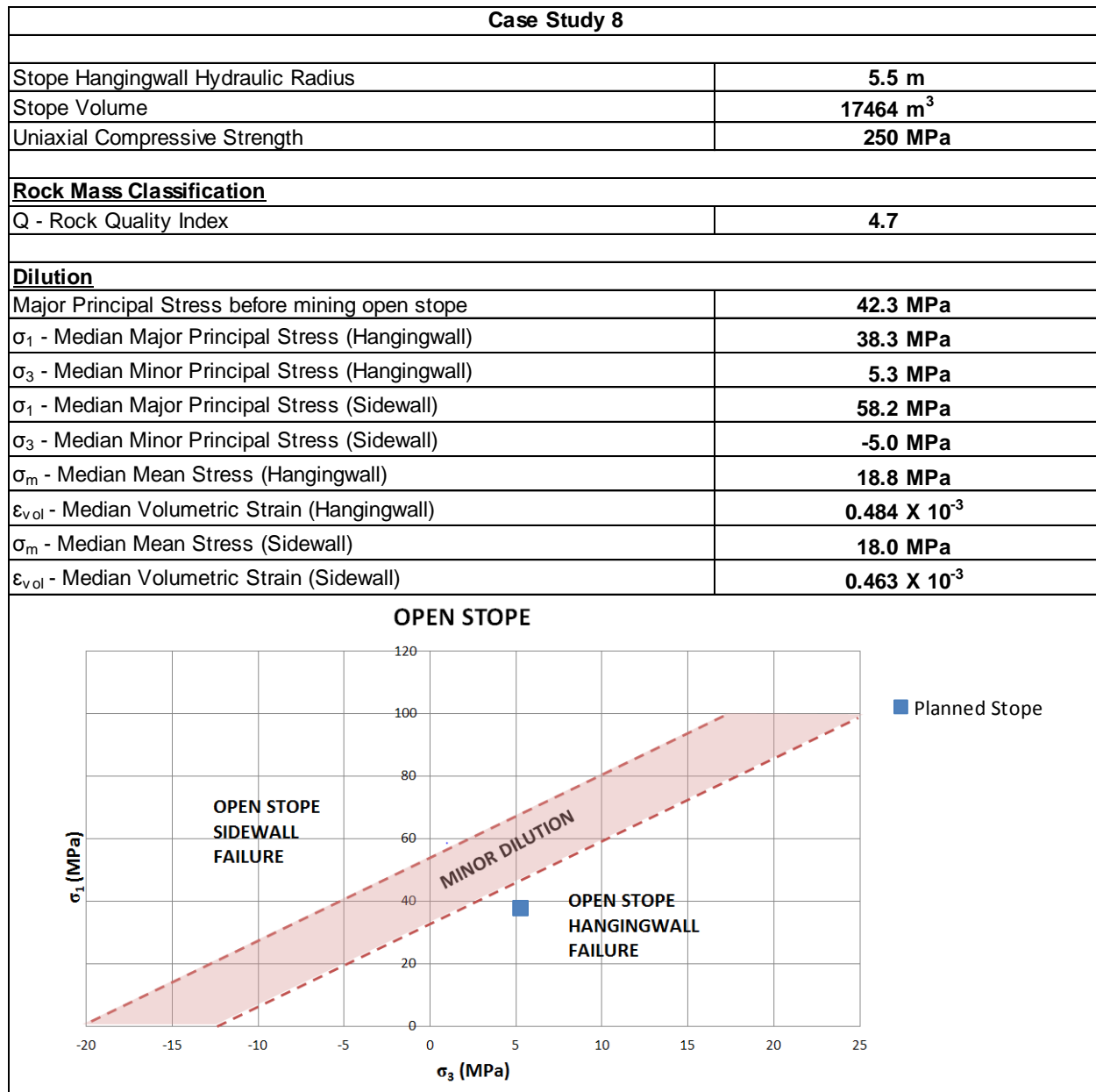
 <p>Graph showing % DILUTION (Y-axis, 0% to 100%) versus HYDRAULIC RADIUS (m) (X-axis, 0 to 30). The graph includes curves for different values of <math>N'</math>:</p> <ul style="list-style-type: none"><li><math>N' \leq 3</math> (Blue)</li><li><math>N' = 4 \text{ to } 10</math> (Red)</li><li><math>N' = 11 \text{ to } 20</math> (Green)</li><li><math>N' = 21 \text{ to } 30</math> (Purple)</li><li><math>N' &gt; 30</math> (Orange)</li></ul> <p>A red square is plotted at approximately 18.5m radius and 60.7% dilation.</p>	<p><b><u>Expected</u></b> <b><u>Dilution (2):</u></b></p>	<p><b>60.7%</b></p>
 <p>Graph showing % DILUTION (Y-axis, 0% to 80%) versus <math>\sigma_m</math> (MPa) (X-axis, -50 to 150) and <math>\epsilon_{vol} \times 10^{-3}</math> (Top X-axis, -1.286 to 3.714). The graph includes curves for different values of <math>N'</math>.</p> <p>A red square is plotted at approximately 30 MPa and 0.0% dilation.</p>	<p><b><u>Expected</u></b> <b><u>Hangingwall</u></b> <b><u>Dilution (3):</u></b></p>	<p><b>0.0%</b></p>
 <p>Graph showing % DILUTION (Y-axis, 0% to 80%) versus <math>\sigma_m</math> (MPa) (X-axis, -50 to 150) and <math>\epsilon_{vol} \times 10^{-3}</math> (Top X-axis, -1.286 to 3.714). The graph includes curves for different values of <math>N'</math>.</p> <p>A red square is plotted at approximately 5 MPa and 41.0% dilation.</p>	<p><b><u>Expected</u></b> <b><u>Sidewall Dilution</u></b> <b><u>(4):</u></b></p>	<p><b>41.0%</b></p>
<p><b>Expected Dilution for Open Stope using OSD</b></p>		<p><b>41.0%</b></p>



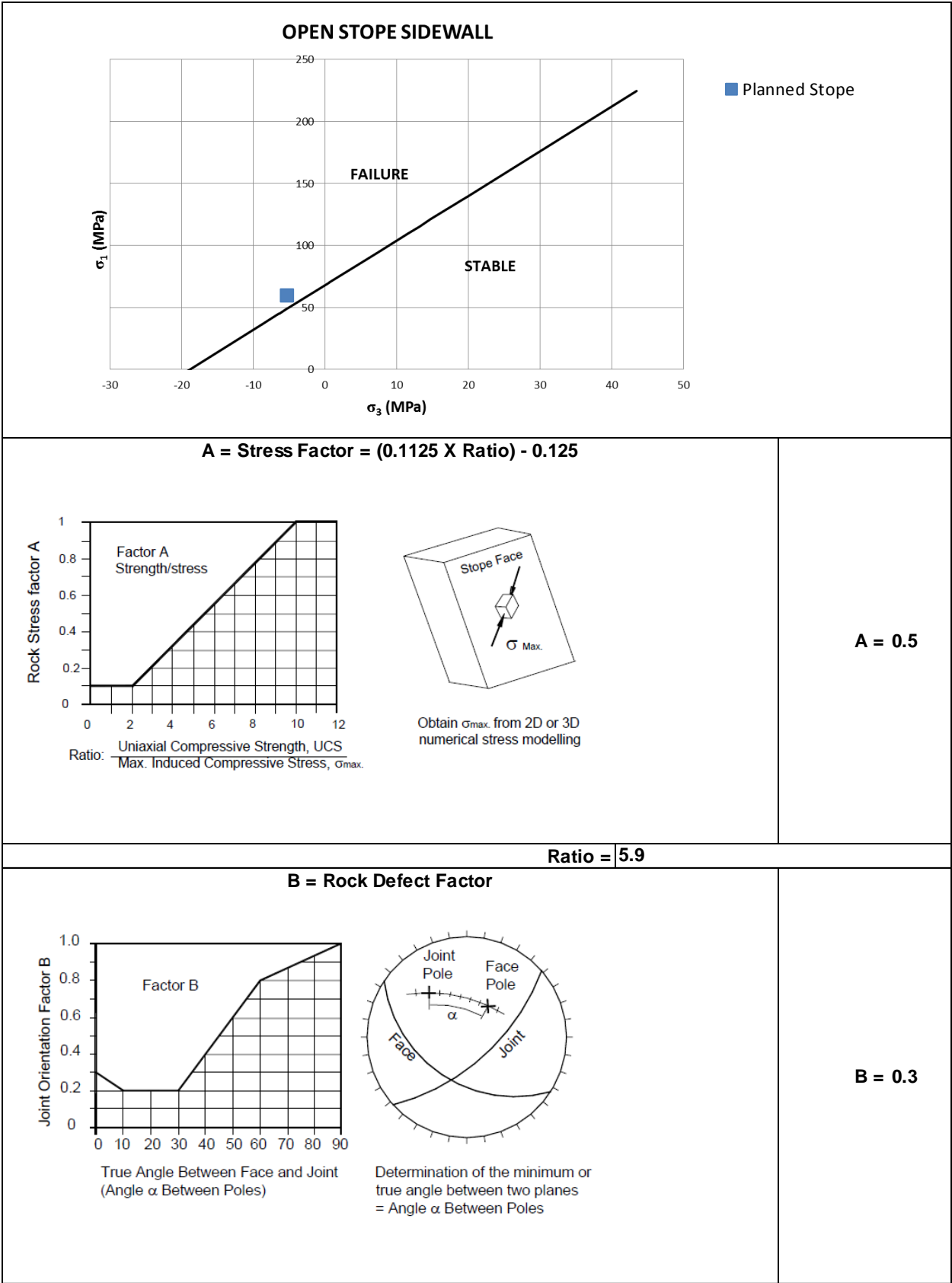




 <p>Graph showing % DILUTION (Y-axis, 0% to 100%) versus HYDRAULIC RADIUS (m) (X-axis, 0 to 30). The graph includes curves for different values of <math>N'</math>:</p> <ul style="list-style-type: none"><li><math>N' \leq 3</math> (Blue line)</li><li><math>N' = 4 \text{ to } 10</math> (Red line)</li><li><math>N' = 11 \text{ to } 20</math> (Green line)</li><li><math>N' = 21 \text{ to } 30</math> (Purple line)</li><li><math>N' &gt; 30</math> (Orange line)</li></ul> <p>A red square is plotted at approximately (15, 58.7%).</p>	<p><b><u>Expected Dilution (2):</u></b></p>	<p><b>58.7%</b></p>
 <p>Graph showing % Dilution (Y-axis, 0% to 80%) versus <math>\sigma_m</math> (MPa) (X-axis, -50 to 150) and <math>\epsilon_{vol} \times 10^{-3}</math> (Top X-axis, -1.286 to 3.714). The graph includes curves for different values of <math>N'</math>.</p> <p>A red square is plotted at approximately (60, 0.0%).</p>	<p><b><u>Expected Hangingwall Dilution (3):</u></b></p>	<p><b>0.0%</b></p>
 <p>Graph showing % Dilution (Y-axis, 0% to 80%) versus <math>\sigma_m</math> (MPa) (X-axis, -50 to 150) and <math>\epsilon_{vol} \times 10^{-3}</math> (Top X-axis, -1.286 to 3.714). The graph includes curves for different values of <math>N'</math>.</p> <p>A red square is plotted at approximately (135, 41.8%).</p>	<p><b><u>Expected Sidewall Dilution (4):</u></b></p>	<p><b>41.8%</b></p>
<p><b>Expected Dilution for Open Stope using OSD</b></p>		<p><b>41.8%</b></p>

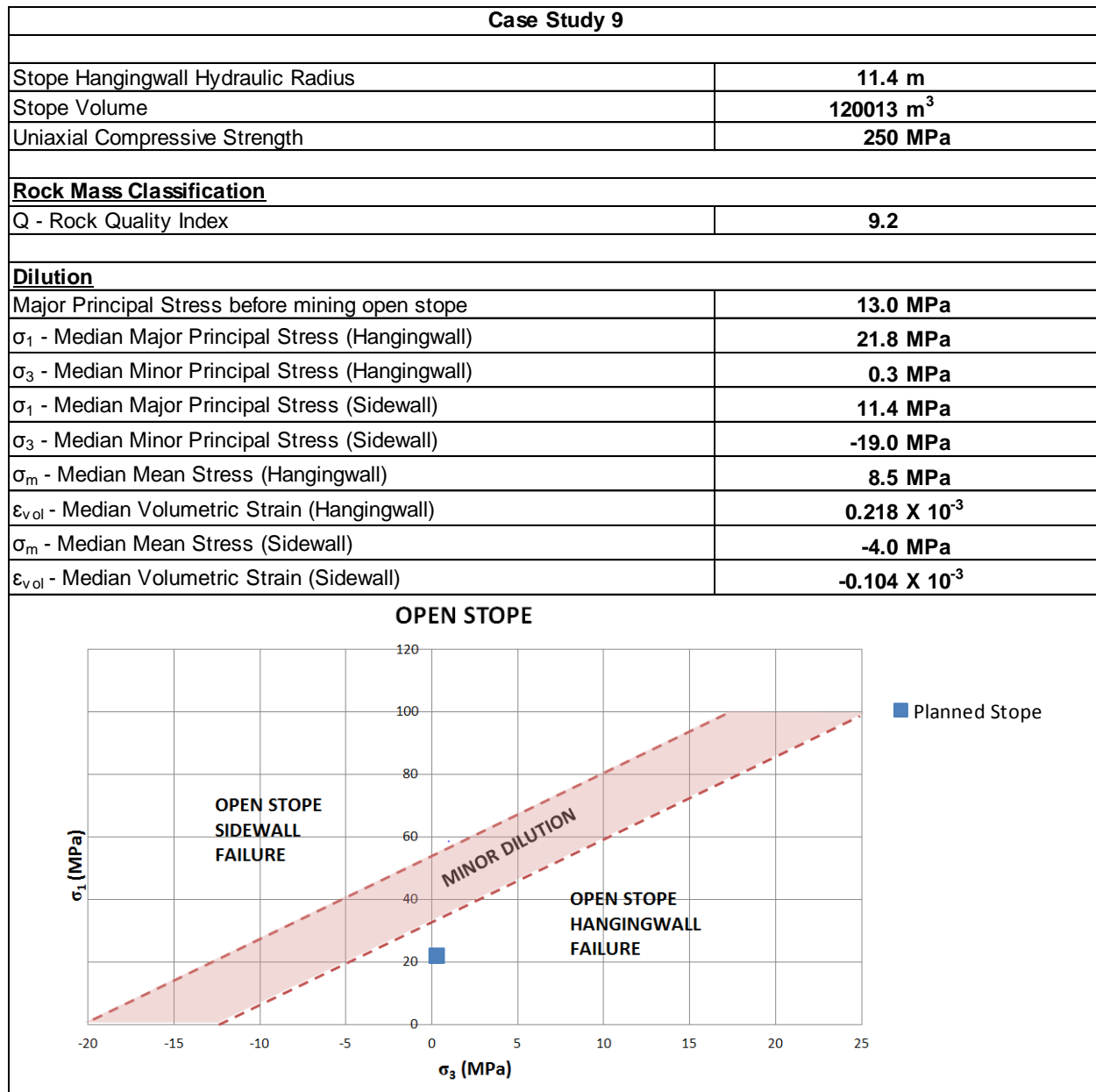


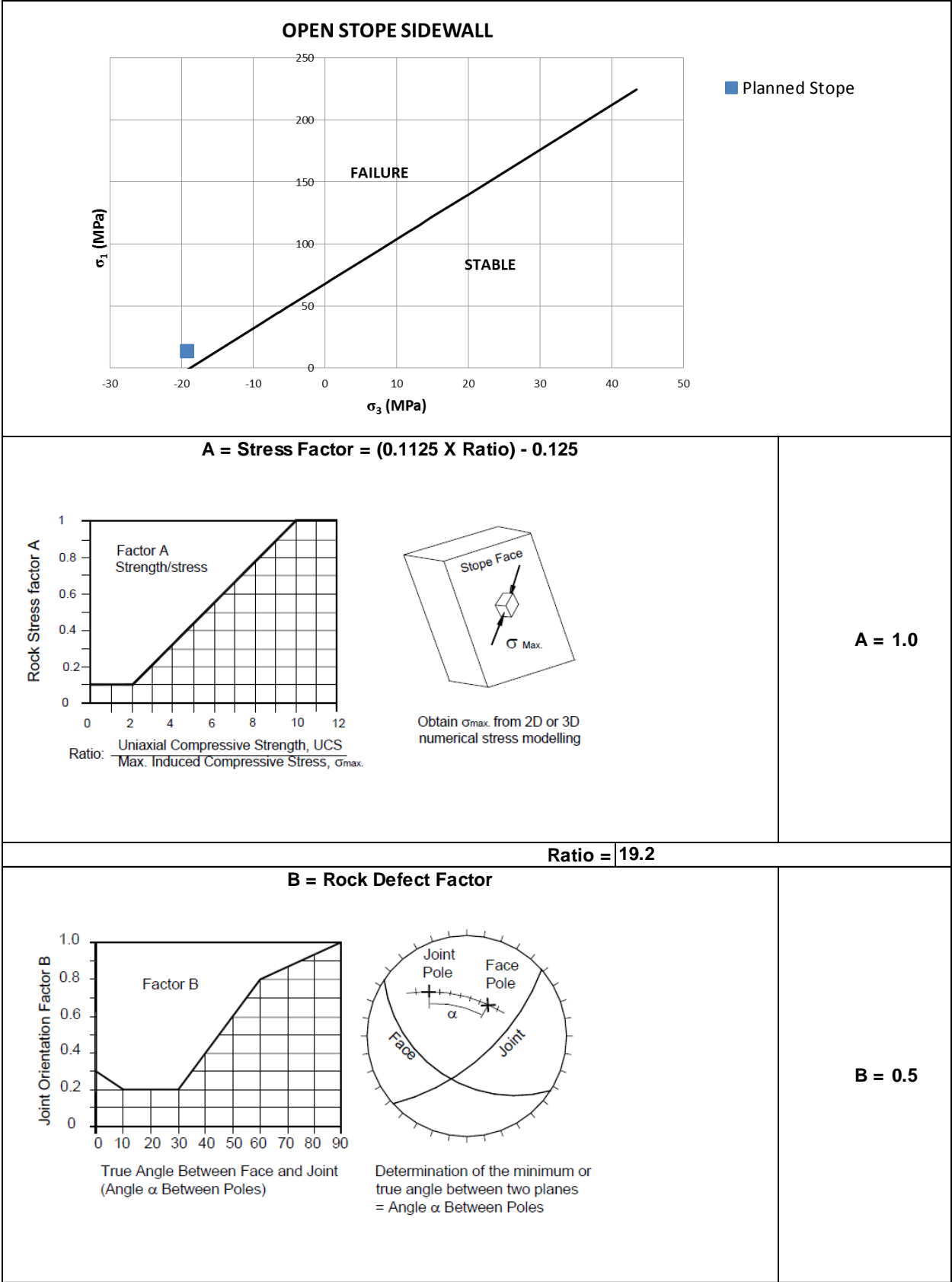




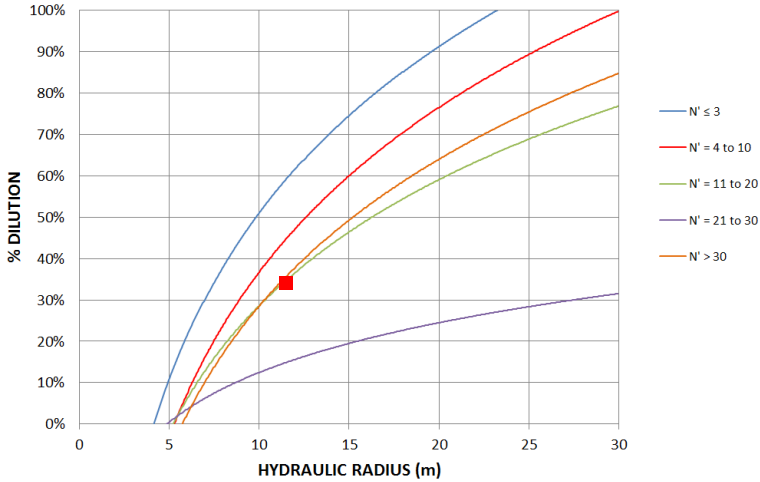
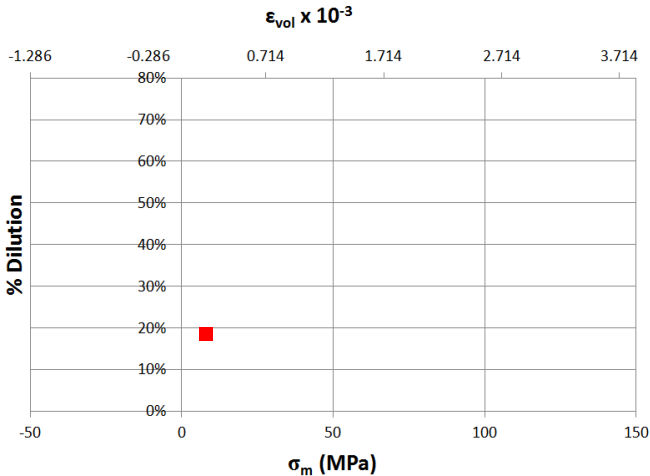
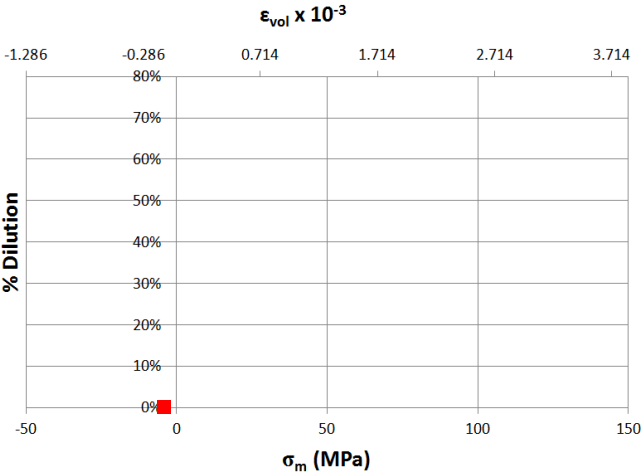
<p style="text-align: center;"><b>C = Slope Orientation Factor</b></p> <div style="display: flex; justify-content: space-around;"> <div style="width: 45%;"> <p>Factor C Gravity Fall &amp; Slabbing</p> <p><math>C = 8 - 6\cos(Dip)</math></p> </div> <div style="width: 45%;"> <p>Face Dip</p> <p>Slope</p> </div> </div> <div style="display: flex; justify-content: space-around; margin-top: 20px;"> <div style="width: 45%;"> <p>Factor C Sliding</p> </div> <div style="width: 45%;"> <p>Joint Dip</p> <p>Slope</p> </div> </div>	<p><b>C = 4.0</b></p>
<p><b>N' = Modified Stability Number = Q' X A X B X C = 3.07</b></p>	
<p style="text-align: center;">MODIFIED STABILITY NUMBER (N')</p> <p style="text-align: center;">HYDRAULIC RADIUS (m)</p> <div style="position: absolute; top: 600px; right: 100px;"> <p>— 10% Dilution</p> <p>— 20% Dilution</p> <p>— 30% Dilution</p> <p>— 40% Dilution</p> <p>— 50% Dilution Estimation</p> <p>— 60% Dilution Estimation</p> </div>	<p><b>Expected Dilution (1): 28%</b></p>

	<p><b><u>Expected Dilution (2):</u></b></p>	<p><b>2.8%</b></p>
	<p><b><u>Expected Hangingwall Dilution (3):</u></b></p>	<p><b>24.5%</b></p>
	<p><b><u>Expected Sidewall Dilution (4):</u></b></p>	<p><b>0.0%</b></p>
<p><b>Expected Dilution for Open Stope using OSD</b></p>		<p><b>24.5%</b></p>

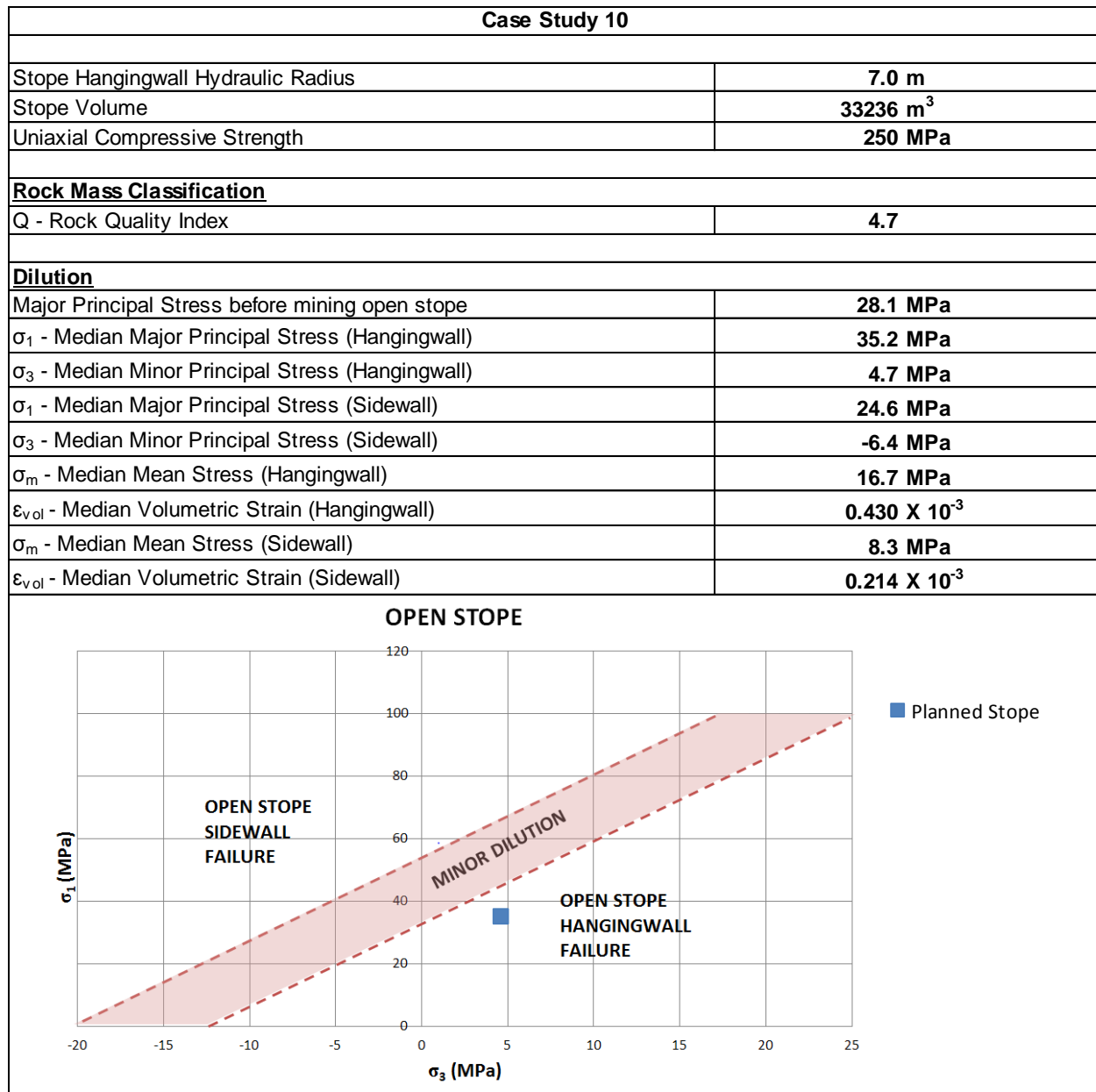


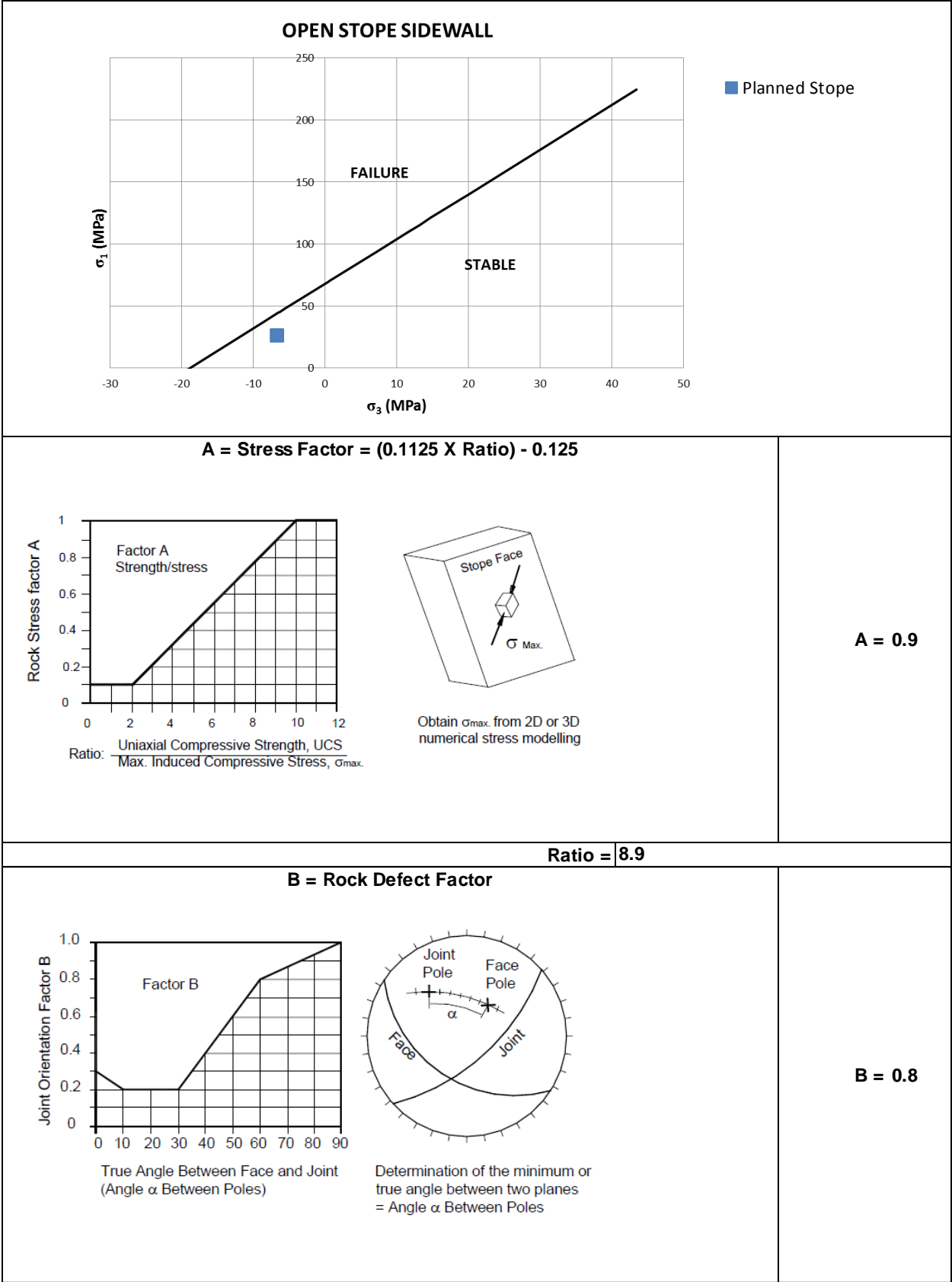


<p style="text-align: center;"><b>C = Slope Orientation Factor</b></p> <div style="display: flex; justify-content: space-around;"> <div style="text-align: center;"> <p>Factor C Gravity Fall &amp; Slabbing</p> <p><math>C = 8 - 6\cos(Dip)</math></p> </div> <div style="text-align: center;"> <p>Face Dip</p> <p>Slope</p> </div> </div> <div style="display: flex; justify-content: space-around; margin-top: 20px;"> <div style="text-align: center;"> <p>Factor C Sliding</p> </div> <div style="text-align: center;"> <p>Joint Dip</p> <p>Slope</p> </div> </div>	<p><b>C = 4.0</b></p>
<p><b>N' = Modified Stability Number = Q' X A X B X C = 18.46</b></p>	
<div style="position: absolute; top: 10px; right: 10px; border: 1px solid black; padding: 5px;"> <p>10% Dilution</p> <p>20% Dilution</p> <p>30% Dilution</p> <p>40% Dilution</p> <p>70% Dilution</p> <p>50% Dilution Estimation</p> <p>60% Dilution Estimation</p> </div>	<p><b>Expected Dilution (1): 45%</b></p>

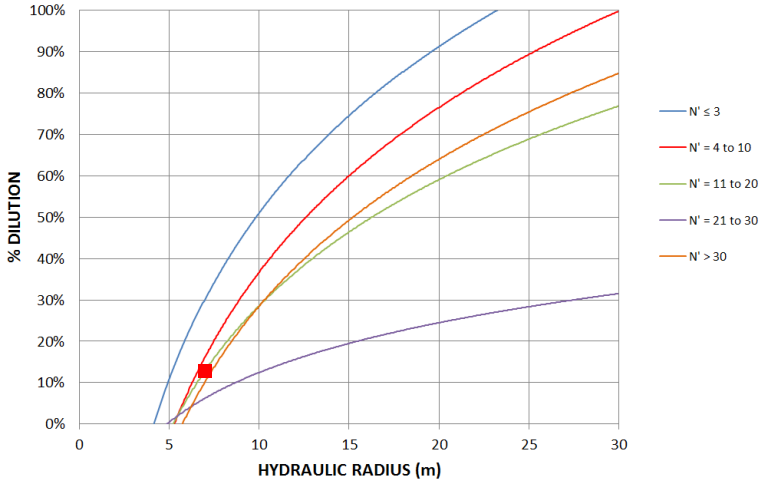
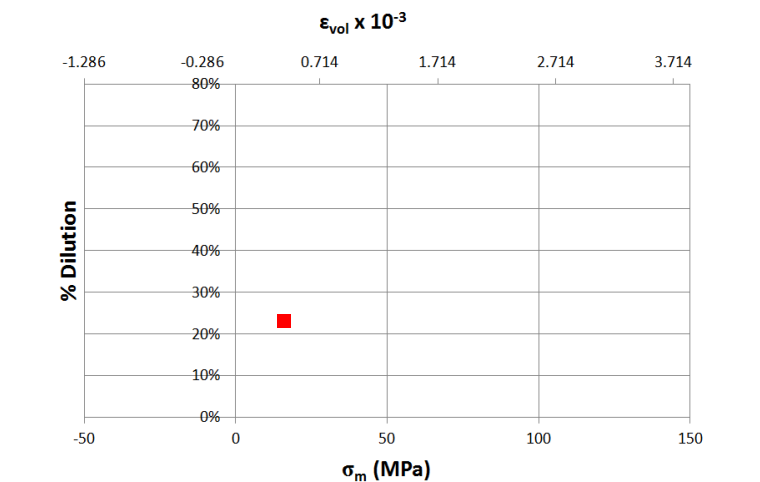
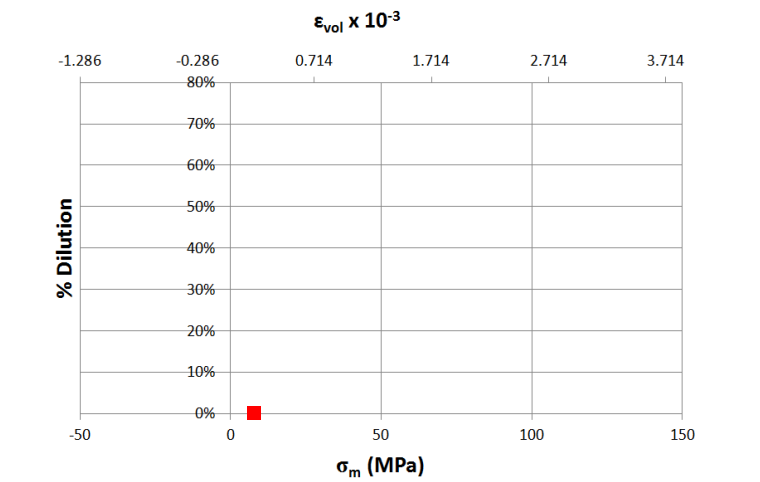
 <p>Graph showing % Dilution (Y-axis, 0% to 100%) versus HYDRAULIC RADIUS (m) (X-axis, 0 to 30). The graph includes curves for different values of <math>N'</math>:</p> <ul style="list-style-type: none"><li><math>N' \leq 3</math> (Blue line)</li><li><math>N' = 4 \text{ to } 10</math> (Red line)</li><li><math>N' = 11 \text{ to } 20</math> (Green line)</li><li><math>N' = 21 \text{ to } 30</math> (Purple line)</li><li><math>N' &gt; 30</math> (Orange line)</li></ul> <p>A red square is plotted at approximately (12, 34.5%).</p>	<p><b><u>Expected Dilution (2):</u></b></p>	<p><b>34.5%</b></p>
 <p>Graph showing % Dilution (Y-axis, 0% to 80%) versus <math>\sigma_m</math> (MPa) (X-axis, -50 to 150). The graph includes curves for different values of <math>\epsilon_{vol} \times 10^{-3}</math>:</p> <ul style="list-style-type: none"><li>-1.286 (Blue line)</li><li>-0.286 (Red line)</li><li>0.714 (Green line)</li><li>1.714 (Orange line)</li><li>2.714 (Purple line)</li><li>3.714 (Brown line)</li></ul> <p>A red square is plotted at approximately (10, 18.2%).</p>	<p><b><u>Expected Hangingwall Dilution (3):</u></b></p>	<p><b>18.2%</b></p>
 <p>Graph showing % Dilution (Y-axis, 0% to 80%) versus <math>\sigma_m</math> (MPa) (X-axis, -50 to 150). The graph includes curves for different values of <math>\epsilon_{vol} \times 10^{-3}</math>:</p> <ul style="list-style-type: none"><li>-1.286 (Blue line)</li><li>-0.286 (Red line)</li><li>0.714 (Green line)</li><li>1.714 (Orange line)</li><li>2.714 (Purple line)</li><li>3.714 (Brown line)</li></ul> <p>A red square is plotted at approximately (0, 0%).</p>	<p><b><u>Expected Sidewall Dilution (4):</u></b></p>	<p><b>0.0%</b></p>
<p><b>Expected Dilution for Open Stope using OSD</b></p>		<p><b>18.2%</b></p>

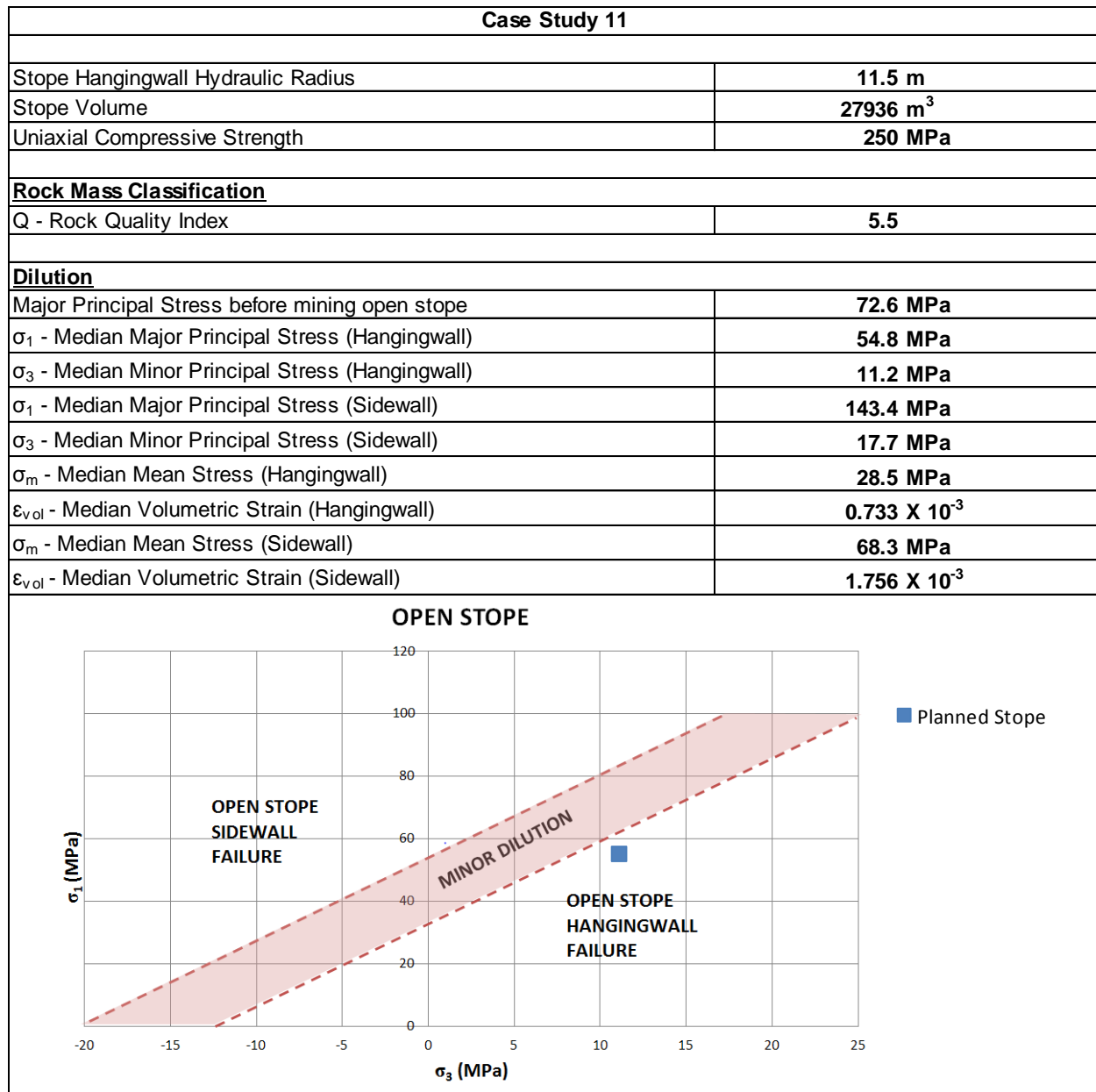


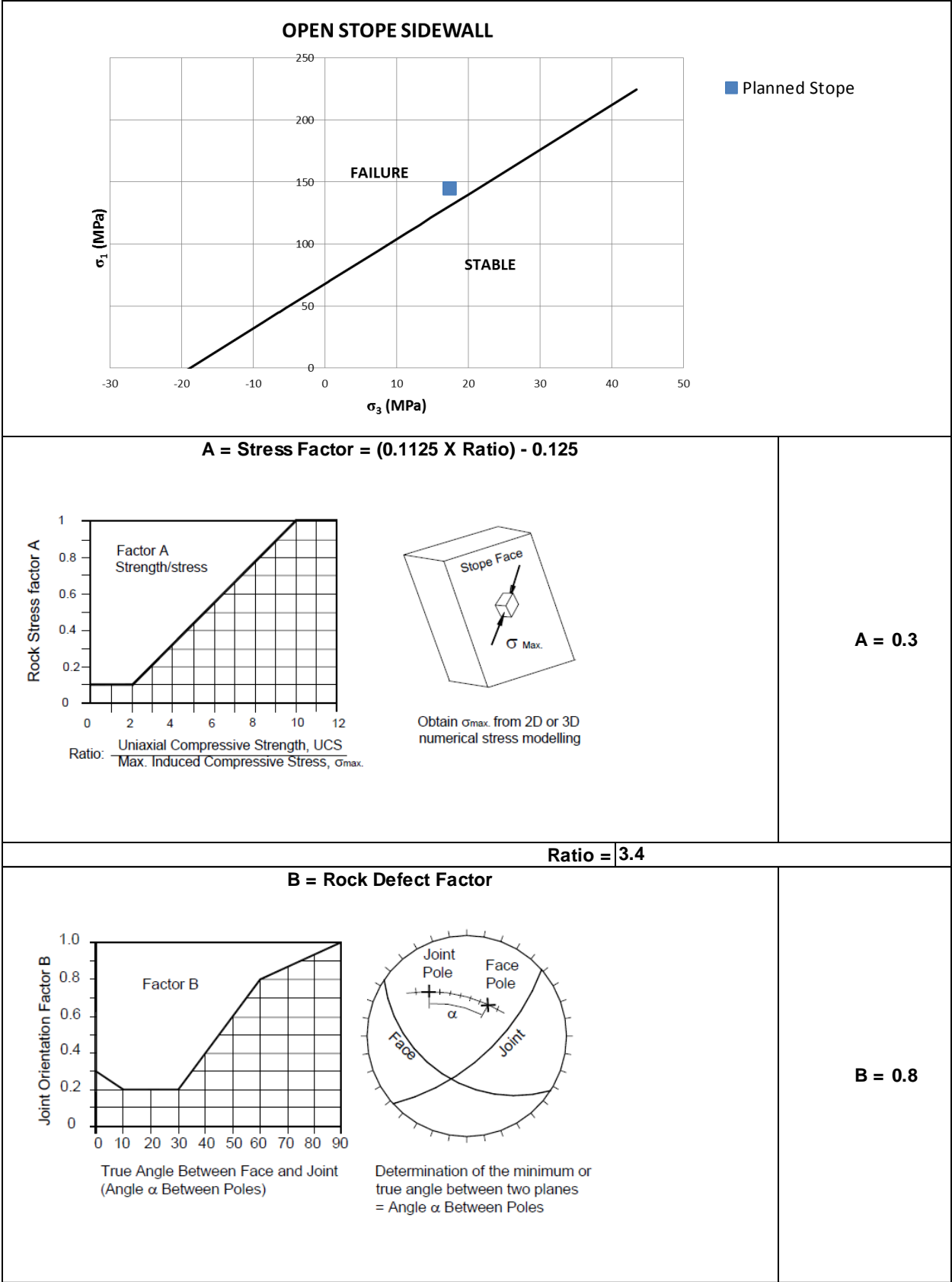


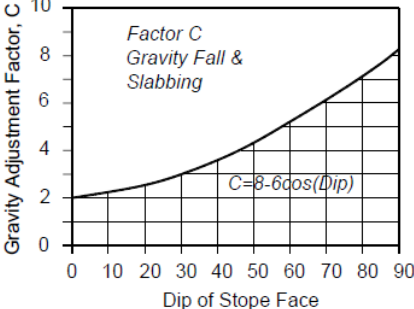
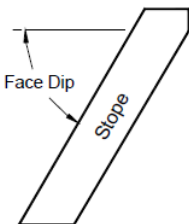
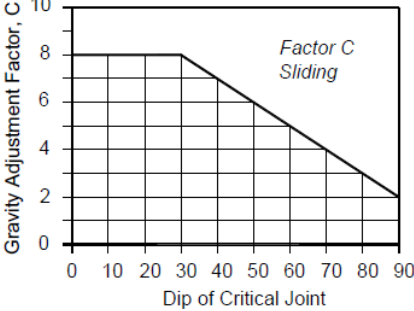
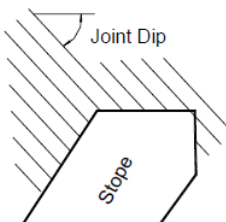
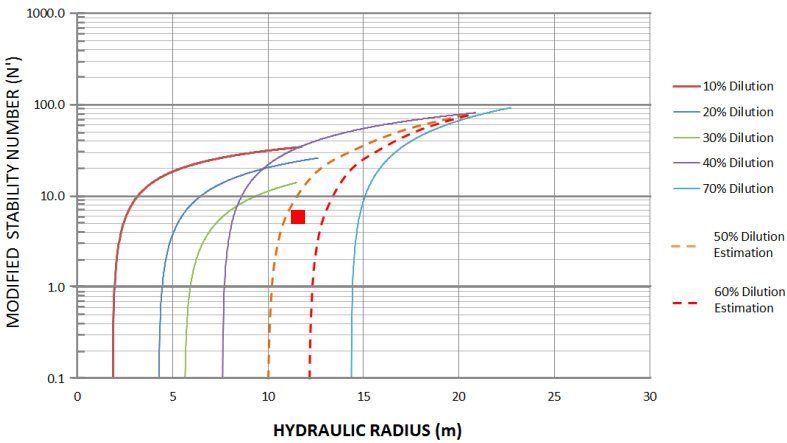




 <p>Graph showing % DILUTION (Y-axis, 0% to 100%) versus HYDRAULIC RADIUS (m) (X-axis, 0 to 30). The graph includes curves for different values of <math>N'</math>:</p> <ul style="list-style-type: none"><li><math>N' \leq 3</math> (Blue line)</li><li><math>N' = 4 \text{ to } 10</math> (Red line)</li><li><math>N' = 11 \text{ to } 20</math> (Green line)</li><li><math>N' = 21 \text{ to } 30</math> (Purple line)</li><li><math>N' &gt; 30</math> (Orange line)</li></ul> <p>A red square is plotted at approximately (7.5, 12.9%).</p>	<p><b>Expected Dilution (2):</b></p>	<p><b>12.9%</b></p>
 <p>Graph showing % Dilution (Y-axis, 0% to 80%) versus <math>\sigma_m</math> (MPa) (X-axis, -50 to 150) and <math>\epsilon_{vol} \times 10^{-3}</math> (Top X-axis, -1.286 to 3.714). A red square is plotted at approximately (15, 23.3%).</p>	<p><b>Expected Hangingwall Dilution (3):</b></p>	<p><b>23.3%</b></p>
 <p>Graph showing % Dilution (Y-axis, 0% to 80%) versus <math>\sigma_m</math> (MPa) (X-axis, -50 to 150) and <math>\epsilon_{vol} \times 10^{-3}</math> (Top X-axis, -1.286 to 3.714). A red square is plotted at approximately (5, 0.0%).</p>	<p><b>Expected Sidewall Dilution (4):</b></p>	<p><b>0.0%</b></p>
<p><b>Expected Dilution for Open Stope using OSD</b></p>		<p><b>23.3%</b></p>

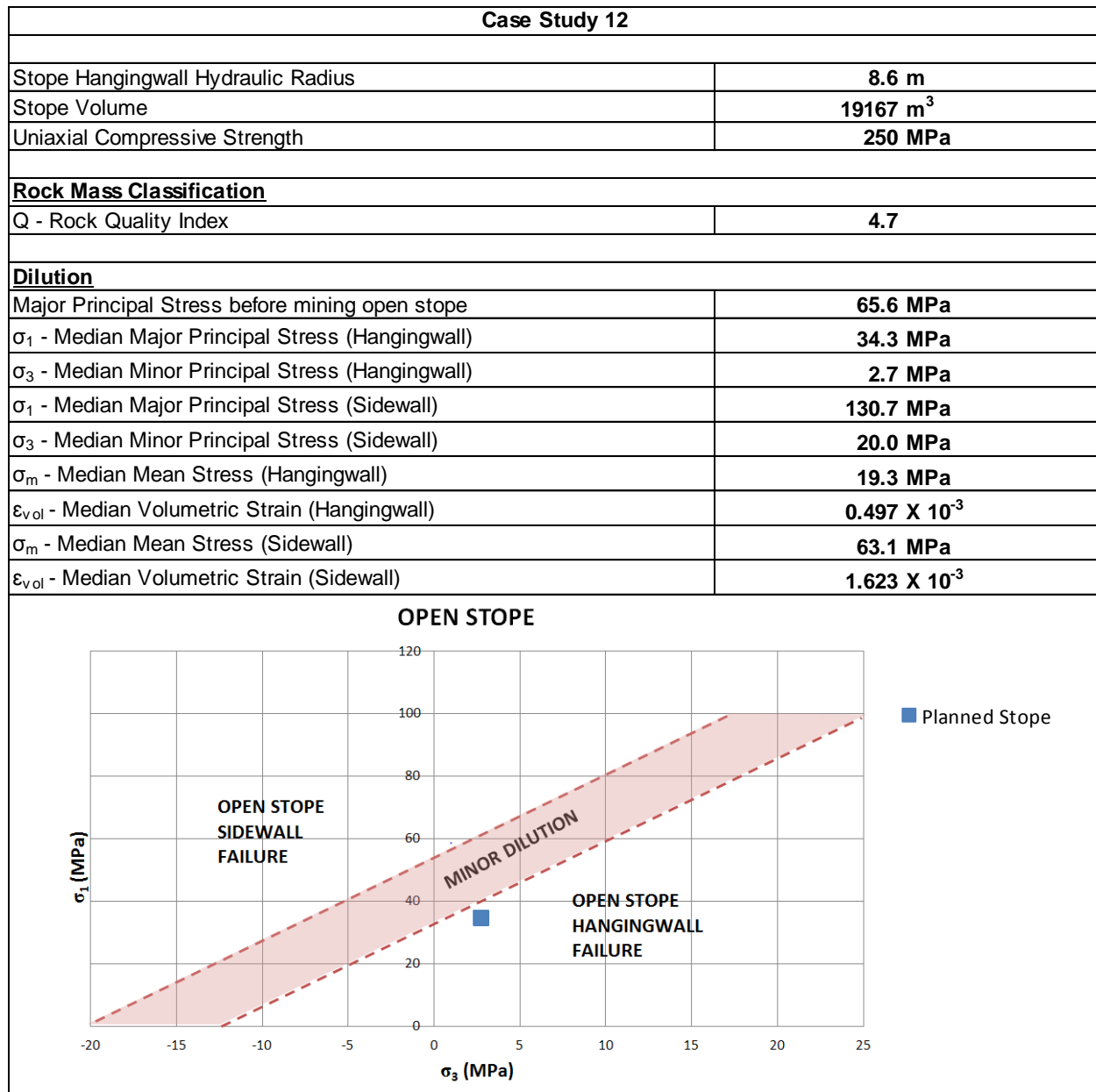


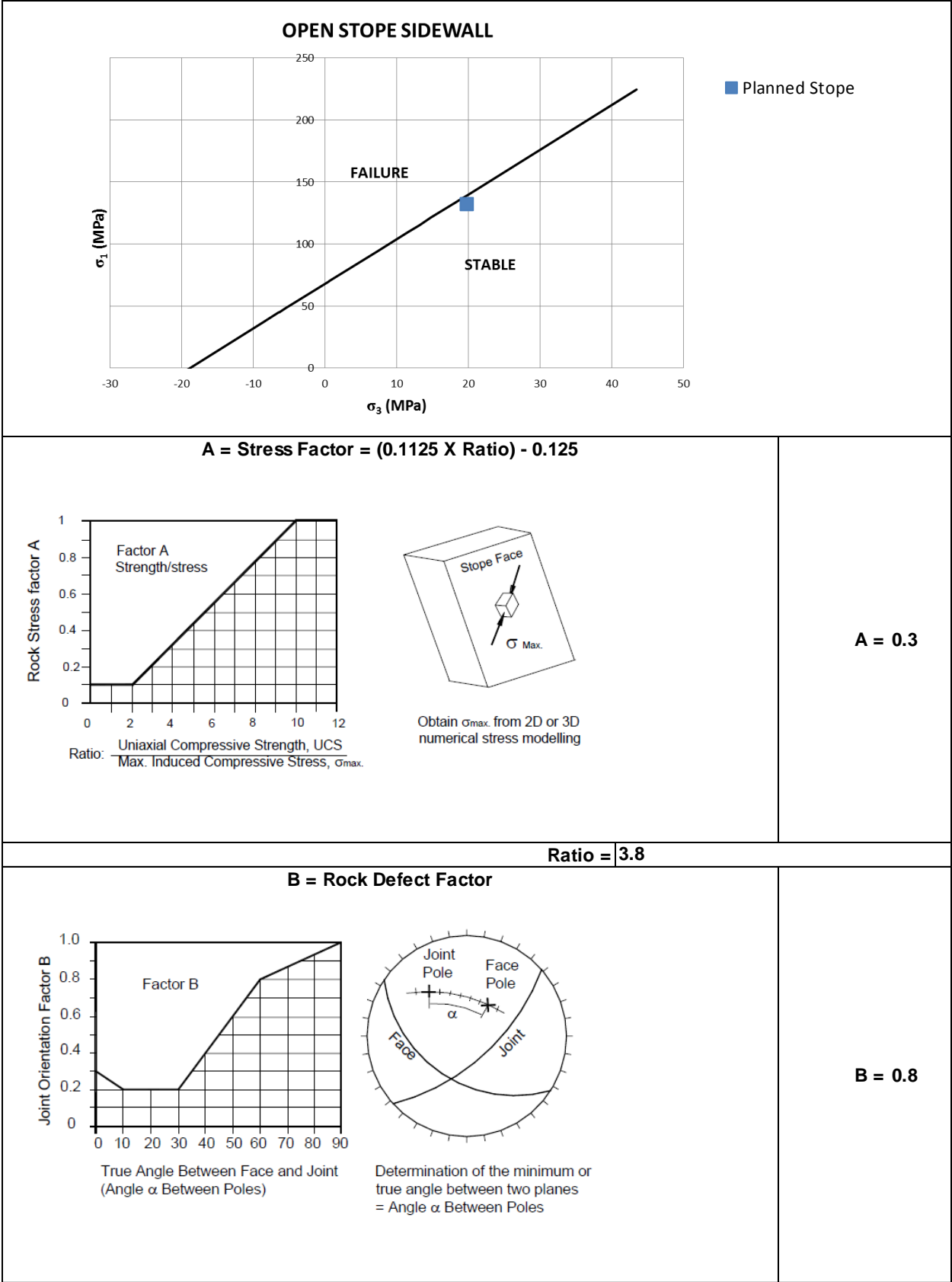


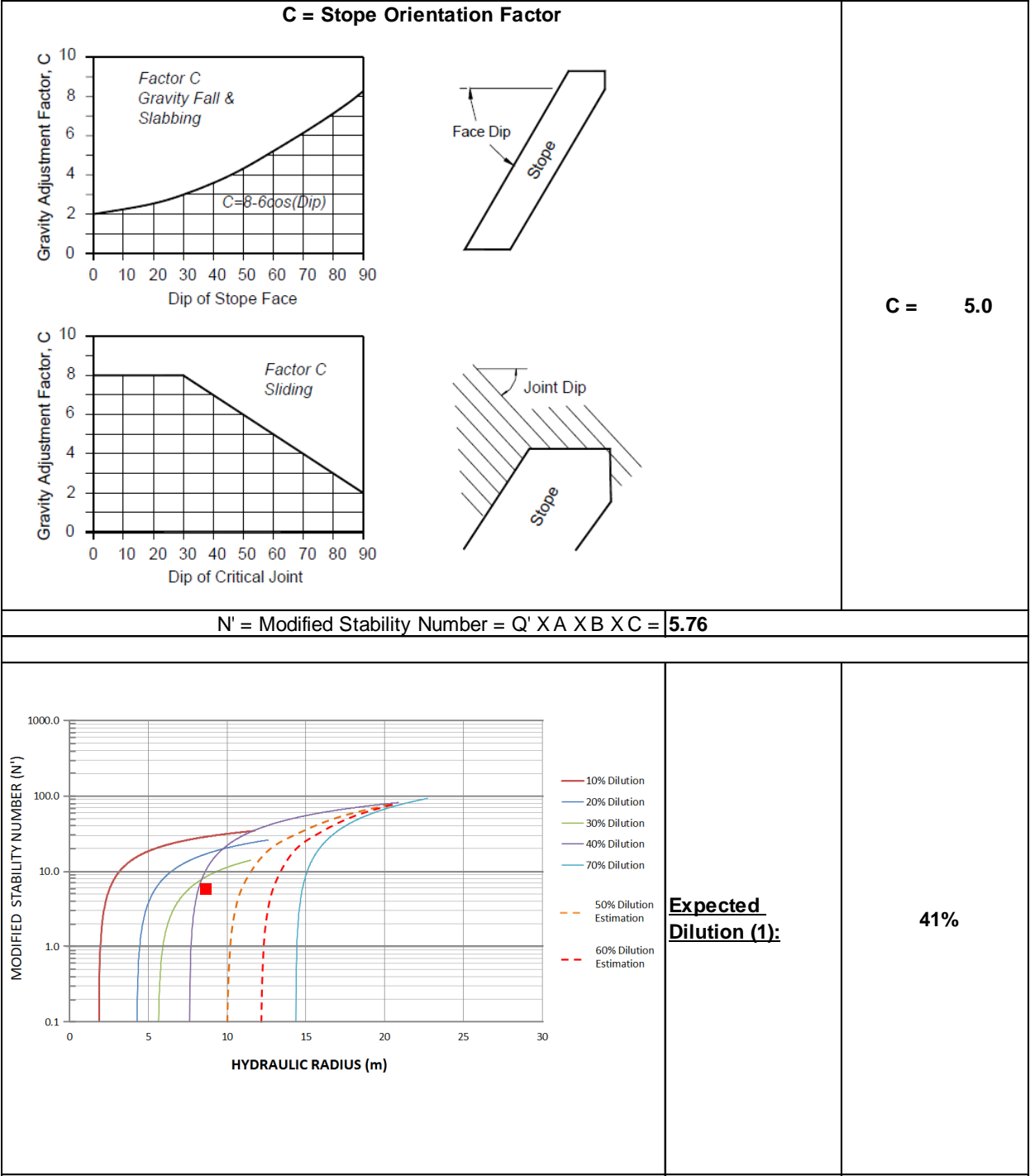
<p style="text-align: center;"><b>C = Slope Orientation Factor</b></p> <div style="display: flex; justify-content: space-around; align-items: flex-start;"> <div style="text-align: center;">  <p>Factor C Gravity Fall &amp; Slabbing</p> <p><math>C = 8 - 6\cos(Dip)</math></p> </div> <div style="text-align: center;">  <p>Face Dip</p> <p>Slope</p> </div> </div> <div style="display: flex; justify-content: space-around; align-items: flex-start; margin-top: 20px;"> <div style="text-align: center;">  <p>Factor C Sliding</p> </div> <div style="text-align: center;">  <p>Joint Dip</p> <p>Slope</p> </div> </div> <div style="text-align: right; margin-top: 20px; font-size: 1.2em;"> <b>C = 5.0</b> </div>	
<b>N' = Modified Stability Number = Q' X A X B X C = 5.74</b>	
 <p style="text-align: center;"><b>HYDRAULIC RADIUS (m)</b></p> <div style="position: absolute; top: 650px; left: 550px;"> <p>10% Dilution</p> <p>20% Dilution</p> <p>30% Dilution</p> <p>40% Dilution</p> <p>70% Dilution</p> <p>50% Dilution Estimation</p> <p>60% Dilution Estimation</p> </div>	<p><b>Expected Dilution (1):</b></p> <p style="font-size: 1.5em;"><b>54%</b></p>



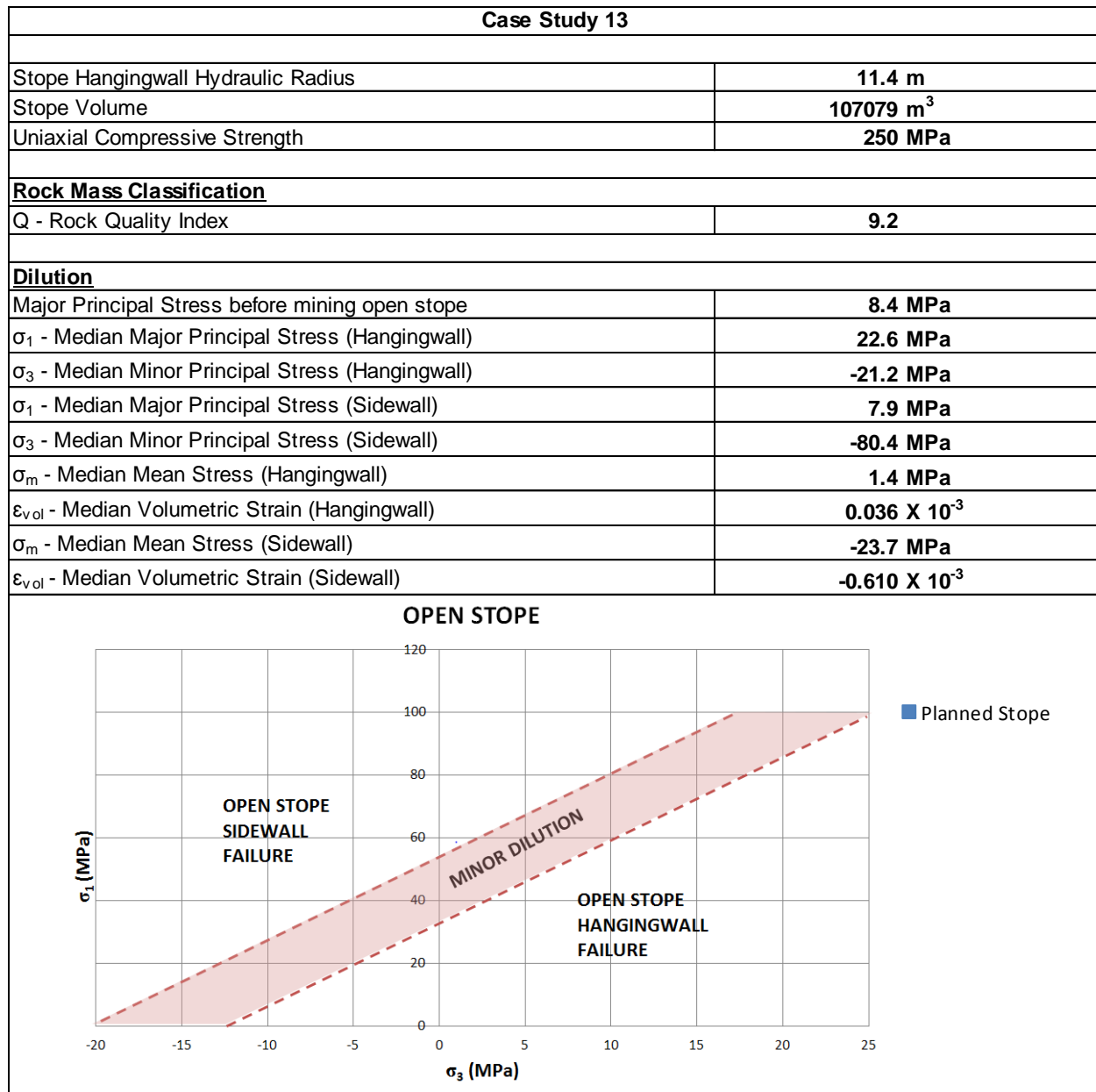
<p>The graph shows % Dilution on the y-axis (0% to 100%) and HYDRAULIC RADIUS (m) on the x-axis (0 to 30). Five curves are shown for different N' values: N' ≤ 3 (blue), N' = 4 to 10 (red), N' = 11 to 20 (green), N' = 21 to 30 (purple), and N' &gt; 30 (orange). A red square is plotted at approximately (11.5, 44.7%).</p>	<p><b><u>Expected Dilution (2):</u></b></p>	<p><b>44.7%</b></p>
<p>The graph shows % Dilution on the y-axis (0% to 80%) and σm (MPa) on the x-axis (-50 to 150). A secondary x-axis at the top shows εvol x 10<sup>-3</sup> values: -1.286, -0.286, 0.714, 1.714, 2.714, 3.714. A red square is plotted at approximately (25, 30.4%).</p>	<p><b><u>Expected Hangingwall Dilution (3):</u></b></p>	<p><b>30.4%</b></p>
<p>The graph shows % Dilution on the y-axis (0% to 80%) and σm (MPa) on the x-axis (-50 to 150). A secondary x-axis at the top shows εvol x 10<sup>-3</sup> values: -1.286, -0.286, 0.714, 1.714, 2.714, 3.714. A red square is plotted at approximately (75, 0.0%).</p>	<p><b><u>Expected Sidewall Dilution (4):</u></b></p>	<p><b>0.0%</b></p>
<p><b>Expected Dilution for Open Stope using OSD</b></p>		<p><b>30.4%</b></p>

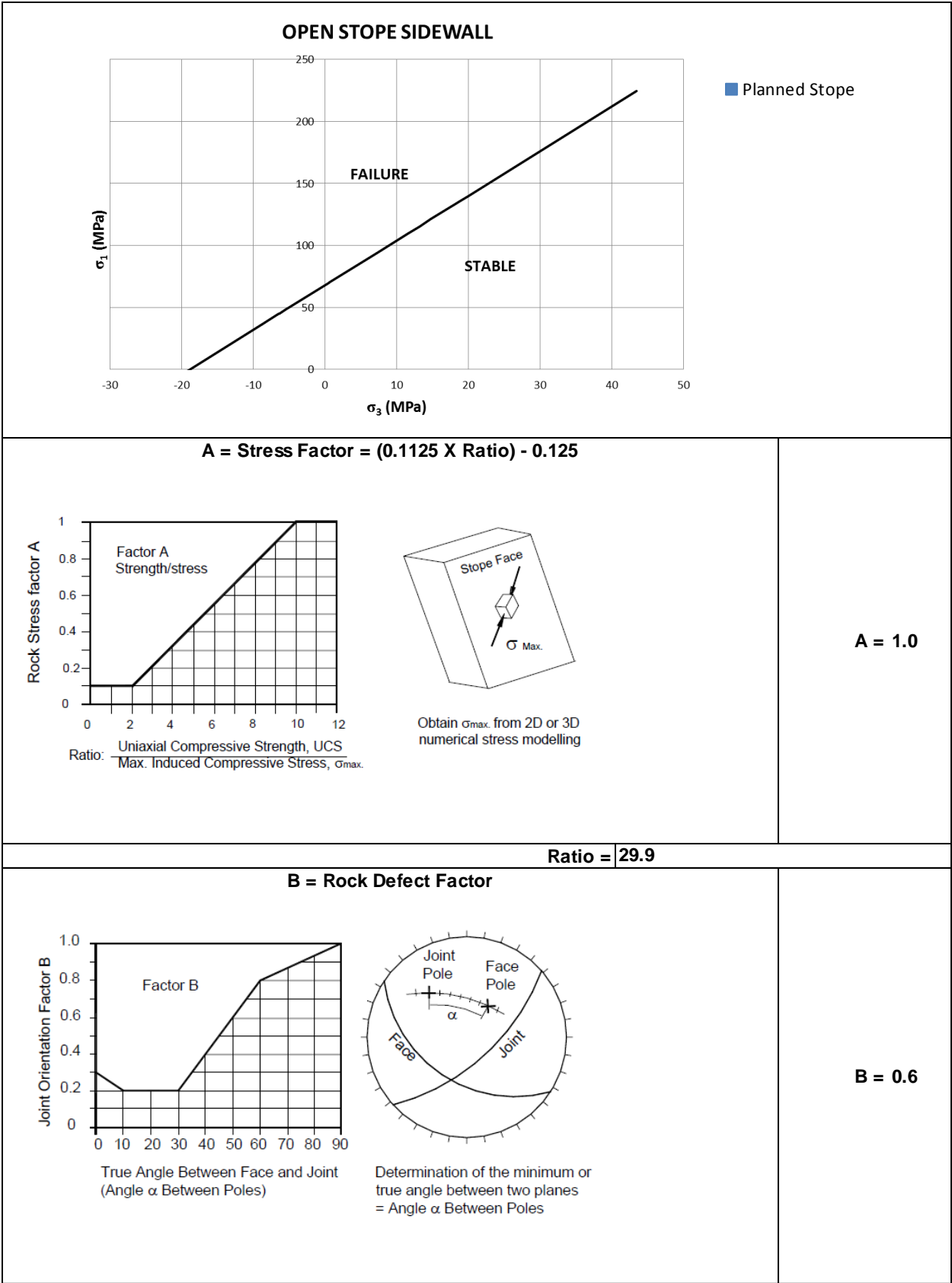






<p>A line graph showing % Dilution (Y-axis, 0% to 100%) versus HYDRAULIC RADIUS (m) (X-axis, 0 to 30). Five curves are plotted for different N' values: N' ≤ 3 (blue), N' = 4 to 10 (red), N' = 11 to 20 (green), N' = 21 to 30 (purple), and N' &gt; 30 (orange). A red square is plotted on the red curve at approximately (8.5, 28.2%).</p>	<p><b><u>Expected Dilution (2):</u></b></p>	<p><b>28.2%</b></p>
<p>A line graph showing % Dilution (Y-axis, 0% to 80%) versus <math>\sigma_m</math> (MPa) (X-axis, -50 to 150) and <math>\epsilon_{vol} \times 10^{-3}</math> (Top X-axis, -1.286 to 3.714). A red square is plotted at approximately (20, 24.9%).</p>	<p><b><u>Expected Hangingwall Dilution (3):</u></b></p>	<p><b>24.9%</b></p>
<p>A line graph showing % Dilution (Y-axis, 0% to 80%) versus <math>\sigma_m</math> (MPa) (X-axis, -50 to 150) and <math>\epsilon_{vol} \times 10^{-3}</math> (Top X-axis, -1.286 to 3.714). A red square is plotted at approximately (60, 0.0%).</p>	<p><b><u>Expected Sidewall Dilution (4):</u></b></p>	<p><b>0.0%</b></p>
<p><b>Expected Dilution for Open Stope using OSD</b></p>		<p><b>24.9%</b></p>

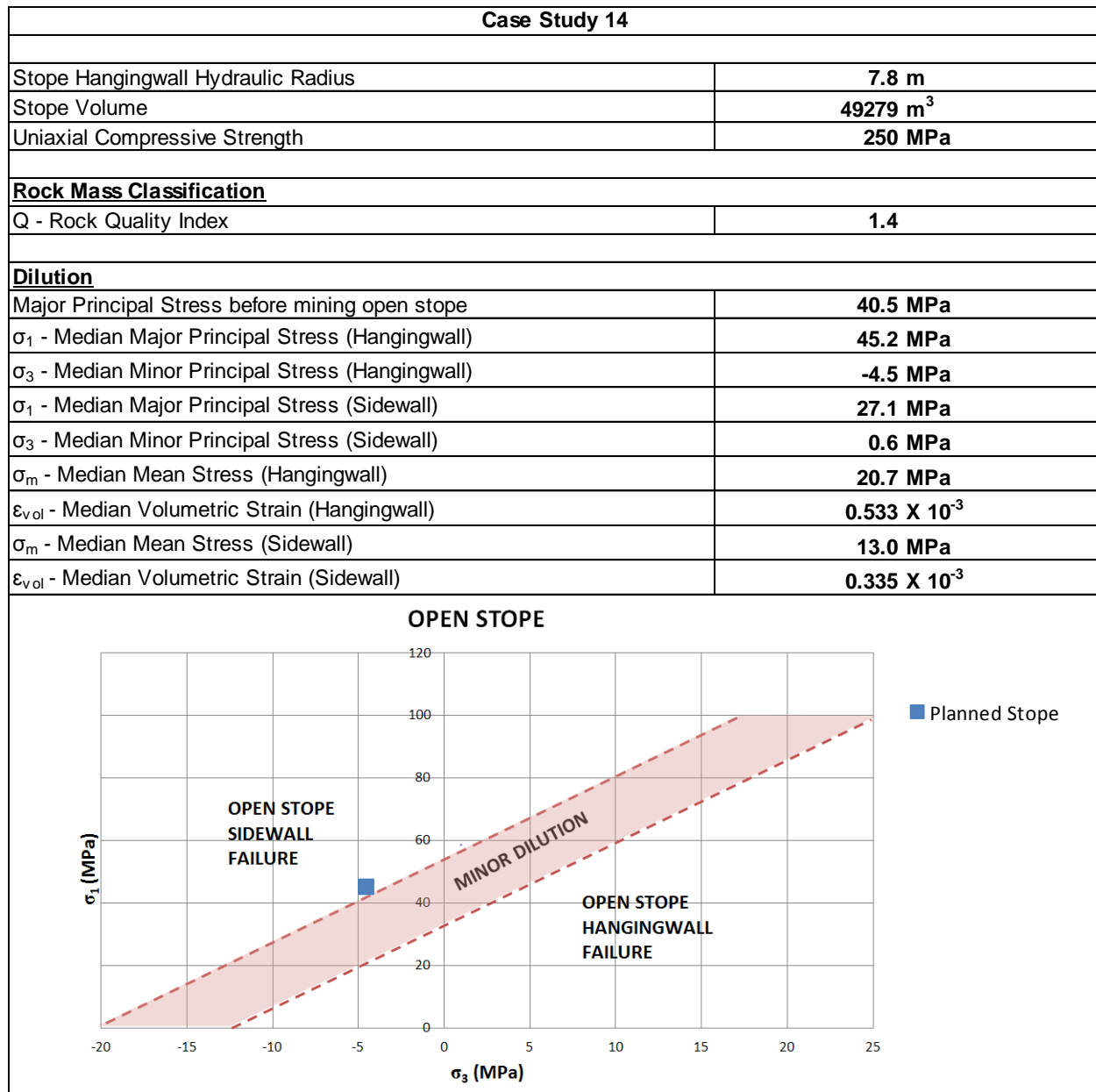


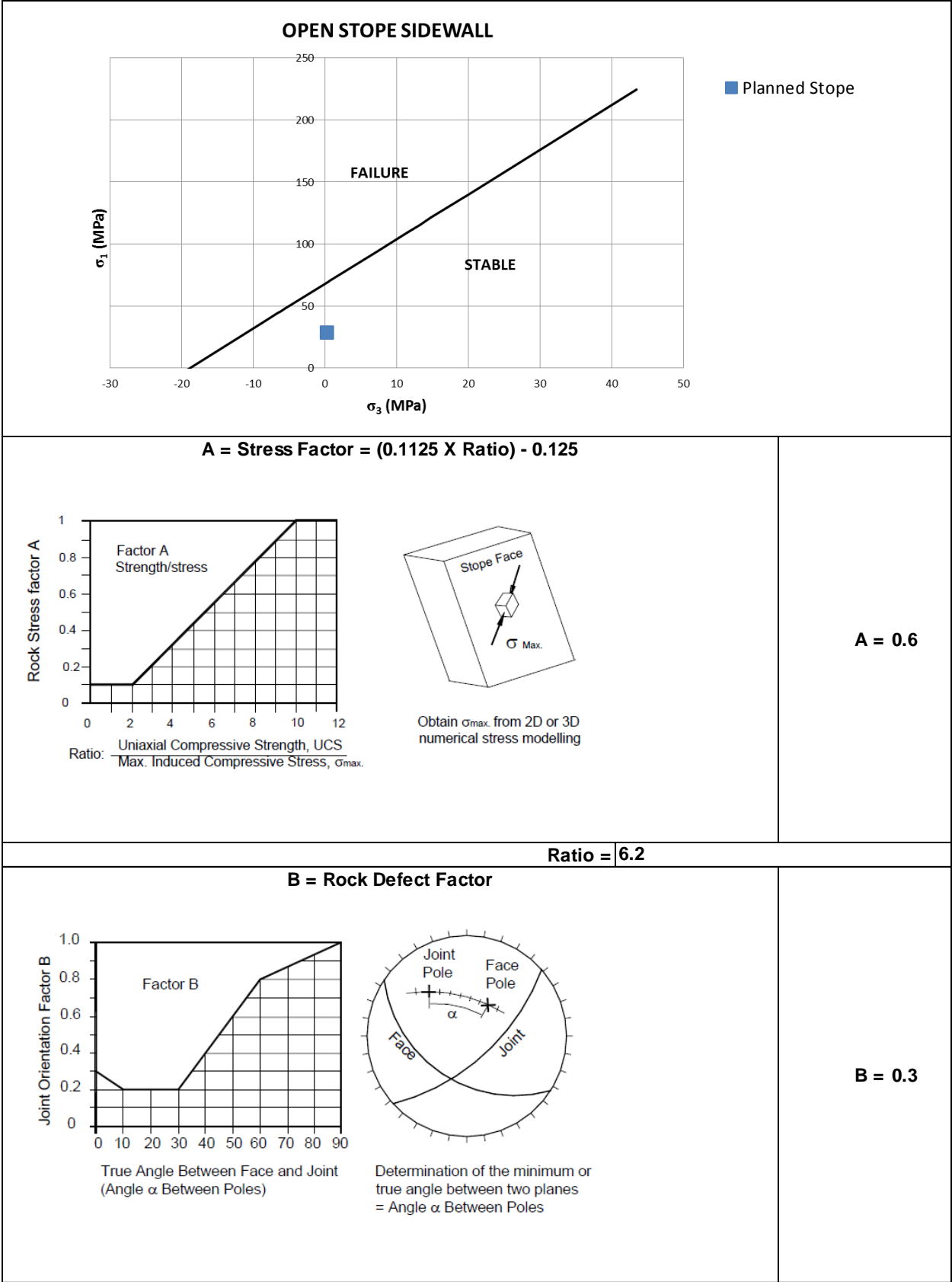






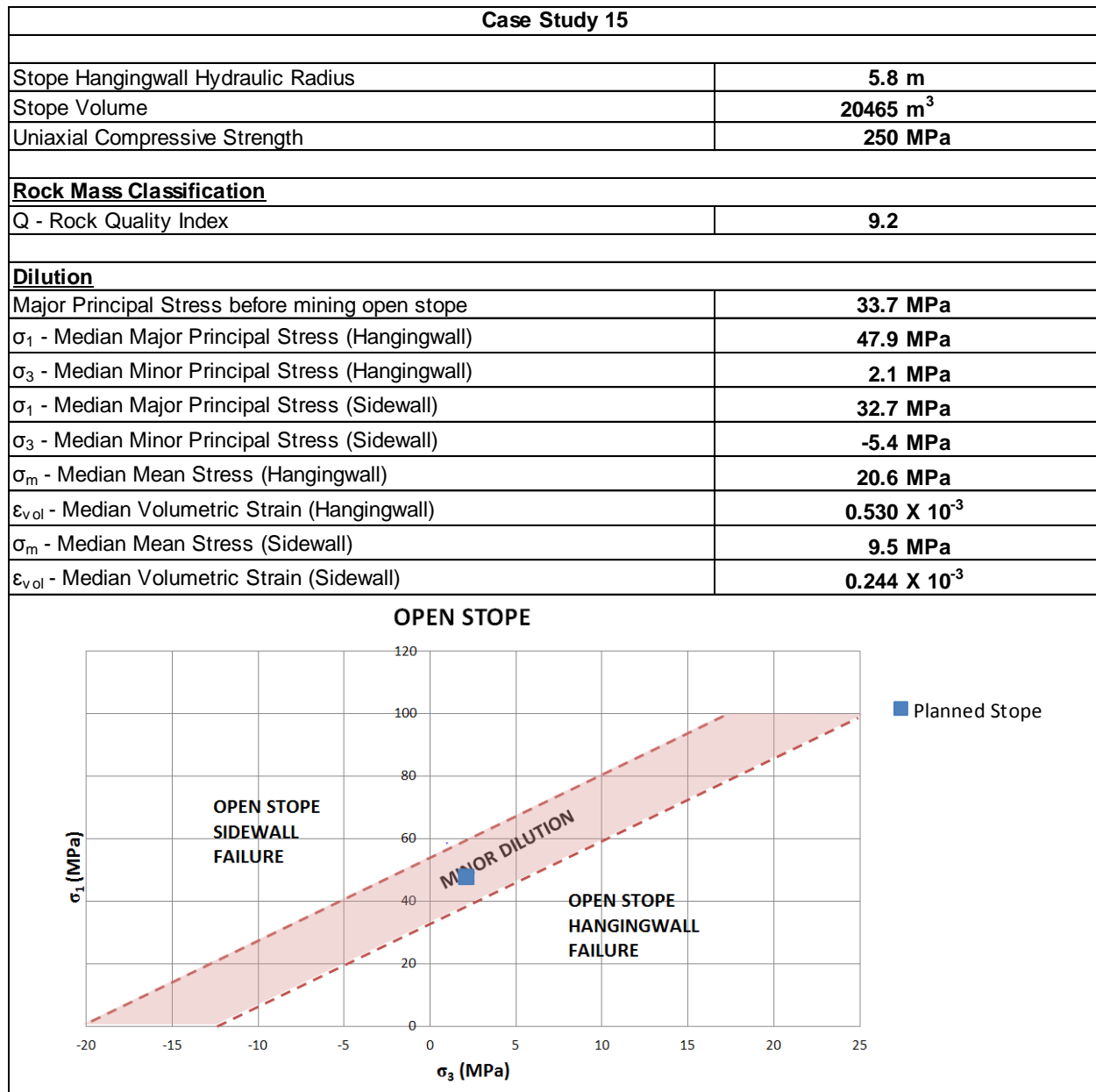
<p>A line graph showing % Dilution (0% to 100%) on the y-axis versus HYDRAULIC RADIUS (m) (0 to 30) on the x-axis. Five curves are shown for different N' values: N' ≤ 3 (blue), N' = 4 to 10 (red), N' = 11 to 20 (green), N' = 21 to 30 (purple), and N' &gt; 30 (orange). A red square is plotted at approximately (12, 15%).</p>	<p><b><u>Expected Dilution (2):</u></b></p>	<p><b>14.8%</b></p>
<p>A line graph showing % Dilution (0% to 80%) on the y-axis versus σ<sub>m</sub> (MPa) (-50 to 150) on the x-axis. The top x-axis shows ε<sub>vol</sub> x 10<sup>-3</sup> values: -1.286, -0.286, 0.714, 1.714, 2.714, 3.714. A red square is plotted at approximately (0, 15%).</p>	<p><b><u>Expected Hangingwall Dilution (3):</u></b></p>	<p><b>13.9%</b></p>
<p>A line graph showing % Dilution (0% to 80%) on the y-axis versus σ<sub>m</sub> (MPa) (-50 to 150) on the x-axis. The top x-axis shows ε<sub>vol</sub> x 10<sup>-3</sup> values: -1.286, -0.286, 0.714, 1.714, 2.714, 3.714. A red square is plotted at approximately (-25, 0%).</p>	<p><b><u>Expected Sidewall Dilution (4):</u></b></p>	<p><b>0.0%</b></p>
<p><b>Expected Dilution for Open Stope using OSD</b></p>		<p><b>13.9%</b></p>

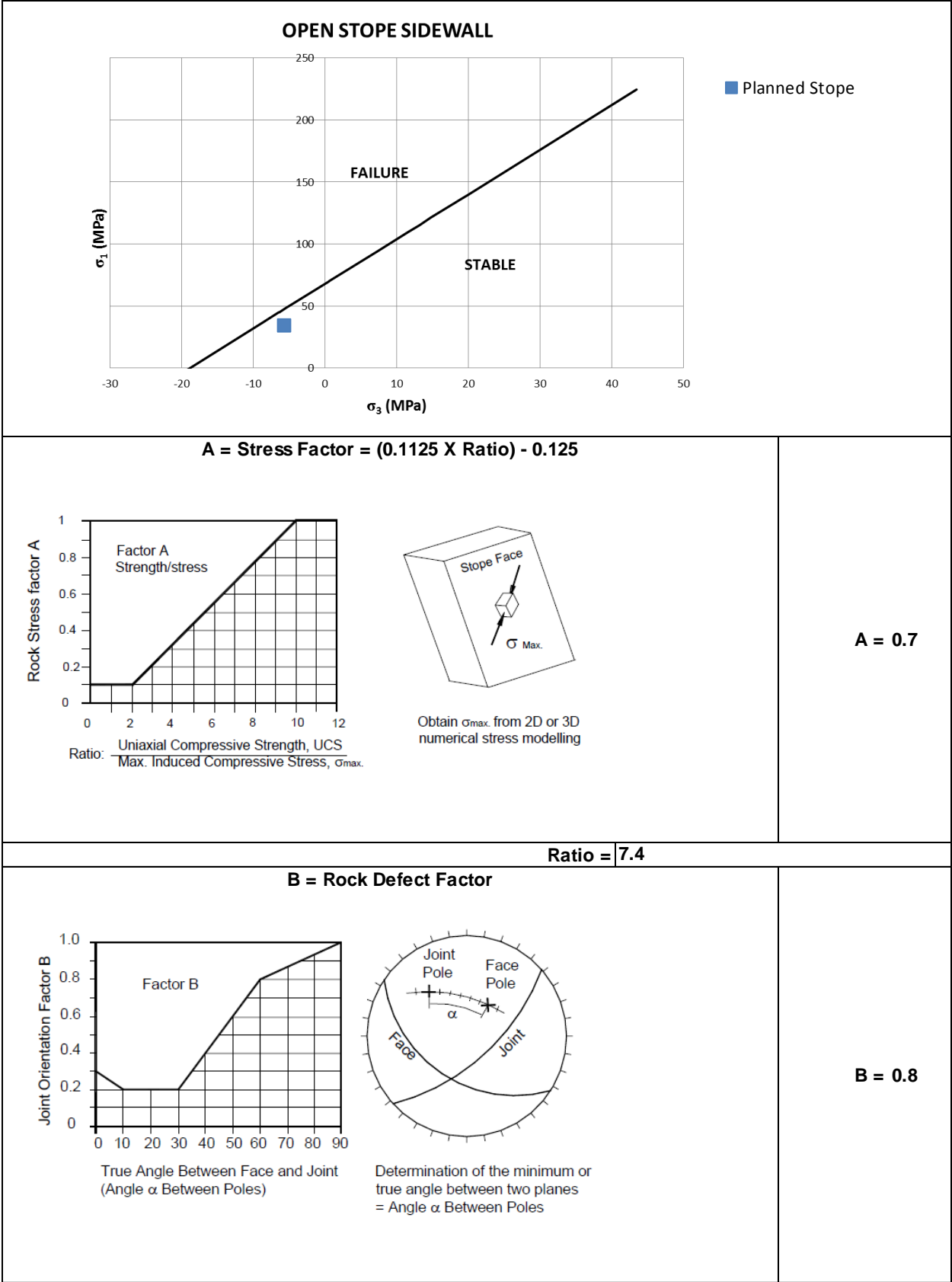




<p style="text-align: center;"><b>C = Slope Orientation Factor</b></p> <div style="display: flex; justify-content: space-around;"> <div style="width: 45%;"> <p>Factor C Gravity Fall &amp; Slabbing</p> <p><math>C = 8.6 \cos(Dip)</math></p> </div> <div style="width: 45%;"> <p>Face Dip</p> <p>Slope</p> </div> </div> <div style="display: flex; justify-content: space-around; margin-top: 20px;"> <div style="width: 45%;"> <p>Factor C Sliding</p> </div> <div style="width: 45%;"> <p>Joint Dip</p> <p>Slope</p> </div> </div>	<p><b>C = 7.0</b></p>
<p><b>N' = Modified Stability Number = Q' X A X B X C = 1.72</b></p>	
<p style="text-align: center;"><b>HYDRAULIC RADIUS (m)</b></p>	<p><b><u>Expected Dilution (1):</u></b></p> <p><b>40%</b></p>

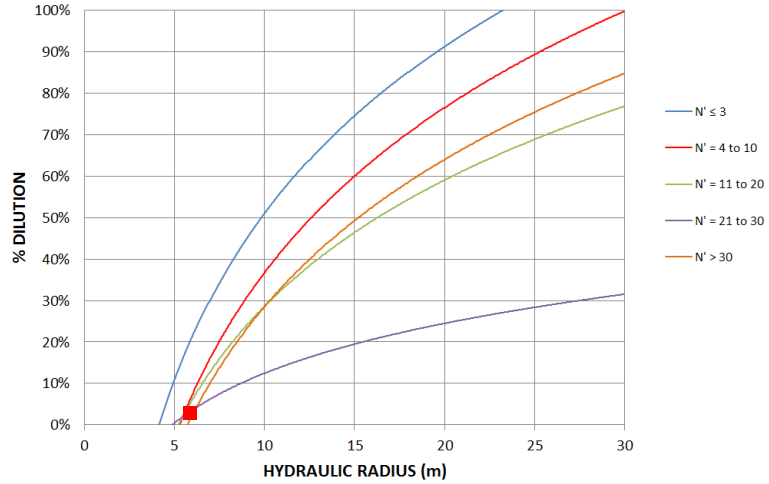
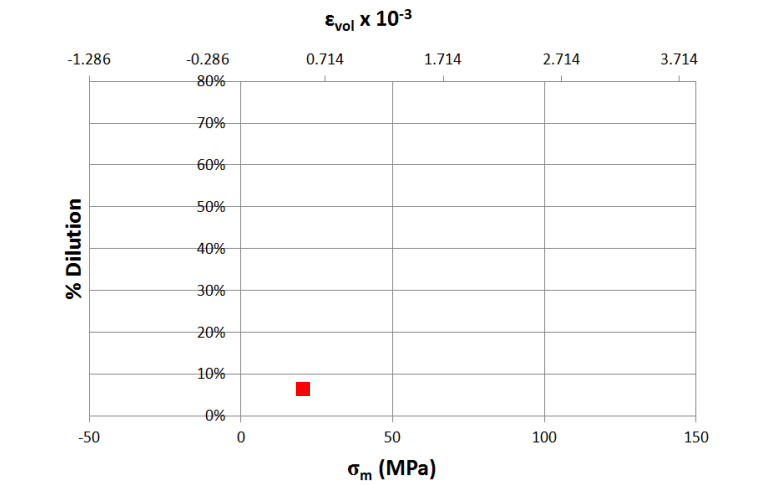
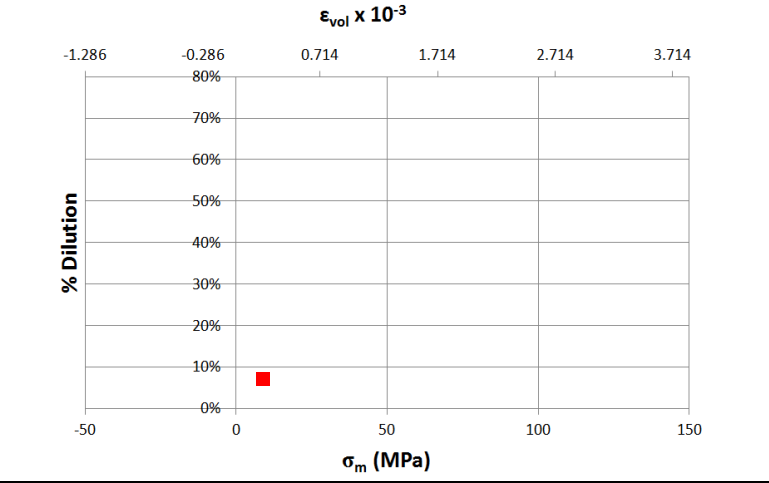
<p>A line graph showing % Dilution (Y-axis, 0% to 100%) versus HYDRAULIC RADIUS (m) (X-axis, 0 to 30). Five curves are plotted for different N' values: N' ≤ 3 (blue), N' = 4 to 10 (red), N' = 11 to 20 (green), N' = 21 to 30 (purple), and N' &gt; 30 (orange). A red square is plotted on the red curve at approximately (7.5, 36.5%).</p>	<p><b><u>Expected Dilution (2):</u></b></p>	<p><b>36.5%</b></p>
<p>A line graph showing % Dilution (Y-axis, 0% to 80%) versus <math>\sigma_m</math> (MPa) (X-axis, -50 to 150). The graph also has a top X-axis for <math>\epsilon_{vol} \times 10^{-3}</math> with values -1.286, -0.286, 0.714, 1.714, 2.714, and 3.714. No curves are visible, and a red square is plotted at approximately (10, 0%).</p>	<p><b><u>Expected Hangingwall Dilution (3):</u></b></p>	<p><b>0.0%</b></p>
<p>A line graph showing % Dilution (Y-axis, 0% to 80%) versus <math>\sigma_m</math> (MPa) (X-axis, -50 to 150). The graph also has a top X-axis for <math>\epsilon_{vol} \times 10^{-3}</math> with values -1.286, -0.286, 0.714, 1.714, 2.714, and 3.714. No curves are visible, and a red square is plotted at approximately (10, 41.1%).</p>	<p><b><u>Expected Sidewall Dilution (4):</u></b></p>	<p><b>41.1%</b></p>
<p><b>Expected Dilution for Open Stope using OSD</b></p>		<p><b>41.1%</b></p>

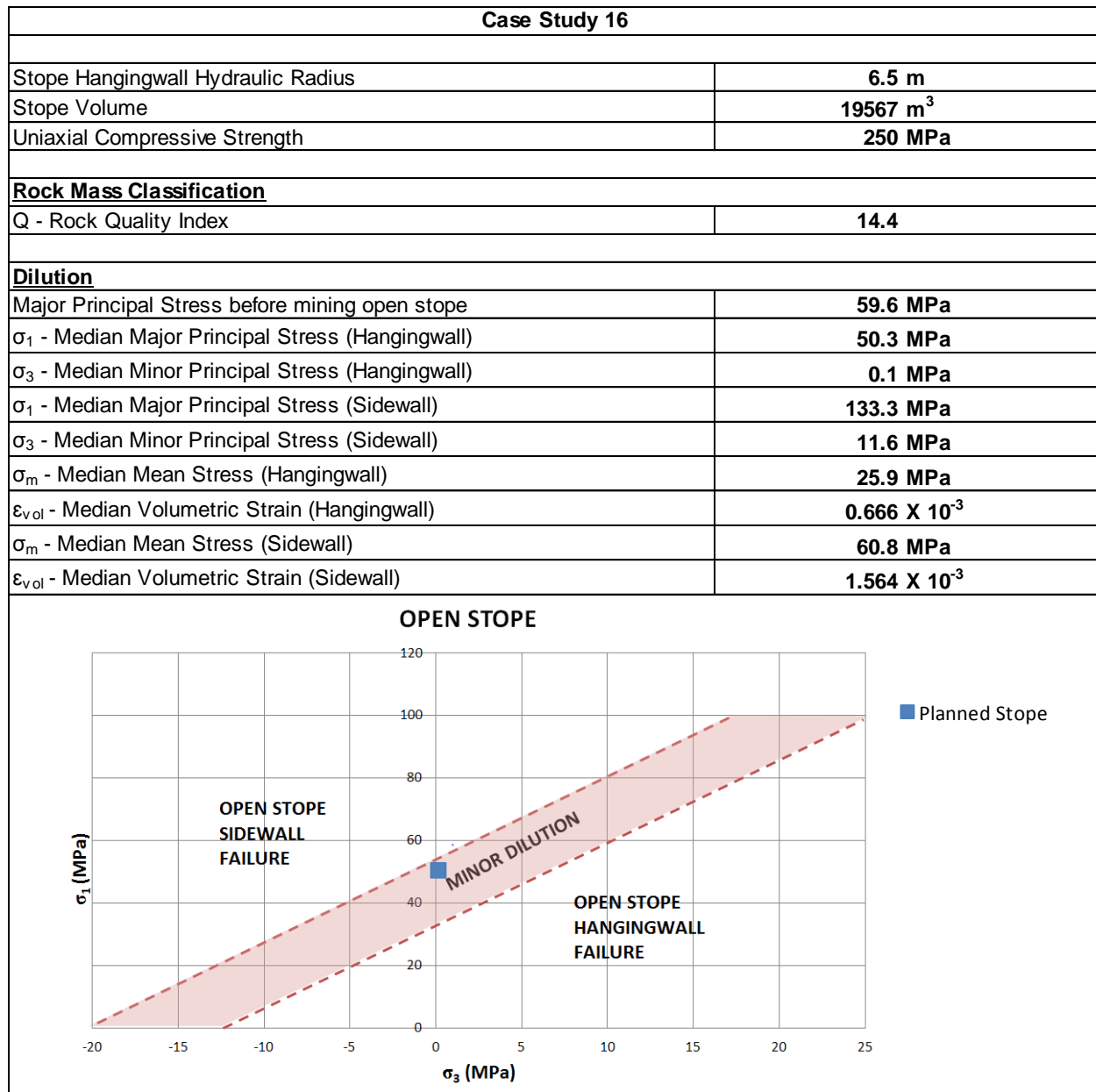


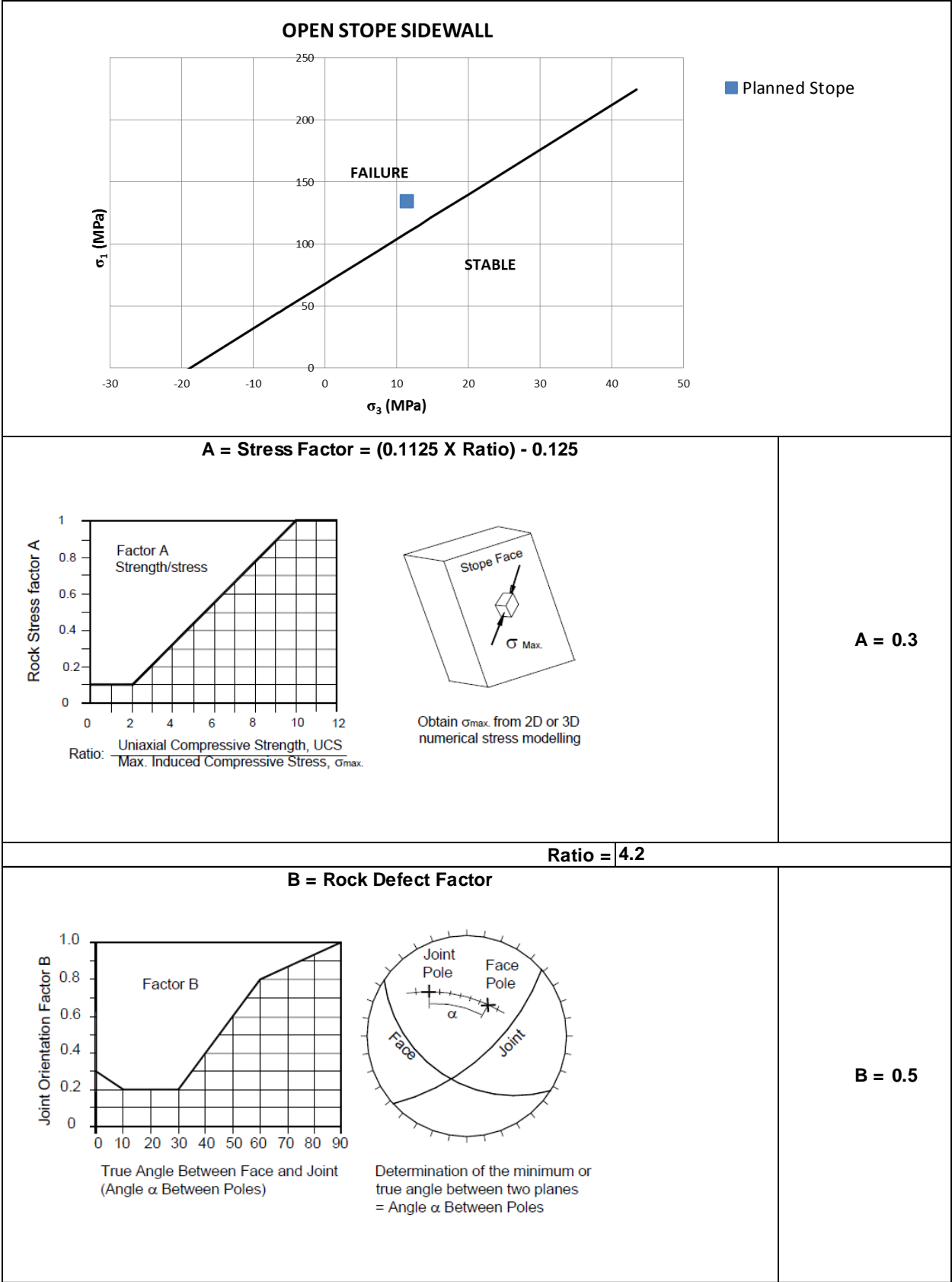


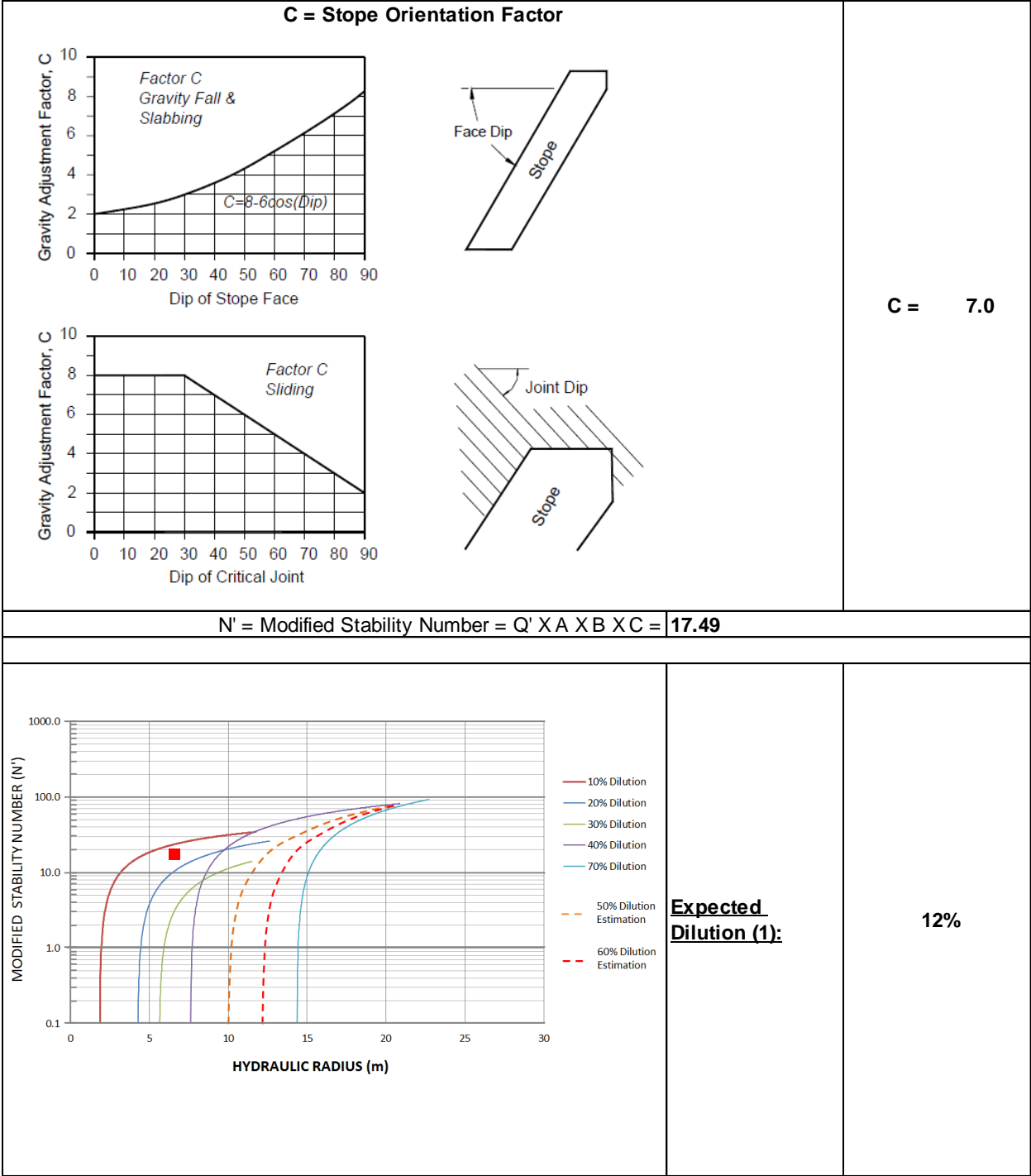




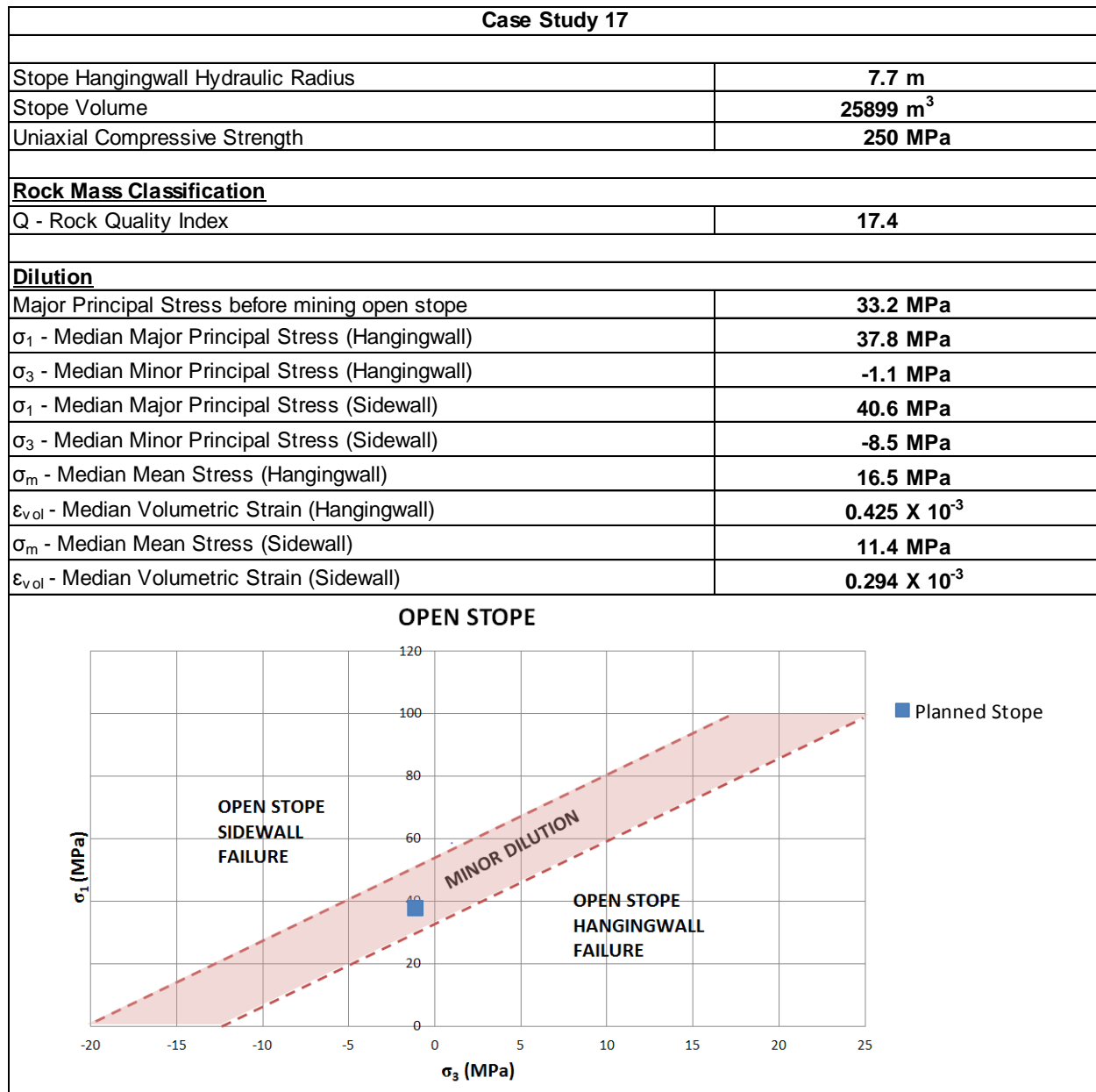
	<p><b><u>Expected Dilution (2):</u></b></p>	<p><b>3.1%</b></p>
	<p><b><u>Expected Hangingwall Dilution (3):</u></b></p>	<p><b>6.2%</b></p>
	<p><b><u>Expected Sidewall Dilution (4):</u></b></p>	<p><b>6.7%</b></p>
<p><b>Expected Dilution for Open Stope using OSD</b></p>		<p><b>6.7%</b></p>

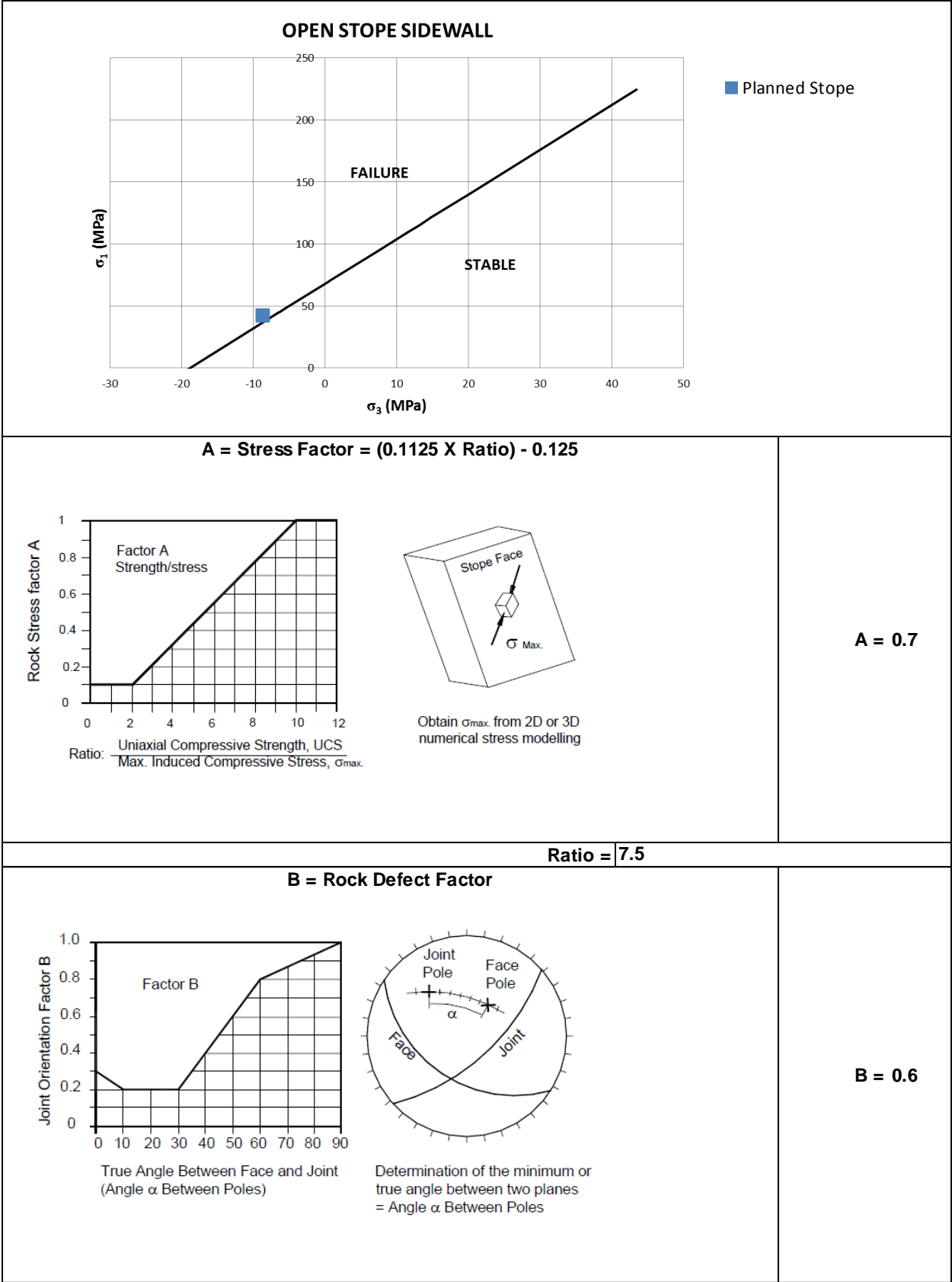






	<p><b><u>Expected Dilution (2):</u></b></p>	<p><b>9.9%</b></p>
	<p><b><u>Expected Hangingwall Dilution (3):</u></b></p>	<p><b>6.5%</b></p>
	<p><b><u>Expected Sidewall Dilution (4):</u></b></p>	<p><b>6.1%</b></p>
<p><b>Expected Dilution for Open Stope using OSD</b></p>		<p><b>6.5%</b></p>

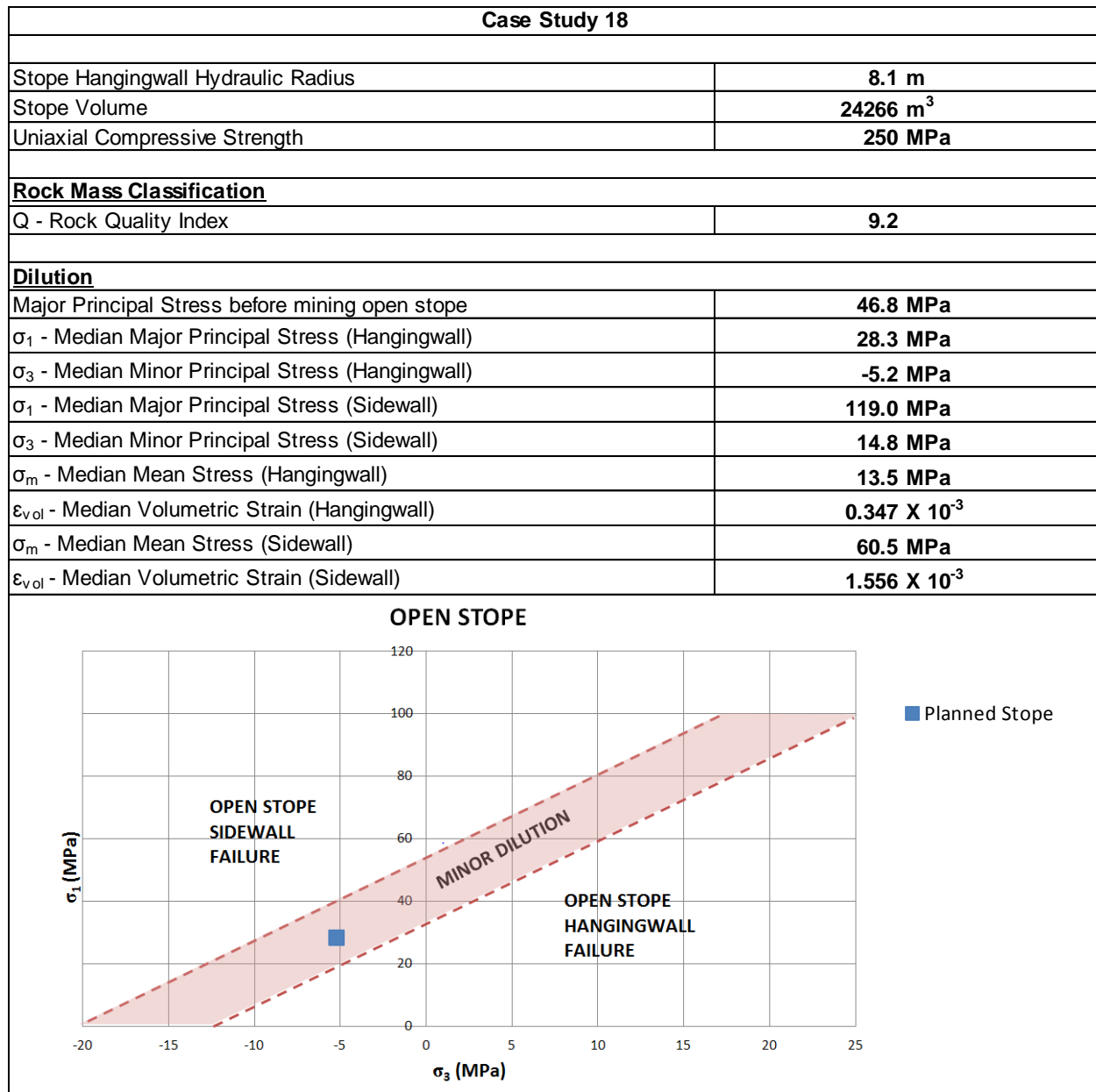


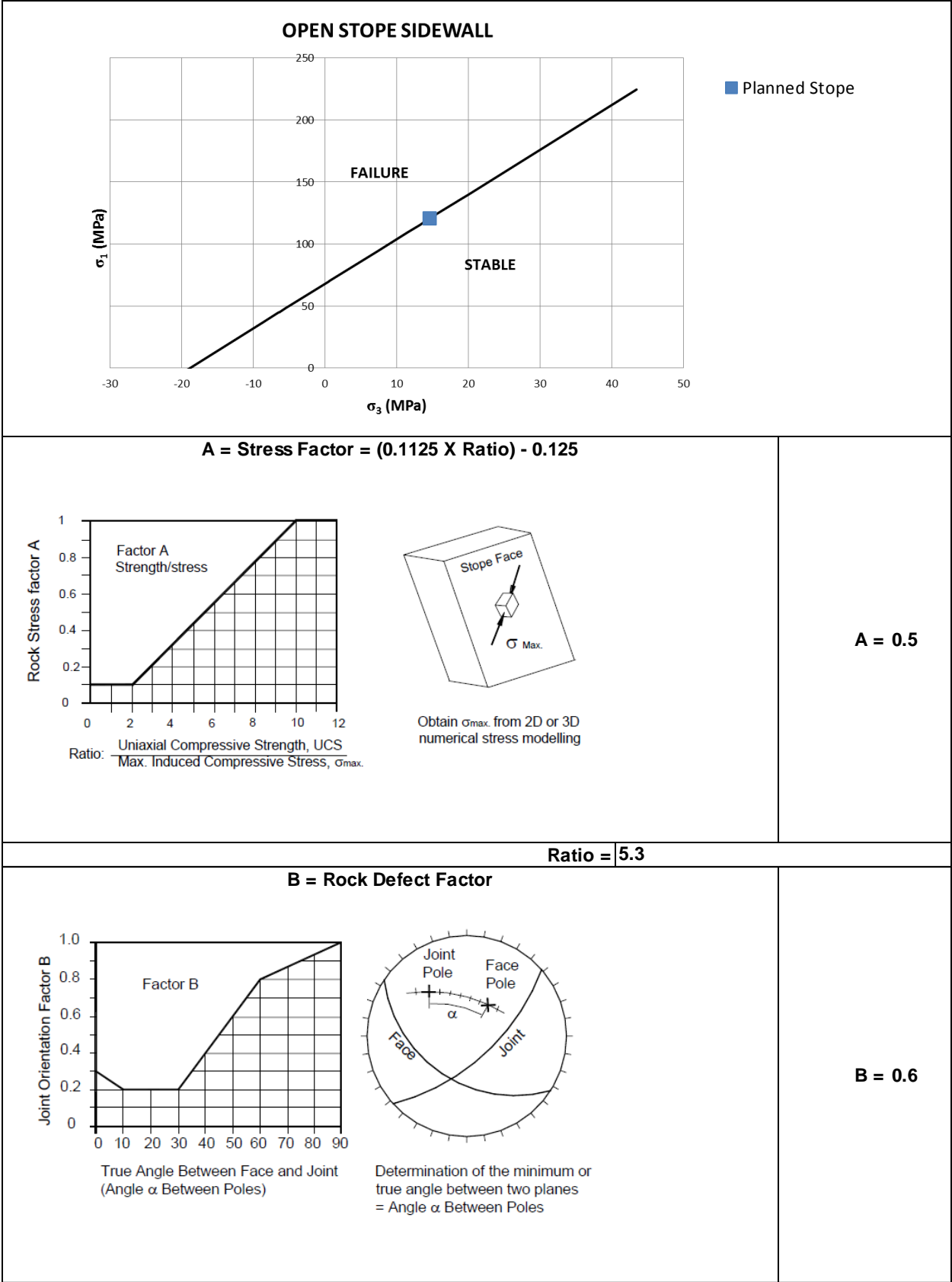




<p style="text-align: center;"><b>C = Slope Orientation Factor</b></p> <div style="display: flex; justify-content: space-around;"> <div style="width: 45%;"> <p>Factor C Gravity Fall &amp; Slabbing</p> <p><math>C = 8 - 6\cos(Dip)</math></p> </div> <div style="width: 45%;"> <p>Face Dip</p> <p>Slope</p> </div> </div> <div style="display: flex; justify-content: space-around; margin-top: 20px;"> <div style="width: 45%;"> <p>Factor C Sliding</p> </div> <div style="width: 45%;"> <p>Joint Dip</p> <p>Slope</p> </div> </div> <div style="text-align: right; margin-top: 20px;"> <p><b>C = 6.0</b></p> </div>	
<p style="text-align: center;"><b>N' = Modified Stability Number = Q' X A X B X C = 45.27</b></p>	
<p style="text-align: center;"><b>HYDRAULIC RADIUS (m)</b></p> <div style="position: absolute; top: 100px; right: 100px;"> <p>1000.0</p> <p>100.0</p> <p>10.0</p> <p>1.0</p> <p>0.1</p> </div> <div style="position: absolute; top: 650px; right: 100px;"> <p>10% Dilution</p> <p>20% Dilution</p> <p>30% Dilution</p> <p>40% Dilution</p> <p>50% Dilution Estimation</p> <p>60% Dilution Estimation</p> </div>	<div style="text-align: center; margin-top: 100px;"> <p><b>Expected Dilution (1):</b></p> <p><b>8%</b></p> </div>

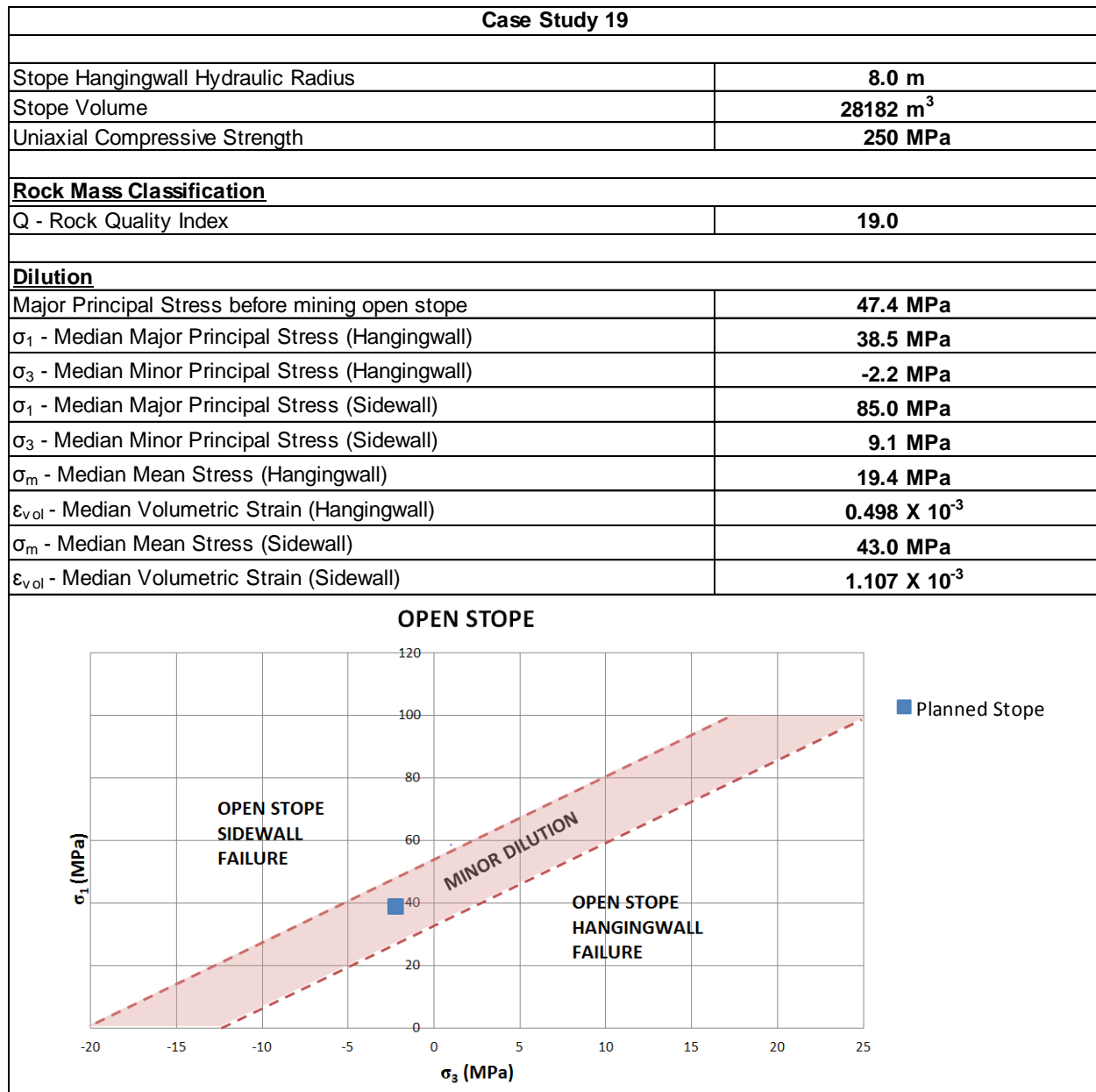
<p>A line graph showing % Dilution (0% to 100%) on the y-axis versus HYDRAULIC RADIUS (m) (0 to 30) on the x-axis. Five curves are plotted for different N' values: N' ≤ 3 (blue), N' = 4 to 10 (red), N' = 11 to 20 (green), N' = 21 to 30 (purple), and N' &gt; 30 (orange). A red square is plotted at approximately (7.5, 15%).</p>	<p><b><u>Expected Dilution (2):</u></b></p>	<p><b>15.0%</b></p>
<p>A line graph showing % Dilution (0% to 80%) on the y-axis versus sigma_m (MPa) (-50 to 150) on the x-axis. The top x-axis shows epsilon_vol x 10^-3 values: -1.286, -0.286, 0.714, 1.714, 2.714, 3.714. A red square is plotted at approximately (10, 6%).</p>	<p><b><u>Expected Hangingwall Dilution (3):</u></b></p>	<p><b>6.0%</b></p>
<p>A line graph showing % Dilution (0% to 80%) on the y-axis versus sigma_m (MPa) (-50 to 150) on the x-axis. The top x-axis shows epsilon_vol x 10^-3 values: -1.286, -0.286, 0.714, 1.714, 2.714, 3.714. A red square is plotted at approximately (10, 6.6%).</p>	<p><b><u>Expected Sidewall Dilution (4):</u></b></p>	<p><b>6.6%</b></p>
<p><b>Expected Dilution for Open Stope using OSD</b></p>		<p><b>6.6%</b></p>

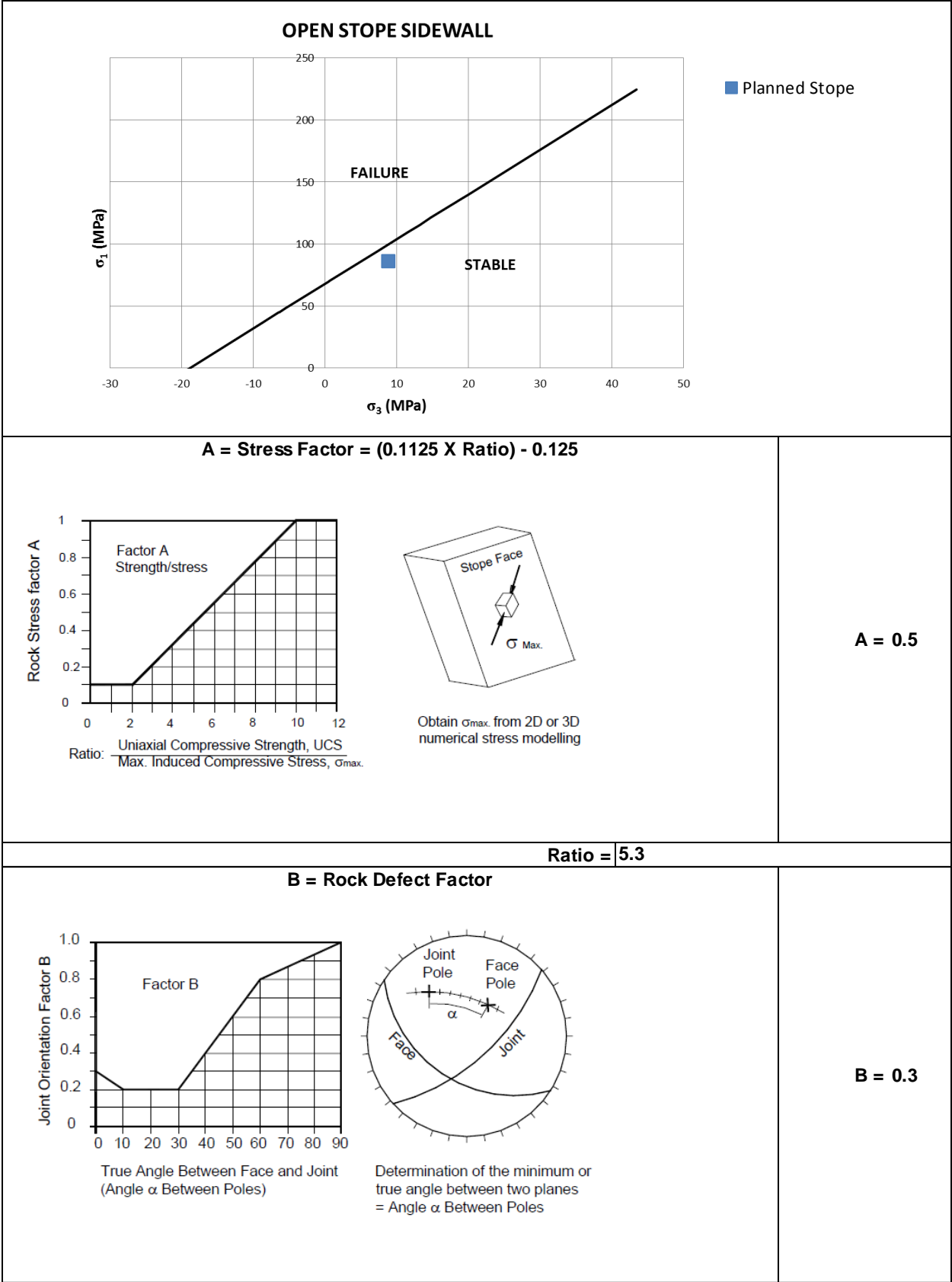




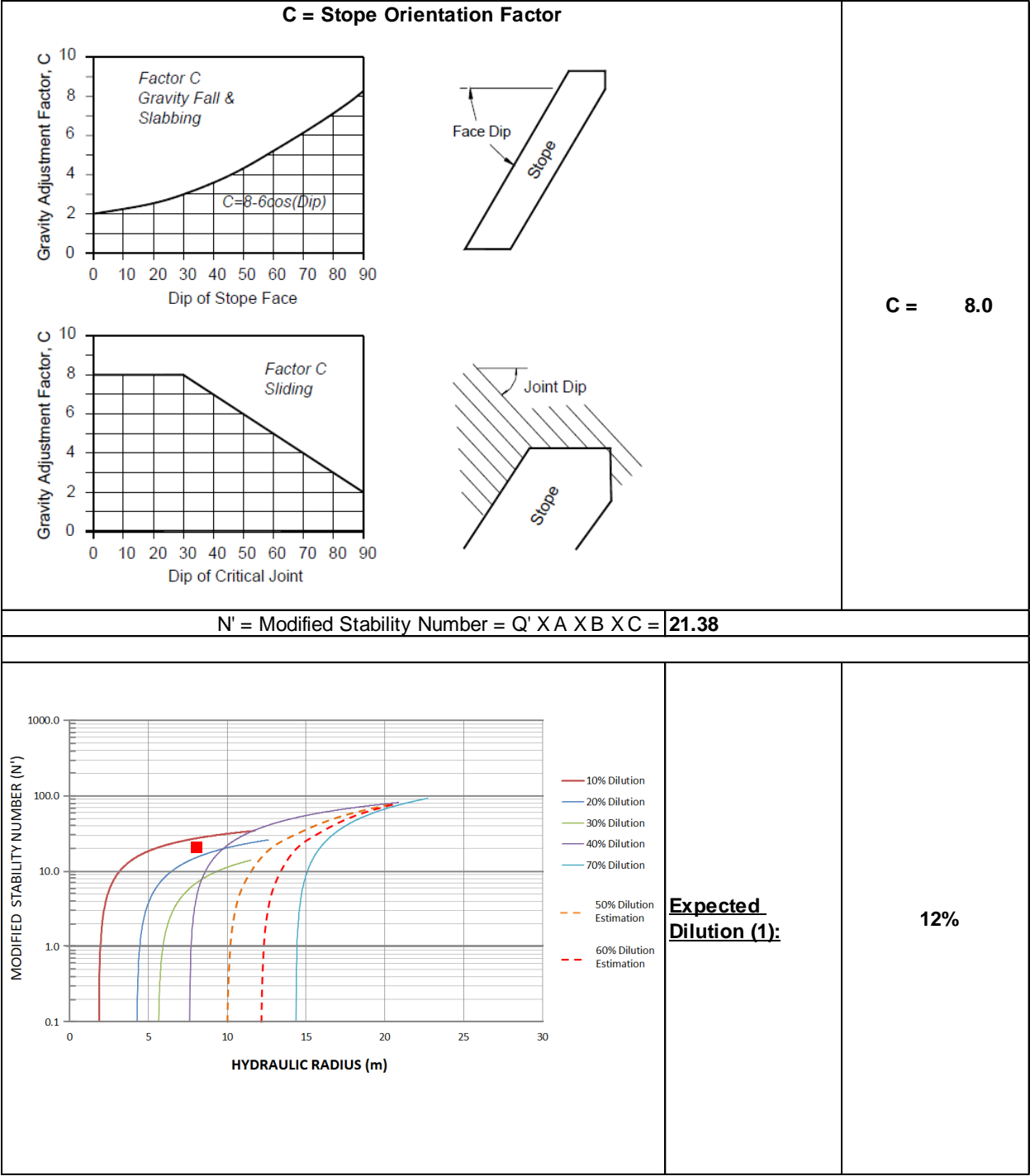


	<p><b><u>Expected Dilution (2):</u></b></p>	<p><b>8.8%</b></p>
	<p><b><u>Expected Hangingwall Dilution (3):</u></b></p>	<p><b>5.9%</b></p>
	<p><b><u>Expected Sidewall Dilution (4):</u></b></p>	<p><b>6.1%</b></p>
<p><b>Expected Dilution for Open Stope using OSD</b></p>		<p><b>6.1%</b></p>

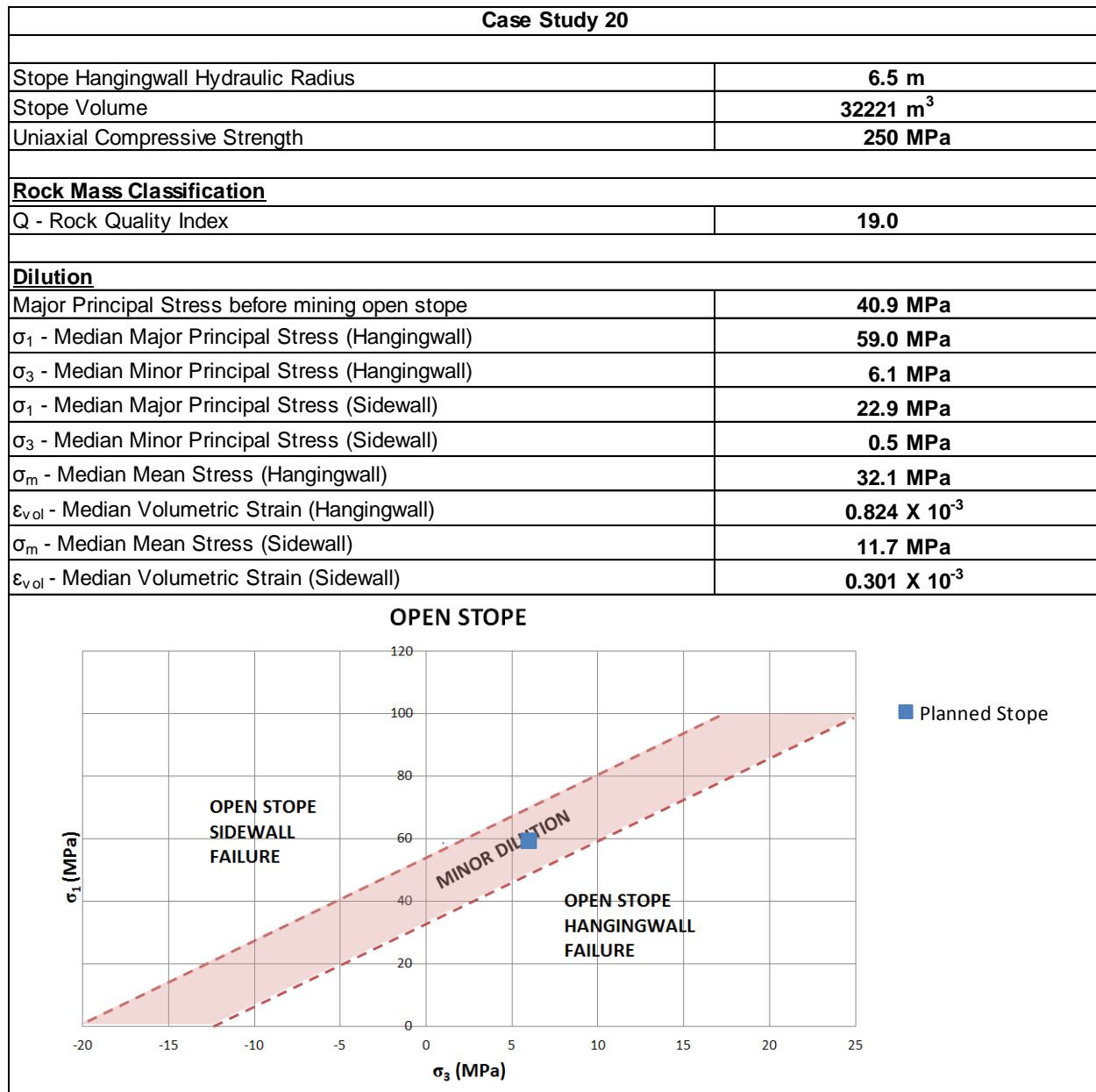


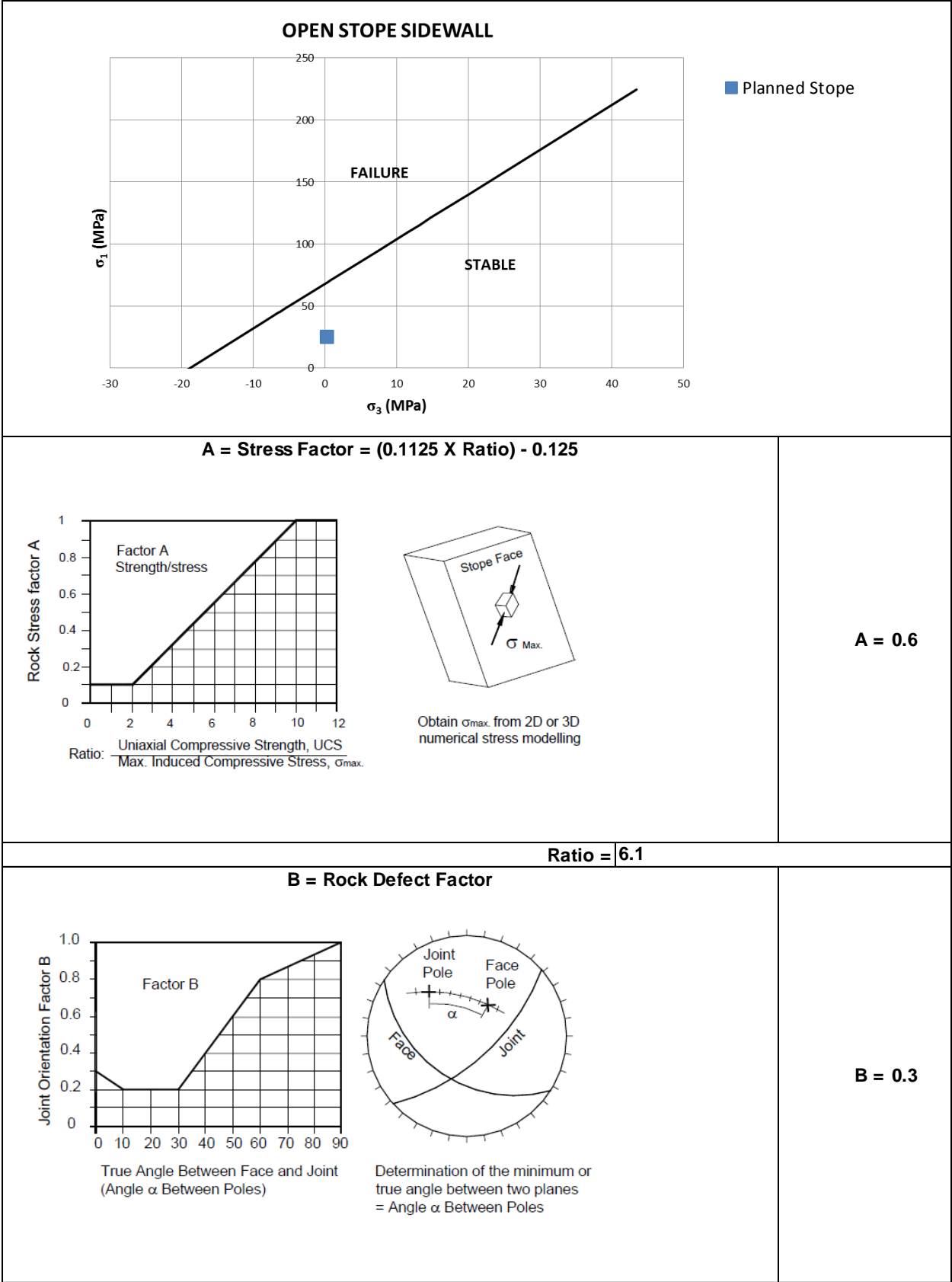






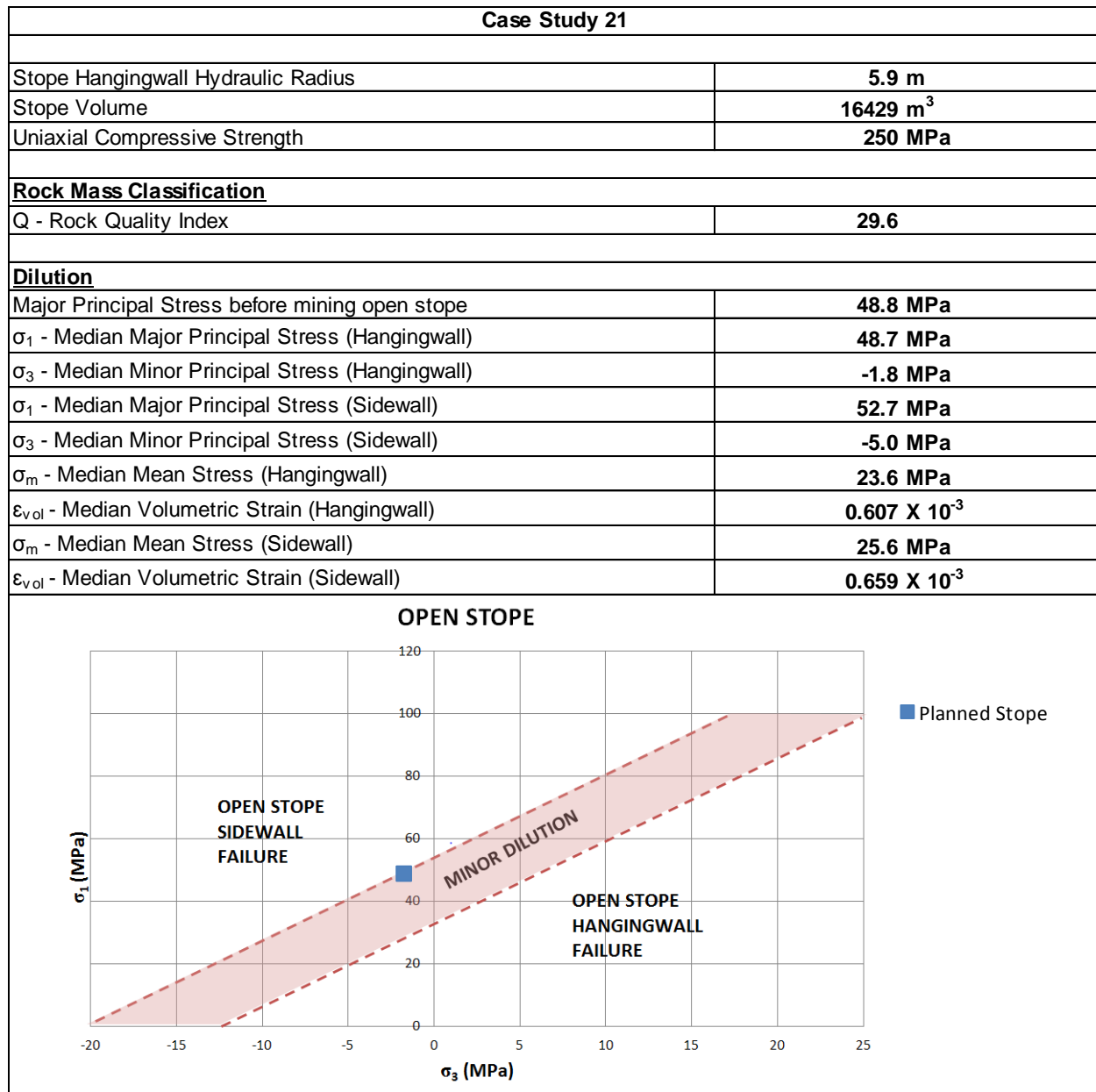
<p>A line graph showing % Dilution (0% to 100%) on the y-axis versus HYDRAULIC RADIUS (m) (0 to 30) on the x-axis. Five curves are shown for different N' values: N' ≤ 3 (blue), N' = 4 to 10 (red), N' = 11 to 20 (green), N' = 21 to 30 (purple), and N' &gt; 30 (orange). A red square is plotted at approximately (8, 10%).</p>	<p><b><u>Expected Dilution (2):</u></b></p>	<p><b>8.6%</b></p>
<p>A graph with % Dilution (0% to 80%) on the y-axis. The bottom x-axis is sigma_m (MPa) from -50 to 150. The top x-axis is epsilon_vol x 10^-3 with values -1.286, -0.286, 0.714, 1.714, 2.714, and 3.714. A red square is plotted at approximately (20, 5%).</p>	<p><b><u>Expected Hangingwall Dilution (3):</u></b></p>	<p><b>6.2%</b></p>
<p>A graph with % Dilution (0% to 80%) on the y-axis. The bottom x-axis is sigma_m (MPa) from -50 to 150. The top x-axis is epsilon_vol x 10^-3 with values -1.286, -0.286, 0.714, 1.714, 2.714, and 3.714. A red square is plotted at approximately (40, 5%).</p>	<p><b><u>Expected Sidewall Dilution (4):</u></b></p>	<p><b>6.3%</b></p>
<p><b>Expected Dilution for Open Stope using OSD</b></p>		<p><b>6.3%</b></p>

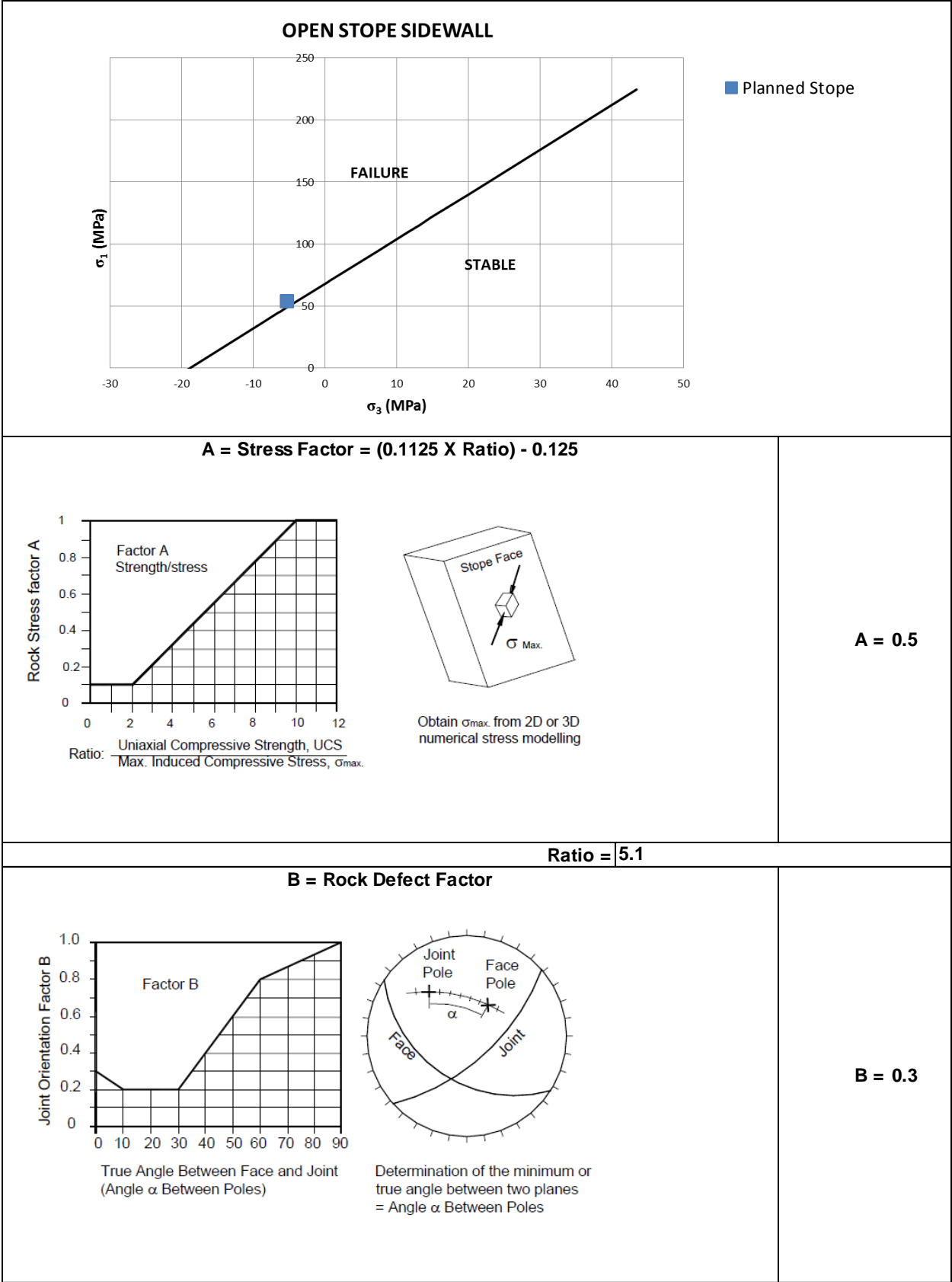






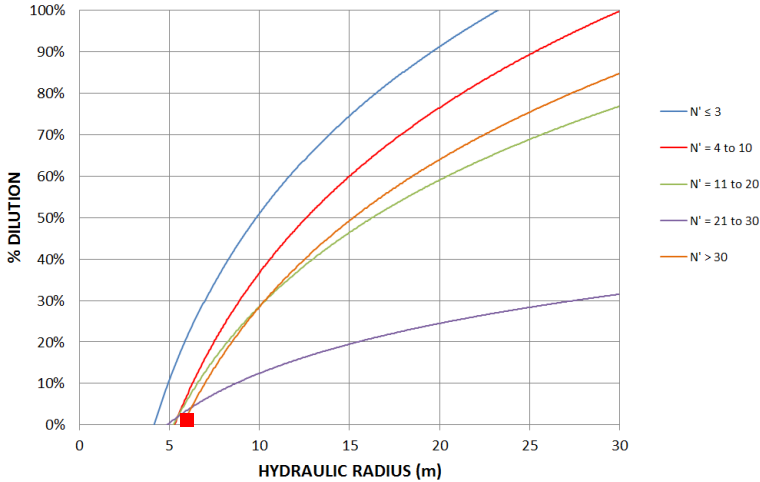
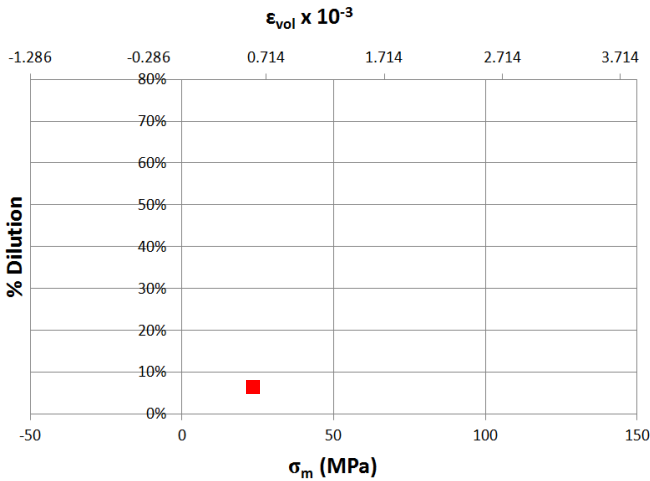
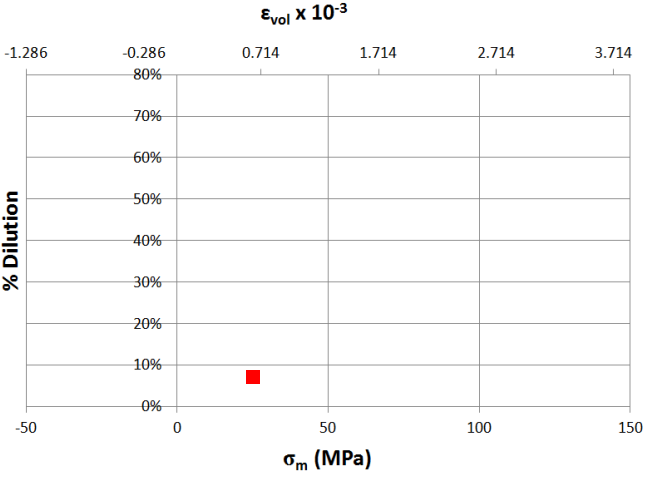
	<p><b><u>Expected Dilution (2):</u></b></p>	<p><b>4.9%</b></p>
	<p><b><u>Expected Hangingwall Dilution (3):</u></b></p>	<p><b>6.8%</b></p>
	<p><b><u>Expected Sidewall Dilution (4):</u></b></p>	<p><b>6.6%</b></p>
<p><b>Expected Dilution for Open Stope using OSD</b></p>		<p><b>6.8%</b></p>

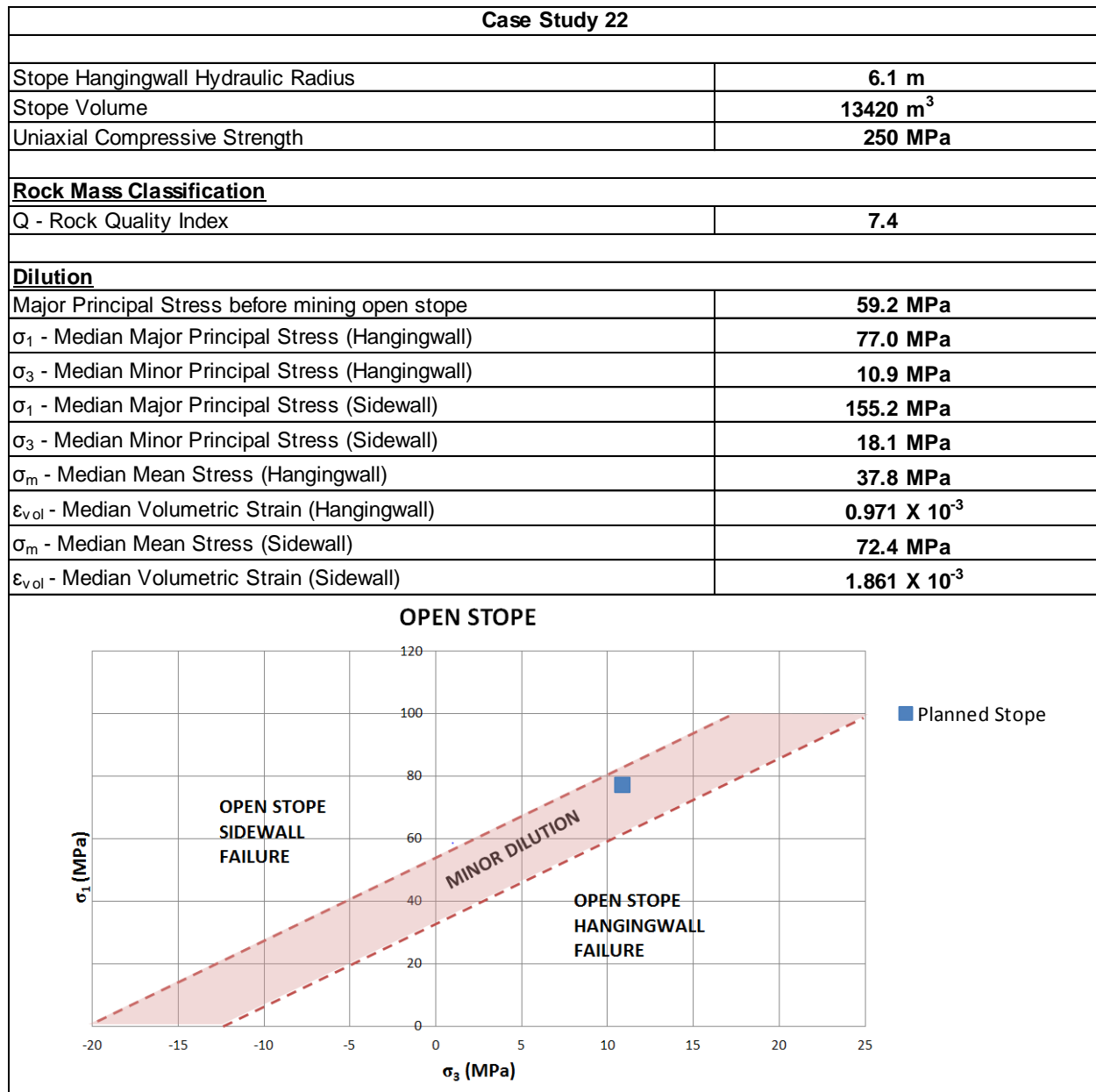


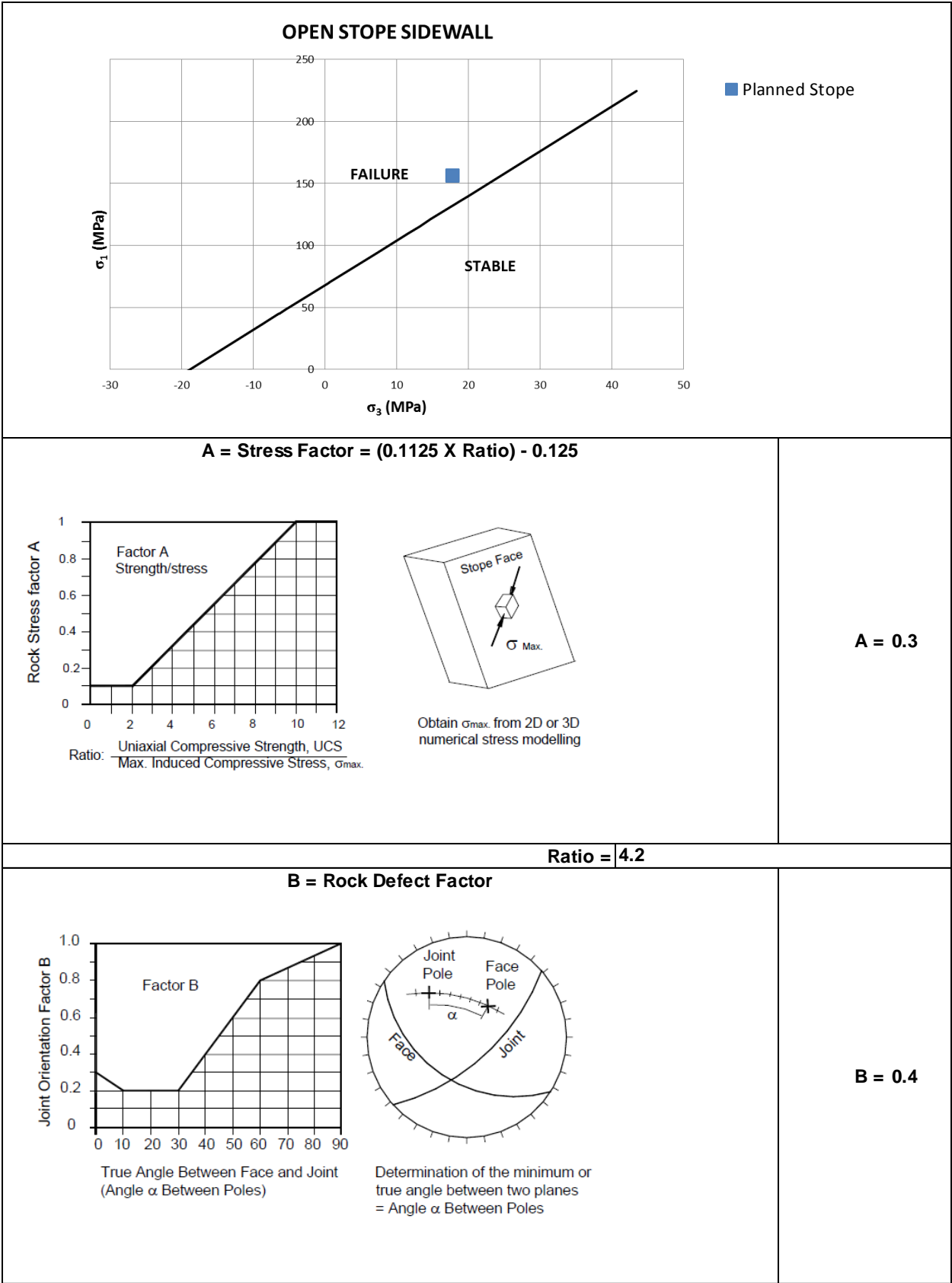




<p style="text-align: center;"><b>C = Slope Orientation Factor</b></p> <div style="display: flex; justify-content: space-around;"> <div style="text-align: center;"> <p>Factor C Gravity Fall &amp; Slabbing</p> <p><math>C = 8 - 6\cos(Dip)</math></p> </div> <div style="text-align: center;"> <p>Face Dip</p> <p>Slope</p> </div> </div> <div style="display: flex; justify-content: space-around; margin-top: 20px;"> <div style="text-align: center;"> <p>Factor C Sliding</p> </div> <div style="text-align: center;"> <p>Joint Dip</p> <p>Slope</p> </div> </div>	<p><b>C = 8.0</b></p>
<p><b>N' = Modified Stability Number = Q' X A X B X C = 32.06</b></p>	
<p style="text-align: center;"><b>HYDRAULIC RADIUS (m)</b></p> <div style="position: absolute; top: 10px; left: 10px; transform: rotate(-90deg);"> <b>MODIFIED STABILITY NUMBER (N')</b> </div> <div style="position: absolute; top: 650px; right: 10px;"> <p>— 10% Dilution</p> <p>— 20% Dilution</p> <p>— 30% Dilution</p> <p>— 40% Dilution</p> <p>— 70% Dilution</p> <p>- - 50% Dilution Estimation</p> <p>- - 60% Dilution Estimation</p> </div>	<p><b>Expected Dilution (1): 8%</b></p>

 <p><b>% DILUTION</b></p> <p><b>HYDRAULIC RADIUS (m)</b></p> <p><math>N' \leq 3</math> <math>N' = 4 \text{ to } 10</math> <math>N' = 11 \text{ to } 20</math> <math>N' = 21 \text{ to } 30</math> <math>N' &gt; 30</math></p>	<p><b><u>Expected Dilution (2):</u></b></p>	<p><b>1.4%</b></p>
 <p><b>% Dilution</b></p> <p><math>\epsilon_{vol} \times 10^{-3}</math></p> <p><math>\sigma_m</math> (MPa)</p>	<p><b><u>Expected Hangingwall Dilution (3):</u></b></p>	<p><b>6.4%</b></p>
 <p><b>% Dilution</b></p> <p><math>\epsilon_{vol} \times 10^{-3}</math></p> <p><math>\sigma_m</math> (MPa)</p>	<p><b><u>Expected Sidewall Dilution (4):</u></b></p>	<p><b>6.5%</b></p>
<p><b>Expected Dilution for Open Stope using OSD</b></p>		<p><b>6.5%</b></p>







<p>A line graph showing % Dilution (0% to 100%) on the y-axis versus HYDRAULIC RADIUS (m) (0 to 30) on the x-axis. Five curves are plotted for different N' values: N' ≤ 3 (blue), N' = 4 to 10 (red), N' = 11 to 20 (green), N' = 21 to 30 (purple), and N' &gt; 30 (orange). A red square is plotted at approximately (6.5, 10%).</p>	<p><b><u>Expected Dilution (2):</u></b></p>	<p><b>8.6%</b></p>
<p>A line graph showing % Dilution (0% to 80%) on the y-axis versus sigma_m (MPa) (-50 to 150) on the x-axis. The top x-axis shows epsilon_vol x 10^-3 values: -1.286, -0.286, 0.714, 1.714, 2.714, 3.714. A red square is plotted at approximately (35, 10%).</p>	<p><b><u>Expected Hangingwall Dilution (3):</u></b></p>	<p><b>7.0%</b></p>
<p>A line graph showing % Dilution (0% to 80%) on the y-axis versus sigma_m (MPa) (-50 to 150) on the x-axis. The top x-axis shows epsilon_vol x 10^-3 values: -1.286, -0.286, 0.714, 1.714, 2.714, 3.714. A red square is plotted at approximately (75, 10%).</p>	<p><b><u>Expected Sidewall Dilution (4):</u></b></p>	<p><b>6.0%</b></p>
<p><b>Expected Dilution for Open Stope using OSD</b></p>		<p><b>7.0%</b></p>

## APPENDIX E

### Application of failure criteria on case studies at Target Mine



Figure E1 Application of the Mohr-Coulomb criterion to case study 1

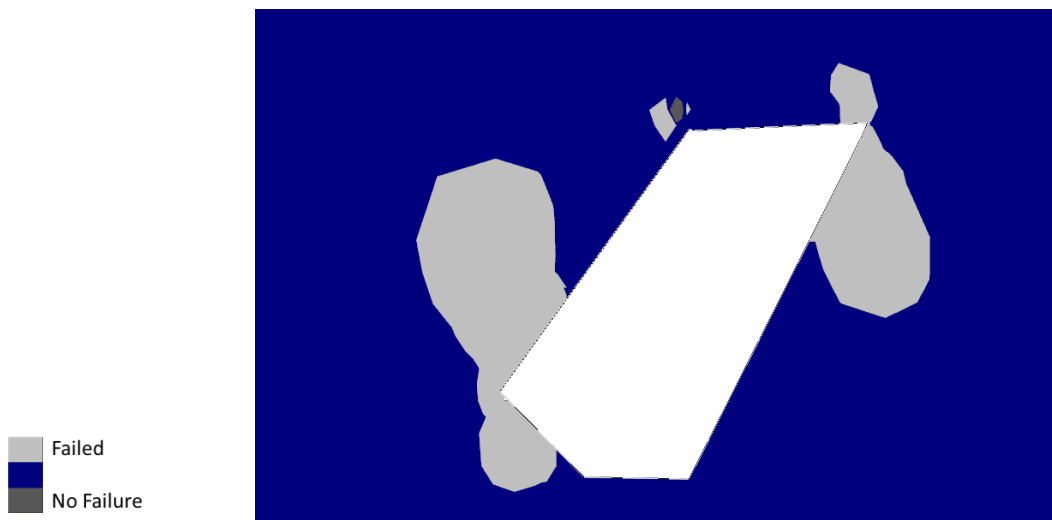


Figure E2 Application of the Hoek-Brown criterion to case study 1

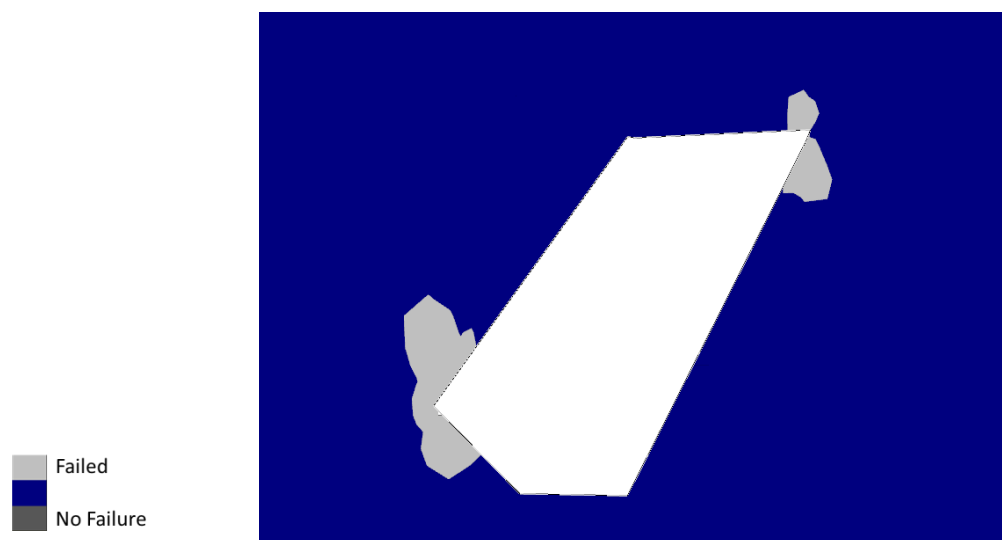


Figure E3 Application of the Zhang–Zhu Criterion to case study 1



Figure E4 Application of the Pan–Hudson Criterion to case study 1



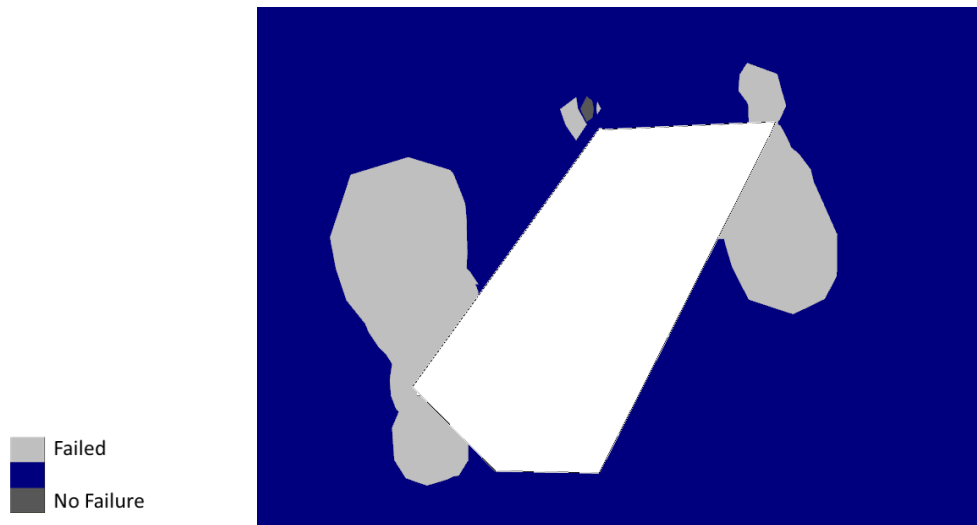


Figure E5 Application of the Priest Criterion to case study 1

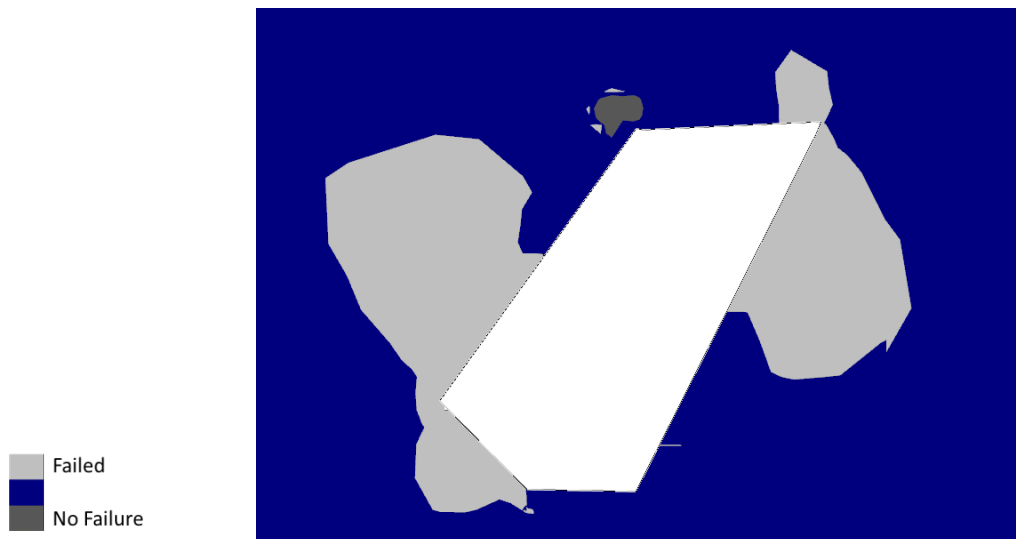


Figure E6 Application of the Simplified Priest Criterion to case study 1

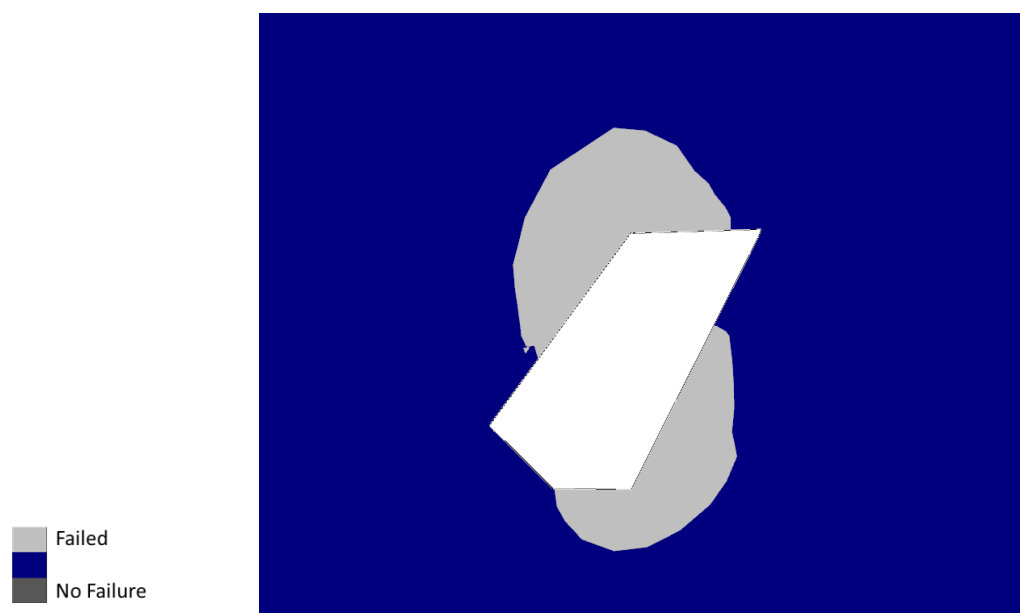


Figure E7 Application of the DSSI design criterion to case study 1

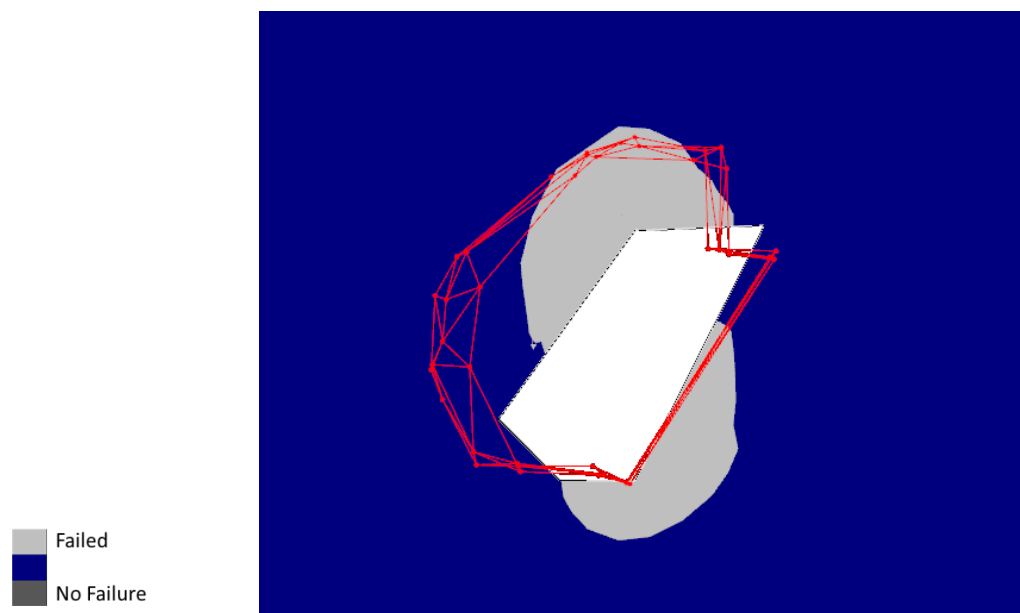


Figure E8 CMS wireframe in red showing actual overbreak of case study 1



Figure E9 Application of the Mohr-Coulomb criterion to case study 2



Figure E10 Application of the Hoek-Brown criterion to case study 2

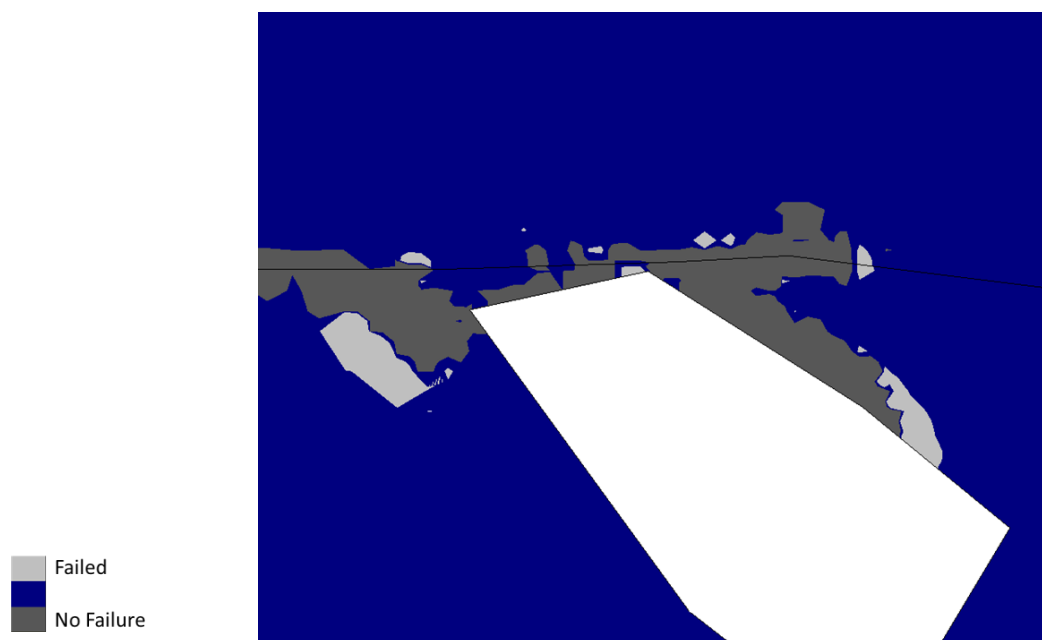


Figure E11 Application of the Zhang–Zhu Criterion to case study 2

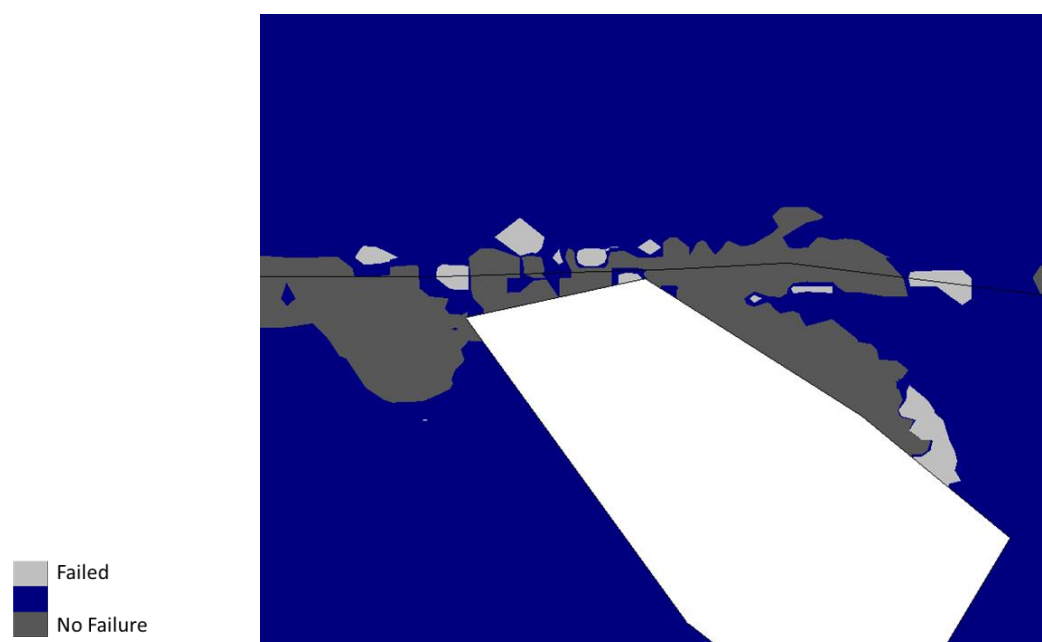


Figure E12 Application of the Pan–Hudson Criterion to case study 2



Figure E13 Application of the Priest Criterion to case study 2



Figure E14 Application of the Simplified Priest Criterion to case study 2

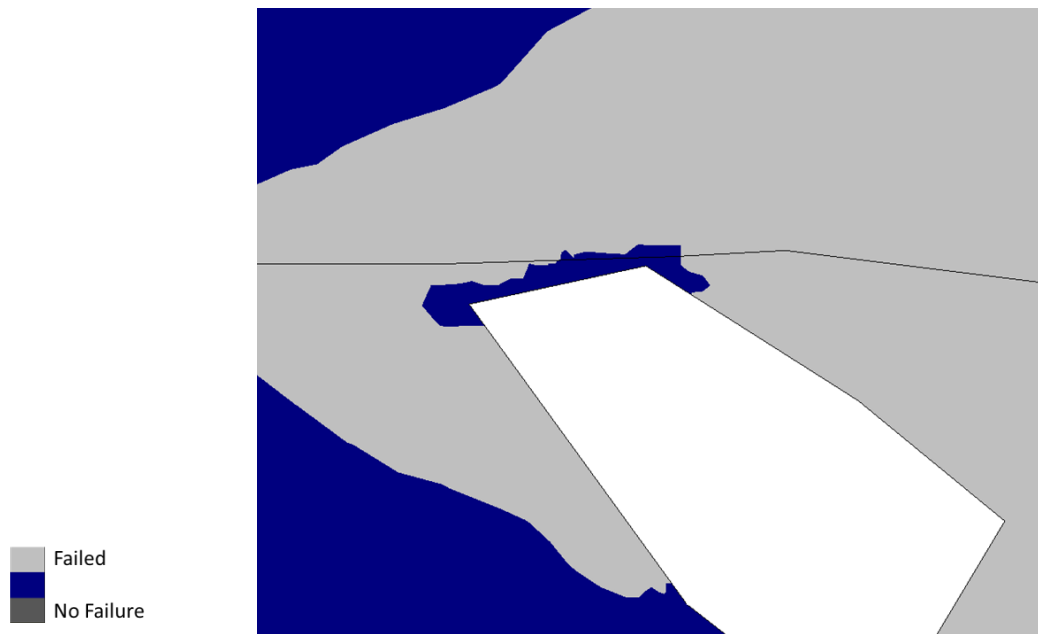


Figure E15 Application of the DSSI design criterion to case study 2

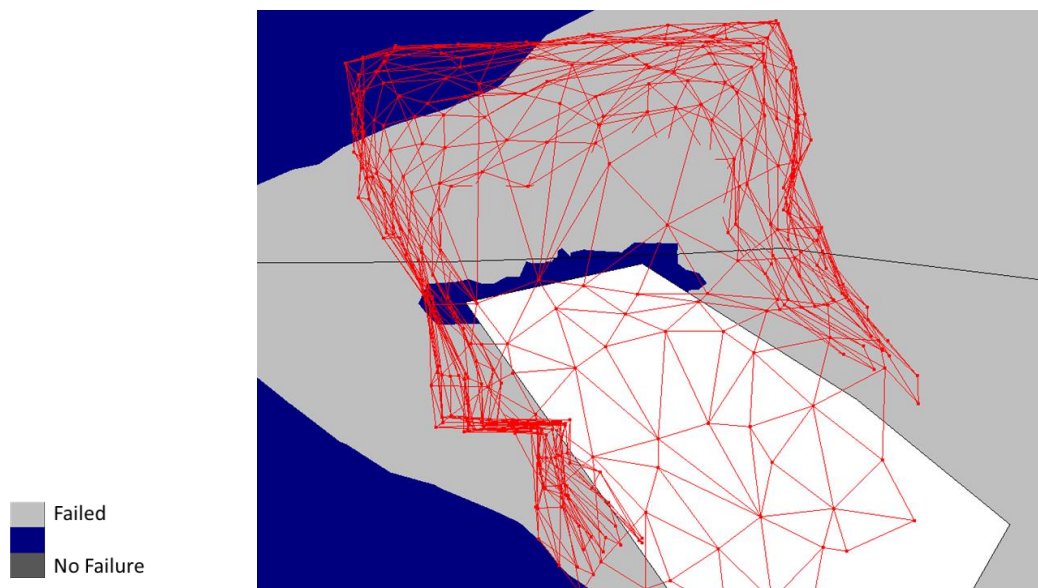


Figure E16 CMS wireframe in red showing actual overbreak of case study 2

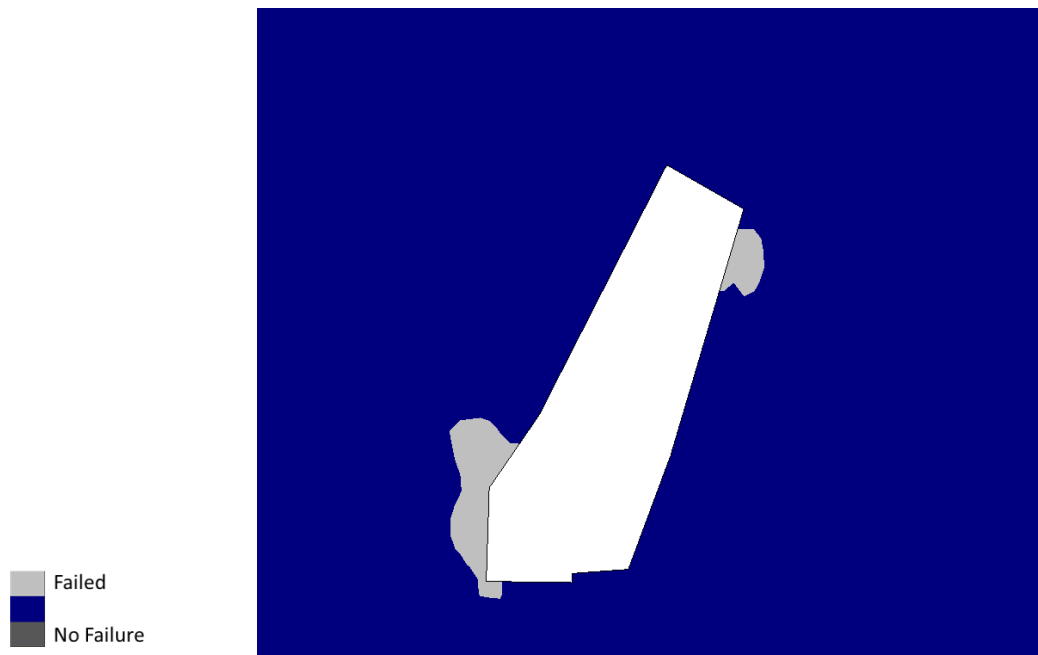


Figure E17 Application of the Mohr-Coulomb criterion to case study 3

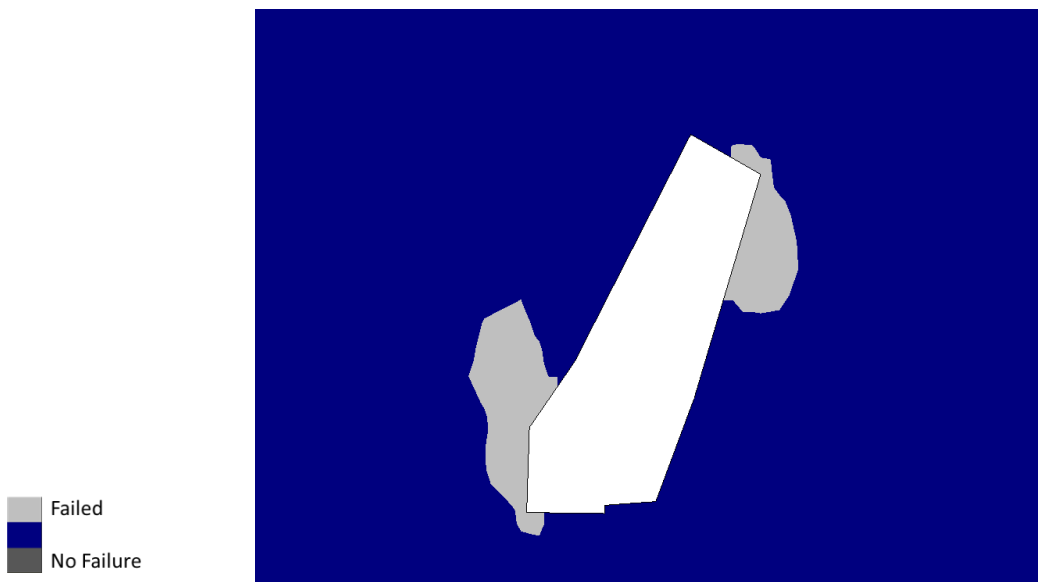


Figure E18 Application of the Hoek-Brown criterion to case study 3

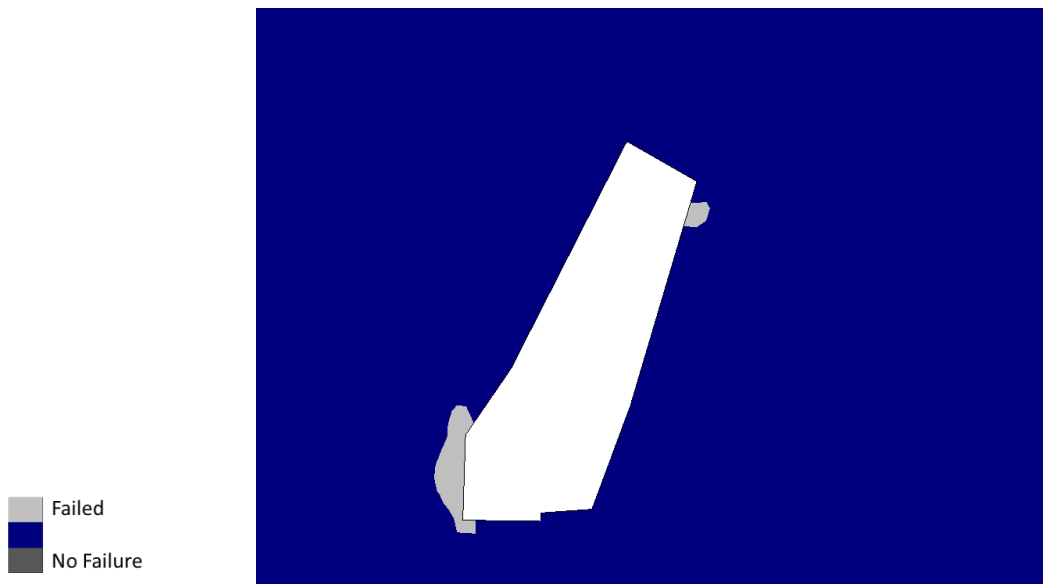


Figure E19 Application of the Zhang–Zhu Criterion to case study 3

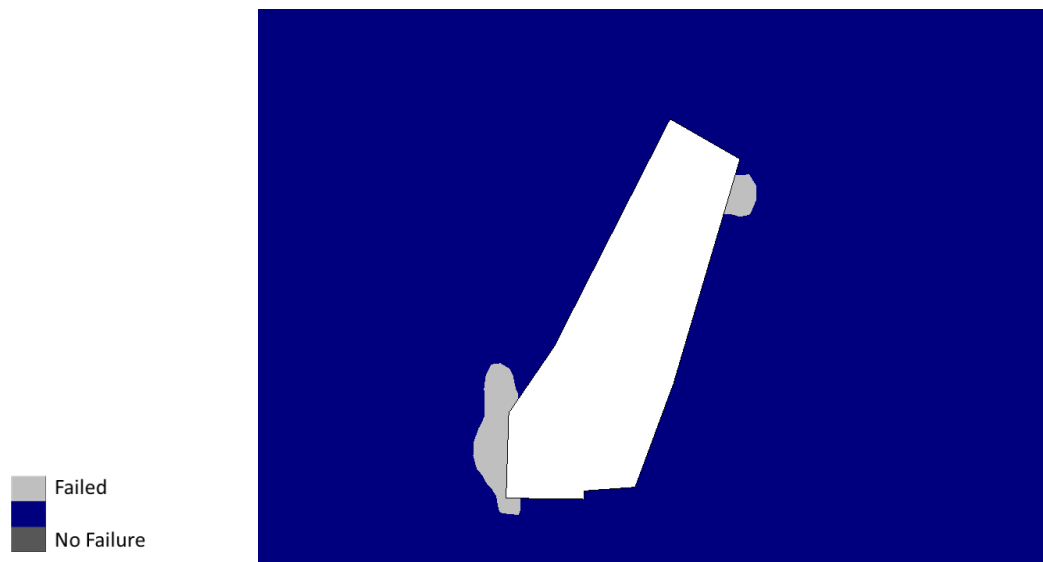


Figure E20 Application of the Pan–Hudson Criterion to case study 3



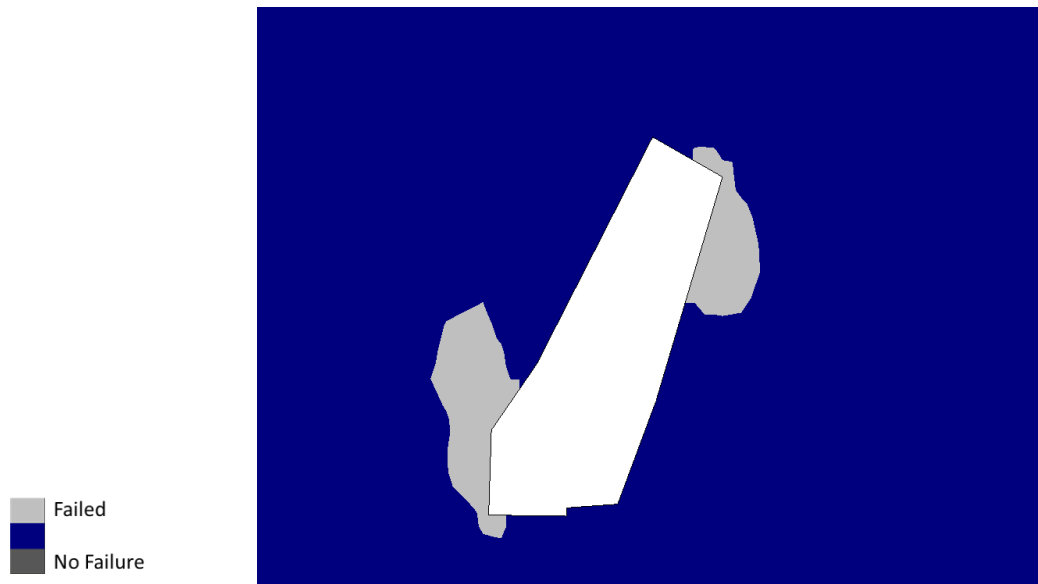


Figure E21 Application of the Priest Criterion to case study 3

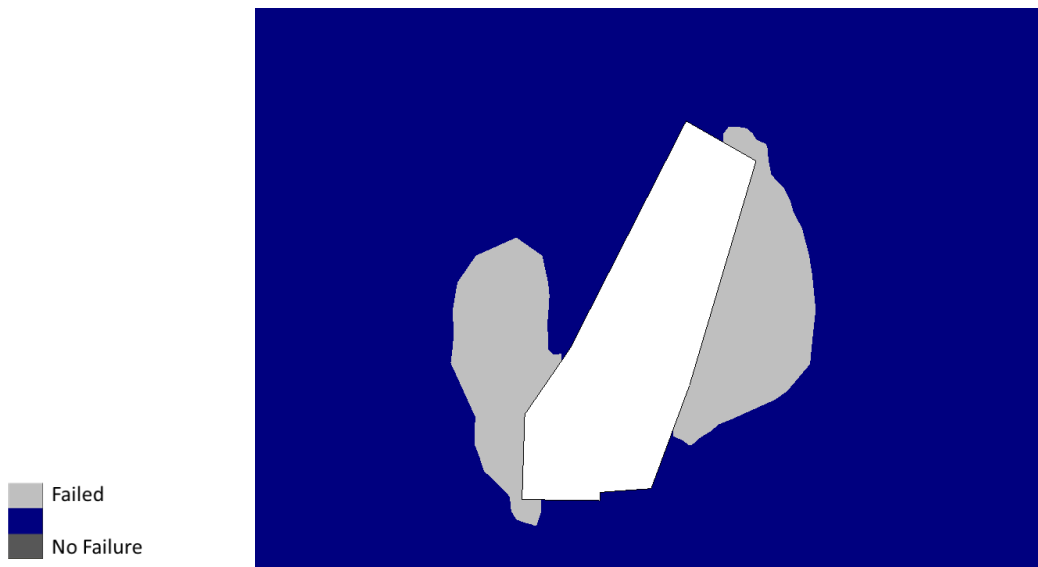


Figure E22 Application of the Simplified Priest Criterion to case study 3

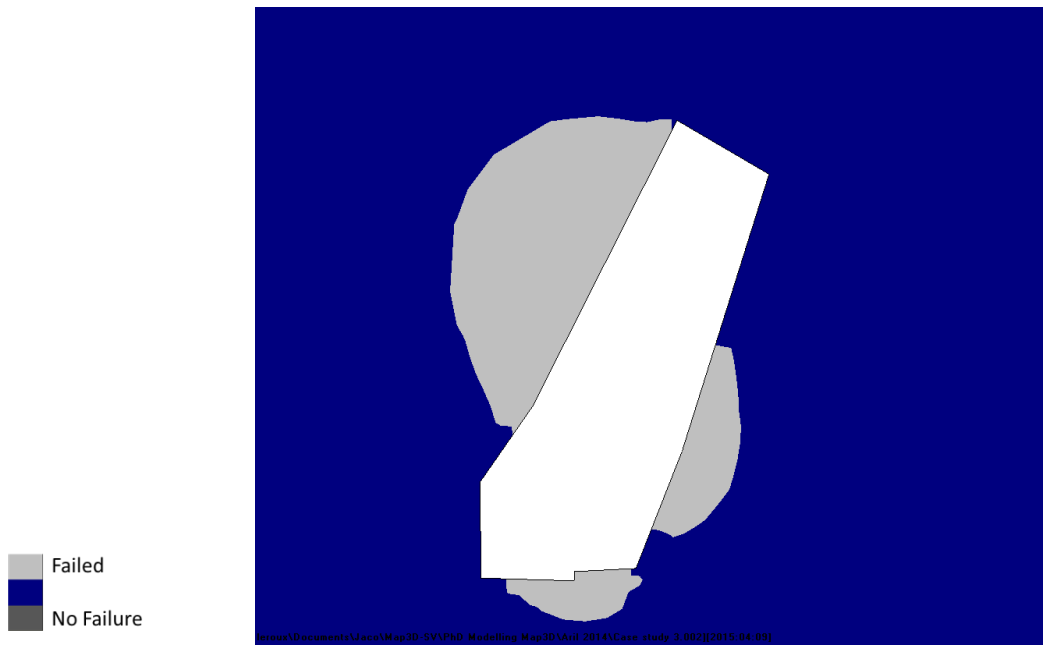


Figure E23 Application of the DSSI design criterion to case study 3

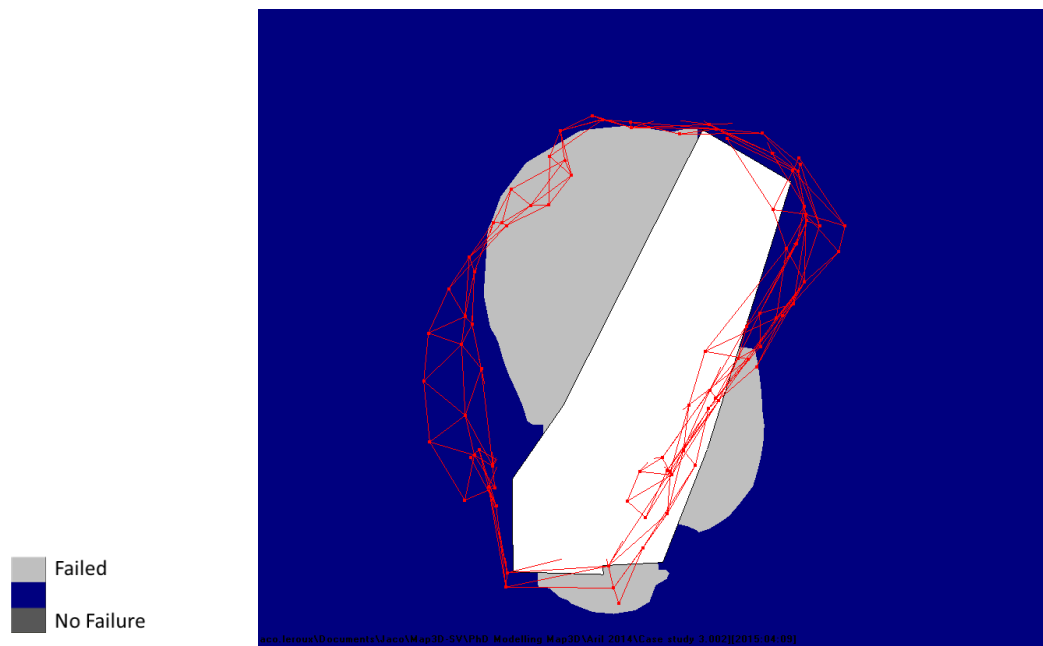


Figure E24 CMS wireframe in red showing actual overbreak of case study 3



Figure E25 Application of the Mohr-Coulomb criterion to case study 4



Figure E26 Application of the Hoek-Brown criterion to case study 4



Figure E27 Application of the Zhang–Zhu Criterion to case study 4



Figure E28 Application of the Pan–Hudson Criterion to case study 4



Figure E29 Application of the Priest Criterion to case study 4



Figure E30 Application of the Simplified Priest Criterion to case study 4

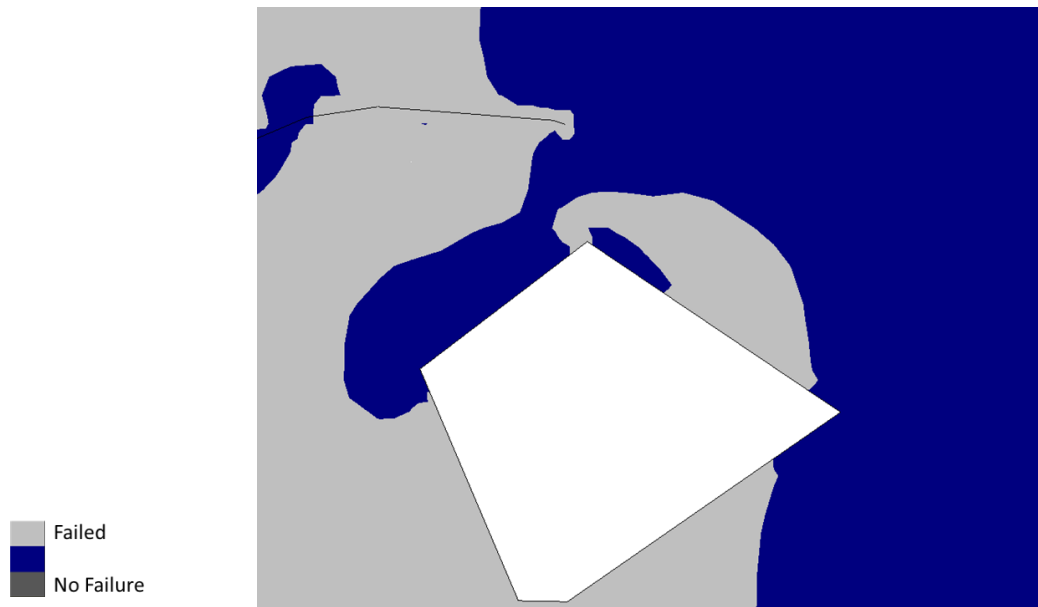


Figure E31 Application of the DSSI design criterion to case study 4



Figure E32 Application of the Mohr-Coulomb criterion to case study 5



Figure E33 Application of the Hoek-Brown criterion to case study 5



Figure E34 Application of the Zhang-Zhu Criterion to case study 5



Figure E35 Application of the Pan-Hudson Criterion to case study 5



Figure E36 Application of the Priest Criterion to case study 5





Figure E37 Application of the Simplified Priest Criterion to case study 5

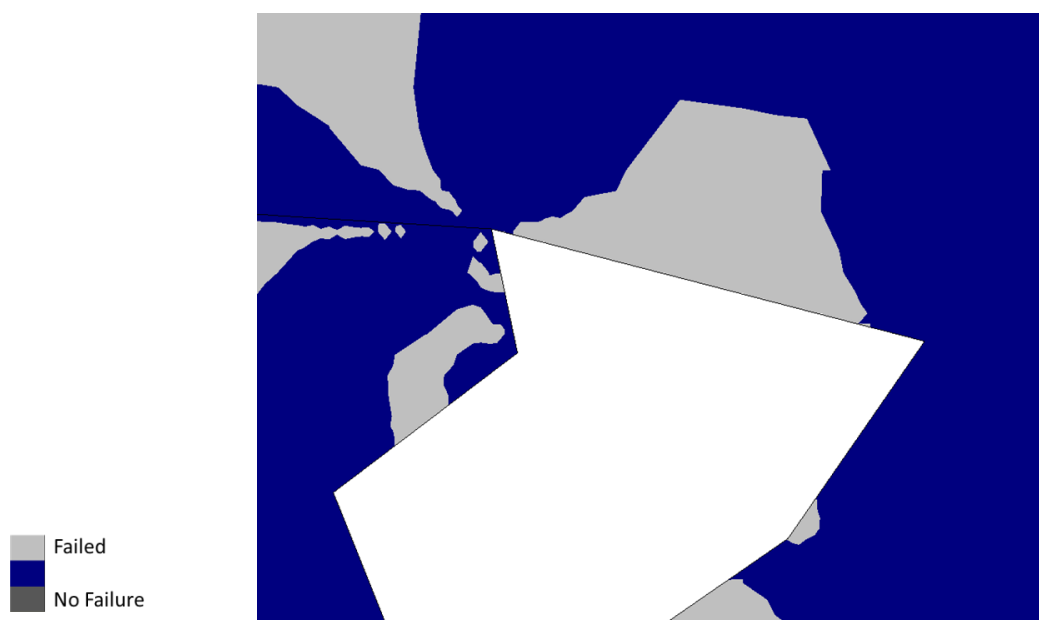


Figure E38 Application of the DSSI design criterion to case study 5

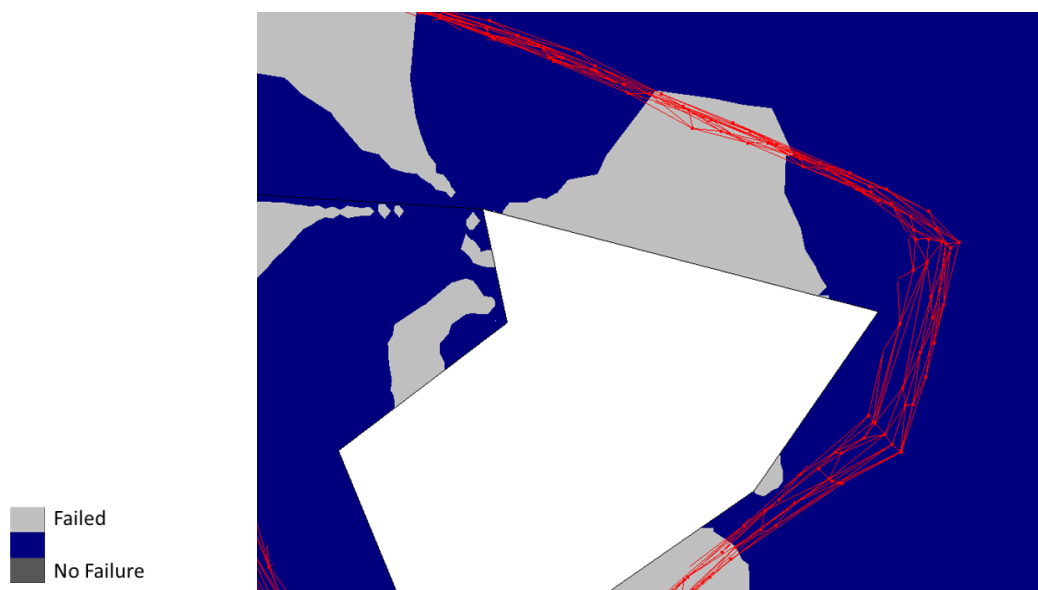


Figure E39 CMS wireframe in red showing actual overbreak of case study 5



Figure E40 Application of the Mohr-Coulomb criterion to case study 6



Figure E41 Application of the Hoek-Brown criterion to case study 6



Figure E42 Application of the Zhang-Zhu Criterion to case study 6



Figure E43 Application of the Pan-Hudson Criterion to case study 6



Figure E44 Application of the Priest Criterion to case study 6

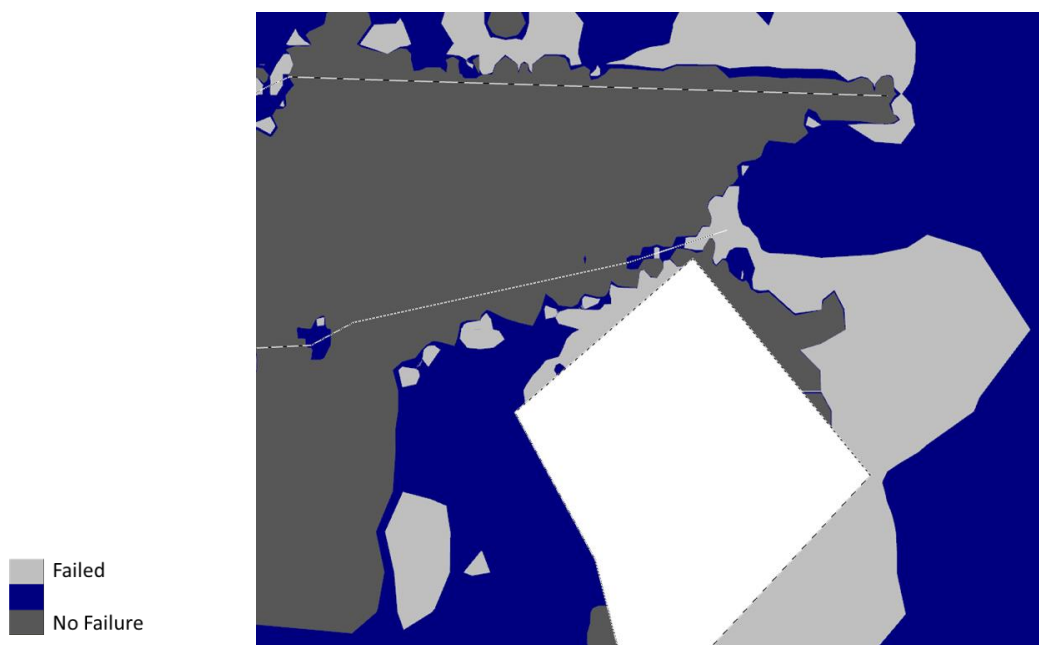


Figure E45 Application of the Simplified Priest Criterion to case study 6

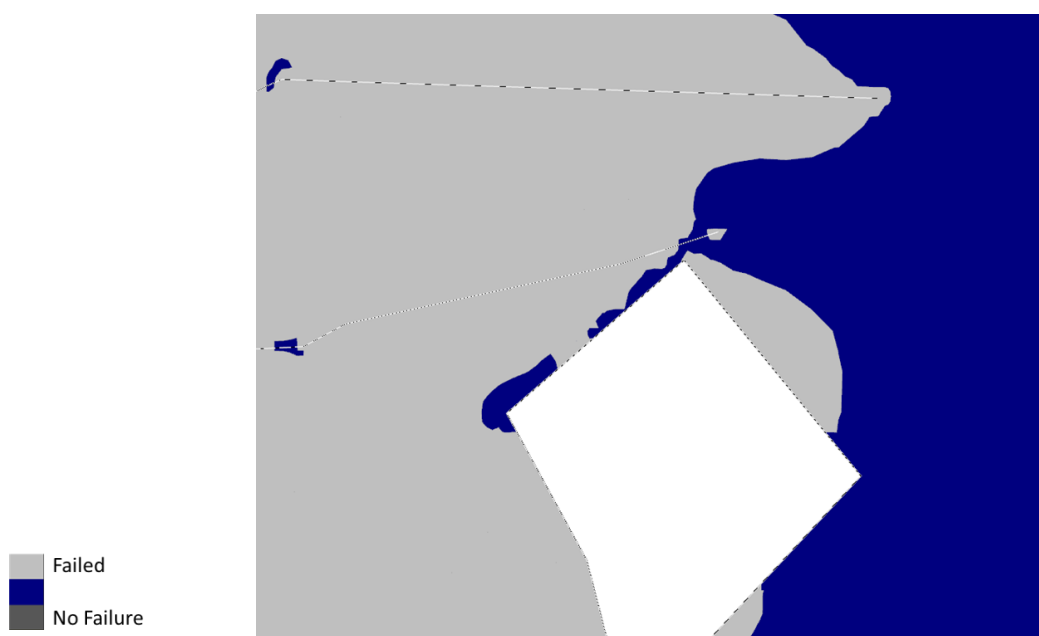


Figure E46 Application of the DSSI design criterion to case study 6



Figure E47 Application of the Mohr-Coulomb criterion to case study 7

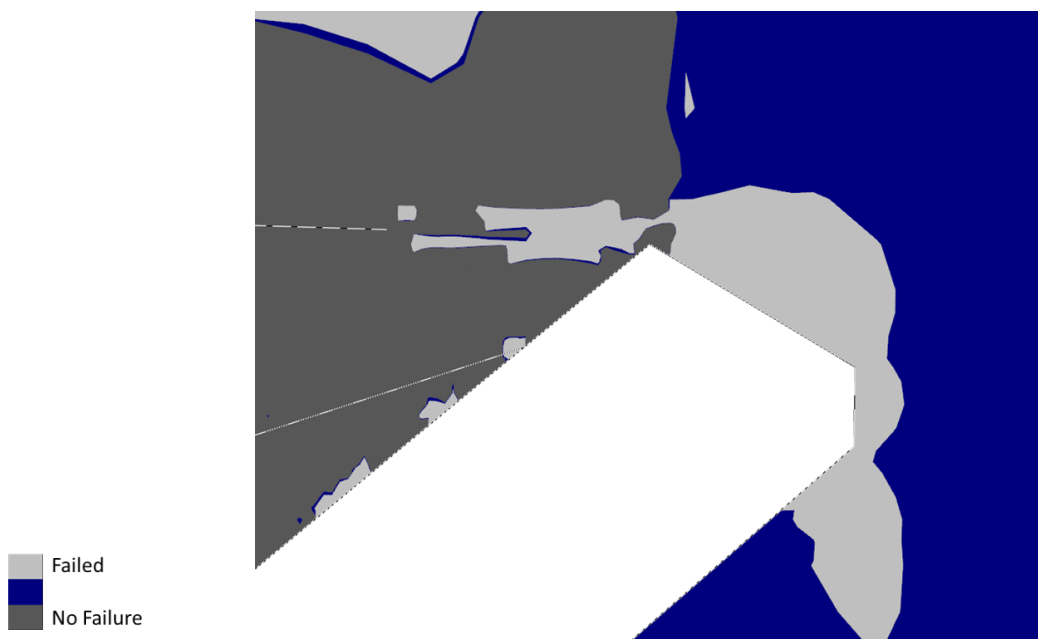


Figure E48 Application of the Hoek-Brown criterion to case study 7

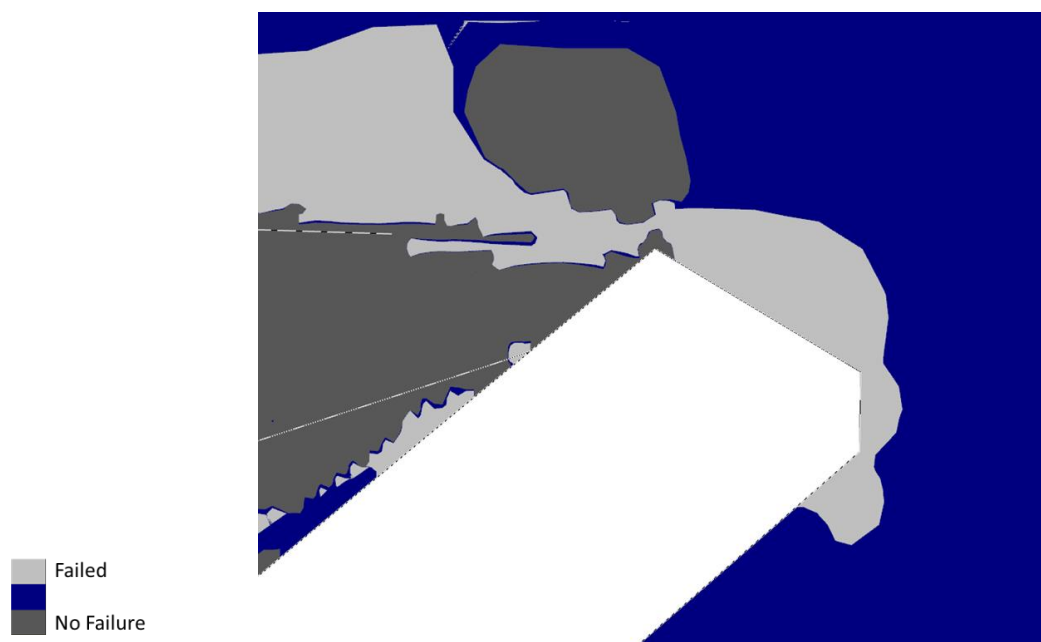


Figure E49 Application of the Zhang–Zhu Criterion to case study 7



Figure E50 Application of the Pan–Hudson Criterion to case study 7

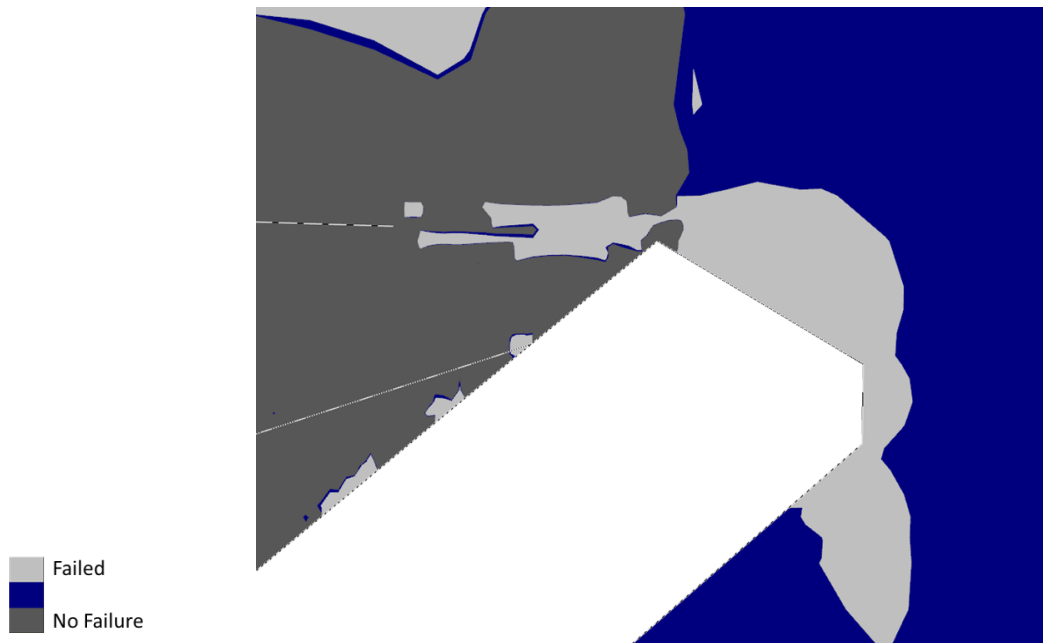


Figure E51 Application of the Priest Criterion to case study 7

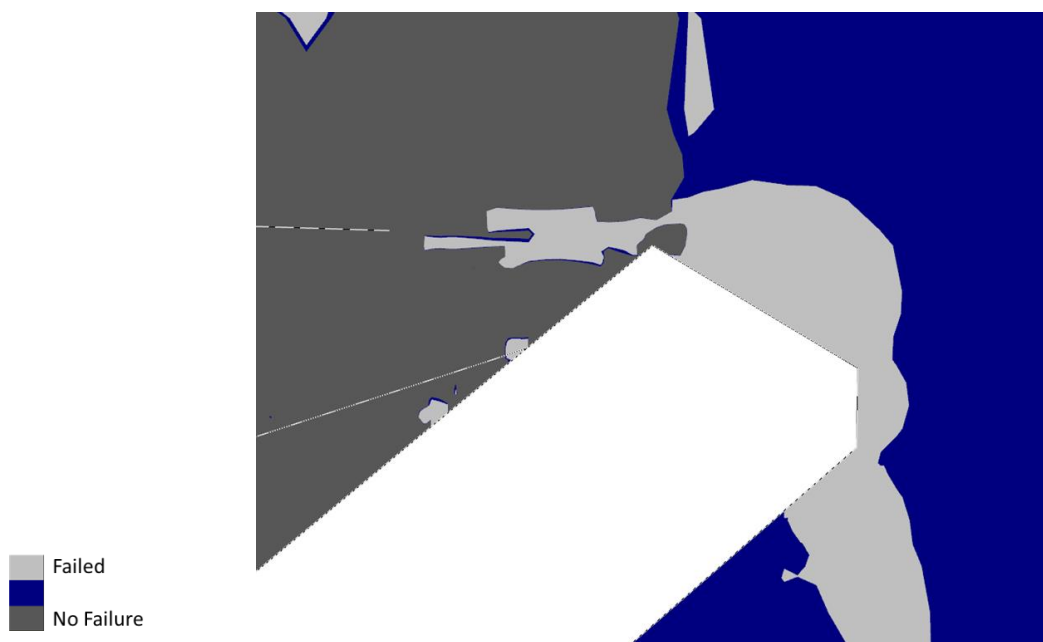


Figure E52 Application of the Simplified Priest Criterion to case study 7





Figure E53 Application of the DSSI design criterion to case study 7

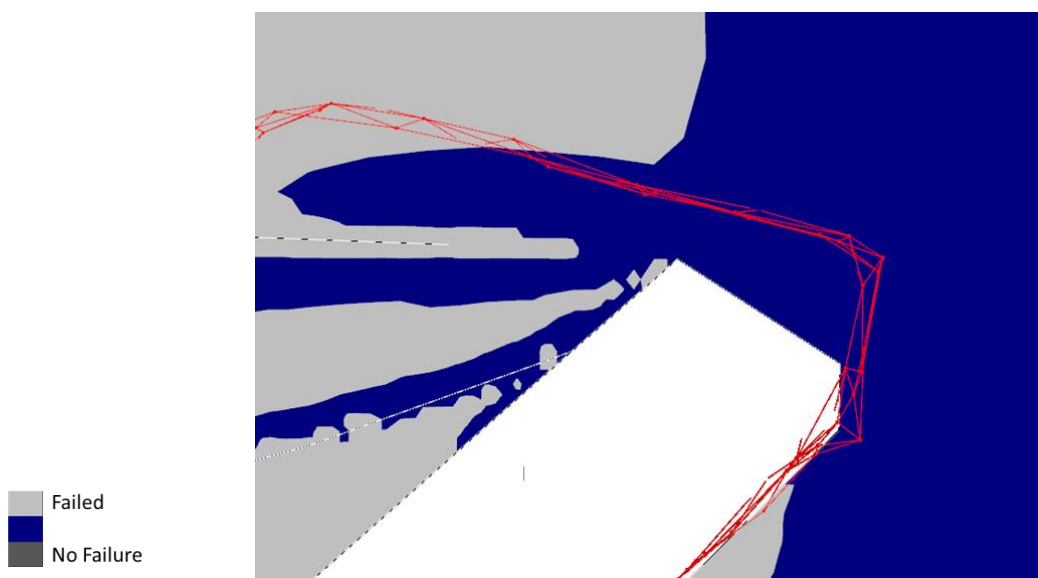


Figure E54 CMS wireframe in red showing actual overbreak of case study 7



Figure E55 Application of the Mohr-Coulomb criterion to case study 8



Figure E56 Application of the Hoek-Brown criterion to case study 8



Figure E57 Application of the Zhang–Zhu Criterion to case study 8



Figure E58 Application of the Pan–Hudson Criterion to case study 8

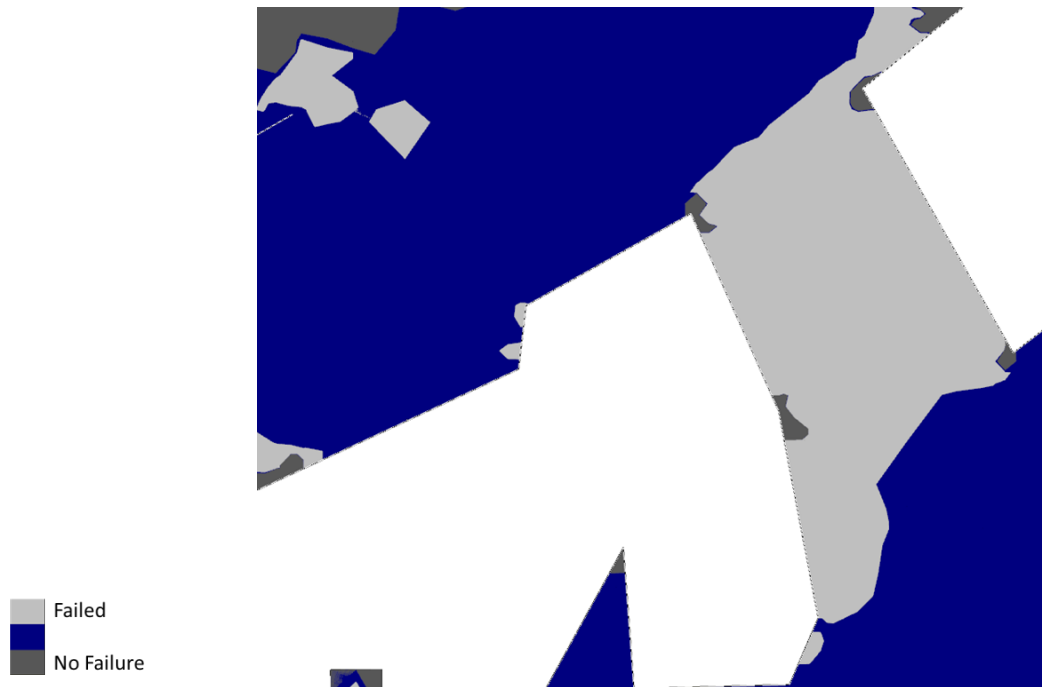


Figure E59 Application of the Priest Criterion to case study 8

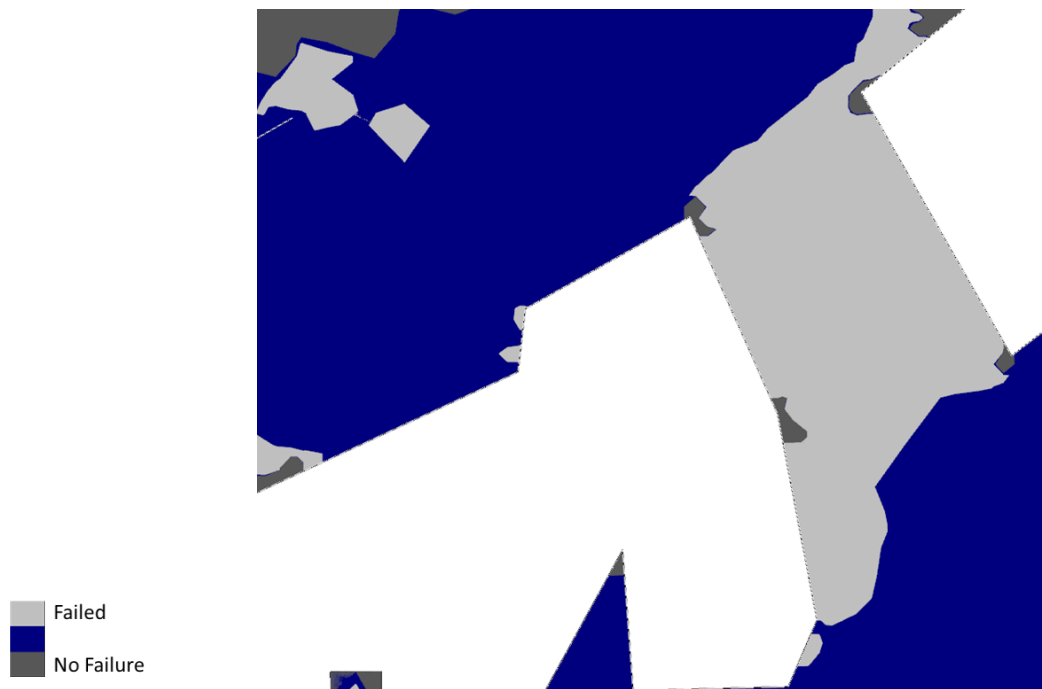


Figure E60 Application of the Simplified Priest Criterion to case study 8

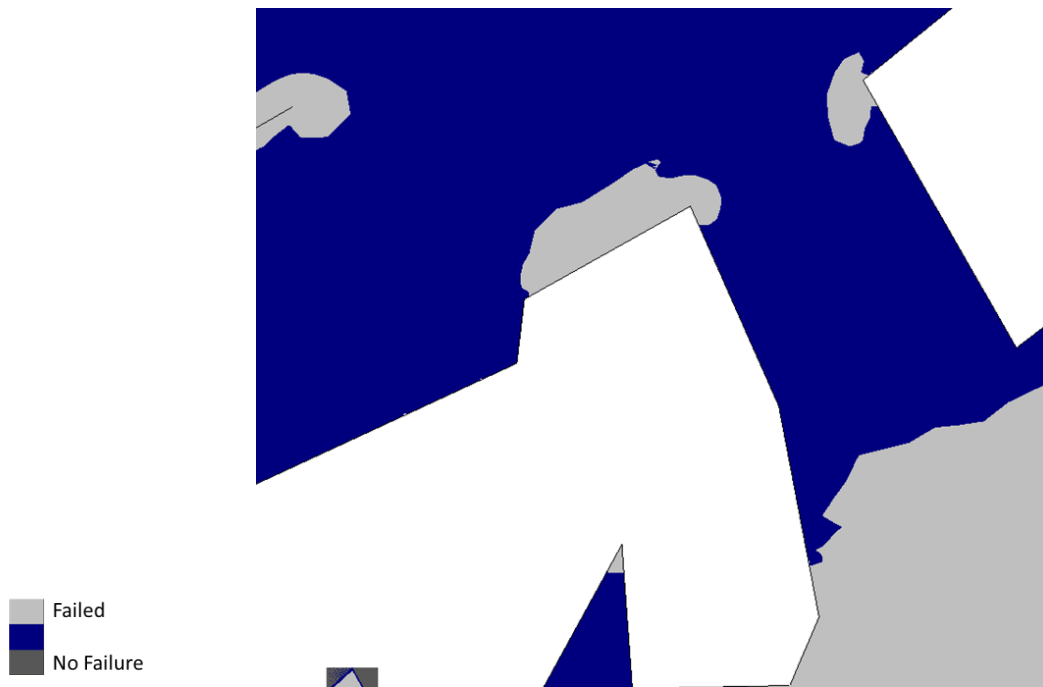


Figure E61 Application of the DSSI design criterion to case study 8

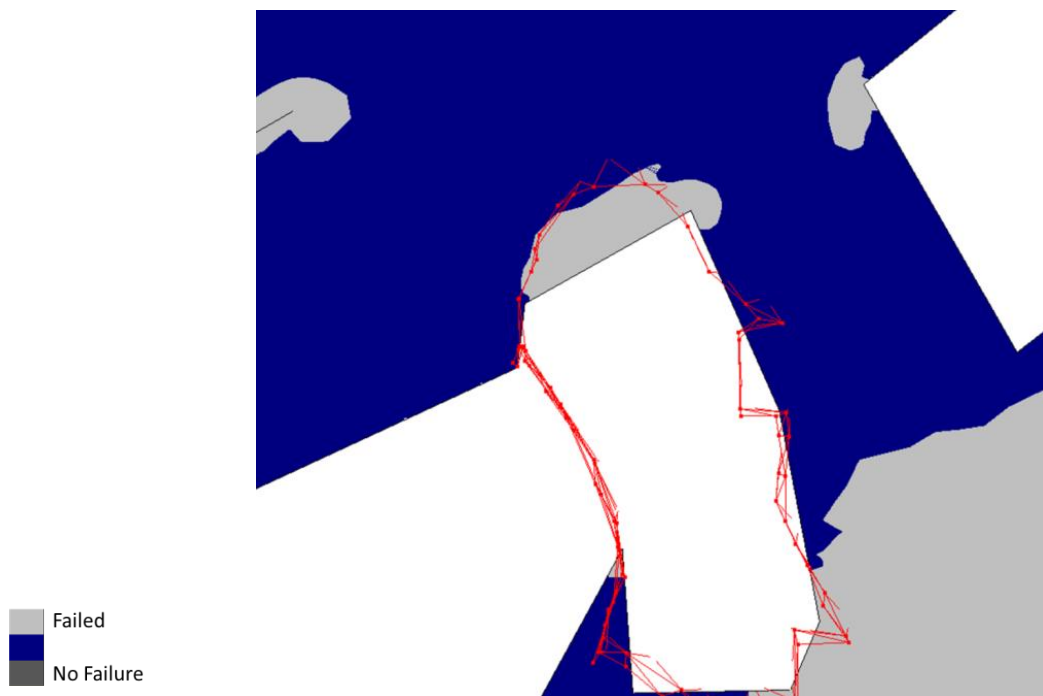


Figure E62 CMS wireframe in red showing actual overbreak of case study 8



Figure E63 Application of the Mohr-Coulomb criterion to case study 9

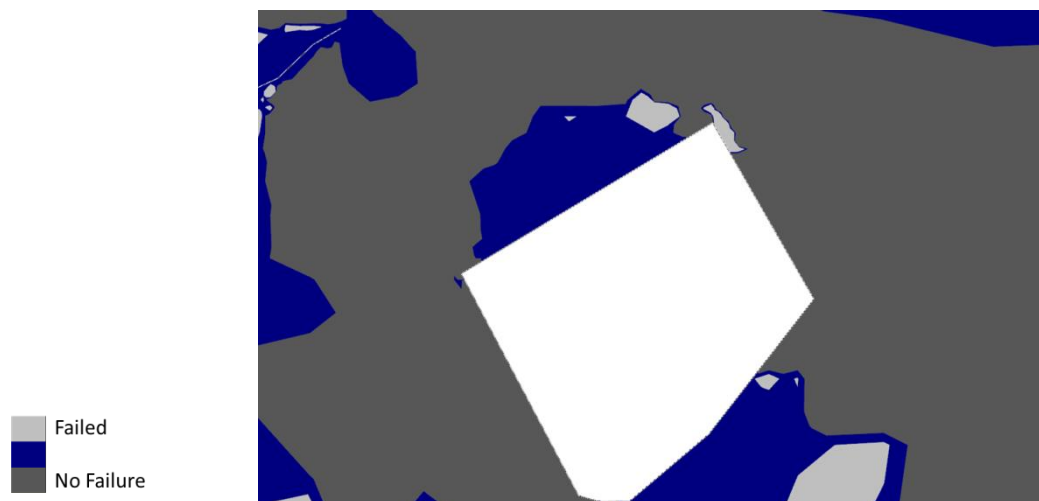


Figure E64 Application of the Hoek-Brown criterion to case study 9

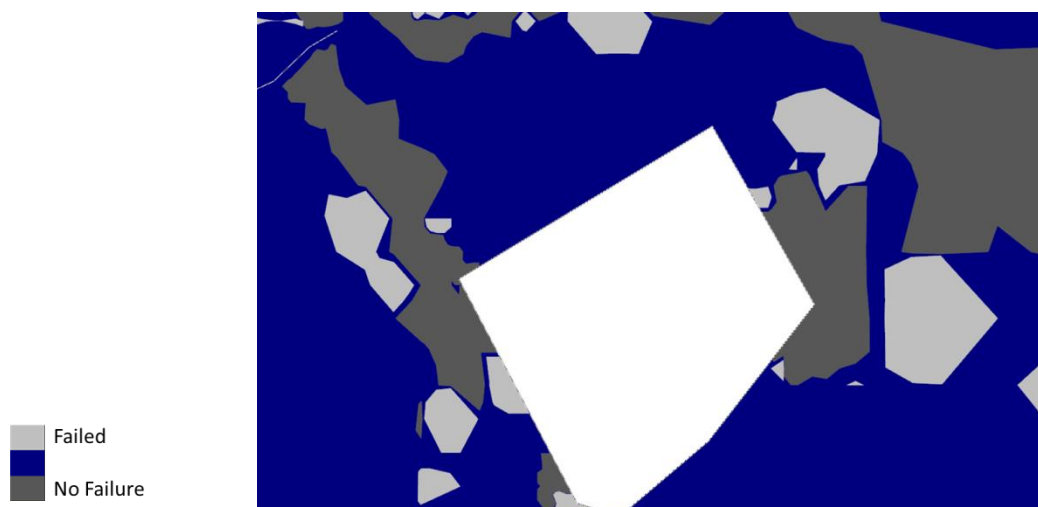


Figure E65 Application of the Zhang–Zhu Criterion to case study 9



Figure E66 Application of the Pan–Hudson Criterion to case study 9

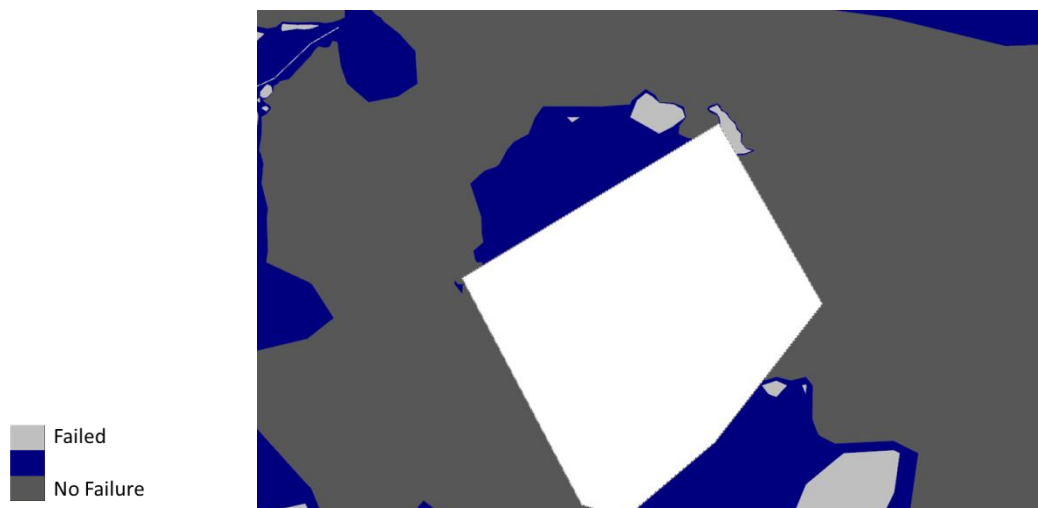


Figure E67 Application of the Priest Criterion to case study 9

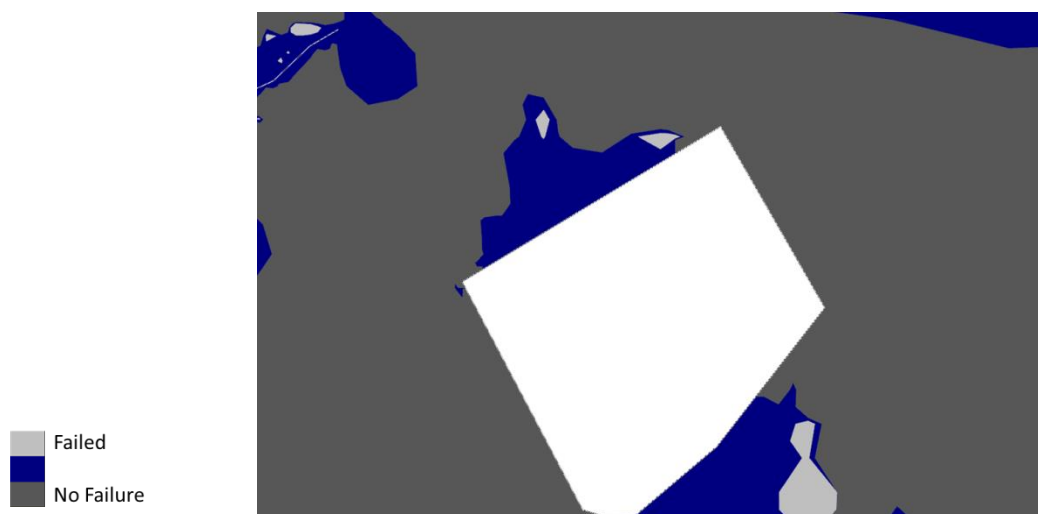


Figure E68 Application of the Simplified Priest Criterion to case study 9

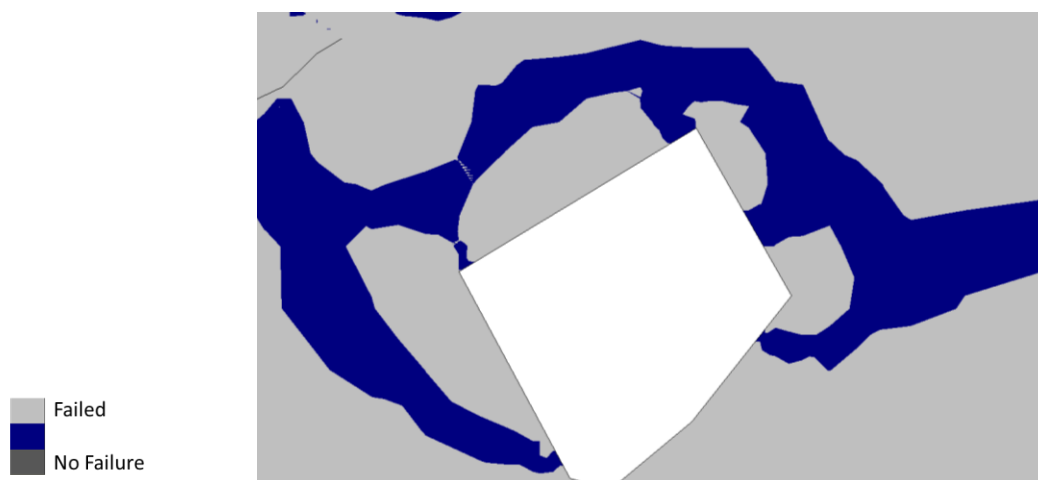


Figure E69 Application of the DSSI design criterion to case study 9



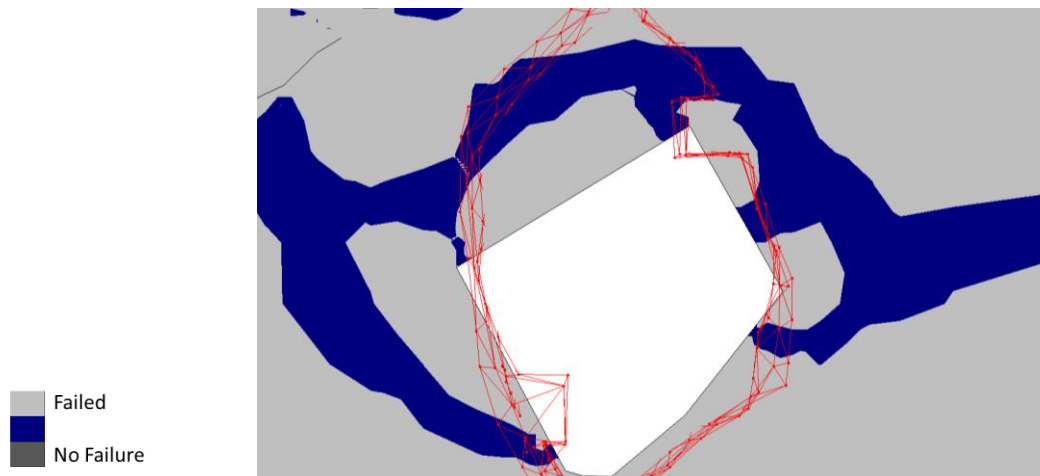


Figure E70 CMS wireframe in red showing actual overbreak of case study 9

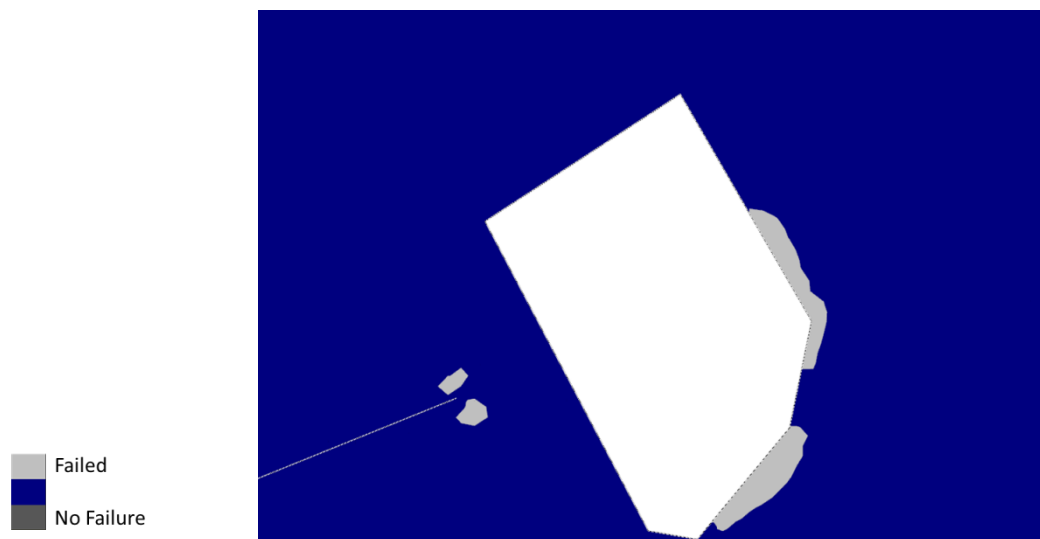


Figure E71 Application of the Mohr-Coulomb criterion to case study 10

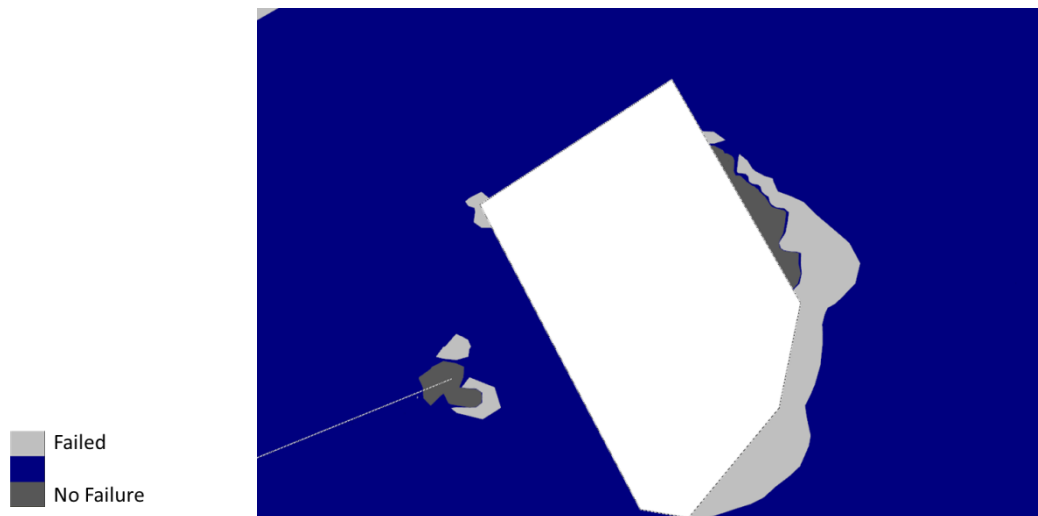


Figure E72 Application of the Hoek-Brown criterion to case study 10

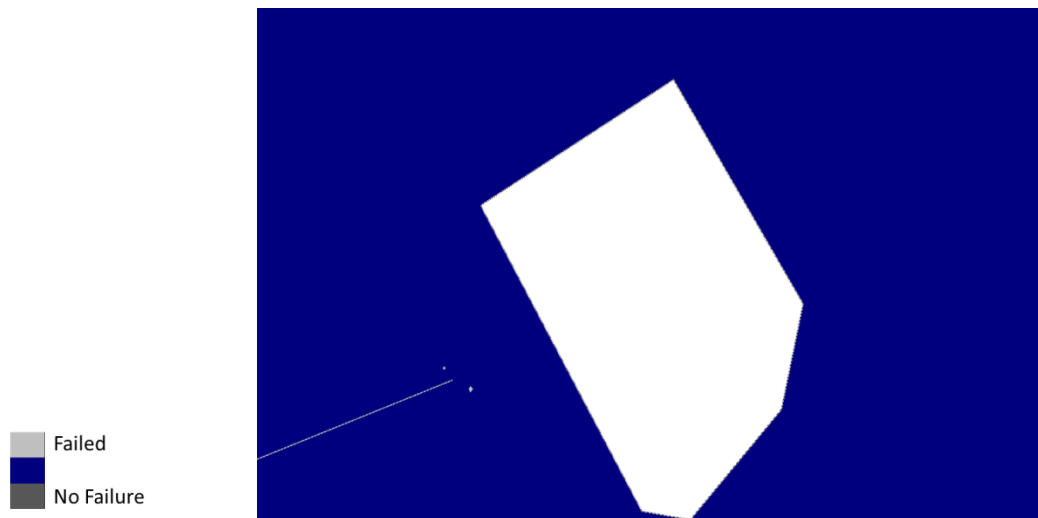


Figure E73 Application of the Zhang-Zhu Criterion to case study 10

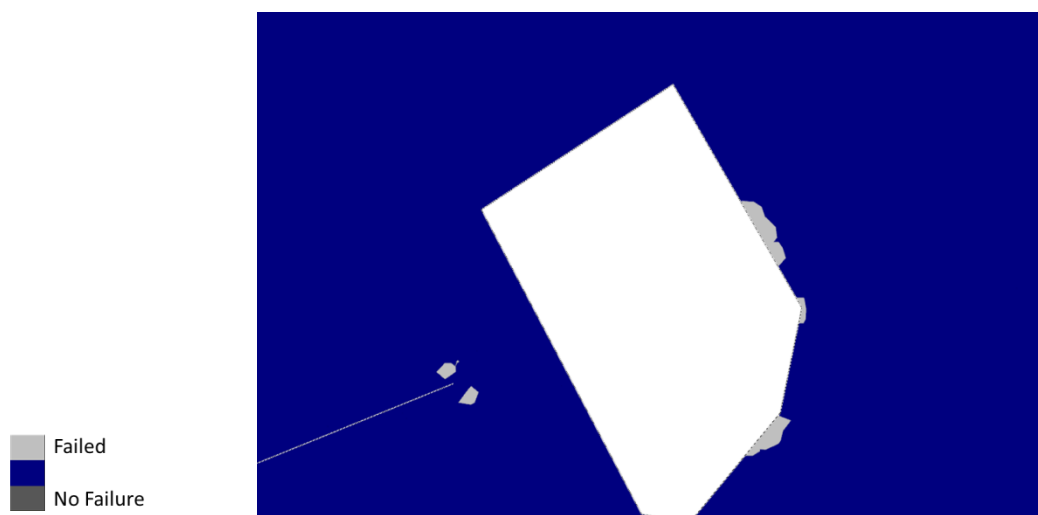


Figure E74 Application of the Pan-Hudson Criterion to case study 10

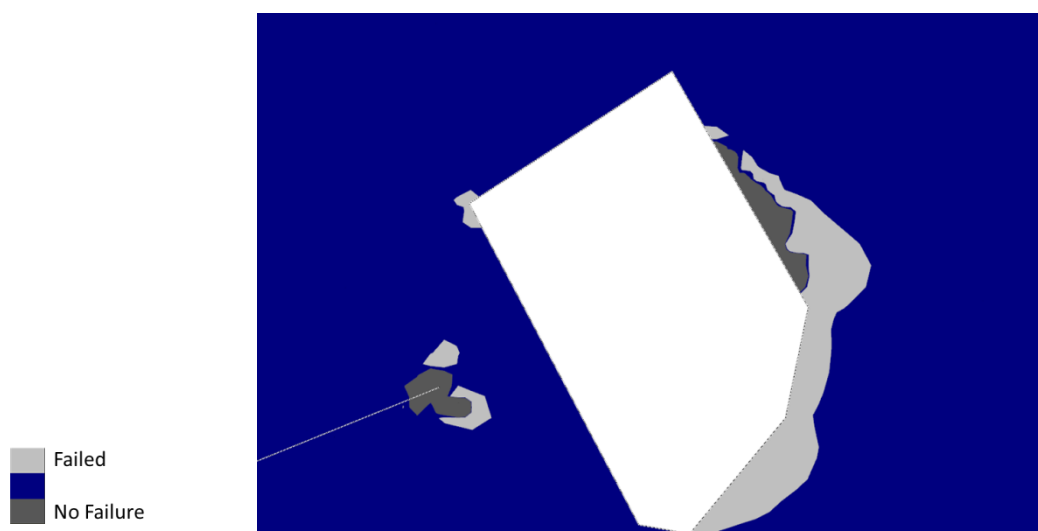


Figure E75 Application of the Priest Criterion to case study 10

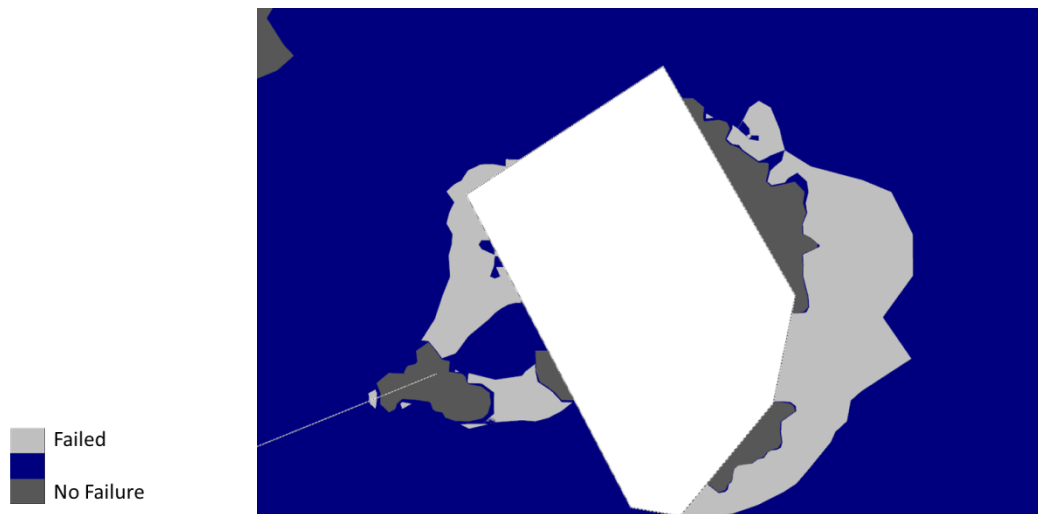


Figure E76 Application of the Simplified Priest Criterion to case study 10

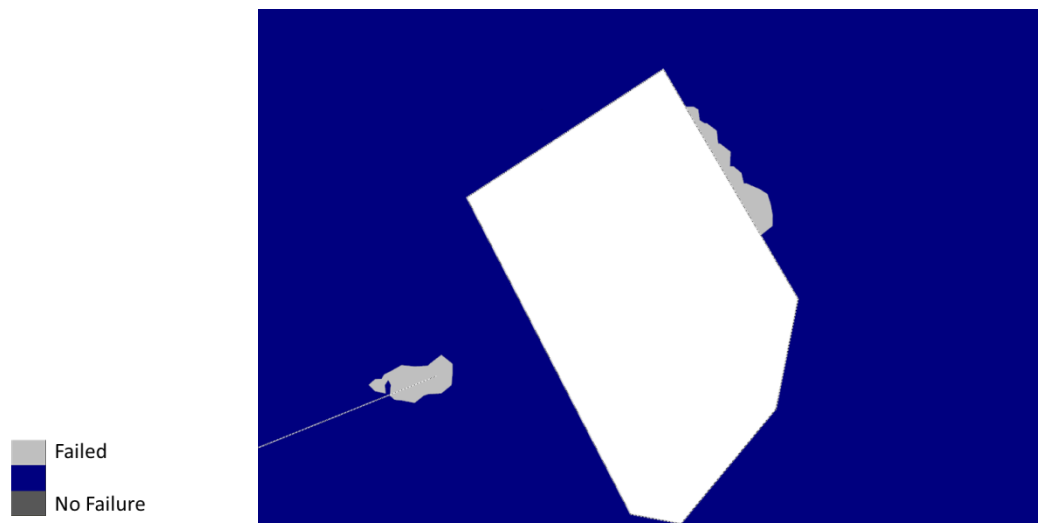


Figure E77 Application of the DSSI design criterion to case study 10

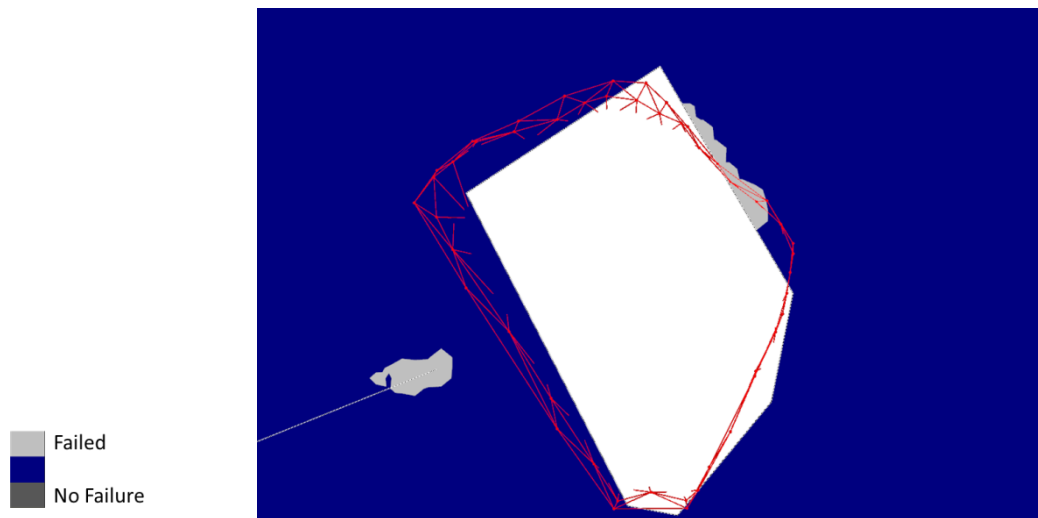


Figure E78 CMS wireframe in red showing actual overbreak of case study 10

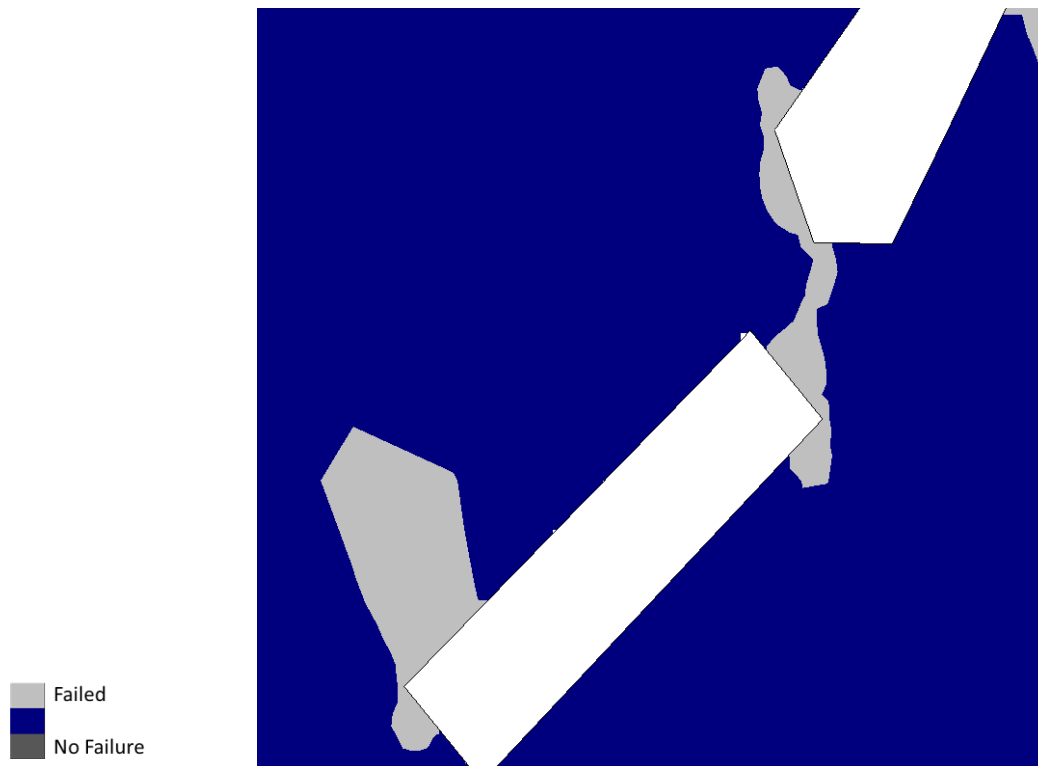


Figure E79 Application of the Mohr-Coulomb criterion to case study 11

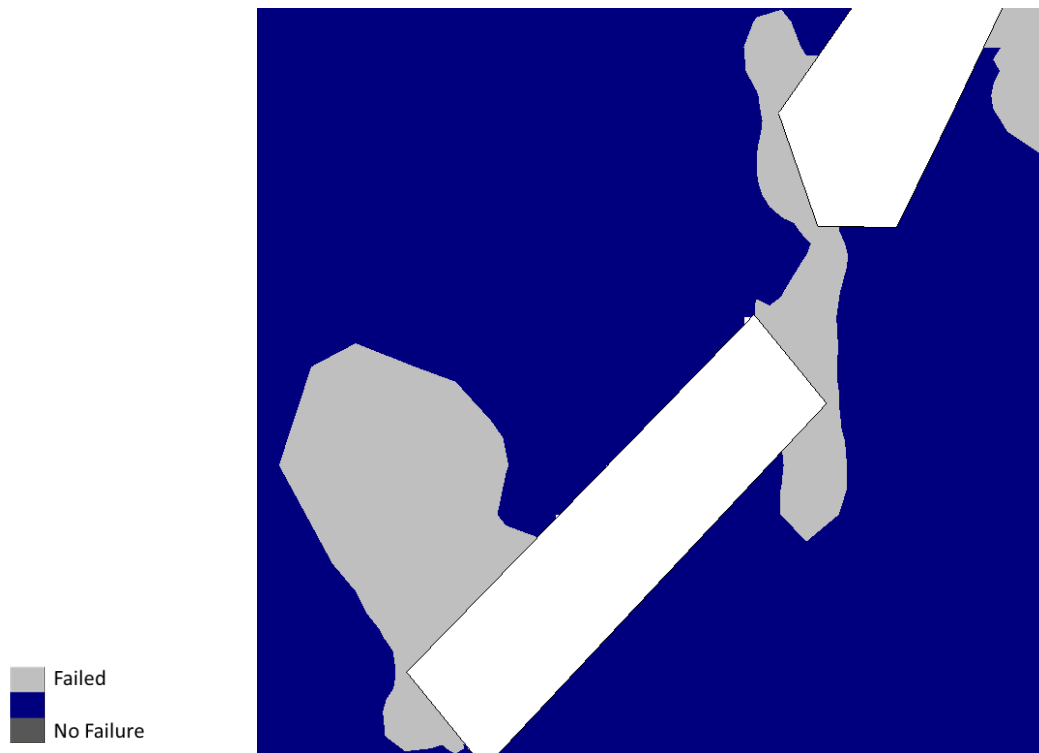


Figure E80 Application of the Hoek-Brown criterion to case study 11

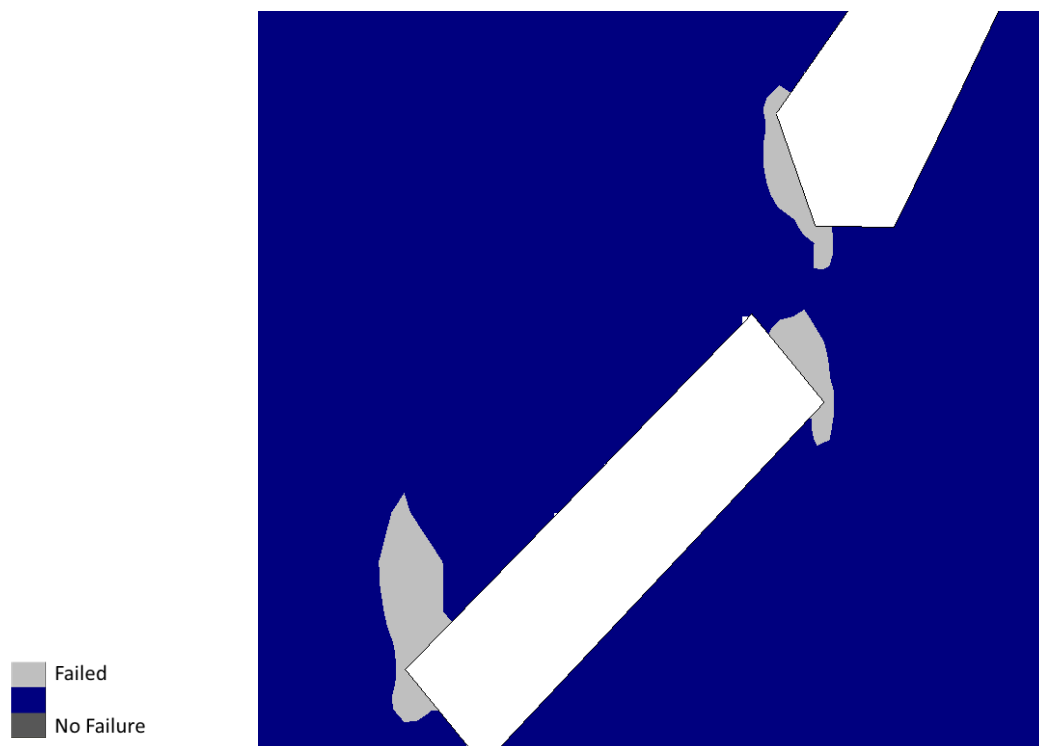


Figure E81 Application of the Zhang-Zhu Criterion to case study 11

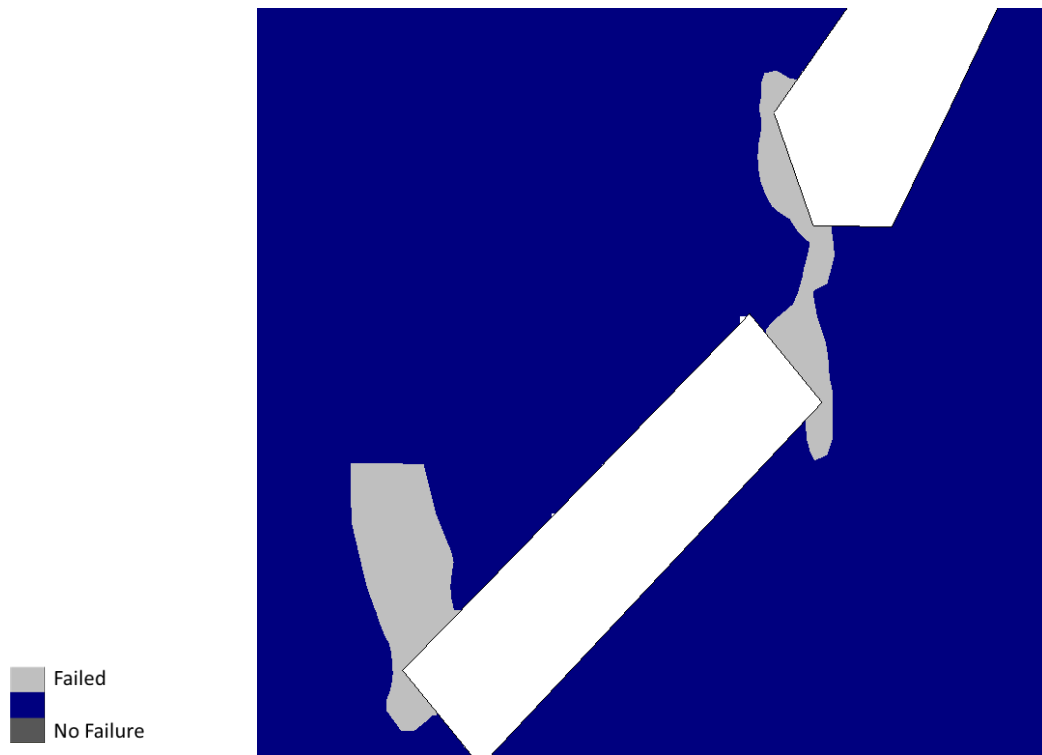


Figure E82 Application of the Pan-Hudson Criterion to case study 11

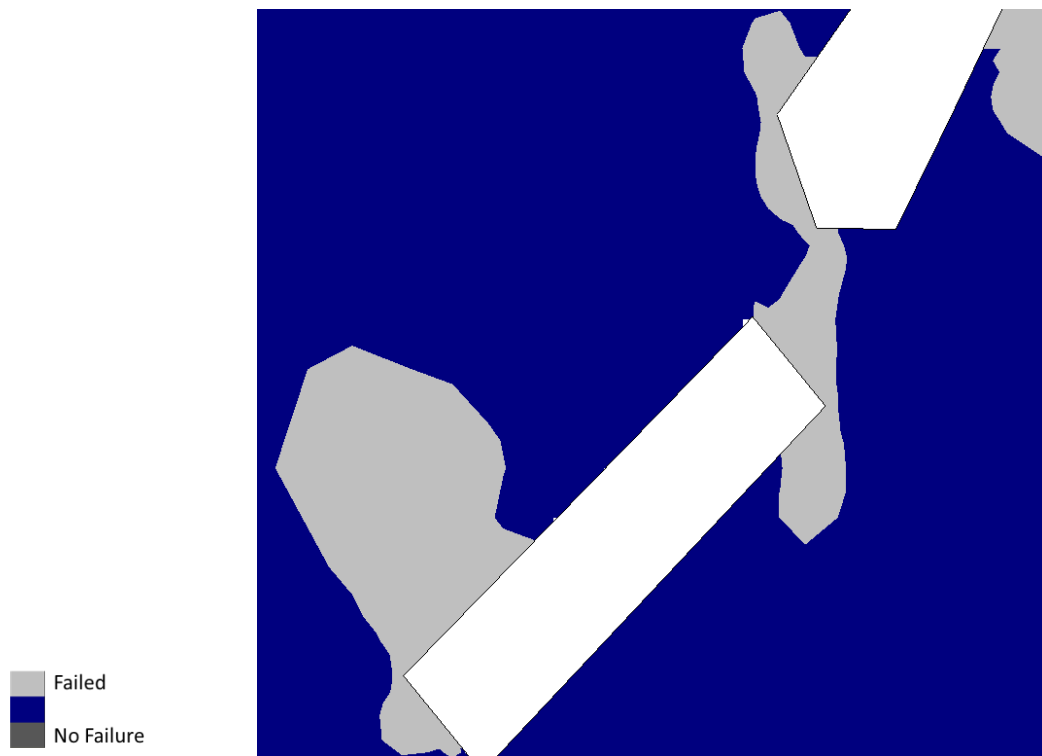


Figure E83 Application of the Priest Criterion to case study 11



Figure E84 Application of the Simplified Priest Criterion to case study 11



Figure E85 Application of the DSSI design criterion to case study 11



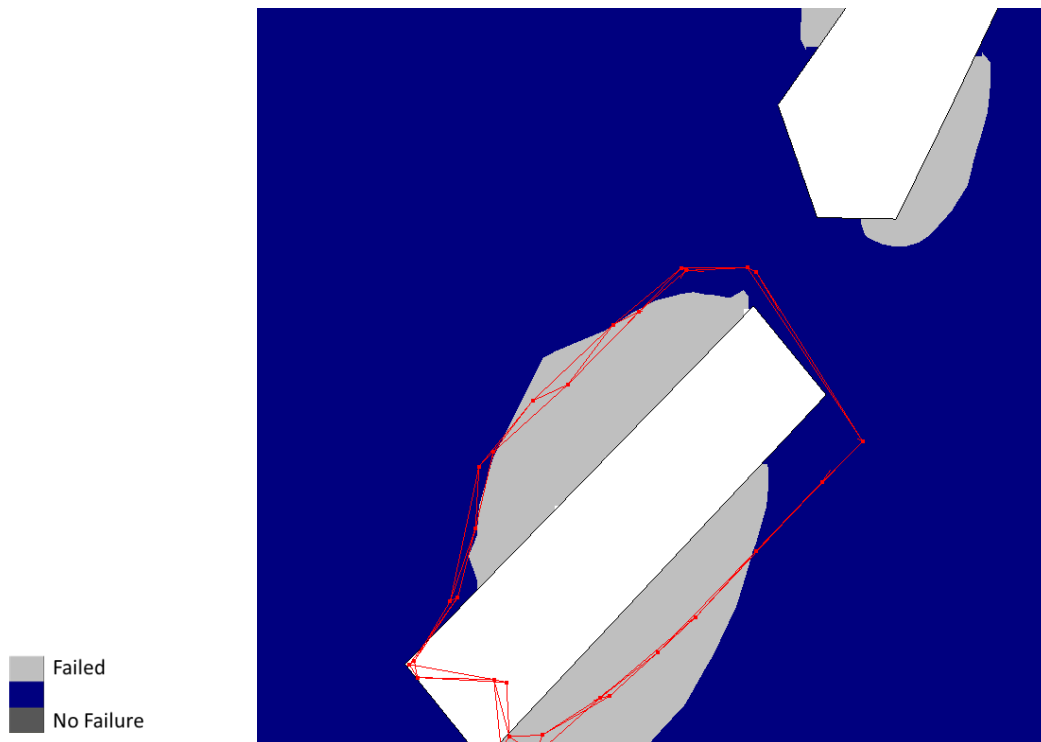


Figure E86 CMS wireframe in red showing actual overbreak of case study 11

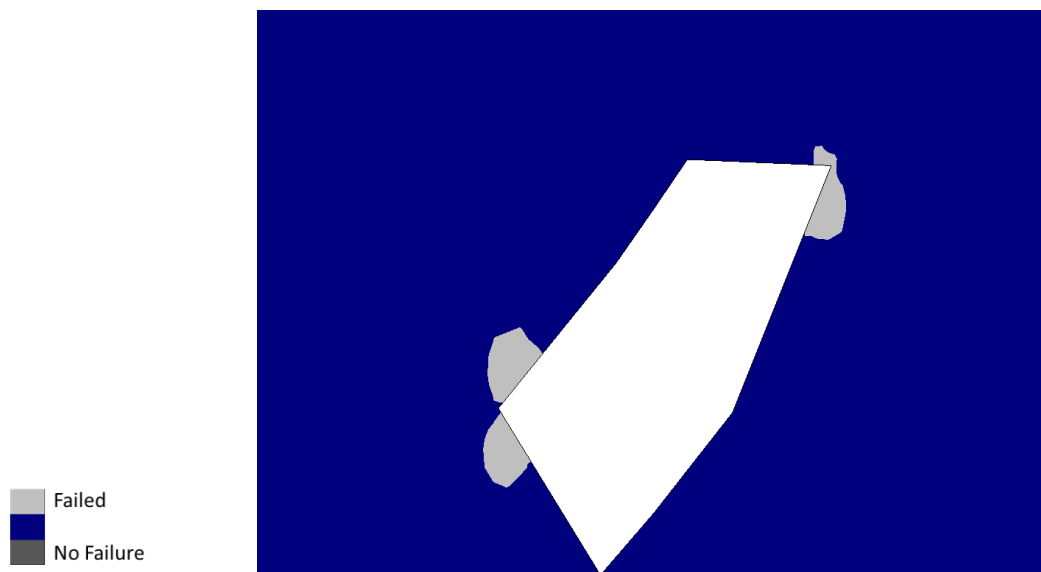


Figure E87 Application of the Mohr-Coulomb criterion to case study 12

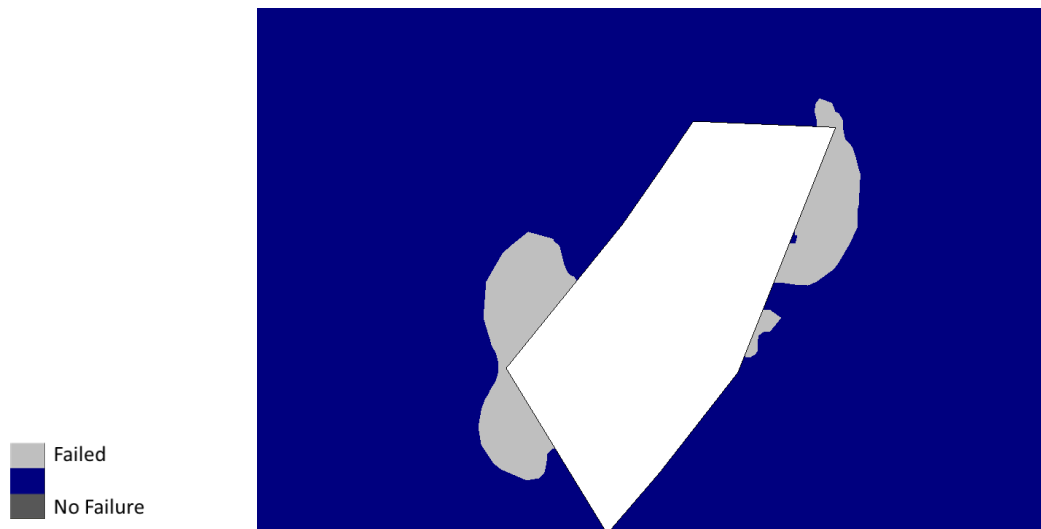


Figure E88 Application of the Hoek-Brown criterion to case study 12

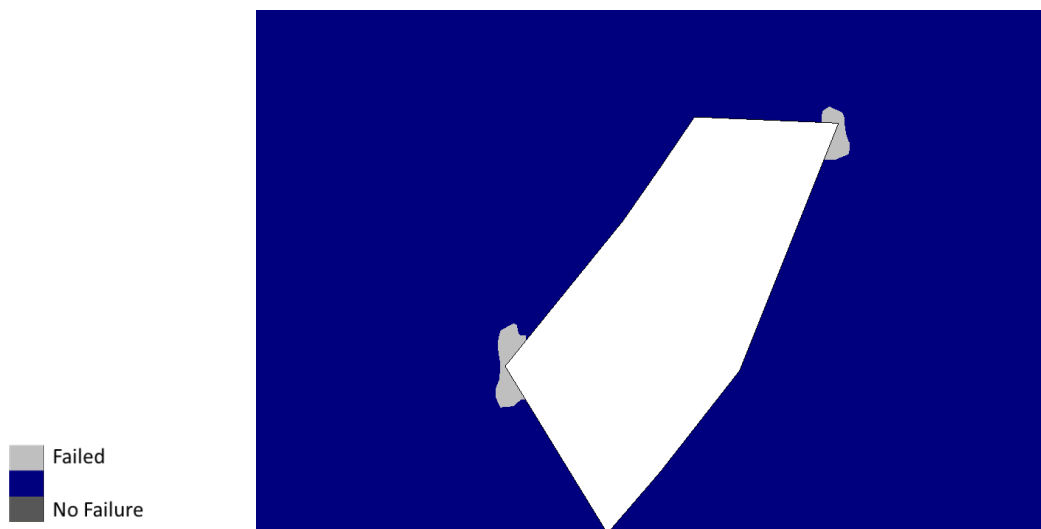


Figure E89 Application of the Zhang-Zhu Criterion to case study 12

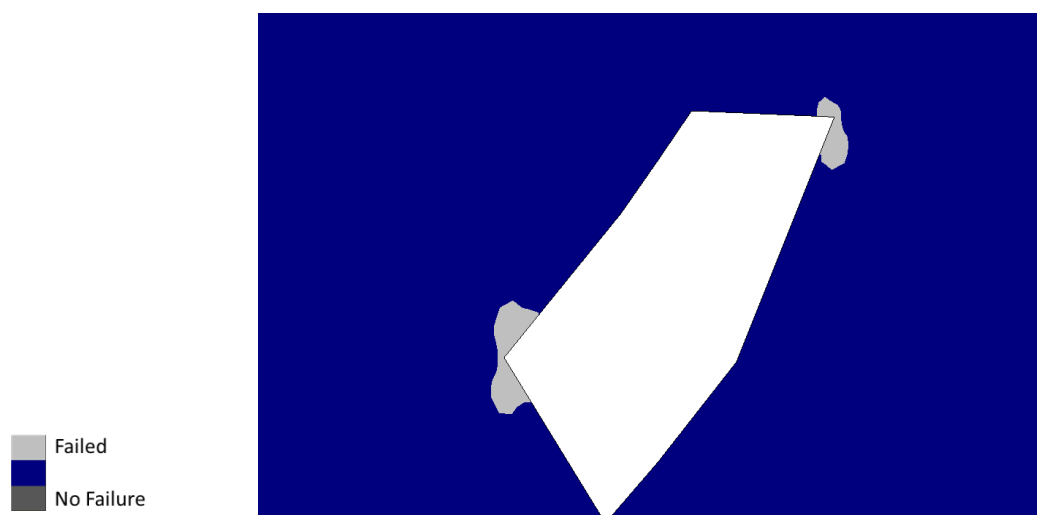


Figure E90 Application of the Pan-Hudson Criterion to case study 12

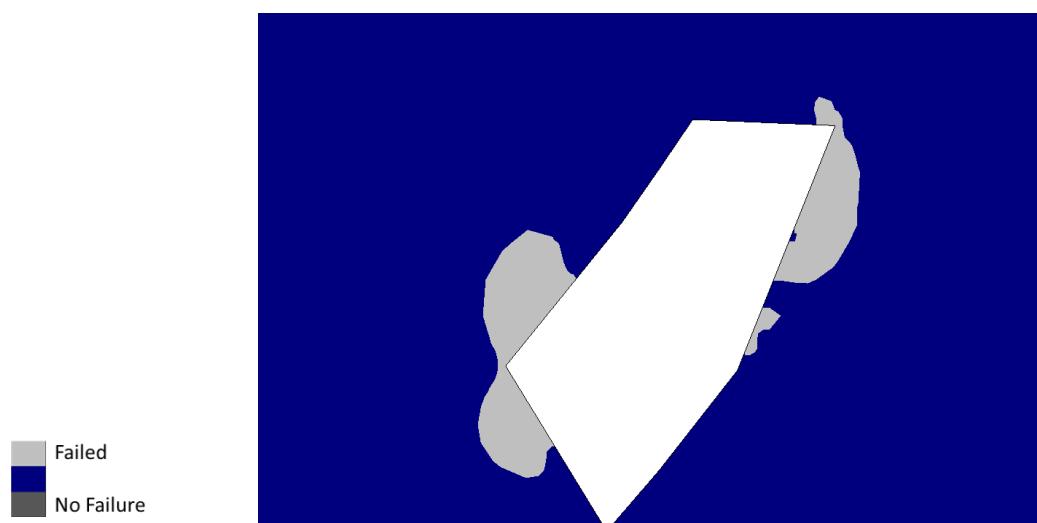


Figure E91 Application of the Priest Criterion to case study 12

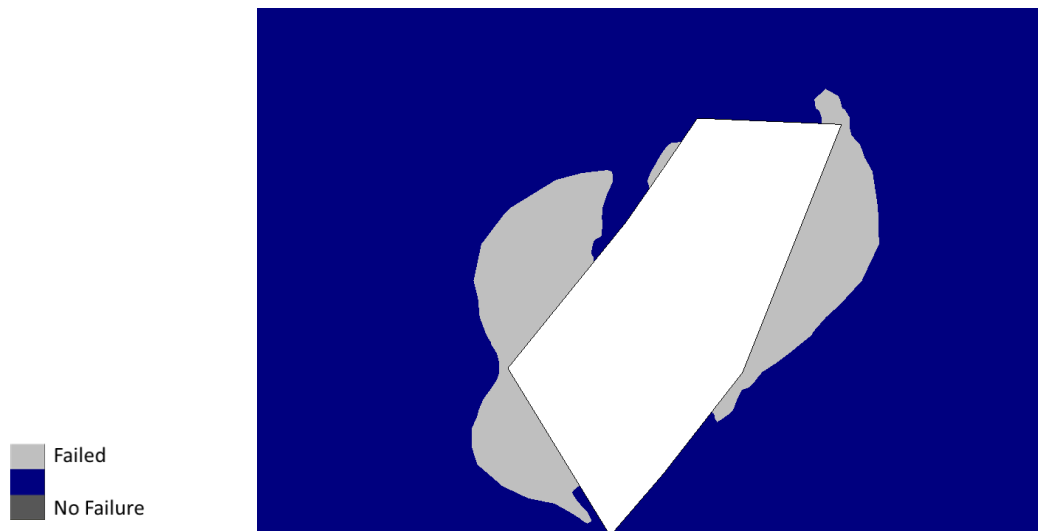


Figure E92 Application of the Simplified Priest Criterion to case study 12



Figure E93 Application of the DSSI design criterion to case study 12

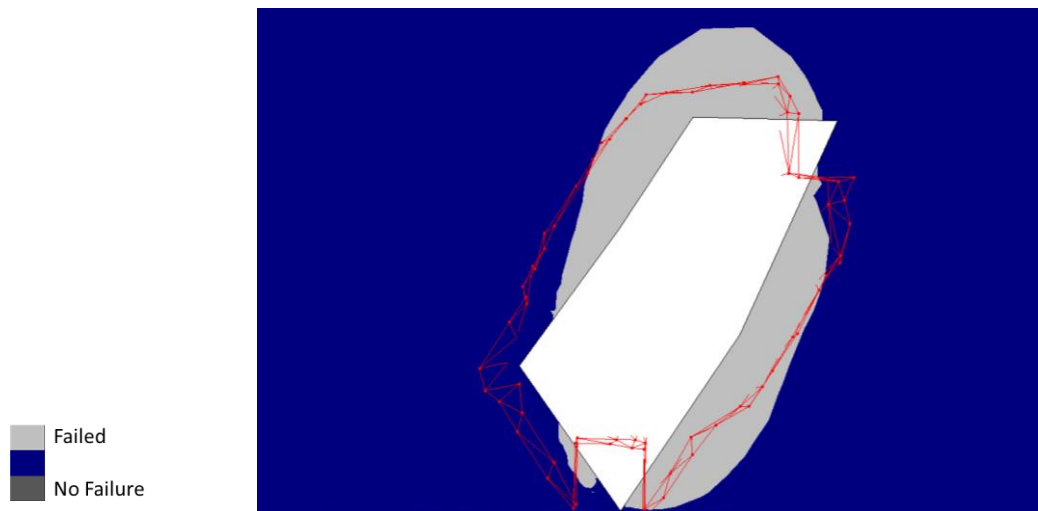


Figure E94 CMS wireframe in red showing actual overbreak of case study 12



Figure E95 Application of the Mohr-Coulomb criterion to case study 13



Figure E96 Application of the Hoek-Brown criterion to case study 13



Figure E97 Application of the Zhang–Zhu Criterion to case study 13



Figure E98 Application of the Pan–Hudson Criterion to case study 13



Figure E99 Application of the Priest Criterion to case study 13



Figure E100 Application of the Simplified Priest Criterion to case study 13



Figure E101 Application of the DSSI design criterion to case study 13

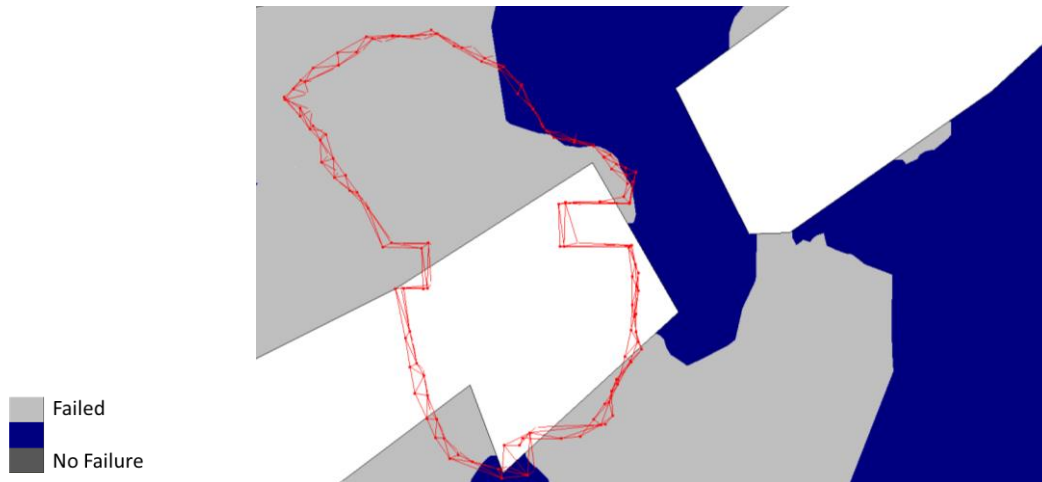


Figure E102 CMS wireframe in red showing actual overbreak of case study 13

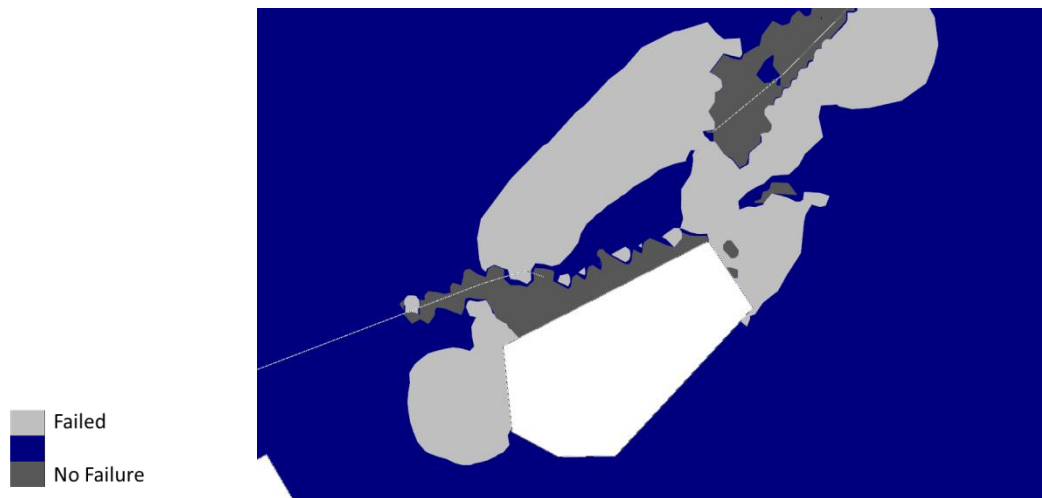


Figure E103 Application of the Mohr-Coulomb criterion to case study 14

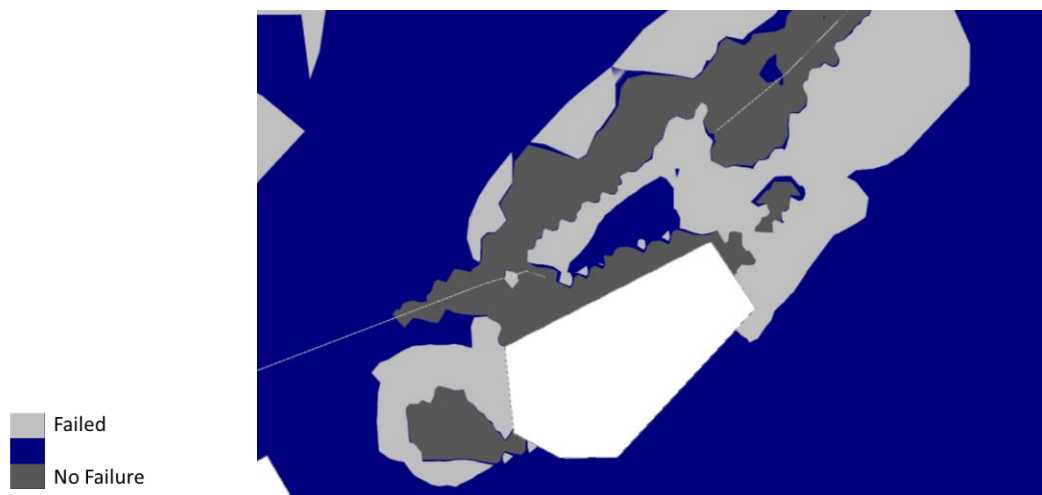




Figure E104 Application of the Hoek-Brown criterion to case study 14

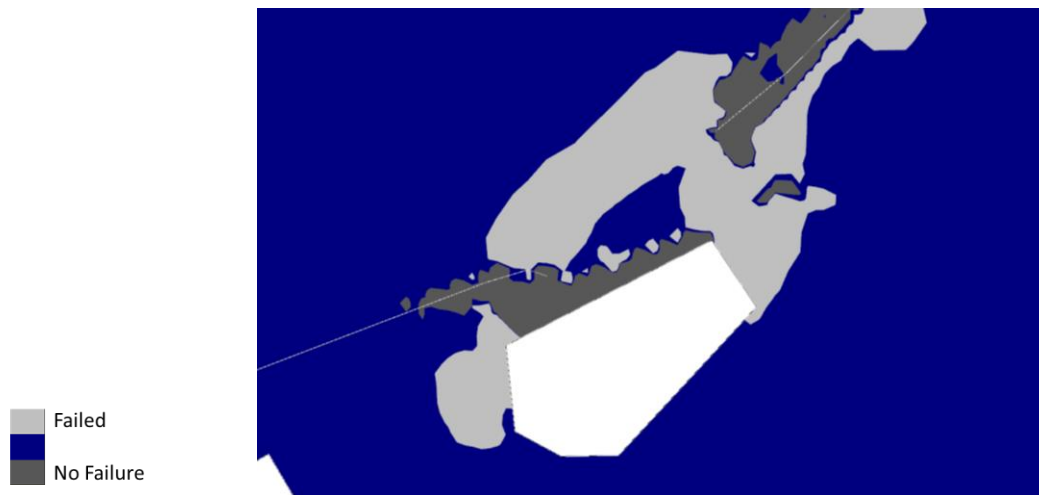


Figure E105 Application of the Zhang–Zhu Criterion to case study 14

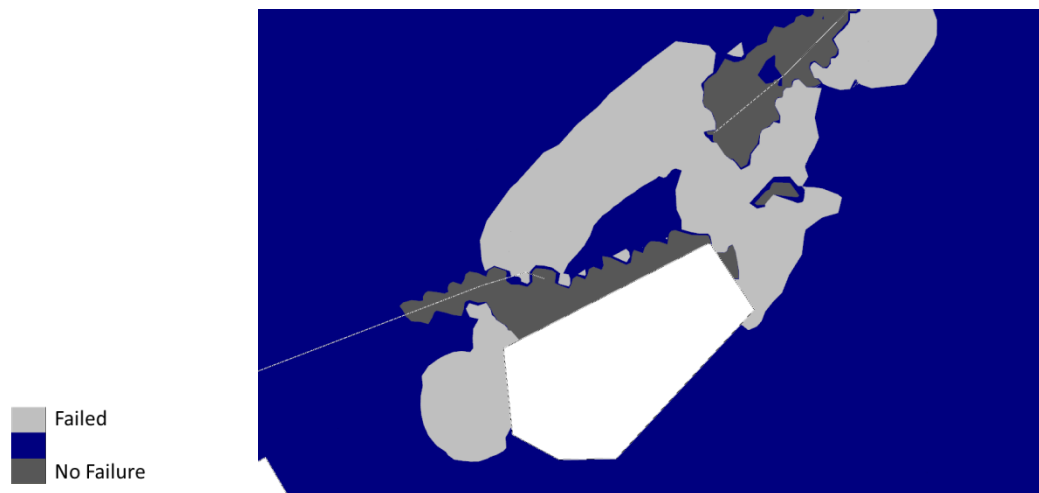


Figure E106 Application of the Pan–Hudson Criterion to case study 14

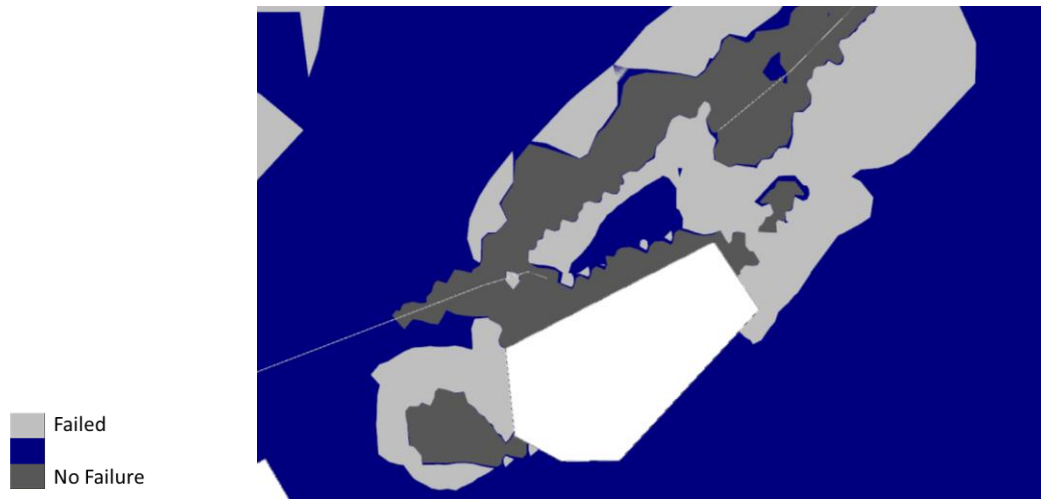


Figure E107 Application of the Priest Criterion to case study 14



Figure E108 Application of the Simplified Priest Criterion to case study 14

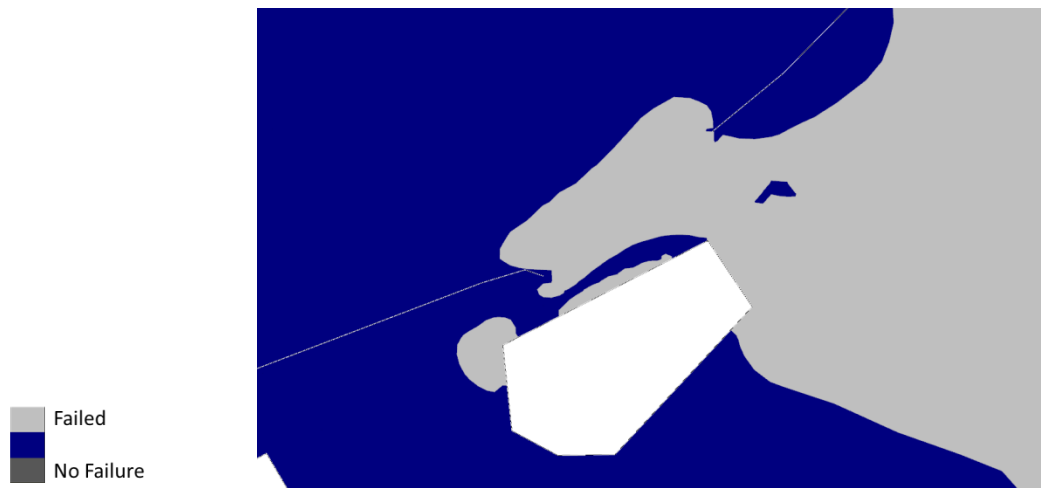


Figure E109 Application of the DSSI design criterion to case study 14

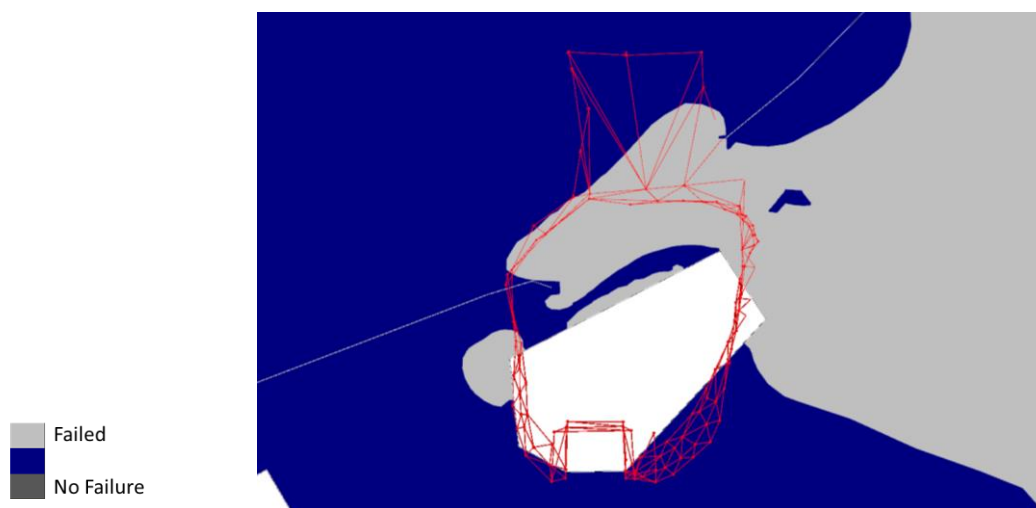


Figure E110 CMS wireframe in red showing actual overbreak of case study 14

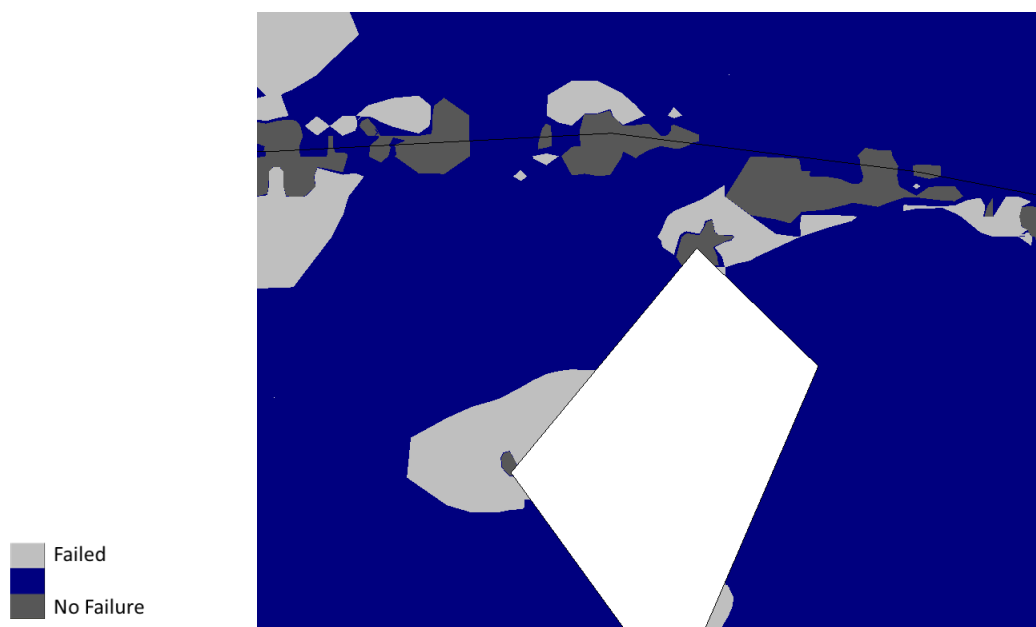


Figure E111 Application of the Mohr-Coulomb criterion to case study 15

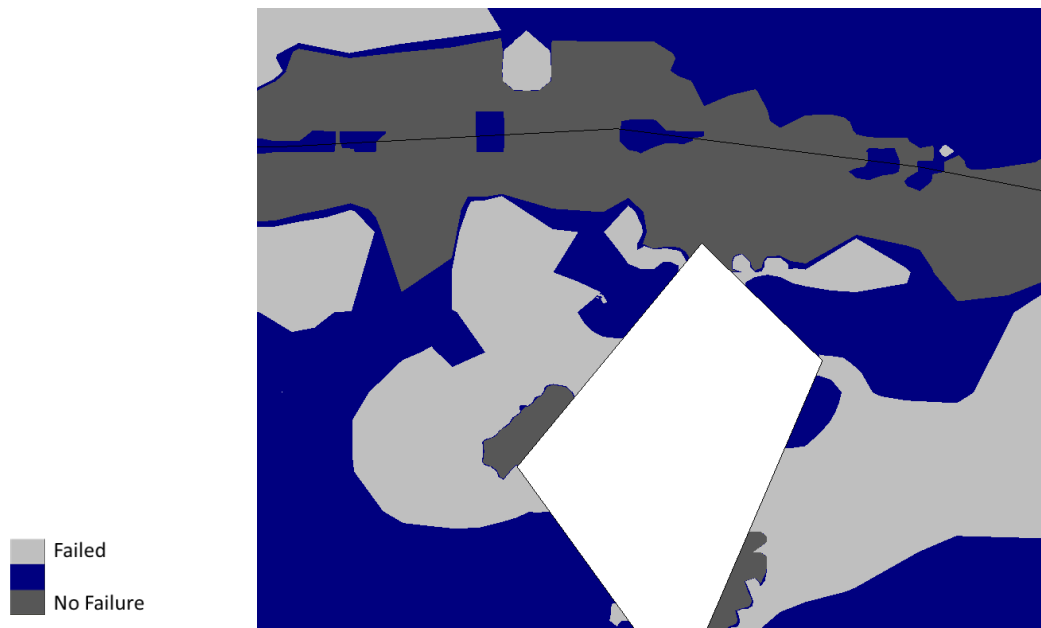


Figure E112 Application of the Hoek-Brown criterion to case study 15

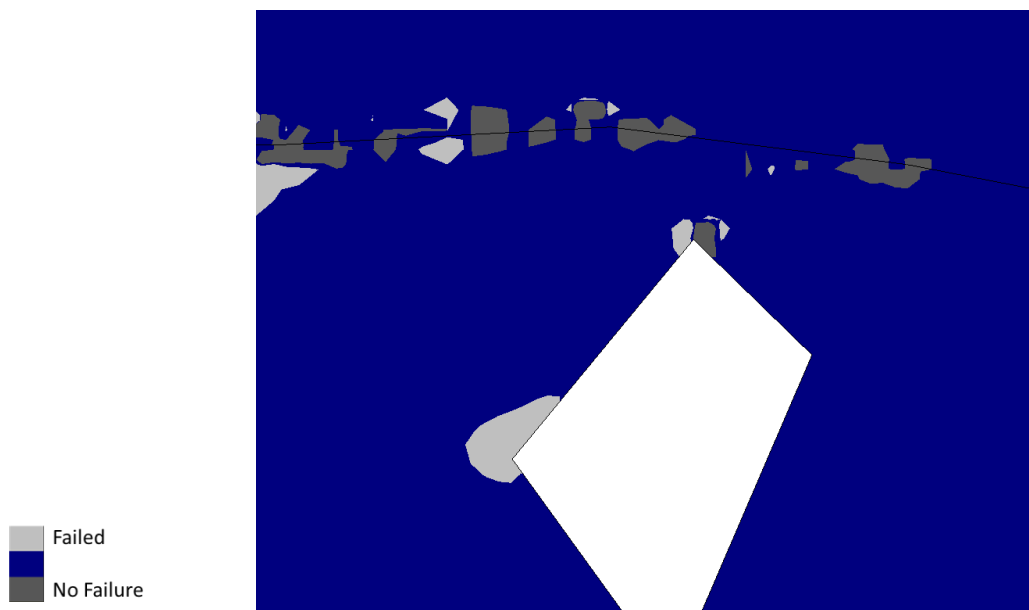


Figure E113 Application of the Zhang-Zhu Criterion to case study 15

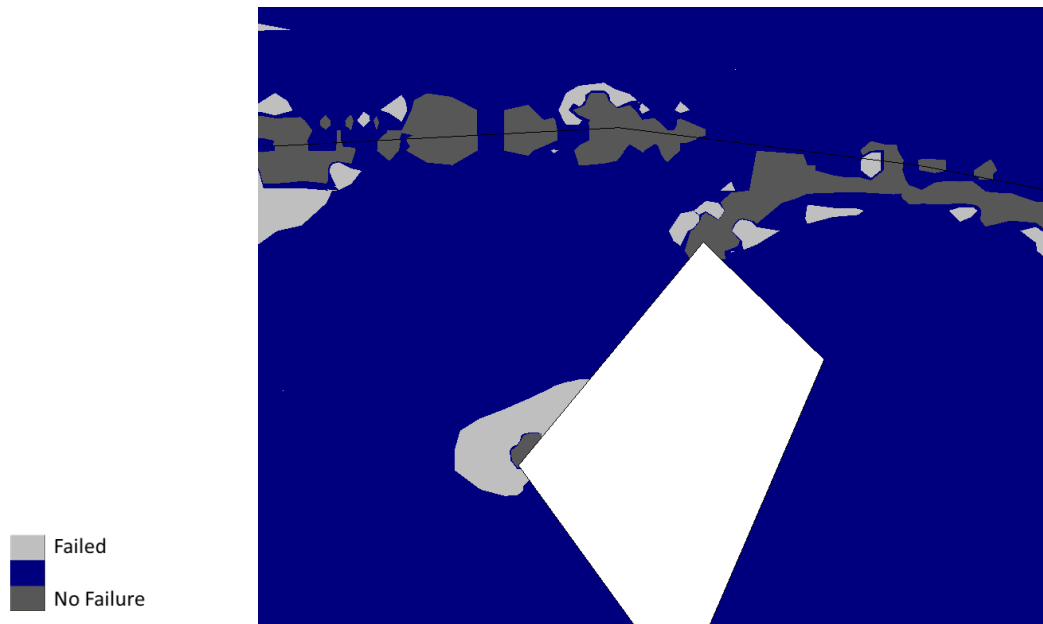


Figure E114 Application of the Pan-Hudson Criterion to case study 15

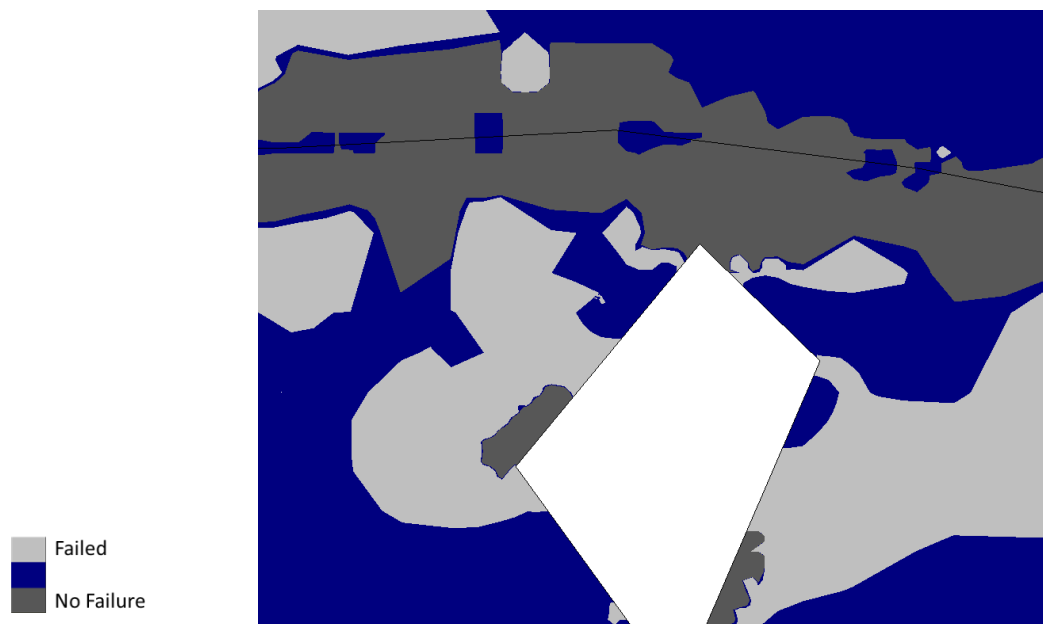


Figure E115 Application of the Priest Criterion to case study 15



Figure E116 Application of the Simplified Priest Criterion to case study 15

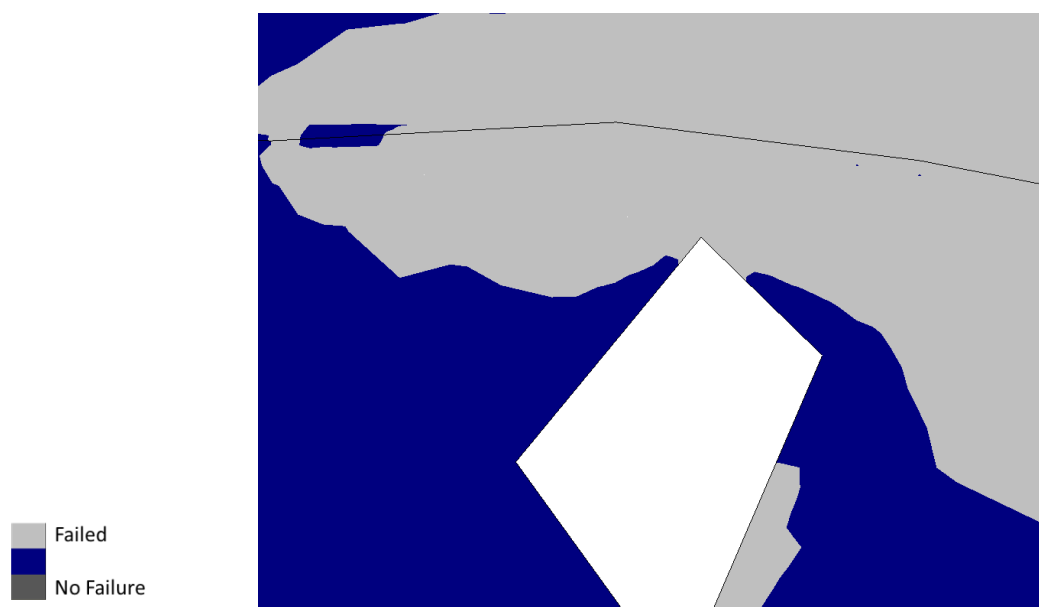


Figure E117 Application of the DSSI design criterion to case study 15

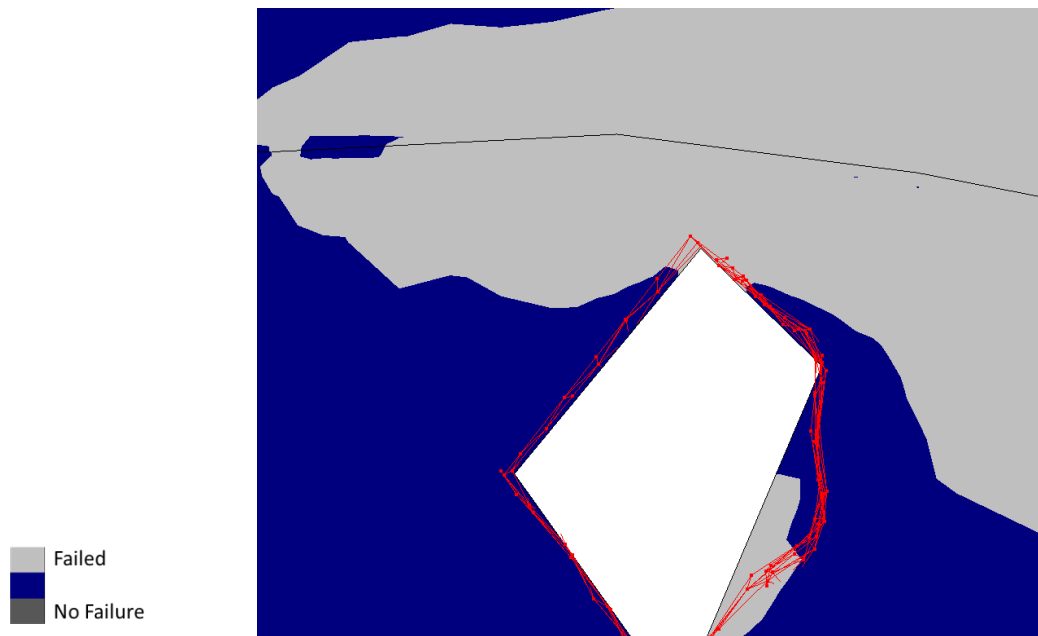


Figure E118 CMS wireframe in red showing actual overbreak of case study 15

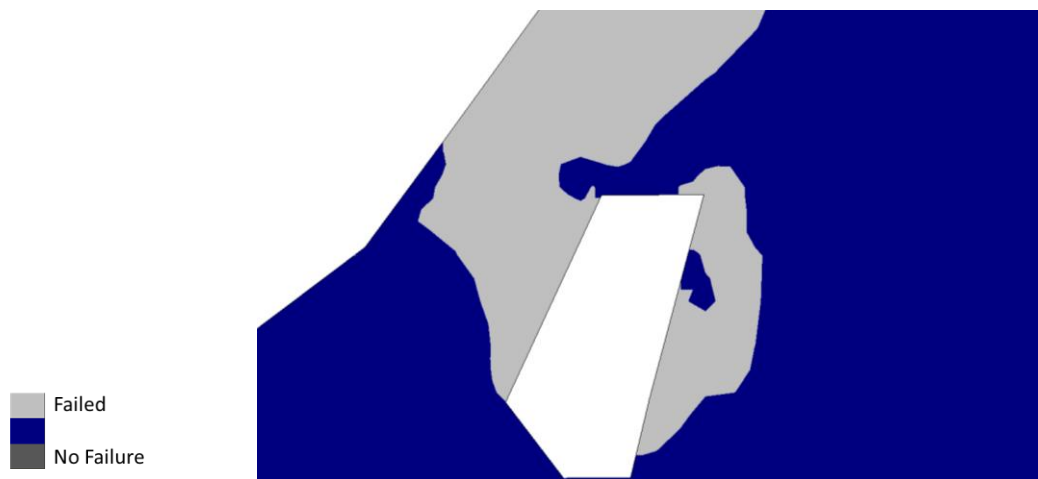


Figure E119 Application of the Mohr-Coulomb criterion to case study 16



Figure E120 Application of the Hoek-Brown criterion to case study 16



Figure E121 Application of the Zhang-Zhu Criterion to case study 16



Figure E122 Application of the Pan-Hudson Criterion to case study 16





Figure E123 Application of the Priest Criterion to case study 16

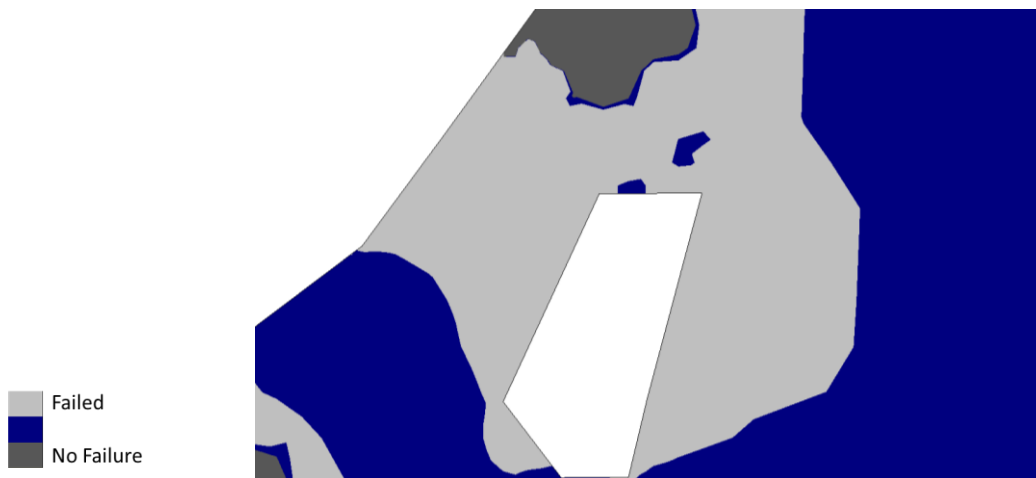


Figure E124 Application of the Simplified Priest Criterion to case study 16



Figure E125 Application of the DSSI design criterion to case study 16

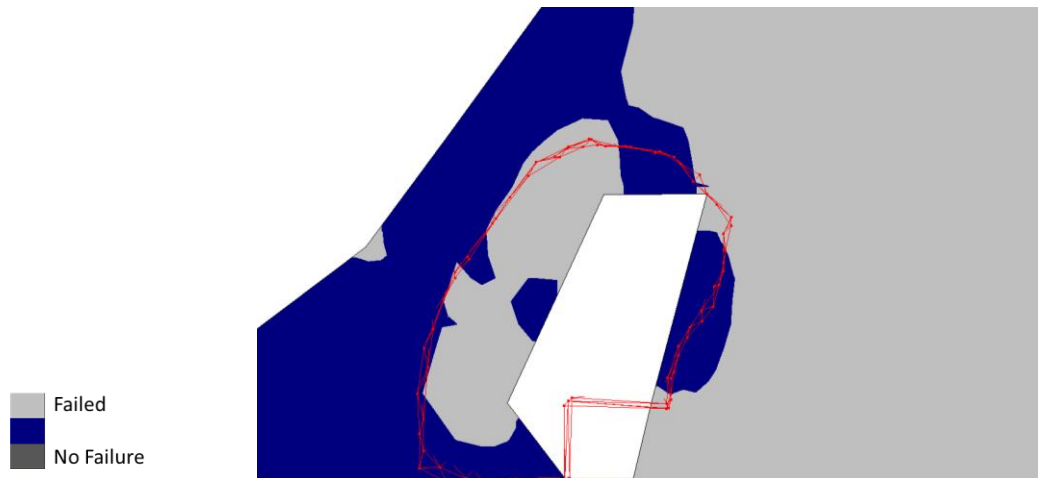


Figure E126 CMS wireframe in red showing actual overbreak of case study 16

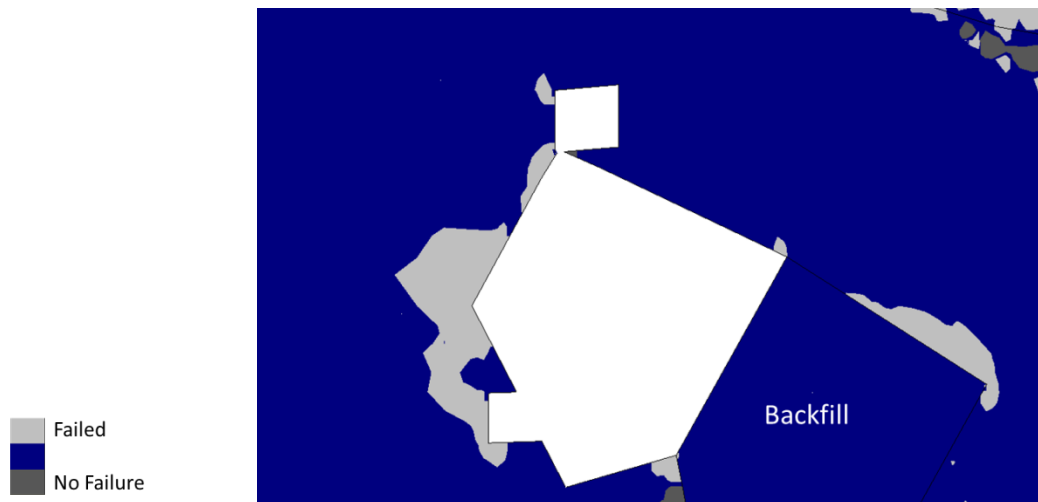


Figure E127 Application of the Mohr-Coulomb criterion to case study 17

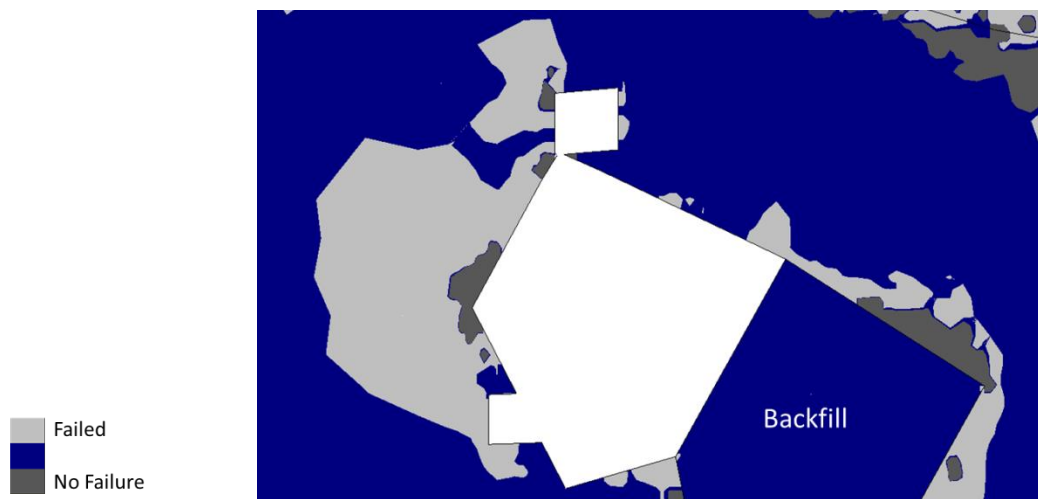


Figure E128 Application of the Hoek-Brown criterion to case study 17

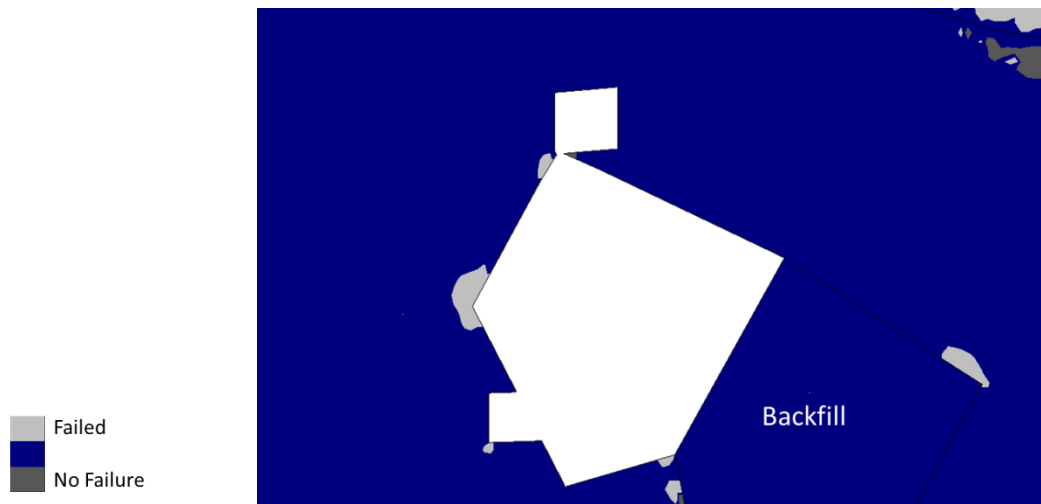


Figure E129 Application of the Zhang–Zhu Criterion to case study 17

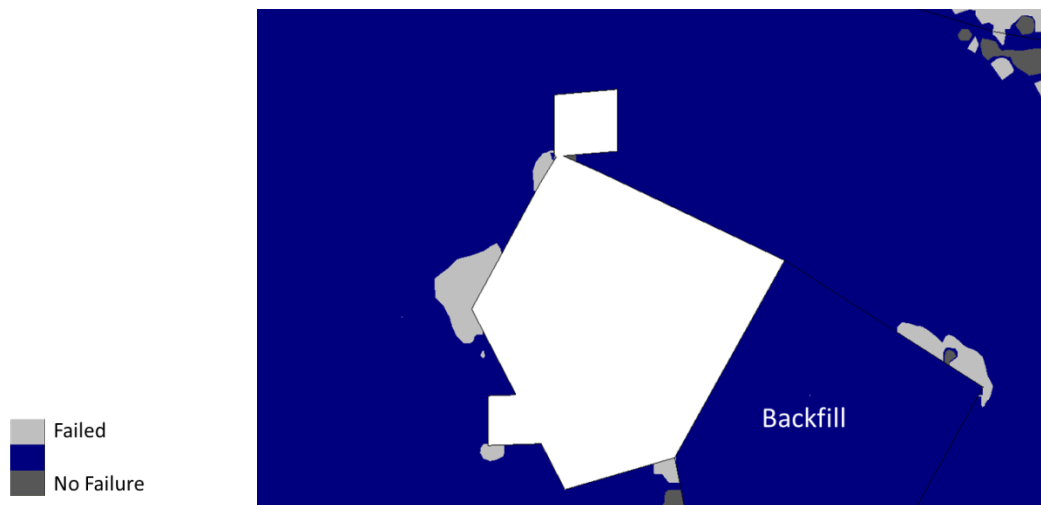


Figure E130 Application of the Pan–Hudson Criterion to case study 17

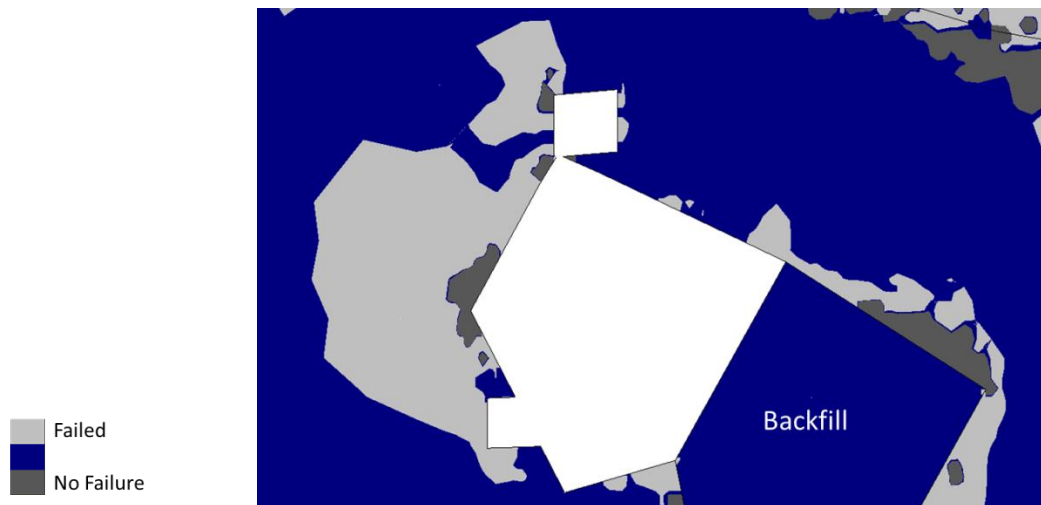


Figure E131 Application of the Priest Criterion to case study 17

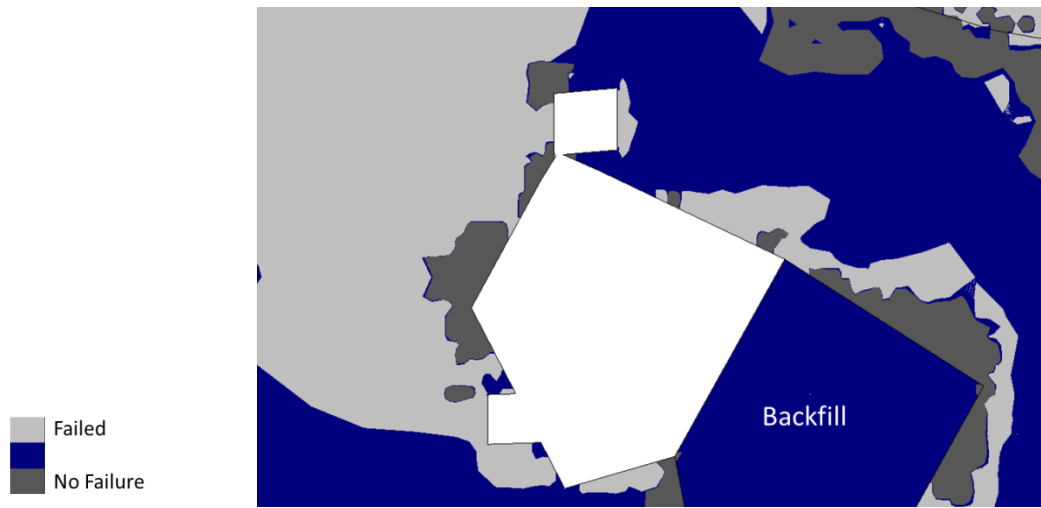


Figure E132 Application of the Simplified Priest Criterion to case study 17

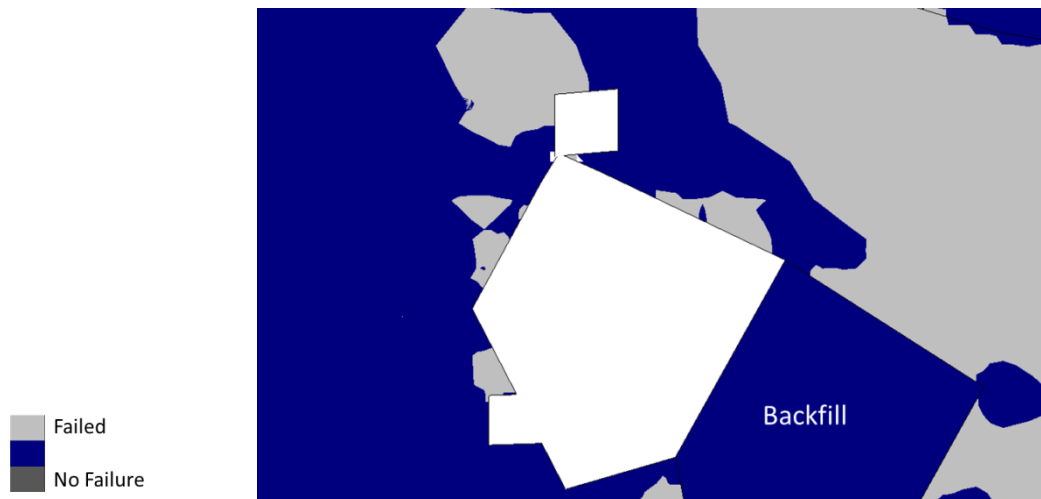


Figure E133 Application of the DSSI design criterion to case study 17

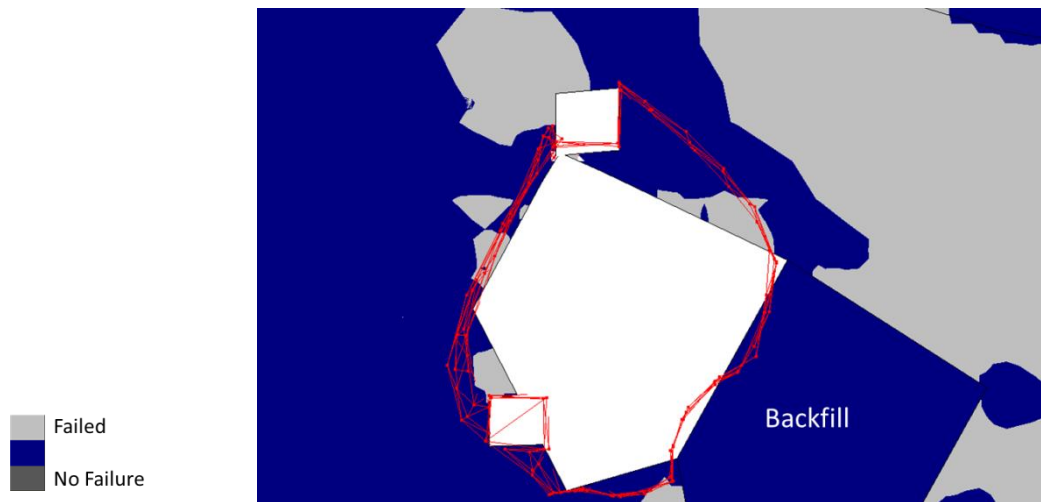


Figure E134 CMS wireframe in red showing actual overbreak of case study 17

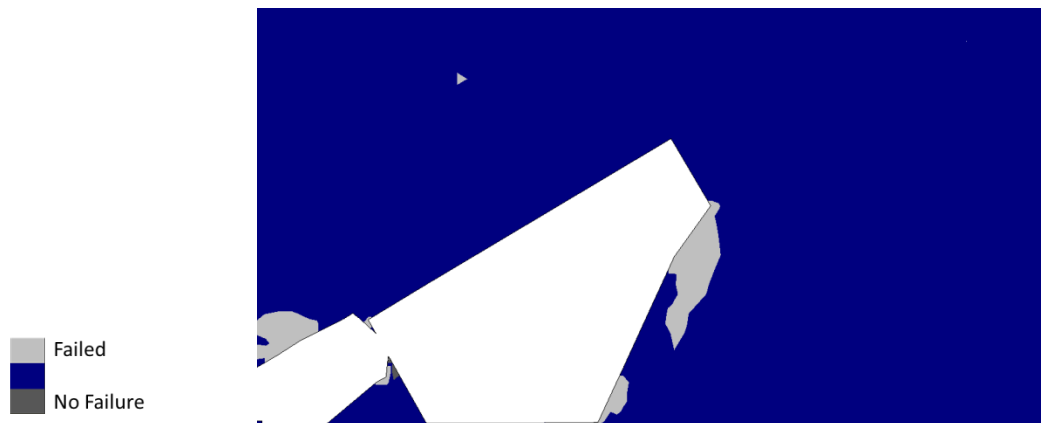


Figure E135 Application of the Mohr-Coulomb criterion to case study 18



Figure E136 Application of the Hoek-Brown criterion to case study 18

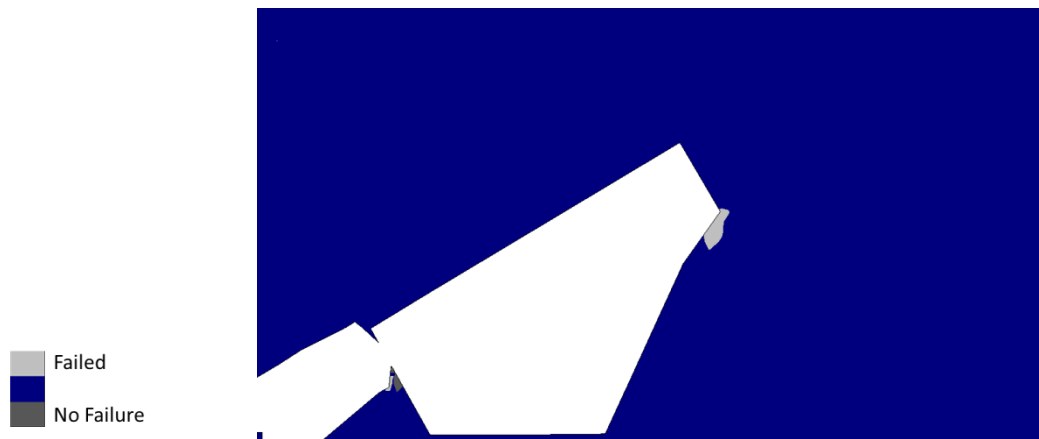


Figure E137 Application of the Zhang–Zhu Criterion to case study 18

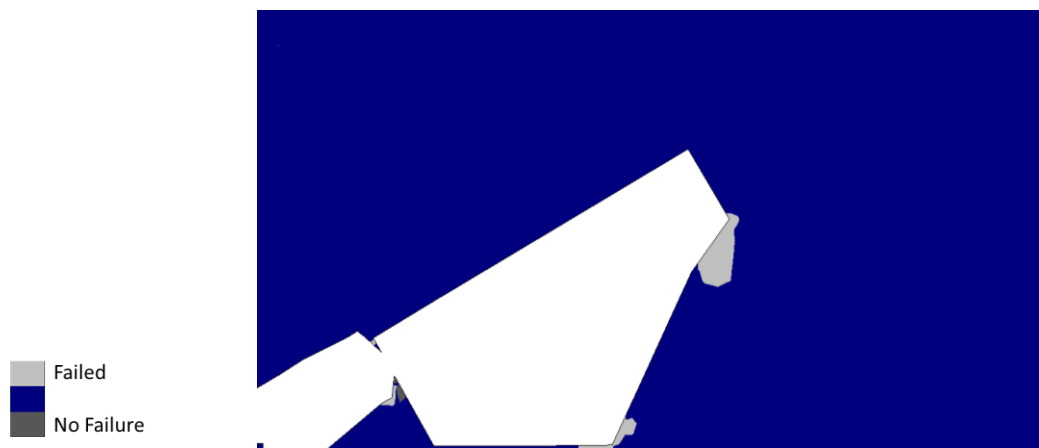


Figure E138 Application of the Pan–Hudson Criterion to case study 18



Figure E139 Application of the Priest Criterion to case study 18



Figure E140 Application of the Simplified Priest Criterion to case study 18

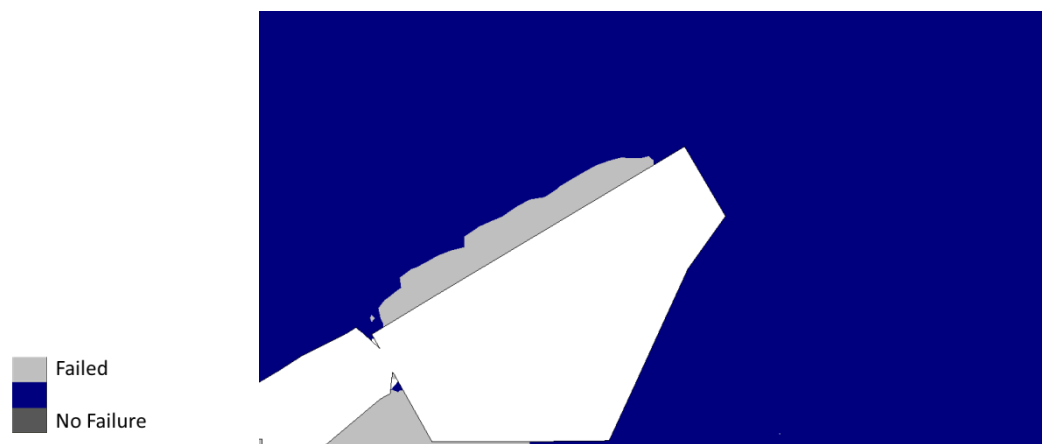


Figure E141 Application of the DSSI design criterion to case study 18

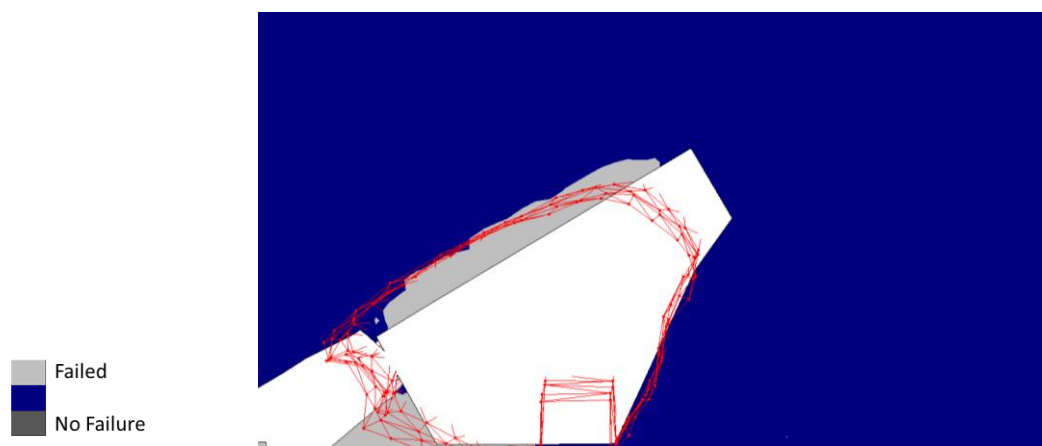


Figure E142 CMS wireframe in red showing actual overbreak of case study 18

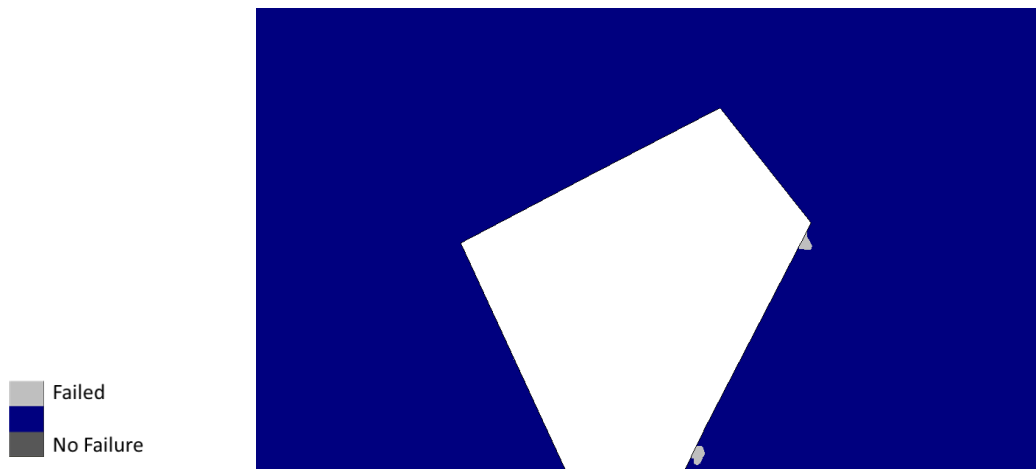


Figure E143 Application of the Mohr-Coulomb criterion to case study 19

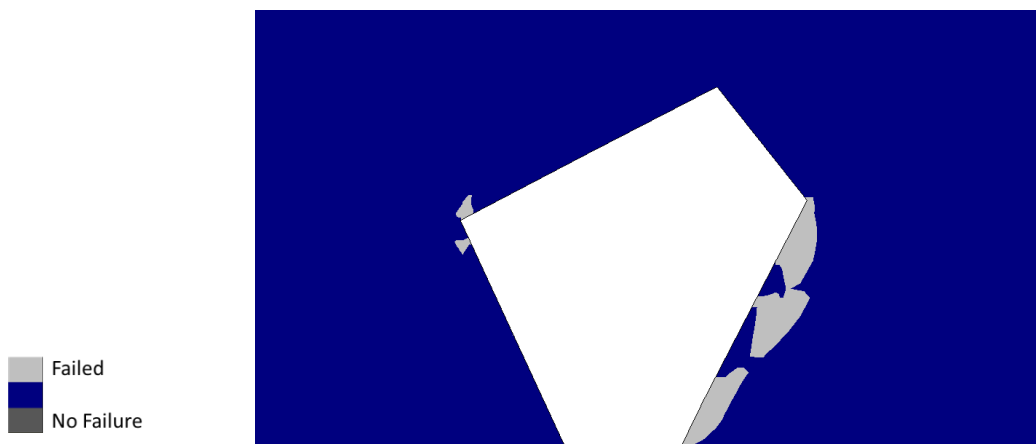


Figure E144 Application of the Hoek-Brown criterion to case study 19

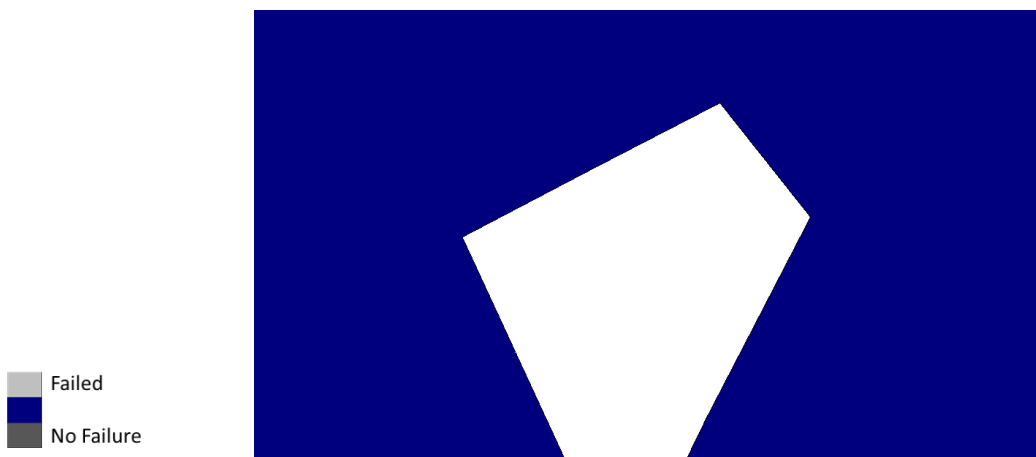


Figure E145 Application of the Zhang-Zhu Criterion to case study 19



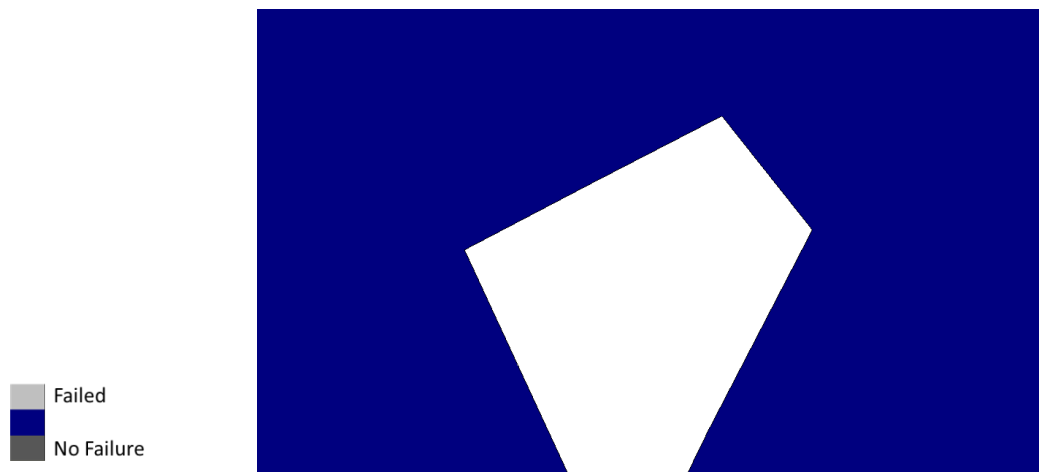


Figure E146 Application of the Pan-Hudson Criterion to case study 19

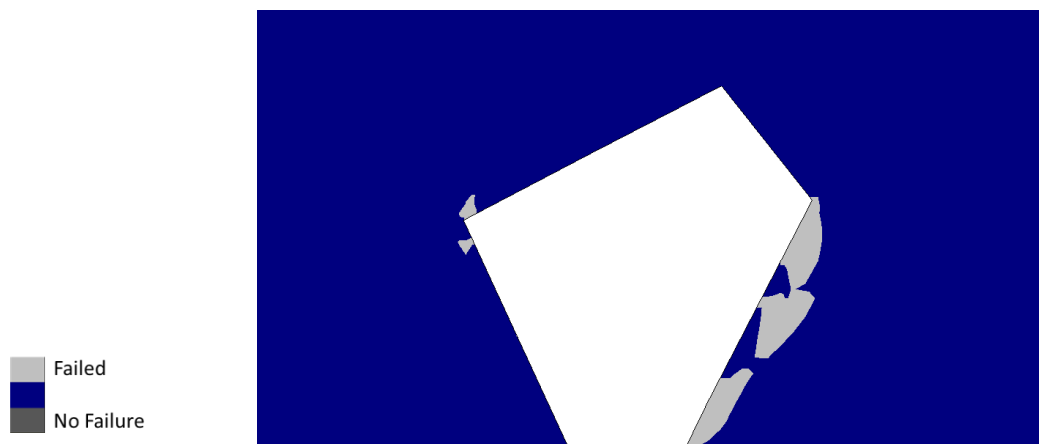


Figure E147 Application of the Priest Criterion to case study 19

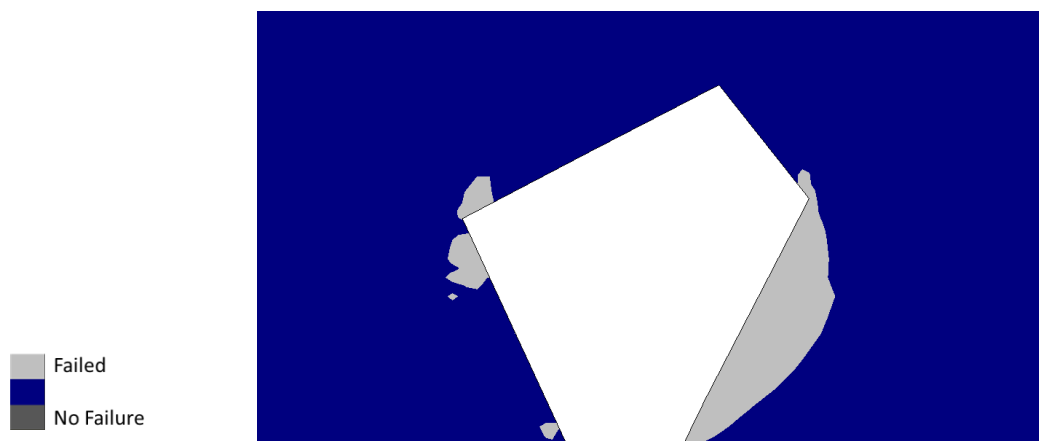


Figure E148 Application of the Simplified Priest Criterion to case study 19

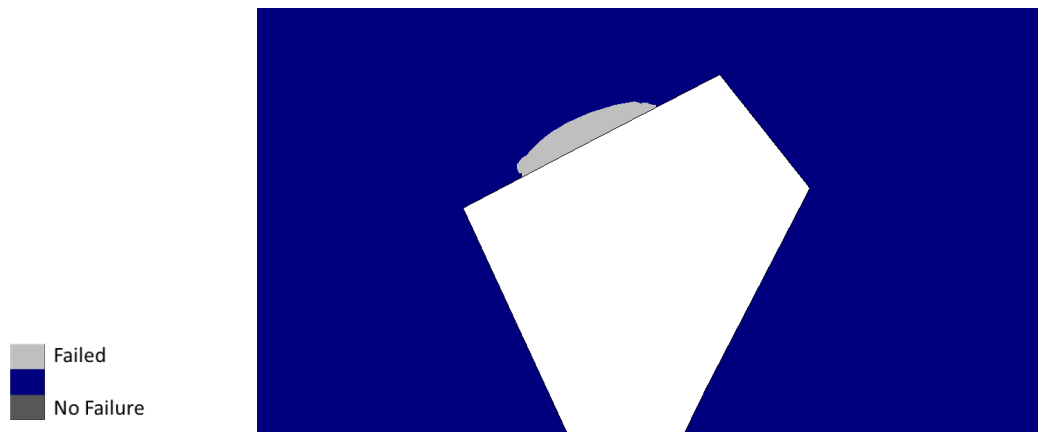


Figure E148 Application of the DSSI design criterion to case study 19

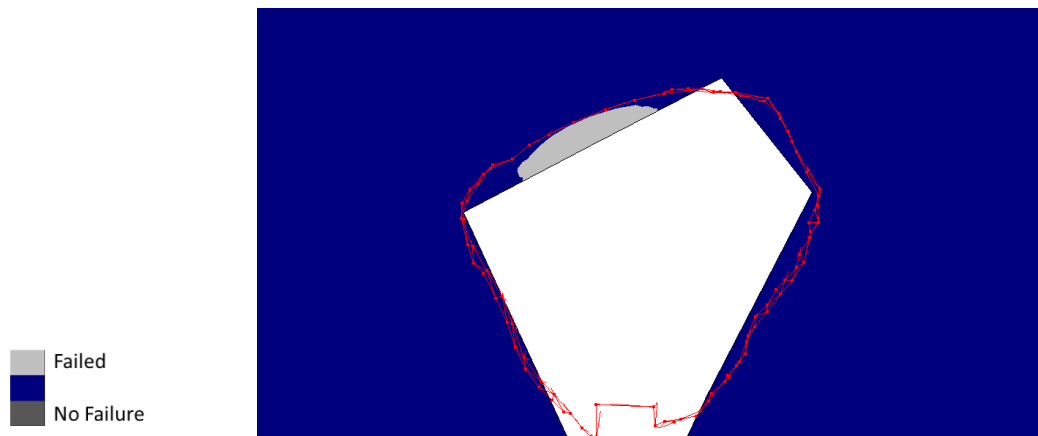


Figure E150 CMS wireframe in red showing actual overbreak of case study 19

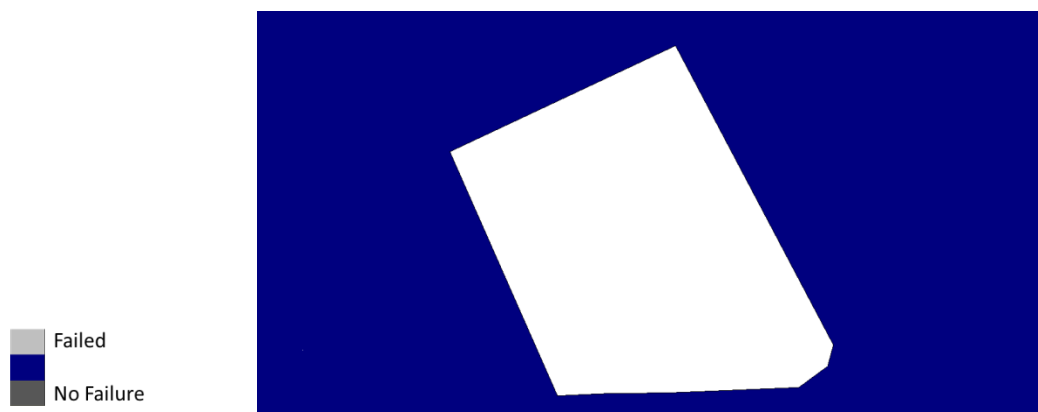


Figure E151 Application of the Mohr-Coulomb criterion to case study 20

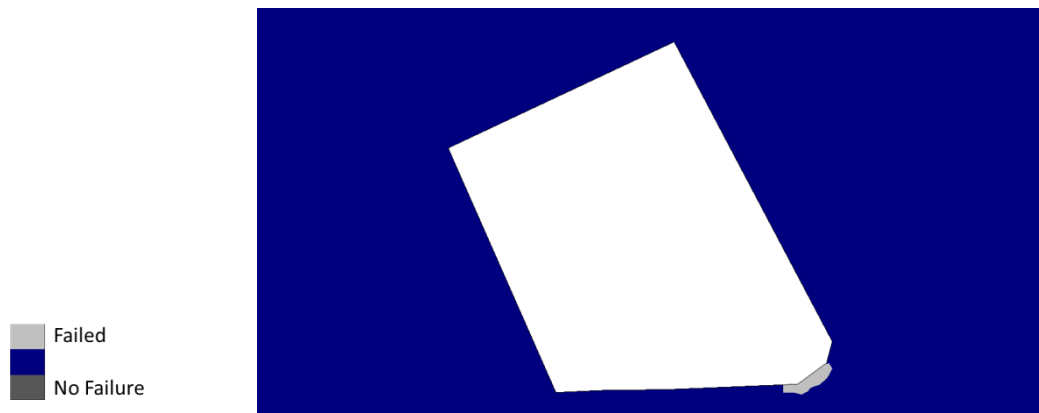


Figure E152 Application of the Hoek-Brown criterion to case study 20

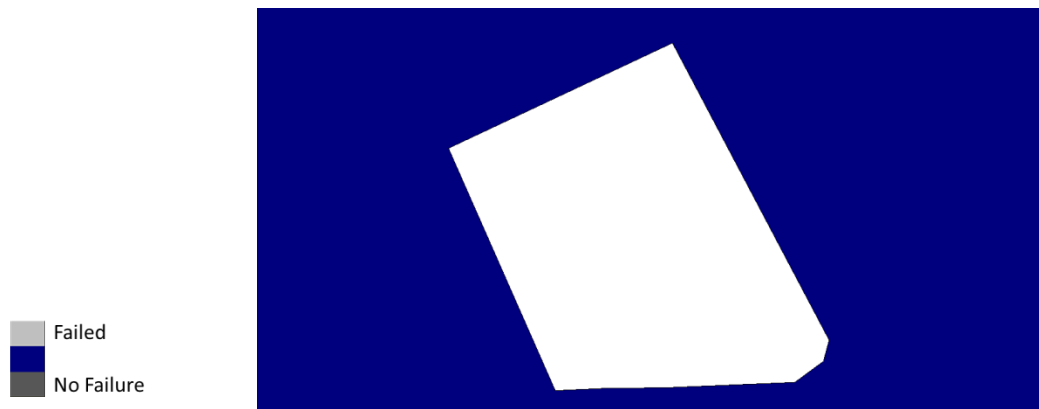


Figure E153 Application of the Zhang-Zhu Criterion to case study 20

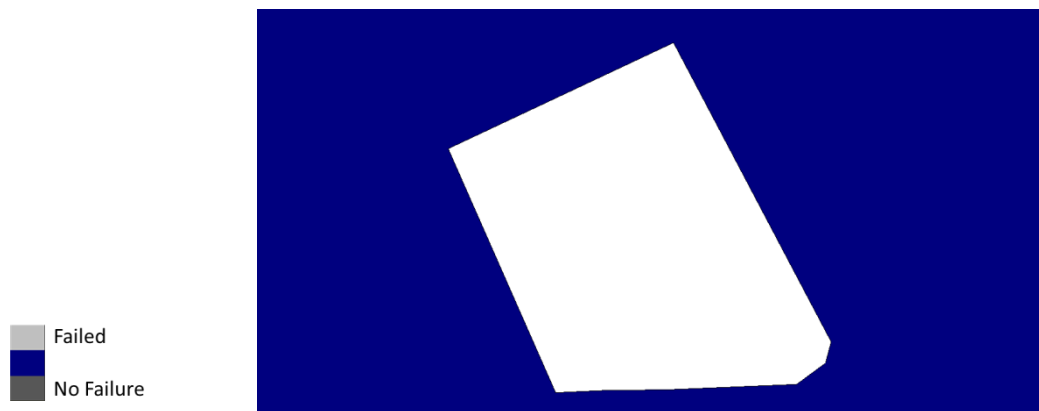


Figure E154 Application of the Pan-Hudson Criterion to case study 20

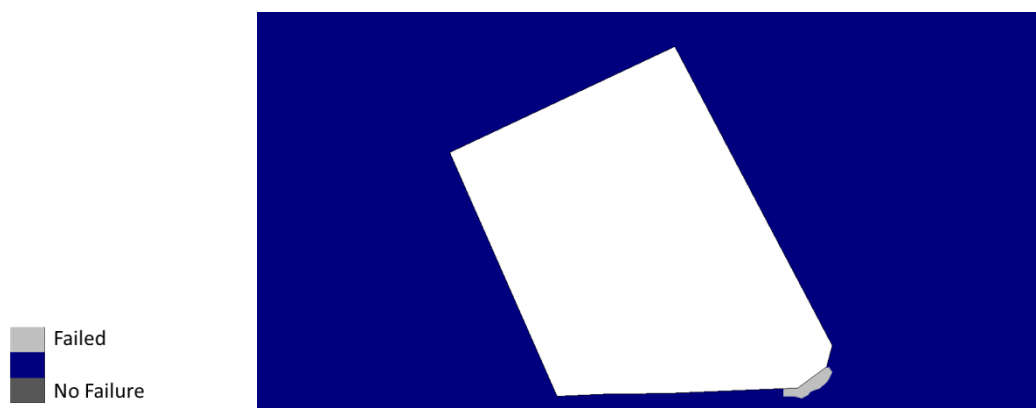


Figure E155 Application of the Priest Criterion to case study 20

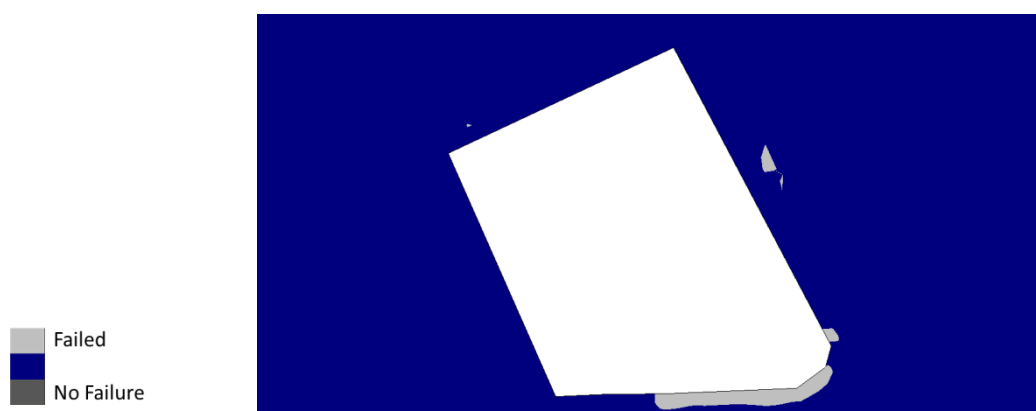


Figure E156 Application of the Simplified Priest Criterion to case study 20

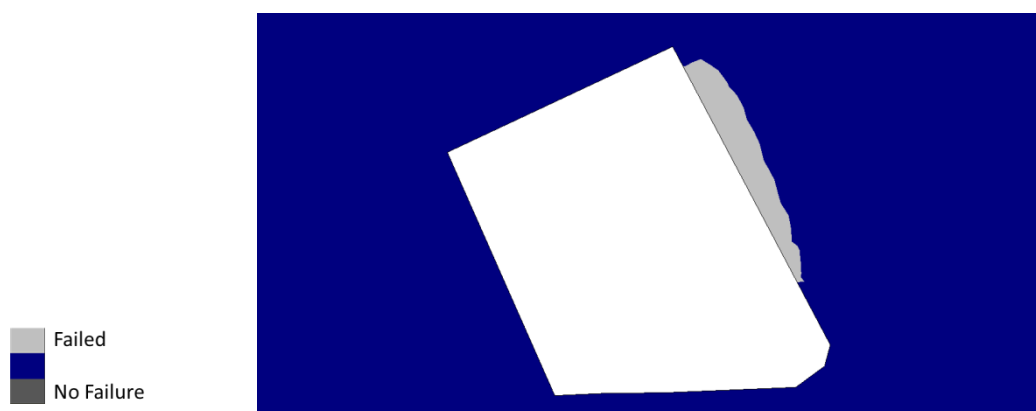


Figure E157 Application of the DSSI design criterion to case study 20

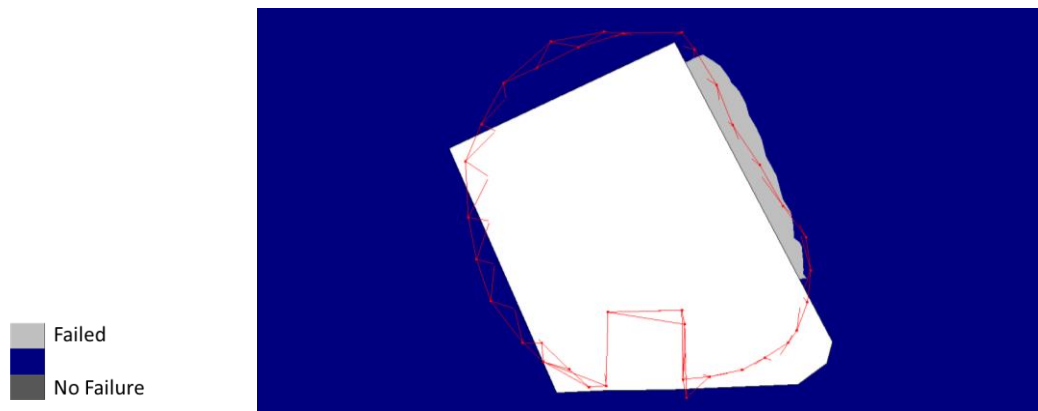


Figure E158 CMS wireframe in red showing actual overbreak of case study 20

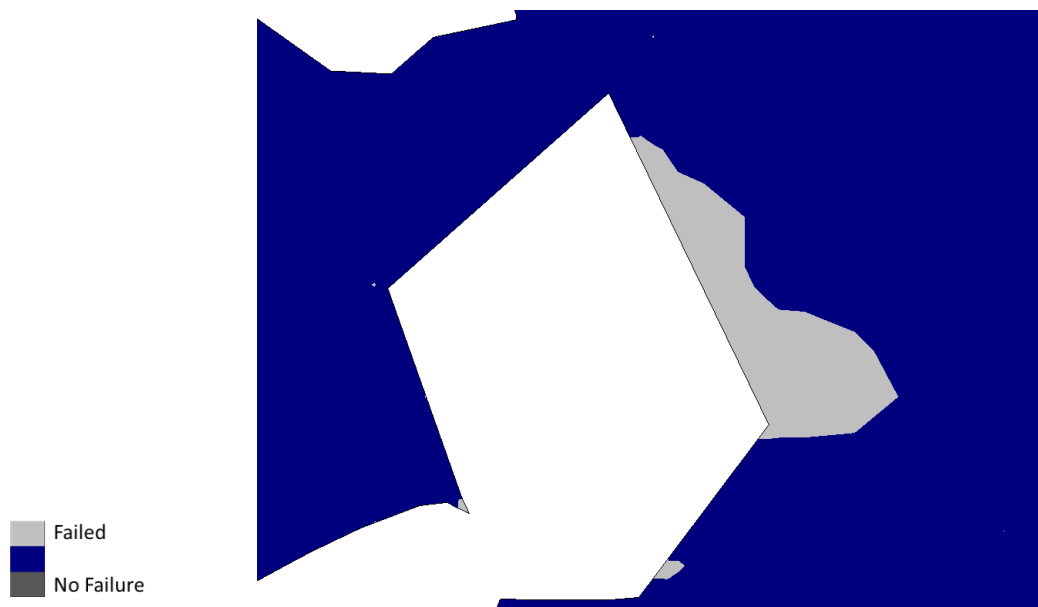


Figure E159 Application of the Mohr-Coulomb criterion to case study 21

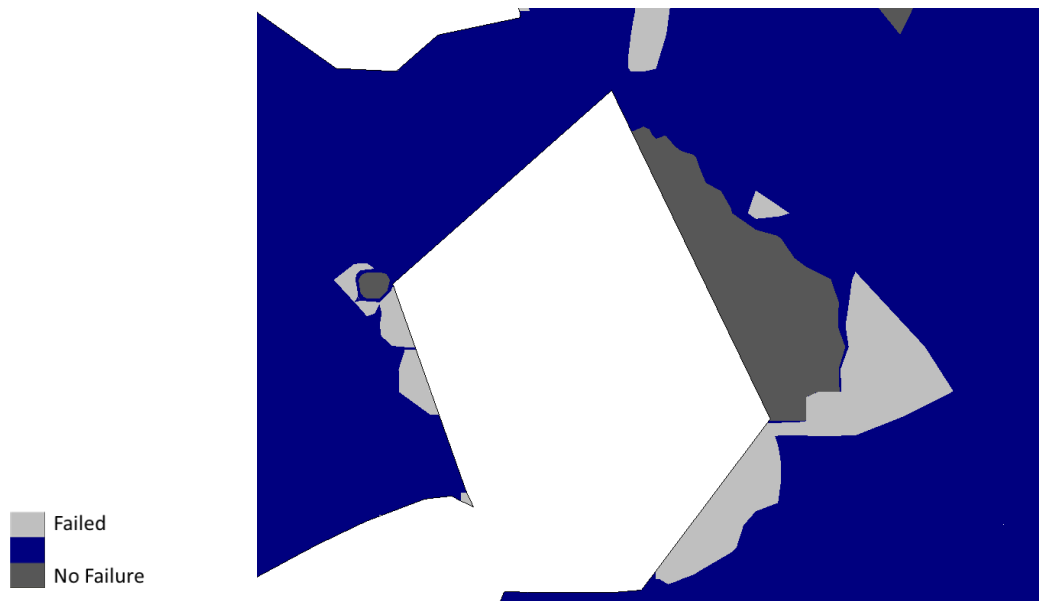


Figure E152 Application of the Hoek-Brown criterion to case study 21

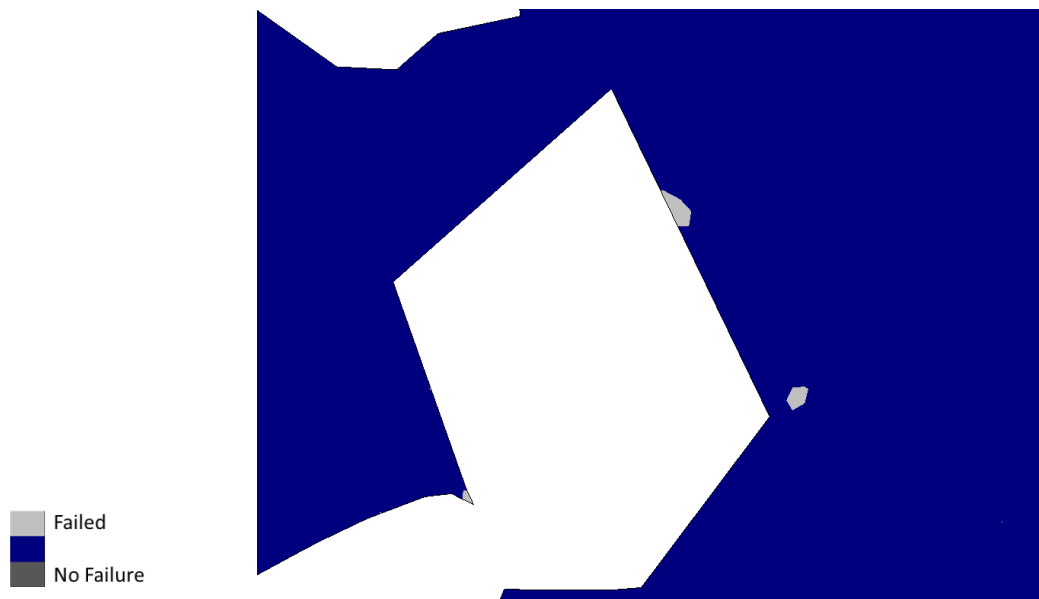


Figure E153 Application of the Zhang-Zhu Criterion to case study 21

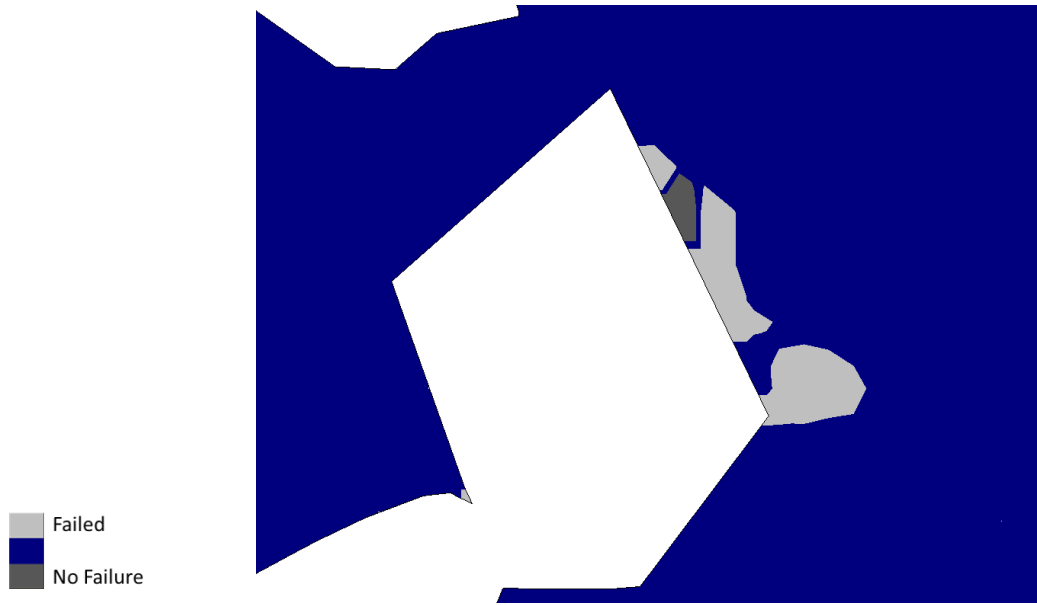


Figure E154 Application of the Pan-Hudson Criterion to case study 21

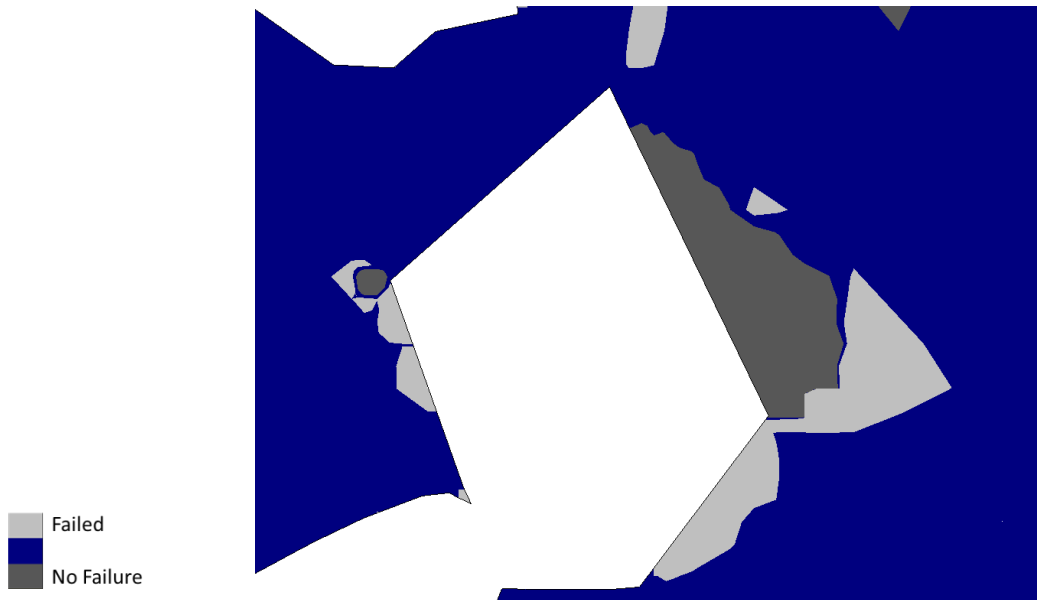


Figure E155 Application of the Priest Criterion to case study 21

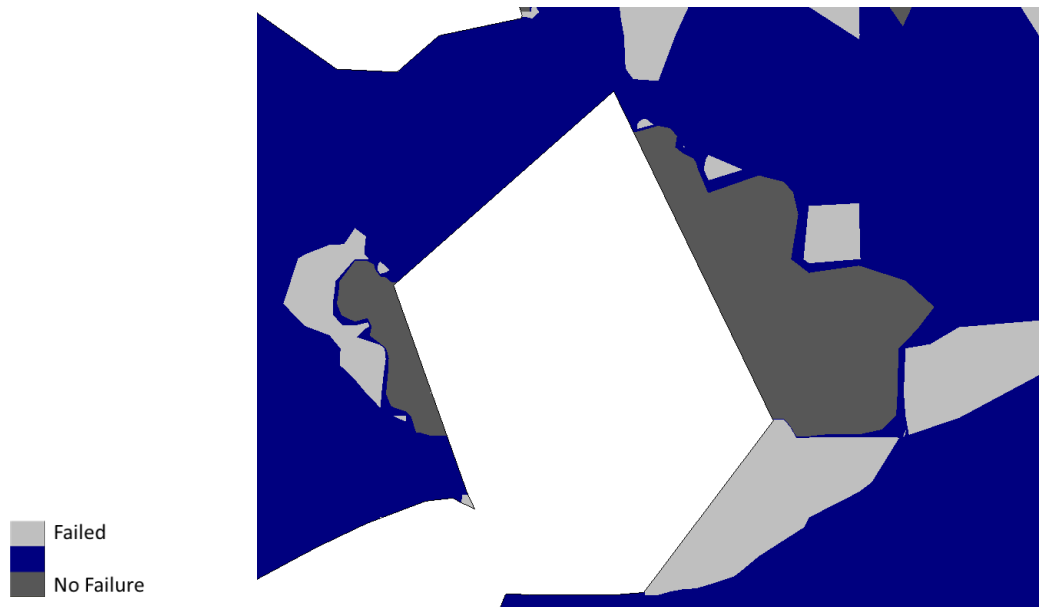


Figure E156 Application of the Simplified Priest Criterion to case study 21

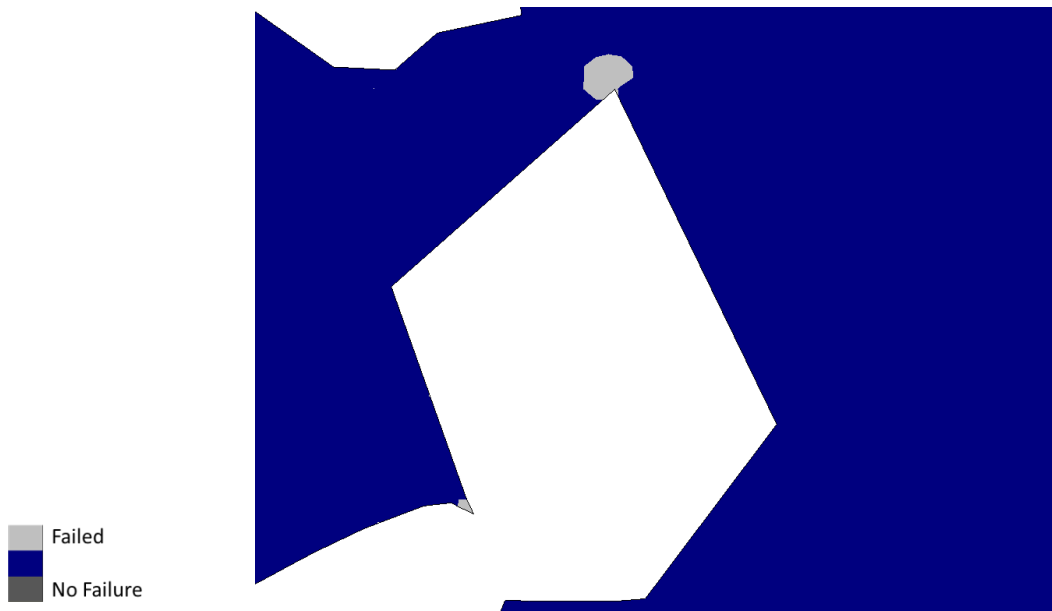


Figure E157 Application of the DSSI design criterion to case study 21



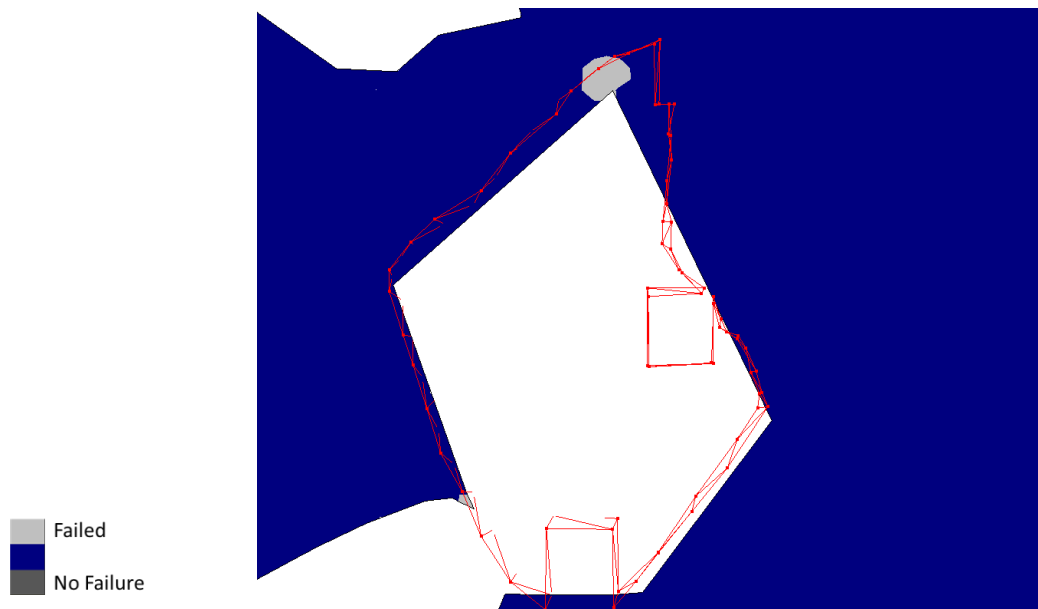


Figure E158 CMS wireframe in red showing actual overbreak of case study 21

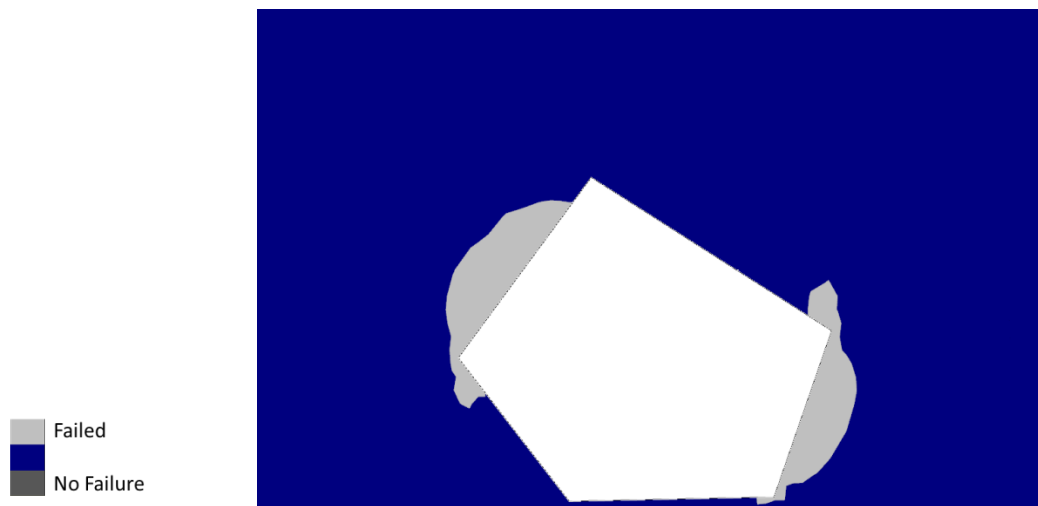


Figure E159 Application of the Mohr-Coulomb criterion to case study 22

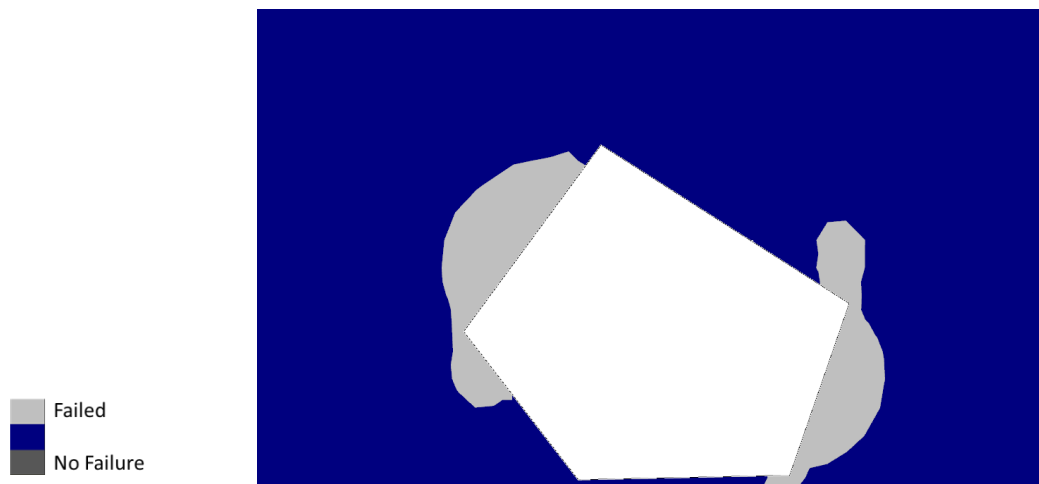


Figure E160 Application of the Hoek-Brown criterion to case study 22

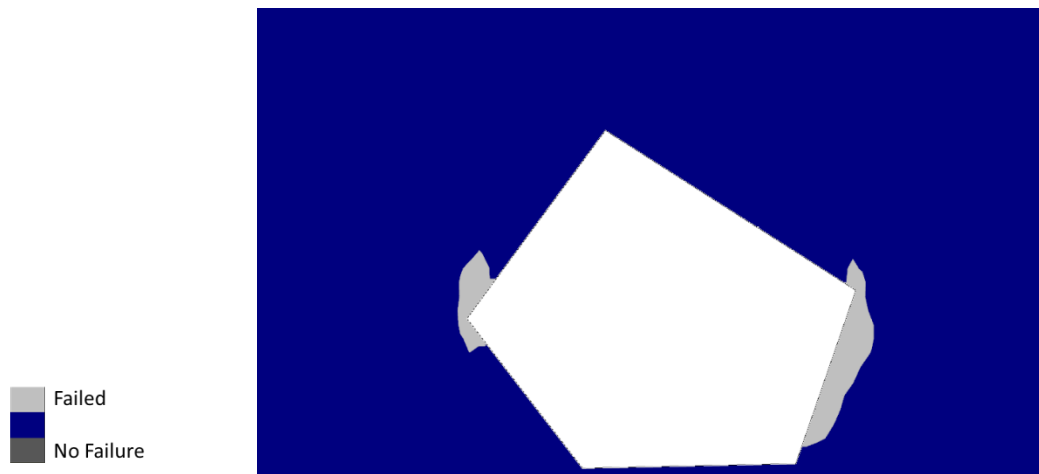


Figure E161 Application of the Zhang-Zhu Criterion to case study 22

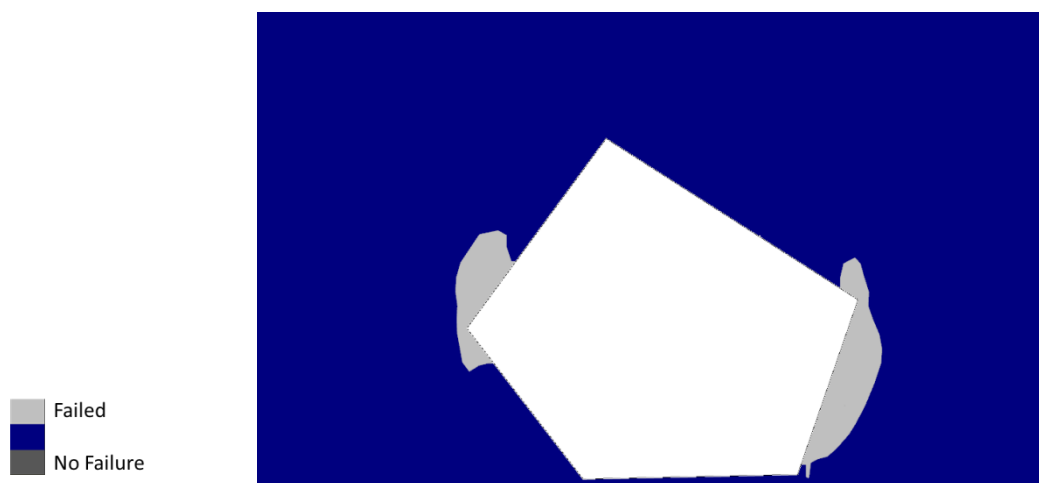


Figure E162 Application of the Pan-Hudson Criterion to case study 22

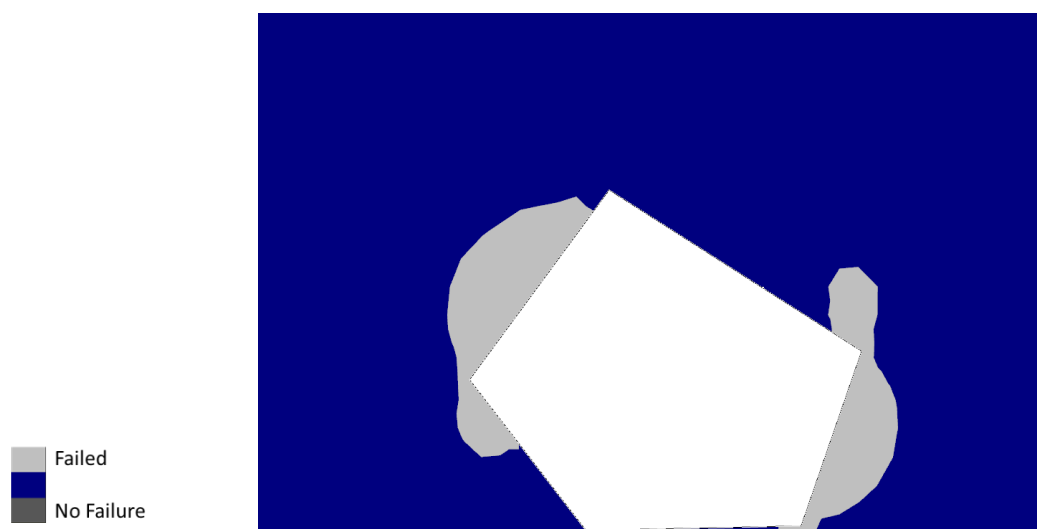


Figure E163 Application of the Priest Criterion to case study 22

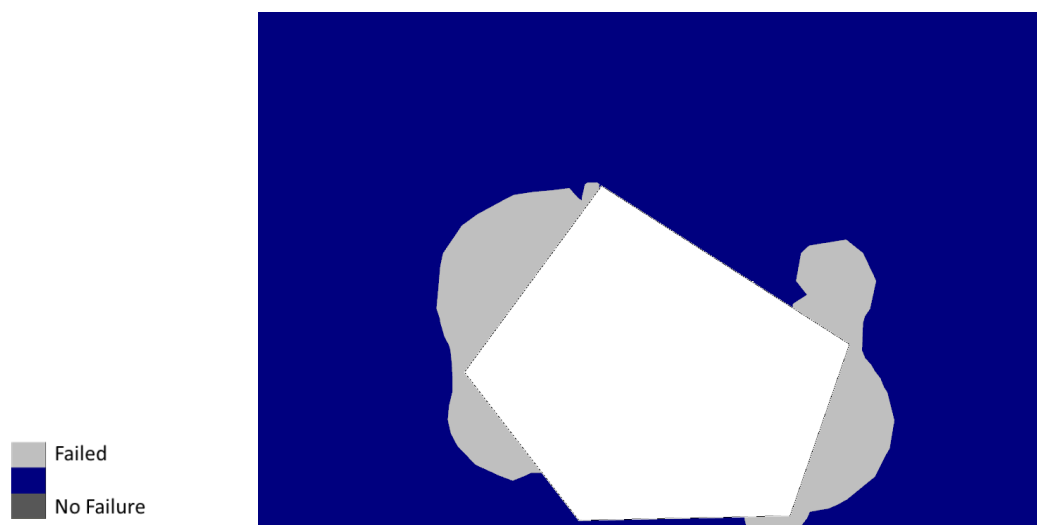


Figure E164 Application of the Simplified Priest Criterion to case study 22



Figure E165 Application of the DSSI design criterion to case study 22



Figure E166 CMS wireframe in red showing actual overbreak of case study 22

## APPENDIX F

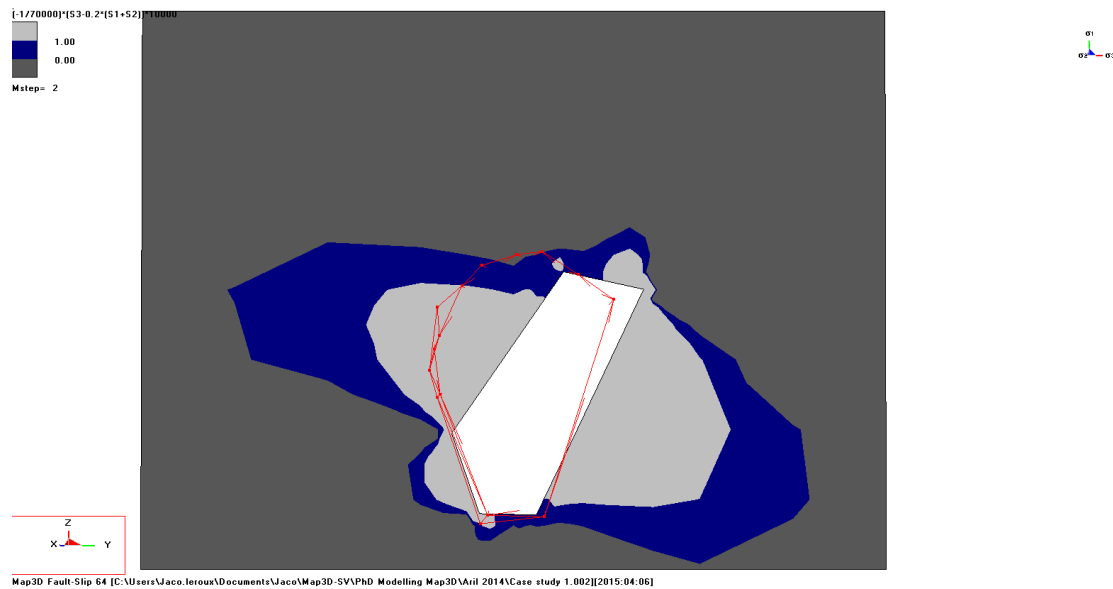
**Application of Strain-Based Failure Criteria to Case Studies**

Figure F1 The extension strain criterion after Stacey, (1981) applied to case study 1 with a modulus of elasticity  $E = 70000$  MPa

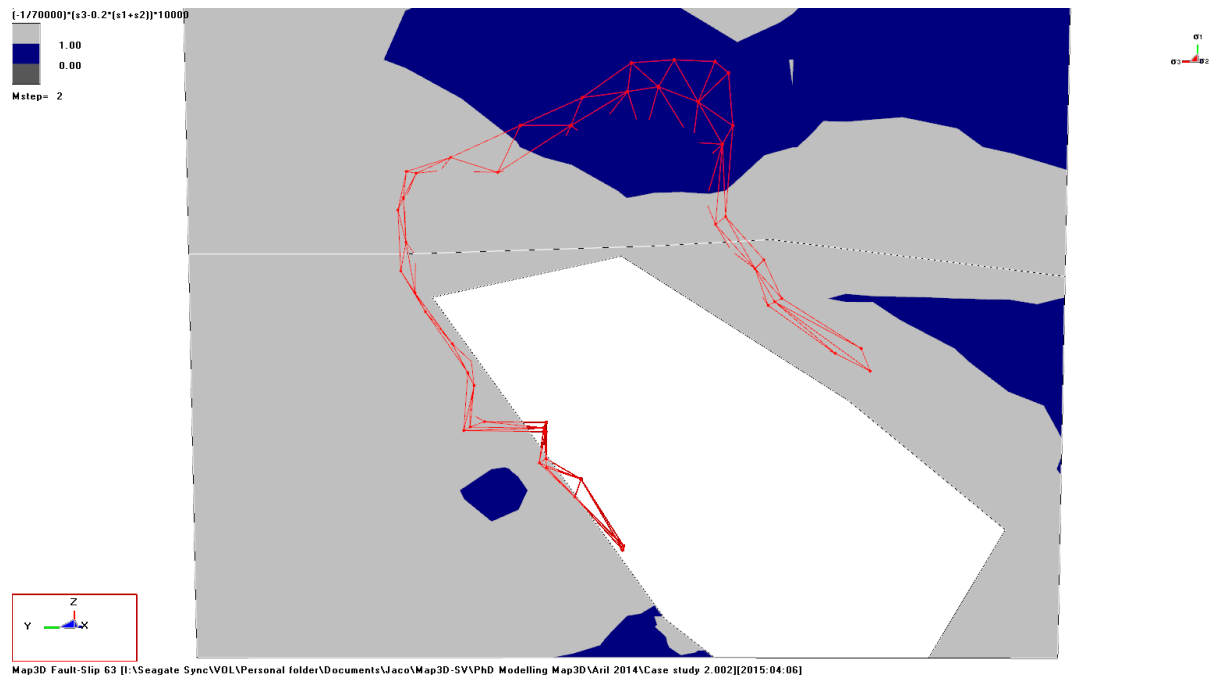


Figure F2 The extension strain criterion after Stacey, (1981) applied to case study 2 with a modulus of elasticity  $E = 70000$  MPa

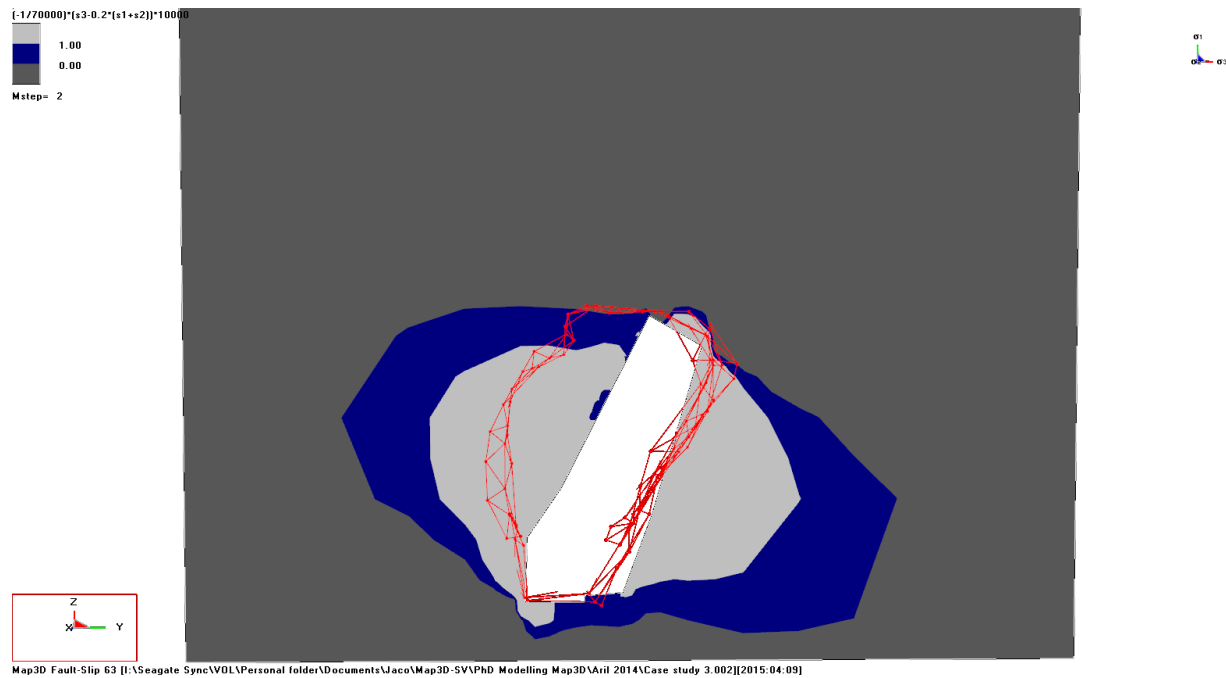


Figure F3 The extension strain criterion after Stacey, (1981) applied to case study 3 with a modulus of elasticity  $E = 70000$  MPa

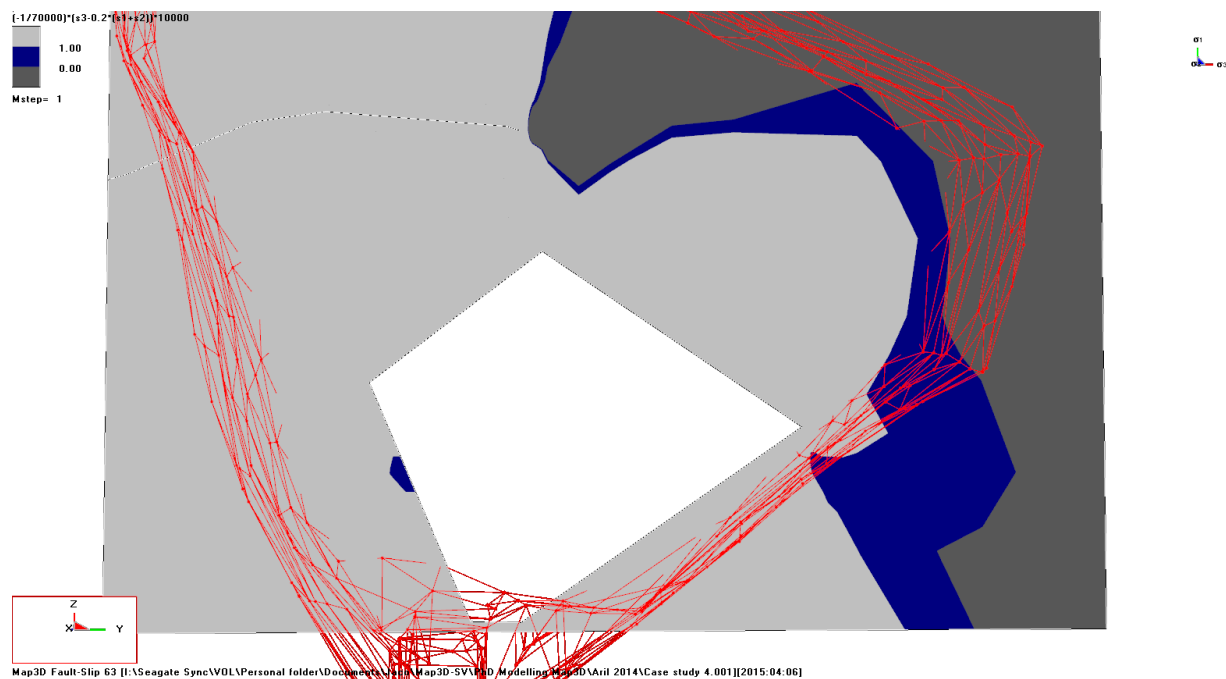


Figure F4 The extension strain criterion after Stacey, (1981) applied to case study 4 with a modulus of elasticity  $E = 70000$  MPa

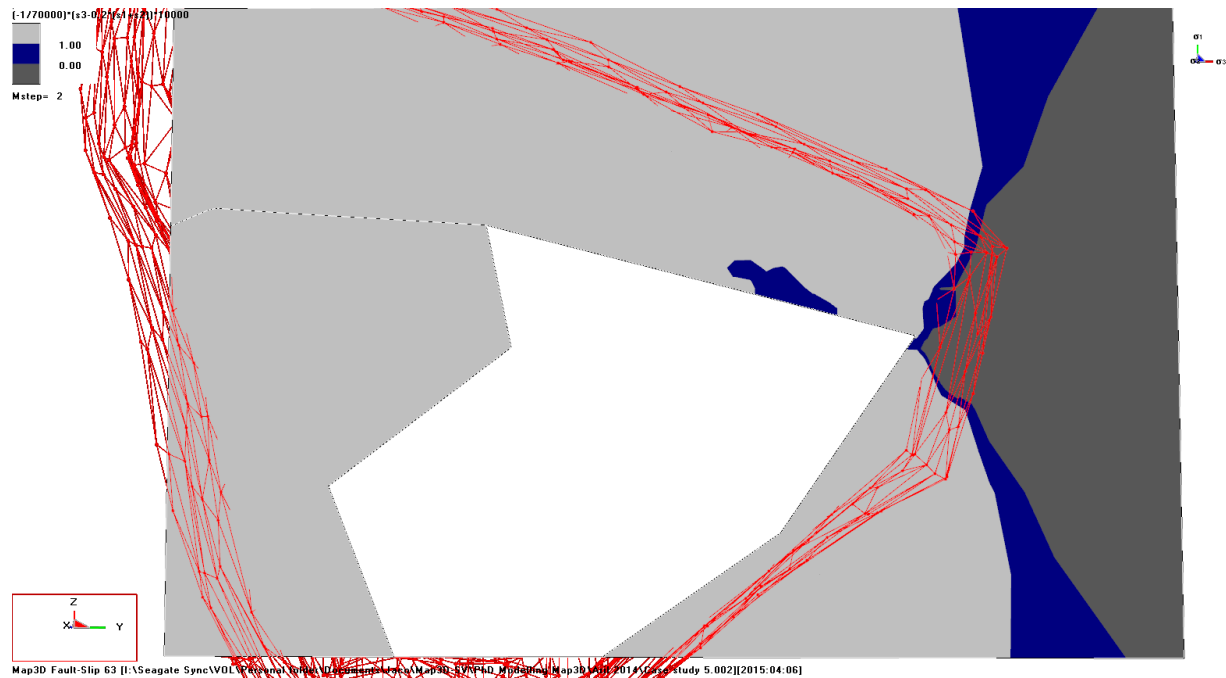


Figure F5 The extension strain criterion after Stacey, (1981) applied to case study 5 with a modulus of elasticity  $E = 70000$  MPa

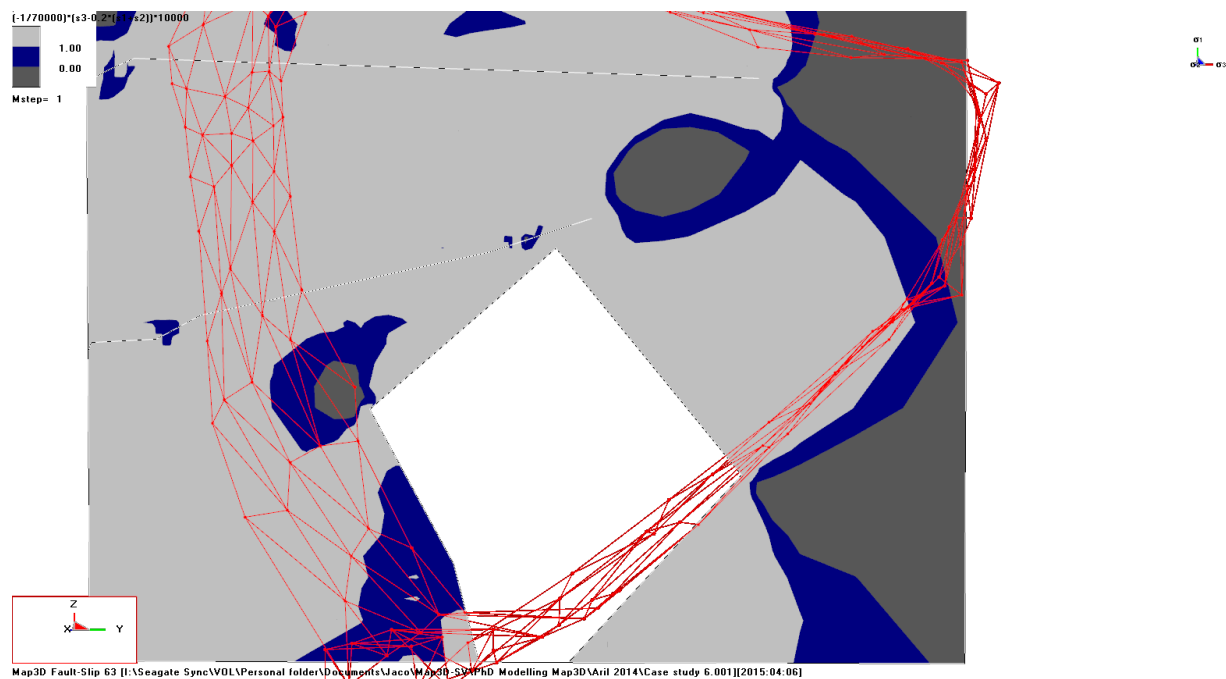


Figure F6 The extension strain criterion after Stacey, (1981) applied to case study 6 with a modulus of elasticity  $E = 70000$  MPa

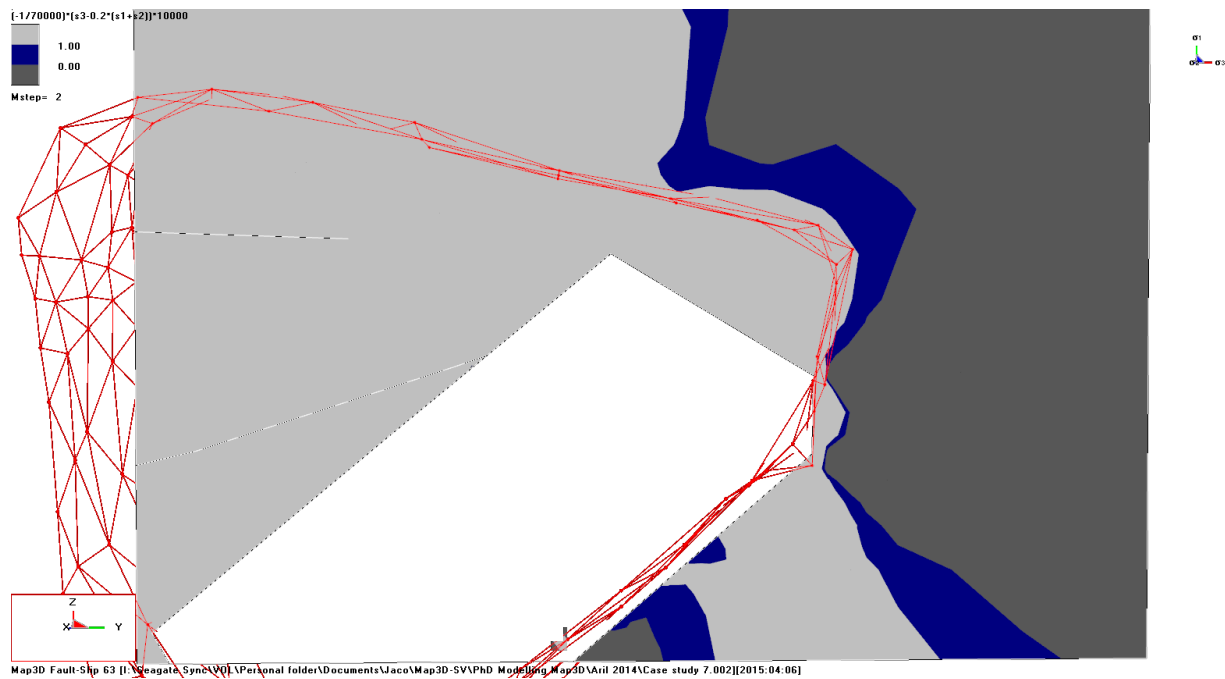


Figure F7 The extension strain criterion after Stacey, (1981) applied to case study 7 with a modulus of elasticity  $E = 70000$  MPa

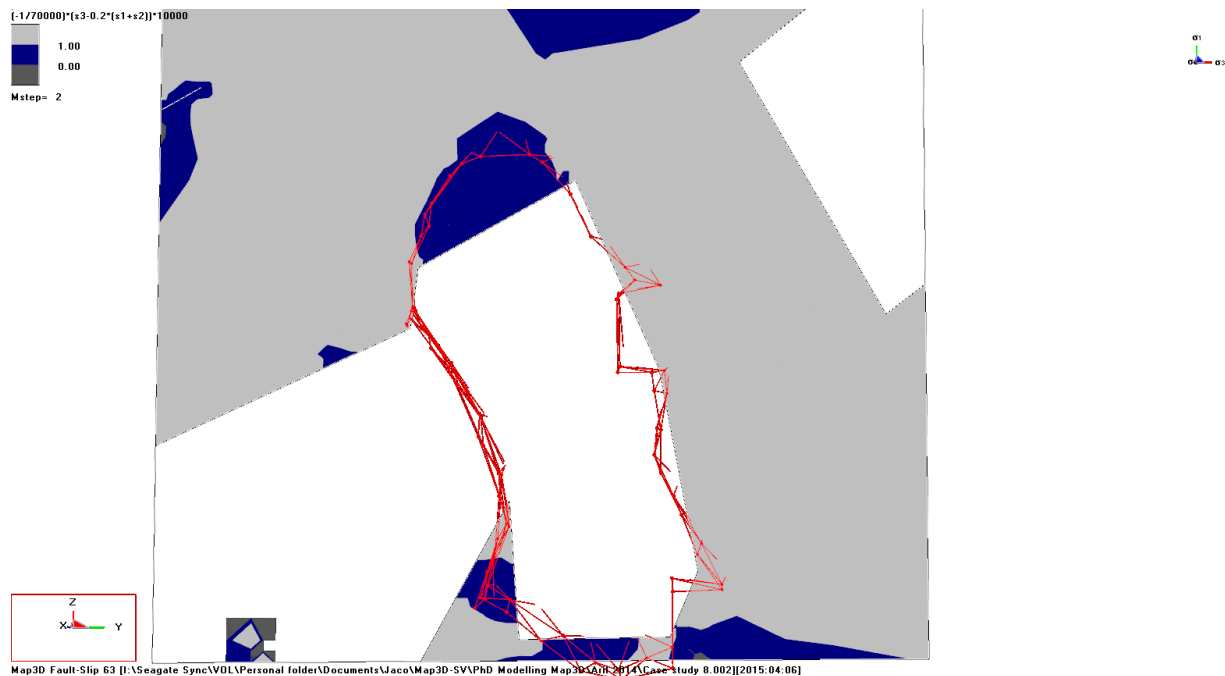


Figure F8 The extension strain criterion after Stacey, (1981) applied to case study 8 with a modulus of elasticity  $E = 70000$  MPa



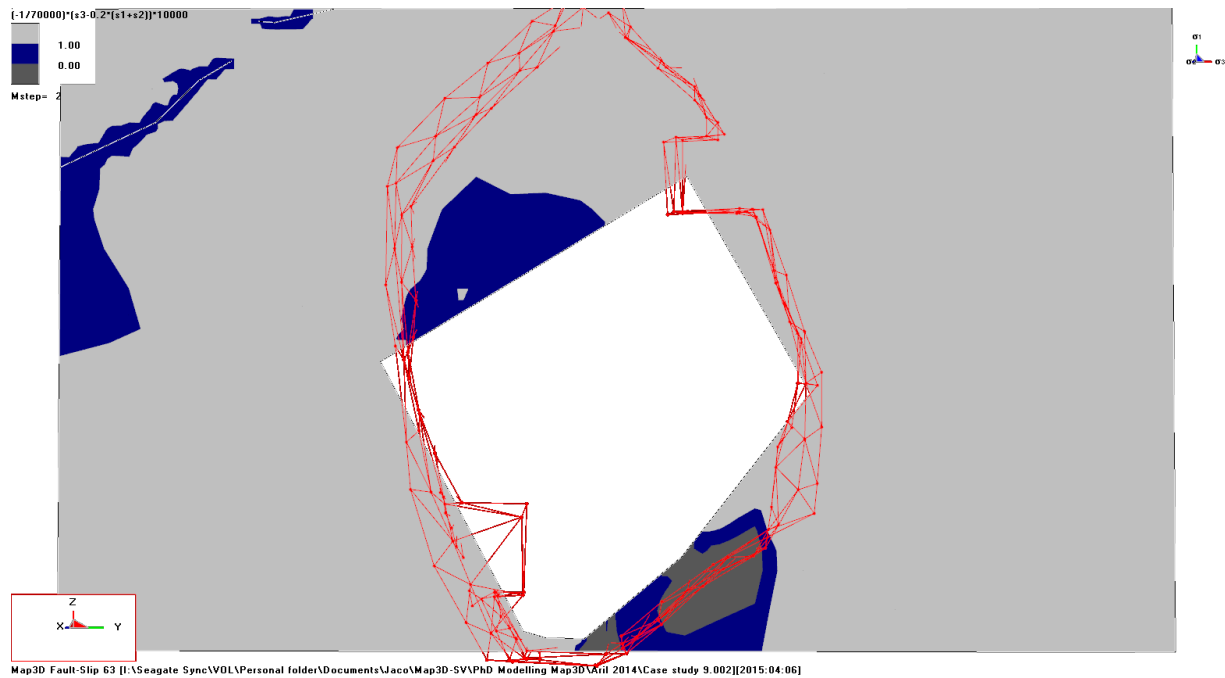


Figure F9 The extension strain criterion after Stacey, (1981) applied to case study 9 with a modulus of elasticity  $E = 70000$  MPa

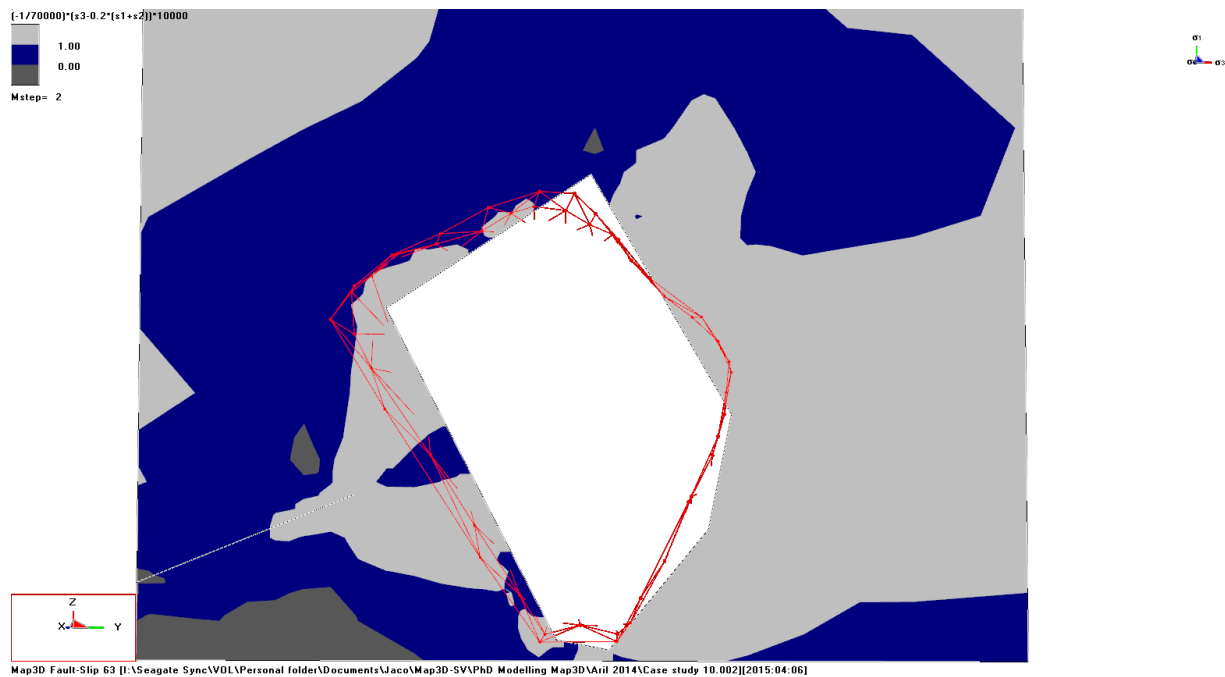


Figure F10 The extension strain criterion after Stacey, (1981) applied to case study 10 with a modulus of elasticity  $E = 70000$  MPa

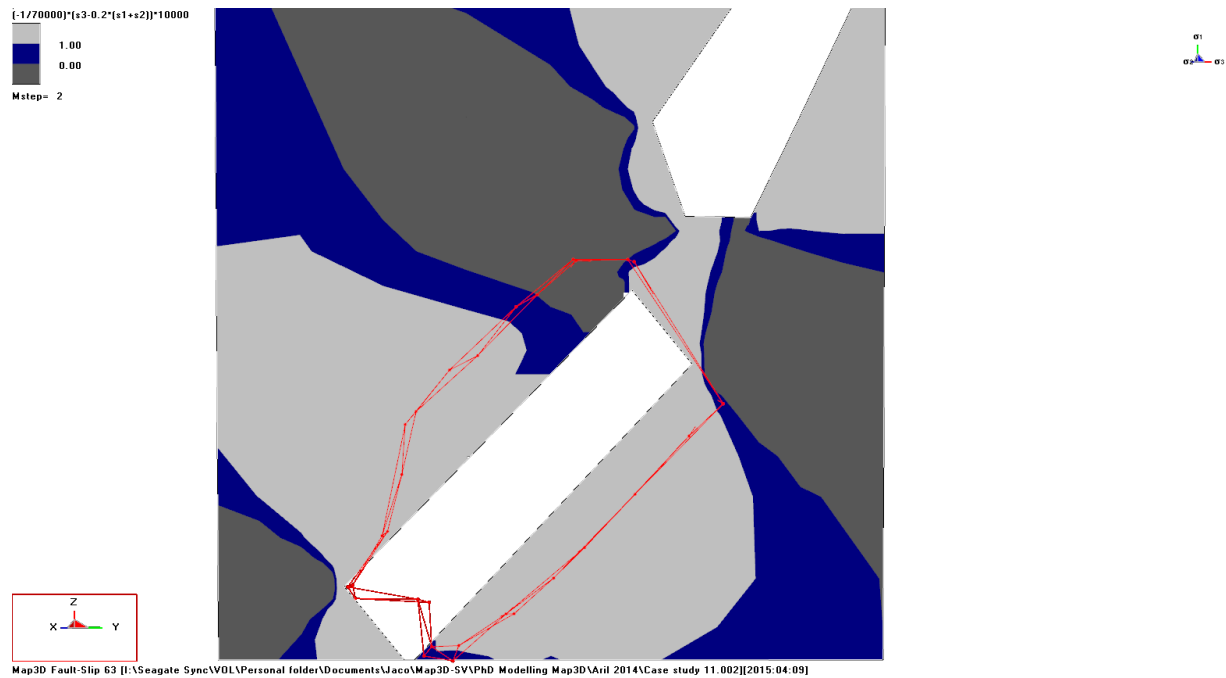


Figure F11 The extension strain criterion after Stacey, (1981) applied to case study 11 with a modulus of elasticity  $E = 70000$  MPa



Figure F12 The extension strain criterion after Stacey, (1981) applied to case study 12 with a modulus of elasticity  $E = 70000$  MPa

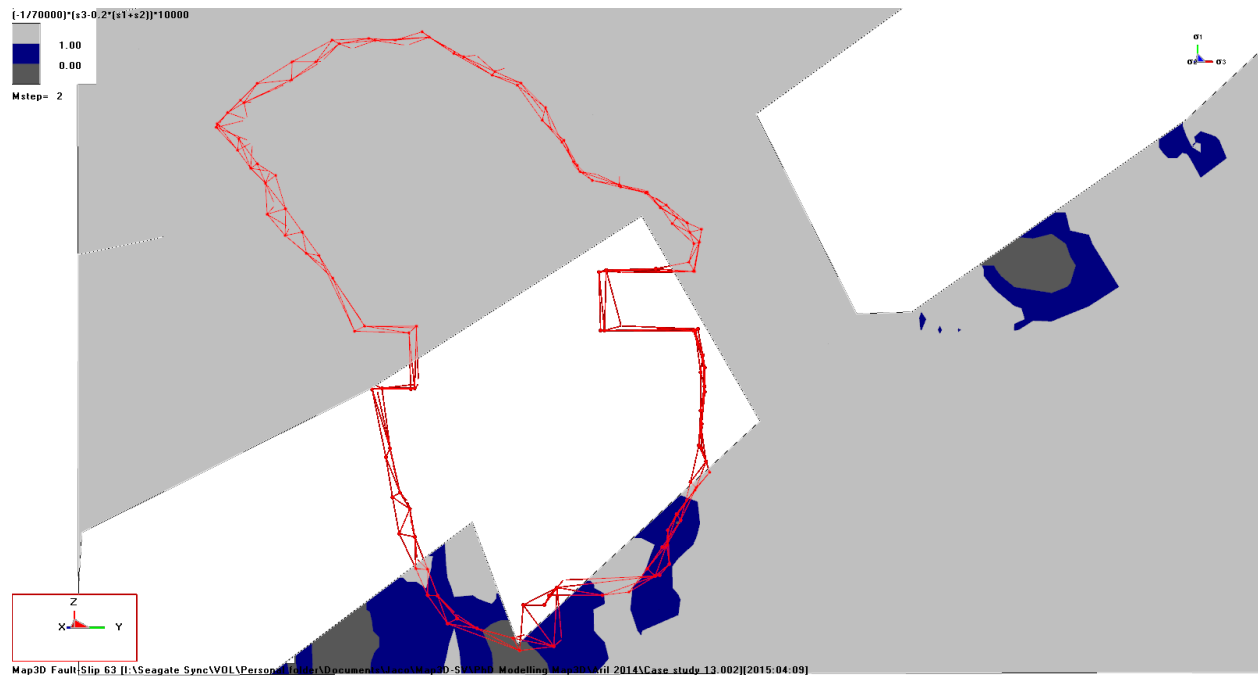


Figure F13 The extension strain criterion after Stacey, (1981) applied to case study 13 with a modulus of elasticity  $E = 70000$  MPa

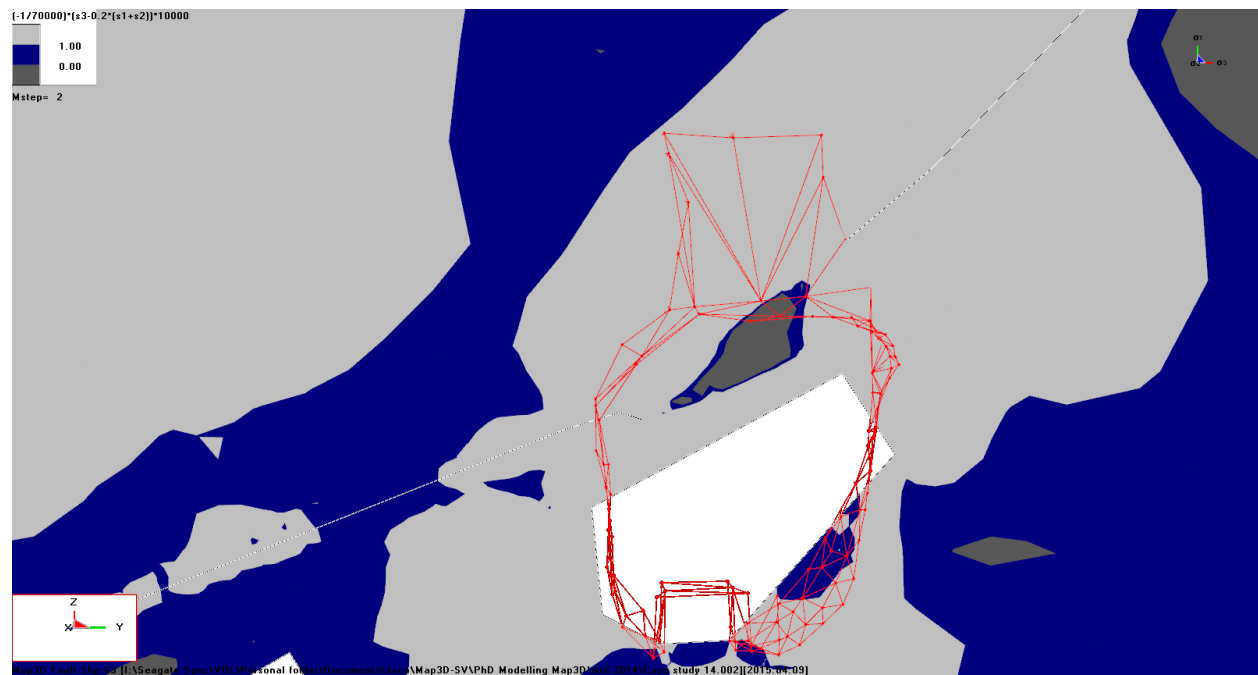


Figure F14 The extension strain criterion after Stacey, (1981) applied to case study 14 with a modulus of elasticity  $E = 70000$  MPa



Figure F15 The extension strain criterion after Stacey, (1981) applied to Mining Site Two mining step 1 with a modulus of elasticity  $E = 60000 \text{ MPa}$

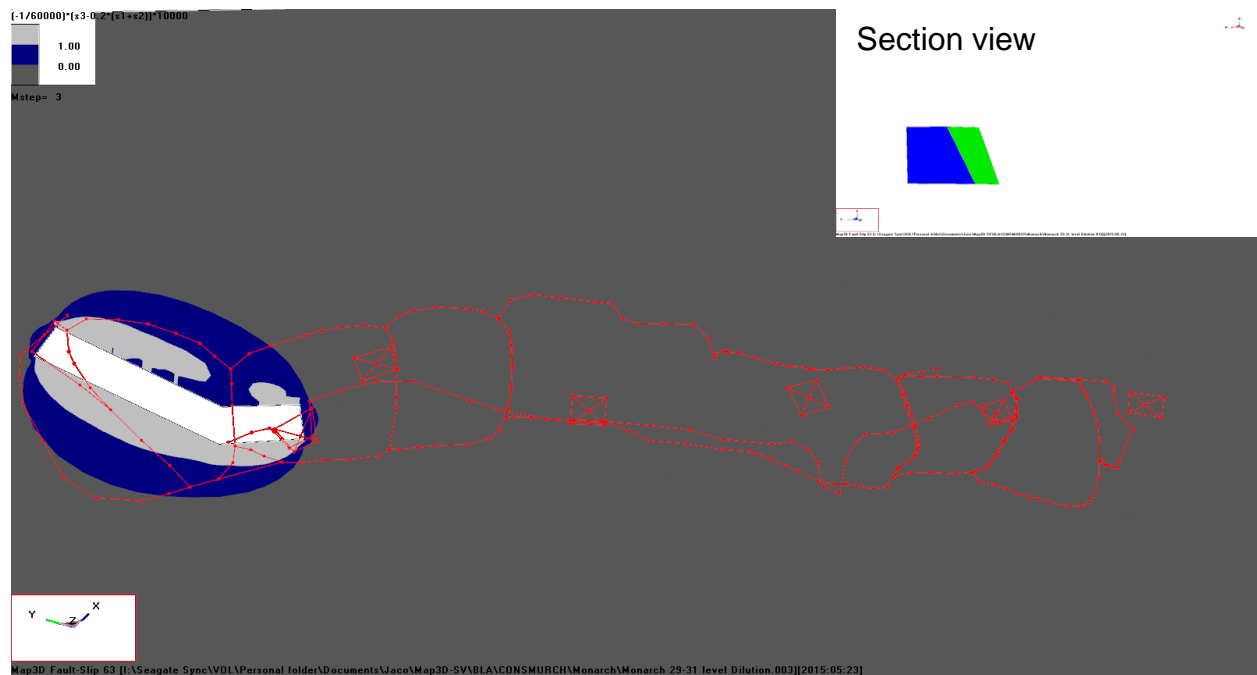


Figure F16 The extension strain criterion after Stacey, (1981) applied to Mining Site Two mining step 2 with a modulus of elasticity  $E = 60000 \text{ MPa}$

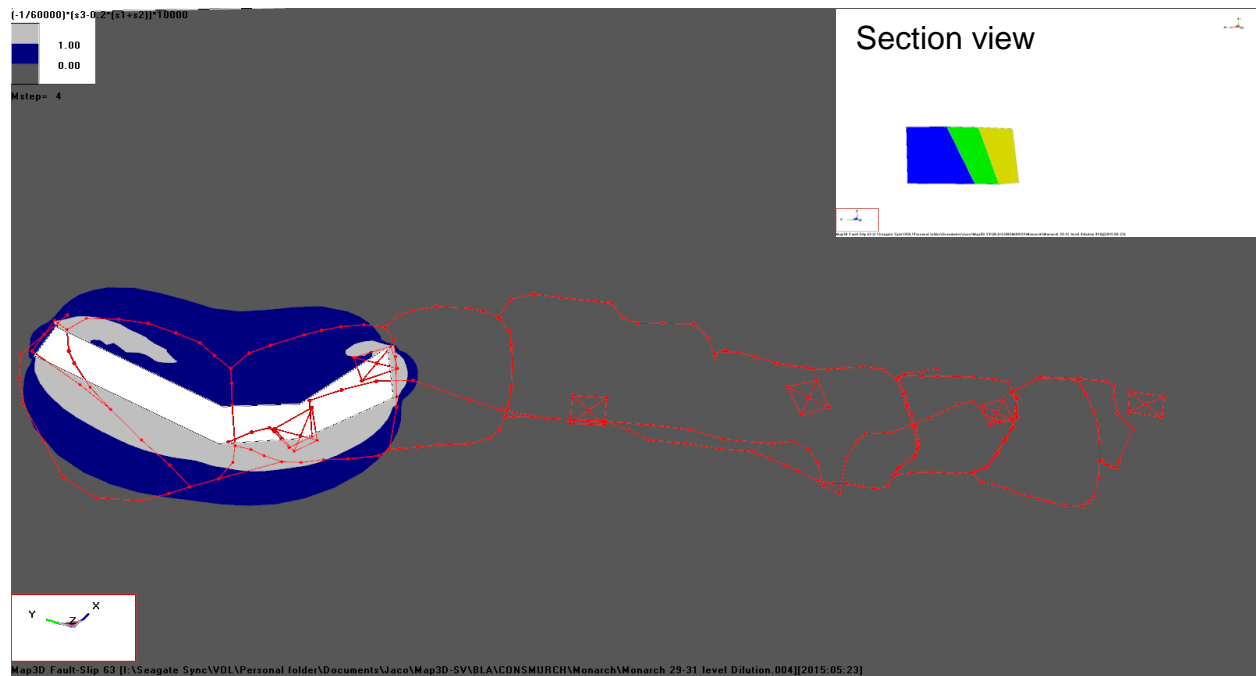


Figure F17 The extension strain criterion after Stacey, (1981) applied to Mining Site Two mining step 3 with a modulus of elasticity  $E = 60000 \text{ MPa}$

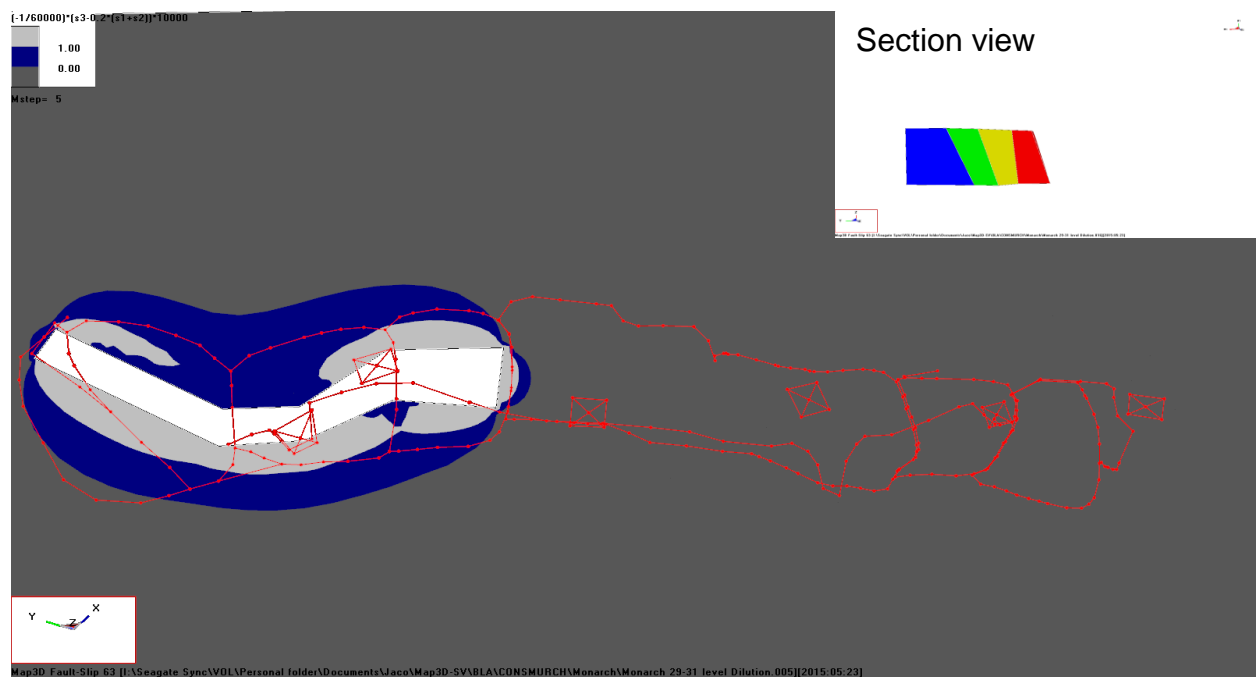


Figure F18 The extension strain criterion after Stacey, (1981) applied to Mining Site Two mining step 4 with a modulus of elasticity  $E = 60000 \text{ MPa}$

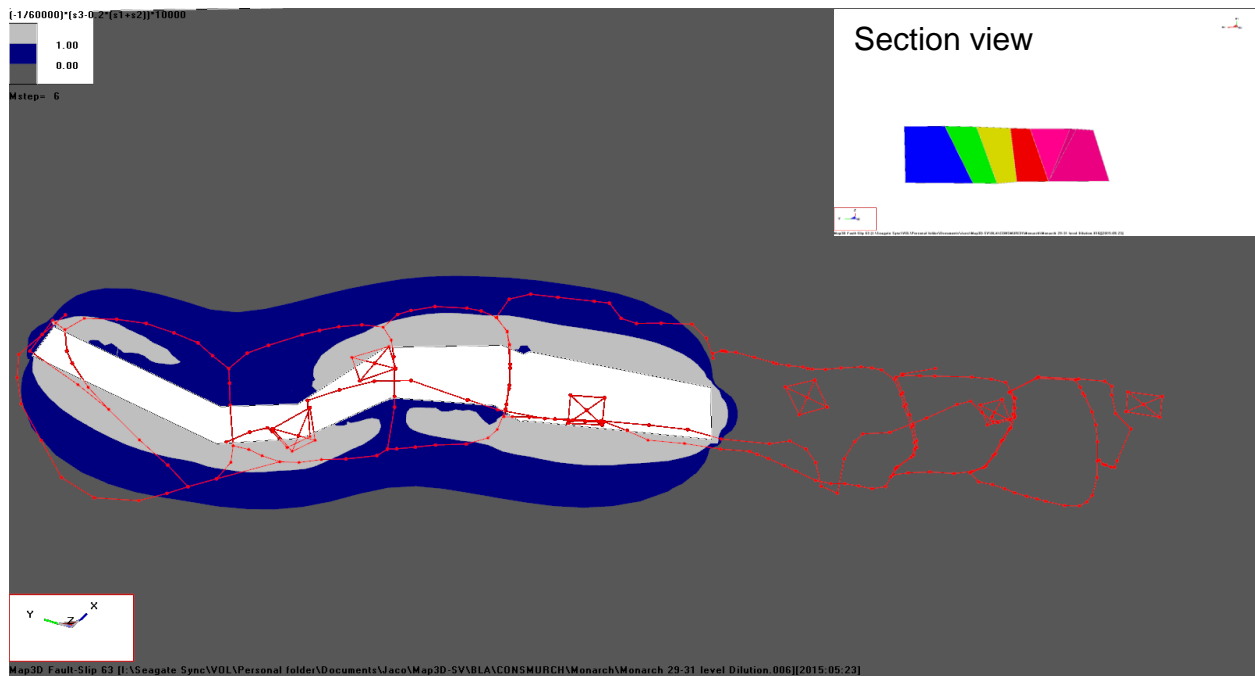


Figure F19 The extension strain criterion after Stacey, (1981) applied to Mining Site Two mining step 5 with a modulus of elasticity  $E = 60000 \text{ MPa}$

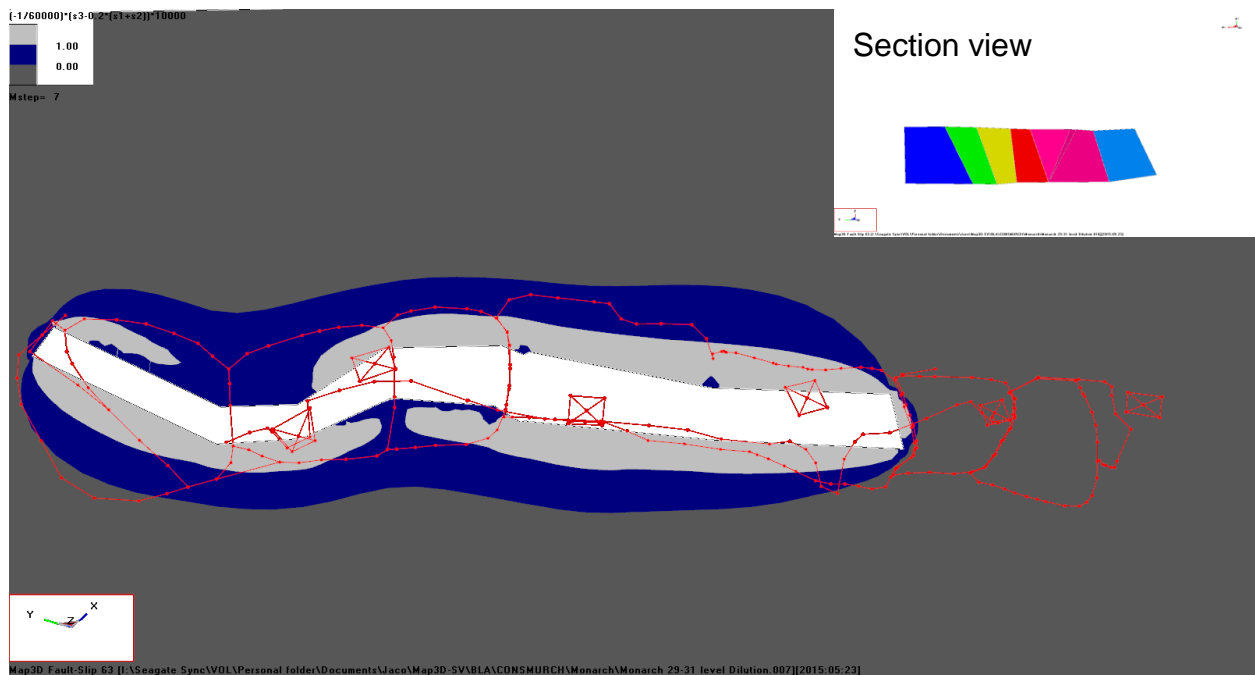


Figure F20 The extension strain criterion after Stacey, (1981) applied to Mining Site Two mining step 6 with a modulus of elasticity  $E = 60000 \text{ MPa}$

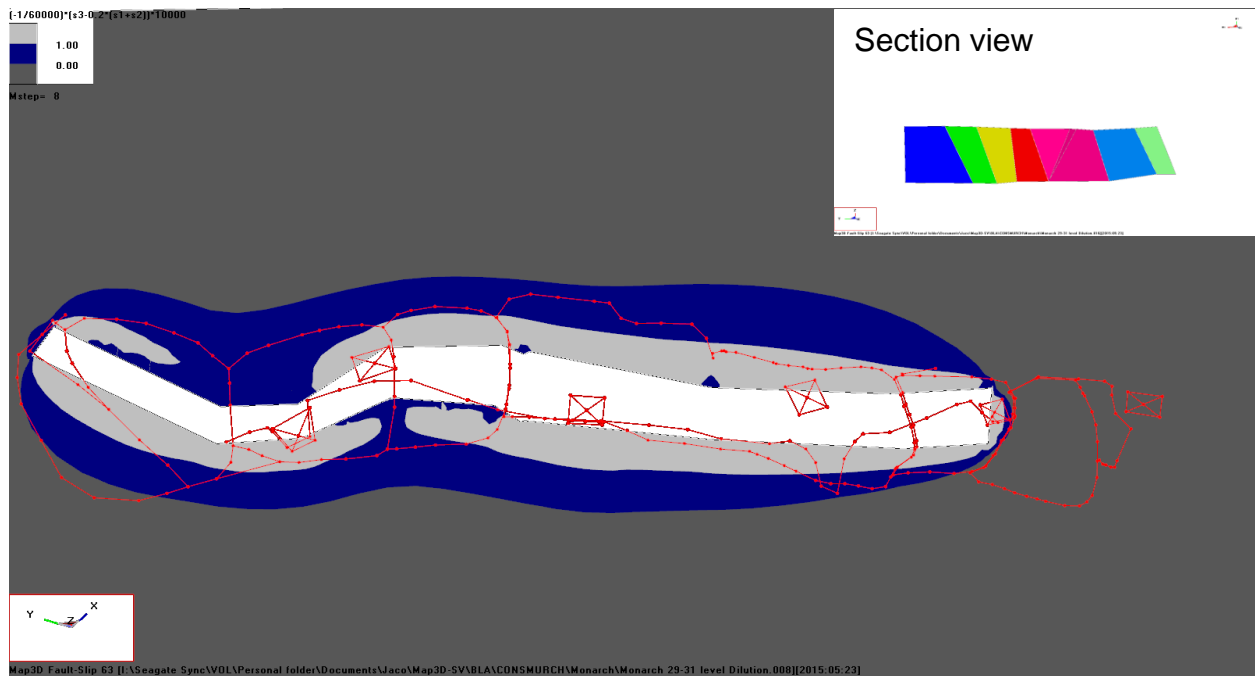


Figure F21 The extension strain criterion after Stacey, (1981) applied to Mining Site Two mining step 7 with a modulus of elasticity  $E = 60000 \text{ MPa}$

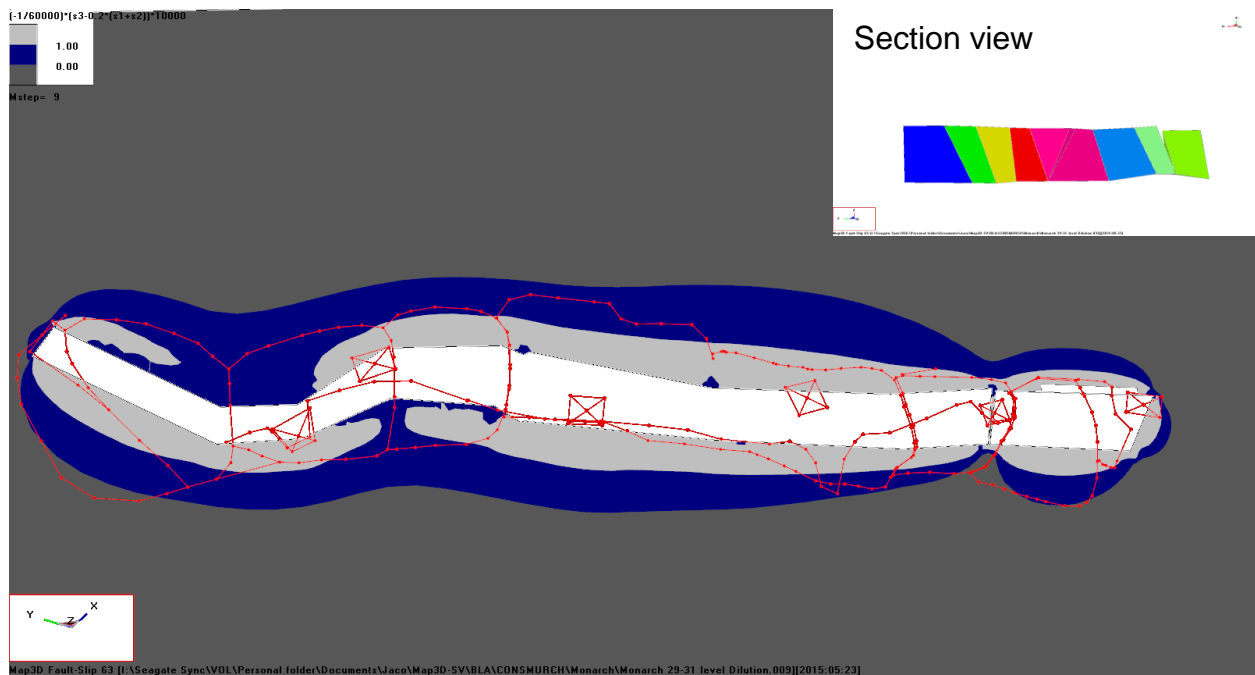


Figure F22 The extension strain criterion after Stacey, (1981) applied to Mining Site Two mining step 8 with a modulus of elasticity  $E = 60000 \text{ MPa}$

## APPENDIX G

### Application of DSSI design criteria on Mining Site Two

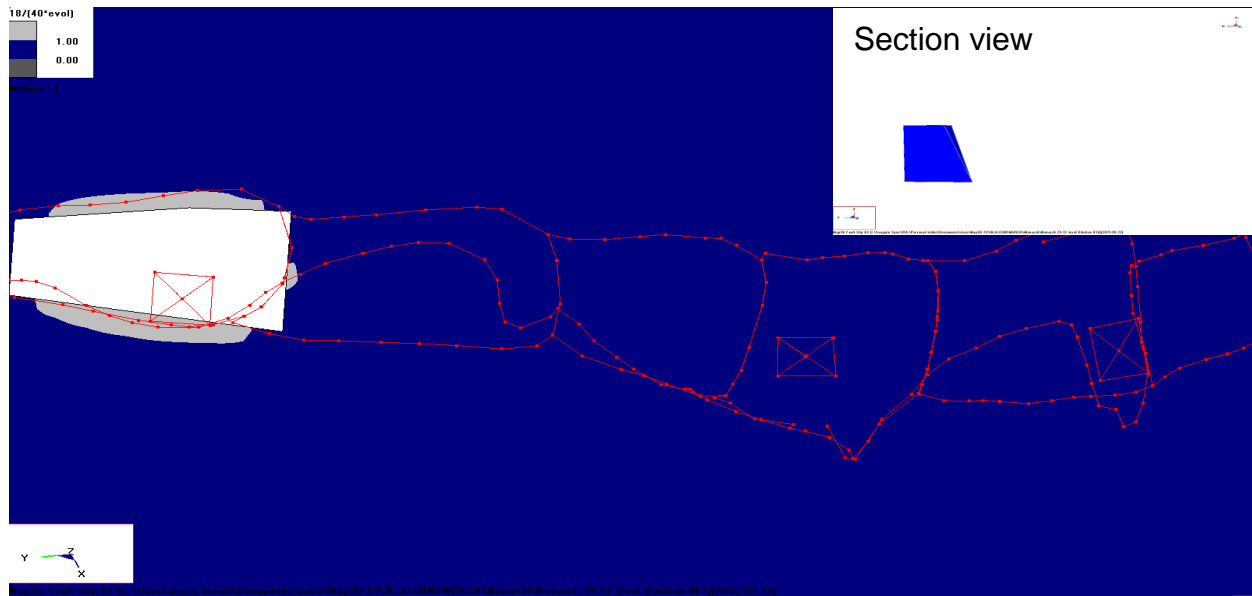


Figure G1 Plan view of the application of the DSSI Design criterion to Mining Site Two at mining step 1

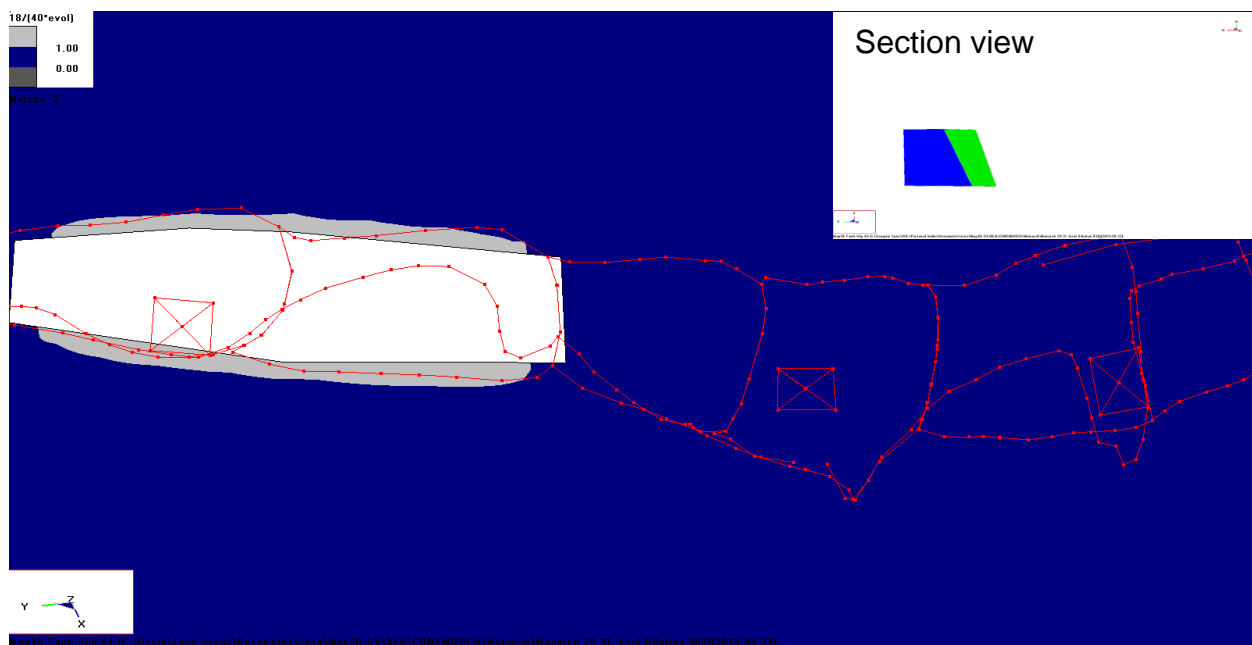


Figure G2 Plan view of the application of the DSSI Design criterion to Mining Site Two at mining step 2



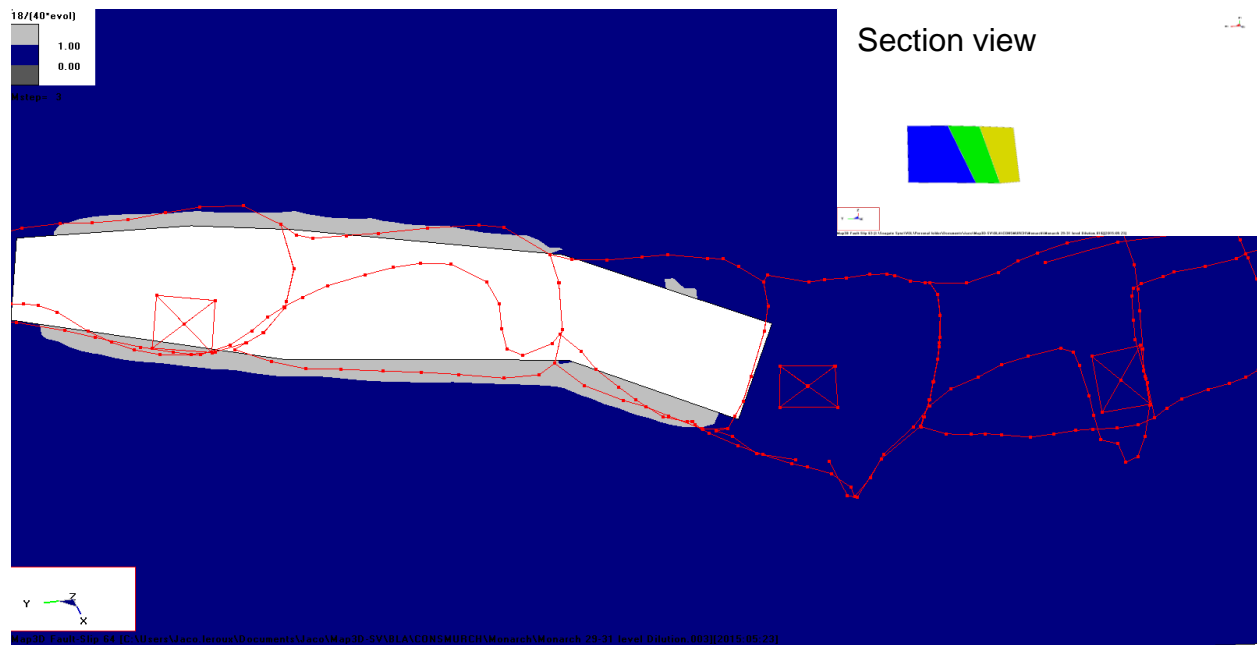


Figure G3 Plan view of the application of the DSSI Design criterion to Mining Site Two at mining step 3

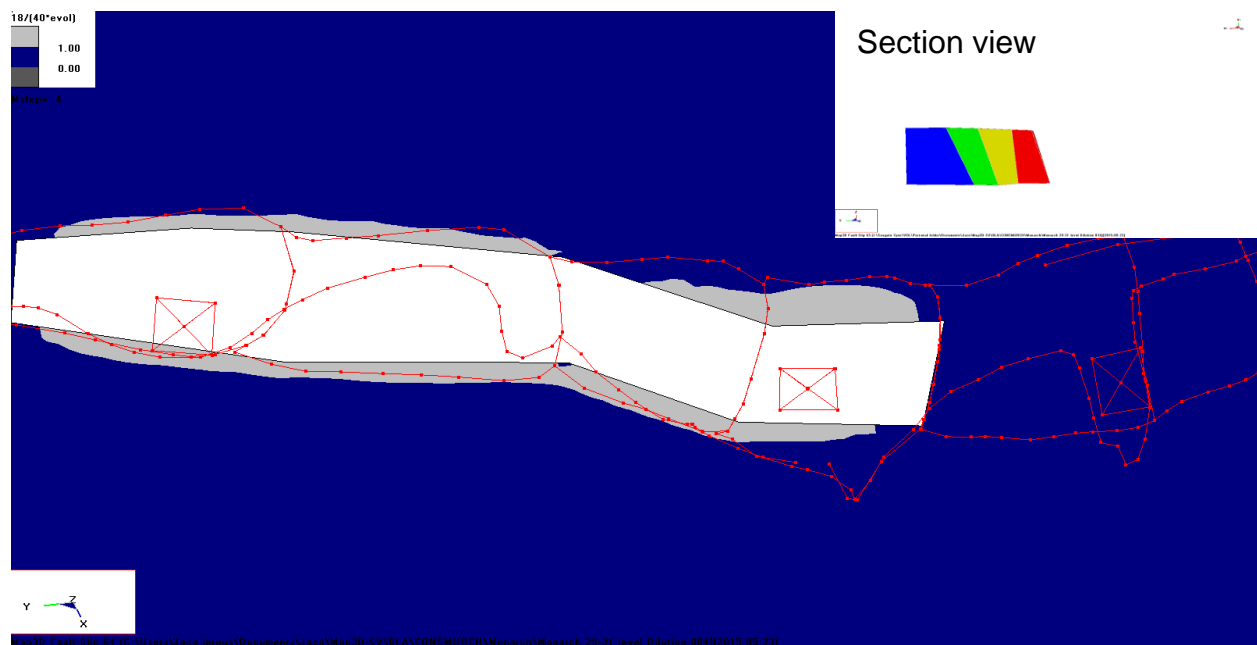


Figure G4 Plan view of the application of the DSSI Design criterion to Mining Site Two at mining step 4

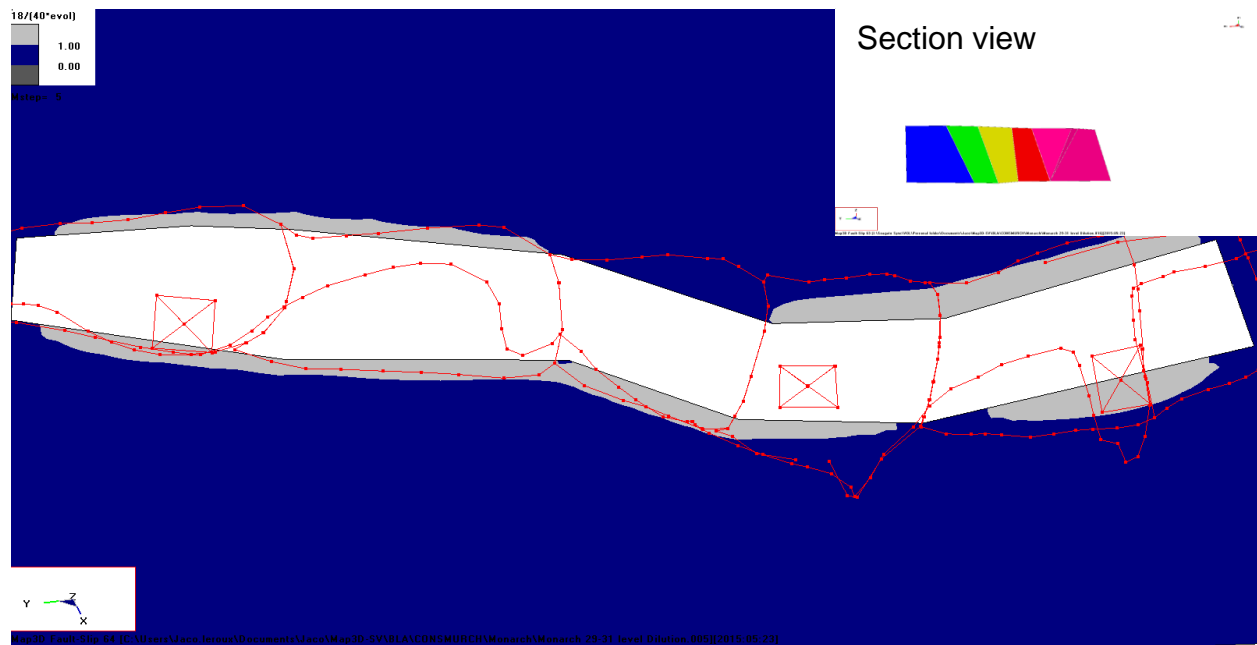


Figure G5 Plan view of the application of the DSSI Design criterion to Mining Site Two at mining step 5